

MRIWA REPORT M532 –
THE GEOLOGY, MINERALOGY AND
GEOMETALLURGY OF EV MATERIALS DEPOSITS
IN WESTERN AUSTRALIA

M Wells, M Aylmore and B McInnes





Government of **Western Australia**
Department of **Mines, Industry Regulation
and Safety**

REPORT 228

MRIWA REPORT M532 – THE GEOLOGY, MINERALOGY AND GEOMETALLURGY OF EV MATERIALS DEPOSITS IN WESTERN AUSTRALIA

Martin Wells*, Mark Aylmore* and Brent McInnes*

* John de Laeter Centre, Curtin University, Perth, Western Australia

With contributions by:

Bryant Ware², Noreen Evans¹, Kai Rankenburgh¹, Bradley McDonald¹, Imogen Fielding, Michael Wingate, Chris Kirkland³
and Aleks Nikoloski⁴

1 John de Laeter Centre, Curtin University

2 Western Australian Argon Isotope Facility, School of Earth and Planetary Sciences, Curtin University

3 Timescales of Mineral Systems Group, Curtin University

4 Murdoch University

PERTH 2022



**Geological Survey of
Western Australia**

MINISTER FOR MINES AND PETROLEUM
Hon Bill Johnston MLA

DIRECTOR GENERAL, DEPARTMENT OF MINES, INDUSTRY REGULATION AND SAFETY
Richard Sellers

EXECUTIVE DIRECTOR, GEOLOGICAL SURVEY AND RESOURCE STRATEGY
Michele Spencer

REFERENCE

The recommended reference for this publication is:

Wells, M, Aylmore, M and McInnes, B 2022, MRIWA Report M532 - The geology, mineralogy and geometallurgy of EV Materials Deposits in Western Australia: Geological Survey of Western Australia, Report 228, 187p.

ISBN 978-1-74168-991-4

ISSN 1834-2280



A catalogue record for this
book is available from the
National Library of Australia

Grid references in this publication refer to the Geocentric Datum of Australia 1994 (GDA94). Locations mentioned in the text are referenced using Map Grid Australia (MGA) coordinates, Zone 50. All locations are quoted to at least the nearest 100 m.



RioTinto

Lithium
Australia



About this publication

John de Laeter Centre acknowledgement

Isotope and element analyses were conducted using the GeoHistory laser-ablation ICP-MS and SHRIMP ion microprobe facilities at the John de Laeter Centre (JdLC), Curtin University, with the financial support of the Australian Research Council and AuScope National Collaborative Research Infrastructure Strategy (NCRIS).

The TESCAN Integrated Mineral Analyser (TIMA) instrument was funded by a grant from the Australian Research Council (LE140100150) and is operated by the JdLC with the support of the Geological Survey of Western Australia, The University of Western Australia and Murdoch University.

Disclaimer

This product uses information from various sources. The Department of Mines, Industry Regulation and Safety (DMIRS) and the State cannot guarantee the accuracy, currency or completeness of the information. Neither the department nor the State of Western Australia nor any employee or agent of the department shall be responsible or liable for any loss, damage or injury arising from the use of or reliance on any information, data or advice (including incomplete, out of date, incorrect, inaccurate or misleading information, data or advice) expressed or implied in, or coming from, this publication or incorporated into it by reference, by any person whatsoever.

Based on consultation with the Western Desert Lands Aboriginal Corporation (WDLAC) on the cultural significance of the name, Waukarlycarly, it has been agreed to change the name of the well to Barnicarndy 1 and the tectonic subdivision to Barnicarndy Graben. This and all future publications will now refer to the Barnicarndy 1 stratigraphic drillhole (previously Waukarlycarly 1) and the Barnicarndy Graben (previously Waukarlycarly Embayment).

Published 2022 by the Geological Survey of Western Australia

This Report is published in digital format (PDF) and is available online at <www.dmirs.wa.gov.au/GSWApublications>.



© State of Western Australia (Department of Mines, Industry Regulation and Safety) 2022

With the exception of the Western Australian Coat of Arms and other logos, and where otherwise noted, these data are provided under a Creative Commons Attribution 4.0 International Licence. (<https://creativecommons.org/licenses/by/4.0/legalcode>)

Further details of geoscience publications are available from:

First Floor Counter, Department of Mines, Industry Regulation and Safety
100 Plain Street, EAST PERTH WESTERN AUSTRALIA 6004
Telephone: +61 8 9222 3459 Email: publications@dmirs.wa.gov.au
www.dmirs.wa.gov.au/GSWApublications

Cover photograph: A 107 x 54 cm polished slab of Pilgangoora Li-Ta pegmatite ore in the collection of Mark Thompson. Spodumene megacrysts (green) are hosted within a coarsely crystalline matrix comprising predominantly alkali feldspar (white) and quartz (tan-grey). Photo by Kai Thompson

Executive Summary

Western Australia currently contributes around 55% of the world's lithium (Li) production (USGS, 2022). With increasing use in the production of Li-ion batteries (LIBs) used to power electric vehicles, the projected global demand for Li is expected to exceed supply by about 2025. Moreover, the transition to increased renewable energy production and utilization will require significant LIB storage capabilities to balance regional electricity grids.

While there are some research publications available on individual LCT (Li, Cs, Ta) pegmatite deposits, there has been no systematic comparative study on Li-ore systems across Western Australia to date. The aim of this work was to develop a geometallurgical framework for Western Australia Li-pegmatite deposits for the purpose of providing fundamental knowledge of Li-orebodies and improving exploration targeting, mineral processing and chemical refining techniques.

The main deliverables and key outcomes from this project were to:

1/ Develop a geological catalogue and database of all LCT pegmatite mineral systems in Western Australia, and compare and contrast these with global equivalents

The geology of LCT pegmatites in Western Australia was assessed in terms of their formation, texture and deposition. Field studies and a sample acquisition program targeted 10, state-wide LCT pegmatites from the Southern Yilgarn (Greenbushes and Mt Cattlin), Eastern Yilgarn (Bald Hill, Mt Marion, Sinclair Caesium Deposit, Dome North, Londonderry, Dalgaranga and Kathleen Valley) and Pilbara Cratons (Pilgangoora).

Mineral mapping established mineral–textural relationships to identify the principal Li host to aid pegmatite classification and aid in understanding the emplacement history, mineral crystallization pathways and genetic associations. All Li deposits investigated in this study form part of the LCT pegmatite family, with sub-types classified as follows:

- Spodumene sub-type (Greenbushes, Kathleen Valley, Dome North and Mt Marion)
- Petalite sub-type (Londonderry)
- Lepidolite sub-type (Sinclair Caesium)
- Albite–spodumene type (Mt Cattlin, Bald Hill and Pilgangoora)
- Albite-type (Dalgaranga) pegmatites.

Geochronology studies provided new zircon U–Pb ages and established that all Western Australian (WA) LCT pegmatites were emplaced during a relatively narrow window in time from 2643 to 2629 Ma. However, the relatively low U content (usually <100 ppm but also <<500 ppm) and relatively small grain size (predominantly <100 µm) of zircon analysed in the current study suggest they are inherited and did not crystallize in the pegmatite. Thus, zircon U–Pb ages place a maximum age constraint on the timing of pegmatite crystallization (i.e. pegmatites must be younger than the rock into which they intrude).

These ages support previous work pointing to a major period of global pegmatite emplacement from 2650 to 2600 Ma. A significant new finding was a revised zircon U–Pb age of 2645 ± 4 Ma for the Greenbushes Deposit, which is much older than earlier work indicating an age of 2527 Ma. $^{40}\text{Ar}/^{39}\text{Ar}$ dating of spodumene was attempted without success. However, muscovite plateau ages indicate that it took up to 40 million years for the pegmatite to cool to temperatures around 300 °C suggesting that they were originally emplaced at mid-crustal levels.

2/ Produce a quantitative understanding of the mineralogical deportment of both economic (e.g. Li, Ta, Nb) and deleterious (e.g. Fe, Mn, F) elements in WA-pegmatitic deposits, and identify factors that may improve or inhibit the economic recovery of Li.

A combination of analytical techniques (SEM-EDS automated mineralogy, laser-ablation inductively coupled plasma–mass spectrometry, focused ion beam-scanning electron microscope/time-of-flight secondary ion mass spectrometry) was used in mineralogical and geochemical assessment of pegmatite samples. The megacrystic nature of spodumene at Mt Cattlin and Bald Hill suggests these pegmatites crystallized from a melt relatively enriched in fluxing agents (H₂O, B, F, P, Be) relative to the other deposits studied, where spodumene was less coarsely crystalline. Compositional trends (K, Rb, Cs, F, Ta) in muscovite–lepidolite–mica are controlled by the degree of magmatic fractional crystallization, and the use of mica chemistry as an exploration targeting tool looks promising.

Two key types of spodumene alteration were observed with the potential to negatively impact ore quality and processing efficiency as follows:

- Dark-green to black, pseudo-morphic replacement of spodumene by massive muscovite (sericite) ± chlorite assemblages are common in zones of post-emplacement hydrothermal alteration. This alteration leads to loss of Li in spodumene and concomitant increases in K, Fe, Mg, Rb and Mn.
- Spodumene–quartz–alkali–feldspar symplectites are quite common across all pegmatite types. This alteration also leads to the loss of Li.

3/ Provide industry with independent verification of the suitability of field portable devices (e.g. laser-induced breakdown spectroscopy) for determining Li abundance and distribution at exploration sites and during drilling operations.

A laser-induced breakdown spectroscopy (LIBS) study of well-characterized Li-bearing samples was undertaken to determine if the technology could be applied in exploration and mining. Using partial least squares analysis, a multi-variate statistical approach of a LIBS analysis was found to produce semi-quantitative results. Quantitative analysis of Li ores is hampered by the fine-scale nature of spodumene alteration products, surface heterogeneities and chemical matrix effects.

4/ Develop a practical geometallurgical model that optimizes the development of Li deposits.

Test work on liberation characteristics, calcination and sulphate leach tests were carried out. The data was then used to develop an understanding of metallurgical properties of different pegmatites to aid in the geometallurgical assessment.

(a) Mineral liberation studies

A systematic study of the liberation characteristics of four LCT pegmatites (Mt Cattlin, Bald Hill, Greenbushes and Pilgangoora) found that Li is predominantly bound within spodumene, and to a lesser extent within Li–mica (lepidolite and zinnwaldite) and petalite. Generally, the coarse nature of spodumene within a quartz–feldspar–muscovite matrix allows for >90% spodumene recovery, with expected Li grades above 3 wt%. Factors that limit recovery and grade include:

- poorly liberated gangue minerals in spodumene in the form of graphic-textured spodumene–quartz–feldspar alteration intergrowth, or partially altered spodumene containing disseminated mica and mica veinlets.
- gangue minerals with specific gravity similar to spodumene diluting the concentrate in dense media and gravity circuits (as high as 20 wt% gangue minerals in concentrates).

Improved spodumene recovery could be achieved by separation of middlings containing high mica and/or quartz–feldspar contents and subjecting them to finer grinding. Techniques such as ore sorting can also be used to reduce mineral impurities to the beneficiation circuit.

Tantalum minerals are mainly associated with gangue minerals and can be concentrated separately from spodumene, whereas cassiterite (SnO₂) is associated with both spodumene and gangue requiring treatment in two separate process streams.

(b) Calcination and acid-bake studies

A two-stage calcination – sulphate-roast testing procedure was used to simulate and assess the Li extraction process. The α – β conversion of spodumene for all ore types was found to occur between 1050 and 1100 °C. The oxidation of Fe and Mn within spodumene during calcination can reduce the calcination transformation temperature. These temperatures exceed the melting point of micaceous and feldspathic gangue minerals, which are commonly present in spodumene concentrates. During calcination, silicate melt products can potentially:

- contribute to glass clinker formation in the calcine roaster leading to production delays and increased maintenance costs
- form glassy coatings around spodumene that can impede β -spodumene conversion and render-coated spodumene refractory to chemical leaching.

Other issues recognized include:

- the exothermic oxidation of Fe and Mn contaminants in spodumene can potentially lead to the uncontrolled production of fine particulates, which can potentially affect the refinery operations
- mineral contaminants, such as quartz gangue, can act as a thermal insulator, which can affect heat transfer to spodumene.

Incomplete Li extraction during the acid-bake and water-leach stage can be attributed to:

- incomplete conversion of α -spodumene to β -spodumene during calcination.
- reduced percolation rate of acid into β -spodumene containing fine particle agglomerates.

Industrial efficiencies can be achieved by minimizing gangue content in Li feedstocks, and the optimization of particle size and roasting time during the calcining process.

(c) Geometallurgical model development

A practical geometallurgical model was developed as a benchmarking tool to identify factors that favour or limit full recoveries in different ore types identified in the 10 pegmatite fields studied in Western Australia. The major issues and impediments for treating pegmatite orebodies and solutions provided cover the effects of mineralogy and specific details of equipment used to treat Li ores. The key factors important in selecting a processing option for treating ores are:

- Lithium mineral host
- grain size of the Li-host
- impurities (Fe, Mn)
- mineral textures, associations and alteration products.

5/ Aid in establishing a multi-institutional 'Centre of Excellence' to foster capability and capacity of Western Australian research institutions to conduct eMaterials-relevant research and provide new opportunities for student involvement in a rapidly developing high technology sector.

The mineralogical understanding and geochemical nature of many of the pegmatite ores presented in this report forms the basis for at least two follow-on applied research activities: 1) A geometallurgical research consultancy will be made available in the John de Laeter Centre to undertake work with industry linking ore body knowledge with improvements in the beneficiation and chemical processing efficiency of lithium minerals; 2) A 'Trusted Supply Chain' project underway in the Future Battery Industries CRC will test whether geochemical fingerprinting techniques can discriminate batteries produced from Australian ores.

Acknowledgements

- Financial support for this study was provided by the Minerals Research Institute of Western Australia (MRIWA), the Geological Survey of Western Australia (GSWA), Lithium Australia, Rio Tinto and Curtin University
- Sample preparation (mounting and polishing) assistance by Payal Panchal, and Selfrag processing and heavy liquid separation by Anusha Kumara (JdLC)
- TIMA measurement and data collection assistance by Alex Prent, Tommaso Tacchetto and Anusha Kumara (all at JdLC). TIMA analysis of Greenbushes sample rounds by Zofia Swierczek and Melissa Narbey (AXT)
- LA–ICP–MS data assistance by Dr Kai Rankenburg and Bradley McDonald
- EPMA measurement and data assistance by Dr Malcolm Roberts (CMCA, UWA)
- SEM and EDS data assistance by Dr Zakaria Quadir, ToF–SIMS data supplied by Assoc Prof William Rickard
- LIBS sample preparation, loan of SciApps 300 instrument, analysis and data reduction assistance kindly provided by Stepan Orlov and Melissa Narbey (AXT)
- Sulphate roasting tests assistance from Prof Aleks Nikoloski and team (Murdoch University)
- Peter Chapman for data collection for DTGA studies (Curtin University)
- DMIRS editing and publishing team for their professionalism in the high level of drafting and formatting quality of the figures and tables

Contents

Introduction.....	1
Nature and types of pegmatites	2
Lithium deposits in Western Australia.....	2
Resource geology and deposit assessment implications.....	4
Process implications	4
Operations in Western Australia	5
Project objectives	6
Project modification	7
Sample acquisition.....	8
Classification and geology of LCT pegmatites in Western Australia	8
Classification and geological assessment methodology	8
Testing of field portable analytical devices	9
Geological setting of LCT pegmatite of the southern region	10
Greenbushes.....	10
Setting	10
Sampling and characterization.....	10
Mt Cattlin	11
Setting	11
Sampling and characterization.....	15
LCT pegmatites of the goldfields.....	15
Sinclair Caesium Deposit.....	19
Setting	19
Sampling and characterization.....	19
Dome North	26
Setting	26
Sampling and characterization.....	26
Bald Hill.....	31
Setting	31
Sampling and characterization.....	31
Mt Marion.....	34
Setting	34
Sampling and characterization.....	35
Londonderry.....	35
Setting	35
Sampling and characterization.....	36
Kathleen Valley	37
Setting	37
Sampling and characterization.....	37
Dalgara.....	43
Setting	43
Sampling and characterization.....	43
LCT pegmatite of the Pilbara region	45
Pilgangoora.....	45
Setting	45
Sampling and characterization.....	45
Geochemical analysis and mineral characterization	48
Bulk-rock composition.....	49
Spodumene composition	50
Spodumene element impurities	51
Mica composition	52
Mica trace element and REE impurities.....	55
Tantalum–niobium geochemistry.....	57
Feldspar composition.....	60
Pegmatite classification.....	60
Complex spodumene sub-type.....	61
Complex petalite sub-type	63
Complex lepidolite sub-type	64
Albite–spodumene type.....	64
Albite type	64
Pegmatite mineral fractionation	64
Caesium mineralization: insight into pegmatite evolution at Greenbushes and Sinclair	66
Spodumene morphology and alteration: indicators of pegmatite crystallization evolution	67
Spodumene–cookeite alteration	67
Graphic spodumene alteration	68
Trace element associations: vein in-filling.....	70
Spodumene textures: implications for pegmatite processing	70
Geochronological characterization.....	70
(U–Pb) dating	73
⁴⁰ Ar/ ³⁹ Ar analysis: spodumene and muscovite	74

Quantitative assessment of pegmatite minerals by LIBS analysis method	76
LIBS methodology.....	76
Sample selection for mineral standards	76
Laser-induced breakdown spectroscopy (LIBS): application for field quantification of pegmatite composition	77
LIBS quantification of LCT pegmatite composition	77
Assessment of physical and chemical processing behaviour of LCT pegmatites	79
Assessment of physical separation behaviour	79
Key findings	79
Sample selection and methodology.....	80
Assessment of mineral content	82
Deportment of lithium and major elements	85
Liberation characteristics of spodumene.....	86
Pilgangoora samples.....	86
Bald Hill samples	86
Mt Cattlin samples	86
Greenbushes samples.....	96
The physical liberation characteristic behaviour of different lithologies for concentrating spodumene.....	96
Liberation characteristics of heavy minerals and pollucite	101
Liberation characteristics – concentrates.....	106
Calcination behaviour of mineral constituents	107
Key findings	107
Methodology for assessment of thermal properties of major mineral components within pegmatites ..	108
Selection and characteristics of samples	108
Morphology and composition of spodumene specimens.....	112
Thermal transformation of primary spodumene and altered spodumene	116
Thermal gravimetric analysis of spodumene and common LCT pegmatite minerals	118
Comparison of the thermal properties of spodumene with common LCT pegmatite minerals	118
Comparison of the thermal properties of different spodumenes	120
Morphology and texture changes during calcination of different spodumenes	122
Phase transformations of different spodumenes at different temperatures	122
Physical characteristics of calcined spodumene grains	122
Surface morphology and textures of calcined spodumene samples	123
Textures of calcined spodumene at different temperatures	123
Partial melting of mica in calcined spodumene.....	129
Feldspar in calcined spodumene	131
Exsolution and oxidation of iron from calcined spodumene.....	133
Quartz in calcined spodumene.....	134
Calcination of other gangue minerals.....	134
Lithium extractability of different lithologies by conventional calcination and sulphate-roasting method	136
Key findings	136
Sample selection.....	136
Calcination and sulphate roasting for lithium recovery methodology	136
Comparison of the calcination properties of different deposits.....	137
Effect of calcination time on spodumene product.....	141
Calcination of concentrates	141
Sulphate roast and lithium extraction.....	141
Effect of lithology and ore deposit on lithium extraction	142
Relationship of lithium extraction to impurity contents.....	142
Morphology and deportment of lithium in acid-baked water-leached residues.....	147
Geometallurgical framework	150
Processing trends in WA LCT pegmatites examined in this study	150
Beneficiation	150
Lithium refineries in Western Australia	152
Comparison with other orebodies	153
Process implications	153
Crushing and grinding.....	153
Beneficiation.....	155
Pretreatment calcination processing.....	156
Acid bake and water leaching	157
Lithium recovery	157
Other mineral recoveries	158
Summary and conclusions.....	158
Further work.....	162
Orebody knowledge	162
Mineralogical analysis	162
Metallurgy considerations	162
Linkage with other projects	163
References	164
Appendices	169

Figures

1.	Distribution of major Li-mineral deposits	1
2.	Summary of classification of rare-element pegmatites	2
3.	Distribution of Western Australian Li resources	2
4.	Global significance of Australia Li hard-rock resources	3
5.	Outline of standard Li extraction and recovery process	4
6.	Structural transformation of spodumene at elevated temperatures	5
7.	Expected global Li market demand and supply balance	5
8.	Outline of work program modules	7
9.	Outline of project analytical workflow	9
10.	Satellite image of proximity of main pits at Greenbushes to town site	11
11.	Aerial views of: a) C3 (Lithium pit); and b) C1 (Central lode) openpits at Greenbushes	12
12.	For drillhole C3DD024: a) Plot of bulk rock Li_2O and Na_2O contents with depth; and b) TIMA mineral maps of selected core intervals	13
13.	Representative examples of pegmatite from C3 and C1 pits at Greenbushes Deposit	14
14.	Simplified geological map of the Ravensthorpe district	14
15.	Aerial view of Mt Cattlin pegmatite openpit, showing sampling sites in Dowling pit, Stage 1F and 2SE Stage 1	16
16.	Examples of pegmatite material collected from Dowling pit, Stage 1F and 2SE Stage 1 at Mt Cattlin	17
17.	Geological and major structural features of the Yilgarn Craton	18
18.	Geological setting of Sinclair Caesium Deposit and near-by Dome North pegmatite field	20
19.	Drillcore imagery of PDD162	21
20.	Close-up view of core sections sampled from PDD162	22
21.	Drillcore imagery of PDD174	23
22.	Close-up view of core sections sampled from PDD174	24
23.	Drillcore imagery of PDD179	25
24.	Aeromagnetic image of Dome North Lithium Project overlain by main geological units and interpreted fault structure	27
25.	Perspective view of the Heller, Davy and Cade pegmatites towards: a) the northwest; and b) an aerial, oblique view of the Cade pegmatite	27
26.	Cross-section on local grid 6486236m showing drillholes PDRCD318 and PDRCD319 intersecting a wire-frame projection of the Cade pegmatite	28
27.	Zone of pegmatite intersection in core PDRCD318 at the Cade pegmatite	29
28.	TIMA mineral map of sample PDRCD318-4 showing the spodumene–petalite crystallization contact	29
29.	Zone of pegmatite intersection in core PDRCD319 at the Cade pegmatite	30
30.	Aerial view of Bald Hill mining pit with three views of the openpit taken in May 2019	31
31.	Bald Hill pit with: a) oblique view of proposed pit design; and b) a wire-frame model of sampling locations on pit floor	32
32.	Representative examples of bulk pegmatite from the low-grade zone at Bald Hill	33
33.	Representative examples of bulk pegmatite from the high-grade zone sampled at Bald Hill	34
34.	Regional geology of the Mt Marion pegmatite suite	35
35.	Geological setting of Lepidolite Hill, Tantalite Hill and Londonderry pegmatite fields	36
36.	Core tray photographs of Londonderry pegmatite drillhole LHD07	36
37.	Photographs of core intervals from drillhole LHD07 selected for analysis	37
38.	Schematic of Mt Mann and Kathleen's Corner pegmatite swarms	38
39.	Proposed openpit at Kathleen Valley and pegmatite block model of underground stopes	38
40.	Core tray images for KVDD0018 with sampled drillcore intervals	39
41.	Close-up of KVDD0018 core intervals	41
42.	Close-up of KVDD0076 core intervals	42
43.	Geological setting of the Dalgara pegmatite field	43
44.	Core tray photographs of Dalgara pegmatite drillhole DD1	43
45.	Core intervals from drillhole DD1	44
46.	Geology of the Pilgangoora District	46
47.	Drillcore intervals of pegmatite at Pilgangoora in mafic host rocks	47
48.	Drillcore intervals of pegmatite at Pilgangoora in ultramafic host rocks	47
49.	Total alkali–silica plot of pegmatite from selected LCT deposits of present study	49
50.	Shand Index plot for pegmatite bulk-rock analyses	49
51.	Li:Si vs Li:Al ratio of spodumene from selected LCT pegmatites	50
52.	Ternary Li–Si–Al plot of spodumene apfu values from various WA LCT pegmatites	51
53.	Impurity content as (Fe+Mn) apfu vs Li:Al (apfu) ratio for spodumene from selected LCT pegmatites	51
54.	Box plot of Na (ppm) content of spodumene from selected WA pegmatites	52
55.	Continental crust normalized trace element plot for spodumene from selected WA LCT pegmatites	52
56.	Box plots of: a) Ga (ppm); and b) Sn (pm) content of spodumene from selected WA LCT pegmatites	53
57.	Continental crust normalized REE plot for spodumene from selected WA rare-element pegmatites	53
58.	Plot of Li wt% vs F wt% for muscovite and lepidolite in LCT pegmatites of current study	53
59.	Plot of: a) Al:Si ratio vs Li wt%; and b) Li:Si vs Li:Al ratio for muscovite and lepidolite LCT pegmatites of current study	54
60.	K:Rb ratio vs Rb (wt%) content of mica in WA LCT pegmatites and their comparison to LCT pegmatites from Scotland and Canada	54
61.	K:Rb vs Cs (wt%) content of mica in WA LCT pegmatites and their comparison to LCT pegmatites from Canada	55

62.	Continental crust normalized trace element plot for muscovite and lepidolite from selected WA rare-element pegmatites	55
63.	Box plots of B, Ga, Nb, Sn and Ta contents of mica for selected WA LCT pegmatites	56
64.	Continental crust normalized REE element plot for muscovite and lepidolite from selected WA rare-element pegmatites	57
65.	Plot of the Ta vs Cs content of muscovite in WA LCT pegmatites	57
66.	Examples of Ta–Nb-bearing phases detected in LCT pegmatites from selected deposits.....	58
67.	Ta/(Ta+Nb) vs Mn/(Mn+Fe) ratios for columbite–tantalite identified by TIMA mineral mapping of WA LCT pegmatites	59
68.	Major element, SiO ₂ –Na ₂ O–Al ₂ O ₃ plot (wt%) for albite from WA LCT pegmatites	60
69.	Classification scheme for rare-element pegmatites	62
70.	Schematic model of rare-element fractionation pegmatite evolution trends and associated changes in rare-element composition in relation to a source granite	65
71.	Pressure–temperature–phase relationships of Li silicates under quartz-saturated conditions	65
72.	Plot of K:Rb vs Rb for LCT pegmatites of present study	66
73.	Generalized mineralization sequence for LCT pegmatites	67
74.	Optical imaging, TIMA mineral and K-K distribution maps of an altered, megacrystic spodumene from Bald Hill.....	68
75.	TIMA mineral map and optical imaging of megacrystic spodumene (a–c) from high-grade zone at Bald Hill, and TIMA mineral and Si–K distribution mapping of coarsely crystalline spodumene (d–f) from Cade Deposit	69
76.	TIMA mineral map of graphic-textured spodumene–quartz alteration between spodumene and K/Na-feldspar for the complex spodumene-type pegmatite from Pilgangoora	71
77.	TIMA mineral maps of Mt Cattlin spodumene showing extensive development of fracture and cleavage-controlled vein alteration	72
78.	⁴⁰ Ar/ ³⁹ Ar apparent age spectra for spodumene from Mt Cattlin, Bald Hill and Pilgangoora that resulted in resolvable age information.....	75
79.	⁴⁰ Ar/ ³⁹ Ar age spectra for muscovite from Mt Cattlin and Bald Hill as single grain analyses plotted against the cumulative percentage of ³⁹ Ar released	75
80.	LIBS spectrum for Mt Cattlin spodumene (MC300) over the 200–1000 nm wavelength.....	77
81.	PLS models of CV-predicted vs measured concentration for Li, Si, Al and Fe.....	78
82.	Outline of sample preparation and test work for characterization of ore materials	80
83.	Particle size distribution of samples from all four deposits	81
84.	Correlation between the chemistry for selected samples from Mt Cattlin, Bald Hill and Greenbushes and Pilgangoora	82
85.	The Li deportment in Pilgangoora, Bald Hill, Mt Cattlin and Greenbushes samples	85
86.	TIMA mineral composition map and mineral abundance in Pilgangoora Altura samples.....	87
87.	Locking characteristics of spodumene, with liberation distribution of spodumene for Pilgangoora Altura samples	87
88.	TIMA mineral composition map and mineral abundance for Pilgangoora Pilbara Minerals samples.....	88
89.	Locking characteristics of spodumene, with liberation distribution of spodumene for Pilgangoora Pilbara Minerals samples	89
90.	TIMA mineral composition map and mineral abundance for Bald Hill samples	90
91.	Locking characteristics of spodumene, with liberation distribution of spodumene for Bald Hill samples	91
92.	TIMA mineral composition map, and mineral abundance for Mt Cattlin samples	92
93.	Locking characteristics of spodumene, with liberation distribution of spodumene for Mt Cattlin samples	93
94.	TIMA mineral composition map and mineral abundance for Mt Cattlin samples.....	94
95.	Locking characteristics of spodumene, with liberation distribution of spodumene for Mt Cattlin samples	95
96.	TIMA mineral composition map, mineral abundance and locking characteristics of spodumene, with liberation distribution of spodumene for Greenbushes samples from the Central lode pit.....	96
97.	TIMA mineral composition map, mineral abundance and locking characteristics of spodumene, with liberation distribution of spodumene for Greenbushes samples	97
98.	TIMA mineral composition map, mineral abundance and locking characteristics of spodumene, with liberation distribution of spodumene for Greenbushes samples	98
99.	TIMA mineral composition map, mineral abundance and locking characteristics of spodumene, with liberation distribution of spodumene for Greenbushes samples	99
100.	Theoretical grade–recovery curves for recovering spodumene for Pilgangoora, Bald Hill, Mt Cattlin and Greenbushes samples with different lithologies	100
101.	Line-up of grains of tantalite and cassiterite for Pilgangoora samples	101
102.	Line-up of grains of tantalite and cassiterite observed in Mt Cattlin samples and the associated mineral-locking characteristics	102
103.	Line-up of grains of tantalite and cassiterite observed in Bald Hill samples and the associated mineral-locking characteristics	103
104.	Line-up of grains of tantalum minerals, cassiterite, pollucite and tourmalines observed in Greenbushes samples and the associated mineral-locking characteristics.....	104
105.	Cross-sections of parabrandidite grains present as inclusions in mineral composition maps, backscatter images and As and Ca distribution maps, with line-up of grains of parabrandidite and associated mineral-locking characteristics for Greenbushes samples.....	105
106.	Examples of concentrates showing spodumene with variation in colour and presence of gangue minerals...	106
107.	Particle size distribution of concentrate samples from different mine sites evaluated	106
108.	Mineral abundance and mineral associations with spodumene for concentrate samples taken from site.....	107
109.	Images of different spodumenes and associated gangue minerals	109

110. Cross-section image and backscatter electron micrograph of white spodumene and potassium Ka energy dispersive elemental map and green spodumene with energy dispersive elemental maps.....	112
111. Optical and mineral composition maps showing mineral impurities within spodumene from Mt Cattlin and Pilgangoora.....	113
112. Rietveld refined X-ray powder diffraction patterns of white spodumene and green spodumene	116
113. XRD analysis of α -spodumene to β -spodumene transformation.....	117
114. The logarithmic concentration of α -spodumene and a tabulation of the calculated rates of α -spodumene transformation for Bald Hill white and green spodumene	118
115. Optical and backscatter electron micrographs, with ToF-SIMS elemental maps of cross-sections of white and green spodumene powdered samples following heating.....	119
116. Comparison of thermal gravimetric analysis of representative mineral examples observed in LCT pegmatites	120
117. Comparison of thermal gravimetric curves of spodumene from Bald Hill, Mt Cattlin and Pilgangoora.....	121
118. Correlation of thermal α - β spodumene conversion temperature with Fe content in spodumene and bulk Fe content of combined spodumene and mineral impurities and mica content	121
119. Relative weight percentage of crystalline phases from Rietveld analysis for different spodumene samples heated in a muffle furnace.....	122
120. The volume change in spodumene vs temperature	123
121. Optical images of sample blocks of spodumene before and after heating.....	124
122. Backscatter electron micrographs showing fragmented surface of calcined spodumenes following heating and conversion to β -spodumene at 1100 °C	125
123. Optical images of sample blocks of spodumene with different Fe contents before and after heating at 1050 °C.....	126
124. Backscatter electron micrographs and mineral composition maps showing a cross-section of calcined spodumene heated at different temperatures	127
125. Backscatter electron micrograph images together with band contrast, orientation, phase and K-K α EDS maps of a cross-section of spodumene calcined at 1050 °C.....	128
126. Backscatter electron micrographs showing regions of partial melting of mica coating and encapsulating spodumene	129
127. Backscatter electron micrographs showing regions of partial melt of micas coating and encapsulating spodumene	130
128. Optical images of muscovite before and after heating and a backscatter electron micrograph of a cross-section of calcined muscovite showing partial melting and retainment of mica structure	131
129. Ternary diagram for the system K ₂ O-Al ₂ O ₃ -SiO ₂ and temperature and phase dominance graph showing impact of temperature on mineral composition	131
130. Backscatter electron micrographs of a cross-section of calcined spodumene showing fractured feldspar particle and partial melted feldspar and mica mixture along a fracture in calcined spodumene particle.....	132
131. Backscatter electron micrographs showing cross-sections of calcined spodumene and exsolution of iron-oxide grains on the edge of open vented structures within β -spodumene particles	133
132. Optical images and mineral composition maps of country rock in Mt Cattlin and Bald Hill samples	134
133. Backscatter electron images, mineral composition maps, and Al and Cs element maps showing association and presence of pollucite with β -spodumene in Greenbushes samples	135
134. Mineral abundance of samples chosen for calcination and sulphate-roast evaluation showing variations in mineral composition.....	136
135. Outline of sample calcination-sulphate-roast testing and test work for characterization of ore materials	137
136. Untreated and calcined images of grains and X-ray powder diffraction patterns, with backscatter electron micrographs showing cross-sections of calcined particles (Mt Cattlin)	138
137. Untreated and calcined images of grains and X-ray powder diffraction patterns, with backscatter electron micrographs showing cross-sections of calcined particles (Bald Hill)	139
138. Untreated and calcined images of grains and X-ray powder diffraction patterns, with backscatter electron micrographs showing cross-sections of calcined particles (Pilgangoora)	139
139. Untreated and calcined images of grains and X-ray powder diffraction patterns, with backscatter electron micrographs showing cross-sections of calcined particles (Greenbushes)	140
140. Graphs showing mineral transformations with time for samples heated at 1100 °C for three hours in a muffle furnace for Mt Cattlin, Greenbushes and the ratio $\beta/(\beta+\gamma)$ spodumene	141
141. Backscatter micrographs, mineral maps, and K and Al elemental maps of calcined concentrate samples	143
142. Comparison of the leaching efficiency of samples and concentrates for different lithologies expressed as percentage of Li and as deportments of Li in filtrate	144
143. Comparison of Li extraction as a function of spodumene conversion ratio expressed as $\beta/(\beta+\gamma)$	144
144. Chemical composition of uncalcined solids and calcined acid-bake and water-leach residues	145
145. Chemical composition of filtrate from filtered solid leached residue following leaching and washings from solid leached residue expressed as a weight %.....	146
146. Backscatter images and ToF-SIMS analyses of leaching residue grains following calcination and sulphate roasting (BH1480)	148
147. Backscatter images and ToF-SIMS analyses of leaching residue grains following calcination and sulphate roasting (BH1480)	149
148. Backscatter images overlayed with Li distribution scanned by ToF-SIMS (C1100P).....	149

Tables

1.	Lithium projects with defined JORC resources in Western Australia	3
2.	Program outline.....	8
3.	Location of samples	8
4.	Trace element contents of mica in drillholes PDD162, PDD174 and PDD179 at the Sinclair Deposit	24
5.	Chemical end-member composition for feldspar from WA LCT pegmatites.....	61
6.	Comparison of muscovite composition from Mt Mann and Kathleen's Corner pegmatite swarms at Kathleen Valley.....	63
7.	Summary of U–Pb dating results for zircon and cassiterite from Greenbushes, Pilgangoora, Dalgaranga, Bald Hill and Londonderry pegmatites	73
8.	Comparison of PLS-predicted and known-element concentrations for Li, Si, Al, Fe, K and Mg in validation samples	79
9.	Sample descriptions	80
10.	Modal mineral abundance from TIMA.....	83
11.	Calculated TIMA chemistry vs measured chemical analysis.....	84
12.	Chemical assays of main elements in concentrates.....	107
13.	Mineralogical analysis by X-ray diffraction studies of mineral specimens	110
14.	Bulk chemical composition of mineral specimens.....	111
15.	Average Li and trace elements composition and standard deviation by LA-ICP-MS analysis of spodumene particles	114
16.	Average Li and trace elemental composition and standard deviation by LA-ICP-MS analysis of micas associated with spodumene particles.....	115
17.	Mineral transformation of other minerals at different temperatures	134
18.	Ore and process characteristics of pegmatites examined in this study	151
19.	A summary of the impact of different ore components on processing for extraction of Li	153

Appendices

1.	Drillcore and pit sample description <i>Available with the PDF online as an accompanying digital resource</i>	
2.	Chemical assays of head samples <i>Available with the PDF online as an accompanying digital resource</i>	
3.	Analytical techniques <i>Available with the PDF online as an accompanying digital resource</i>	
4.	Pegmatite mineral association and alteration characterization <i>Available with the PDF online as an accompanying digital resource</i>	
5.	X-ray diffraction analysis <i>Available with the PDF online as an accompanying digital resource</i>	
6.	Composition of Ta–Nb phases detected by TIMA mineral mapping <i>Available with the PDF online as an accompanying digital resource</i>	
7.	Department of lithium and major elements in liberation analysis samples	170
8.	Acid-bake and water-leaching tests.....	174

The geology, mineralogy and geomettallurgy of EV materials deposits in Western Australia

Martin Wells*, Mark Aylmore* and Brent McInnes*

* John de Laeter Centre, Curtin University, Perth, Western Australia

Introduction

Lithium is an important commodity used in glass and ceramics (35%), rechargeable batteries (29%), lubricating grease (9%), air treatment by CO₂ capture (5%), continuous casting mould flux powders (6%) and polymer production (5%). The demand for Li has increased significantly in recent years and is forecast to grow by 350% by 2030 because of its increasing use in the production of Li-ion batteries (LIBs) used to power electric vehicles (EVs), and grid storage (Tarascon, 2010; Grosjean et al., 2012; Mohr et al., 2012; Cano et al., 2018; Wietelmann and Klett, 2018). Government incentives, designed to reduce reliance on fossil fuels and reduce greenhouse gas emissions, are helping to drive the increasing demand for lithium.

The largest concentrations of Li minerals (spodumene, petalite, lepidolite and zinnwaldite) are found in granitic pegmatites in Australia, Canada, Zimbabwe and China (Fig. 1). Tantalum–niobium phases (e.g. columbite and tantalite) and rare earth minerals often associated with these deposits are potential industrial byproducts. A large lepidolite resource in Yichun, Jiangxi province of China, is currently obtained as flotation tailings of Ta and Nb (Guo et al., 2019). Other important sources of Li come from low-grade brine solutions found in Argentina, Bolivia, Chile, China and the United States. Other Li-bearing minerals found in secondary mineral deposits (e.g. hectorite and jadarite) are also being investigated for commercial production (e.g. Jadar Li-borate deposit in Serbia), although Li-bearing clays, such as found in volcano-sedimentary rocks, are often of lower grade and are difficult to process. Pegmatites have a wider geographic distribution than brines, are less susceptible to supply disruptions and have high-grade Li compositions, which make them more flexible to market changes (Kesler et al., 2012).

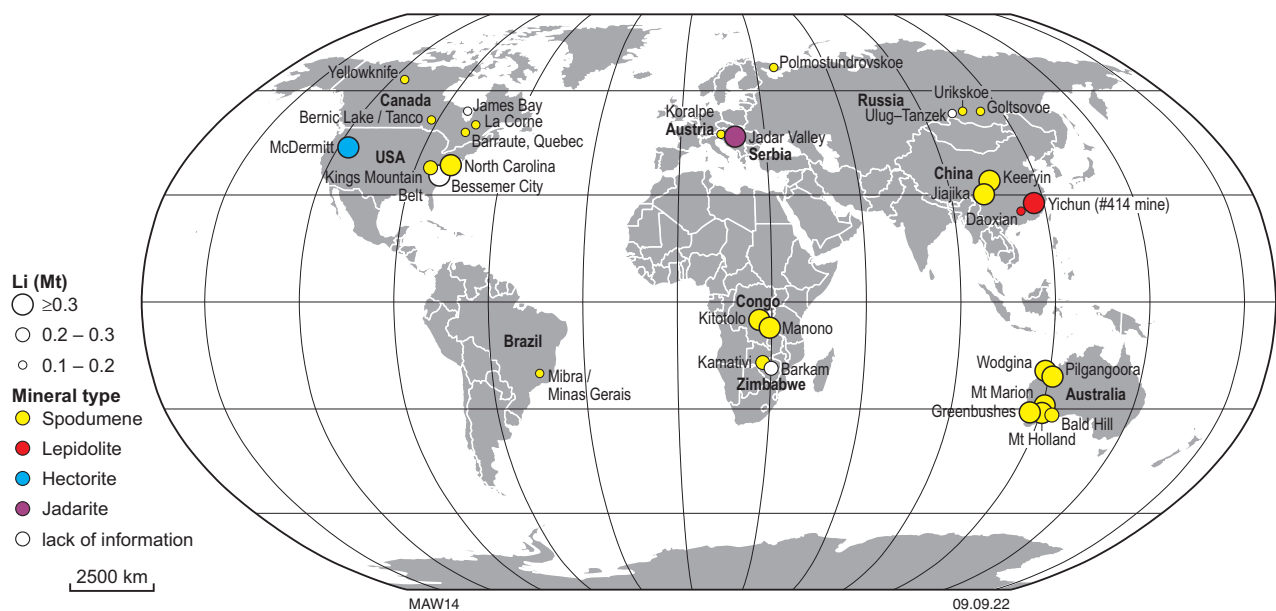


Figure 1. Distribution of major Li-mineral deposits (≥0.1 Mt) of the world. After Li et al. (2019)

Nature and types of pegmatites

Granitic pegmatites are well known and important sources of rare metals including Li, Sn, Ta, Nb, Be, Cs, Rb, Sc, Th, U and rare earths (London, 2008). Although granitic pegmatites are common and widespread, only approximately 0.1% are rare-element pegmatites, with Li-rich pegmatites only making up a fraction of rare-metal pegmatites (Laznicka, 2006). Almost all Li-rich pegmatites contain other rare metals such as Sn, Be, Ta and Nb (Kesler et al., 2012). Pegmatites have been categorized into five groups of which the rare-element pegmatite group can be further classified into the NYF (niobium, yttrium, fluorine) and LCT (lithium, caesium, tantalum) pegmatite families, based on different mineral assemblages and textures as illustrated in Figure 2.

Pegmatites are igneous rocks that form during the final stage of magma crystallization under conditions that favour large crystals of felsic minerals. They either form concentric-zoned or alternating coarse-grained and fine-grained layer-structured deposits. Fluorine, Li, Ta, Cs, Rb and rare earths, which are incompatible in minerals formed in the early-stage magma crystallization, can be concentrated and crystallized in such deposits (Bradley and McCauley, 2013). LCT pegmatites are usually related to fractionated (termed fertile or specialized) granites and may occur sporadically within less evolved S-type granite pegmatite bodies. The identification of mineral fractionation trends within granitic rocks is an important step in evaluating LCT pegmatite potential on a regional scale. For example, the use of Rb:K and Cs:K ratios of pegmatitic K-feldspars and muscovite can provide a measure of the degree of fractionation of a pegmatite (Selway et al., 2005; Linnen et al., 2012), as well as the Ta:Nb ratio of columbite–tantalite oxides (e.g. Shaw et al., 2016). The colour and geochemistry of garnets (Mn vs Fe), tourmaline (Li, Mn), muscovite (Sn) and beryl minerals that may also be present in pegmatites has also been used to establish fractionation of pegmatites (Selway et al., 2005).

Lithium deposits in Western Australia

Lithium deposits and prospects (and Ta-ores containing Li) are known to occur at six major locations in Western Australia as shown in Figure 3. The main documented lithium deposits occur at:



Figure 3. Distribution of Western Australian Li resources (mines, deposits and prospects). After GSWA, Lithium Investment Opportunities (2020)

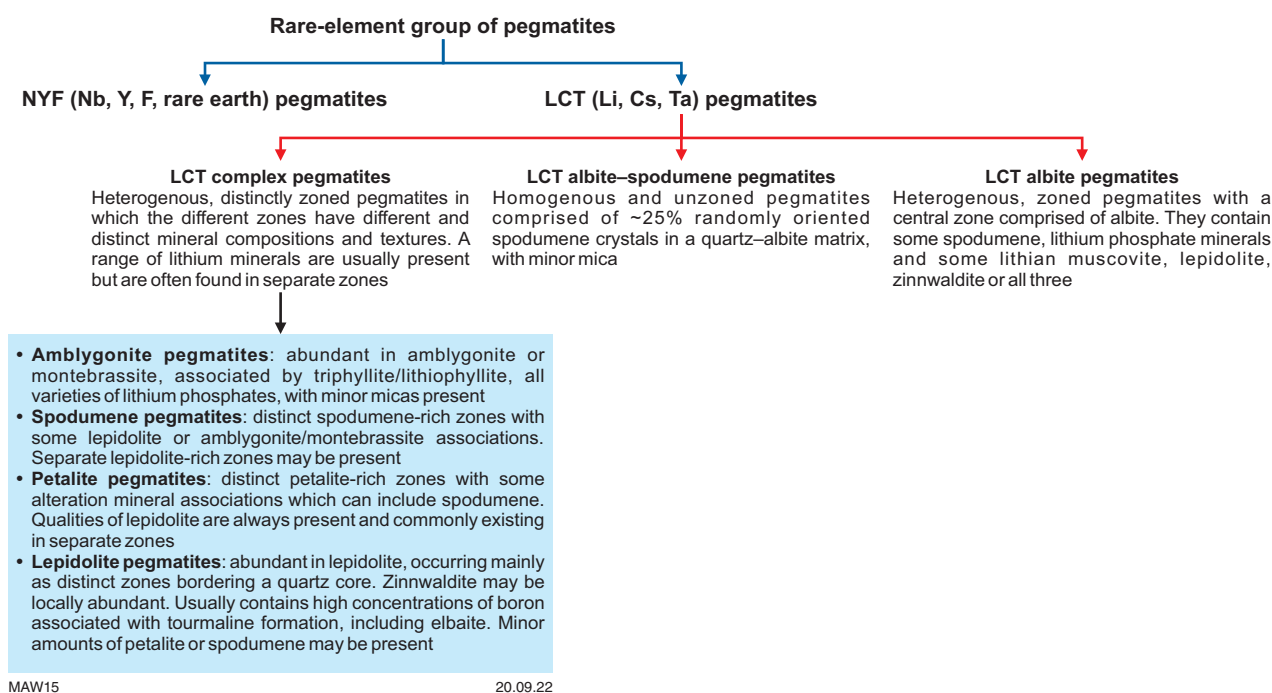


Figure 2. A summary of the classification of rare-element pegmatites. After Černý (1991)

- Greenbushes (about 90 km southeast of Bunbury)
- Mt Marion (about 40 km south of Kalgoorlie)
- Mt Cattlin (about 2 km north of Ravensthorpe)
- Earl Grey at Mt Holland (about 160 km southwest of Coolgardie)
- Kathleen Valley (about 680 km northeast of Perth or 50 km north of Leinster)
- Pilgangoora (about 90 km south of Port Hedland).

Australia's economically defined lithium resources (estimated at 15.2 M tonnes) occur exclusively within hard-rock pegmatite deposits, within the Archean Yilgarn and Pilbara Cratons of Western Australia. Rare-element pegmatites are known in other districts in Proterozoic terrains throughout Australia, such as the Curnamona, Arunta and Pine Creek provinces (e.g. Pollard, 2017) but all current Li production to date is from WA LCT pegmatites. The JORC defined resource estimates, as collated by the Geological Survey of Western Australia (GSWA) for the different pegmatite deposits, are shown in Table 1.

A comparison of the Li grade and size of resources in Australia compared with other major hard-rock Li-bearing deposits is shown in Figure 4. The Greenbushes lithium mine is the world's largest and highest grade spodumene deposit, supplying 50% of the world's Li production at the time of writing. Other companies such as Pilbara Minerals, Mineral Resources and Liontown Resources have defined significant resources (Table 1). Other significant deposits are located at Cinovec in Europe (European Metals Holdings), with Li hosted by mica (zinnwaldite), and in the Manono

Table 1. Lithium projects with defined JORC resources in Western Australia

Mining company/Deposit/ Project	Ore (Mt)	Average Grade Li ₂ O (%)	Contained Li ₂ O (Mt)
Mineral Resources – Wodgina ¹	259.2	1.17	3.03
Pilbara Minerals – Pilgangoora (Altura project – Pilgangoora²)	309.0 (50.5 ²)	1.14 (1.02 ²)	3.51 (0.5 ²)
Covalent Lithium – Mt Holland	189	1.5	2.84
Talison – Greenbushes	196.8	1.90	3.75
Liontown Resources – Kathleen Valley	156	1.35	2.10
Mineral Resources – Mt Marion	72.9	1.37	1.00
Alita Resources³ – Bald Hill	26.5	0.97	0.26
Alkem Limited⁴ – Mt Cattlin	11.0	1.20	0.13
Pilbara Minerals – Lynas Find	5.3	1.56	0.1
Total	1225.7		16.72

NOTE: * Pre-mining reserves and inferred, ¹under care and maintenance. ²Formerly Altura Resources now owned by Pilbara Minerals and incorporated in Pilbara Minerals updated resource. ³Formerly Alliance Minerals, under care and maintenance at the time of writing. ⁴Formerly Galaxy Resources. Samples obtained from Bald Hill and Mt Cattlin were subsequent to this research but prior to publication of this report. Lithium projects highlighted in bold were included as part of this study. Data source: GSWA (2022), Lithium investment opportunities, January 2022 Flyer, obtained from: <https://dmpbookshop.eruditetchnologies.com.au/product/lithium-investment-opportunities-western-australia-geographical-product-n20bz.do>

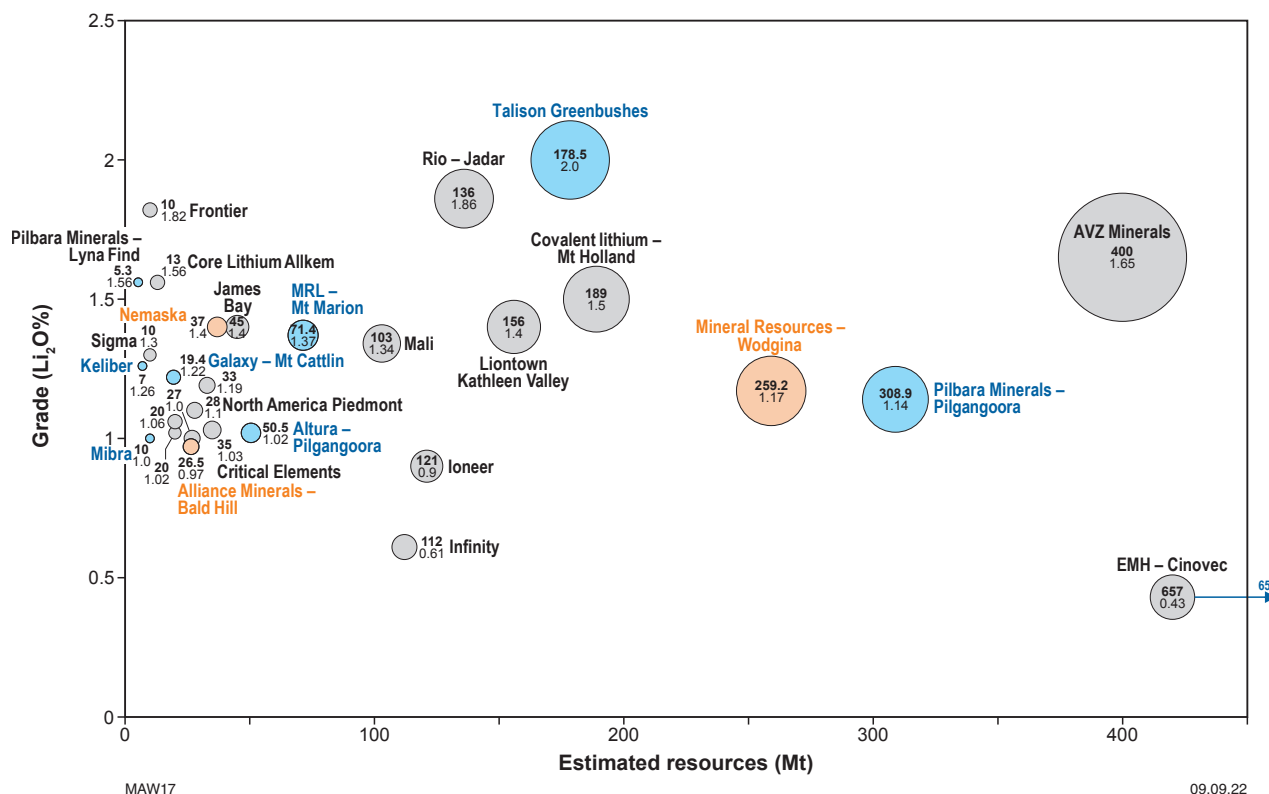


Figure 4. Global significance of Australia lithium hard-rock resources. Key: operational mines (blue); mines under care and maintenance (orange); deposits under development (grey)

project in Democratic Republic of Congo in Africa (AVZ minerals), where Li occurs as spodumene. Both deposits are undertaking feasibility studies and are not operational.

The pegmatite fields of Western Australia were known to mineralogists from the early 1900s as a source of gem-quality beryl, tourmaline, petalite and other lithium minerals (Jacobson et al., 2007). Most pegmatites in Western Australia are hosted by Archean mafic–ultramafic greenstone belts that have experienced upper greenschist to lower amphibolite metamorphism (e.g. Greenbushes, Kathleen Valley, Mt Marion and Londonderry). However, other deposits, such as Bald Hill and Dome North, intrude metasedimentary sequences. Regardless, as pegmatite emplacement post-dates the host rock, the depth in the crust at which emplacement occurred and the P – T conditions to which the pegmatite was subjected does not necessarily correspond to the conditions under which the host rocks were metamorphosed (e.g. Bradley et al., 2017). The exception of the Western Australian pegmatites examined in this work is the giant Greenbushes pegmatite swarm, which is interpreted to have intruded synchronous with regional deformation associated with the Donnybrook–Bridgetown shear zone under conditions of medium to high temperature and medium-pressure metamorphism (e.g. Partington et al., 1995). Further details of the geological setting of each of the pegmatites examined in the current study are discussed in detail in the section Classification and geological assessment methodology.

Resource geology and deposit assessment implications

Overall:

- While the deposits in Western Australia can be classified as LCT pegmatites, there is limited detail on mineralogy and deportment of lithium and other rare elements associated with many of the Western Australian deposits.
- Conventional X-ray based techniques do not have the ability to detect Li and other low atomic number elements (Be, B, C). Only with advanced analytical techniques coupled with mass spectrometry can the deportment of Li-minerals and its complexity with other associated minerals be evaluated (e.g. Aylmore et al., 2017; Aylmore et al., 2018a,b).
- The documentation of the geochemistry of mineral constituents (e.g. rutile or feldspars) within pegmatites as an exploration tool is limited. Further work is required to identify mineral fractionation trends, which can aid in identifying Li and rare-metal minerals during the early stages of exploration.

In recent times, hand-held X-ray fluorescence (XRF) and laser induced breakdown spectroscopy (LIBS) devices (e.g. produced by Bruker, Hitachi and SciApps) have been produced which allow the geologist in the field to determine grade and some elemental associations in pegmatite deposits. However, these portable techniques are matrix dependent and need to be calibrated using laboratory-based analytical techniques (e.g. X-ray diffraction [XRD] analysis) before they can be used quantitatively.

Process implications

Various processes have been developed and reported in the literature to recover Li from silicate minerals and some approaches are dependent on the ore mineralogy (Brandt and Haus, 2010; Meshram, et al., 2014; Choubey, et al., 2016; Li et al., 2019). An outline of the conventional processing route for treatment of spodumene ores is illustrated in Figure 5.

Processing of hard-rock material requires physical beneficiation (grinding, sizing, flotation, gravity, reflux classifier and/or heavy media/magnetic separation) to liberate and concentrate the Li-bearing minerals and to remove gangue minerals, which are made up mainly of quartz, feldspars and micas. Processes involved in crushing and liberating Li-bearing minerals from gangue minerals have been reviewed and published by others (Gibson et al., 2017; Tadesse et al., 2019).

Lithium is extracted from silicate concentrates usually by a combination of elevated temperature and chemical treatment processes (e.g. sulphation, carbonation or chlorination roasting). The treatment of spodumene concentrate conventionally involves a calcination step ($\sim 1100^\circ\text{C}$) to convert the natural low-temperature, monoclinic α -spodumene into the tetragonal β -spodumene form, which is a more open crystalline structure where the Li ion can be more readily extracted through reaction with acid or alkali reagents (Ellestad and Leute, 1950; Salakjani et al., 2017; Aylmore et al., 2018b). The structural transformation of spodumene is illustrated in Figure 6.

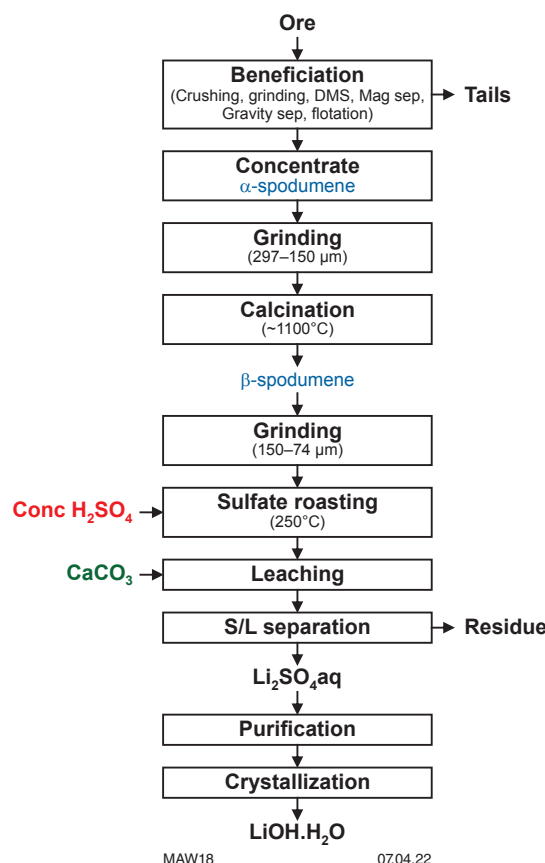


Figure 5. Outline of standard lithium extraction and recovery process

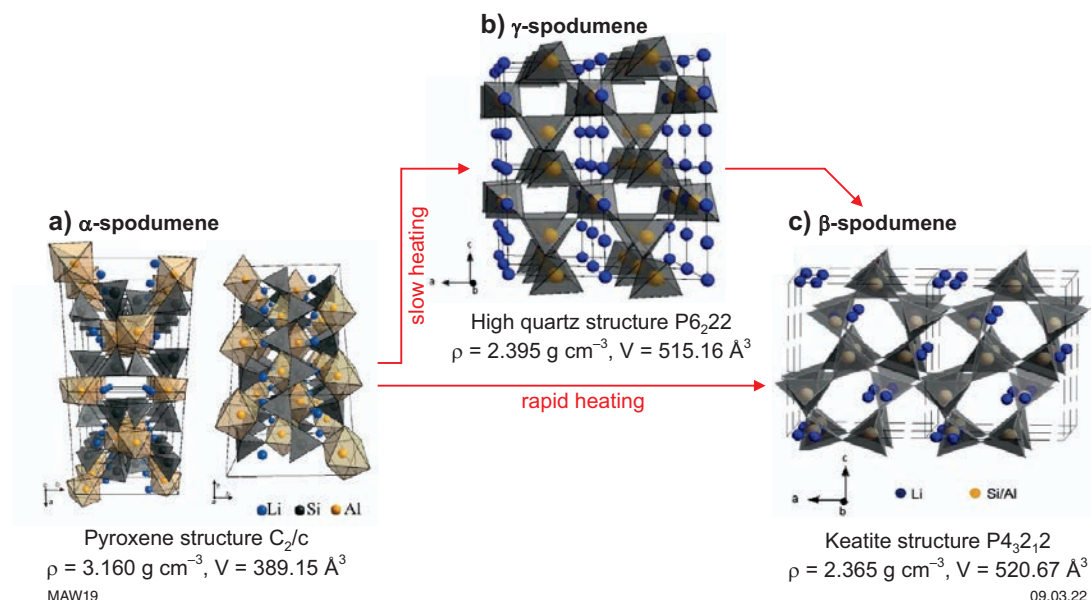


Figure 6. Structural transformation of spodumene at elevated temperatures

The thermal transformation of α-spodumene to β-spodumene has been studied in detail and involves different pathways. Formation of intermediate transformation phases has been attributed to the nature of the grain size, concentration of impurities and amorphous material formed in grinding as well as different heating rates and techniques (Peltosaari et al., 2015; Salakjani et al., 2016, 2017, 2019; Moore et al., 2018; Abdullah et al., 2019).

Conventional roasting with chemical reagents has been used for treating micaceous minerals, such as lepidolite and zinnwaldite, prior to leaching the lithium into aqueous solutions. The sulphation process has been the most prominent leaching approach. Other processes such as chlorination requires corrosion-resistant plant equipment, although chlorination has the advantage of forming more highly soluble species (LiCl) than the carbonation and sulphation of minerals.

Recovery of Li from pregnant liquors can be a challenge and is dependent upon the amount of other dissolved species (e.g. Na, K, Ca, Mn, Fe, F, Si, Al) that occur through the dissolution of silicate minerals.

Operations in Western Australia

In Western Australia, spodumene concentrates produced from Talison Lithium's Greenbushes mine, Galaxy Resources' Mt Cattlin mine, Mineral Resources' Mt Marion mine and Pilbara Minerals' Pilgangoora mines are currently shipped to Chinese converter plants for processing. Pilbara Minerals' current 2 million tonne per annum (tpa) mining and processing operations produce ~330 000 tpa of ~6 wt% Li_2O spodumene concentrate. Pilbara Minerals has acquired the Ngungaju plant (formally Altura Lithium Operations) and is expecting these operations to increase production by ~180 000 to 200 000 dry metric tonnes (dmt) by mid-2022, resulting in a combined production capacity of ~580 000 tpa. Mining operations at Wodonga and Bald Hill were shut down when the lithium price decreased but are expected to recommence production in the future.

In 2017, Australian production of spodumene concentrate was worth \$1 billion. With the expected rise in demand for lithium, the value of Australia concentrate production is predicted to increase to \$10 billion by 2025. Globally, projected lithium demand is expected to exceed supply in about 2025 (Fig. 7).

A key issue for the Western Australian spodumene industry is that many of the existing beneficiation plants have struggled to meet design recovery rates. In order to meet converter specifications, spodumene miners often sacrifice recovery for grade, culminating in loss of spodumene to waste and poor overall resource utilization. It is estimated that \$713 million worth of spodumene production is reporting to waste every year, mainly in the form of fines, which otherwise could potentially be recovered through improvements in processing technology (Harman, 2019).

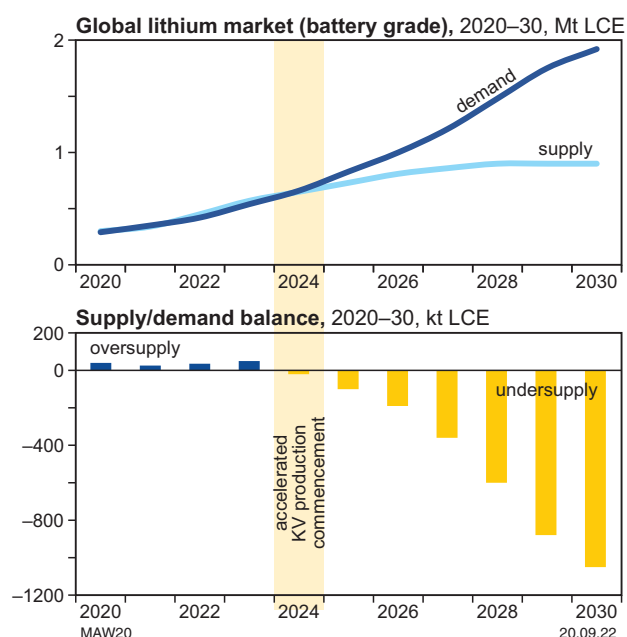


Figure 7. Expected global lithium market demand and supply balance (kt Lithium Carbonate Equivalent (LCE)). After Roskill (Aug 2021)

In 2017, the Li refinery global market was worth around \$2 billion, and the refinery industry is expected to balloon in value to \$65 billion by 2025 (Talbot and Watts, 2020). The first Li refinery in Australia run by a joint venture between IGO Ltd (49%) and Tianqi Lithium Corporation (51%) has been commissioned at Kwinana. The commissioned first train is expected to reach 24 000 tpa capacity by the end of 2022. A second production train is under construction and scheduled for commissioning in 2024 to enable a total of 48 000 tpa of battery grade lithium hydroxide. Further expansion to 96 000 tpa is expected in the following years. The Kwinana plant will produce lithium hydroxide from spodumene concentrate trucked from the Greenbushes mine. Early commissioning of the plant was stalled in 2020 due to process engineering problems and the drop in lithium hydroxide price.

The approval by the Western Australia's Environmental Protection Authority for construction and operation of Covalent Lithium's 45 000 tpa lithium hydroxide refinery in Kwinana has been granted enabling the early commencement of construction works at the site, with production expected to start in the second half of 2024 (www.australianmining.com.au/news/covalent-lithium-begins-mt-holland-construction).

Development of a processing plant by Liontown (Kathleen Valley) progressed through to the definitive feasibility study (DFS) in November 2021 with the final investment decision confirmed in June 2022. Production of battery grade lithium hydroxide is not expected until the second quarter of 2025 (Liontown, 2022).

The processing of Li-rich micaceous deposits has yet to be developed on a commercial scale in Australia. These have previously been considered as uneconomic. For the treatment and extraction of lithium from Li-mica ores, sulphate roasting is best undertaken with CaSO_4 and Ca(OH)_2 , followed by water leaching. In this process F present in the Li-mica is fixed by the formation of F-containing compounds to prevent HF formation. Other process options (e.g. halide based SiLeach process, L-Max Technology) have been developed that may allow treatment of more complex Li-feedstock and utilize the HF generated during acid leaching breakdown and recovery of lithium from mica. Lithium Australia has reported on testing of the Lepidolite Hill ore in Western Australia using their atmospheric halogen-based SiLeach process.

Overall, the key impediments to the economic processing of Li-mineral ores are considered as follows:

- It is important during the beneficiation stage that high-grade Li concentrates are produced with little or no gangue material. Li-bearing minerals can be interlocked within gangue minerals requiring a finer grind to liberate. The thermal decomposition or dissolution of gangue material in the downstream process can reduce Li recovery.
- Existing technology for refining lithium is not suitable for treating the variability in some Li-bearing pegmatite ores. Mineral and elemental impurities (e.g. K, Na, Fe, Mn) associated with concentrates can lead to clinker formation and agglomeration of particles within the calcine convertor kilns, which leads to frequent shut-downs for maintenance and reduction in lithium recoveries.
- The deportment and management of deleterious elements such as F and Mn from mica can be problematic and important in considering process paths for treatment.
- Lithium products must meet a certain quality standard to be used in producing Li-batteries. The high-purity product yield of Li_2CO_3 and LiOH are in demand for battery production (Meshram et al., 2014; Choubey et al., 2016). Hence, knowledge of elemental impurities within the host Li-bearing minerals is important.
- Continued work is still required on developing novel, environmentally friendly processes to minimize harmful byproducts (e.g. HF and SO_2 gas emissions and energy for roasting process). Other process issues such as scaling (e.g. gypsum precipitation), water usage and minimization of power costs remain important.

To facilitate further process development, a comprehensive understanding of the deportment of Li and associated minerals in potential orebodies and linking the mineralogy to the fundamental processes of mineral liberation, thermal alteration and chemical dissolution is essential to allow the industry to predict the response of ore reserves to metallurgical treatment options.

Project objectives

The aim of this work was to develop a geomettallurgical framework for Western Australian Li-pegmatite deposits that will lead to improved efficiencies in exploration, mineral beneficiation and processing techniques.

The whole project was divided into three integrated modules of geology, mineralogy and metallurgy as outlined in Figure 8.

The **Geology module** focused on assessing the geology of LCT pegmatites in Western Australia in terms of the formation, texture and deposition. Field studies to collect samples from mine sites and the acquisition of drillcore samples were carried out and targeted the main LCT pegmatites and regions in Western Australia. Minerals commonly found in pegmatites (e.g. feldspars, rutile, zircons, garnets and beryl muscovite) and their geochemistry signature were examined to identify pegmatite associations that can assist in targeting LCT pegmatites. Although granitic pegmatites are common and widespread, less than 0.1% are Li-enriched and can be considered as a legitimate eMaterial resource. In addition, work was carried out to produce a petrochronological and geochemical synthesis of LCT pegmatite mineral systems in Western Australia. The work looked to produce a classification scheme useful in both exploration targeting for economic LCT pegmatites and grade control in mining operations.

The **Mineralogy module** focused on understanding the deportment of Li and other elements of interest in pegmatite deposits and improving the accuracy and precision of analytical techniques used to measure mineral components in pegmatites. Samples from mine sites taken from field studies and drillcore samples were examined as well as specimens from the Western Australian Boola Bardip museum.

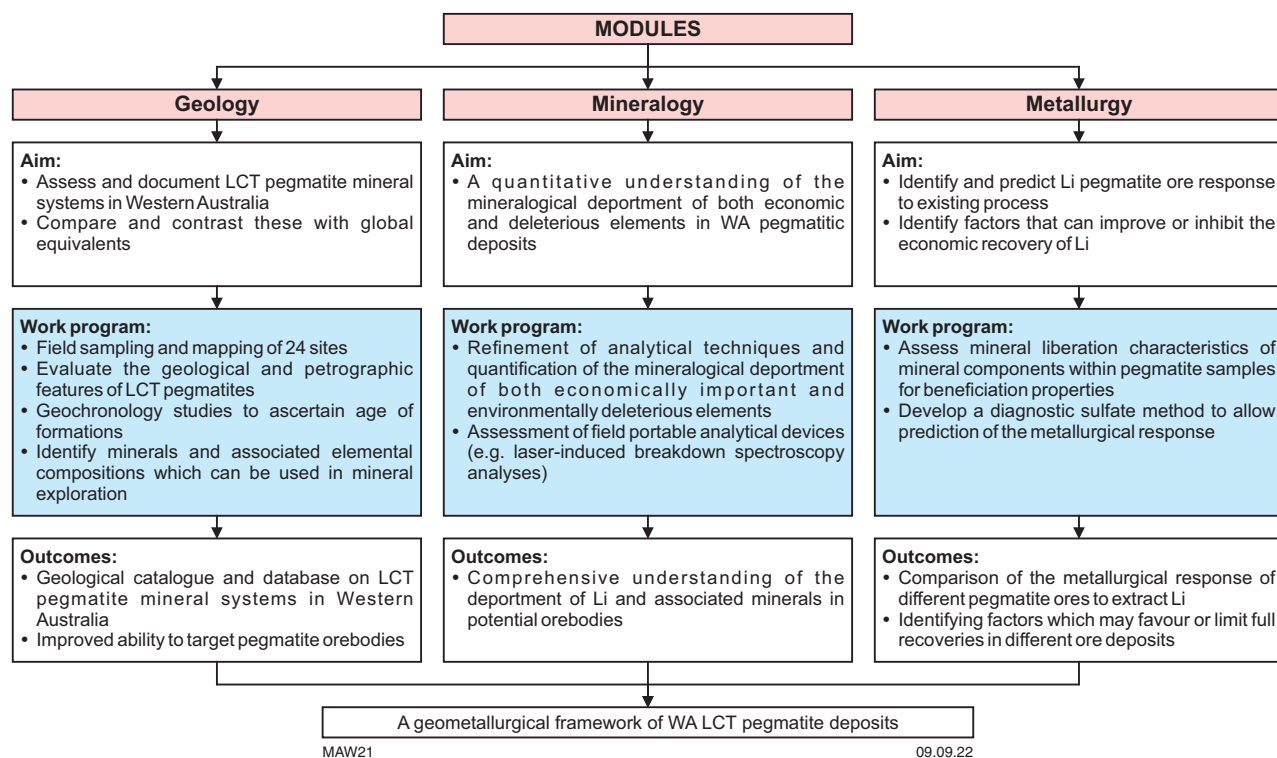


Figure 8. Outline of work program modules

In addition, the work assessed the accuracy and precision of novel, hand-held field portable analytical devices employing laser-induced breakdown spectroscopy (LIBS) techniques to measure Li concentrations in outcrop and hand samples. Emphasis was on assessment of the effectiveness of techniques and the correlations that can be made with the mineralogy of pegmatites.

From this work, assessment of the deportment of Li and other elements of interest and associated minerals in pegmatite deposits was obtained, and an independent assessment on the practical application of LIBS technology for exploration and mining operations was carried out.

For the **Metallurgy module**, the physical liberation characteristics of Li-bearing mineral particles and chemical processing behaviour of LCT pegmatites were correlated to the mineralogy data collated in the geology and mineralogy studies. Processing of hard-rock material is highly operating-expenditure intensive, involving beneficiation to liberate and concentrate the Li-bearing minerals and a combination of elevated temperature and chemical treatment processing (e.g. sulphation, carbonation or chlorination roasting) to recover Li from silicate minerals. Mineral liberation characteristics provide information about the required particle size to liberate and concentrate minerals of interest in the different pegmatite ores for grade control. A suite of samples representing different lithologies in the orebodies were examined.

A study on the thermal decomposition of different pegmatite constituents under conventional calcination treatment conditions was undertaken to link the mineralogical properties to the metallurgical response of different pegmatite ores. Further studies examined the whole calcination and acid-bake process to correlate lithium extraction parameters to lithology.

A comparison between pegmatite ore types and processing options that are either currently used or are reported as suitable for processing Western Australian pegmatite type ores were examined. A summary of the issues and impediments of processing Western Australian lithium ores, which identified factors that favour or limit full recoveries in different ore deposits, is provided.

Project modification

The work was split into two programs to accommodate constraints in the budget as outlined in Table 2.

In this report, the results from both programs have been combined. The report is set out into the following main sections:

- Classification and geology of LCT pegmatites in Western Australian
- Geochemical analysis and mineral characterization
- Quantitative assessment of pegmatite minerals by LIBS analysis method
- Assessment of physical and chemical processing behaviour of LCT pegmatites
- Geometallurgical framework.

Table 2. Program outline

	Program 1 (MRIWA, GSWA, Rio Tinto, Lithium Australia)	Program 2 – extended project (GSWA)
Sites	Focus on seven sites , mainly spodumene-type ores collected	Samples from additional sites covering other significant pegmatite deposits
Program	All three modules Work on Li–mica-type deposits specified by Lithium Australia ceased and other major deposits (e.g. Kathleen Valley, Mt Marion and Pioneer Dome) not examined. Mineralogical analysis and metallurgical studies reduced to reflect the reduction in number of sites and samples examined	Geology module Focused on petrology, mineralogical analysis and geochronological studies
Project time frame	18 months	6 months

Sample acquisition

Sampling targeted the four main LCT pegmatite regions in Western Australia (Pilbara, Murchison, Goldfield and Southern regions) as outlined in Table 3.

Pegmatite material for analysis was sourced from either drillcore and/or from pit wall exposures at various deposits. The team worked with geological and metallurgical personnel on site to ensure representative samples were collected from the different regions. Sampling details of drillcore from the Greenbushes, Sinclair Caesium Deposit, Dome North, Kathleen Valley, Pilgangoora, Londonderry and Dalgaranga pegmatites are provided in Appendix 1.

Sampling of Greenbushes drillcore C3DD024 was undertaken at the GSWA Carlisle Core Library Facilities, whereas drillcore from the Sinclair, Londonderry and Dalgaranga pegmatites was sampled at the GSWA Joe Lord Core Library Kalgoorlie. Pit sampling from the Bald Hill (while still in operation) and Mt Cattlin pegmatite deposits was undertaken during a site visit in May 2019, whereas pit sampling at Greenbushes was undertaken during a site visit in August 2020. Samples were categorized and classified using the classifying scheme of Černý (1991). Industry and Curtin protocols for occupational health and safety were adhered to for fieldwork in remote locations and mine visits, classification and geology of LCT pegmatites in Western Australia.

Table 3. Location of samples

	Sampling location	Sample type
Pilbara	Pilgangoora region	Drill-core Hand specimens
Murchison/ Gascoyne	Dalgaranga– Kathleen Valley	Drill-core
Goldfields	Londonderry Bald Hill Pioneer Dome and Dome North Mt Marion	Drill-core Pit/ROM Drill-core Concentrate
Southern Region	Mt Cattlin Greenbushes	Pit/ROM pad Drill-core, pit

Classification and geology of LCT pegmatites in Western Australia

The geology of LCT pegmatites in Western Australia were assessed in terms of their formation, texture and deposition characteristics. The range of LCT pegmatites examined in the current study includes those that have been in operation for a prolonged period (e.g. Greenbushes for 120+ years and Mt Cattlin since mid-1900s), those that are now historical deposits (e.g. Dalgaranga/Mt Farmer and Londonderry), those that have only recently begun production (e.g. Pilgangoora), those that are now being evaluated as prospective (e.g. Dome North and Kathleen Valley), those that have, for economic reasons, recently been exhausted (e.g. Sinclair Caesium Deposit), and those that have recently been shut-down or are under care and maintenance (e.g. Bald Hill). Consequently, there are limited publicly available, geological descriptions for some deposits (e.g. Dalgaranga and Bald Hill), while other deposits have been extensively investigated (e.g. Greenbushes). Hence, the following section provides a summary of the geological setting of each of the 10 pegmatite deposits, located in the Archean Yilgarn and Pilbara Cratons of Western Australia, examined in the current study. For reasons previously outlined, geological descriptions for some deposits will be less comprehensive compared to those deposits that have been more extensively investigated.

This section describes:

- the methodology used for characterizing drillcore and representative examples of LCT pegmatites
- the geological setting of the deposits examined in this work, which includes most of the significant (e.g. Greenbushes, Kathleen Valley and Pilgangoora) LCT pegmatites in Western Australia
- the mineralogy and textures of the samples collected.

Classification and geological assessment methodology

Pegmatite samples were systematically characterized following the workflow procedures as outlined in Figure 9.

Test work consisted of the following:

- **Textural** – brief sample descriptions of all drillcore and pit samples collected summarize the general mineral–textural relationships. Refer to Appendix 1.

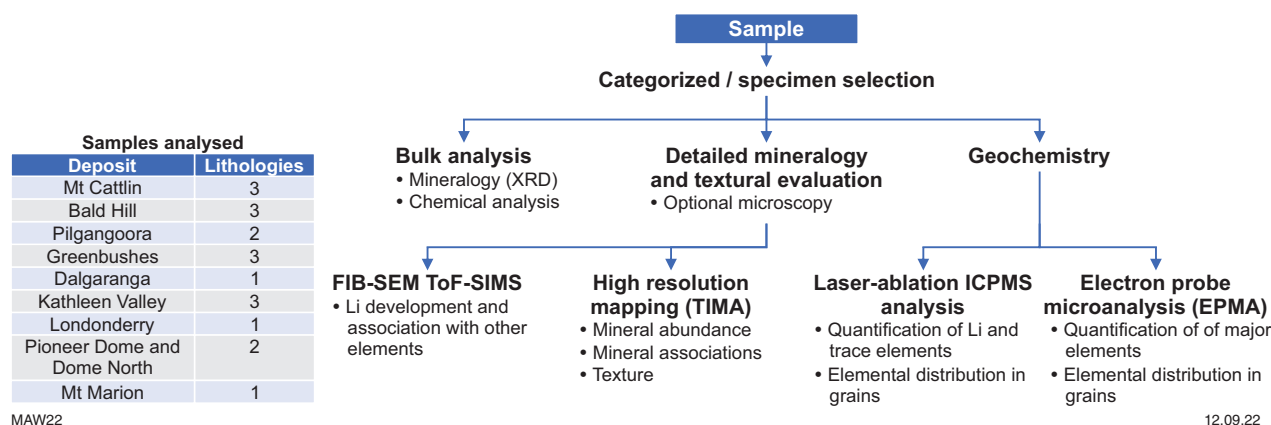


Figure 9. Outline of the project analytical workflow

- **Preliminary bulk chemical and mineralogical analyses** – a full elemental suite analyses (Appendix 2) and quantitative X-ray powder diffraction (XRPD) analyses (Appendix 3) was carried out to characterize sub-samples of pegmatite from all sites.
- **Mineralogy and textural evaluation** – polished sections or thin sections of suitable rock specimens were produced at the John de Laeter Centre (JdLC), Curtin University. The identification of tourmaline, garnet, Ta–Nb-oxide, beryl and other minerals associated with fractionated pegmatites was carried out within the mineralogy module.
- A combination of **optical and electron microscopy** instruments at the JdLC were utilized, including the:
 - **Tescan Integrated Mineral Analyser (TIMA)** which uses a scanning electron microscopy – energy dispersive X-ray system (SEM–EDS) to generate mineral maps and characterize textural features and mineral associations. Detailed TIMA mineral mapping of all pegmatite drillcore and pit samples is provided in Appendix 4.
 - focused ion beam-scanning electron microscope (FIB-SEM) which uses a time-of-flight secondary ion mass spectrometry (ToF-SIMS) to produce light element (Li and B) maps.
- **Geochemical signature of pegmatites** – minerals commonly found in pegmatites and their geochemical signatures were examined to assist in targeting LCT pegmatites. Major element compositions were determined using electron probe microanalysis (EPMA) measurements of an 11-element suite (Si, Al, Fe, Mn, K, Ca, Mg, Na, F, Rb, Cs) at the Centre for Microscopy, Characterisation and Analysis (CMCA), University of Western Australia. The trace geochemical analysis of a 40-element suite of selected mineral grains was then quantified by laser-ablation inductively coupled plasma–mass spectrometry (LA-ICP-MS) at the JdLC for both geochronology and the assessment of the degree of fractionation of pegmatites in this study. In particular, the following investigations were undertaken to determine whether it is possible that geochemical trends can be used to determine the degree of fractional crystallization experienced by the pegmatite which might be applied as a ‘fertility’ or ‘prospectively’ indicator:
 - The K:Rb and K:Cs ratios of pegmatitic mica.
 - Lithium, K, Rb, Cs, and Ta in muscovite.
 - Elemental composition of Ta–Nb-oxide minerals.
- **Dating techniques** – several geochronological techniques were applied to place temporal constraints regarding the timing of emplacement or crystallization of the host pegmatite:
 - Zircon U–Pb geochronology using JdLC GeoHistory Facility (LA-ICP-MS)
 - Spodumene and muscovite Ar–Ar geochronology using the $^{40}\text{Ar}/^{39}\text{Ar}$ geochronological technique using the JdLC Western Australian Argon Isotope Facility.
- **Lithium isotope analysis** – the isotopic homogeneity of selected spodumene crystals was determined to assess if a Li-isotope standard could be developed that may have application as a provenance indicator of the material source of mined spodumene ore concentrates:
 - $^6\text{Li}/^7\text{Li}$ analysis was undertaken using the JdLC GeoHistory Facility (LA-ICP-MS).

Details of all analytical procedures are outlined in Appendix 3.

Testing of field portable analytical devices

Application of a field portable analytical device for quantitative compositional analysis was tested using LIBS of well-characterized, pressed-powder discs of pulped samples with known composition. Details of the technique is given in Appendix 3.

Geological setting of LCT pegmatite of the southern region

Pegmatites hosted in the southern region of Western Australia, along the southwestern margin of the Yilgarn Craton, included in this study were from the Greenbushes and Mt Cattlin Deposits.

Greenbushes

Setting

The Greenbushes pegmatite swarm is located approximately 350 km south of Perth, and about 80 km southeast of Bunbury (Fig. 3), occurring within the Archean South West Terrane (Partington et al., 1995; Quentin de Gromard et al., 2021). Mining for Sn began in 1888 and has since been in continuous production, making Greenbushes the longest operating mine in Western Australia (Partington et al., 1995). Jacobson et al. (2007) provide a detailed account of the mining history of the deposit. Work by Partington et al. (1995) provide a detailed account of the geological setting of the Greenbushes pegmatite, which is summarized here.

The pegmatite swarm at Greenbushes consists of north-trending pegmatites, the largest trending north-northwest for up to 2500 m, emplaced into dioritic gneiss, amphibolite, granofels, ultramafic schist and banded iron formation of the Archean South West Terrane greenstones (Quentin de Gromard et al., 2021), informally referred to as the 'Balingup metamorphic belt' (Wilde, 1996; Fig. 10). The pegmatite swarm intruded close to, and parallel with, the north to north-northeasterly trending Donnybrook–Bridgetown shear zone (Partington et al., 1995; Fetherston, 2004; Partington, 2017). The Donnybrook–Bridgetown shear zone is a 150-km long regional lineament that trends northerly, subparallel to the Darling Fault in the north of the Balingup metamorphic belt and northwest–southeast oblique to the Darling Fault in the south (Partington et al., 1995). U–Pb zircon age of 2641 ± 4 Ma, undertaken in the present study of grains, interpreted to be inherited in origin (refer to the section (U–Pb) dating), updates the earlier U–Pb zircon age of 2527 ± 2 Ma of the Greenbushes pegmatite as reported by Partington et al. (1995) and Kendall-Langley et al. (2020). While our findings reduce the age disparity between the older Greenbushes pegmatite and the younger Logue Brook granite at 2612 ± 5 Ma (Fetherston, 2004), the age difference may dispel previous proposals for a genetic link between the Logue Brook granite and the Greenbushes pegmatite (Partington et al., 1995).

Emplacement and crystallization of the Greenbushes pegmatite is considered pre- or near synchronous with regional deformation within the Donnybrook–Bridgetown shear zone as evidenced by heterogeneous deformation, recrystallization and mylonitization of parts of the pegmatite (Partington et al., 1995; Fetherston, 2004). Despite the fine-grained and sheared nature of the pegmatite, four layered, major mineralogical zones are identified (Fig. 10) consisting of a contact zone (mainly albite–quartz), a K-feldspar zone (microcline–quartz), a Na-feldspar zone (albite–quartz) containing the main Ta mineralization, and a Li-zone (spodumene–quartz) as the main source of Li mineralization (Partington et al., 1995; Fetherston, 2004; Partington, 2017). Ta-bearing ore consists of tantalite, tantalite-enriched cassiterite, stibiotantalite and minor Ta minerals (e.g. wodginite, tapiolite and microlite).

The highly evolved or fractionated nature of the layered pegmatite units has resulted in the development of discrete Ta–Sn and Li-rich spodumene lodes. This is evident at Greenbushes with major Sn–Ta mineralization occurring in the Cornwall and Hanging Walls lodes mined in the Cornwall pit, and Li mineralization (spodumene) occurring mainly in the Lithium pit (C3 pit) (Fetherston, 2004). The Central or C1 pit has discrete occurrences of both mineralization types (Fetherston, 2004). The C3 pit contains the main Li deposit, occurring in the upper part of a 250-m wide Li-enriched pegmatite. The pegmatite ore zone comprises a quartz–spodumene body up to 100 m wide and 600 m long, dipping at 30–80° west to southwest (Porter Geo, 2019: www.portergeo.com.au/database/mineinfo.asp?mineid=mn508, viewed 13-06-2021). Lithium mineralization within the C1 pit is hosted by an approximately 500-m long by 150-m wide ore zone in the pegmatite (Porter Geo, 2019). A third pit, C2, is situated between C3 and C1 but only limited mining has been undertaken and is currently not in production.

Sampling and characterization

Greenbushes samples for this study included drillcore materials obtained from the GSWA Carlisle core library (C3DD024) and during a visit to site in August 2020. The location of the drillcore and pit samples are shown in Figure 11. For drillhole C3DD024, downhole logging records show changes in bulk rock; weight percent Li_2O and Na_2O contents and hyper-spectral data were used to aid the selection of core intervals for mineralogical and geochemical investigation (Fig. 12). A montage of TIMA mineral mapping results referenced to the compositional downhole logging is useful in characterizing the mineralogical and textural evolution of the Greenbushes pegmatite. The Li-zone, approximately 120 m thick (0–120 m), consists mainly of spodumene–quartz mineralization, with spodumene occurring as both tabular laths 3–4 cm in length and as smaller poikiloblastic blebs (Fig. 12). Minor albite occurs sporadically in the Li-zone and lepidolite is present as an additional, late-stage Li-bearing phase (e.g. #241170), as evidenced by crosscutting textures with spodumene (Appendix 4).

At depths >120 m, the Li-zone grades sharply into the Na-zone that continues to end of hole (EOH), associated with the more common occurrence of albite (Fig. 12). This zone is also marked by the variable occurrence of K-feldspar as supported by a variable K_2O content of approximately 4–6 wt% (Fig. 12). TIMA mineral mapping highlights a distinct textural change within the Na-zone as evidenced by a decrease in spodumene crystal size to 1-cm long laths at the top of the Na-zone to granular, 'ovoid' 1-mm sized spodumene grains that form raft-like aggregates or show deformation in the form of grain elongation and grain wrapping (e.g. #241174 and #241175; Appendix 3). This imparts a distinct foliation, with segregation of apatite, in the Na-zone towards the base of the hole (Fig. 12). These mylonitic-like textures are consistent with and support the heterogeneous deformation and recrystallization of the pegmatite synchronous with the regional deformation and metamorphic events within the Donnybrook–Bridgetown shear zone (Partington et al., 1995; Fetherston, 2004).

Pit sampling at Greenbushes was restricted to the C3 (Lithium pit) and C1 (Central lode) openpits (Fig. 11); access to the Cornwall pit farther to the north was not possible. Anecdotally, mine geologists note a difference in spodumene crystal size, with spodumene crystals in the C1 pit generally larger than spodumene in the C3 pit (Husein Al Shakarji,

written com., August 2020). Representative examples of bulk material collected from the C3 and C1 pits are shown in Figure 13, with a detailed description of the pit samples provided in Appendix 1.

TIMA mineral mapping results, as detailed in Appendix 4, confirmed the dominant quartz–spodumene mineralogy of the C3-300 series and C1-100 series samples (Fig. 13). These are representative of high-grade, Li-zone pegmatite that display a similarly dominant spodumene–quartz textural intergrowth as mapped for Li-zone samples in C3DD024 drillcore (Appendix 4; Fig. 12 in TIMA mineral maps for selected samples). The similar foliated texture of the low-grade, Na-zone, albite–pegmatite example, C3-100, is texturally comparable to the inferred zone of mylonization in drillcore C3DD024 as exemplified by sample #241175 (e.g. Appendix 4) and supports localized re-crystallization and pegmatite deformation in the C3 pit.

A feature of the C1, high-grade, Na- and Li-zone samples is the occurrence of megacrystic (+10-cm sized), tabular spodumene as white, pale-grey and pink crystals (Fig. 13). The poikiloblastic nature (i.e. symplectic texture) and smaller size of spodumene in samples collected from the C3 pit suggests the relatively rapid and synchronous crystallization of spodumene and quartz (Fig. 13). The similarity of the graphic spodumene–quartz texture mapped in samples collected from the high-grade zone in the C3 pit to that mapped in the

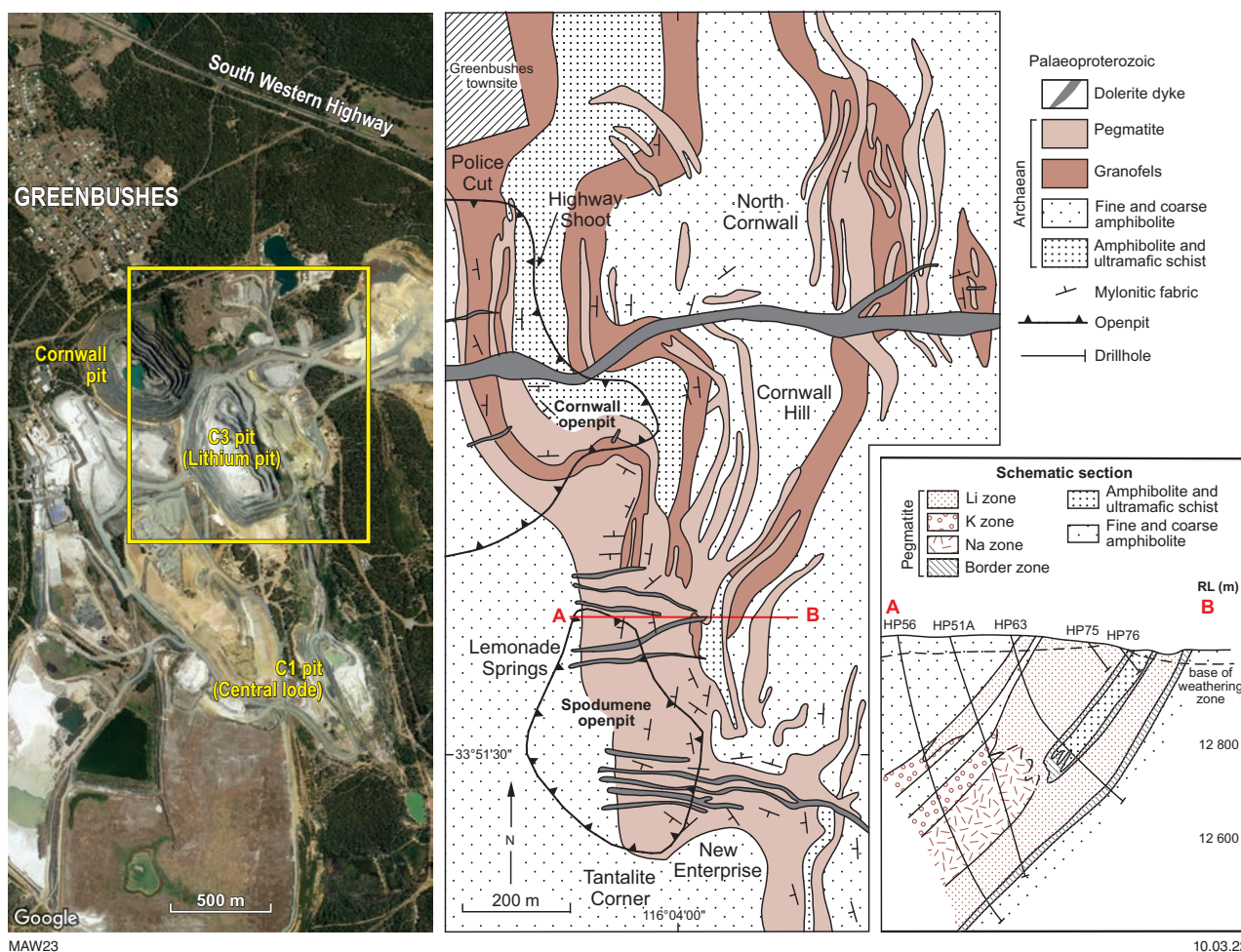
upper part of drillcore C3DD024 (Fig. 12) is discussed further in section, Pegmatite mineral fractionation. In contrast, the tabular nature of spodumene at C1 indicates that spodumene formed first prior to final cooling of the pegmatite.

Mt Cattlin

Setting

The Mt Cattlin pegmatite, also known as the Cattlin Creek pegmatite, is situated about 2 km north of Ravensthorpe and 400 km southeast of Perth (Fig. 3). The deposit occurs at the southeast margin of the Yilgarn Craton within the Southern Cross Domain of the Youanmi Terrane (Blewett et al., 2010; see Fig. 14).

The pegmatite at Mt Cattlin is a spodumene-rich, Ta-bearing body, hosted by the Ravensthorpe quartz diorite and greenstone belt (Fig. 14), where the granitic rocks are dated at about 3.0 – 2.95 Ga (Myers, 1993). The Ravensthorpe greenstone belt is restricted to the north-closing, south-plunging Beulah synform (Witt, 1999; Porter, 2017). The eastern and western limbs of the Beulah synform define the Carlingup and Cocanarup domains, respectively (Porter, 2017). Both are composed of quartzo–feldspathic gneiss, schist, iron formation of metasedimentary origin and 2.96 Ga felsic and ultramafic volcanic rocks (Porter, 2017).



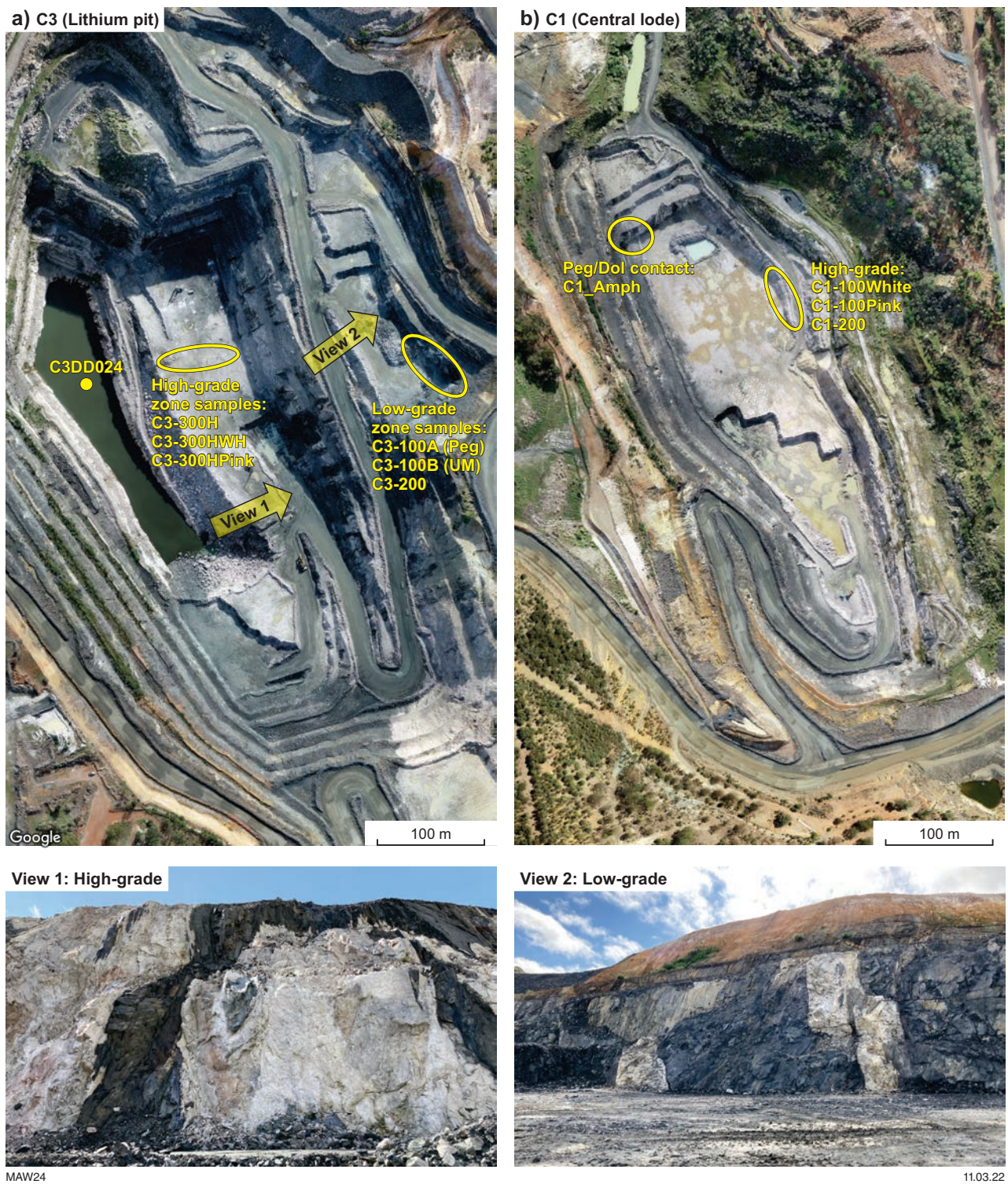


Figure 11. Aerial views of the: a) C3 (Lithium pit); and b) C1 (Central lode) openpits at Greenbushes pegmatite mine. Sample locations, in low-grade and high-grade zones, are indicated by yellow ovals in the C1 and C3 pits. Sample names and descriptions are provided in Appendix 1. At the pegmatite–dolerite contact (Peg/Dol) in the C1 pit, an example of the exposed amphibolite (C1-Amp) was sampled. The direction of views 1 and 2 in the Lithium pit show exposure of the pegmatite. Location of drillhole C3DD024 (Appendix 13) is shown by the red dot in the (submerged) section of the pit floor in the Lithium pit. Aerial views of the C3 and C1 pits provided by Greenbushes Operations (Husein Al Shakarji, Mine Geologist, August 2020)

Greenbushes: C3DD024

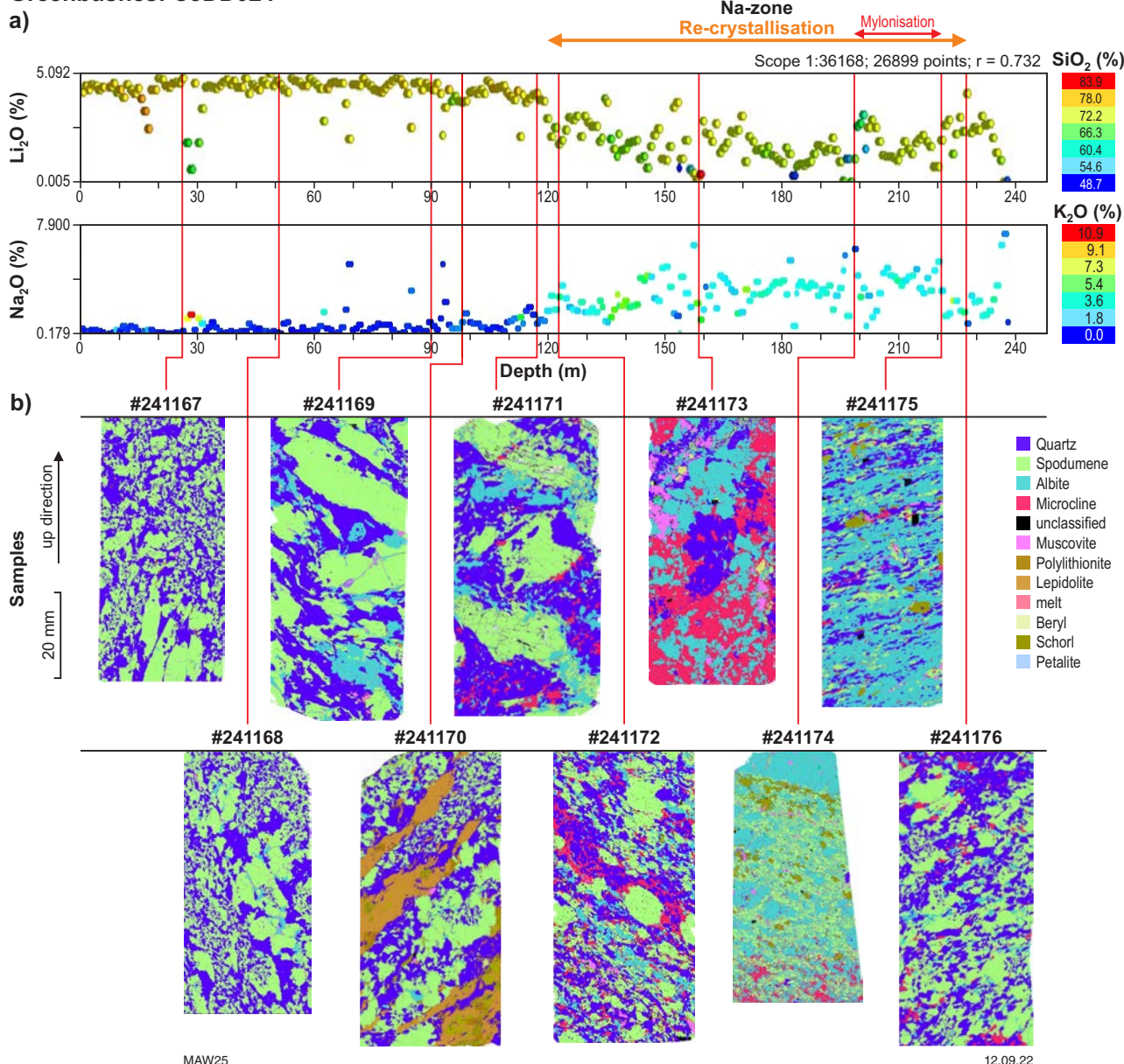


Figure 12. For drillhole C3DD024: a) Plot of the bulk rock Li₂O and Na₂O contents with depth in drillcore C3DD024; and b) TIMA mineral maps of selected (e.g. #241168) core intervals. Weight percent Li₂O and Na₂O values coloured by corresponding wt% SiO₂ and K₂O contents. Red arrows locate core intervals selected for detailed characterization in present study. Corresponding TIMA mineral maps of each interval are presented below the depth log plots to aid visualization of the mineralogical and textural evolution of the drillcore with depth (see mineral legend). Re-crystallization and heterogeneous deformation within the Na zone (see grey-shading) is evidenced by a decrease in spodumene grain size at the start of the Na zone (#241172) and development of mylonitic-type textures towards the base of the Na zone (e.g. #241174 and 241175) that impart a well-developed foliation

The main mineralized body occurs as a 1–20-m thick, shallow-dipping to flat-lying pegmatite dyke (Area = 1 x 1.5 km; Fig. 14) near the Beulah synform axis. Multiple, flat-lying Li–Ta pegmatites occur below the main pegmatite (Porter, 2017). Tantalum mineralization is mainly confined to a high-grade zone of Ta-rich lenses and pods (Fetherston, 2004).

All dykes are hosted by the Archean Annabelle Volcanics, a sequence of metamorphosed ultramafic, mafic and felsic rocks (Porter, 2017), with dating of rhyolite in the Annabelle Volcanics at 2989 ± 11 Ma (Witt, 1999). To the east, another swarm of north-trending pegmatites intrude both the Annabelle Volcanics and the adjoining Archean,

calc-alkaline Manyutup Tonalite (Fetherston, 2004). At Kundip, approximately 18 km southwest of Ravensthorpe, coarse-grained tonalite was dated at 2965 ± 12 Ma (U–Pb zircon) (Witt, 1999). In the same area, a tonalite porphyry dyke was dated at 2989 ± 7 Ma (zircon U–Pb) identical to the reported age of the Annabelle Volcanics (Witt, 1999). The Ravensthorpe pegmatite swarm may be related to a late-phase, Archean (Sapkota and Wyche, 2022) granite (quartz-monzonite) located about 7 km to the northeast (Fetherston, 2004).

The flat-lying, tabular pegmatite sheets at Mt Cattlin are grouped into the Western Pegmatite Sheet exposed in the Dowling pit and the Eastern Pegmatite Sheet exposed in the

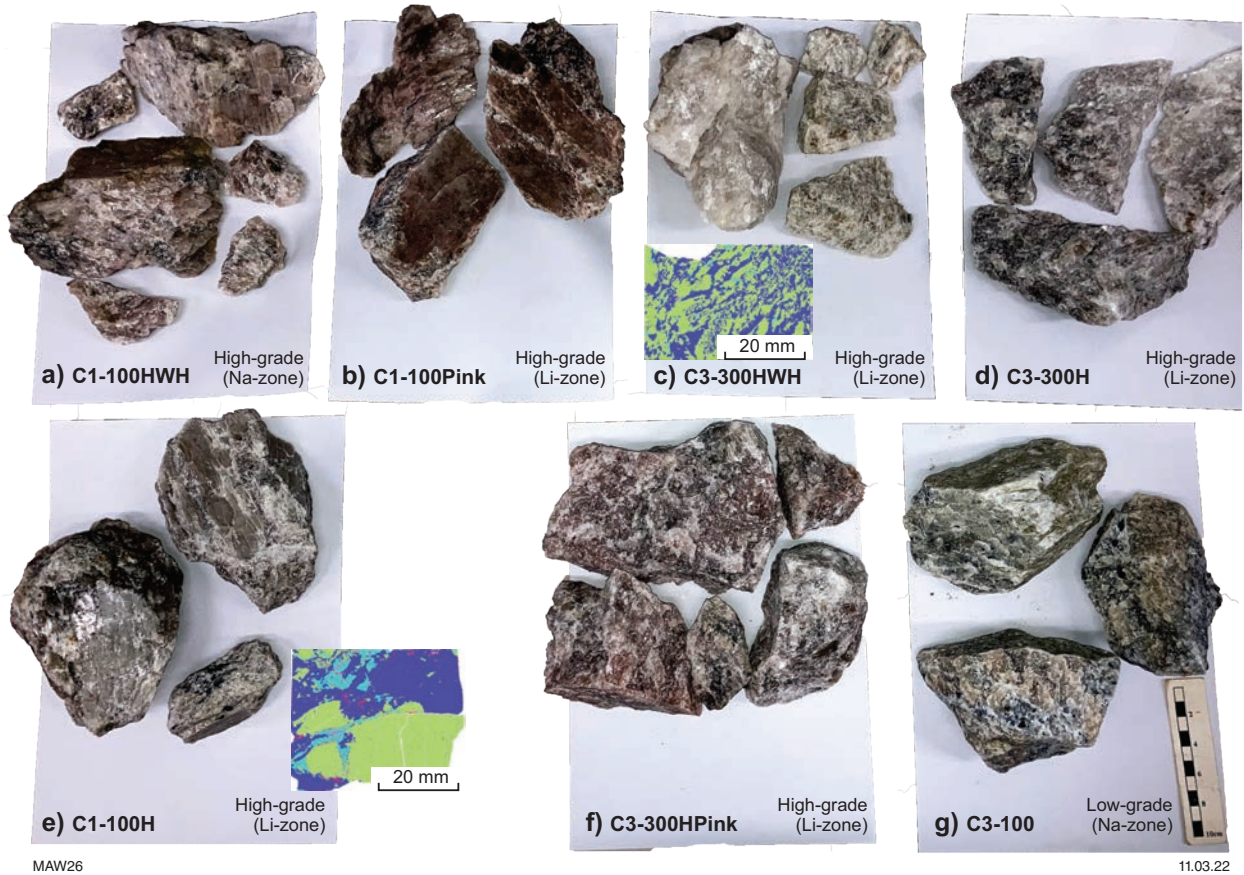


Figure 13. Representative examples of pegmatite from the C3 and C1 pits at the Greenbushes Deposit. Pegmatite material includes examples from the Li and Na zones. Scale bar with sample C3-100 (g) is 10 cm long (marked in 1 cm intervals). TIMA mineral mapping highlights the markedly (e) larger crystal size of tabular spodumene in the high-grade, Li zone at C1 compared to the smaller, lath-like spodumene in the (c) high-grade, Li zone at C3 (green = spodumene, dark-blue = quartz, pale-blue = albite). All C3 and C1 pegmatite samples shown here were included in the liberation and chemical processing study as described in section, Assessment of physical and chemical processing behaviour of LCT pegmatites

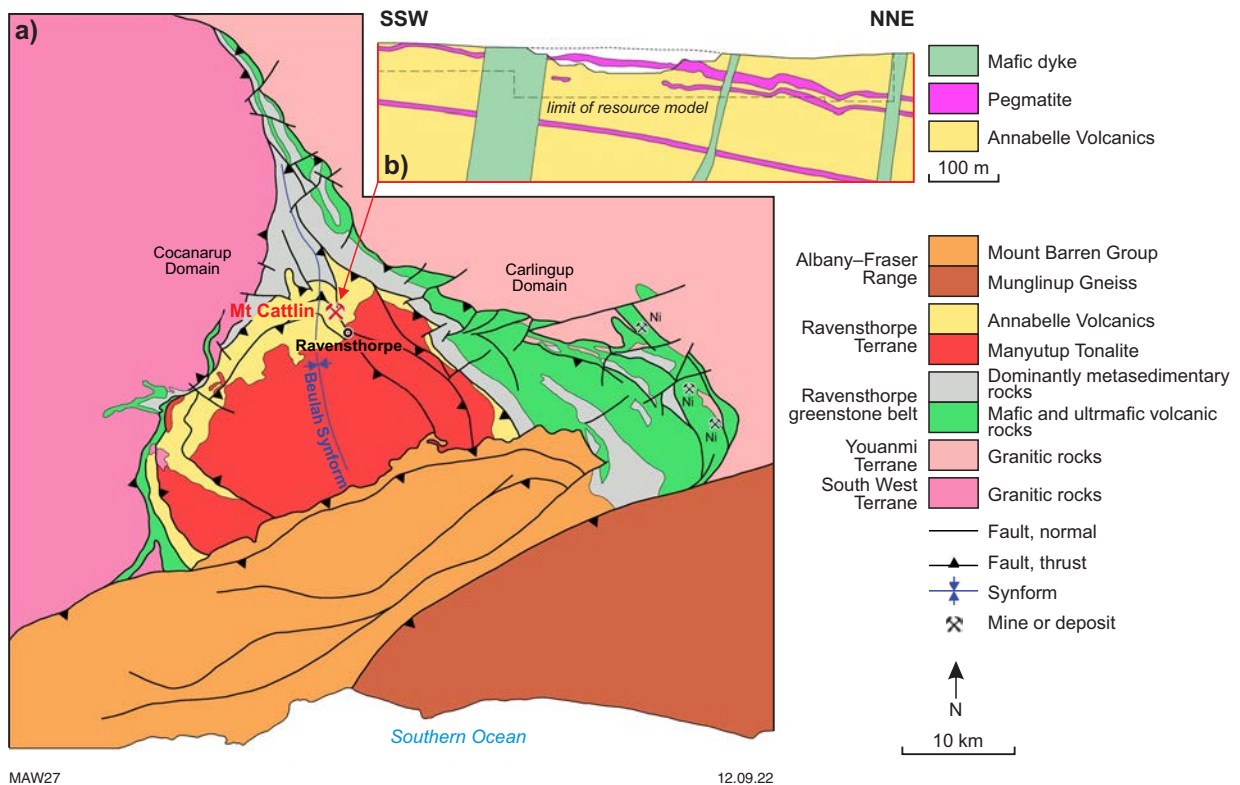


Figure 14. Simplified geological map of the Ravensthorpe district showing: a) the location and setting of the Mt Cattlin Li-Ta pegmatite deposit; with b) inset of an oblique cross-section, oriented south-southwest to north-northeast, showing the flat-lying, sheet-like nature of the Mt Cattlin Deposit. After Porter (2017)

northwest (e.g. Stage 1F) and to the southeast (2SE Stage 1) as denoted by Galaxy Resources (e.g. Fig. 14; Urgine, 2016). These authors describe important mineralogical and textural differences between the Western and Eastern Pegmatite Sheets. Primary spodumene mineralization in the Western Pegmatite Sheet is hosted by two zones that comprise nearly 75% by volume of the deposit, with an extremely coarse-grained (megacrystic) spodumene zone that comprises about 80% of mineralization overlying a medium-coarse grained spodumene zone (Urgine, 2016). In both units, green spodumene (i.e. partially altered) predominates over white–grey (i.e. unaltered) spodumene. Spodumene alteration is largely restricted to the western edge of the sheet, where the pegmatite sheet abruptly terminates against a north-northwesterly trending fault (Urgine, 2016).

Though uncommon to rare in the Mt Cattlin pegmatite types examined in the present study, the main Ta-bearing phases identified were columbite–tantallite (e.g. MC750 and MC1900) and microlite (e.g. MC1600_B1/B4) (Appendix 3). In addition, a single, large (500 µm), complex, Nb-depleted, Ta–(U?)–oxide phase was mapped in MC1500 (Appendix 4). A conspicuous feature of the main albite–spodumene pegmatite is the extensive alteration of spodumene, which is described in more detail in section, Spodumene–cookeite alteration.

The megacrystic spodumene–albite pegmatite is laterally extensive and is the main pegmatite type occurring in the Eastern Pegmatite Sheet (Urgine, 2016). Spodumene alteration is less well developed with about 60% white to pale-grey spodumene and 40% green spodumene. In addition, Urgine (2016) describes locally variable lepidolite mineralization, which is more important in the central eastern pegmatite sheet (e.g. Stage 1F), and a locally developed K-feldspar zone that occurs mainly in the Western Pegmatite Sheet. This contrasts to the occurrence of a coarsely crystalline, basement albitic zone, which is more uniformly developed across both pegmatite sheets (Urgine, 2016).

Sampling and characterization

Sampling at Mt Cattlin was mainly from two central pit locations as shown in Figure 15. Additional samples were also collected from the Dowling pit to the west and from the ROM pad (Appendix 1). Samples from the ROM pad consisted mainly of fragments of tabular, pale-grey and green spodumene megacrysts (+20 cm long) (Appendix 1). Pegmatite material collected across the Mt Cattlin Deposit hosts spodumene as fragments of acicular, or more typically lath-like, megacrysts, with pegmatite material collected from the Dowling pit and the SE pit (2SE Stage 1) representative of the megacrystic, spodumene–albite pegmatite zone (Fig. 16). Pegmatite collected from the Stage 1F pit is also representative of the spodumene–albite pegmatite with locally developed lepidolite mineralization (Fig. 16).

Megacrystic spodumene exhibits marked differences in colour and various alteration textures (Fig. 16). Unaltered spodumene is generally pale-grey, whereas partially altered spodumene is green–grey and may display a darker green alteration rim along crystal margins (Fig. 16). As pseudo-morphic alteration progresses to completion, spodumene displays a massive dull, green–black or waxy-

mottled appearance (Fig. 16). Unaltered or partially altered spodumene is mainly hosted by a highly fractured, pale-blue albite–quartz matrix (with minor Li-mica/muscovite and accessory tourmaline) compared to the massive, milky white (secondary?) albite matrix where spodumene alteration has gone to completion (Fig. 16).

Such alteration is consistent with previous descriptions of altered pegmatite mineralogy at Mt Cattlin, where Grigson (2011) and Urgine (2016) described the alteration mineralogy as (secondary) finely crystalline muscovite. Less commonly, spodumene may be replaced by finely crystalline lepidolite, evidenced as pink spodumene (e.g. Grigson, 2011); examples of such altered spodumene were not collected in the present study.

However, TIMA mineral mapping of examples of megacrystic spodumene–albite pegmatite (e.g. Appendix 4) demonstrate that spodumene alteration is mineralogically complex (Appendix 4; Fig. 16), where replacement is predominantly a fine-grained mixture of secondary micaceous phases (e.g. MC1200; Fig. 16). In comparison, where spodumene replacement is near completion, pseudo-morphic alteration by intimately associated, secondary albite+lepidolite/polyolithionite (e.g. as for MC1600, Appendix 4) or by patchy albite–quartz–lepidolite/polyolithionite replacement, which produces the distinctive waxy-mottled texture, may occur (e.g. MC1900; Fig. 16). Element distribution mapping clearly shows that alteration is associated with coincidentally elevated K and Mg contents (Appendix 4). A more detailed discussion of spodumene alteration, across all LCT pegmatites investigated in the current study, is provided in section, Spodumene morphology and alteration: indicators of pegmatite crystallization evolution.

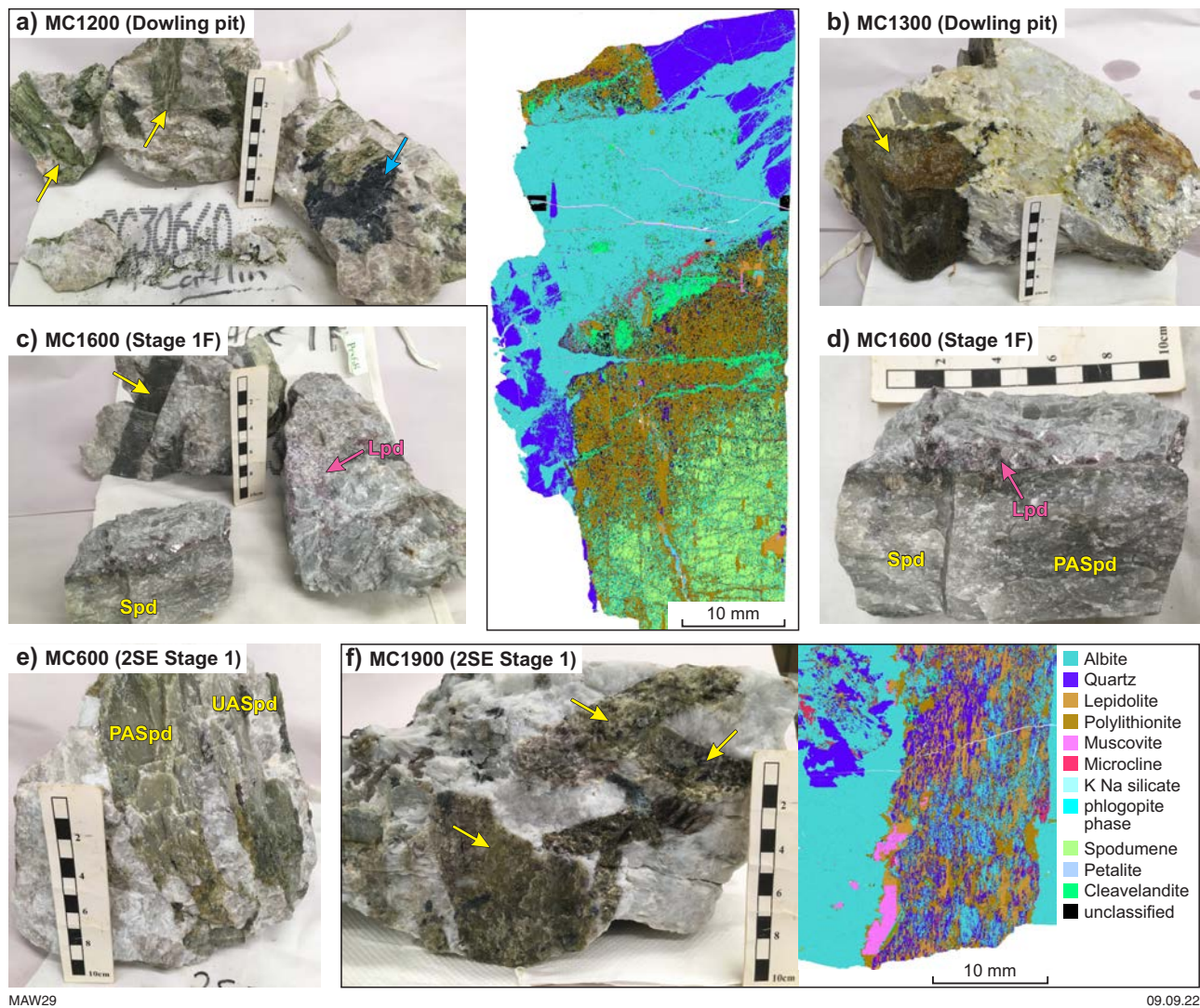
LCT pegmatites of the goldfields

Due to the proximity of several rare-element pegmatites to the major regional centre of Kalgoorlie–Boulder and their occurrence in the eastern Yilgarn, the regional geology and location of the Sinclair Caesium, Dome North, Bald Hill, Mt Marion and Londonderry pegmatites are shown together in Figure 17. The Sinclair Caesium, Dome North, Mt Marion, Londonderry and Lepidolite Hill pegmatites occur within the Coolgardie Domain of the Norseman–Wiluna greenstone belt in the Kalgoorlie Terrane (Fig. 17). The Bald Hill pegmatite occurs near the western margin of the Kurnalpi Terrane in proximity to the Ockerburry Fault hosted within the Belches Basin (Fig. 17). Kathleen Valley occurs to the north and along the western margin of the Kalgoorlie Terrane, within the Yakabindie Domain of the Norseman–Wiluna greenstone belt, in proximity to the Ida Fault (Fig. 17).

The Goldfields LCT pegmatites occur within the central-western portion of the Eastern Goldfields Superterrane (EGST), which comprises the Kalgoorlie, Gindalbie and Kurnalpi Terranes (Fig. 17), and the Burtville and Yamarna Terranes to the east (Cassidy et al., 2006; Witt et al., 2020). The EGST is highlighted by the Sm–Nd isotope model age map, where the Ida Fault separates the older crustal domain in the west from the younger crustal domains in the east (Champion and Huston, 2016; Witt et al., 2020). The Kalgoorlie Terrane forms a north-northwesterly to south-southeasterly trending



16



MAW29

09.09.22

Figure 16. Representative examples of pegmatite material collected from the Dowling pit (MC1200, MC1300), Stage 1F (MC1600) and 2SE Stage 1 (MC600, MC1900) locations at Mt Cattlin. In all sampled areas, megacrystic spodumene is variously altered as evidenced by various texture and changes in colour associated with alteration: a) randomly oriented, dark-grey-green spodumene laths (to +10 cm x 4 cm) hosted in fractured quartz-albite matrix with coarsely crystalline (≈ 1 cm) silvery-white muscovite booklets. Coarse-crystal groupings (to 6 cm) of dull (altered), blue-black tourmaline (blue arrow) with evidence of alteration. TIMA mineral map of partially-altered spodumene in the extreme left of the image; b) megacrystic (+10 cm) spodumene-lath fragments are completely replaced by massive brown-black, fine-grained micaceous(?) alteration (arrowed), hosted in a (secondary) albitic+minor quartz matrix; c) variously altered, acicular (green-black crystal – yellow arrow) and green-grey, lath-like spodumene (Spd) associated with highly-fractured, pale-blue-grey albite, pale-brown quartz and lilac lepidolite. The blocky, spodumene lath and in close-up; (d) displays a dark-green-grey alteration rim about the crystal margin, with <1 cm sized lepidolite flakes formed; e) lath-like, unaltered pale-grey spodumene (UASpd) and partially altered grey-green spodumene (PASpd) in massive, albitic-quartz matrix; and f) randomly oriented, waxy-mottled textured, tabular spodumene (arrowed), pseudo-morphically replaced by secondary albite-micaceous association. TIMA mineral map of a completely replaced spodumene in MC1900 highlights the mineralogically complex nature of alteration

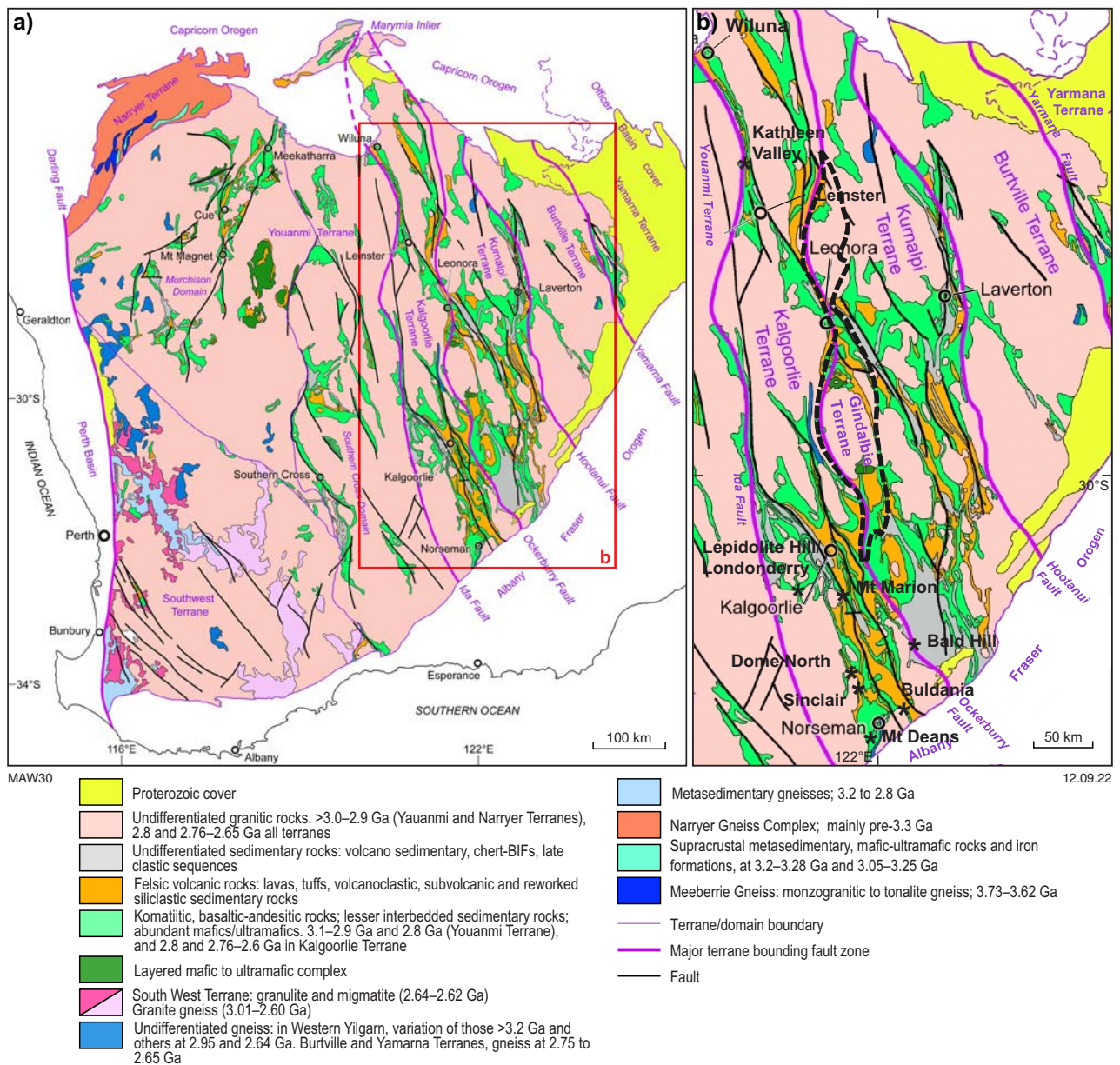


Figure 17. Geological and major structural features of, a) the Yilgarn Craton. Inset outline, b) shows detail of the regional geological setting and major fault systems of the Eastern Goldfields Superterrane (EGST), and location of the Sinclair, Dome North, Bald Hill, Mt Marion, Lepidolite Hill, Londonderry and Kathleen Valley LCT pegmatites. The thick, dashed outline more clearly defines the Gindalbie Terrane. Other pegmatite deposits, such as Lepidolite Hill, the Mt Deans (Aruma Resources) and Buldania (Liontown Resources) prospects are also shown. Mt Deans occurs within the Norseman Domain, while Buldania sits in the Kambalda Domain. Bald Hill intrudes metasedimentary rocks of the Mt Belches Formation, mapped as the grey, undifferentiated sedimentary rocks southeast of Kalgoorlie. Modified from the PorterGeo Database (2019) (<http://www.portergeo.com.au/>).

strip varying in width from 50 to 120 km and a length of ~800 km. Representing the westernmost structural element of the Eastern Goldfields Superterrane, the Kalgoorlie Terrane abuts the Youanmi Terrane across the east-dipping Ida Fault and is adjacent to the Kurnalpi Terrane across the east-dipping Ockerburry Fault (Fig. 17). The Kalgoorlie Terrane is interpreted as a basinal formation initiated by a rifting event at ~2810 Ma into which the younger sequences of the terrane were deposited (e.g. Wyche and Wyche, 2017; PorterGeo Database, 2019).

The Kurnalpi Terrane is considered to have formed as part of the same rift complex as the Kalgoorlie Terrane but with a different suite of supracrustal formations, related to calc-alkaline volcanism (e.g. Witt et al., 2020). Exposed over a strike length of 650 km and varying in width from ~50 to 150 km, the Kurnalpi Terrane abuts the older Burtville Terrane to the east and its eastern margin is interpreted to define the eastern extent of the Kalgoorlie–Kurnalpi rift (Witt et al., 2020). The similarity of crystallization ages and Nd signatures of the oldest rocks in the Kalgoorlie and Kurnalpi Terranes to granites and greenstones of the Youanmi Terrane is interpreted to indicate that attenuated crust of the Youanmi Terrane forms the basement to supracrustal rocks of the Kalgoorlie and Kurnalpi Terranes (Czarnota et al., 2010).

Sinclair Caesium Deposit

Setting

The history and geology of the Sinclair Caesium Deposit is described in detail by Crook et al. (2019). The deposit is situated 125 km south-southeast of Kalgoorlie or 35 km north-northwest of Norseman, within the Coolgardie Domain of the Norseman–Wiluna greenstone belt. The southern extent of the Coolgardie Domain is marked by the occurrence of two granitoid bodies, the 2690–2664 Ma Pioneer Monzogranite (formerly referred to as the Pioneer Dome) and the 2687 Ma Burra Monzogranite (formerly referred to as the Widgiemooltha Dome) (Hall, 2022a). The east–west trending Proterozoic Binneringie Dyke (c. 1258 Ma) transects the sequence between the Pioneer and Burra Monzogranites. The Pioneer Monzogranite is inferred to be younger than the Burra Monzogranite as the porphyritic Pioneer Monzogranite Monzogranite lacks the foliation evident in the Burra Monzogranite (Griffin, 1989). The Pioneer Dome core intrudes the 2664 ± 5 Ma Fifty Mile Tank Gneiss (Nelson, 1997), Archean and a younger sedimentary sequence (Crook et al., 2019).

Pegmatites have preferentially intruded the Kalgoorlie Group greenstone sequence along a 20-km long strike length, faulted on the eastern margin of the Pioneer Dome (Fig. 18). With at least 13 pegmatite clusters identified, including LCT-types, the pegmatite dykes form a narrow (<1 km wide) north–south trending corridor along the eastern flank of the Pioneer Dome (Crook et al., 2019). Evidence for several episodes of pegmatite intrusion is shown by less deformed pegmatites crosscutting more deformed pegmatites (Crook et al., 2019).

The pegmatites are zoned mineralogically with cores containing quartz, microcline, Li–micas lepidolite and

zinnwaldite, and petalite and pollucite and contact zones limited to quartz, K/Na-feldspar and muscovite (Fig. 18; Crook et al., 2019). Massive mono-mineralic lenses of pollucite ranging from 2 to 10 m in length typically occur adjacent to quartz and are nearly always rimmed by Cs-bearing clays. Lithium mineralization also occurs in the pegmatite cores, hosted by massive lepidolite, petalite, eucryptite, zinnwaldite and rarer amblygonite (Crook et al., 2019).

Discovered in 2016, the Sinclair Caesium Deposit at the time represented only the third known, commercially viable source of Cs along with the Tanco Mine in Manitoba, Canada and the Bikita Mine, Zimbabwe (Crook et al., 2019). Now exhausted, Essential Metals (formally own by Pioneer Resources) are exploring the potential for further Cs mineralization in the area.

Sampling and characterization

As access to the Sinclair Caesium Deposit was not possible, a request was submitted (November 2020) to view drillcores PDD162, PDD174 and PDD179 at the Joe Lord Core library facilities, Kalgoorlie. The location of hole PDD162 is shown in Figure 18 and intersects the main Cs mineralization. The associated lithological logging (121412_135034_M63_665_WADL4_Lithology) and assay (121412_13509_M63_665_WADL4_XRD) reports, initially prepared by Pioneer Resources Ltd., were used to aid drillcore sampling to target selected intervals of interest for follow-up study. Drillcore imagery from recent HyLogging line scans (completed in May 2020) for holes PDD162 PDD174 and PDD179 are presented in Figures 19, 21 and 23, respectively, with core intervals selected for analysis also shown (Figs 20, 22, 23). A brief description of the core intervals selected for sampling from PDD162, PDD174 and PDD179 is listed in Appendix 1.

Holes PDD162 and PDD174 intersect Cs mineralization as shown in depth plots of the Cs-assay data for both holes (Figs 19, 21), whereas PDD179 intersected the pegmatite wall zone (Fig. 23). It must be noted that for PDD162 and PDD174 prior sampling for assay analysis did not leave sufficient core to enable material for other analysis, particularly for PDD162, where only ¼-core remained. Hence, sampling of the Cs-mineralized zone in PDD162 was not possible. In addition, with few exceptions, for those core intervals that were selected across all three holes, only 25-mm diameter, polished rounds were prepared for study (e.g. refer to Appendix 4).

The pegmatite sequence intersected by PDD162 and PDD174 are representative of the complete pegmatite mineral zonation as described in the cross-section of the Sinclair pegmatite (Crook et al., 2019). In PDD162, fractured, blocky, perthitic microcline occurs over the 0 – 37.55-m depth interval, hosting two prominent muscovite bands, as an upper thinner band (0.55 m thick) and a deeper, nearly 2-m thick band (e.g. sample #3; Figs 19, 20; Appendix 4). This overlies and grades sharply to an 11-m thick zone of high-grade pollucite (Fig. 19; Appendix 1). Zones of pollucite–amblygonite–albite interspersed within the pollucite zone account for the varied Cs₂O content in the mineralized zone (Fig. 19). The pollucite zone transitions sharply to the underlying, approximately 12-m thick (from 49.35 to 63 m) lepidolite-bearing zone, as an albite–lepidolite–quartz pegmatite type

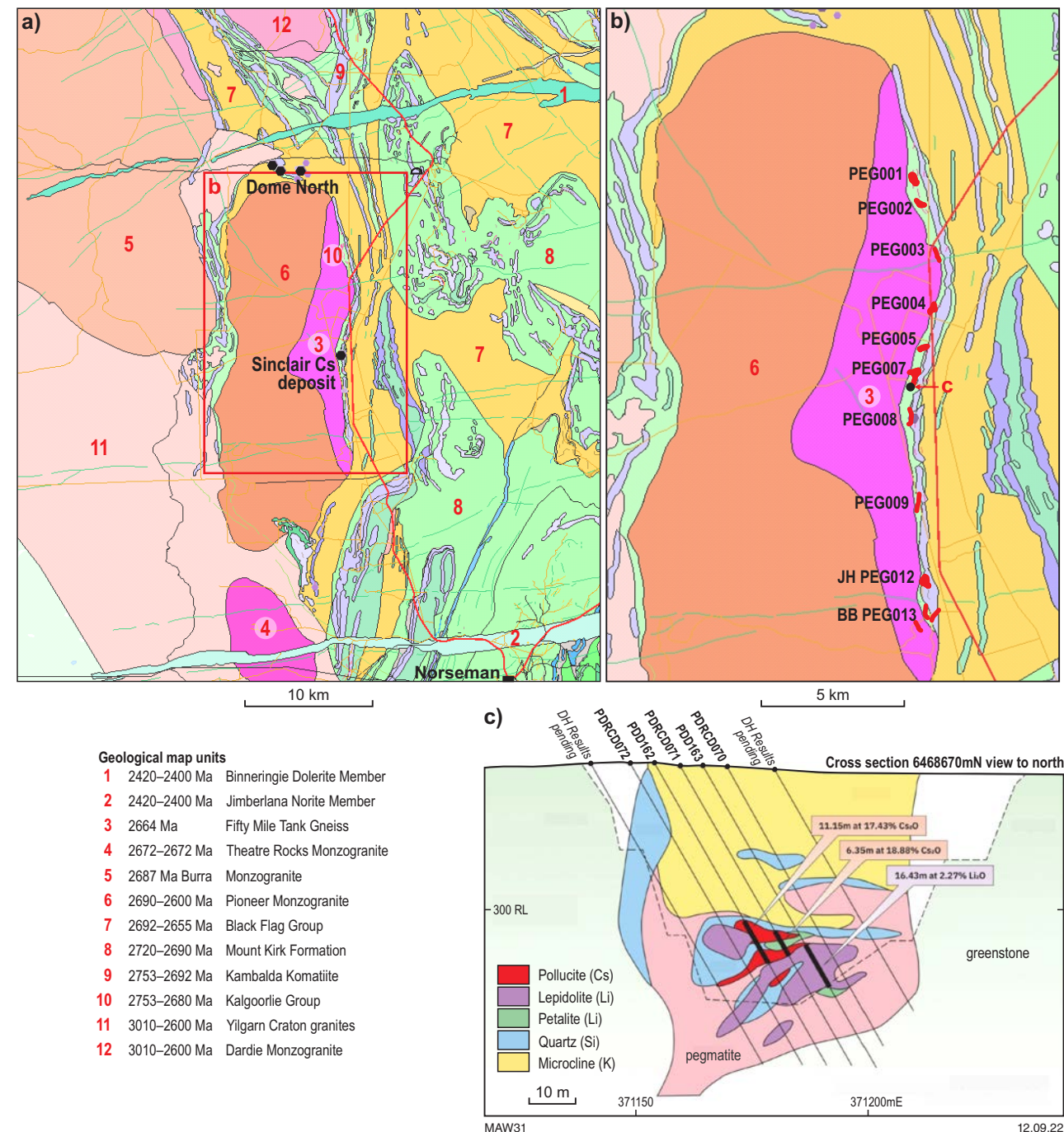


Figure 18. Geological setting of Sinclair Caesium Deposit and near-by Dome North pegmatite field: a) Image source from GSWA GeoView, 1:100 000 interpreted bedrock geology map. After: 1 (Wingate and Romano, 2022a); 2 (Sapkota, 2022a); 3 (Wyche and Sapkota, 2022a); 4 (Sapkota, 2022b); 5 (Hall, 2022a); 6 (Sapkota, 2022c); 7 (Hall et al., 2022a); 8 (Sapkota, 2022d); 9 (Hall and Wyche, 2020a); 10 (Wyche and Sapkota, 2022b); 11 (Wyche et al., 2022); 12 (Hall, 2022b); b) detailed view of north–south trending pegmatites emplaced in the Kalgoorlie Group along the eastern margin of the Pioneer Monzogranite; and c) geological cross-section of Sinclair in the area between pegmatites PEG007 and PEG008, as shown in b) at 6468670mN. The main mineralogical zones are identified, with drillhole PDD162 as sampled for this study highlighted. Cross-section modified from Batt et al. (2020)

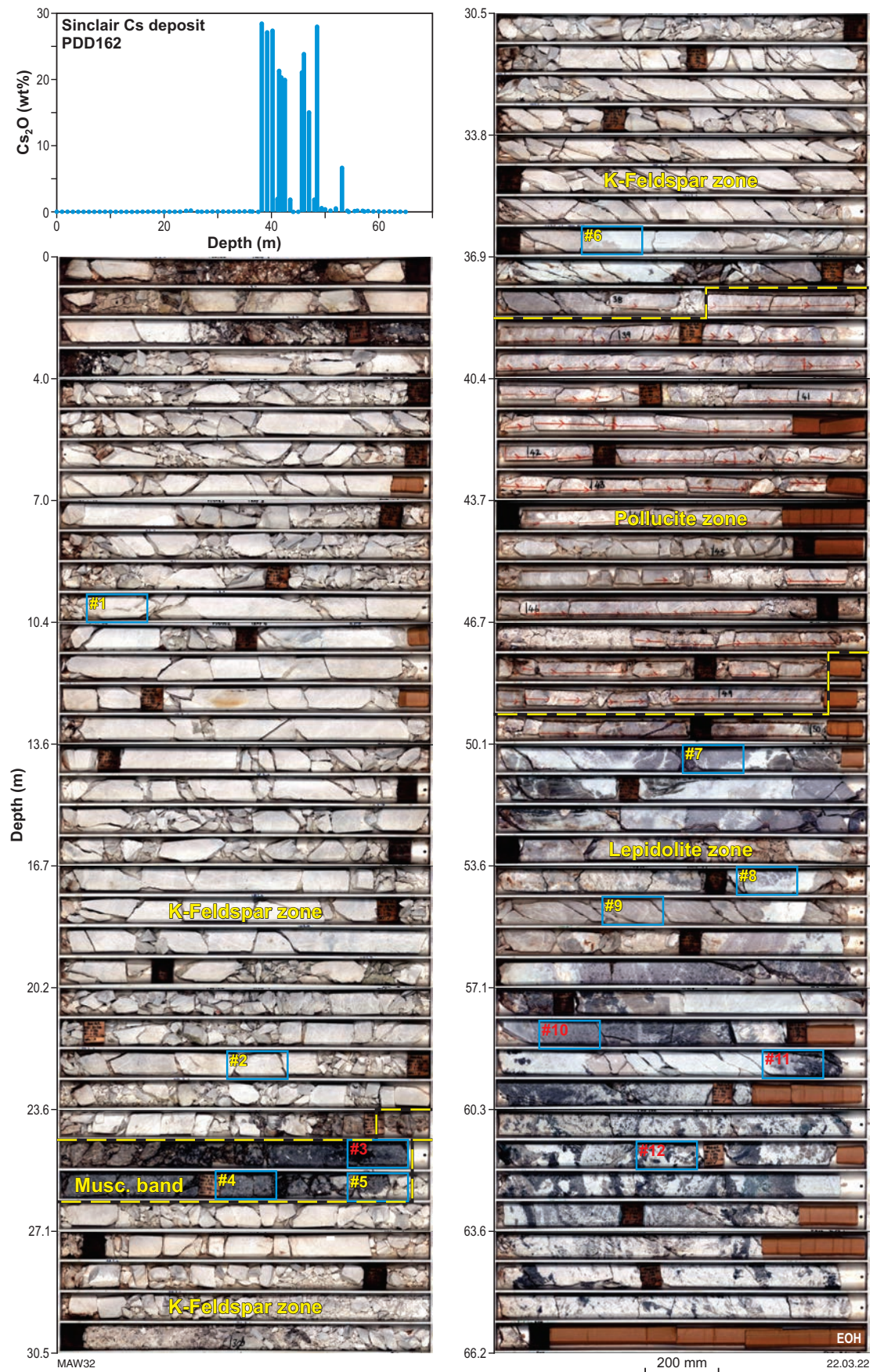


Figure 19. Drillcore imagery of PDD162. Yellow numbered blue rectangles (e.g. #4) denote core sections selected along the drillcore. Red numbered blue rectangles (e.g. #3) denote samples used for further analysis, such as TIMA mapping and mineral (Appendix 4). The dotted yellow outline denotes the zone of Cs (pollucite) mineralization also shown in the depth plot for assayed wt% Cs₂O contents. Other lithological zones are also indicated. No sampling from the Cs mineralized zone was allowed for this study. Core tray imagery was captured by line scanning using the CSIRO HyLogging™ system

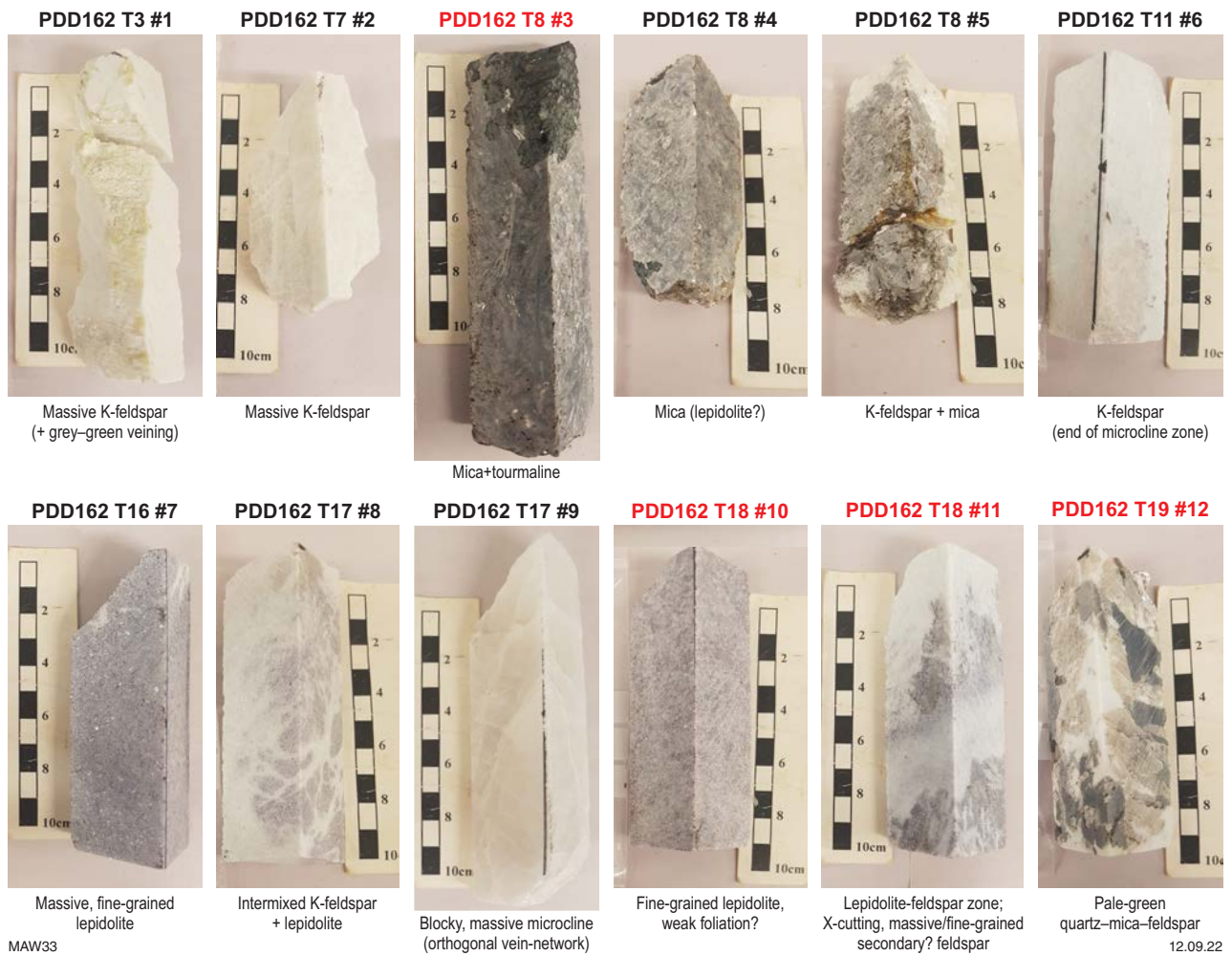


Figure 20. Close-up view of core sections sampled from PDD162. Core sections labelled in red were prepared for further analysis

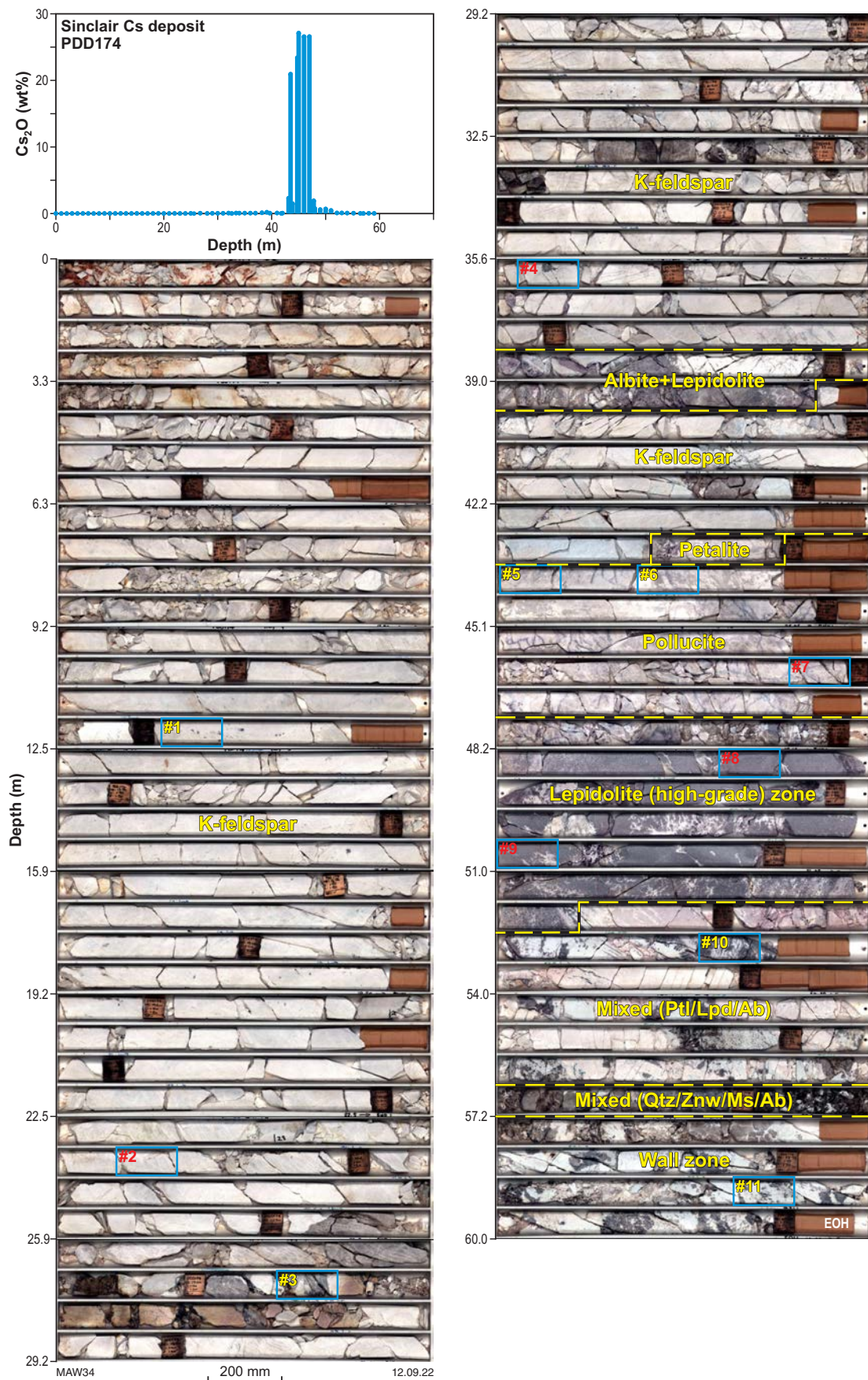


Figure 21. Drillcore imagery of PDD174. Yellow numbered blue rectangles (e.g. #1) denote core sections selected along the drillcore. Red numbered blue rectangles (e.g. #3) denote samples used for further analysis, such as TIMA mapping and mineral (Appendix 4). The dotted yellow outline denotes the zone of Cs (pollucite) mineralization also shown in the depth plot for assayed wt% Cs₂O contents. Other lithological zones are also indicated. Core tray imagery was captured by line scanning using the CSIRO HyLogging™ system



Figure 22. Close-up view of core sections sampled from PDD174. Core sections labelled in red were prepared for further analysis

(e.g. samples #9 and #10; Appendix 4) with lepidolite-free, quartz–albite zones hosting blocky muscovite books (e.g. sample #12; Fig. 19; Appendix 4).

The same mineralized sequence is intersected by PDD174 (Appendix 1) but the mineralized Cs-zone is hosted above and below by lepidolite-bearing zones, which in turn host Li mineralization as petalite, with the hanging wall lepidolite–petalite units comparatively thinner than the footwall units (Appendix 1).

The sequence intersected by PDD179 consists of the lower portion of an upper weathered ultramafic unit and an unaltered, 12-m thick, highly foliated footwall greenstone (metasediment – refer to slide #14; Appendix 4) hosting an approximately 43-m thick pegmatite unit (Appendix 1). Metasedimentary rocks are strongly foliated with amphibole, albite, biotite, zinnwaldite and minor sulphides (Appendix 4). The pegmatite consists of a highly fractured and mixed albite–quartz–microcline wall zone with variable muscovite that can be coarsely crystalline (e.g. sample #5; Fig. 23). The mixed wall zone continues below the greenstone unit (Appendix 1).

Semi-quantitative EDS analysis of the mica (muscovite, lepidolite and zinnwaldite) composition (F, Cs, Mn and Fe contents) in TIMA mineral maps of the Sinclair pegmatite (Appendix 4) are summarized in Table 4. Although the trace element compositions are similar, there are some important differences. Muscovite contains a moderate F content (2–3 wt%), comparable to zinnwaldite (3.3 wt%), whereas

lepidolite/polyolithionite has a tendency to contain the highest F content of about 6 wt% (Table 4). The Fe content in muscovite and lepidolite/polyolithionite was variably low to moderate, in contrast to the very high Fe content of zinnwaldite at about 13 wt% (Table 4). Caesium was not detected in muscovite, whereas all other micas showed consistently low contents in the range 0.4 – 0.7 wt% (Table 4). The significance of the observed distribution of Cs and how it relates to the mineral evolution at Sinclair is discussed in more detail in the section Caesium mineralization.

Table 4. Trace element (F, Cs, Mn, Fe) contents of mica in drillholes PDD162, PDD174 and PDD179 at the Sinclair Deposit

	Drillhole	F (wt%)	Cs (wt%)	Mn (wt%)	Fe (wt%)
Muscovite	PDD162	2-3	nd	0.1-0.2	3-4
	PDD174	3	nd	0.4	0.9
	PDD179	1.6-2.3	nd	0.06	0.66-2.5
Lepidolite	PDD162	3	0.5	0.5-1.5	nd
	PDD174	6	0.4-0.7	0.2-1.5	<0.8
	PDD179				
Polyolithionite	PDD174	6.5	0.6	0.6-1.5	0.8
Zinnwaldite	PDD179	3.3	0.6	0.5	13



Figure 23. Drillcore imagery of PDD179 (a, b). Yellow numbered blue rectangles (e.g. #3) denote core sections selected along the drillcore. Red numbered blue rectangles (e.g. #8) denote samples used for further analysis, such as TIMA mapping and mineral (Appendix 4). The main lithological units are indicated. Core tray imagery was captured by line scanning using the CSIRO HyLogging™ system. Close-up view of core sections sampled from PDD179 (c) are also shown with sections labelled in red prepared for further analysis

Dome North

Setting

The Dome North Lithium Project is situated approximately 48 km north-northwest of Norseman in the Coolgardie Domain of the Norseman–Wiluna greenstone belt (Figs 17, 18). Discovered in June 2019 by Essential Metals, the Dome North Lithium Project represents one of the newest pegmatite discoveries in Western Australia, with a current defined mineral resource of 11.2 Mt @ 1.21% Li₂O (Essential Metals, 2021).

Felsic–metasedimentary rocks of the 2692–2655 Ma Black Flag Group (Hall et al., 2022a), interfingering with greenstone units of the 2706 ± 36 Ma Kambalda Kommatiite (Foster et al., 1996), wrap around the northern margin of the Pioneer Monzogranite (Fig. 18), and define a regional, deformation fabric (Fig. 24). Multiple north-northeasterly trending faults are inferred in the northern host rocks, and this observation is consistent with a dominant north-northeasterly oriented fabric recorded in metasedimentary and greenstone units exposed along the eastern margin of the granitoid (Griffin, 1989).

The Dome North Lithium Project currently comprises three, subparallel, north-northwesterly striking, rare-element pegmatites located ~2 km north of the northern margin of the Pioneer Monzogranite (Fig. 24). The westernmost Heller pegmatite and the central Davy pegmatite, hosted by greenstone units of the Kalgoorlie Group, crosscut the regional fabric (Fig. 24). The largest, eastern Cade Deposit has intruded, en echelon style, subparallel to the regional fabric developed in the Black Flag group (Fig. 24; Jessica Booth, Essential Metals geologist, written com, December 2020). The north-northwesterly trending, steeply dipping (near vertical) Cade pegmatite has a strike length of 860 m and is up to 20 m in width (Fig. 25).

Sampling and characterization

Core sections from two drillholes were kindly provided by Essential Metals for inclusion in the present study. Holes PDRCD318 and PDRCD319 were drilled at the north-northeast extent of the main Cade pegmatite body with collars at local grid references X = 367588m, Y = 6486236m (#318) and X = 367966m, Y = 6486236m (#319). The holes are declined to the west and intersect the approximately 20-m thick pegmatite at relative levels of 220 m (#318) and 160 m (#319), approximately 60 m apart (Fig. 26).

Drillcore for each of the pegmatite sections intersected by PDRCD318 and PDRCD319 are shown in Figures 27 and 28, respectively, with sampling locations of core intervals examined also shown; an accompanying core description for each interval is provided in Appendix 1.

Hanging wall metasedimentary rocks (within 10 m of the pegmatite contact) in PDRCD318 are weakly foliated and mainly comprise quartz–biotite–albite(cleavelandite)–siderophyllite with minor almandine garnet and pyrrhotite detected by TIMA mineral mapping (Appendix 4). Footwall metasediments in PDRCD319 are more strongly foliated, with the foliation defined by intimately associated lobate and elongate grains of quartz and pyrrhotite, 200 x 1000 µm (e.g. Appendix 4).

The pegmatite intersection within PDRCD318 contains a 1-m thick petalite-rich zone consisting of massive petalite that grades into a predominantly muscovite–quartz–albite pegmatite, with subparallel bands of muscovite and coarsely crystalline (3–4 cm) green tourmaline (Appendix 1; Appendix 4). Textural evidence in the form of poikiloblastic intergrowths of quartz–spodumene–petalite provide an example of the formation of symplectic SQL (spodumene–quartz intergrowth, e.g. Bradley et al., 2017) where the intrusion crystallized along the spodumene–petalite-phase equilibrium line (Fig. 28). This is discussed in more detail in the section Pegmatite mineral fractionation.

For the Cade pegmatite intersected at depth by PDRCD319, the hanging wall contact zone consists of an equigranular spodumene-free quartz–muscovite, with subhedral, 1–2 mm sized, fractured garnet (almandine–spessartine) as the main accessory phase (Appendix 4). This grades into the main pegmatite body consisting of a quasi-homogeneous, quartz–spodumene–albite mineralogy with rare muscovite (Appendix 4.). Subparallel alignment of acicular, white spodumene imparts a conspicuous lineation as evident in the drillcore imagery (Fig. 29); in cross-section spodumene displays a mottled texture (Appendix 4). Albite is present as randomly distributed, uncommon blocky laths ranging from 2 to 5 cm in size (Appendix 1; Appendix 4).

Spodumene displays a distinct change in size in relation to proximity to the hanging wall and footwall contacts compared to the centre of the pegmatite body. Below the hanging wall contact zone, spodumene occurs as acicular crystals 3 x 0.5 cm in size, increasing to 5 x 0.5 cm in the central portion of the Cade pegmatite (e.g. sample #15; Appendix 3). Proximal to the footwall contact, spodumene again decreases in size (e.g. 2.5 x 0.5 cm; sample #19) becoming more lath-like, occurring as rare, stunted laths approximately 5–6 mm long at the top of the wall zone (e.g. sample #20; Appendix 1; Appendix 4).

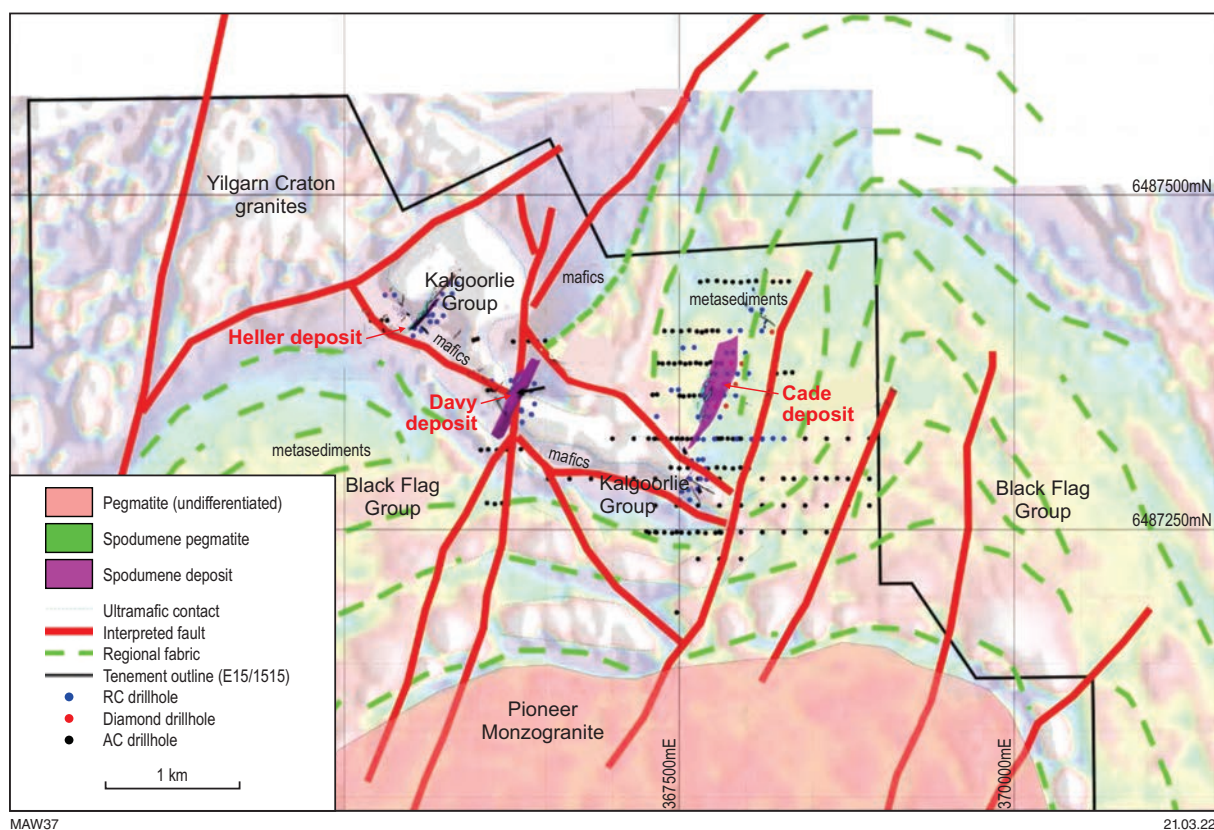


Figure 24. Aeromagnetic image of the Dome North Lithium Project area overlain by the main geological units and interpreted fault structure. Modified image provided by Essential Metals (Essential Metals, 2020)

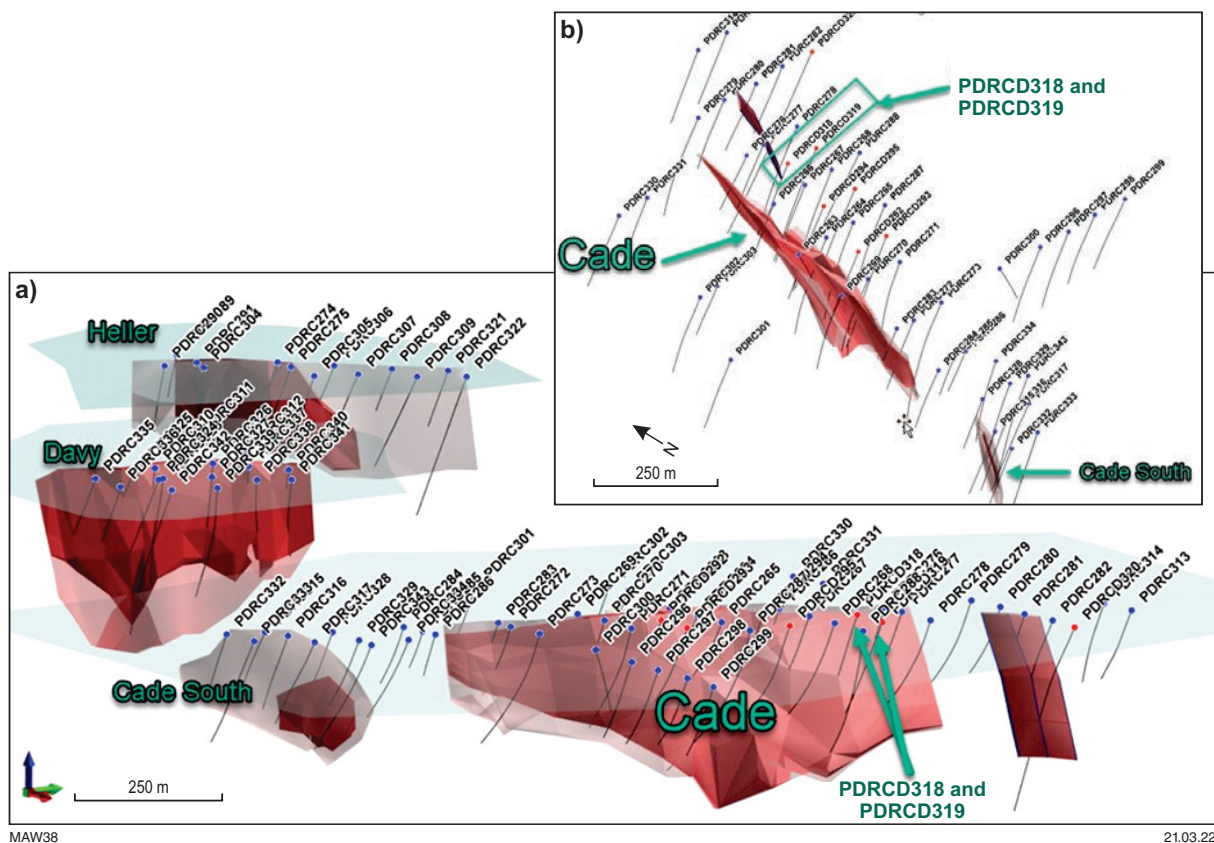


Figure 25. Perspective view of the Heller, Davy and Cade pegmatites towards: a) the northwest; and b) an aerial, oblique view of the Cade pegmatite. The location of drillholes PDRC018 and PCRD019 used in the current study are shown (arrowed). Image provided by Essential Metals (Jessica Booth, written com., December 2020)

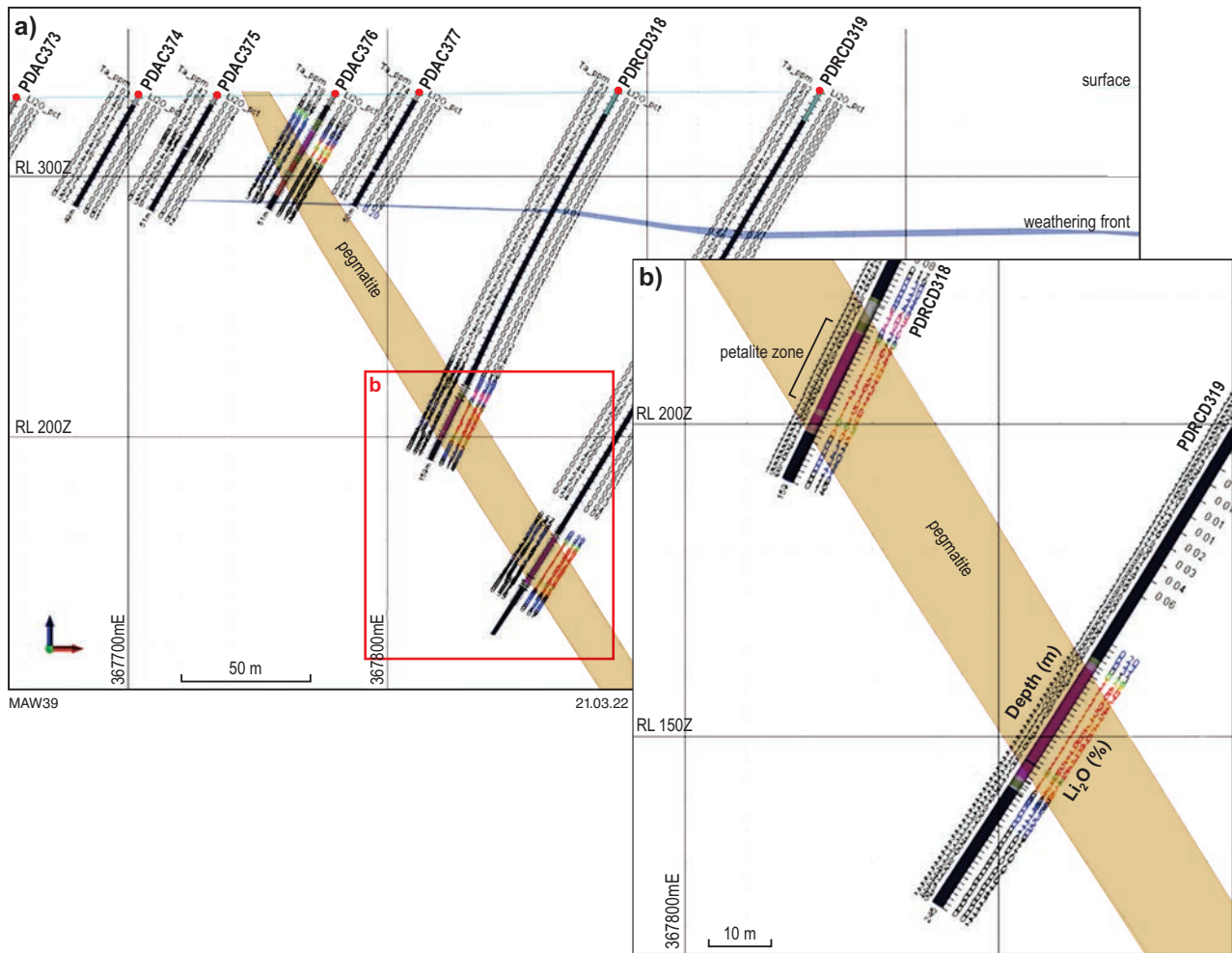


Figure 26. Cross-section on (a) local grid 6486236m showing drillholes PDRCD318 and PDRCD319 (boxed in red) intersecting a wire-frame projection of the Cade pegmatite (pink outline). Drillhole collars are indicated by the red dots along the surface trace (light-blue). The weathering front (base of oxidation) is shown in dark-blue and (b) detail of the zone of drillhole intersection with the pegmatite in purple and wall zone contacts in grey

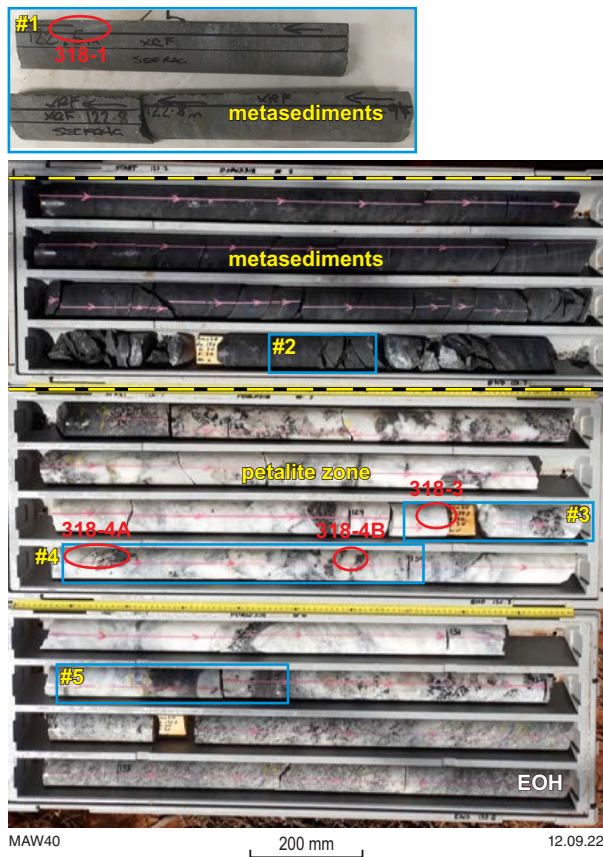


Figure 27. Zone of pegmatite intersection in core PDRCD318 at the Cade pegmatite. Blue rectangular outlines show the core intervals (#2–5) received by Curtin University for examination. No core tray imagery was available for section #1 (Tray #1). Instead, imagery of the core section is shown. Red ovals denote the location of samples prepared for detailed analysis (refer to Appendix 4)

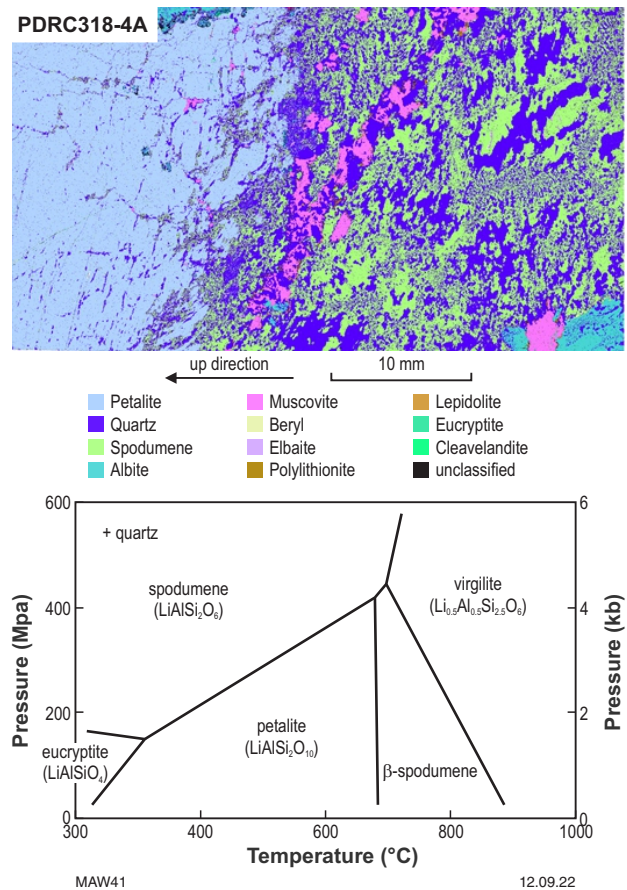


Figure 28. TIMA mineral map of sample PDRCD318-4 (@ 129.4 – 130.3 m) showing the spodumene–petalite crystallization contact. During cooling of the pegmatite, P – T conditions followed the spodumene–petalite reaction equilibrium enabling both phases to crystallize. Phase–equilibrium diagram modified from Bradley et al. (2017). Arrow shows the upward direction of the core sample

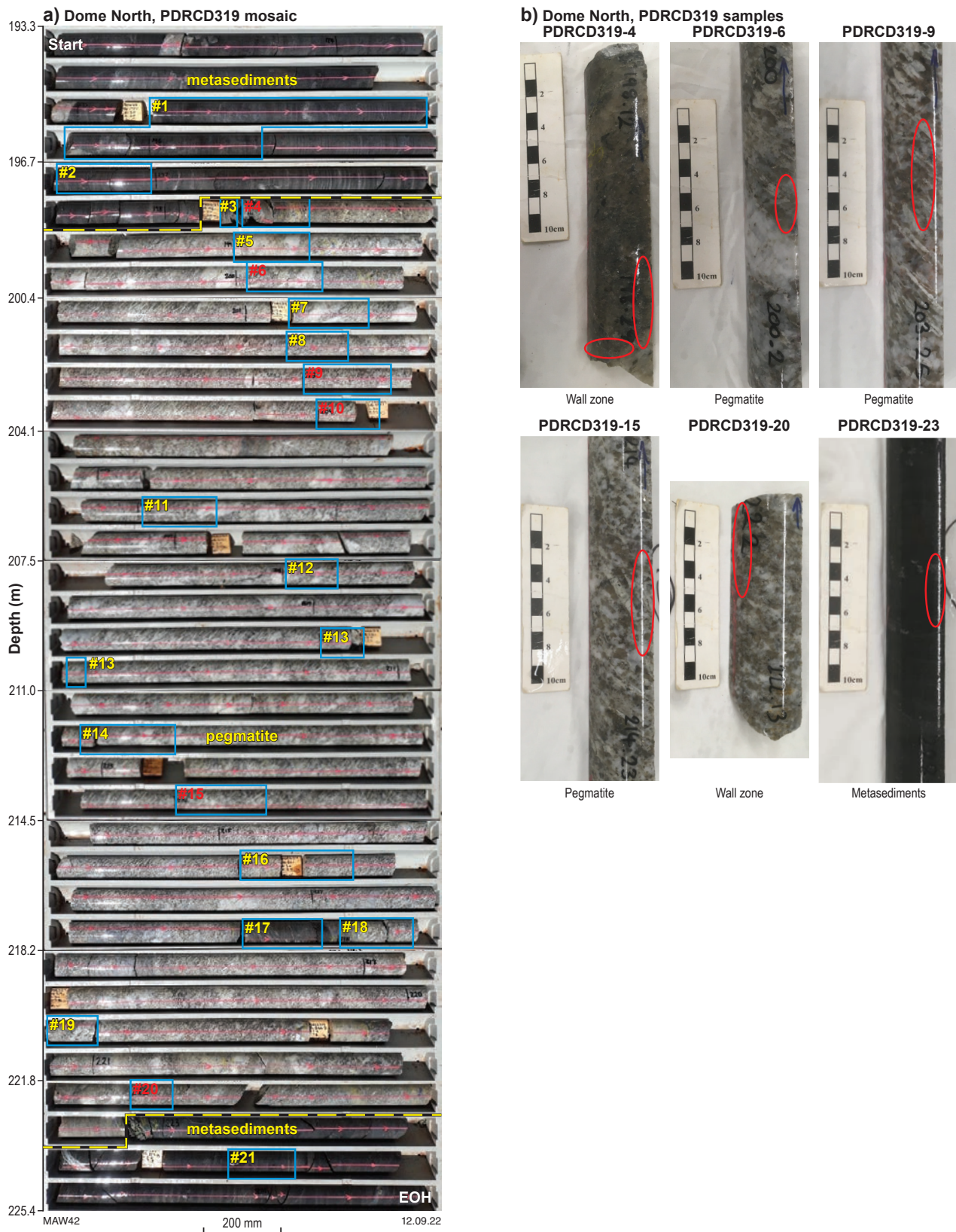


Figure 29. Zone of pegmatite intersection in core PDRCD319 at the Cade pegmatite. In a) yellow numbered blue rectangles show the core intervals made available by Essential Metals to Curtin University. Core intervals with the sample number highlighted in red were prepared as polished round mounts or slabs for further mineral analysis. The main lithological units are shown. In b) close-up views of the core sections selected for further analysis show the locations (red ovals) from which round or slab mounts were taken (refer to Appendix 4)

Bald Hill

Setting

The Bald Hill Deposit is located about 50 km southeast of Kambalda within the Kurnalpi Terrane of the Eastern Goldfields (see Fig. 17). The Ta-rich pegmatite is typically 1–8 m thick in the vicinity of the mine and varies from horizontal to gently west-dipping to a depth of about 30 m (Fetherston, 2004).

The main pegmatite unit strikes north–south and is surrounded by several, smaller subparallel pegmatites with a total strike length of 1245 m and width of 990 m with an overall depth interval of ~195 m (Tawana Resources NL and Alliance Mineral Assets Ltd, 2018). The Bald Hill pegmatites intrude into and crosscut foliation in metasedimentary host rocks of the 2666 ± 5 Ma (zircon U–Pb) Mt Belchers Formation (MBF) (<https://asud.ga.gov.au/search-stratigraphic-units/results/35605>), which are best exposed in the vicinity of the Randall Dome, a regional feature up to 30 km wide that incorporates units of the MBF and granitoid intrusions (Painter and Groenewald, 2001). The MBF is comprised of a distinct package of multiply deformed

metasediments ranging from wackestone to mudstone (Painter and Groenewald, 2001).

Bald Hill was commissioned in March 2018 with initial production of 155 000 tpa of spodumene concentrate. In early 2019, Bald Hill was reported to contain a total Li resource of 26.5 Mt at 1.0 wt% Li_2O and Ta resource of 4.4 Mt at 336 ppm Ta_2O_5 at a combined cut-off of 0.3 wt% Li_2O and 149 ppm Ta_2O_5 , respectively (Source: www.allianceminerals.com.au/projects/, viewed 21–02–2019). In July 2019, Alliance Minerals changed its name to Alita Resources. However, Bald Hill was placed under care and maintenance in August 2019.

Sampling and characterization

Sampling at Bald Hill was from the northern section of the main pit, with bulk material collected from low-grade (samples denoted as BH2 series) and high-grade zones (samples denoted as BH1 series), the locations of which are shown in Figures 30 and 31. Representative examples of low-grade pegmatite are shown in Figure 32. Randomly oriented, prismatic, lath-like spodumene megacrysts (+10–15 cm in length), as fragments of larger crystals, are

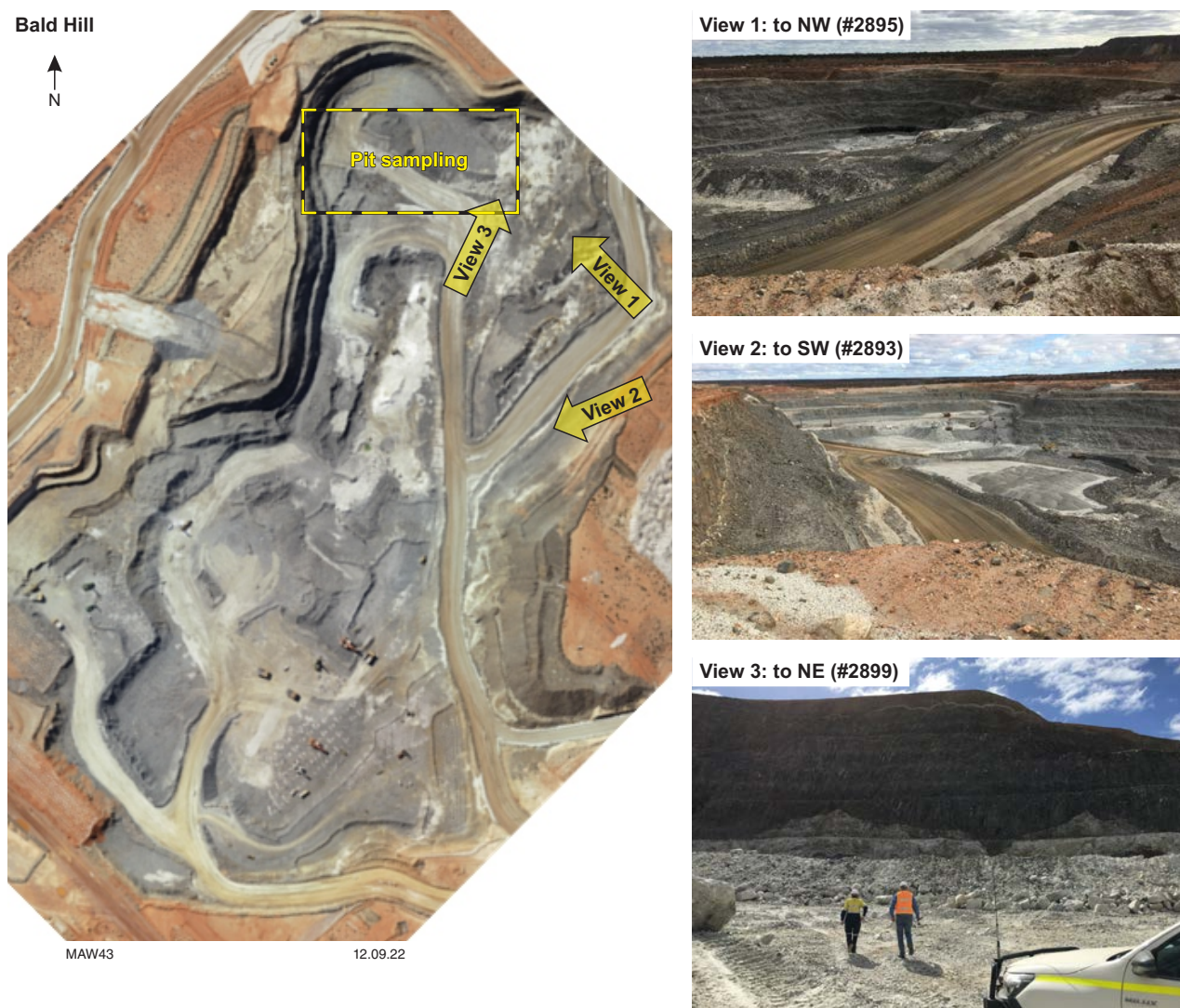


Figure 30. Aerial view of the Bald Hill mining pit with three views of the openpit taken in May 2019. Exposure of the flat-lying pegmatite is shown in View 3. The sampling area from the Bald Hill pit floor is marked by the dashed yellow outline in the aerial view

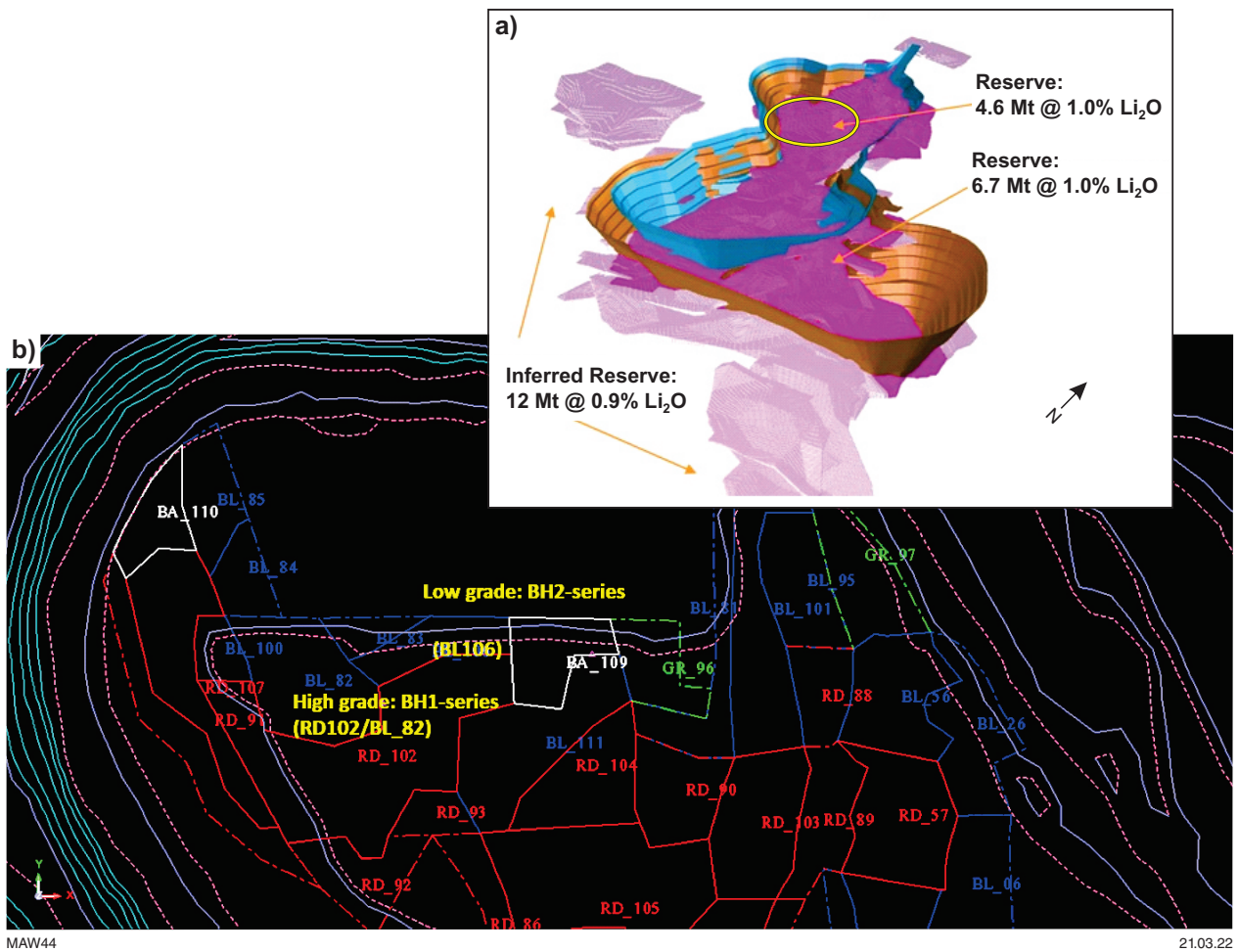


Figure 31. The Bald Hill pit with: a) oblique view of proposed pit design, with the blue pit shell denoting the current pit outline and a proposed pit outline shown in brown; and b) a wire-frame model of sampling locations on the pit floor. Samples were taken from high-grade (BH1-series) and low-grade (BH2-series) zones. Refer to Appendix 10 for more detailed sample description. Image kindly provided by Alliance Minerals. (Source of pit shell models: modified from AMAT JOGMEC Site Visit presentation, 2019)

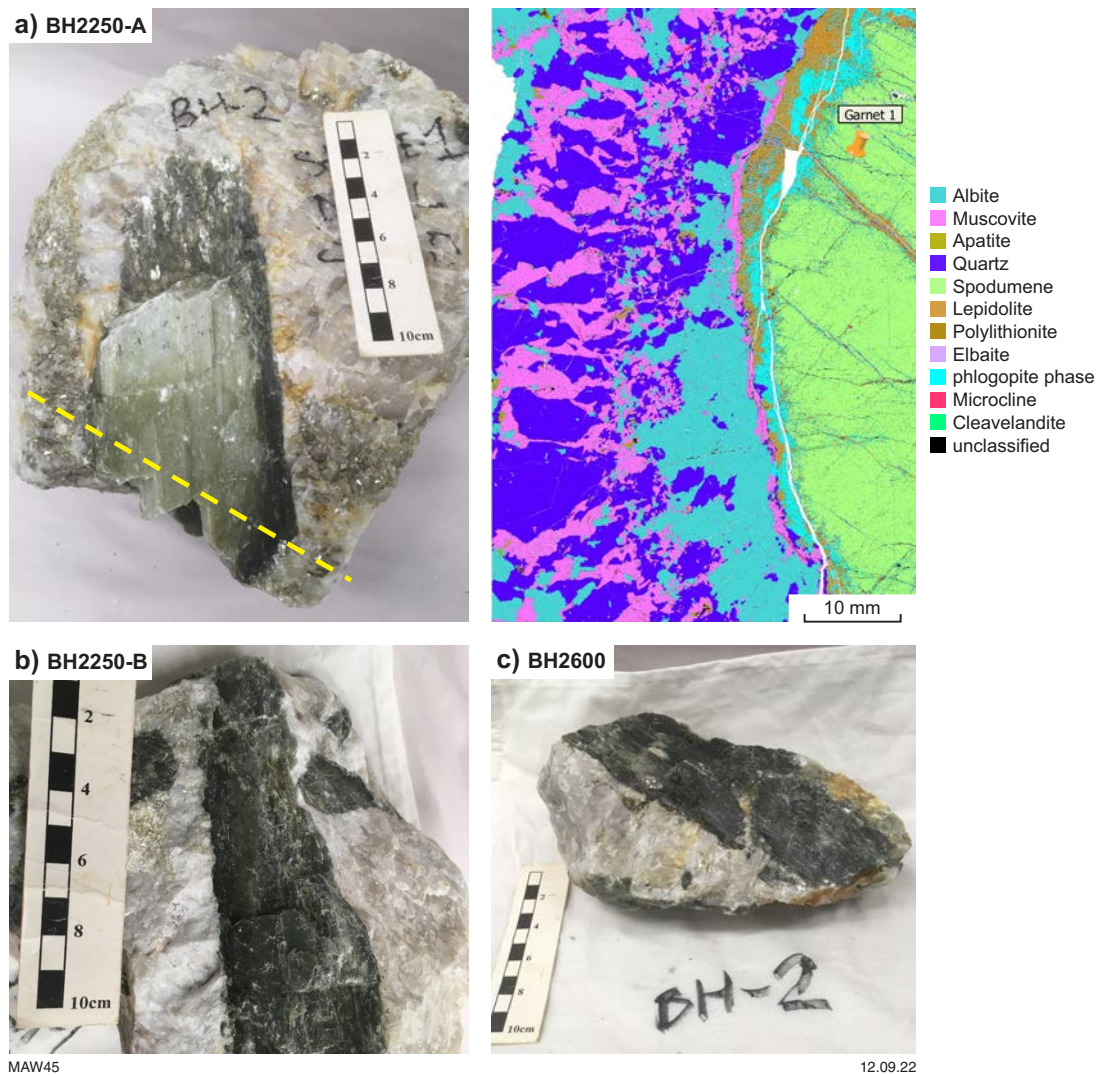


Figure 32. Representative examples of bulk pegmatite from the low-grade zone at Bald Hill. Laths of megacrystic (+10 cm sized) green-grey spodumene, as fragments of larger crystals hosted within an albite-quartz-muscovite matrix, are pseudomorphically altered to dark-green-black, fine-grained Li-mica (muscovite/lepidolite)-chloritic mixture. Alteration occurs congruently from the crystal margin and proceeds inwards along fractures and spodumene cleavage planes as illustrated in the TIMA mineral map for #BH2250-A (also refer to Appendix 4). The TIMA mineral map is for the cross-section (yellow dashed line) through the single, large spodumene megacryst, BH2250-A

hosted in a quartz–albite–muscovite (silvery–white) matrix (Fig. 32). Primary spodumene is pseudo-morphed by a dark-green–black, fine-grained, Li–mica/chlorite assemblage that imparts a waxy lustre to the altered crystal. Alteration may either completely replace primary spodumene or be preserved as a ‘reaction rim’ about the crystal margin enveloping a residual, green–grey spodumene core (Fig. 33). Though not obvious in hand specimens, TIMA mineral mapping clearly shows that alteration proceeds congruently from the margin to the interior of the crystal along cracks and cleavage planes (e.g. Appendix 4).

In examples of high-grade pegmatite, megacrystic spodumene is highly fractured and displays a pronounced tabular habit (Fig. 33). Spodumene that is visibly unaltered is pale-grey or green–grey (e.g. BH1300 and BH1400), whereas where alteration is more obvious, spodumene is a darker grey–green (e.g. BH2700; Fig. 33). High-grade pegmatite examples BH1300 and BH2700 were included for detailed liberation analysis (refer to section, Assessment of physical and chemical processing behaviour of LCT pegmatites).

Mt Marion

Setting

The Mt Marion pegmatite suite is located approximately 40 km south of Kalgoorlie at 31°04'41"S and 121°28'00"E (Fig. 17; Smith and Ross, 2017). Jacobson et al. (2007) provide a detailed account of the history of the deposit with a more recent account by Smith and Ross (2017). Pegmatite bodies are located within the northwest–north-northwesterly striking Archean Saddle Hills greenstone belt. The Mt Marion pegmatite field comprises eight subparallel, northeast–southwesterly striking pegmatites, seven of which are mineralized with the westernmost pegmatite as unmineralized aplite (Fig. 34a). The pegmatites appear to be associated with fault splays conjugate to the north–northwesterly trending Karamindie shear zone on the eastern side of the Coolgardie Domain (PorterGeo Database, 2019, www.portergeo.com.au/database/mineinfo.asp?mineid=mn1543).

The pegmatites intrude Archean, high-Mg basalts such as the 2753–2692 Ma Lunnon Basalt (Hall and Wyche, 2020b), including komatiitic basalt, amphibole–chlorite, talc–carbonate and serpentinite rocks, separated by interflow sediments including sulphidic black shale (Smith and Ross, 2017). A more formal description of the associated rock units is shown in Figure 34. The pegmatite swarm at Mt Marion occurs over a strike length of approximately 10 km in a series of gently dipping (15–30° west) subparallel sills with thickness of 2–30 m (Fig. 34a). The largest pegmatite, the No. 1 deposit, crops out over a strike length of approximately 400 m, with a typical cross-section through the pegmatite shown in Figure 34b (Smith and Ross, 2017).

All but one of the pegmatite bodies are unzoned, with limited textural inhomogeneity and a relatively uniform mineralogy, consisting of spodumene (as the only Li-bearing phase), quartz, albite, with lesser amounts of microcline and muscovite (Smith and Ross, 2017). The exception, pegmatite body No. 3, occurs to the north of pegmatite No. 2 (not shown in Fig. 34a). The No. 3 pegmatite is zoned and is significantly more coarse-grained than the southern pegmatites, with core mineralogy consisting



Figure 33. Representative examples of bulk pegmatite (a, b and c) from the high-grade zone sampled at Bald Hill. Megacrystic spodumene displays a pronounced tabular habit and is generally less altered (dark green–black) than spodumene sampled in the low-grade zone. The large, tabular, pale-green–grey crystal in BH1300 (a) was used in subsequent, liberation analysis and chemical processing work (refer to the section Assessment of physical and chemical processing behaviour of LCT pegmatites)

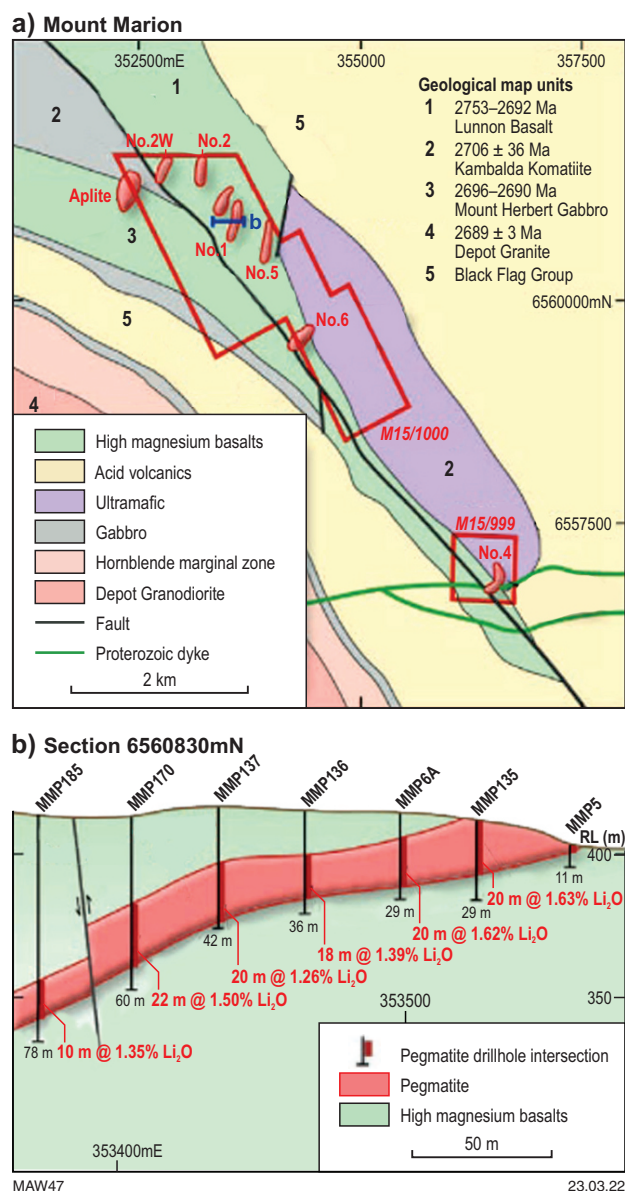


Figure 34. Regional geology of the Mt Marion pegmatite suite a), and b) cross-section through the largest No. 1 pegmatite body. Figures modified from Smith and Ross (2017). Key to main geological units after 1 (Hall and Wyche, 2020b); 2 (Foster et al., 1996); 3 (Hall and Wyche, 2020c); 4 (Lu et al., 2016); 5 (Hall et al., 2022a)

of quartz–spodumene–albite±muscovite and an outer wall zone of microcline–quartz–plagioclase–muscovite (Jacobson et al., 2007).

The Mt Marion pegmatites are considered by Jacobson et al. (2007) as representative of (predominantly) unzoned quartz–spodumene pegmatites, whereas Smith and Ross (2017) classify the pegmatites as albite–spodumene type. Textural evidence and the decrease in spodumene content with proximity to the 2689 ± 3 Ma (zircon U–Pb) Depot Granodiorite (Lu et al., 2016) suggests a potential genetic link between pegmatite intrusion and the Depot Granodiorite.

Sampling and characterization

The project team was unable to arrange for a site visit to the Mt Marion Deposit. However, Mineral Resources kindly provided a 10 kg sub-sample of their coarse ore concentrate.

The concentrate has an average Li₂O grade of 5.41 wt% (± 0.45%), with an average P80 size of 4.69 mm (Ervin Ozolins, Laboratory Supervisor, Mineral Resources, written com., December 2020).

TIMA mineral mapping results (Appendix 4) reveal that >95% of the ore concentrate consists of five mineral phases. In decreasing order of abundance these are spodumene, quartz, muscovite, albite and microcline, and they contain a few, residual grains of country rock (greenstone) with a mineralogy consisting of actinolite–siderophyllite–biotite–cleavelandite (Appendix 4). Of the more common accessory phases carried over into the concentrate, large (2 mm-sized), Mn-bearing (F)–apatite and rare, large (2 mm-sized), highly fractured garnet (spessartine–almandine) grains were mapped (e.g. Appendix 4). Some grains occur as compound forms, mapped as an aggregate of K-feldspar–quartz–spodumene–albite (Appendix 4). Coarsely granular spodumene is commonly included with quartz and to a lesser extent muscovite. Mapping of the Si distribution highlights these inclusions and the graphic textured, alkali alteration along margins of spodumene in contact with K-/Na-feldspars (e.g. Appendix 4).

Based on the mapped phase abundance, the bulk composition of the concentrate can be calculated. From the averaged mineral content for two aliquots of the ore concentrate scanned using the TIMA, an equally weighted average Li₂O content of 6.12 wt% was close to the measured Li₂O grade of 5.41%, as provided by Mineral Resources. A single polished round mount of hand-picked spodumene grains and muscovite books was prepared for EPMA and LA-ICP-MS analysis (Appendix 4).

Londonderry

Setting

The Londonderry pegmatite field is situated in the Coolgardie Domain (refer to Fig. 17), located approximately 25 km southwest of Coolgardie (Dittrich et al., 2019). The Londonderry pegmatite field is hosted by the Archean Kangaroo Hills greenstone belt, a northeast–southwest striking structure about 20 km in length (Dittrich et al., 2019), confined to the west and south by granitic and gneissic rocks of unknown affinity (Fig. 35). Both the greenstone terrane and post-collisional granites, related to D2 deformation during a tectonic regime with a prevalent north–northwest contraction (Dittrich et al., 2019), are cross-cut by an east–northeast to west–southwest striking Proterozoic mafic/ultramafic dyke that may be related to either the 2420–2400 Ma Randalls or the 2420 ± 30 Ma Celebration dyke systems (Turek, 1966 as cited by Dittrich et al., 2019), which are both part of the Widgiemooltha Dolerite (Wingate and Romano, 2022b).

The Londonderry pegmatite field consists of four known pegmatites (Fig. 35): Londonderry Feldspar Quarry, Lepidolite Hill, Tantalite Hill and the Bon Ami pegmatite (Dittrich et al., 2019), of which Londonderry is the most prominent pegmatite in the field. The pegmatite at Londonderry is approximately 1000 m long, 200–280 m wide and 15–66 m thick. It is described as tadpole in shape, with a northern bulbous end (Jacobson et al., 2007). The pegmatite is asymmetrically zoned from the hanging wall to the footwall, but lateral zonation is also reported (Jacobson et al., 2007). The principal

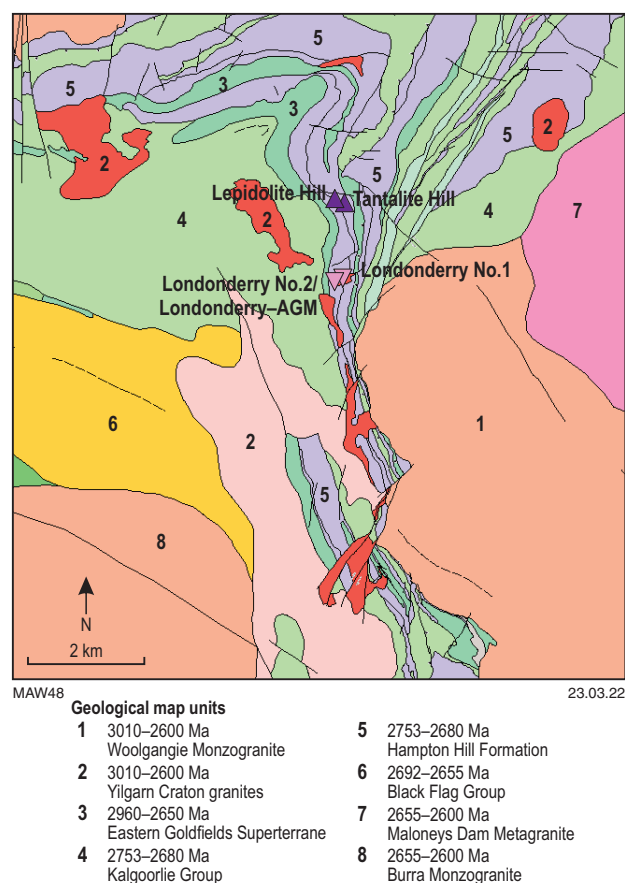


Figure 35. Geological setting of the Lepidolite Hill, Tantalite Hill and Londonderry pegmatite fields. Image source from GSWA GeoView, 1:100 000 interpreted bedrock geology map. Legend after 1 (Hall, 2022d); 2 (Sapkota and Wyche, 2022); 3 (Drummond and Wyche, 2022); 4 (Wyche et al., 2022); 5 (Hall and De Paoli, 2020); 6 (Hall et al., 2022a); 7 (Libby and Wyche, 2019); 8 (Hall, 2022a)

Li-bearing phase is petalite, with petalite–quartz and petalite–quartz–albite–muscovite assemblages occurring in the central zone of the pegmatite (Dittrich et al., 2019).

Sampling and characterization

As access to the Londonderry pegmatite was not possible, a request was submitted to view drillcores LHD07 and LHD19 at the Joe Lord Core library facilities. From the core logging description in the historical Western Mining Corporation (WMC) logging report (Report A126, M267/6 Item 10717) as summarized in Appendix 1, only LHD07 was sampled, with 16 intervals sampled (Fig. 36) of which eight intervals were selected for analysis (Fig. 37; Appendix 1 – selected intervals outlined in red in core tray images). It is noted that the selected core intervals were not large enough to prepare polished slabs, so only polished rounds (25 mm diameter) were prepared for study.

The pegmatite has sharp contacts with hanging wall and footwall greenstone units, with aplitic-chilled margins about 20 cm thick (Fig. 36; Appendix 1). The hanging wall aplite grades into an albite–quartz–muscovite pegmatite before the main quartz–petalite/petalite-ore zone (Appendix 1). The main petalite-ore zone is highlighted in Figure 36, with petalite-bearing intervals selected for analysis shown in more detail in Figure 37. The albite–quartz–muscovite zone

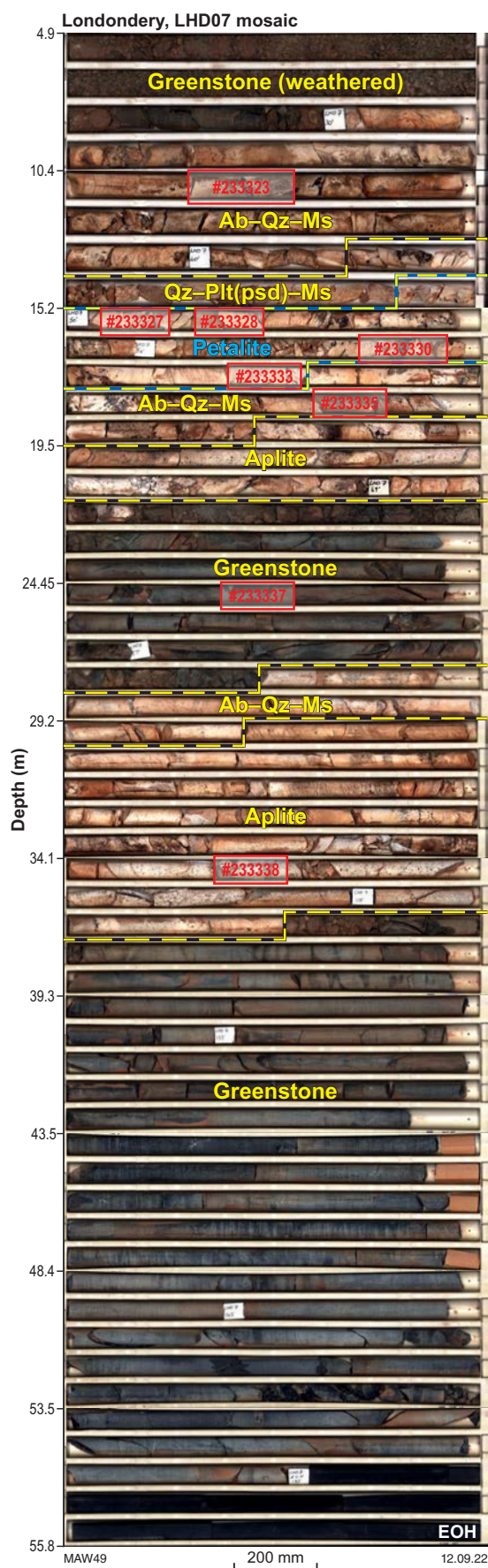


Figure 36. Core tray photographs of Londonderry pegmatite drillhole LHD07, with sample intervals selected for analysis outlined in red rectangles. The main petalite-ore zone is highlighted by the dotted yellow outline, with other lithological units also marked

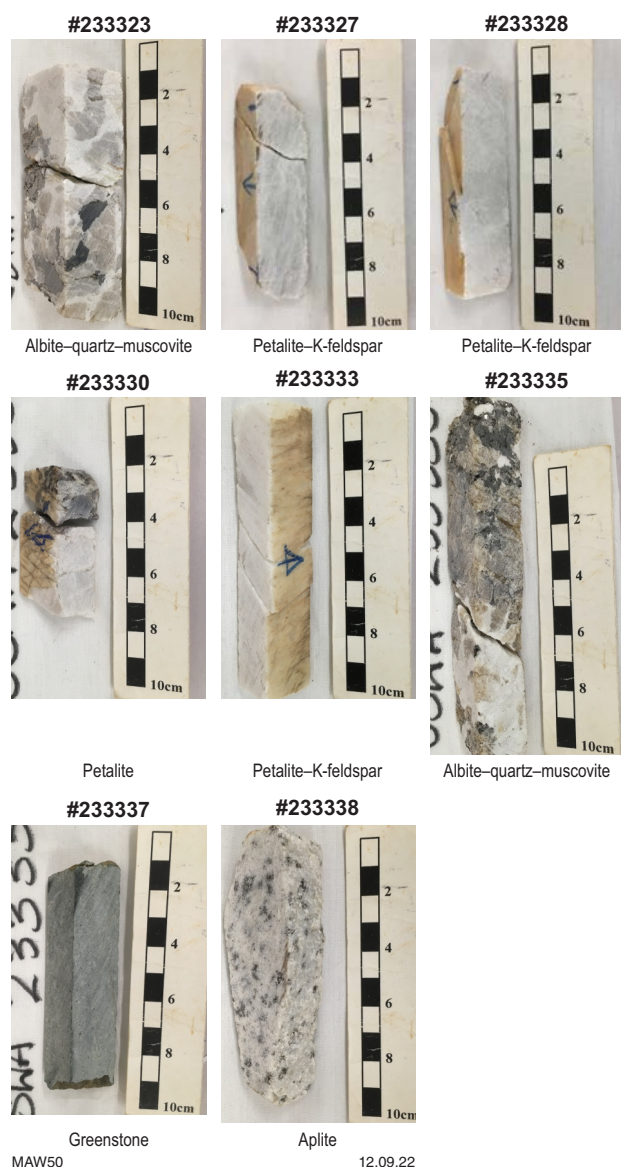


Figure 37. Photographs of core intervals from drillhole LHD07 selected for analysis, with the dominant lithology noted in each case. Note that only polished round mounts were prepared for analysis

repeats below the petalite zone, interspersed with aplitic zones that envelope local, thinner greenstone units (Fig. 36; Appendix 1). Examples of albite-quartz-muscovite (hanging and footwall) and aplite zones and the greenstone host rock, also selected for analysis, are shown in Figure 37.

Kathleen Valley

Setting

The Kathleen Valley Lithium-Tantalum Project is located approximately 50 km north of Leinster or 680 km northeast of Perth (Jacobson et al., 2007), on the western edge of the Kalgoorlie Terrane in the Yakabindie Domain of the Norseman-Wiluna greenstone belt (see Fig. 17). The belt consists predominantly of mafic (2817–2736 Ma Mt Goode Basalt) and ultramafic volcanics as well as considerable volumes of clastic sediments (2665–2640 Ma Jones Creek Conglomerate), minor felsic volcanics and

the 2735 ± 3 Ma Kathleen Valley Gabbro (e.g. Bunting and Williams, 1979; Wyche, 2021). In the Kathleen Valley area greenstones have been metamorphosed to upper greenschist – lower amphibolite facies metamorphic grade (Liontown Resources, 2021).

The Kathleen Valley pegmatite was previously reported as one of nine pegmatite occurrences trending north-south along a strike length of approximately 10 km (Jacobson et al., 2007). However, new work by Liontown Resources has delineated twenty mineralized pegmatites occurring as two, northwest-southeast trending pegmatite swarms defined by the Mt Mann pegmatite (Jacobson et al., 2007) and the Kathleen's Corner pegmatite swarm situated about 1.7 km to the north (Fig. 38a; Liontown Resources, <https://www.ltresources.com.au/kathleen-valley-lithium-project>, viewed 11-06-21). The shallow dipping Kathleen's Corner swarm, which contains about 90% of the project pegmatites, and the steeper dipping, southwestern Mt Mann pegmatite are interpreted to merge at depth to form a single, thick and moderately dipping mineralized body (Fig. 38b). Currently, the Kathleen Valley project has a mineral resource estimate of 156 Mt @ 1.4% Li₂O and 130 ppm Ta₂O₅ (Liontown Resources, <https://www.ltresources.com.au/kathleen-valley-lithium-project>, viewed 11-06-21). Currently, there is limited description available for the pegmatite mineralogy or textural relationships of the host pegmatites.

The Mt Mann and Kathleen's Corner pegmatite swarms are hosted by the 2735 ± 3 Ma Kathleen Valley Gabbro (Jacobson et al., 2007). This is an overturned, composite, layered intrusion of predominantly gabbroic nature with anorthosite to amphibolitized pyroxenite, formed from at least two episodes of magma emplacement (Bunting and Williams, 1979). The gabbro was intruded by dolerite dykes, presumably related to the 2400 Ma Widgiemooltha dyke suite, prior to the onset of regional metamorphism (Bunting and Williams, 1979). Textural evidence is consistent with a younger age for granite to the north of the gabbro (Bunting and Williams, 1979), such as the 2689 ± 17 Ma Mt Keith Granodiorite (Roddick et al., 1976 – whole rock Rb-Sr age) in the area between the Jones Creek and Mount Keith Homestead.

Sampling and characterization

Access to drillcores at the Kathleen Valley Deposit was kindly made available by Liontown Resources (Jamie Day, Exploration Manager, written com., February 2021). Four drillcores were made available for sampling: KVDD0018, KVDD0049, KVDD0076 and KVG008, with their locations at the Kathleen Valley Deposit shown in Figure 39. Of these, holes KVDD0018 (local grid coordinates X = 256623m; Y = 6958310m) and KVDD0076 (local grid coordinates X = 257865m; Y = 6959337m) were selected for inclusion in the present study. KVDD0018 intersects the southern extent of the Mt Mann pegmatite (Fig. 38) and is lepidolite-bearing, whereas KVDD0076 is lepidolite-free and intersects high-grade Li and is tentatively interpreted by Liontown Resources as the merged zone of the Mt Mann and Kathleen's Corner pegmatite swarms (e.g. Fig. 38).

Core tray imagery for KVDD0018 is shown in Figure 40, with sampling locations highlighted and shown in more detail in Figure 41. Core intervals sampled from KVDD0076 are presented in Figure 42. The single, thickest portion of the Mt Mann pegmatite intersected by KVDD0018, as exposed in the core trays presented, is first encountered at approximately

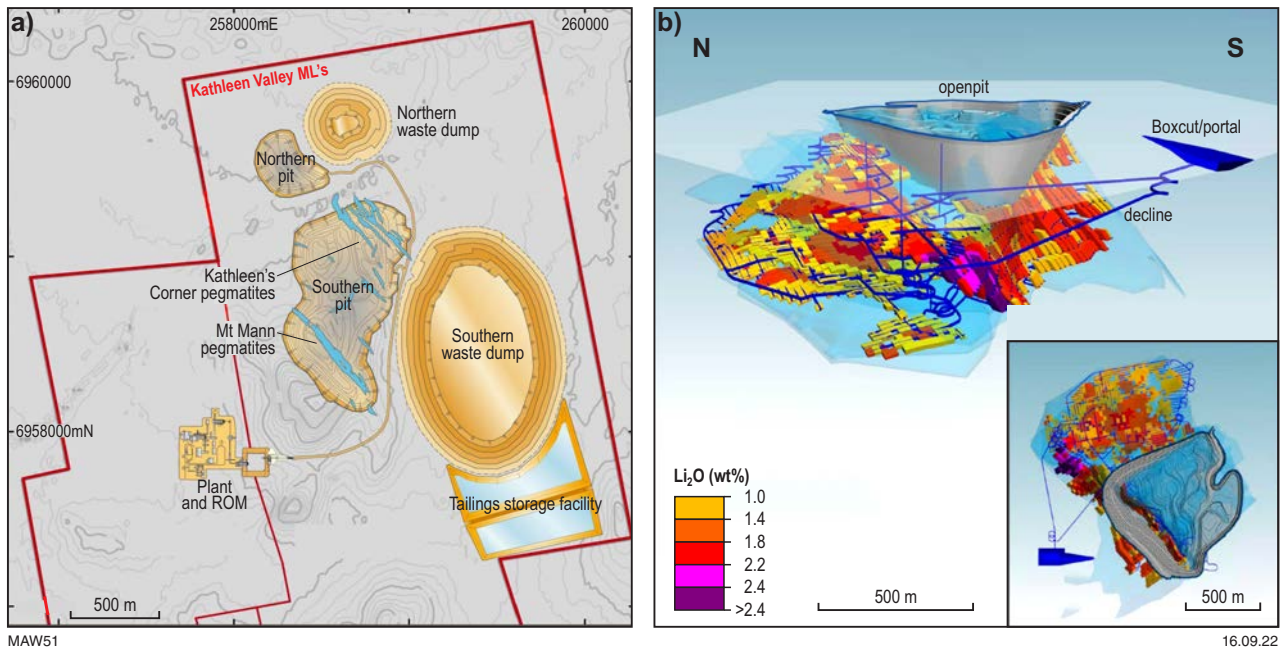


Figure 38. Schematic of the Mt Mann and Kathleen's Corner pegmatite swarms that comprise: a) the Kathleen Valley Project and proposed pit and site layout as planned in 2019; and b) pegmatite resource model delineation and planned openpit and underground workings

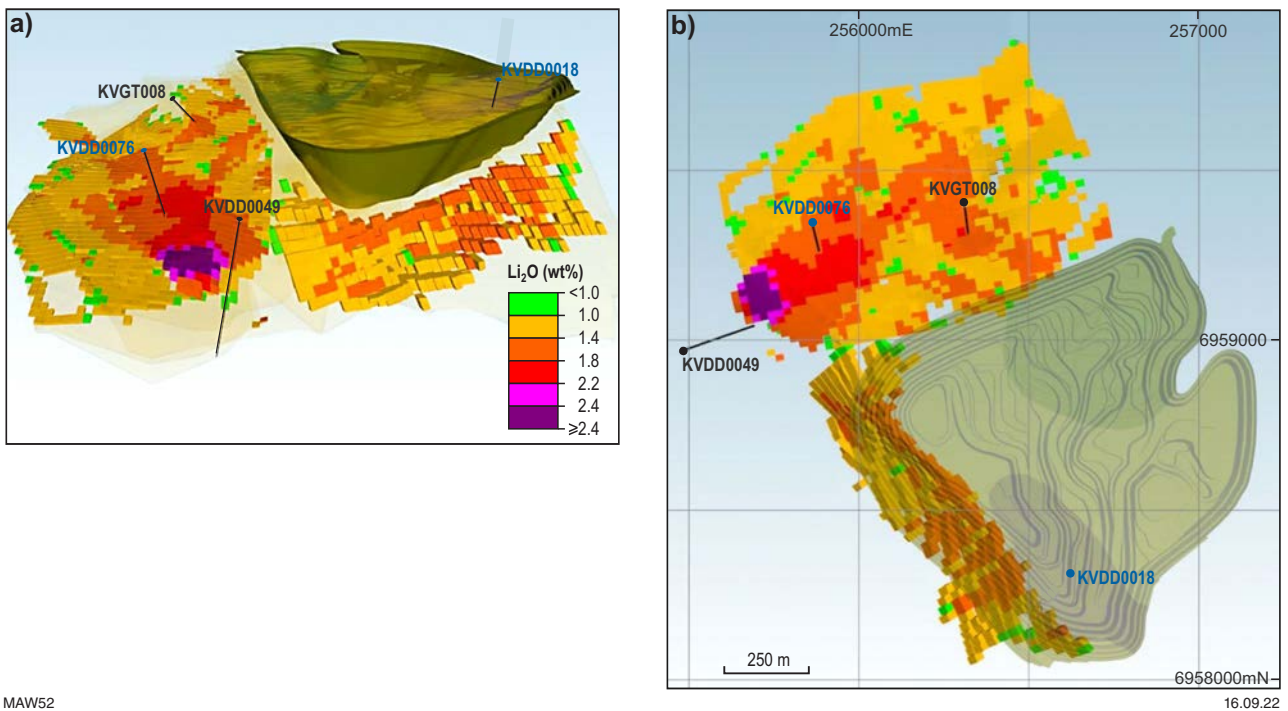


Figure 39. Proposed openpit at Kathleen Valley and pegmatite block model of the underground stopes, coloured by wt% Li_2O content, by: a) an elevated perspective view (looking due east) of the drillhole collars (blue dots) and core strings of the drillholes made available for sampling; and b) an aerial view. Drillholes KVD0018 and KVDD0076 (highlighted in blue) were selected for further analysis. Images kindly provided by Jamie Day (Exploration Manager, Liontown Resources)

42.0 m and continues to a depth of approximately 62 m (Fig. 40). Close to the upper pegmatite–greenstone contact, the pegmatite consists of a 2-m thick zone, with the middle, 1-m thick portion comprising fine-grained lepidolite in a granular quartz matrix, with fine, acicular (4–5 cm long x 1–2 mm wide), pink–lilac spodumene. The fine-grained lepidolite imparts a strong purple colour to the pegmatite. Either side of this first lepidolite zone, the pegmatite consists of a

variably coloured, granular textured albite–quartz zone, free of spodumene (e.g. sample #2; Fig. 41; Appendix 4).

The main pegmatite body, over a depth of 46–62 m, consists of quartz–spodumene with variably distributed albite, as massive, blocky crystals to +10 cm in size, and fine-grained lepidolite. Spodumene occurs as randomly oriented, pale-grey–lilac, acicular crystals generally 4–5 cm long and

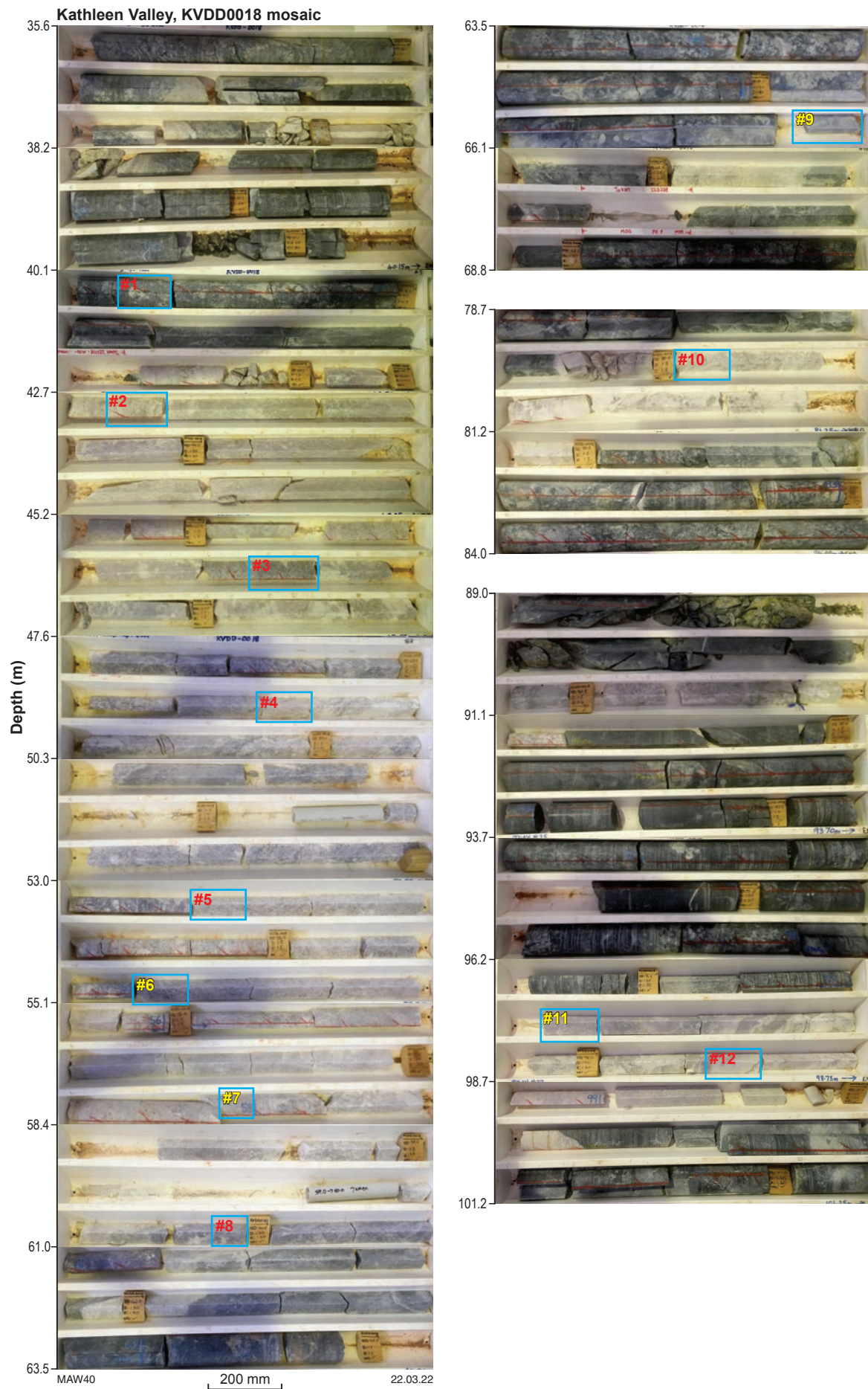


Figure 40. Core tray images for KVDD0018 with sampled drillcore intervals highlighted by the red numbered blue rectangles. Intervals selected for follow up mineral are denoted by the red numbering (e.g. sample #2). Note: The crossed-purple shading effect apparent in the core images is due to the lighting conditions of the core storage facilities

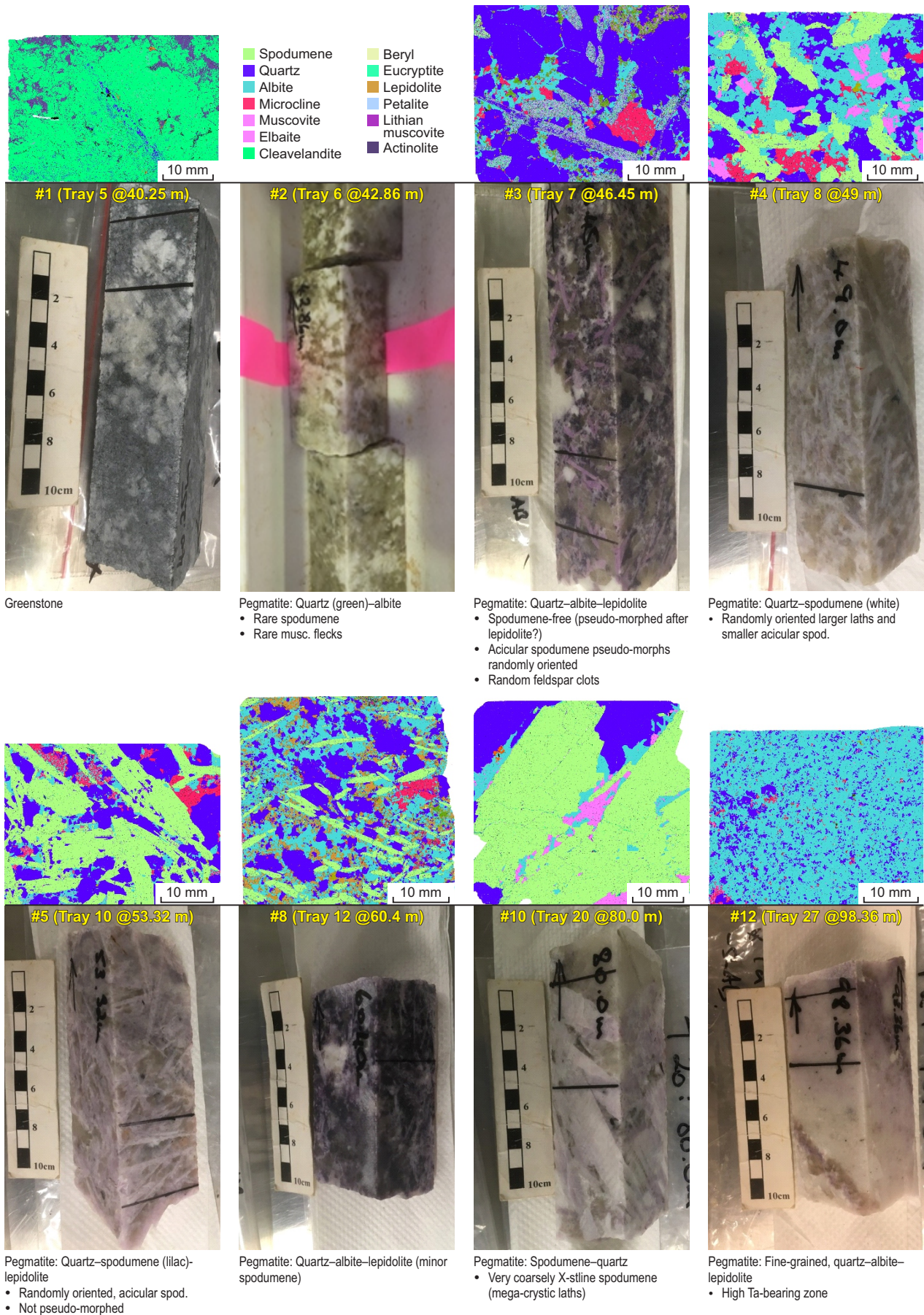
3–4 mm wide that display as an inter-woven, mesh texture (e.g. samples #4 and #5; Fig. 41) but can develop an extreme acicular habit with crystals +10 cm in length and 3 mm wide, grading towards the middle of this zone (Fig. 41).

Fine-grained (primary) lepidolite imparts a purple colour to the pegmatite, particularly for the upper and lower margins of the 'meshed' spodumene zone. Spodumene in the upper 'mesh' zone has been altered, pseudo-morphically replaced by a secondary 'quartz–elbaite–cleavelandite–beryl' mixture with minor, residual spodumene as detected by TIMA mineral mapping (e.g. sample #3; Appendix 4).

Below the main pegmatite body, comparatively thin pegmatite units interfinger with thicker greenstone units (e.g. 66.7 – 79.6 m and 81.5 – 91.0 m; Fig. 42; Appendix 1). In underlying, intersected pegmatite units (e.g. #10 @ 80 m), spodumene is very coarsely crystalline with a lath-like habit to +10 cm long x 10 mm wide (Appendix 1). In the deepest units, pegmatite consists of fine-grained, spodumene-free, quartz–albite–lepidolite hosting elevated Ta mineralization (e.g. sample #12; Fig. 42).

On the basis of the drillcore available for examination, KVDD0076 intersected two main pegmatite bodies (Appendix 1; Fig. 42). Greenstone at 189.3 m (base) and 238.8 m (top) constrains a quartz–spodumene pegmatite type, with white, coarsely crystalline, acicular (+10 cm long x 10 mm wide) spodumene (Fig. 42; Appendix 3). Pegmatite within the wall contact zone displays the classic quartz–albite, graphic texture (Appendix 1). Spodumene can be crosscut by albite–muscovite veins (e.g. Fig. 42; Appendix 3), which can make up a significant proportion of the pegmatite composition (e.g. sample #2, Fig. 42; Appendix 4).

The deeper pegmatite body intersected in KVDD0076, over the depth range 258.26 – 293.5 m (Appendix 1), is mineralogically monotonous, consisting of quartz–albite–muscovite–spodumene in varying proportions, but is texturally highly variable (Fig. 42). Towards the top of this pegmatite unit, bi-coloured megacrysts of spodumene are randomly distributed within a massive quartz matrix (e.g. sample #4; Fig. 42) with zones of granular textured quartz–albite hosting few muscovite booklets and smaller, acicular (3 cm x 1 mm) spodumene (Appendix 1). With depth, the white–tan coloured pegmatite displays a predominantly granular texture consisting of white, randomly oriented, acicular spodumene with quartz–albite and less commonly muscovite (Fig. 42; Appendix 1).



MAW54

16.09.22

Figure 41. Close-up of KVDD0018 core intervals selected for detailed follow-up mineral characterization. Marked-up locations for each interval show the location from which sub-samples were prepared for subsequent analysis, e.g. as polished rounds or slabs (refer to Appendix 3). TIMA mineral maps for each selected sample highlight the mineralogical associations and textural changes throughout the pegmatite. Scale bar in each TIMA map is 10 cm

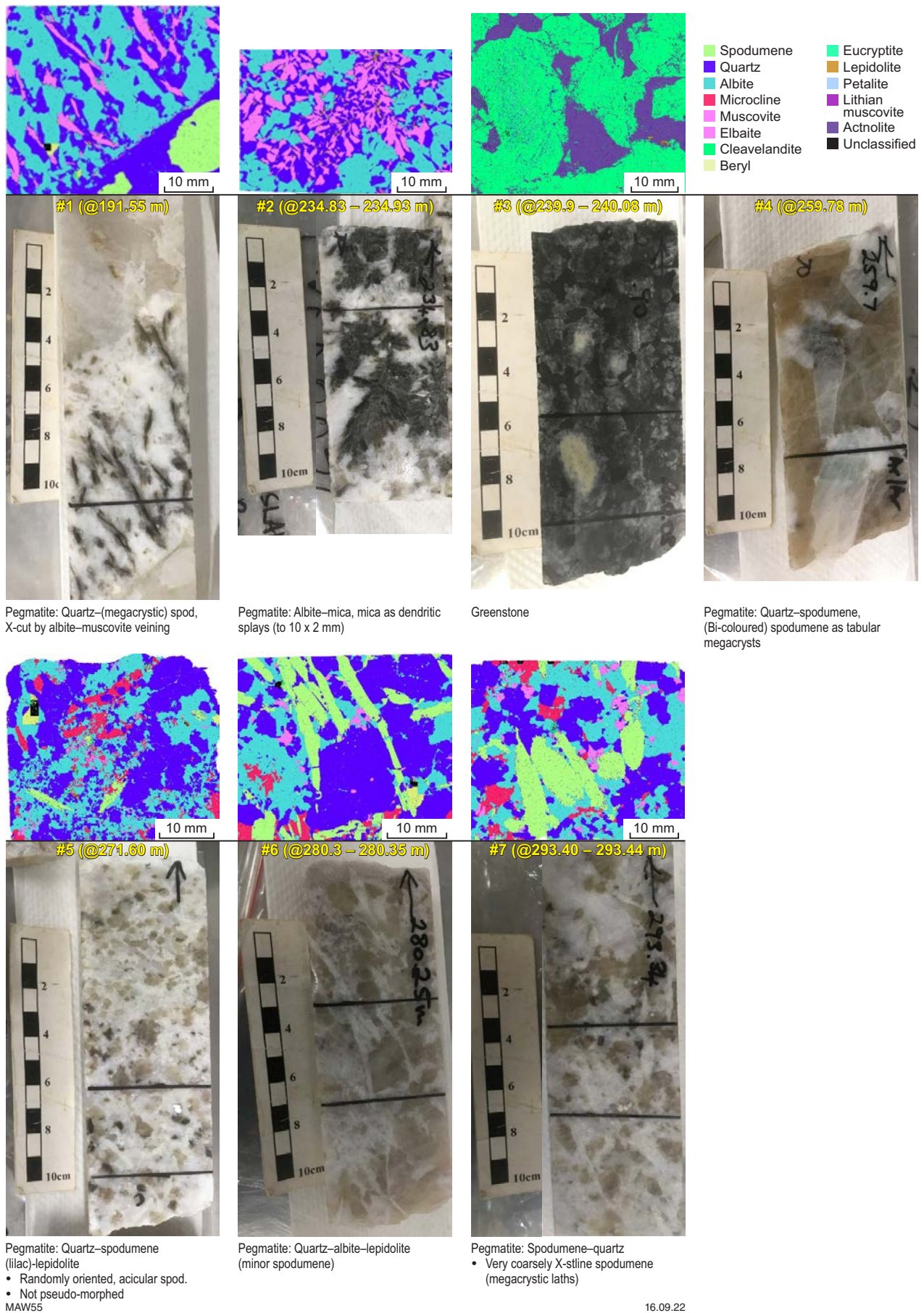


Figure 42. Close-up of KVDD0076 core intervals selected for detailed follow-up mineral characterization. Marked-up locations for each interval show the location from which sub-samples were prepared for subsequent analysis, e.g. as polished rounds or slabs (refer to Appendix 3). TIMA mineral maps for each selected sample highlight the mineralogical associations and textural changes throughout the pegmatite. Scale bar in each TIMA map is 10 cm

Dalgaranga

Setting

The Dalgaranga pegmatite is located approximately 70 km northwest of Mount Magnet (Fig. 17) and forms part of the Dalgaranga pegmatite field, which also includes the Niobe (formerly Mount Farmer) and Breakaway pegmatites (Jacobson et al., 2007). The Dalgaranga pegmatite is the most significant pegmatite in the field and is hosted in gabbroic rocks of the 2735–2711 Ma Yalgowra Suite (Ivanic, 2019) and peltitic schist of the 2670–2635 Ma Greensleeves Formation (Van Kranendonk et al., 2013) that forms part of the Dalgaranga greenstone belt in the western Youanmi Terrane. Greenstones are intruded by granitic rocks of the c. 2790 Ma Big Bell Suite to the southeast, northwest and northeast and the 2787–2733 Ma Cullculli Suite (Zibra, 2022) to the southwest. It is typical for greenstones to be in sheared contacts with these granitic suites (Fig. 43).

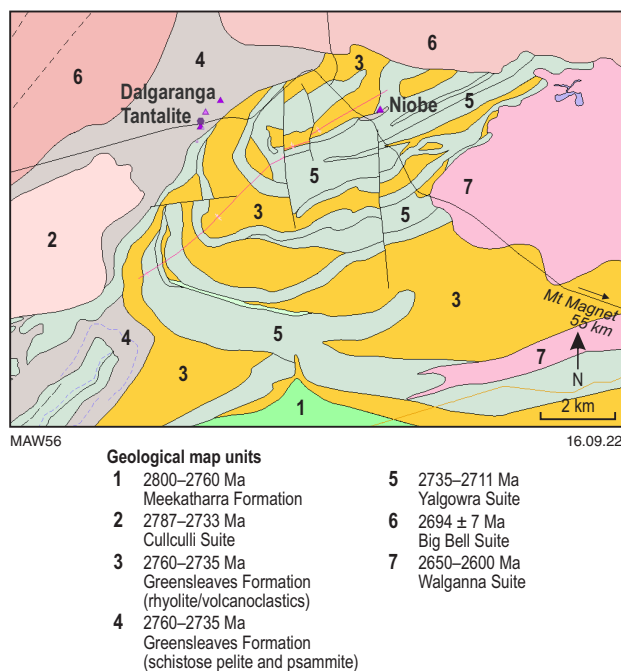


Figure 43. Geological setting of the Dalgaranga pegmatite field. Image sourced from the GSWA GeoView, 1:100 000 interpreted bedrock geology map, with exposure of the Dalgaranga field (modified from Fetherston, 2004) and exposure of the Dalgaranga pegmatite in the openpit, view to the south-southwest (Source: Krakatoa Resources Ltd, media release, p. 14., viewed 21-0-2019)

Striking northeast, the pegmatite outcrops for about 137 m in length, is 12 m wide and shows a moderate dip (20–40°) to the southeast (Jacobson et al., 2007). Compositional zoning is expressed downwards from the hanging wall as consisting of a 0.5-m thick zinnwaldite zone, a 1-m thick albite–zinnwaldite zone and a 2–3-m thick core of grey quartz (Fig. 43). The albite–zinnwaldite and zinnwaldite sequence repeats to the footwall (Jacobson et al., 2007). The deposit has been mined for beryl and tantalite for nearly 80 years, with Ta mineralization occurring mainly as tapiolite and tantalite, with lesser microlite (Fetherston, 2004).

Sampling and characterization

Site access to the Dalgaranga pegmatite was not possible, although drillcore DD1 was available to the project via the Joe Lord Core Library. Based on details provided by Pancontinental Mining Ltd, Annual Mining Report (Hall, 1988), DD1 is located approximately 10 m north of the quartz core of the Dalgaranga pegmatite, at the gabbro–pegmatite hanging wall contact (local grid E = 9993m, N = 10195.5m). DD1 is declined to the south and intersects the quartz–albite zone and quartz–albite–zinnwaldite footwall zone, underlying the quartz core (Hall, 1988). An approximately 1.3-m thick zone of Ta mineralization, occurring within mainly massive albite towards the base of the quartz–albite zone (e.g. Appendix 3), is intersected by DD1 at a depth of ≈18.5 m with a Ta-grade of 2000 ppm (Hall, 1988).

Core tray photographs (Fig. 44) show the location of the 16 core intervals sampled (numbered, yellow rectangular outlines), with intervals selected for detailed analysis numbered in blue (Fig. 45). Core intervals selected for

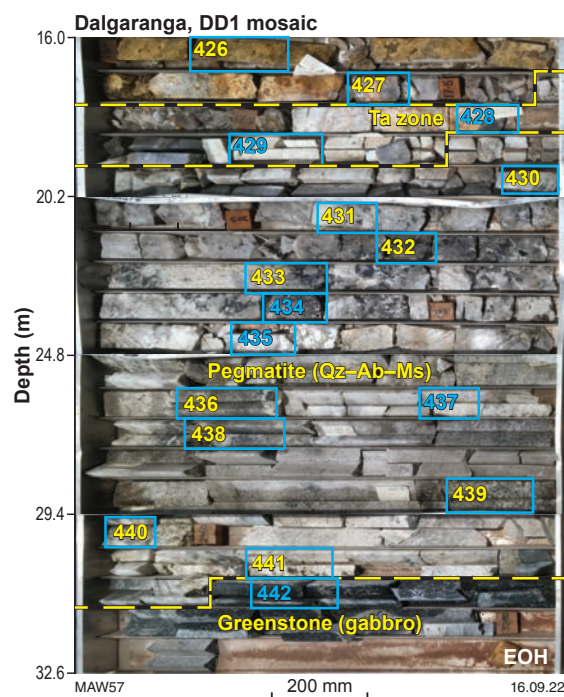


Figure 44. Core tray photographs of Dalgaranga pegmatite drillhole DD1. Sample intervals are shown by the numbered (e.g. #241426) blue rectangles. Samples examined in the current study are shown by sample numbers given in blue (e.g. #428). The core outlined in dotted yellow defines the zone of reported Ta mineralization (Hall, 1988) towards the bottom of the quartz–albite zone at/close to the contact of the quartz–albite–zinnwaldite zone

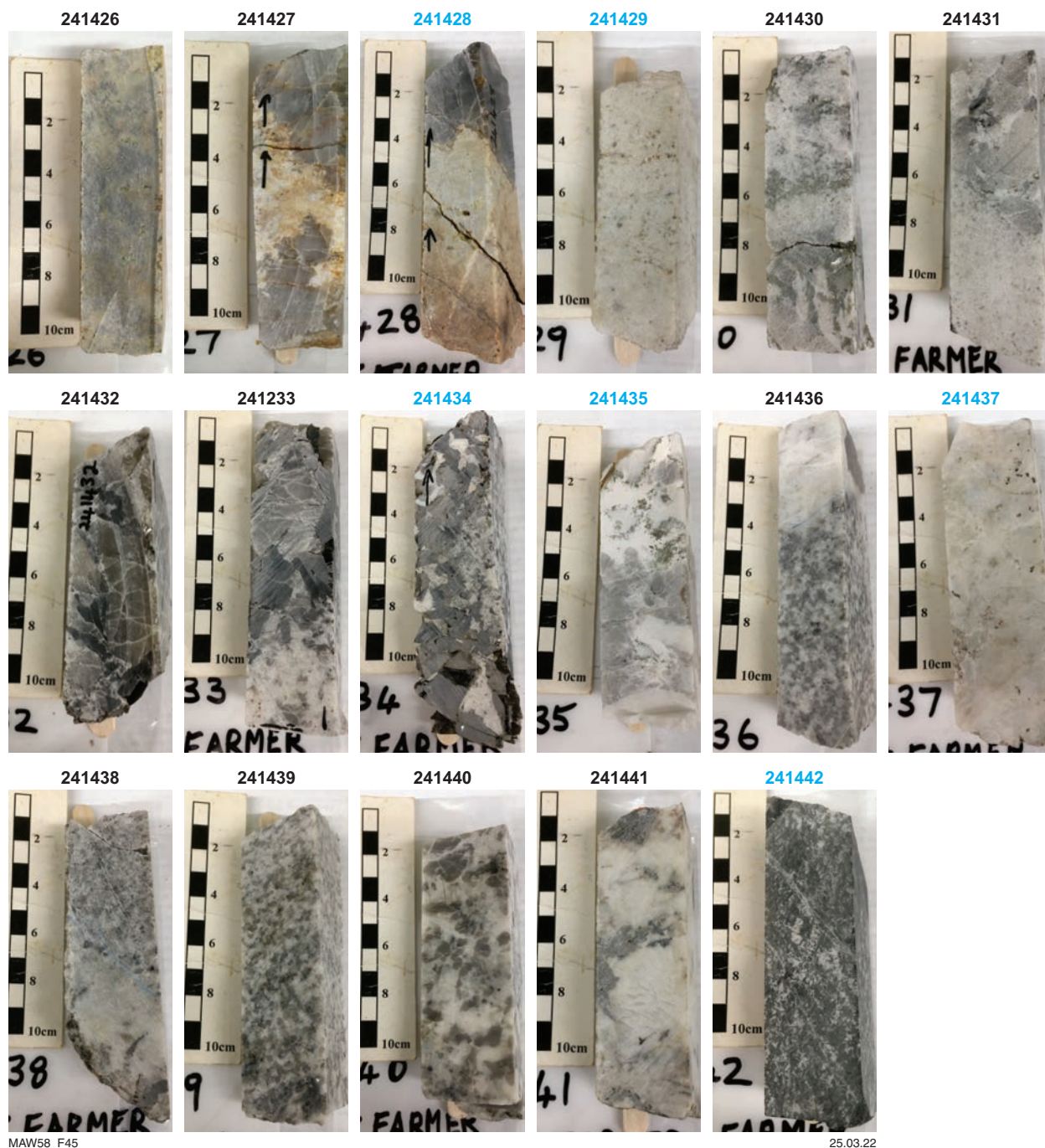


Figure 45. Core intervals from drillhole DD1. Samples numbered in blue were selected for further detailed analysis

analysis focused on the zone of Ta mineralization (#241428 and #241429; Fig. 12; Appendix 3), quartz–albite–muscovite zone (#241434, #241435 and #241437) and footwall gabbro (#241442) (Fig. 45; Appendix 3).

Localized occurrences of massive albite were detected in the underlying quartz–albite–muscovite zone (e.g. #241437; Fig. 45), which also hosts minor Ta mineralization (Appendix 13). Fetherston (2004) reports that Ta mineralization occurs mainly as tapiolite, $(\text{Fe}^{2+}, \text{Mn}^{2+})(\text{Ta}, \text{Nb})_2\text{O}_6$ and tantalite, $(\text{Mn}, \text{Fe})\text{Ta}_2\text{O}_6$, with lesser microlite, $(\text{Na}, \text{Ca})_2\text{Ta}_2\text{O}_6(\text{O}, \text{OH}, \text{F})$. However, Hall (1988) considers that microlite is the principal source of Ta at Dalgara. Characterization of the Ta mineralogy at Dalgara is discussed in more detail in Tantalum–niobium geochemistry.

LCT pegmatite of the Pilbara region

Pilgangoora

Setting

Pilgangoora is located about 97 km south-southeast of Porth Hedland (Fig. 3), situated on the western side of the McPhee Range (Fetherston, 2004). The geological setting of the Pilgangoora pegmatites was only briefly summarized by Fetherston (2004) in relation to Sn–Ta mineralization but was recently described in more detail by Sweetapple (2017). Pegmatites are hosted by the north-trending, East Strelley greenstone belt, as part of the east Pilbara terrane, in a sequence of highly deformed, fault bounded, mafic-dominated rocks that protrude into the Carlindi Batholith (Sweetapple, 2017). Rock units assigned to the Euro Basalt (dated at 3350–3335 Ma) form the lower part of the Kelly group (Fig. 19). Schistose and sheared talc–chlorite–carbonate ultramafics (Dalton Suite at 3185 Ma) occur along the eastern boundary, which also hosts the abandoned Iron Stirrup Au Deposit (Baker et al., 2002, as cited by Sweetapple, 2017).

In the project area, tholeiitic basalt is the dominant lithology with a thin, interflow sequence of metasediments (e.g. lithic wacke/siltstone+quartz, greywacke and conglomerate). In the centre of the project area a 500-m thick, intrusive sequence of layered ultramafics (peridotite, pyroxenite and Mg–Fe–dolerite) occurs (Sweetapple, 2017; Fig. 46). The Pilgangoora pegmatites are moderately dipping (20–60°) to the east, occurring as en echelon dykes and sills (Sweetapple, 2017). Columbite–tantalite at Pilgangoora was dated by secondary ion mass spectrometry Pb–Pb analysis to yield a date of 2879 ± 5 Ma (Kinny, 2000).

The Pilgangoora pegmatites occur as three main groups (Sweetapple, 2017) in the central project area (Western, Centre and Eastern groups), with the Southern and north Monster pegmatites as outlying groups (Fig. 46). Pegmatites at Pilgangoora are quasi-homogeneous, although anisotropic mineral assemblages are noted and include very coarse or megacrystic spodumene, aplitic layering (finer-grained, quartz–feldspar granite-type) and locally distinct border units (Sweetapple, 2017). Compared to pegmatites of the Western and Central units, the Eastern group pegmatite is texturally and mineralogically distinct and contains more lepidolite, (grey) spodumene and discrete albitic units (Sweetapple, 2017).

Sampling and characterization

Selected intervals of drillcore (PD001 to PD008) from the Western Pegmatite group (Fig. 46; Appendix 4) were kindly provided by Altura Mining (Stephen Barber) for inclusion in the present study. LCT pegmatite hosted in both mafic and ultramafic units were provided to enable a comparative evaluation of the host rock on pegmatite formation (Appendix 4). Photographs of Pilgangoora drillcore hosted in either mafic or ultramafic are shown in Figures 46 and 47, respectively. Several of the core intervals provided are comparatively short (≈ 10 cm in length), with the thickness of the pegmatite unit and relative position of the core section within each pegmatite unit unknown.

However, interrogation of the optical imaging (Figs 47, 48) and TIMA mineral mapping results (Appendix 4) have been useful in determining the source pegmatite lithology in each case. As reported by Jacobson et al. (2007), Pilgangoora pegmatites are classified into three main compositional groups: quartz–spodumene–albite–microcline, quartz–microcline–albite (acc. muscovite) and quartz–muscovite–microcline (+accessory cassiterite and plagioclase) pegmatites. All pegmatite examples occurring in mafic host rocks (Fig. 46) can be classified as belonging to the quartz–spodumene–albite–microcline lithology, which can be considered as high-grade according to Sweetapple (2017). Of the pegmatite examples hosted in ultramafic units, spodumene-free PD002 (@29.95 m) is classified as low-grade, quartz–muscovite–microcline pegmatite, and the deeper interval (@192.8 m) in drillhole PD004 as an aplite (low-grade, albite–quartz) pegmatite (Fig. 48). The remaining pegmatite intervals can also be classified as examples of high-grade, quartz–spodumene–albite–microcline pegmatite (Fig. 48).

Fluorapatite is uncommon in the quartz–spodumene–feldspar-type pegmatite and in the quartz–muscovite pegmatite lithology. Where present, (F)–apatite occurs as large, subhedral grains to ≈ 600 μm , with variable Mn contents of 1.6 – 5.1 wt% (e.g. PD004-67.8 m, PD001-36 m; PD005-83.9 m). Manganiferous, (F)–apatite containing about 3 wt% Mn is more common in the aplite pegmatite types and exhibits well-developed lobate and poikiloblastic forms (e.g. PD004-191.8 m). TIMA mineral mapping also detected several accessory phases, such as garnet (PD002-29 m, PD004-67 m, PD004-191 m in skeletal form), PD006-66 m, PD008-66 m fractured/altered large 3-mm zoned grain. A single, 500- μm sized, fractured (Ce)–monazite grain was mapped in PD005-46.5 m (refer to Appendix 4).

Discrete Ta–Nb mineralization was uncommon in the pegmatite examined from Pilgangoora, occurring mainly as rare, columbite–tantalite typically 20–50 μm in size, occasionally to 100–150 μm in size and rarely as larger prismatic grains to about 1 mm in size (#PD005-84 m, Appendix 4). Columbite–tantalite detected at Pilgangoora exhibits a variable Ta:Nb ratio and no consistent trend in the Ta:Nb ratio could be attributed to the host rock type (i.e. mafic vs ultramafic).

TIMA mineral mapping also identified extensive development of graphic-textured alteration of spodumene along crystal margins in contact with Na/K-feldspars, particularly where spodumene contacts albite (e.g. PD003-33 m, Appendix 4). In addition, extensive Fe–chlorite alteration of spodumene was detected, mapped as veins crosscutting crystals and developed along cleavage planes (e.g. PD008-66.5 m, Appendix 4). This is discussed in more detail in section, Spodumene morphology and alteration: indicators of pegmatite crystallization evolution.

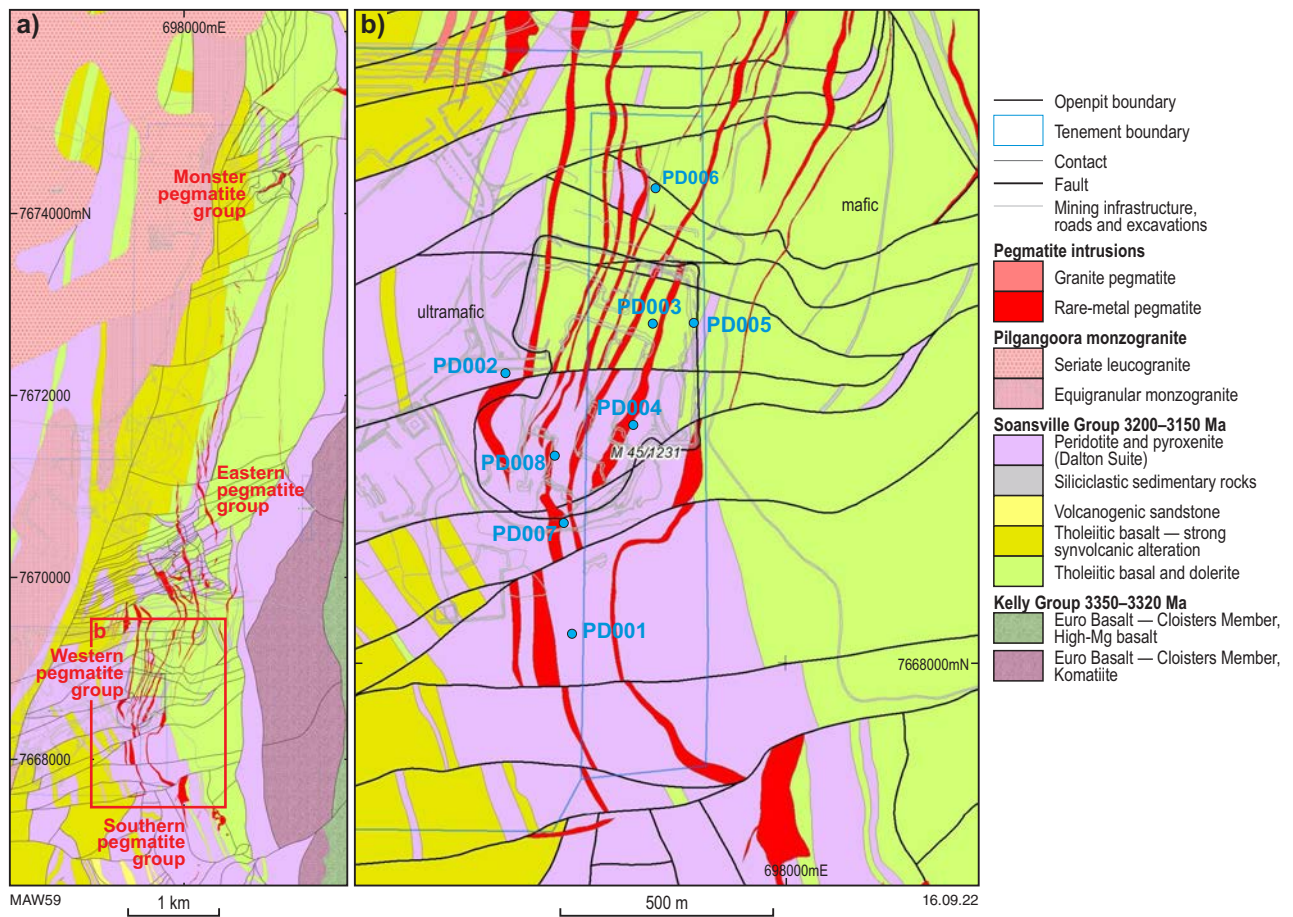


Figure 46. Geology of the Pilgangoora District showing: a) the three main pegmatite groups; and b) detail of the area hosting the Western Pegmatite group showing the location of drillholes from Pilgangoora (black outline), provided by Altura Mining (Stephen Barber, written com., April 2020) for examination in the present study. A description of the drillholes examined including the intervals selected and the host rock type is given in Appendix 1

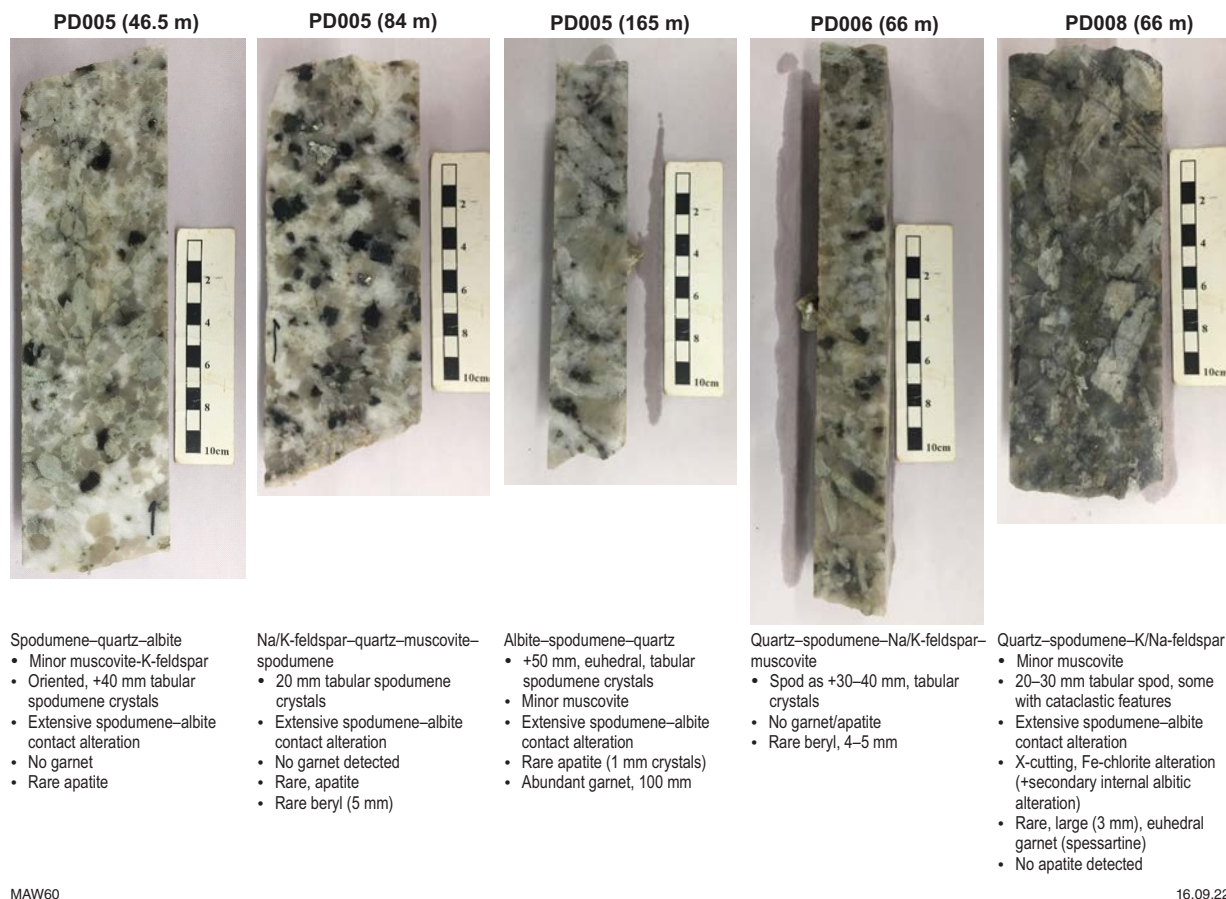


Figure 47. Drillcore intervals of pegmatite at Pilgangoora in mafic host rocks. A brief mineralogical description, based on TIMA mineral mapping results (refer to Appendix 3), is provided for each core interval. All pegmatite examples can be classified as belonging to the high-grade, quartz-spodumene-albite-microcline compositional group (Jacobson et al., 2007)

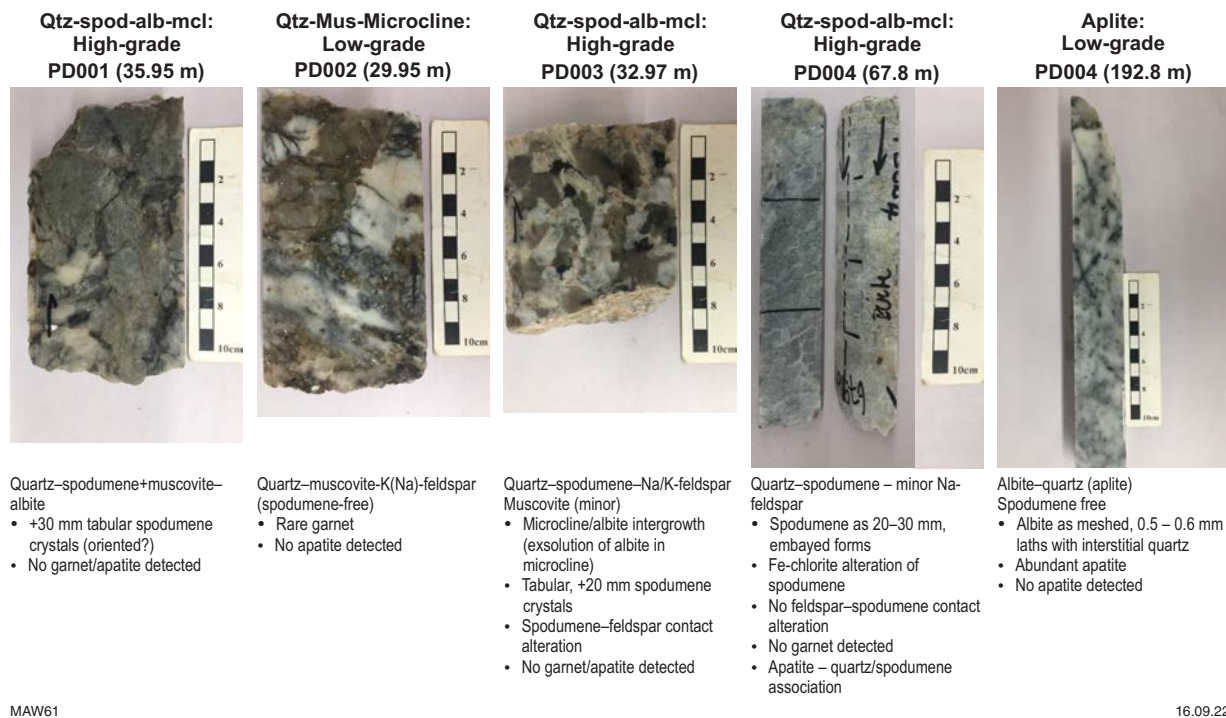


Figure 48. Drillcore intervals of pegmatite at Pilgangoora in ultramafic host rocks. A brief mineralogical description, based on TIMA mineral mapping results (refer to Appendix 3), is provided for each core interval. Pegmatite examples in drillcore PD001_35.95 m, PD003_32.97 m and PD004_67.8 m can be classified as belonging to the high-grade, quartz spodumene-albite-microcline compositional group (Jacobson et al., 2007). In contrast, pegmatite PD002_29.95 m and the core interval deeper in PD004 (192.8 m) are examples of low-grade quartz-muscovite-microcline and aplitic (albite type) pegmatite, respectively

Geochemical analysis and mineral characterization

Initial geochemical characterization was undertaken to enable the comparative analysis of pegmatite deposits using bulk-rock compositional data. However, due to the coarsely crystalline and heterogeneous nature of the study samples, only those samples (pit and drillcore) where sufficient volumes of represented material were collected and submitted for bulk geochemical analysis.

To further aid the assessment and geological classification of the LCT pegmatites examined in this study, their mineralogical associations and textural features were characterized by extensive application of TIMA mineral mapping. TIMA mineral-mapping results and interpretations for each rare-element pegmatite deposit examined in this study are summarized in Appendix 3. These results were used to aid mineral identification, provide textural information through mineral-mineral associations, inform the geochemical and phase compositional analysis of phases of interest at each deposit, and aid in interpretation of their crystallization sequence and characterization of alteration styles and associated mineralogy.

Initial TIMA mineral mapping was used to identify regions of interest, specifically minerals suitable for follow-up compositional analysis by LA-ICP-MS and EPMA measurement (refer to Appendix 2). This section first describes the bulk-rock chemical composition of pegmatite before discussion of more detailed compositional analysis.

Though typically present in pegmatites, minerals such as beryl, garnet, rutile and zircon occurred sporadically as accessory phases in the LCT pegmatites examined. Thus, quantitative mineral compositional analysis focused on the mineral chemistry of spodumene, feldspar and mica (as muscovite and lepidolite) to identify compositional trends with potential application as exploration tools or as indicators of pegmatite provenance. Established mineral compositional trends were compared to other global LCT deposits, where possible, to place a comparative ranking of WA LCT pegmatites on a global scale. In addition, semi-quantitative SEM-EDS analysis of the Ta-Nb-bearing mineralogy was used to characterize trends in the fractionation evolution of the pegmatites as expressed in changes in the Ta:Nb and Fe:Mn ratios.

The main objectives and key findings of the work undertaken in this section are summarized below:

- 1 Geochemistry signature of minerals to identify pegmatite associations, which can assist in targeting LCT pegmatites:
 - Changes in mica (muscovite/lepidolite) composition followed well-correlated and highly predictable trends in relation to their Li and F contents, Li:Al and Li:Si, and K:Rb ratios.
 - Changes in mica composition described may provide a useful tool in greenfields/brownfields exploration in assessing pegmatite mineralization potential (Li, Ta) based on mica composition as in the field:
 - Mica (muscovite/lepidolite) is more easily identified compared to the typically white, Li-bearing and barren (feldspar, quartz) phases that also occur
 - Mica is typically present as coarsely crystalline 'books' of well-defined crystals
- 2 Assessment of the deportment of Li and other elements of interest and associated minerals in pegmatite deposits, through a quantitative understanding of the mineralogical deportment of both economically important (Li, Nb, Ta) and environmentally deleterious (F, Mn) elements within minerals associated with pegmatite ores:
 - Spodumene typically has Li-Al-Si contents close to stoichiometric $\text{LiAlSi}_2\text{O}_6$:
 - Alteration systematically removes Li from spodumene (at 8.03 wt% for the pure pyroxene), with lowest Li_2O content of 5.15 wt% for spodumene at Mt Cattlin
 - Iron and Mn (max. 1.2 wt% combined) were the main impurities
 - Sodium, at 500–1200 ppm, was the other main trace impurity.
 - Based on their textural characteristics, two main pegmatite-alteration styles that preferentially impact spodumene were defined:
 1. Complete/near-complete, pseudo-morphic replacement of spodumene by a massive, dark-green-black, Li-mica/cookeite assemblage
 - Associated with thermal overprinting event/s, possibly related to dyke intrusion
 - Alteration introduces significant K (+Fe, Mg, Rb and Mn) with near-complete loss of Li.
 2. Symplectic (graphic-textured), in-situ alteration where spodumene is in contact with Na/K-feldspar
 - Forms microscopic, graphic-textured, quartz-spodumene intergrowth (SQL-type)
 - Affects nearly all LCT pegmatites examined.
- 3 Derive a classification scheme that is useful in exploration targeting for economic LCT pegmatites and grade control in mining operations:
 - The majority of pegmatites belong to one of three main complex sub-types:
 - Spodumene — Greenbushes, Kathleen Valley, Dome North, Mt Marion
 - Petalite — Londonderry
 - Lepidolite — Sinclair Caesium.
 - Exceptions are Mt Cattlin, Bald Hill and Pilgangoora, classed as albite-spodumene types, and the Dalganga pegmatite, which is classed as an albite-type.
- Mica highly amenable to compositional analysis using field portable instruments (e.g. XRF, LIBS).
- Changes in the Ta-Nb mineralogy (e.g. Ta:Nb and Mn:Fe ratios) may provide an additional exploration tool useful for assessing pegmatite fractionation and mineralization style (i.e. Ta vs Nb content).

- Pegmatite classification is important to informing the most appropriate processing route that accommodates differences in the main Li host and associated mineralogy.
- 4 Petrochronological and geochemical synthesis of LCT pegmatite mineral systems in Western Australia:
 - Geochronological characterization of the Greenbushes, Pilgangoora, Dalgaranga, Bald Hill and Londonderry LCT pegmatites was undertaken by:
 - U–Pb dating of zircon
 - $^{40}\text{Ar}/^{39}\text{Ar}$ dating of spodumene
 - $^{40}\text{Ar}/^{39}\text{Ar}$ dating of muscovite.
 - Zircon U–Pb ages of 2643–2629 Ma obtained for project samples, consistent with other WA LCT pegmatites:
 - Coincides with a major period of global pegmatite emplacement from 2650–2600 Ma
 - A revised, older age for Greenbushes pegmatite at 2631 ± 4 Ma is a significant new finding
 - The relatively low U content (usually <100 ppm but also <<500 ppm) and relatively small grain size (predominantly <100 μm) of zircon analysed in the current study suggest they are inherited and not of pegmatitic origin
 - Thus, zircon U–Pb ages place a maximum age constraint on the timing of pegmatite crystallization.
 - $^{40}\text{Ar}/^{39}\text{Ar}$ dating determined a robust, plateau age of c. 2605 Ma for muscovite from Bald Hill:
 - Compares to 2643 ± 10 Ma zircon U–Pb age for Bald Hill, indicating that cooling took place deep in the crust over a period of ≈ 40 Ma
 - Similar interpretation made for Londonderry LCT pegmatite.
 - $^{40}\text{Ar}/^{39}\text{Ar}$ dating of Mt Cattlin spodumene established a robust plateau age of c. 1100 Ma:
 - Possibly related to spodumene alteration by a hydrothermal resetting event, from fluid flow associated with localized, mafic dyke emplacement.

Bulk-rock composition

Bulk compositional results indicate that the majority of pegmatite samples have SiO_2 contents >65 wt% and plot in the granite and granodiorite fields in the total alkali–silica diagram (Fig. 49). The sample plotting in the ‘Diorite’ field is sample BH1480, whereas gabbroic and doleritic samples from Mt Cattlin plot near the ‘Gabbro’ field (Fig. 49). Shand index plots, A/NK vs A/CNK (molar $\text{Al}_2\text{O}_3/(\text{Na}_2\text{O}+\text{K}_2\text{O})$ vs $\text{Al}_2\text{O}_3/(\text{CaO}+\text{Na}_2\text{O}+\text{K}_2\text{O})$), confirm that all examined pegmatites are strongly per-aluminous ($A/CNK \gg 1$), while a few samples (Pilgangoora, Greenbushes – Partington et al., 1995 and GSWA) are mildly per-aluminous with A/CNK values of 1.0–1.2 (Fig. 50). The per-aluminous nature is suggestive of S-type granitic melts as the parent source of the pegmatite (e.g. Bradley et al., 2017). Sample data points that plot on or close to a line of unit slope attest to the very low Ca content of the pegmatites examined in this study (Appendix 3).

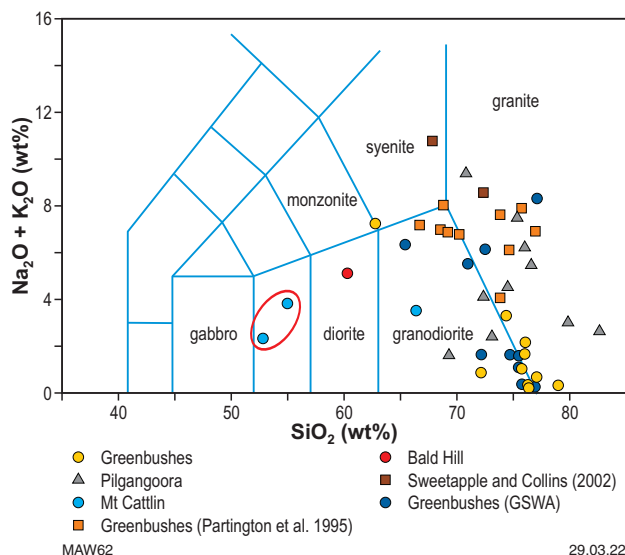


Figure 49. Total alkali–silica plot of pegmatite from selected LCT deposits examined in the present study. Previously published data for other LCT pegmatites include Greenbushes from Partington et al. (1995) and GSWA, and Wodgina and Mt Cassiterite (Sweetapple and Collins, 2002)

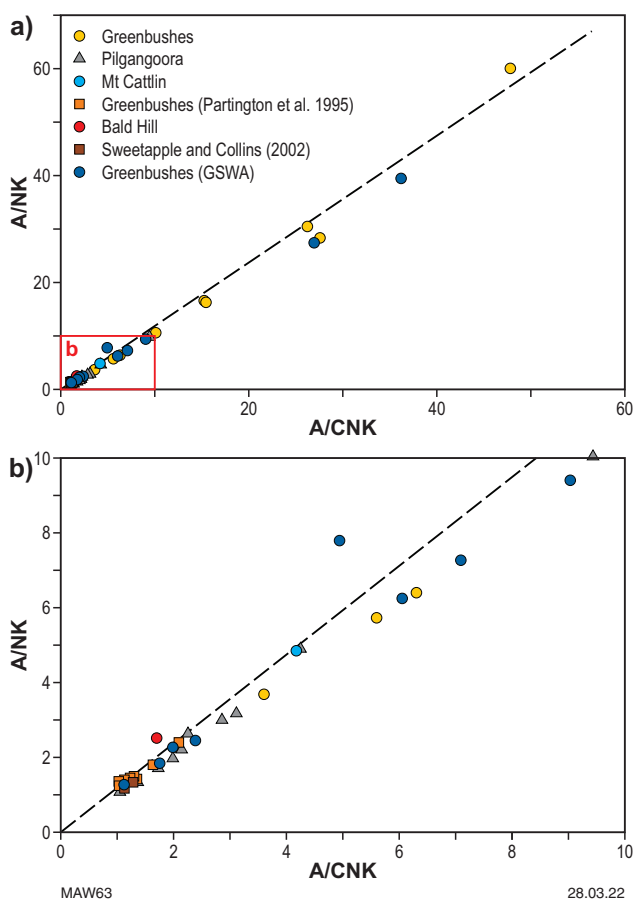


Figure 50. Shand Index plot for pegmatite bulk-rock analyses. Plots a) and b) show the same data, with plot b) an expanded view of the red rectangle in plot a), where A/NK = molar $(\text{Al}_2\text{O}_3/(\text{Na}_2\text{O}+\text{K}_2\text{O}))$ and A/CNK = molar $(\text{Al}_2\text{O}_3/(\text{CaO}+\text{Na}_2\text{O}+\text{K}_2\text{O}))$. The dashed line in plot b) is a line of unit slope. Previously published data for other LCT pegmatites include Greenbushes from Partington et al. (1995) and GSWA, and Wodgina and Mt Cassiterite (Sweetapple and Collins, 2002)

Spodumene composition

While spodumene compositions do not show any significant deviation from the ideal formula, $\text{LiAlSi}_2\text{O}_6$, they can contain minor contents of Fe, Mn, Na, K, Mg and Ca in the structure (Deer et al., 1980; London and Burt, 1982). A slight excess of SiO_2 is also reported for some spodumene analyses for Si atoms per formula unit (apfu) values slightly greater than 2 for stoichiometric spodumene (Deer et al., 1980). This may represent small amounts of SiO_2 originally in solid-solution with the high-temperature polymorph, β -spodumene (Deer et al., 1980). Discussion of the phase-stability relationships of Li–aluminosilicates is given in the section Pegmatite mineral fractionation. Alternatively, the common occurrence of small-phase inclusions, such as mica (as described in detail in section, Trace element associations: vein in-filling), may also account for the slight excess in silica.

A plot of the Li:Si vs Li:Al ratio, as derived from a combination of LA-ICP-MS analysis of Li (refer to Appendix 3) and EPMA analysis of Al and Si (e.g. Appendix 3), enables an evaluation of the relative enrichment or depletion of Li in spodumene (Fig. 51). Spodumene Li:Si and Li:Al (apfu) ratios are strongly correlated, with the majority of the spodumene analysed close to or slightly depleted compared to stoichiometric

spodumene (Fig. 51). Some spodumene from Bald Hill, Mt Marion and Dome North are slightly enriched in Li compared to stoichiometric spodumene (Fig. 51). In contrast, Pilgangoora spodumene is either slightly enriched (mafic host) or depleted (ultramafic host) in silicon. Spodumene from the Greenbushes C3 and C1 pits has a Li content very close to that expected for pure spodumene, while spodumene in drillcore C3DD024 is moderately depleted in Li (Fig. 51). Spodumene from Mt Cattlin displays the greatest variation in Li content, with spodumene being slightly enriched in Li to spodumene being the most severely depleted at a Li content of 0.7191 apfu (equivalent to 2.55 wt% Li – LA-ICP-MS analysis) (Fig. 51), compared to a Li content of 3.73% for stoichiometric spodumene.

The change in spodumene composition follows a highly predictable ($r^2 = 0.992$) and consistent trend (i.e. decrease), with the relative change (Δ) in apfu following the trend $\text{Li} > \text{Al} > \text{Si}$ (e.g. $\text{Li } \Delta\text{apfu} \approx 28\%$; $\text{Al } \Delta\text{apfu} \approx 4\%$; $\text{Si } \Delta\text{apfu} \approx 2.8\%$). Images of the Mt Cattlin spodumene samples analysed in Figure 51 show a progressive darkening from pink–white (MC100/MC200) to khaki (MC500) to green (MC300) or grey (MC1500) to spodumene that is completely,

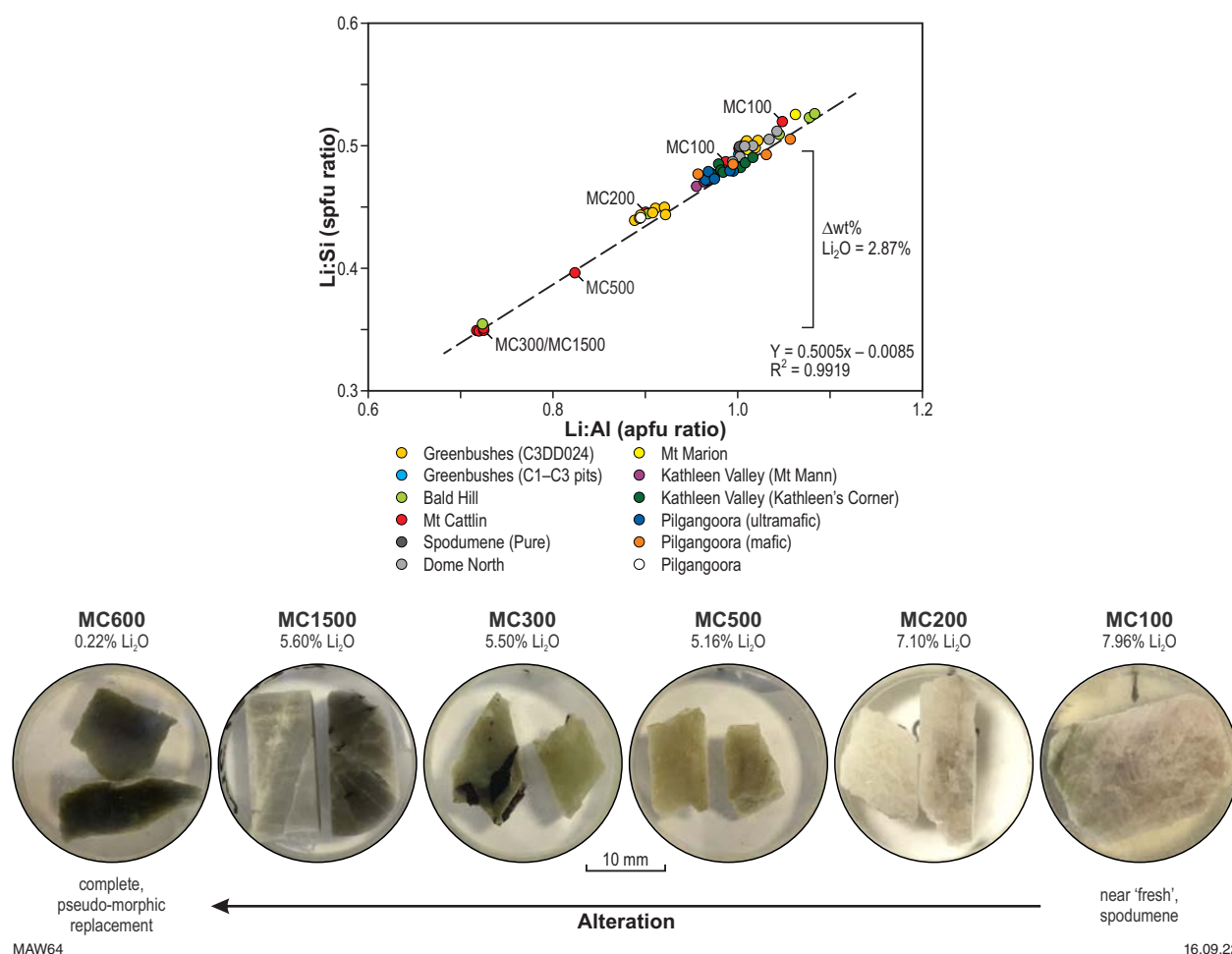


Figure 51. Li:Si vs Li:Al ratio of spodumene from selected LCT pegmatites. The black data point at Li:Si = 0.5 and Li:Al = 1.0 is for stoichiometric spodumene and was not included in the regression analysis. Al and Si apfu values were calculated from EPMA data, whereas Li apfu values are from LA-ICP-MS analyses. Decrease in the Li:Al and Li:Si values is mostly related to the leaching of Li with increasing alteration of Mt Cattlin spodumene. Examples of Mt Cattlin spodumene, as indicated in the plot, are presented below and show a progressive change in colour from pink–white to green to grey in response to increasing spodumene alteration, and finally to black–green ‘spodumene’ that is completely pseudo-morphically replaced by secondary, low Li-bearing mica

pseudo-morphically replaced by black–green secondary Li-bearing micas (MC600) in response to increasing spodumene alteration with almost the complete loss of Li (Fig. 51).

A ternary, Li–Si–Al plot more clearly demonstrates the change in spodumene composition in response to the effect of alteration, particularly for Mt Cattlin spodumene (Fig. 52). The structural formulae of the majority of spodumene in WA LCT pegmatites included in this study plot close to that expected for stoichiometric spodumene (Fig. 51). However, the composition of spodumene in the Greenbushes drillcore and, in particular, from Mt Cattlin shows a consistent loss of Li (i.e. leaching) and concomitant increase in the Si (apfu) content (Fig. 52) as the severity of alteration increases (refer to Fig. 52). In contrast, Al apfu values are relatively unchanged; that is, they are unaffected by alteration (Fig. 52).

Spodumene element impurities

The most significant impurities in spodumene are Fe and Mn with contents ranging from 500 to 1200 ppm. Figure 53 shows the variation in Fe and Mn content, expressed as apfu, observed in the structure of spodumene in samples collected in this study.

At Kathleen Valley, spodumene from Kathleen's Corner is markedly enriched in Fe and Mn compared to spodumene from Mt Mann (Fig. 53). In the drillcore samples examined at Pilgangoora, there was no obvious difference between Fe and Mn content in spodumene for pegmatites hosted in ultramafic or mafic rocks. For spodumenes from other deposits there were no obvious trends in the Fe and Mn compositions with host-rock type. High Fe and Mn spodumene in Mt Cattlin can be attributed to spodumene which has undergone late-stage alteration.

The (Fe+Mn) impurities appear unrelated to changes in the Li:Al (apfu), which for stoichiometric spodumene has a value of 1 (Fig. 53). A slight depletion in the Li content for spodumene in the Greenbushes core decreases the Li:Al ratio (to about 0.9), whereas alteration of spodumene and the associated loss of Li results in the altered spodumene from Bald Hill (concentrate) and Mt Cattlin, with a near-constant Li:Al apfu value of 0.72. (Fig. 53). Comparable (Fe+Mn) apfu values (0.02 – 0.034) were reported for spodumene from the Kolmozero pegmatite field, in the Kola region, Russia (Morozova et al., 2020), and for spodumene (0.006 – 0.035, up to 0.088 apfu) from predominantly Canadian and US pegmatites (Filip et al., 2006). Incorporation within spodumene is considered to be accommodated by a portion of Fe^{2+} substituting for Al^{3+} on the M1 site, with minor replacement of Li^+ by Fe and Mn on the M2 site (Morozova et al., 2020). Although Fe is generally assigned to the ferrous state, Mössbauer's spectroscopic analysis of spodumene confirmed that both Fe^{2+} and Fe^{3+} can be hosted by spodumene (e.g. Filip et al., 2006). The partitioning of Fe across the M1 and M2 sites within spodumene may account for the relatively constant behaviour of the Li:Al ratio with increasing impurity content (Fig. 53). The presence of element impurities, particularly elevated contents of Fe and Mn has implications for the calcination processing of spodumene, where exsolution of Fe and Mn from spodumene, as oxides associated with 'blow-out' structures, may promote spodumene decrepitation, as discussed in section, Partial melting of mica in calcined spodumene.

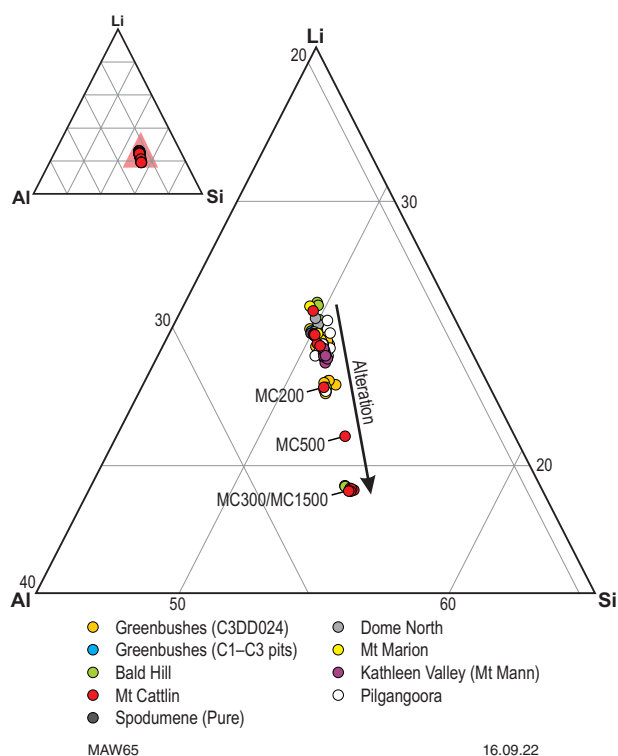


Figure 52. Ternary Li–Si–Al plot of spodumene apfu values from various WA LCT pegmatites. The inset Li–Si–Al plot shows detail of the larger ternary plot as outlined by the red triangle. Li, Al and Si apfu values for stoichiometric spodumene are shown by the black data spot. Mt Cattlin samples MC200, MC500 and MC300 define an increasing trend of a loss of Li and relative increase in Si with increasing spodumene alteration (refer to Fig. 50). Compositional Al (apfu) values are relatively unaffected by alteration

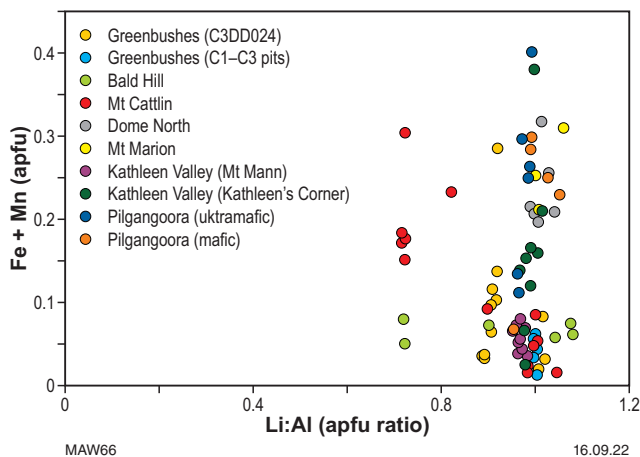


Figure 53. Impurity content as (Fe+Mn) apfu vs Li:Al (apfu) ratio for spodumene from selected LCT pegmatites. Al apfu values and Fe+Mn (apfu) contents were calculated from EPMA data, whereas Li apfu values were determined by LA-ICP-MS analysis

The other major element impurity of significance measured in spodumene was Na, which showed comparable and consistent contents ranging from 500 to 1200 ppm across all pegmatite deposits (Fig. 54). Similar Na contents were reported for spodumene (1039–1558 ppm Na) from the Kolmozero pegmatite (Morozova et al., 2020); in the Leviäkangas, Syväjärvi and Rapasaaret pegmatites (668–1261 ppm Na), Finland (Ahtola et al., 2015); and in spodumene (from 668 ppm up to 5267 ppm) examined by Filip et al. (2006). At the Tanco pegmatite, Na can occur as the dominant trace element impurity, particularly in secondary spodumene formed by the replacement of petalite (e.g. Černý et al., 1996; Stilling et al., 2006). The presence of Na likely occurs via the replacement of small amounts of Li on the M2 site of spodumene (Deer et al., 1980; Filip et al., 2006).

Normalized, trace element patterns for spodumene from selected WA LCT pegmatites show variable enrichment–depletion patterns for the majority of the trace elements

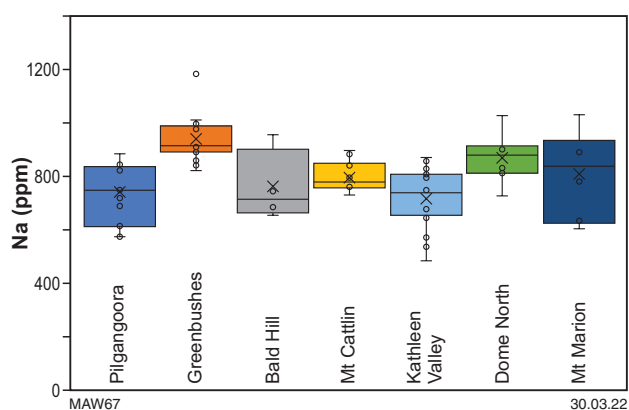


Figure 54. Box plot of the Na content (ppm, LA-ICP-MS analysis) of spodumene from selected WA pegmatites

analysed (Fig. 55). Though highly variable, only Ga (32–147 ppm; average 85 ppm) and Sn were consistently enriched in spodumene across all LCT pegmatites, with enrichment of Sn varying by two orders of magnitude from 8 ppm to ≈ 700 ppm (e.g. Fig. 56).

The REE contents of spodumene are unsurprisingly low due to their incompatibility (large ionic radius, trivalent coordination) in the spodumene structure (Fig. 57). However, there was no consistent depletion trend or anomaly that might enable discrimination of the WA LCT pegmatites. Future work should consider comparing REE patterns for spodumene from other Australian (not accessible in the current study) and worldwide LCT pegmatites to determine if such plots could be applied as a provenance indicator to ‘fingerprint’ the regional (country) source of LCT pegmatites.

Mica composition

Micas can be an important host for Li mineralization, although they may comprise only a relatively small proportion of pegmatite-phase composition. The lepidolite solid-solution series of Al-bearing micas, polyolithionite–trilithionite, represent a sequence of high-grade Li (polyolithionite) to low-grade Li (trilithionite) tri-octahedral micas (Aylmore et al., 2018a). Di-octahedral, Al–mica muscovite is a low-grade host of Li with contents up to 1.5% Li (Aylmore et al., 2018a). Micas can also be a source of deleterious elements such as F, which can be problematic in the processing of pegmatite ore (Aylmore et al., 2018a).

In the process of crystallization of a pegmatite melt, the relative abundance of incompatible elements like Rb, Cs, Li, Mn, Ga, Tl, Sn, Ta and F increases, such that the composition of the final crystallization products, as expressed by element ratios such as K:Rb, K:Cs,

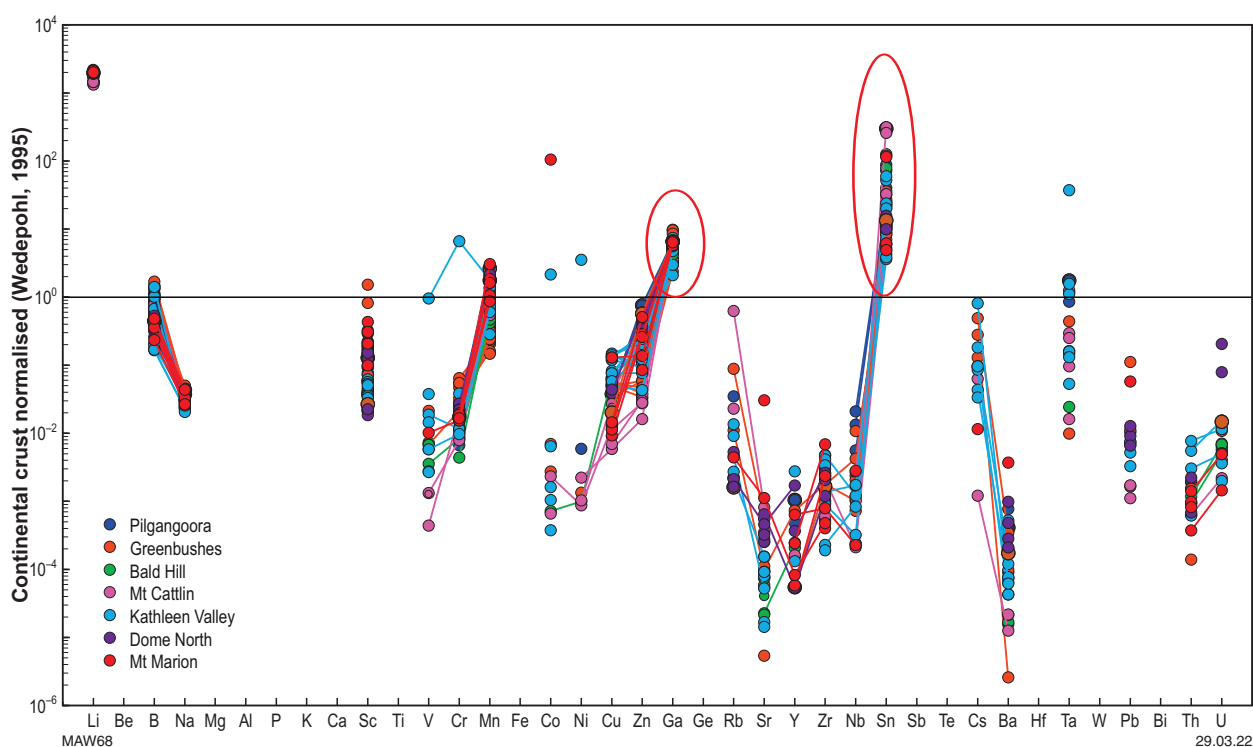


Figure 55. Continental crust normalized trace element plot for spodumene from selected WA LCT pegmatites. Plots constructed using normalizing factors from Wedepohl (1995). Trace element analyses by LA-ICP-MS analysis. Only Ga and Sn (circled) are consistently enriched in spodumene

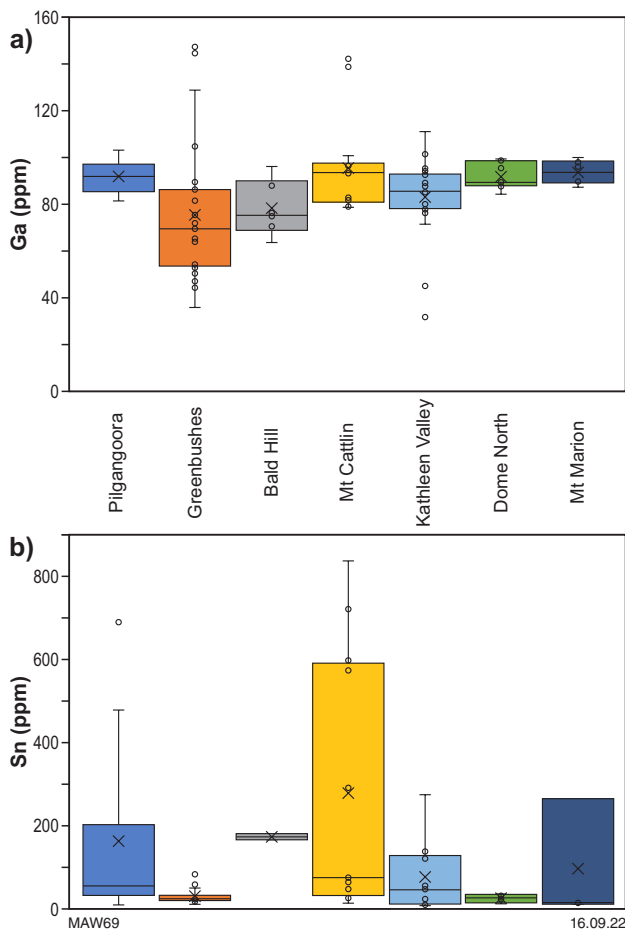


Figure 56. Box plots of: a) Ga (ppm); and b) Sn (ppm) content of spodumene for selected WA LCT pegmatites. Data are from LA-ICP-MS analysis

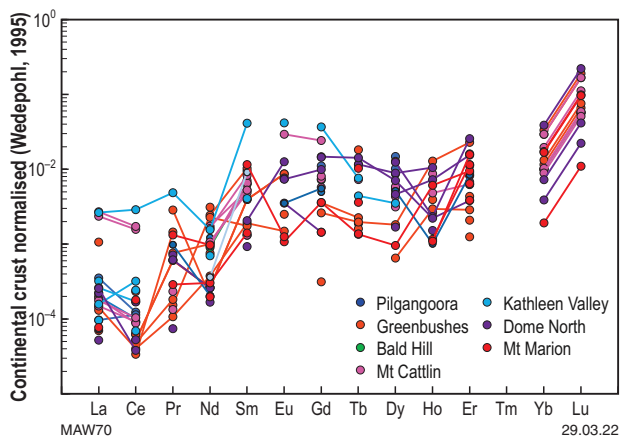


Figure 57. Continental crust normalised REE plot for spodumene from selected WA rare-element pegmatites. Plots constructed using normalizing factors from Wedepohl (1995). Trace element analyses by LA-ICP-MS analysis

K:Ti, Fe:Mn and Al:Ga, can potentially be used as a measure of the relative degree of crystal fractionation in a variety of pegmatites (e.g. Shaw et al., 2016). As the fractionation evolution continues, the concentration of these incompatible elements increases, resulting in the concomitant decrease in element ratios such as K:Rb, K:Cs, K:Ti, Fe:Mn and Al:Ga (Shaw et al., 2016). As the mica structure is capable of hosting most of these elements, compositional analysis of mica (muscovite and lepidolite) was undertaken to characterize the deportment of deleterious elements, such as F, and to determine if trends in K:Rb, K:Cs, K:Ti, Fe:Mn and Al:Ga exist that can be used to infer fractionation evolution (Shaw et al., 2016).

Measured Li and F contents of muscovite and lepidolite show a strong, positive relationship (Fig. 58), consistent with previous work (Aylmore et al., 2018a), indicative of the simultaneous uptake of Li and F during mica crystallization. The same trend is observed for micas from Canadian rare-metal pegmatites, including the Tanco Deposit (e.g. Černý et al., 1996; Černý et al., 2012b; Fig. 58). The Mt Cattlin and Sinclair lepidolites are the most fluorinated with contents of ≈ 4.5 wt% F and with correspondingly elevated Li contents of about 2.2 – 2.5 wt% (Fig. 58). In contrast, Mt Marion and Dome North muscovite were consistently the least fluorinated and contained the least Li (Fig. 58). Bridging the compositional 'end-member' extremes, muscovite from the Sinclair, Londonderry and Mt Cattlin displayed the greatest variation in Li and F composition (Fig. 58).

Values of the mica Al:Si ratio were strongly ($R^2 = 0.872$) and inversely related to Li content (Fig. 59a), similar to the findings of Aylmore et al. (2018a), indicating that the uptake of Li replaces Al in the mica octahedral site (Aylmore et al., 2018a). The strongly related, curvi-linear

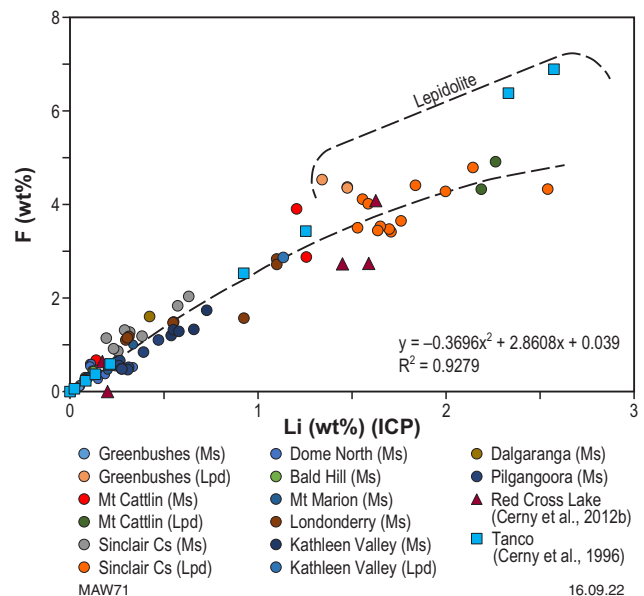


Figure 58. Plot of Li wt% vs F wt% for muscovite (Ms) and lepidolite (Lpd) in LCT pegmatites of the current study. Weight percentage F values are from EPMA analysis, while Li wt% values were measured by LA-ICP-MS analysis. Lepidolites are more highly fluorinated with a correspondingly greater Li content than muscovite. Comparative data for the analysis of mica from Canadian pegmatites (e.g. Tanco – Černý et al., 1996; and the Red Cross Lake pegmatite – Černý et al., 2012b) were excluded from the regression analysis

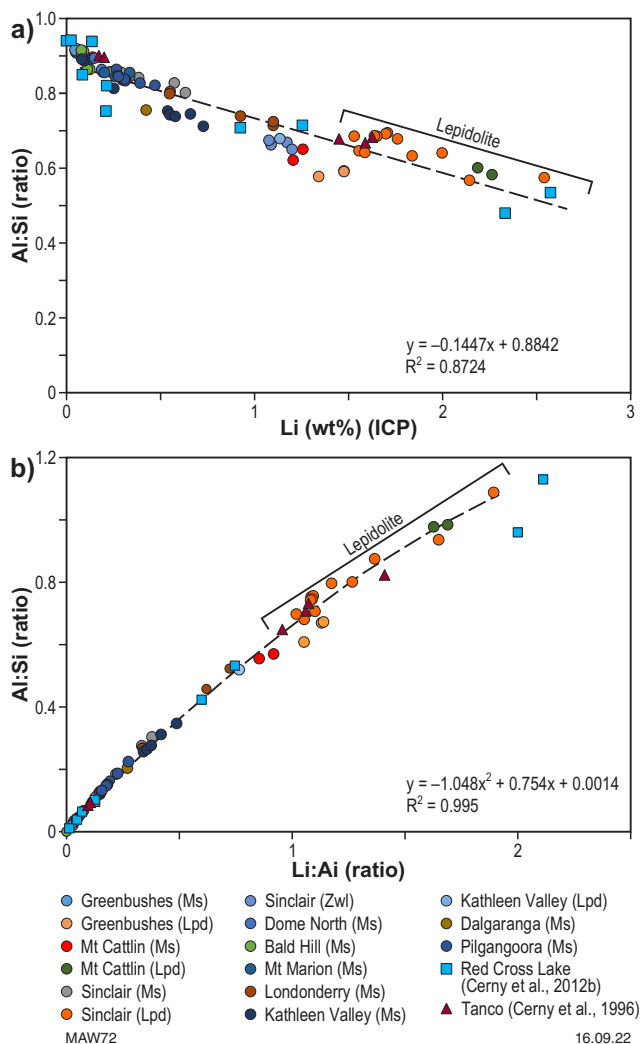


Figure 59. Plot of: a) Al:Si ratio vs Li wt%; and b) Li:Si vs Li:Al ratio for muscovite (Ms) and lepidolite (Lpd) LCT pegmatites of the current study. Element ratio values for muscovite and lepidolite were calculated from EPMA (Al, Si) and LA-ICP-MS (Li) analyses. Lepidolite data points are bracketed. Data for muscovite and lepidolite in Canadian pegmatites (Tanco – Černý et al., 1996; Red Cross Lake pegmatite – Černý et al., 2012b) were excluded from the regression analysis

relationship between Li:Si and Li:Al ratios (Fig. 59b), across the muscovite and lepidolite compositional range, also supports the depletion of Si from the tetrahedral site in the di- and tri-octahedral micas. While it is considered that Li uptake in di-octahedral muscovite occurs via the substitution of octahedral Al^{3+} (Aylmore et al., 2018a), these results indicate that the substitution mechanism of Li in muscovite is more complex and continues into tri-octahedral lepidolite. As noted for the relationship between the F and Li content of muscovite (e.g. Fig. 58), the Sinclair and Mt Cattlin lepidolite, with the highest Li content (about 2.3 – 2.5 wt%) were also the most depleted in Al. Similarly, Bald Hill and Kathleen Valley muscovite were the least depleted in Al (Fig. 59).

Mica K:Rb ratio values for pegmatite samples are presented in Figure 60 to enable comparison with published data, with values <20 indicating that the host pegmatites are highly fractionated, more so than Scottish and Red Cross Lake rare-metal pegmatites (Fig. 60a). Muscovite at Mt Cattlin

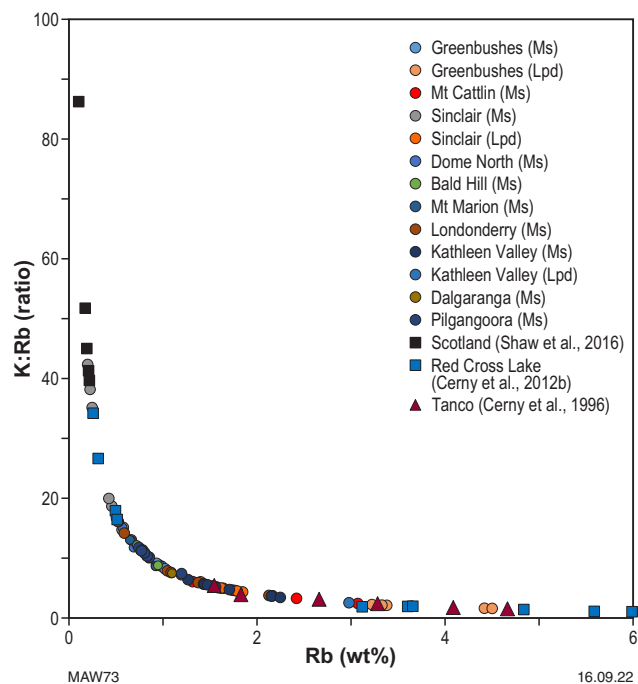


Figure 60. K:Rb ratio vs Rb (wt%) content of mica (muscovite [Ms] and lepidolite [Lpd]) in Western Australian LCT pegmatites, and their comparison to LCT pegmatites from Scotland and Canada (e.g. Tanco – Černý et al., 1996; Red Cross Lake pegmatite – Černý et al., 2012). EPMA data was used to calculate the K:Rb ratio. Published data are for examples from Scotland (Shaw et al., 2016) and Canada (Černý et al., 1996, 2012), and were not included in the regression analyses

showed the lowest K:Rb ratio value (<2.5) and highest Rb content (>3 wt%) revealing the host pegmatite to be the most highly fractionated of the muscovite-bearing, WA LCT pegmatites (Fig. 60b). Conversely, muscovite analyses for the Londonderry and Sinclair LCT pegmatite suggest these were comparatively the least fractionated of the WA pegmatites.

Of the WA lepidolite-bearing, rare-element pegmatites, the examples from Greenbushes were the most highly fractionated and were comparable to the extremely fractionated Canadian lepidolites, including lepidolite from the Tanco Deposit (Fig. 60), which has been described as one of the most highly fractionated LCT pegmatite deposits in the world (e.g. London, 2008 as cited by Bradley et al., 2017). To remove the closure effect that operates when plotting X/Y vs Y, which accounts for the highly correlated nature between K and Rb, the mica K:Rb vs Cs composition was assessed as an indicator of pegmatite fractionation (Fig. 61).

Changes in the mica K, Rb and Cs composition display a well-correlated fractionation trend (Fig. 61) similar to that based on the K and Rb composition (Fig. 60). Similarly, Mt Cattlin muscovite and Greenbushes lepidolite were the most highly fractionated of the WA pegmatites samples examined, comparable to mica from the highly fractionated Tanco and Red Cross Lake pegmatites (Fig. 61). This demonstrates the potential for changes in the mica K, Rb and Cs composition to be applied as a valuable exploration tool in assessing the mineralization potential of a pegmatite deposit.

Further discussion of the relative changes in the inferred fractionation trends for the different WA pegmatites is given in section, Pegmatite mineral fractionation.

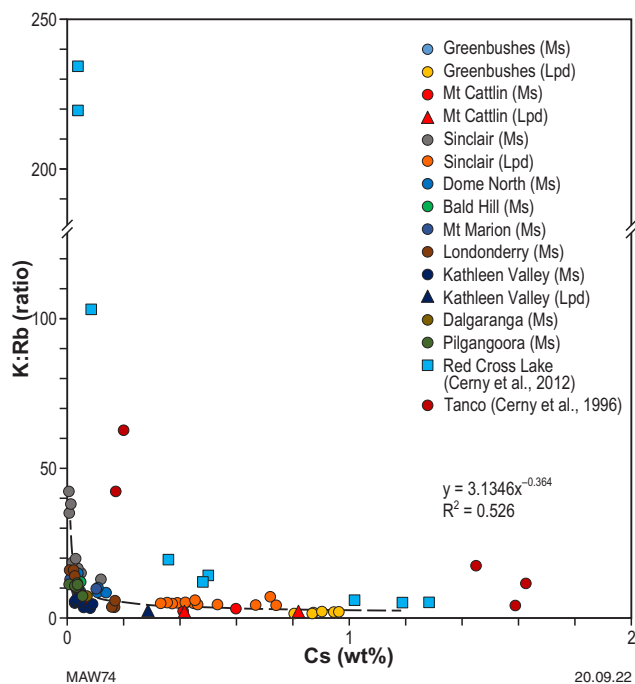


Figure 61. K:Rb vs Cs (wt%) content of mica (muscovite [Ms] and lepidolite [Lpd]) in Western Australian LCT pegmatites, and their comparison to LCT pegmatites from Canada (e.g. Tanco-Černý et al., 1996; Red Cross Lake pegmatite – Černý et al., 2012). EPMA data was used for measurements of K, Rb and Cs content. Published data for examples from Canada (Černý et al., 1996, 2012) were not included in the regression analyses

Mica trace element and REE impurities

Continental crust normalized plots of mica (muscovite+lepidolite) trace element composition show highly varied enrichment–depletion trends, with mica from WA LCT pegmatites most strongly enriched in Li, Rb, Sn, Cs and Ta, and with lesser enrichment in B, Ga and Nb (Fig. 62). Owing to the nature of the mica structure, K can be replaced by Na, Rb, Cs, Ca and Ba (Deer et al., 1992), octahedral Al may be substituted by Mg, Fe²⁺, Fe³⁺, Li, Mn, Ti, Cr and V (Deer et al., 1992; Li et al., 2021), and Si may be replaced by Al, B, Be and Fe³⁺ (Li et al., 2021). In our case, enrichment in Sn, Ga and Nb is likely to occur by the replacement of Al³⁺ in the mica structure (e.g. Li et al., 2021), due to the similar ionic size of Sn⁴⁺ (0.69 Å), Ga³⁺ (0.62 Å) and Nb⁵⁺ (0.64 Å) compared to Al³⁺ at 0.535 Å (e.g. Shannon, 1976).

Box plots for selected trace elements (B, Ga, Nb, Sn, Ta) are presented in Figure 63. Overall, these trace elements are enriched to similar orders of magnitude with contents generally in the range 50–500 ppm, excluding outliers (Fig. 63). Comparable enrichment in Nb (110–258 ppm – Li et al., 2021; to 782 ppm – Shaw et al., 2016), Ta (to 148 ppm – Shaw et al., 2016; 15–88 ppm – Li et al., 2021), Ga (to 224 ppm – Shaw et al., 2016) and Sn (101 ppm – Shaw et al., 2016) was reported for muscovite hosted by rare-metal pegmatites in Scotland (Shaw et al., 2016) and in the Renli Deposit, Hunan, China (Li et al., 2021).

Globally, changes in the mica trace element composition (e.g. Figs 62, 63) do not show any regional trends that may enable the identification of individual LCT deposits. However, at the Sinclair Caesium Deposit, marked differences in the B, Nb and Ta enrichment in mica may be attributed to the crystallization evolution associated with increasing fraction during cooling of

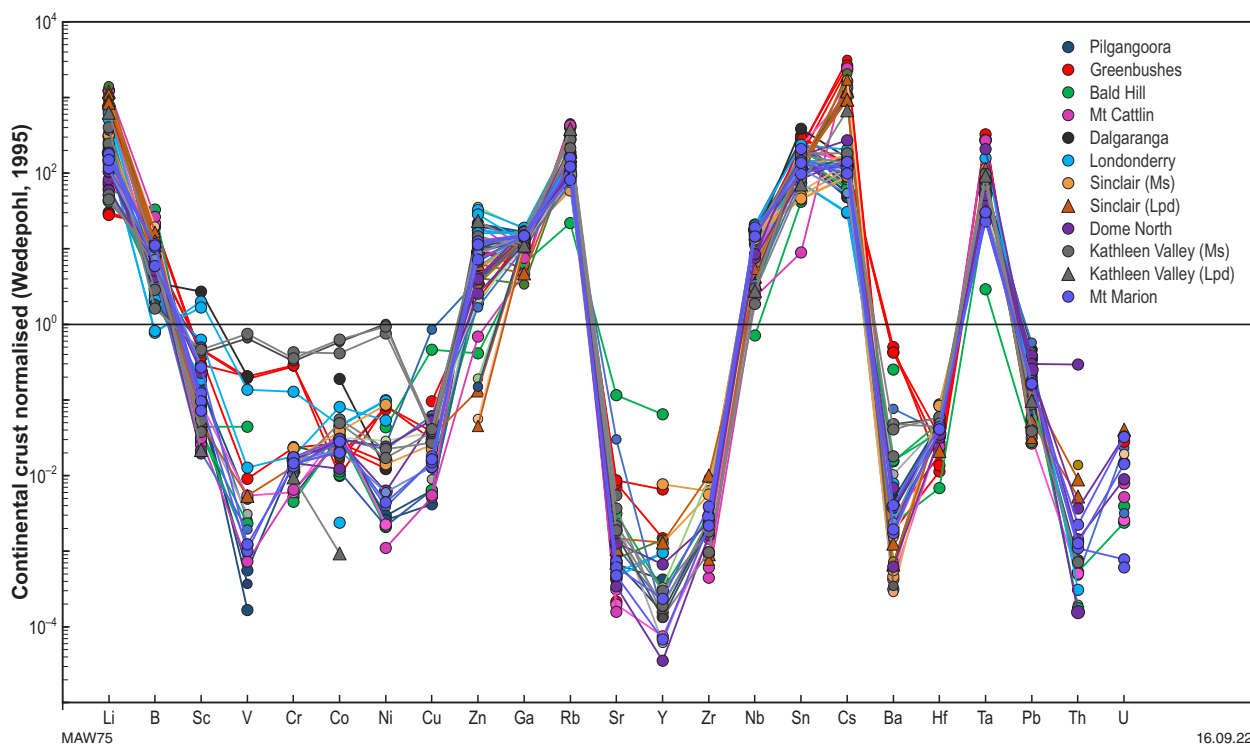


Figure 62. Continental crust normalized trace element plot for muscovite and lepidolite from selected WA rare-element pegmatites. Mica, as muscovite and lepidolite, is most strongly enriched in Li, Rb, Sn, Cs and Ta, with lesser enrichment in B, Ga and Nb. Plots constructed using normalizing factors from Wedepohl (1995). Trace element measurement by LA-ICP-MS analysis

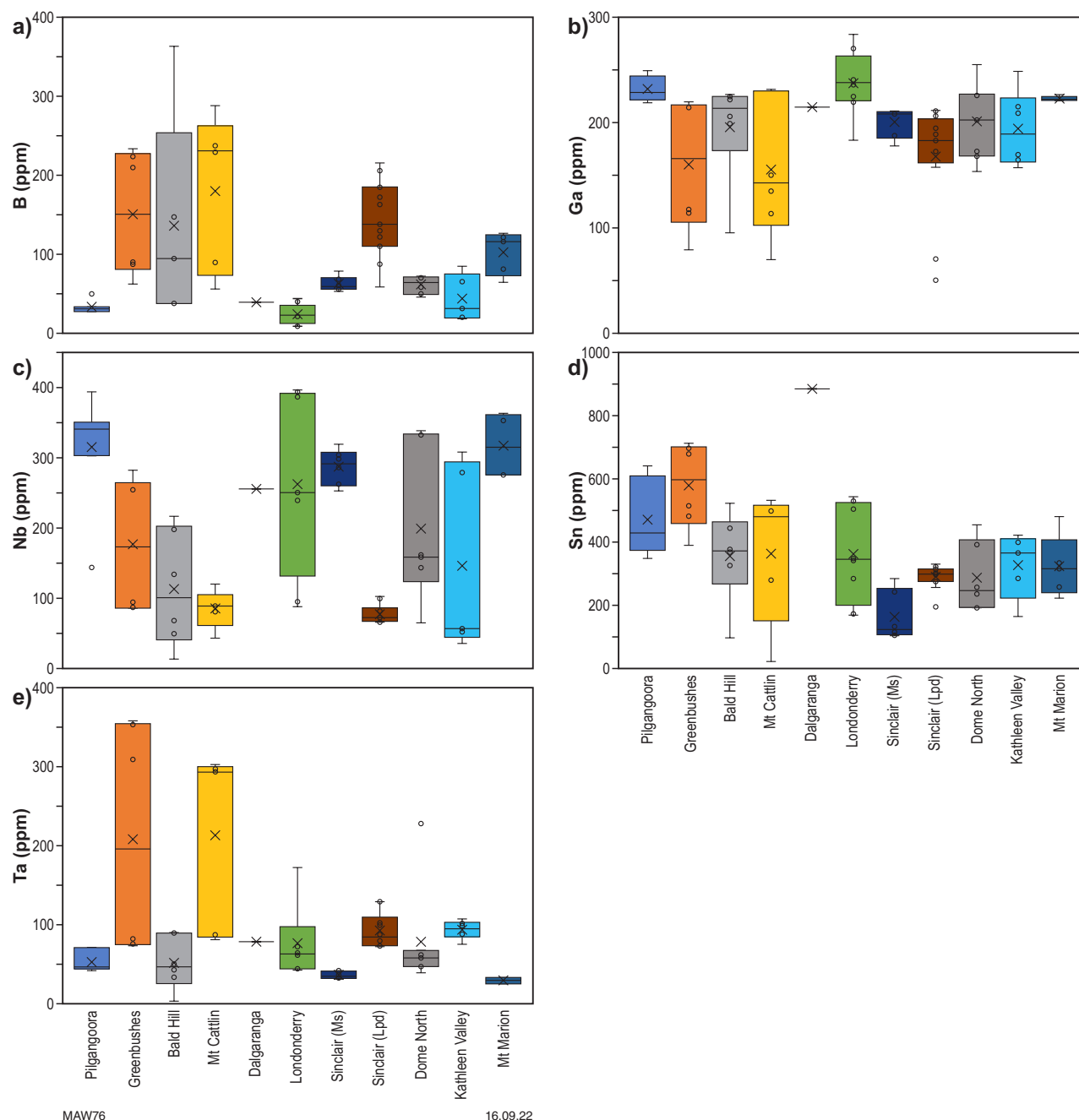


Figure 63. Box plots of the B, Ga, Nb, Sn and Ta contents of mica (muscovite, Ms and lepidolite, Lpd) for selected WA LCT pegmatites. Data are from LA-ICP-MS measurements (units as ppm)

the pegmatite melt. Early crystallization of muscovite results in the relative enrichment of Nb, whereas later crystallization of lepidolite (e.g. refer to section, Pegmatite mineral fractionation) enables the uptake of B and Ta to approximately 2–3 times the content in muscovite (Fig. 63).

Continental crust normalized plots of the mica REE composition show a strong depletion of all REEs across all the LCT pegmatites examined (Fig. 64). As is the situation for spodumene, it would be interesting to determine if the same depletion trend occurs for other Australian and worldwide LCT pegmatites and, if so, if this may have application as a potential provenance indicator tool for characterizing the LCT pegmatite source.

Being enriched in mica, the Cs and Ta composition of muscovite has been identified as an exploration tool for

identifying potential Ta mineralization in pegmatites (e.g. Selway et al., 2005; Shaw et al., 2016). As demonstrated by Selway et al. (2005), pegmatite containing muscovite with a Ta content >65 ppm and a Cs content >500 ppm is highly likely to host Ta–Nb mineralization.

A plot of the Ta and Cs contents of muscovite in LCT pegmatites is presented in Figure 65, compared against the suggested muscovite Ta and Cs contents as indicators of potential Ta mineralization (e.g. Selway et al., 2005). Measured Ta and Cs contents of lepidolite were not included as the Ta content of lepidolite can be comparable to muscovite, whereas the Cs content of lepidolite is significantly enriched relative to muscovite. For example, at Kathleen Valley, the Ta content of 102 ppm for Mt Mann lepidolite (KVDD0018_#5) is comparable to the average Ta content of 82 ppm for

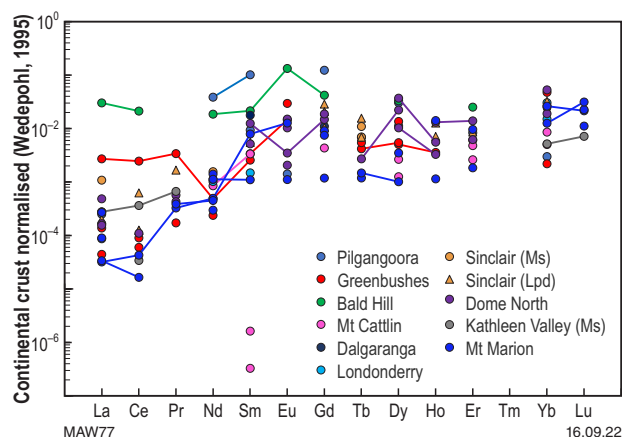


Figure 64. Continental crust normalized REE element plot for muscovite (Ms) and lepidolite (Lpd) from selected WA rare-element pegmatites. Micas are strongly depleted in REEs across all the pegmatite deposits examined. Plots constructed using normalizing factors from Wedepohl (1995). REE measurements by LA-ICP-MS analysis

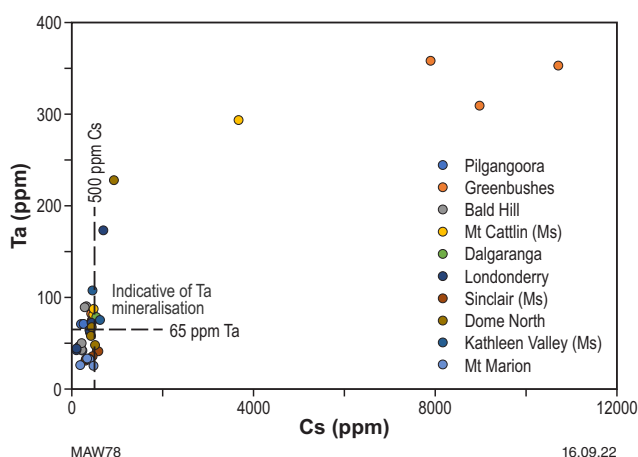


Figure 65. Plot of the Ta vs Cs content of muscovite in WA LCT pegmatites. Ta and Cs limits indicative of the potential for Ta mineralization (e.g. Selway et al., 2005) are shown by the dashed lines. Measurement of the Ta and Cs content are from LA-ICP-MS analyses. Lepidolite was not included due to the relative enrichment of Cs compared to Ta for this mica type (refer to discussion)

muscovite (KVDD0018_#6). In contrast, the Cs content of lepidolite in this sample at 2300 ppm is double that measured for muscovite at 904 ppm. Similarly, at the Sinclair Caesium Deposit, the Cs content of lepidolite (3320–7090 ppm) is ≈ 8 –10 times greater than the Cs content of muscovite (300–580 ppm), whereas enrichment of Ta in lepidolite (72–130 ppm) is approximately 2–4 times that in muscovite (31–41 ppm).

Muscovite from LCT pegmatites that plot in the lower left quadrant of the Ta vs Cs plot (i.e. Ta < 65 ppm and Cs < 500 ppm) or contain Cs contents < 500 ppm are unlikely to contain significant Ta mineralization (Fig. 65). Such LCT pegmatites include the Sinclair Caesium Deposit, Mt Marion, Londonderry and the Pilgangoora pegmatites. Individually, while Ta–Nb oxides were detected in these deposits by TIMA mineral mapping (refer to Appendix 3), Ta–Nb oxides were absent or rare to uncommon, occurring as disseminated grains, generally < 50 μm but up to 200–600 μm in size.

At the Dome North Cade pegmatite, the Ta and Cs composition of all muscovite examined, bar one sample, does not support the presence of potential Ta mineralization (Fig. 65). This is consistent with the current resource estimate (indicated+inferred) of 33 ppm Ta_2O_5 for the Cade Deposit (Essential Metals, 2021). This is also consistent with the lack of columbite–tantalite detected by TIMA mineral mapping in drillcore examined from the Cade Deposit. Further indication of the relatively poor Ta mineralization at Cade, may be derived from the few columbite–tantalite grains that were detected (e.g. Appendix 4). For example, rare columbite–tantalite occurred as < 50 to 250 μm long laths, with phase composition of Nb > Ta and Fe > Mn, as indicated by EDS analysis (refer to samples PDRC319_#9-slide #9; PDRC319_#15-slide #12 and PDRC319_#20-slide #14 in Appendix 4). Despite the poor quality of the EDS signal, the inferred Nb > Ta and Fe > Mn compositional trends indicate a ferrocolumbite dominated mineralogy (refer to Appendix 4) for a pegmatite melt that has undergone limited fractionation. Changes in the columbite–tantalite, Ta:Nb and Mn:Fe composition and their relationship to pegmatite fractionation is discussed in more detail in section, Tantalum–Niobium geochemistry.

In contrast, the known Ta-bearing LCT pegmatites, such as the Greenbushes, Mt Cattlin, Londonderry and Kathleen Valley Deposits, all plot in the upper right quadrant, with muscovite Ta and Cs contents indicative of Ta mineralization (Fig. 65). The exceptions to this were for muscovite from Bald Hill, a known Ta producer (refer to the section Bald Hill), and the Dome North Cade pegmatite which all contained < 500 ppm Cs but were variably enriched in Ta (e.g. to 228 ppm Ta at Dome North; Fig. 65). A reason for the discrepancy between our study and the reported Ta content at Bald Hill may be attributed to pit sampling at Bald Hill not targeting known Ta mineralization at the pegmatite. At the time of our site visit to Bald Hill, sampling was restricted to pit exposures only of the pegmatite; access to drillcore was limited or not available.

Hence, a more comprehensive characterization of mica composition at Bald Hill is required to establish if the Ta and Cs composition of muscovite can be established as a universal tool for identifying potential Ta mineralization across all WA rare-element pegmatites. However, overall, this study tends to support the hypotheses of Selway et al. (2005) and Shaw et al. (2016) that Cs and Ta enrichment in muscovite is a potential indicator of Ta-mineralized pegmatites. A good rule of thumb in greenfield exploration would be to consider using threshold values of 65 ppm Ta and 500 ppm Cs in muscovite.

Tantalum–niobium geochemistry

Tantalum mineralization in rare-element pegmatites typically occurs as columbite–tantalite, $(\text{Mn,Fe})[\text{Nb,Ta}]_2\text{O}_6$ (Bradley et al., 2017). Fetherston (2004) provide a detailed description of the characteristics of Ta mineralization associated with mainly hard-rock (i.e. pegmatite) occurrences in Western Australia. Phase composition and Nb–Ta–Sn–Ti-oxide mineralogy can be useful in assessing the degree of fractionation in LCT pegmatites (e.g. Shaw et al., 2016). With increasing fractionation, columbite–tantalite composition evolves through an enrichment of Ta over Nb and Mn over Fe, so that the Ta:Nb and Mn:Fe ratios increase as the pegmatite evolves (Bradley et al., 2017).

The evolution or increasing fractionation of LCT pegmatites may be reflected in the evolution of Ta–Nb mineralogy,

with the least evolved, parental pegmatites characterized by complex Ta:Nb minerals such as aeschynite-(Y) – $(Y, \text{Ln}, \text{Ca}, \text{Th})_9 \text{Ti}_2 (\text{Nb})_2 (\text{O}, \text{OH})_6$ and euxenite-(Y) – $(Y, \text{Ca} < \text{Ce}, \text{U}, \text{Th}) (\text{Nb}, \text{Ta}, \text{Ti})_2 \text{O}_6$. Highly evolved pegmatites contain oxides dominated by Ta, such as ixiolite $(\text{Ta}, \text{Nb}, \text{Sn}, \text{Fe}, \text{Mn})_4 \text{O}_8$ and wodginite $(\text{MnSnTa}_2 \text{O}_8)$ (Fetherston, 2004).

Phase distribution characterization by TIMA mapping identified the occurrence of Ta–Nb-bearing phases in several of the rare-element pegmatites examined. Representative

examples of Ta–Nb oxides and other exotic phases detected in these deposits is shown in Figure 66, with EDS composition analysis of Ta:Nb-bearing phases detected tabulated in Appendix 6. For Mt Marion, Dome North and Sinclair Deposits, the quality of the EDS analysis was poor, and so no analysis was possible.

The most common Ta–Nb-bearing phase identified in the LCT pegmatites examined in our study was present as a low Ca-bearing (mainly 1–2% but up to 5%), potentially

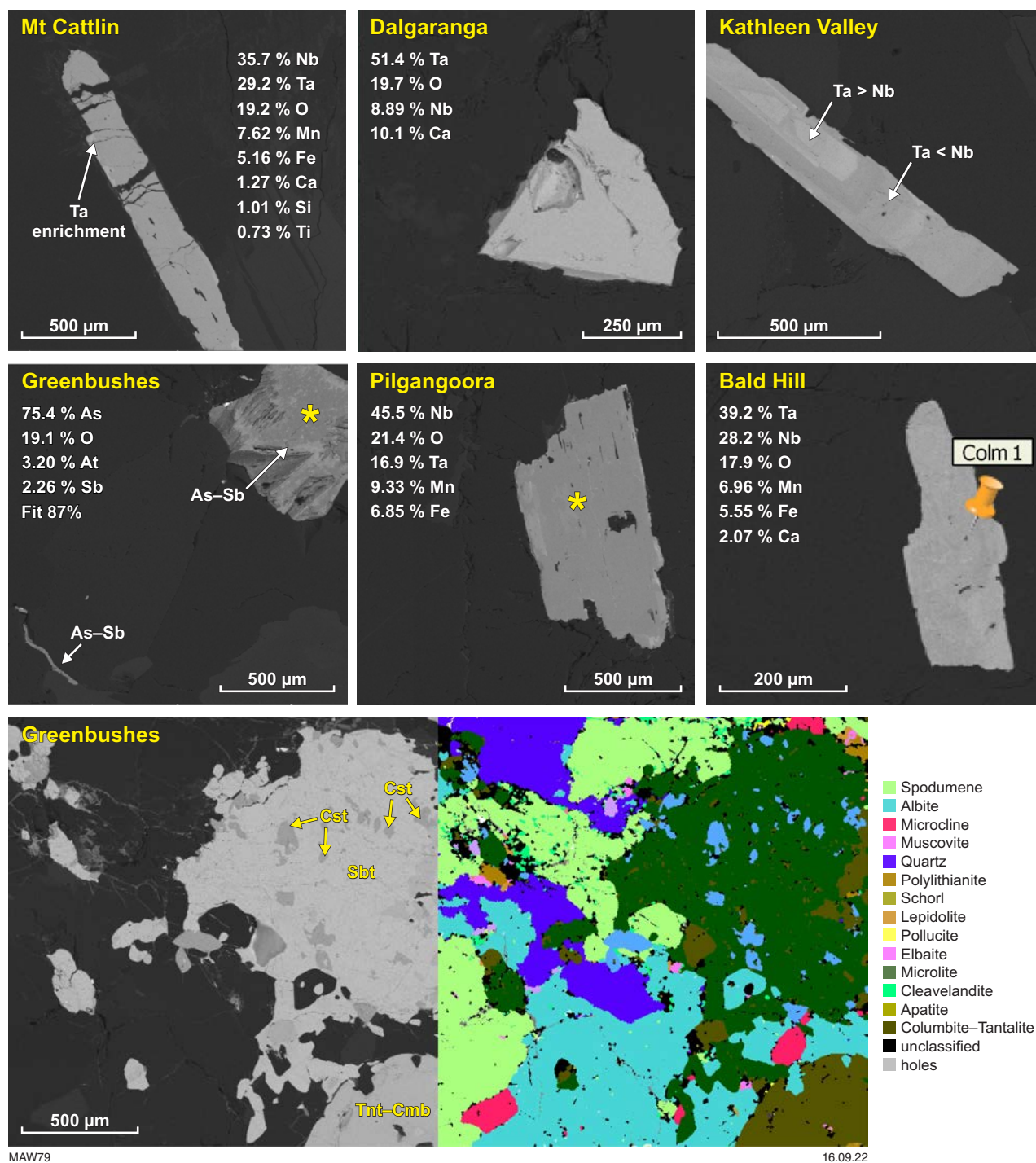


Figure 66. Representative examples of Ta–Nb-bearing phases detected in LCT pegmatites from the Mt Cattlin, Dalgaranga, Kathleen Valley, Bald Hill and Pilgangoora pegmatites. In addition, an exotic As–Sb–At-bearing phase was detected at Greenbushes (drillcore C3DD024) as a large, equant grain and as vein in-fill within apatite. Tantalite–columbite grains often show Ta enrichment along the grain margins as evidenced by brighter BSE contrast, as shown at Mt Cattlin or as compositional zoning that likely occur from changes in Ta:Nb and Mn:Fe ratios during crystal growth (Kathleen Valley). Two Ta-mineral series were identified at Greenbushes, comprising a (Sb-free) tantalite–columbite Lseries and a Sb-bearing stibiotantalite (Sbt), which also hosts (Ta-bearing) cassiterite (Cst)

low Tm-bearing, tantalite–columbite solid–solution series as typically prismatic or blocky, lath-like crystals (e.g. Fig. 66; Appendix 6). Notable examples of LCT pegmatite Ta mineralization include compositionally complex, acicular (to 1000 µm) Nb>Ta oxide at Mt Cattlin, with evidence of Ta enrichment about the grain margin (Fig. 66; slide #18, Appendix 4). Similarly, at Kathleen Valley, euhedral tantalite–columbite laths display alternating, dark–light backscattered electron (BSE) image contrasts that may indicate changes in relative Ta:Nb and/or Mn:Fe ratio during crystallization (e.g. Fig. 66).

At Greenbushes, as well as columbite–tantalite, a Sb-bearing, Mn/Fe-free phase, tentatively identified as stibiotantalite, of ideal formula SbTaO_4 (Fetherston, 2004) was detected both in drillcore (e.g. #241167-slide #17; 241170-slide #21, #241173-slide #24, associated with feldspar) and in pit material (e.g. #C1-200-slide #8, Appendix 4). Greenbushes was the only LCT pegmatite examined in the current study where this phase was identified. Stibiotantalite occurs as large (to ~1 mm), irregular, blocky, poikiloblastic grains that host smaller grains of albite, tantalite–columbite and fractured cassiterite (~200 µm), which may also be Ta-bearing (~2–3 wt%) as indicated by EDS analysis (e.g. Fig. 66). Tantalum is known to substitute for Sn in cassiterite (e.g. Fetherston, 2004), but confirmation requires further analysis. As noted by Boyle and Jonasson (1984), in pegmatites antimony may be concentrated in minerals, such as tantalite–columbite and stibiotantalite, and related phases. In addition, a low Sb–At, high As-bearing oxide, tentatively identified as arsenolite, ideally As_2O_3 , was also detected at Greenbushes, occurring as equant grains or as fracture-fill in apatite (#241170; Fig. 66), suggesting a later-stage, remobilization and crystallization of this phase.

At Dalgaranga, a Ta–Nb phase enriched in Ca, and potentially Tm-bearing (Appendix 6) was detected associated with albite, with a Ta:Nb ratio of 2.24–3.07 and consistent Ca content averaging 9.95 wt% (e.g. Fig. 66; Appendix 6; slides #7–8, Appendix 4). This phase was initially identified as calciotantalite, $\text{CaTa}_4\text{O}_{11}$, but did not account for the presence of Nb. A check against a published summary of Ta-group minerals, provided by Fetherston (2004), indicates this phase is likely microlite, part of the Euxenite Group with general formula, ABO_4 , where A = Y, Er, Ce, La, Nd, Dy, U, Zr, Th, Ca, Fe^{2+} , and B = Nb, Ta, Ti, Sn and W. This supports the earlier observation of Hall (1988) that microlite, ideally $(\text{Ca},\text{Na})_2(\text{Ta},\text{Nb})_2(\text{O},\text{OH},\text{F})$, is the main source of Ta at Dalgaranga. Minerals of this group occur in peralkaline granites/syenites, and subordinately in rare-metal (Li–F) granites and granitic rare-metal pegmatites (Fetherston, 2004). This is supported by the presence of fluorite, CaF_2 , hosted by massive albite in several samples (e.g. DD1-241429, Appendix 4).

The Sinclair Caesium Deposit was generally free or showed only trace amounts of Ta–Nb mineralization, which were mostly developed in albite–lepidolite–quartz zones (e.g. PDD162_#10 or PDD174_#10, Appendix 3) as single, large grains of Fe-free and Ta–Sn–Mn-bearing ($\text{Ta} \gg \text{Nb}$), as infill between lepidolite flakes.

At Dome North, the upper (petalite) zone of the pegmatite was free of Ta–Nb oxides. At depth, Ta–Nb oxides were rare to uncommon, and where detected, generally comprised columbite–tantalite as rounded laths <50 µm

but up to 250 µm long, with $\text{Fe} > \text{Mn}$ and $\text{Nb} \gg \text{Ta}$ (Appendix 4). Similarly, at Mt Marion, the few grains of Nb–Ta oxides detected consisted of rounded laths, 50–100 µm in size, also with $\text{Nb} \gg \text{Ta}$ and $\text{Fe} > \text{Mn}$ (Appendix 4). TIMA EDS quality of Ta–Nb oxides detected at Sinclair, Dome North and Mt Marion was poor, partly due to their generally small grain size, and so no EDS analysis was possible.

In the Mt Mann pegmatite at Kathleen Valley, Ta–Nb oxides were generally rare, occurring mainly as small (about 50 µm), irregular grains of calcio–tantite, with $\text{Ta} \gg \text{Nb}$ and trace Mn (e.g. KVDD0018_#3, slide #5, Appendix 4) or as sub-20 µm grains of microlite with $\text{Ta} \gg \text{Nb}$, free of Mn and Fe (e.g. KVDD0018_#10, slide #16, Appendix 4). In the high Ta-bearing zone, several (to 600 µm) prismatic tantalite–columbite grains with $\text{Ta} \gg \text{Nb}$ and $\text{Mn} > \text{Fe}$ (e.g. KVDD0018_#12, slide #17, Appendix 4) were detected. Similarly, within the Kathleen's Corner pegmatite swarm, Ta–Nb oxides ($\text{Mn} \gg \text{Fe}$, low Ca, $\pm \text{Ti}$) were commonly present as coarse laths, 0.4 – 1 mm, with evidence of compositional zoning reflecting changes in the Ta:Nb and Mn:Fe ratios during crystal growth (e.g. KVDD0076_#7, slide #31, Appendix 4; Fig. 66).

Changes in the Ta:Nb and Mn:Fe ratios of the tantalite–columbite solid–solution series composition (Fig. 67) were used as a means of assessing the degree of fractionation of the LCT pegmatites (e.g. Shaw et al., 2016). Although some caution is necessary because the calculated Ta:Nb and Mn:Fe ratios are based on semi-quantitative EDS analysis, a plot of the Ta:Nb vs Mn:Fe ratios shows that the majority of tantalite–columbite analysed are Mn-enriched (i.e. $\text{Mn} > \text{Fe}$) and occupy the middle portion of the manganocolumbite–manganotantalite solid–solution series (Fig. 67). Columbite–tantalite from Kathleen Valley was the most Mn-enriched, with an overall averaged Mn content of 10.2 wt% (Appendix 6).

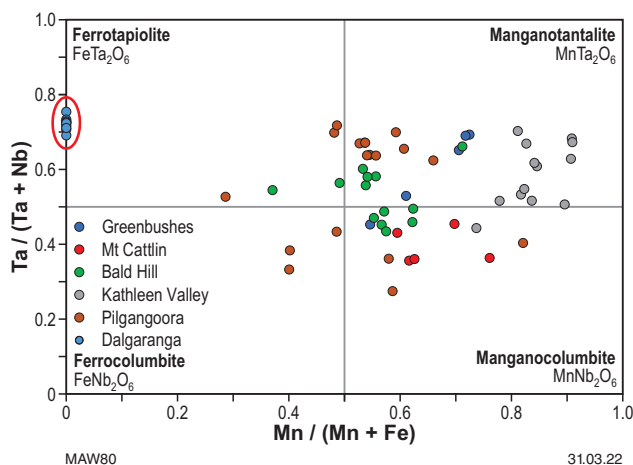


Figure 67. Ta/(Ta+Nb) vs Mn/(Mn+Fe) ratios for columbite–tantalite identified by TIMA mineral mapping of WA LCT pegmatites. Data are from EDS measurements as tabulated in Appendix 5. Data excludes the Sn- and Sb-bearing phases detected at Greenbushes. The Mn/Fe-free, Ca-microlite identified at Dalgaranga (circled) displays a relatively consistent Ta:Nb ratio of approximately 0.70 – 0.75. The majority of tantalite–columbite samples are Mn rich, with Kathleen Valley exhibiting the highest Mn contents and generally occupying the middle ground of the manganocolumbite–manganotantalite solid–solution series

This result is somewhat surprising given that based on the mica K, Rb and Cs composition, Greenbushes is inferred to present as the most highly fractionated WA LCT pegmatite (e.g. Figs 60, 61). It would follow that the associated Ta–Nb oxides at Greenbushes would also display a more fractionated nature compared to other pegmatites of this study. As noted by Linnen et al. (2012), key minerals such as Ta–Nb oxides record but do not control the fractionation behaviour of rare elements (e.g. Ta, Nb). Changes in the rare-element composition of these key pegmatite phases can vary continuously from barren to complexly evolved pegmatites, and in early or late assemblages within individual pegmatites (Linnen et al., 2012). Other associated phases where Mn and Fe are either essential components, such as in garnet (Fe-bearing spessartine), or present as impurities (e.g. (F)–apatite, tourmaline, mica) may influence the partitioning of these elements during pegmatite crystallization. For example, at Kathleen Valley (e.g. slide #26, 31, Appendix 4) and Pilgangoora (e.g. slide #36, Appendix 4) Fe-bearing spessartine is a common accessory phase, whereas at Greenbushes garnet was absent or only present in trace amounts as very small (<10–50 µm) grains (e.g. slides #6, 24, 26, Appendix 4). Hence, the comparative enrichment of Mn in Ta–Nb oxides at Kathleen Valley may not arise through pegmatite fractionation but may reflect a pegmatite melt inherently enriched in Mn prior to the onset of crystallization.

Feldspar composition

Albite was the predominant feldspar detected by TIMA mineral mapping, hence the majority of EPMA and LA-ICP-MS analyses presented are for sodic alkali feldspar. The compositional range of albite measured by EPMA, expressed as end-member compositions, varied from $Ab_{94.3}$ to $Ab_{99.6}$ with a maximum orthoclase content of 4.7% (Table 5). Conversely, the limited analysis of K-feldspar measured in WA LCT pegmatites varied from $Or_{91.0}$ to $Or_{98.2}$, with a maximum albite composition of $Ab_{9.0}$ (Table 5). The Ca-feldspar, end-member anorthite was only detected at the Dome North (Cade) and Kathleen Valley LCT pegmatites but limited to <8.0% An (Table 5), with the more calcic albite occurring in the Kathleen Corner pegmatite (KVDD0076) as compared to examples from the Mt Mann pegmatite (KVDD0018) (Table 5).

An Al–Si–Na ternary plot of LCT pegmatite albite identified two compositional trends in relation to the expected composition for stoichiometric albite (Fig. 68). The first trend is a small increase in the alumina content from 19.4 wt% (stoichiometric albite) to 20.2 wt% Al_2O_3 for albite from Dalgara and Kathleen Valley at the expense of silica (about 67 wt% SiO_2 for Dalgara and 66.6 wt% SiO_2 for Kathleen Valley) while maintaining a relatively constant Na_2O content at about 11.6 and 11.5 wt%, respectively (Fig. 68). A more significant trend is evidenced by albite from the Londonderry, Mt Cattlin and Greenbushes (pit) pegmatites which show a comparative enrichment in Na_2O (to 16.7 wt%, Greenbushes-pit; C3-100/C3-300H-Pink) also at the expense of silica (e.g. 65.2 wt%, Greenbushes-pit) while maintaining a near constant alumina content (about 19.1 wt%) relative to stoichiometric albite at 11.8 wt% Na_2O , 68.7 wt% SiO_2 and 19.4 wt% Al_2O_3 (Fig. 68). Interestingly, albite in Greenbushes core (C3DD024) is slightly enriched

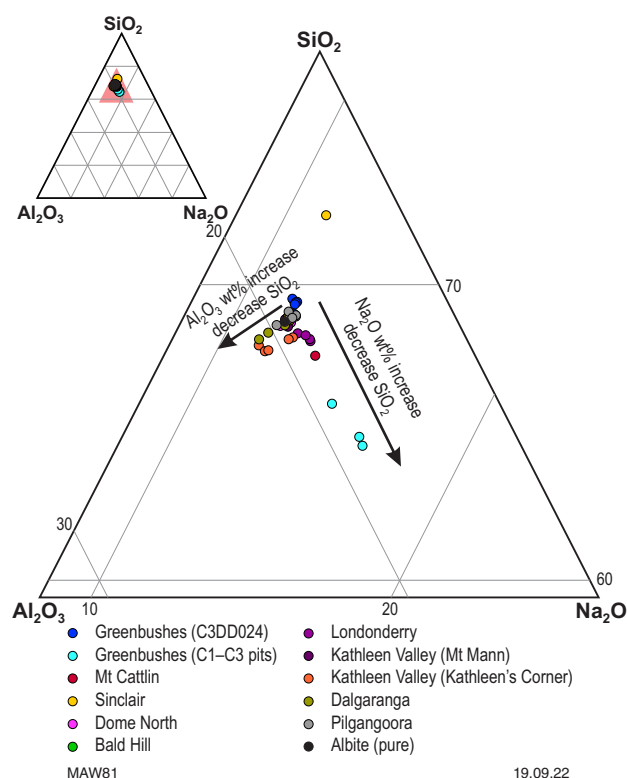


Figure 68. Major element, SiO_2 – Na_2O – Al_2O_3 plot (wt%) for albite from WA LCT pegmatites. The inset ternary plot shows detail of the area marked by the red triangle in the larger SiO_2 – Na_2O – Al_2O_3 ternary plot. Two compositional trends are indicated: an increase in Na_2O content from 11.8 wt% (pure albite) to 16.7 wt% (Greenbushes), and a smaller increase in alumina content from 19.4 wt% for stoichiometric albite to 20.2 wt% for albite from Dalgara

in silica to about 69.1 wt% compared to 68.7 wt% for stoichiometric albite, whereas the albite example from Sinclair shows significant enrichment in silica to about 72.1 wt% (Fig. 68).

Pegmatite classification

As previously described in section, Nature and types of pegmatites, pegmatites (including rare-element types) may be classified into one of five groups on the basis of their trace-element signatures as reflected by their mineral composition (e.g. Černý et al., 2012a). The recent review of LCT pegmatite deposit formation by Bradley et al. (2017) provides a useful summary of the history of pegmatite research and evolution of pegmatite classification schemes. The currently accepted system of pegmatite classification adapts the earlier scheme of Černý (1991) (refer to section on Nature and types of pegmatites) whereby pegmatite families are identified by their diagnostic trace-element composition and pegmatite class, which incorporates mineralogy and emplacement depth (Bradley et al., 2017) (Fig. 69).

Pegmatite classification, as well as enabling a means of identifying and comparing LCT pegmatite types, importantly informs the most appropriate processing route applicable to the pegmatite mineralogical and textural characteristics, expected on the basis of its classification. This is extensively discussed in detail in

Table 5. Chemical end-member composition (AbOr) for feldspar measured by EPMA from WA LCT pegmatites

		%Ab	%Or	%An			%Ab	%Or	%An
Greenbushes	GB_241168_Albite_71-80	99.1	0.2		Londonderry (LHD07)	LHD07_233328_Ortho 51-60	6.1	93.8	
	GB_241168_Albite_81-85	99.4	0.2			LHD07_233328_Albite 61-75	99.5	0.4	
	GB_241171_Albite_39-41	99.4	0.1			LHD07_233328_Ortho 76-85	9.0	91.0	
	GB_241172_Albite_133-140	99.2	0.3			LHD07_233328_Albite 86-95	99.6	0.3	
	GB_241173_Albite_152-160	99.1	0.3			LHD07_233335_Albite 172-181	98.1	0.2	
	GB_241173_Ortho_161-168	3.8	96.1			LHD07_233338_Albite 134-141	98.4	0.6	
	GB_241175_Albite_112-122	99.1	0.6		Kathleen Valley	Av.KVDD18_3_Albite_21-25	97.2	0.4	2.5
	Av.C3-100_Albite_112-120	98.9	0.8			Av.KVDD18_4_Albite_56-61	97.7	0.3	1.9
	Av.C3-100_Albite_121-130	98.8	0.9			Av.KVDD18_5_Albite_76-80	98.4	0.3	1.3
	Av.C1-100Pink_Microcline_161-170	4.8	95.1			Av.KVDD18_6_Albite_121-125	97.7	0.3	1.9
	Av.C3-300H_Pink_Albite_211-220	99.6	0.4			Av.KVDD76_1_Albite_156-160	91.2	0.7	8.0
Mt Cattlin	MtC1600_B4_Albite_81-91. Av	99.6	0.3			Av.KVDD76_2_Albite_1-5	92.3	0.3	7.4
Sinclair Cs	Av. PDD162_10_Albite 41-45	99.7	0.1			Av.KVDD76_5_Albite_51-55	93.1	0.4	6.6
	Av.PDD162_10_Albite_51-55	99.6	0.2			Av.KVDD76_6_Albite_81-85	97.3	0.3	2.3
	Av.PDD162_11_Albite_66-75	99.5	0.1			Av.KVDD76_7_Albite_101-105	96.8	0.3	2.8
	Av.PDD162_11_Albite_76-80	99.5	0.2			Av.KVDD18_3_Micro_26-30	5.5	94.5	0.0
	Av.PDD174_4_Albite_131-135	99.8	0.2			Av.KVDD76_5_Micro_36-45	6.3	93.7	0.0
	Av.PDD174_10_Albite_26-30	99.5	0.1			Av.KVDD76_7_Micro_86-95	6.8	93.2	0.0
	Av.PDD179_4_Albite_75-80	96.1	0.3		Dalgaranga	DD1_241428_Albite 1-10. Av	98.9	0.3	
	Av.PDD174_2_Micro_121-125	6.2	93.8			DD1_241428_Albite 11-20. Av	98.8	0.3	
	Av.PDD174_4_Micro_126-130	4.1	95.9			DD1_241429_Albite 21-30. Av	97.9	0.4	
	Av.PDD174_4_Micro_136-140	5.0	95.0			DD1_241429_Albite 31-40. Av	97.6	0.4	
						DD1_241434_Albite 71-80. Av	94.5	0.4	
Dome North	Av.PDRC319_9 Albite_31-35	99.4	0.4	0.2		DD1_241435_Albite 101-110. Av	98.2	0.3	
	PDRC319_10 Albite_66-70	97.5	0.4	2.1		DD1_241437_Ortho. 111-122. Av	1.7	98.2	
	Av.PDRC319_20 Albite_111-115	99.3	0.4	0.3		DD1_241437_Albite 123-131. Av	94.3	4.7	
	Av.PDRC319_10 Micro_51-55	3.5	96.5	0.0	Pilgangoora	PD003_32.96m_Albite_51-60	98.3	1.1	
	Av.PDRC319_10 Micro_56-60	4.4	95.6	0.0		PD003_32.96m_Ortho_61-70	2.5	97.4	
	Av.PDRC319_10 Micro_61-65	4.4	95.6	0.0		PD004_192m_Albite_61-70. Av	99.2	0.4	
	Av.PDRC319_15 Micro_76-80	5.7	94.3	0.0		PD004_192m_Albite_71-80. Av	99.2	0.3	
	Av.PDRC319_15 Micro_81-85	4.7	95.3	0.0		PD005_46.5m_Albite_96-100	95.7	0.3	
Bald Hill	BH1475_Albite_41-50	99.2	0.5			PD005_83m_Albite_191-200	98.8	0.4	
	BH1600_1_Albite_91-100	99.1	0.5			PD005_165.08m_Albite_159-170	99.1	0.3	
	BH1600_1_Albite_111-120	99.2	0.4						
	BH2250_A_Albite_161-170	99.0	0.5						

section, Assessment of physical and chemical processing behaviour of LCT pegmatites and underpins the basis of a geomettallurgical framework for WA LCT pegmatites as described in section, Geomettallurgical framework.

Based on this classification scheme, all WA pegmatites examined in this study belong to the LCT family of pegmatites (Fig. 69), grouped into three sub-types (complex spodumene, petalite and lepidolite) and two pegmatite types (albite–spodumene and albite) (Fig. 69). As a comparison, the well-known Tanco (Canada) and Bikita (Zimbabwe) pegmatite deposits are also included in the classification scheme (Fig. 69). However, compared to WA LCT pegmatites, these are highly zoned and mineralogically complex deposits, with Li mineralization hosted by

spodumene, petalite and lepidolite, with massive pollucite (Cs) mineralization. Until a few years ago, these deposits including the Sinclair Caesium Deposit were the only three known sources of economic pollucite.

The following discussion describes the main characteristics of each of the WA LCT pegmatites, grouped according to the classification scheme.

Complex spodumene sub-type

Greenbushes — This is a large Sn–Ta–spodumene deposit and is classed as a member of the complex spodumene sub-type (e.g. Fetherston, 2004, p. 18). TIMA mineral mapping detected

the occurrence of Na-bearing, pollucite $(\text{Cs,Na})_2(\text{Al}_2\text{Si}_4\text{O}_{12}) \cdot 2\text{H}_2\text{O}$, or ideally as $\text{CsAlSi}_2\text{O}_6$ (Bradley et al., 2017), in trace amounts in spodumene sub-type examples from the C1 and C3 pits (e.g. C1-100H, C1-100Pink, C3-300White) and as a minor phase associated with spodumene, polyolithionite and Na/K-feldspar in an albite–spodumene type example (C1-200) (refer to Appendix 4). Phase-liberation analysis (refer to the section Assessment of physical and chemical processing behaviour of LCT pegmatites) detected up to 4–5 wt% pollucite in sample C1-200 (refer to section, Liberation characteristics of heavy minerals and pollucite), containing approximately 36 wt% Cs (EDS analysis); stoichiometric pollucite has a Cs content of 42.6 wt% (as $\text{CsAlSi}_2\text{O}_6$). The conditions of Cs mineralization and implications for the crystallization evolution at Greenbushes and for the Sinclair Caesium deposit are discussed in more detail in the section Caesium mineralization: insight into pegmatite evolution at Greenbushes and Sinclair.

The presence of pollucite was previously reported at Greenbushes (Partington et al., 1995), though not described in detail by these authors, and is inferred by Talison Lithium from drillhole assay data but is currently considered as uneconomic (Husein Al Shakarji, Mine Geologist, written com. August 2020). Economic pollucite mineralization is known only from three

locations worldwide: the Bernic Lake Mine or Tanco Mine, Manitoba, Canada; the Bikita Mine, Zimbabwe; and the Sinclair Caesium Deposit, 125 km south-southeast of Kalgoorlie (e.g. Crook et al., 2019).

Mt Marion — Smith and Ross (2017) classify the Mt Marion pegmatite swarm as representative of the albite–spodumene type, whereas Jacobson et al. (2007) considers the pegmatites as representative of (predominantly) unzoned quartz–spodumene pegmatites. TIMA mineral mapping of the ore-concentrate, with a mineralogy comprising predominantly of spodumene–quartz–albite with lesser microcline and muscovite, supports the classification of Jacobson et al. (2007). However, as only a sub-sample, presumably representative of the concentrate that was made available for characterization, our classification may require further confirmation (Fig. 69).

Dome North — Classification of the Cade rare-element pegmatite is complicated as Li is hosted by both petalite and spodumene. Below the weathering front, TIMA mineral mapping of the shallowest portion of the pegmatite intersected by drilling upper confirmed Li mineralization is variably hosted by massive petalite that grades to a predominantly

Class	Subclass	Type	Subtype	Family	WA pegmatite example	
Abyssal	HREE	NYF				
	LREE					
	U	NYF				
	BBe	LCT				
Muscovite						
Muscovite-rare element	REE	NYF				
	Li	LCT				
Rare element	REE	allanite–monazite euxenite gadolite	NYF			
	Li	beryl	beryl–columbite beryl–columbite–phosphate			
		complex	spodumene		Greenbushes, Mt Marion*, Dome North^ (spodumene), Kathleen Valley, Londonderry (petalite), Tanco (Canada)# , Bikita (Zimbabwe)#	
			petalite			
			lepidolite	LCT		
			elbaite amblygonite		Sinclair Cs — lepidolite/petalite (+albite/microcline)	
		albite–spodumene albite				
					Mt Cattlin, Bald Hill, Pilgangoora	
					Dalgaranga(+eucryptite)	
	Miarolitic	REE	topaz–beryl gadolite–fergusonite	NYF		
		Li	beryl–topaz spodumene petalilte lepidolite	LCT		

* Classification of the Mt Marion pegmatite is based on characterisation of ore concentrate, and may be biased

^ Li mineralisation at Dome North is hosted by either an upper petalite-zone and a larger underlying spodumene-zone

The Tanco and Bikita pegmatites are highly-zoned, mineralogically complex pegmatites, mined for Cs

MAW82

19.09.22

Figure 69. Classification scheme for rare-element pegmatites. LCT and Western Australian rare-element pegmatites examined in the current study are also included. Image modified from Černý et al. (2012a). The Li subclass of REE pegmatites is highlighted by the larger font compared to other pegmatite classes and subclasses. The Tanco and Bikita pegmatite deposits are included as examples of other well-known pegmatites

(spodumene-free) muscovite–quartz–albite-type pegmatite (e.g. Appendix 4). Within the zone of massive petalite, TIMA mineral mapping provides textural evidence of graphic quartz–spodumene (e.g. Fig. 28) in contact with massive petalite, supporting their synchronous crystallization as the pegmatite cooled (Appendix 4).

In the thicker, main pegmatite body at depth as intersected by PDRC319 (Fig. 26), minor petalite persists closest to the pegmatite/metasedimentary, hanging wall zone that grades into a predominantly feldspar (microcline–albite)–spodumene–quartz–pegmatite type (e.g. Appendix 4). As the main body of the pegmatite comprises spodumene as the principal Li host, the Dome North Deposit is classified as a complex spodumene sub-type (Fig. 69). The occurrence of petalite and spodumene in close association may provide insight into the temperature–pressure conditions under which the pegmatite crystallized. This is discussed in more detail in section, Pegmatite mineral fractionation.

Kathleen Valley — There is limited detailed description of the pegmatite mineralogy or textural relationships of the host pegmatites at Kathleen Valley. The current classification is based on the examination of discontinuous sections of drillcore kindly made available by Lontown Resources.

Lithium mineralization in the Mt Mann pegmatite section examined in this study is hosted by both spodumene and lepidolite, with the main pegmatite body consisting of quartz–spodumene with variably distributed albite and fine-grained, primary lepidolite (e.g. Appendix 4). This classifies the pegmatite as a complex spodumene sub-type (e.g. Fig. 69). Similarly, in the pegmatite characterized as part of the Kathleen's Corner swarm, mineralization is hosted by quartz–spodumene–albite (\pm muscovite) (refer to the section LCT pegmatites of the goldfields), which also classifies the pegmatite as a complex-spodumene sub-type (Fig. 69).

However, the upper and lower margins of the main pegmatite body at Mt Mann includes Li hosted by fine-grained lepidolite, which imparts a strong purple colour to the pegmatite (e.g. Appendix 4). In addition, spodumene in the upper lepidolite zone has been altered pseudo-morphically and replaced by a secondary mixture mapped as quartz–elbaite–cleavelandite–calcite–beryl with some relict, primary spodumene (Appendix 4). However, XRD analysis of a hand-picked, altered spodumene in the upper lepidolite zone detected quartz–mica–Li–chlorite with minor laumontite and calcite (e.g. Appendix 3). In contrast, lepidolite was not detected/mapped in core from Kathleen's Corner.

The shallow dipping Kathleen's Corner pegmatite swarm and the more steeply dipping Mt Mann pegmatite suite are interpreted by Lontown Resources to merge at depth to a single pegmatite body (refer to section Kathleen Valley). Although this may be possible, the different structural aspects of the Mt Mann and Kathleen's Corner pegmatite suites compared to the generally subparallel emplacement of pegmatites in other pegmatite swarms, such as Greenbushes, Mt Cattlin, Dome North, Bald Hill and Mt Marion (refer to the section Classification and geology of LCT pegmatites in Western Australia) puts this interpretation in question. In addition, the occurrence of lepidolite in the Mt Mann pegmatite (and its absence at Kathleen's Corner) suggests that the pegmatite bodies are the products of different fractional crystallization sequences. Support for our interpretation is evidenced by the marked compositional difference of muscovite examined from the different

pegmatite swarms, with significant differences in composition highlighted in green in Table 6.

Muscovite from the Kathleen's Corner swarm is comparatively enriched in Li, Mg, Fe and F, and is hosted by a more highly fractionated pegmatite, as indicated by the larger K:Rb ratio, than muscovite from the Mt Mann pegmatite swarm (Table 6). In contrast, muscovite from the Mt Mann pegmatite swarm is relatively enriched in Rb and contains a significantly greater Al content (Table 6): muscovite composition for all other elements (not highlighted in green) are similar between the two pegmatite swarms.

Complex petalite sub-type

Londonderry — TIMA mineral mapping detected petalite as the principal Li-bearing phase at Londonderry, thereby classifying the pegmatite as belonging to the complex petalite sub-type (Fig. 69). Out of the main ore zone, the pegmatite is described as an albite(–quartz–muscovite) type. Within the main ore zone at Londonderry (e.g. Fig. 36), zones of massive petalite (confirmed by XRD; Appendix 5) are interspersed with zones of quartz–mica (muscovite–trilithionite) (e.g. #233323, #2333330) and zones of massive perthitic-textured microcline with exsolved albite lamellae (#233328) (Appendix 4). The main petalite zone at Londonderry is essentially free of any accessory or exotic phases (e.g. zircon, apatite and garnet) with only a few rare zircon grains (30–50 μ m) and a single, euhedral columbite–tantalite grain detected in sample #233335. A solitary, 500- μ m sized garnet (almandine–spessartine) grain was detected towards the base of the pegmatite in the aplite zone (#233338) (Appendix 4, slide #14). Additionally, Dittrich et al. (2017) report that until 2017, the Londonderry pegmatite field was the sole Australian locality for which pollucite was recorded.

Table 6. Comparison of muscovite composition (EPMA) from the Mt Mann and Kathleen's Corner pegmatite swarms at Kathleen Valley

Element (wt%)	Mt Mann (KVDD0018)	Kathleen's Corner (KVDD0076)
Li (ppm)*	806-936	2512-5788
Ca	0	0
Si	20.9-21.0	20.8-21.0
Mg	0.05-0.08	0.41-0.93
Mn	0.34-0.35	0.28-0.37
Fe	0.58	2.2-3.33
Al	18.6	15.4-16.9
K	7.7-7.8	8.1-8.2
Na	0.33-0.35	0.23-0.35
Cs	0.05-0.08	0.03-0.05
Rb	2.15-2.24	1.27-1.47
F	0.26-0.29	0.65-1.32
K:Rb	3.44-3.64	5.56-6.39

*Li analysis from LA-ICP-MS measurement

Complex lepidolite sub-type

Sinclair Caesium Deposit — This deposit was developed and mined as a source of Cs until mid-2020. The pegmatite core also hosts Li mineralization, as Li–micas (lepidolite), petalite, eucryptite and rarer amblygonite (Crook et al., 2019). The mineralized pegmatite sequence examined in the current study (e.g. refer to the section Sinclair Caesium Deposit; Appendix 4) broadly consists of a perthitic microcline zone, overlying high-grade pollucite which transitions sharply to an underlying albite–lepidolite–quartz pegmatite (Fig. 19). Petalite occurs within the lepidolite zones above and mainly below the mineralized Cs zone (e.g. Crook et al., 2019).

Therefore, this deposit can be classified as a complex petalite/lepidolite sub-type (Fig. 69), although the existing classification scheme does not take into account the occurrence of massive Cs mineralization. This may, in part, reflect the fact that very few pegmatites host economically viable deposits of Cs (e.g. Tanco, Bikita and Sinclair).

Albite–spodumene type

Mt Cattlin — Regional pegmatite zonation developed at Mt Cattlin results in the flat-lying pegmatite being classified as simple (albite or beryl), albite–spodumene (two types distinguished on the basis of spodumene crystal size) and complex lepidolite types (Fetherston, 2004, p123). The albite–spodumene pegmatite type represents the main orebody at Mt Cattlin. Hence, Mt Cattlin is classified as a Ta-bearing, albite–spodumene type pegmatite (Urgine, 2016; Fig. 69).

Bald Hill — Based on the TIMA mineral mapping characterization of ore material sampled from the main pit at Bald Hill (Appendix 4), the main pegmatite unit can be classified as an albite–spodumene type (Fig. 69). TIMA mineral mapping detected few Ta:Nb-bearing phases, which were mainly present as isolated, ~50-µm sized grains of columbite–tantallite and microlite (e.g. #BH2250_A/BH2250). Other accessory phases detected include sphalerite (to 200 µm), pyrite (to 200 µm), cassiterite (<20 µm) and garnet (<20 µm) (e.g. #BH2250, #BH1475). Similar to pegmatite collected from Mt Cattlin, megacrystic spodumene hosted in a massive albite–granular quartz matrix is extensively altered, particularly those from the low-grade zone (e.g. Fig. 32; Appendix 4). This is discussed in more detail in section, Spodumene morphology and alteration: indicators of pegmatite crystallization evolution.

Pilgangoora — Pegmatites at Pilgangoora can be classified into three compositional groups: high-grade, quartz–spodumene–albite–microcline (source of alluvial Sn); quartz–microcline–albite; and quartz–muscovite–microcline (e.g. Fig. 69; Jacobson et al., 2007). The quasi-homogeneous nature and textural characteristics of the Pilgangoora pegmatites that include coarse to megacrystic spodumene (e.g. PD001, PD005-all samples) and aplitic layering (e.g. PD004-191.88 m) are characteristics of albite–spodumene type, LCT pegmatites (e.g. Fig. 41; Sweetapple, 2017).

Albite type

Dalgaranga — This is classed as an albite-type pegmatite with spodumene+eucryptite as the main Li hosts (Fig. 69). TIMA mineral mapping and EDS analysis confirmed the presence of microlite as the only Ta-bearing phase detected at Dalgaranga in samples examined from drillhole DD1 (refer to Appendix 4; e.g. sample #241429, #241437), supporting the earlier description by Hall (1988) of Ta principally hosted by microlite. The presence of fluorite (associated with microlite, e.g. #241429,) and less commonly (F)–apatite (#241429), along with eucryptite (associated with fluorite, e.g. #241429) and the secondary, Be-bearing phase bavenite, $\text{Ca}_4\text{Be}_2\text{Al}_2\text{Si}_9\text{O}_{26}(\text{OH})_2$, (e.g. #241435, #241437 — as confirmed by XRD analysis) probably as a weathering product of beryl, infers that Dalgaranga derived from a rare-metal, flux-bearing (Li–F–Be) granitic melt.

Pegmatite mineral fractionation

District-scale changes in LCT mineralogy and associated rare-element geochemistry can define a broad, concentric zonation developed about an inferred or exposed parental granite (e.g. Linnen et al., 2012; Bradley et al., 2017 and the references therein). Pegmatites proximal to the source granite are the least evolved, consisting only of the typical granitic phases, such as quartz, K-feldspar, Na-plagioclase, muscovite and biotite, with accessory garnet, apatite, tourmaline and zircon (Bradley et al., 2017). With increasing distance from the source granite, the pegmatite melt cools further and continues to fractionate so that in distal and evolved pegmatites Ta and Li–alumino silicates crystallize (Fig. 70), and finally in extremely evolved and most distal pegmatites pollucite precipitates (e.g. Bradley et al., 2017), as previously described.

Petalite, a Li-bearing phyllosilicate, $\text{LiAlSi}_4\text{O}_{10}$, as occurs at Londonderry and Dome North, is generally associated with highly differentiated LCT pegmatites, forms at lower pressure compared to spodumene at the same temperature conditions (Fig. 71; e.g. Linnen et al., 2012). Conversely, under the same pressure conditions, petalite forms at higher temperatures than spodumene (Fig. 71). Thus, the presence of petalite may be useful as an approximate geobarometer (Bradley et al., 2017). Decreases in temperature and pressure following crystallization can result in the alteration of either spodumene or petalite to eucryptite (Jacobson et al., 2007). Symplectite spodumene–quartz intergrowth (SQI) textures are a common feature of LCT pegmatites and result from the replacement of petalite to a mixture of spodumene and quartz, under changing (decreasing) P – T conditions (e.g. Bradley et al., 2017, London, 2017).

The occurrence of petalite as the principal source of Li at Londonderry suggests that the crystallization cooling history occurred at a relatively low pressure, c. <2 kb (e.g. Jacobson et al., 2007; Fig. 71). The lack of SQI textures in the pegmatite examples examined from Londonderry (refer to the section Spodumene morphology and alteration: indicators of pegmatite crystallization evolution) infer that during crystallization, cooling of the melt did not cross the spodumene–petalite equilibrium reaction (London, 2017). The eucryptite+spodumene association identified in the feldspar-rich Dalgaranga pegmatite (refer to Appendix 4) suggests the late stage, hydrothermal alteration

of spodumene formed eucryptite under reduced P – T conditions (Fig. 71; e.g. London, 2017).

At the Dome North Deposit within the upper section of the Cade pegmatite intersected by hole PDRC318, the zone of massive petalite mineralization displays the typical graphic or SQI texture (slide #5, Appendix 4) that can result by the alteration of petalite to a spodumene–quartz mixture (London, 2017). During cooling of the pegmatite, P – T conditions intersected and continued past the petalite–spodumene equilibrium reaction, as inferred by the dashed blue cooling trend (Fig. 71) enabling alteration of petalite. The timing of alteration must have occurred co-incidental to final solidification of the pegmatite, which prevented petalite alteration going to completion (Fig. 28).

At Greenbushes, mineral textural relationships and fluid inclusion studies place P – T constraints on Li mineralization (e.g. Partington et al., 1995; Partington, 2017). In the footwall Li zone, the absence of petalite and fluid inclusion work indicate formation of (feldspar-free) quartz–spodumene assemblage at 770 °C and at 5–5.5 kbars (Partington et al., 1995; Partington, 2017). This places initiation of Li mineralization, not in the spodumene stability field as suggested by Partington et al. (1995), but within the virgilite stability field (Fig. 71). Under cooling conditions, the melt is inferred to have crossed the virgilite–spodumene-phase equilibrium at approximately 710 °C and transformed to spodumene in the presence of free quartz (Fig. 71). In the same way that the alteration of petalite at Dome North explains the classic SQI-texture identified in this deposit, the development of (near-identical) symplectic spodumene–quartz mapped in the C3 pit at Greenbushes (e.g. Fig. 12; drillcore and Fig. 13; C3 pit samples) may have formed by the alteration of virgilite during cooling of the pegmatite melt (Fig. 71).

Based on the fractionation trend derived from changes in mica (muscovite+lepidolite), K and Rb composition (Fig. 60) and taking into account the classification of the rare-element pegmatites as presented in Figure 69, we can begin to develop a comparative ranking of the Western Australian rare-element pegmatites (Fig. 72). As based on the muscovite K–Rb composition (refer to the section Mica composition), Western Australian rare-element pegmatites in this study are, in the main, highly fractionated compared to other LCT pegmatites worldwide (refer to Fig. 60). Muscovite from the Sinclair Caesium Deposit, with a Rb content of <0.6 wt%, associated with the wall rock zone, is the least fractionated of all mica investigated in this study (Fig. 72). The majority of the rare-element pegmatite deposits characterized with Rb contents in the range 0.6 – 1.2 wt% may be considered as moderately fractionated (Fig. 72).

Muscovite from the Londonderry pegmatite shows a degree of fractionation comparative to the majority of the pegmatites investigated, but the slightly greater Rb contents (to about 1.8 wt% Rb) support a more fractionated system that overlaps into the lower part of the fractionation trend for the Mt Cattlin and Kathleen Valley pegmatites (Fig. 72). This appears to mark a crossover zone in pegmatite fractionation where both muscovite and lepidolite host similar Rb contents. As the Rb content increases, associated with an implied increase in fractionation of the host pegmatite, in the most highly fractionated of WA's pegmatites (Greenbushes) mica presents as lepidolite,

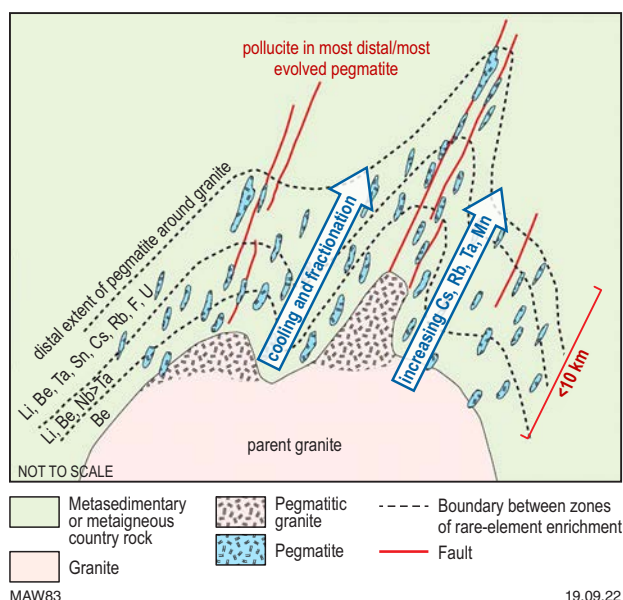


Figure 70. Schematic model of rare-element fractionation pegmatite evolution trends and associated changes in rare-element composition in relation to a source granite. The characteristic rare-element suite for each zone is indicated. Modified after Bradley et al. (2017) and Duuring (2020)

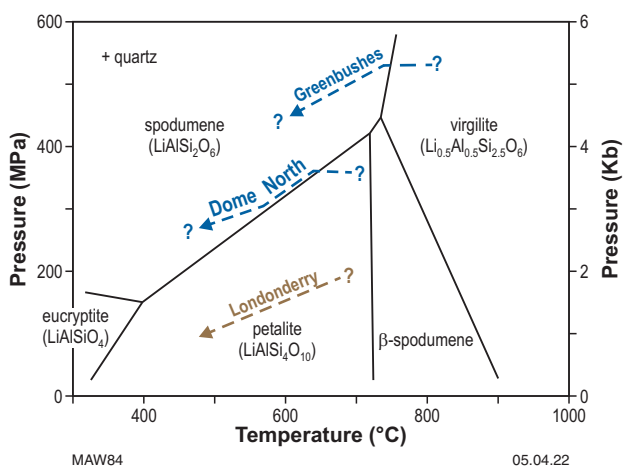


Figure 71. Pressure–temperature–phase relationships of Li silicates under quartz-saturated (mica+feldspar-free) conditions. The arrows (blue and hashed brown) show the interpreted cooling trend of the Dome North (blue), Greenbushes (blue) and Londonderry (brown) inferred from the main Li-bearing phases detected in these pegmatites. P – T conditions for Londonderry are based on those reported by Jacobson et al. (2007). Phase relationship diagram is modified after Linnen et al. (2012), Bradley et al. (2017) and the references therein. Note that eucryptite is regarded as hydrothermal in origin, whereas spodumene and petalite are primary Li–aluminosilicates (London, 2017)

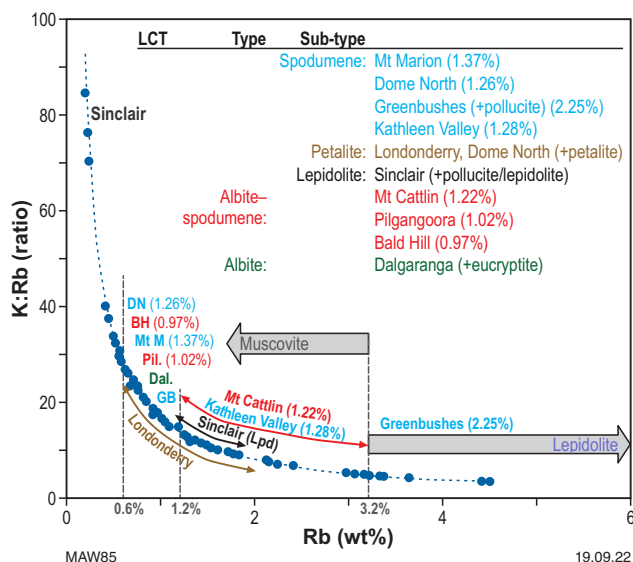


Figure 72. Plot of the K/Rb vs Rb for LCT pegmatites of the present study. Depending on the measured Rb content, fractionation zones may be inferred into which the different WA LCT pegmatites may be allocated (e.g. DN = Dome North; BH = Bald Hill), coloured by their pegmatite classification (inset) as denoted in Figure 57. The most highly fractionated mica forms as lepidolite, with Rb contents >3.2 wt%. Mica with Rb contents in the range 1.2 – 1.8 wt%, mark a fractionation crossover zone, where the same degree of pegmatite fractionation is manifested in the similar composition of muscovite and lepidolite. K and Rb contents are from EPMA measurements

with Rb contents in the range 3.2 – 4.5 wt% (Fig. 72). This suggests a structural limit to the incorporation of Rb within muscovite, with a maximum Rb content of ≈ 3.2 wt% (Fig. 72). This is consistent with the very high Rb contents of lepidolite from the extremely fractionated Red Cross Lake and Tanco pegmatites (refer to Fig. 60).

However, the occurrence of lepidolite does not necessarily infer a high degree of fractionation, as shown by lepidolite from the Sinclair Caesium Deposit with Rb contents in the range 1.2 – 1.8 wt%, which overlaps with muscovite from the Londonderry, Mt Cattlin and Kathleen Valley pegmatites. Further analysis is required to understand how the pegmatite fractionation behaviour is manifested or influences changes in mica composition.

As noted by Linnen et al. (2012), key minerals such as K-feldspar, Nb–Ta oxides and muscovite record but do not control the fractionation behaviour of rare elements (e.g. Li, Rb, Cs, Ta, Nb). Changes in the rare-element composition of these important pegmatite phases can vary continuously from barren to complexly evolved pegmatites, and in early or late assemblages within individual pegmatites (Linnen et al., 2012). Hence, fractionation of the crystal melt may not be the only process driving the observed mineral compositional changes (Linnen et al., 2012). This may be the case for the Sinclair pegmatite and help to explain the overlapping fractionation trends recorded by muscovite and lepidolite for Rb contents between 1.2 and 3.2 wt%.

Caesium mineralization: insight into pegmatite evolution at Greenbushes and Sinclair

Recent detailed characterization of Cs-enriched, LCT pegmatites in Zimbabwe and Western Australia, with a focus on the main economic pollucite deposits at Bikita and Tanco, established a genetic model for the formation of massive pollucite mineralization (Dittrich et al., 2019). According to Dittrich et al. (2019), massive Cs mineralization requires some very specific conditions that enable discrete Cs phases (pollucite) to form which bridge the apparent miscibility gap between Cs-bearing micas (e.g. muscovite, lepidolite and zinnwaldite), with maximum Cs contents of ≈ 1 –2 wt%, and discrete pollucite mineralization, with Cs contents of $> \sim 25$ wt% (Dittrich et al., 2019). This is discussed in more detail in the following section.

As discrete Cs mineralization occurs in only the most fractionated rare-element pegmatites (e.g. Bradley et al., 2017; Duuring, 2020), the occurrence of pollucite has implications for the fractionation evolution of the Greenbushes pegmatite. In the genetic model proposed by Dittrich et al. (2019), initial fractionation of a Cs-bearing melt results in the segregation of a proportionally smaller, immiscible melt of composition $(\text{Al}_2\text{O}_3 + \text{Na}_2\text{O}) \gg \text{SiO}_2$ that enables the crystallization of analcime, $\text{Na}(\text{AlSi}_2\text{O}_6) \cdot \text{H}_2\text{O}$. Segregation and accumulation of the immiscible analcime melt occurs in the upper part of the pegmatite while continuing to be enriched in Cs from the host melt (Dittrich et al., 2019). Final crystallization of the pegmatite occurs with formation of massive Ca–analcime, coupled with fluid-controlled Cs enrichment that shifts the composition from Ca–analcime to Na–pollucite. Final cooling and late-stage, hydrothermal alteration continue the Cs enrichment within the massive pollucite mineralization (Dittrich et al., 2019).

At Greenbushes, pollucite was most common in sample C1-200, with a mineralogy characterized by predominantly coarsely crystalline spodumene–albite (+minor microcline), and the near-absence of quartz (Appendix 4). Pollucite solubility in granitic melts is strongly dependent on temperature (Linnen et al., 2012). A granitic melt at about 390 °C can be saturated with pollucite at a Cs concentration of ≈ 4700 ppm (Linnen et al., 2012). Melt composition and temperature conditions may have limited Cs enrichment in the Greenbushes pegmatite melt, resulting in only minor, localized pollucite crystallization at Greenbushes.

For pegmatite intersected by drillhole PDD179 at Sinclair, only one sample examined in the current study provided an example of massive pollucite mineralization at this deposit (sample #PDD179_7 @47.2 – 47.3 m; refer to Appendix 4, slide #8). From the mineral associations and textural features mapped in this example, in comparison to those described by Dittrich et al. (2019), an inferred mineralization sequence may be described as:

- 1 Initial albite crystallization with incorporation of disseminated, early muscovite
- 2 Massive pollucite crystallization
- 3 Fracture development and increase in porosity (decrease in bulk density). Evidence of radial fracture development in albite, and block fracturing in pollucite
- 4 Later-stage crystallization of pollucite in void space within albite

- 5 Fracture and vein infilling, mapped as lepidolite/'elbaite', and with penetration into early formed albite
- 6 Microcline (exsolution?) and (secondary), later-stage albite crystallization as evidenced by albite+microcline infilling previous fractures.

This inferred mineralization sequence at Sinclair is consistent with a generalized LCT pegmatite sequence of mineral formation (Fig. 73) as developed by Dittrich et al. (2019). Textural characteristics revealed by TIMA mineral mapping are also consistent with the genetic model for massive Cs mineralization, whereby following initial, magmatic controlled crystallization of pollucite, cooling of the pegmatite melt to temperatures below 400 °C results in the formation of shrinkage cracks and fractures (Dittrich et al., 2019). Below this temperature, the main process operating as the pegmatite cools further changes to one more consistent with hydrothermal processes. This open network allows the continued circulation of hydrothermal fluids through the pegmatite resulting in further enrichment in Cs of the pollucite mineralization via hydrothermally driven alteration. These cracks and fractures also provide the sites for late-stage crystallization of lepidolite, quartz and feldspar (Dittrich et al., 2019).

Spodumene morphology and alteration: indicators of pegmatite crystallization evolution

Mineral-textural relationships, as characterized in this study by detailed TIMA mineral mapping, can provide a useful insight of pegmatite alteration during or following crystallization. From the mineralogical and textural characteristics of Western Australian rare-element pegmatites examined in the current study, two alteration styles were observed to predominate:

- Pseudo-morphic alteration of spodumene, which is replaced by a dark-green to black, fine-grained, Li-mica/chlorite assemblage that imparts a massive dull, green-black, waxy-mottled texture (e.g. Fig. 16; Mt Cattlin) or imparts a waxy lustre to the altered crystal (e.g. Fig. 32; Bald Hill). Alteration may either completely (or near completely) replace primary spodumene or is preserved as a 'reaction' rim about the crystal margin.
- In situ, graphic-textured (i.e. symplectite), contact alteration where spodumene juxtaposes sodic feldspar (predominantly albite). Alteration is typically mapped as a microscopic, inter-growth of spodumene-quartz-beryl(-elbaite-eucryptite) (e.g. Dome North—#PDRC319_15-slide#12; Kathleen Valley—KVDD0078_#6, slide #23; Pilgangoora—#PD005 @165 m, slide #36, Appendix 3).

Spodumene-cookeite alteration

The first style of alteration is almost exclusively confined to or affects megacrystic (+20 cm sized), tabular and lath-form spodumene at Bald Hill and Mt Cattlin (Fig. 16; Mt Cattlin and Fig. 32; Bald Hill). In contrast, the second style of alteration is present to varying degrees throughout all the rare-element pegmatites examined in the current study, with the exception of the Sinclair Caesium Deposit. The extremely coarsely

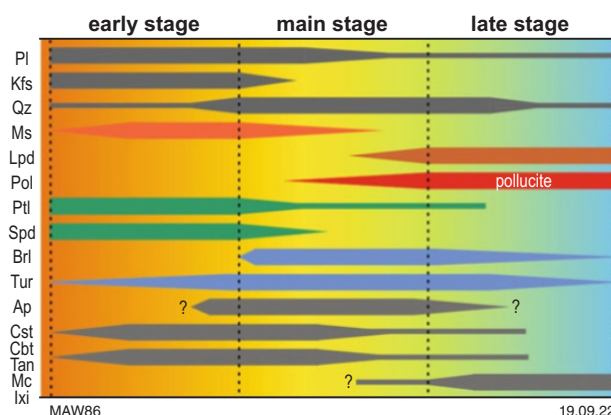


Figure 73. A generalized mineralization sequence for LCT pegmatites as described by Dittrich et al. (2019). Mineral key (top-to-bottom) Pl = plagioclase, Kfs = K-feldspar, Qz = quartz, Ms = muscovite, Lpd = lepidolite, Pol = pollucite, Ptl = petalite, Spd = spodumene, Brl = beryl, Tur = tourmaline, Ap = apatite, Cst = cassiterite, Cbt = columbite, Tan = tantalite, Mc = microcline, Ixl = ixiolite

crystalline nature of spodumene at Mt Cattlin and Bald Hill may provide insight into the syn-/post-crystallization evolution of pegmatite and of the origin of spodumene alteration at these deposits.

Formation of megacrystic to giant crystals (meters in size) has been related to the mechanism of constitutional zone refining (CZR) (e.g. London and Morgan, 2012, and the references therein), which can enable very rapid rates of crystallization over a surprisingly short period of weeks to years (e.g. Bradley et al., 2017; Duuring, 2020). In the CZR process, a well-known metallurgical refining technique, the presence of incompatible components, such as H₂O, B, F, P and Be, act as fluxing agents in the rare-element pegmatite melt that can undercool or suppress the melt liquidus temperature by up to 150–200 °C below that normally expected for the onset of crystallization (London and Morgan, 2012). As the melt cools, continued fractionation further enriches the fluxing components (and incompatible elements), which modifies the melt structure, decreases the melt density and lowers the melt viscosity. The effect is to increase the rate of ionic diffusion, which during crystal growth results in the development of a flux-enriched, boundary-layer liquid at the rapidly progressing crystal front that enables such large crystal sizes to be attained (London and Morgan, 2012; Bradley et al., 2017). Thus, the comparatively more coarsely crystalline nature of spodumene at Mt Cattlin and Bald Hill suggests these pegmatites crystallized from a melt relatively enriched in fluxing agents. This contrasts to the less coarsely crystalline nature of spodumene in the remaining LCT pegmatites, which suggest these crystallized from a melt low in fluxing components.

As the pegmatite melt cools to <400 °C, the process of pegmatite consolidation switches from a process of crystallization to one of hydrothermal alteration (e.g. London, 2017; Dittrich et al., 2019). As revealed by TIMA mineral mapping, alteration of megacrystic spodumene at Bald Hill occurs congruently at the crystal margin and proceeds inwards along fractures and spodumene cleavage planes, marked by a significant influx of K (Fig. 74) and the removal of nearly all Li (refer to Fig. 51). TIMA mapping also reveals a distinct change in the morphology of primary muscovite from coarsely crystalline, subparallel booklets to a finer grained,

'disaggregated' state (Fig. 74). This textural change may define a decomposition front developed concentrically about the margin of spodumene alteration as muscovite is progressively decomposed as the front moves outward consuming muscovite. This provides the source of K that feeds the inward progression of spodumene replacement (Fig. 74).

Though mapped by TIMA as a mixture of lepidolite+phlogopite, XRD analysis confirmed the absence of spodumene and the presence of cookeite (Fig. 74). Cookeite is a Li-bearing, di-trioctahedral chlorite, with ideal formula $(\text{Al}_2\text{Li})\text{Al}_2(\text{AlSi}_3\text{O}_{10})(\text{OH})_2$, containing 2.86% Li_2O , though small amounts of Fe and Mg can replace Li in the octahedral sheet (Bobos et al., 2007). The occurrence of cookeite is known in several pegmatite fields worldwide (Bobos et al., 2007) and has been reported at three Western Australian localities (Lepidolite Hill, Londonderry and Mt Cattlin) (e.g. www.mindat.org/min-1121.html). Cookeite may form during the hydrothermal replacement of spodumene and other Li–alumino silicates (e.g. petalite, eucryptite and lepidolite), with studies (Bobos et al., 2007) indicating that spodumene–cookeite assemblages in equilibrium with kaolinite±mica±quartz are stable at ≈ 2.2 kbar and 220 °C, with the lower P – T limits of stability for cookeite at 205 °C and 2 kbar.

A similar style of alteration was noted in the upper lepidolite zone of the main pegmatite body in the Mt Mann suite

at Kathleen Valley, where acicular spodumene has been completely, or near-completely, pseudo-morphically replaced by a fine-grained mixture, mapped as 'quartz–elbaite–cleavelandite–calcite–beryl' with some relict spodumene (refer to Fig. 41). XRD analysis of a hand-picked, altered crystal of spodumene confirmed the mineralogy of the spodumene alteration as consisting of quartz–cookeite as the major phases, with muscovite/lepidolite, laumontite? (a zeolite) and calcite (refer to slide 74#, Appendix 5).

Graphic spodumene alteration

Symplectic spodumene–quartz intergrowth or SQI is the textural term used to describe the classic, fine-grained intergrowth texture of spodumene and quartz formed by the alteration of petalite (London, 2008; Bradley et al., 2017; Liera et al., 2019; Lima and Dias, 2019), as described in the petalite zone of the Dome North Deposit (e.g. see section, Dome North; Fig. 28). Although texturally similar, the microscopic, symplectitic quartz–spodumene (graphic) textures, formed between Na/K-feldspar and spodumene, as characterized by TIMA mineral mapping of the rare-element pegmatites investigated in this work, did not involve petalite as a precursor phase due to the absence of this phase in the many examples where this texture was identified (e.g. Fig. 75).

The graphic textured, SQI developed in the high-grade zone example from Bald High (BH1200; Fig. 75a–c) shows the

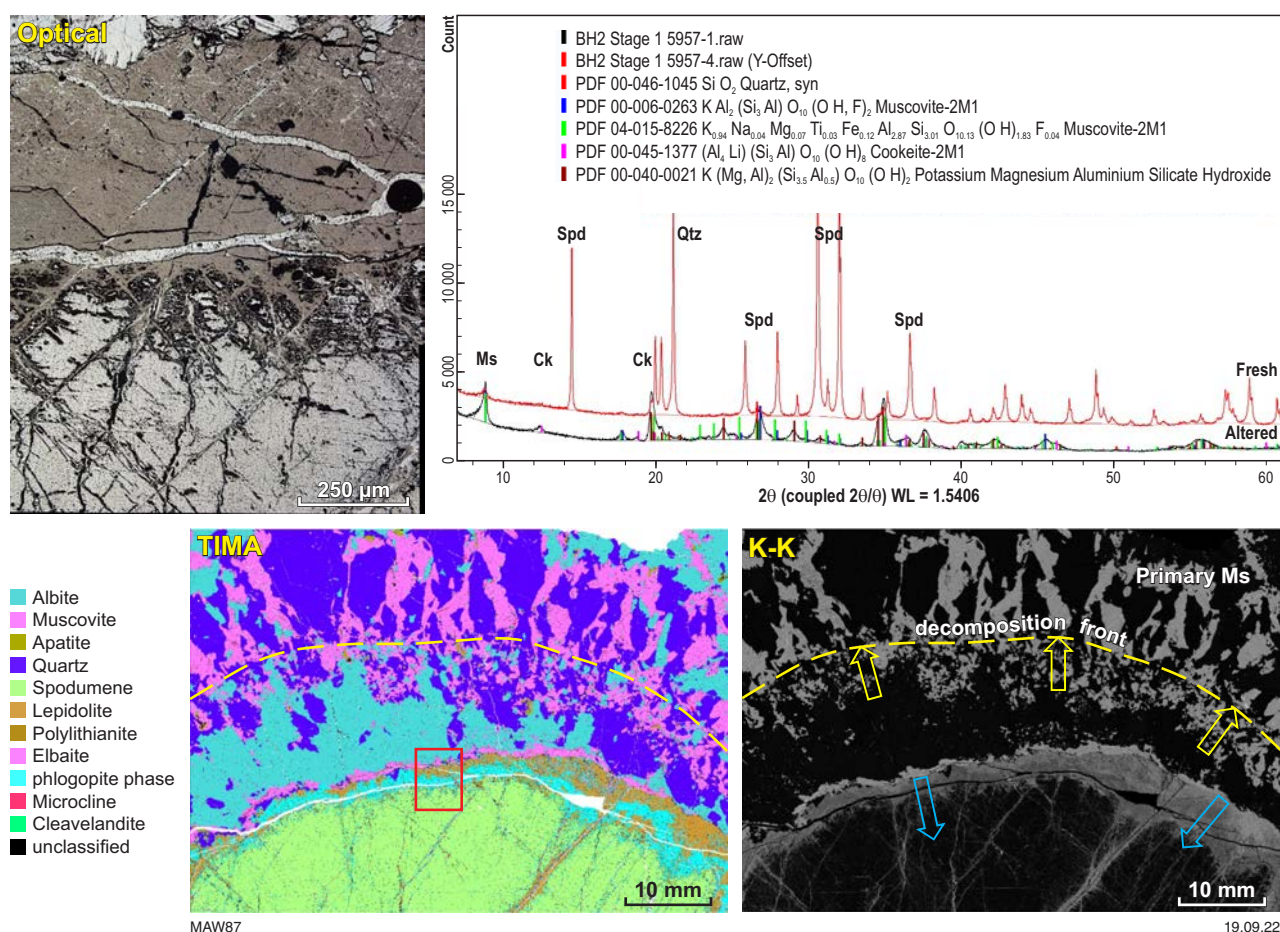


Figure 74. Optical imaging, TIMA mineral and K-K distribution maps of an altered, megacrystic spodumene from Bald Hill (sample #BH2250). The reflected light image of the area marked by the red rectangle in the TIMA mineral map shows detail of the blocky nature of spodumene alteration concentrated along fractures and cleavage planes. Blue arrows in the K–K distribution map show the direction of K influx, associated with spodumene alteration, that is likely sourced from the decomposition of muscovite along an outward moving 'decomposition' front (yellow arrows). XRD analysis of the spodumene alteration rim confirmed the presence of cookeite as one of the alteration products of spodumene

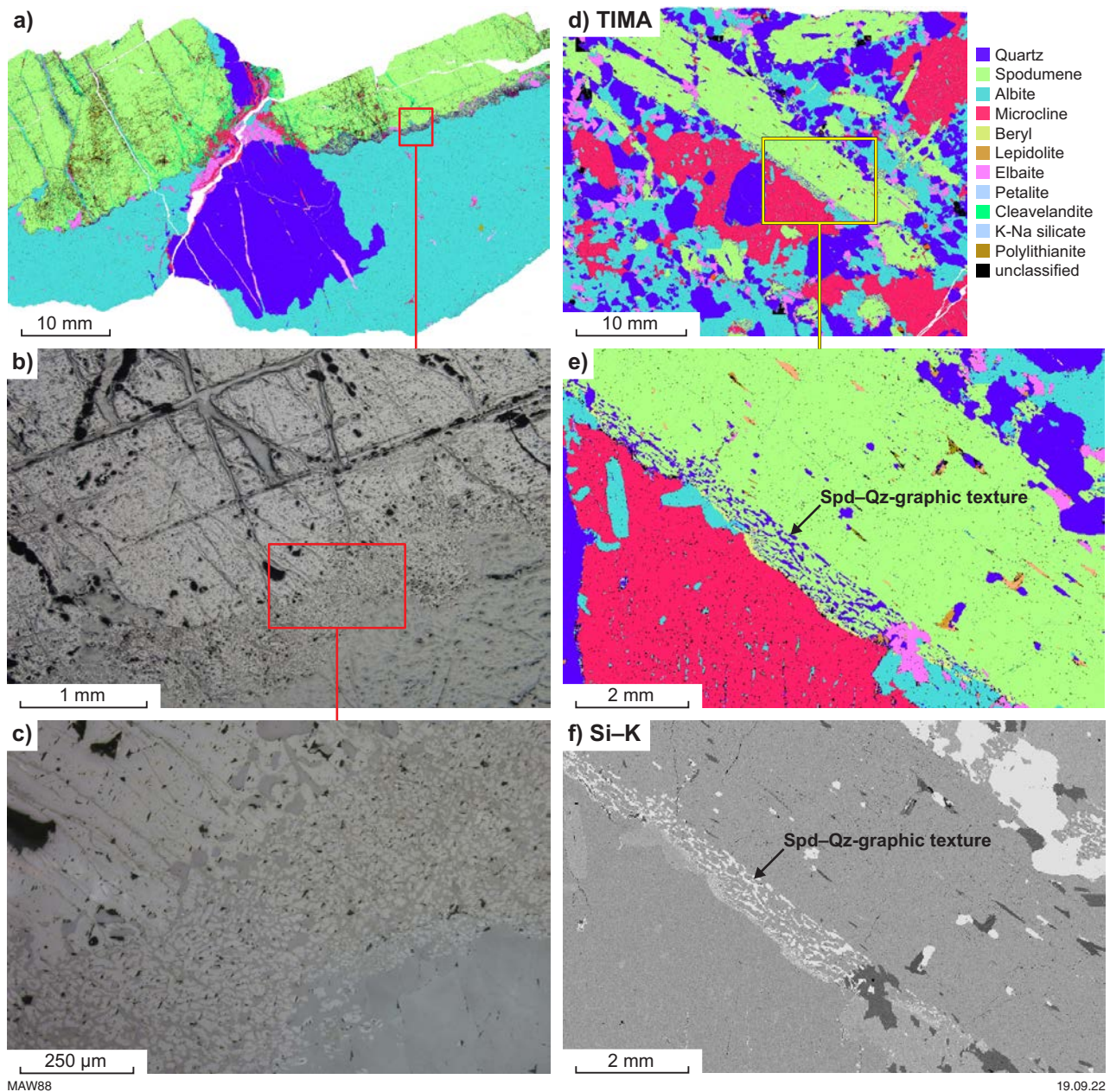


Figure 75. TIMA mineral map and optical imaging of megacrystic spodumene (#BH1200 (a-c) from the high-grade zone at Bald Hill (a-c) and TIMA mineral and Si-K distribution mapping of coarsely crystalline spodumene (d-f) from the Cade Deposit (sample PDD319_#15). Optical images in (b) and (c) show increasing detail of the symplectic spodumene-albite-alteration zone in the area marked by the yellow square in the TIMA map (a). The TIMA mineral map e) shows the intimately mixed nature of the symplectic spodumene-quartz alteration in the Cade pegmatite example (red box in (a)). Mapping of the Si-K distribution (f) more clearly defines the textural characteristics of the alteration

'mottled'-like alteration of spodumene as sub-rounded to rounded blebs in a zone up to 500 µm wide. Such relic, spodumene 'islands' decrease in size with distance from the spodumene grain margin as they are progressively assimilated within albite (Fig. 75c). Similarly, for the coarsely crystalline, complex spodumene deeper in the pegmatite body at the Dome North Cade Deposit (Fig. 75d–f), the interspersed secondary quartz 'domains' occur as elongated to lobate forms (to 500 µm long). Mapping of the Si distribution, in this case, clearly delineates the occurrence and form of the spodumene–quartz graphic intergrowth (Fig. 75f). Other prominent examples of this style of spodumene alteration include Mt Marion (slide #4; Appendix 4), Kathleen Valley (sample KVDD0076-#7, slide #32; Appendix 4) and Pilgangoora (sample PD005, slide #30; Appendix 4).

Modelling the alteration of Li-bearing aluminosilicates and their exchange reactions between alkali-feldspars (Wood and William-Jones, 1993) established that with decreasing temperature more Li goes into solution at the expense of spodumene. This suggests that the symplectic SQIs represent a late-stage, re-equilibration or replacement reaction prior to final solidification of the pegmatite, which results in the loss (leaching) of essentially all Li and Al from spodumene that leaves residual Si in the form of secondary, low Al-bearing (1–2%) quartz (e.g. Fig. 76; Pilgangoora). ToF-SIMS mapping of a symplectic interface between K-feldspar and spodumene in the quartz–spodumene pegmatite from Pilgangoora highlights the abrupt changes in composition associated with this type of alteration (Fig. 76). Where spodumene is in contact with quartz, this texture type does not form (it appears that the end result of the replacement is quartz, so that primary quartz acts as a buffer in some way).

Hence, care must be exercised when interpretation of the conditions of pegmatite crystallization is based solely on mineral–textural considerations. Though superficially very similar to the classic SQI texture often described in LCT pegmatites (as noted for the Dome North Deposit) formed by the alteration of petalite, in this case, the symplectic texture is formed by an entirely different process, that is, the alteration of spodumene. In addition, this textural type has implications for the processing of such ores where fine-grained intergrowth may require finer grinding to more effectively liberate spodumene (refer to the section Assessment of physical separation behaviour for a more detailed discussion regarding ore processing).

Trace element associations: vein in-filling

Aside from the above alteration styles characterized in the rare-element pegmatites examined, spodumene inherently contains inclusions of contaminant phases such as Na/K-feldspar, quartz, garnet fragments and tourmaline. In addition, spodumene universally displays secondary 'sericitic-like' alteration as microscopic veining, generally not visible to the naked eye, controlled by internal fractures and cleavage plane surfaces of the pyroxene structure. Lithium-bearing aluminosilicates are particularly susceptible to alteration compared to the bulk of the pegmatite mineralogy (e.g. feldspars and mica), in part, because coordination of the Li cation in the octahedral site of spodumene is destabilized due to the small size of the Li ion, which is too small to effectively fill the site (e.g. London, 2017). This is manifested as a decrease in the Li content of spodumene as demonstrated in section, Spodumene composition. During cooling, one of the octahedral oxygen

atoms rotates away from Li in spodumene, which essentially breaks the bond (Cameron et al., 1973).

Secondary alteration veining is predominantly K-rich but also introduces other trace element impurities such as Mg, Fe and Rb that are ultimately hosted by spodumene. For example, EPMA-wavelength dispersive X-ray spectrometry (WDS) mapping of an alteration veining assemblage consisting of a 'elbaite–phlogopite–lepidolite', as mapped by TIMA, in spodumene from Mt Cattlin, highlights the textural variability and compositional complexity associated with such alteration (Fig. 77).

Secondary vein alteration is likely to be site specific and may not be developed at all deposits. For example, spodumene in some of the Pilgangoora rare-element pegmatites hosts extensive, Fe–chlorite (as mapped) veining as shown by TIMA mapping in slides #20–21 (Appendix 4). More detailed work is required to confirm the mineralogy of this particular vein-alteration style. However, where it does exist, it will be carried through to the final, coarse grind spodumene concentrate. This has implications for the calcination processing of spodumene where thermal decomposition of secondary (and primary) micas can lead to the formation of melts that have the potential to limit the amenability of Li to acid leaching. This is discussed more fully in section, Calcination behaviour of mineral constituents.

Spodumene textures: implications for pegmatite processing

Mineral–textural associations are key to establishing the most appropriate processing strategy (e.g. grinding and recovery route) that accommodates differences in the Li-host phase and associated mineralogy. In the current study, spodumene is overwhelmingly the major Li-bearing phase, though petalite (e.g. Dome North, Londonderry) and, to a lesser extent, mica are also important hosts of Li. The occurrence of megacrystic spodumene, as characterized at Mt Cattlin and Bald Hill, is more suited to a (coarse) grind only processing approach, whereas the intimately associated, symplectic SQI, as developed at Greenbushes and at Dome North, and the mesh-textured, acicular spodumene intergrowths as developed at Kathleen Valley (Mt Mann pegmatite), would benefit by a two-stage process of a coarse–fine grind followed by flotation to more effectively recover spodumene. The textural implications in relation to establishing the most effective processing workflow are discussed in more detail in section, Calcination behaviour of mineral constituents.

Geochronological characterization

Zircon (and some cassiterite) U–Pb and spodumene/muscovite $^{40}\text{Ar}/^{39}\text{Ar}$ dating was undertaken on several LCT pegmatites in order to place age constraints on emplacement, crystallization and/or alteration of the host pegmatite. Details of the sampling methodology and techniques used are described in Appendix 3, which includes discussion and treatment of the results for individual samples. The following discussion considers the application of the different dating techniques and what may be inferred from the findings.

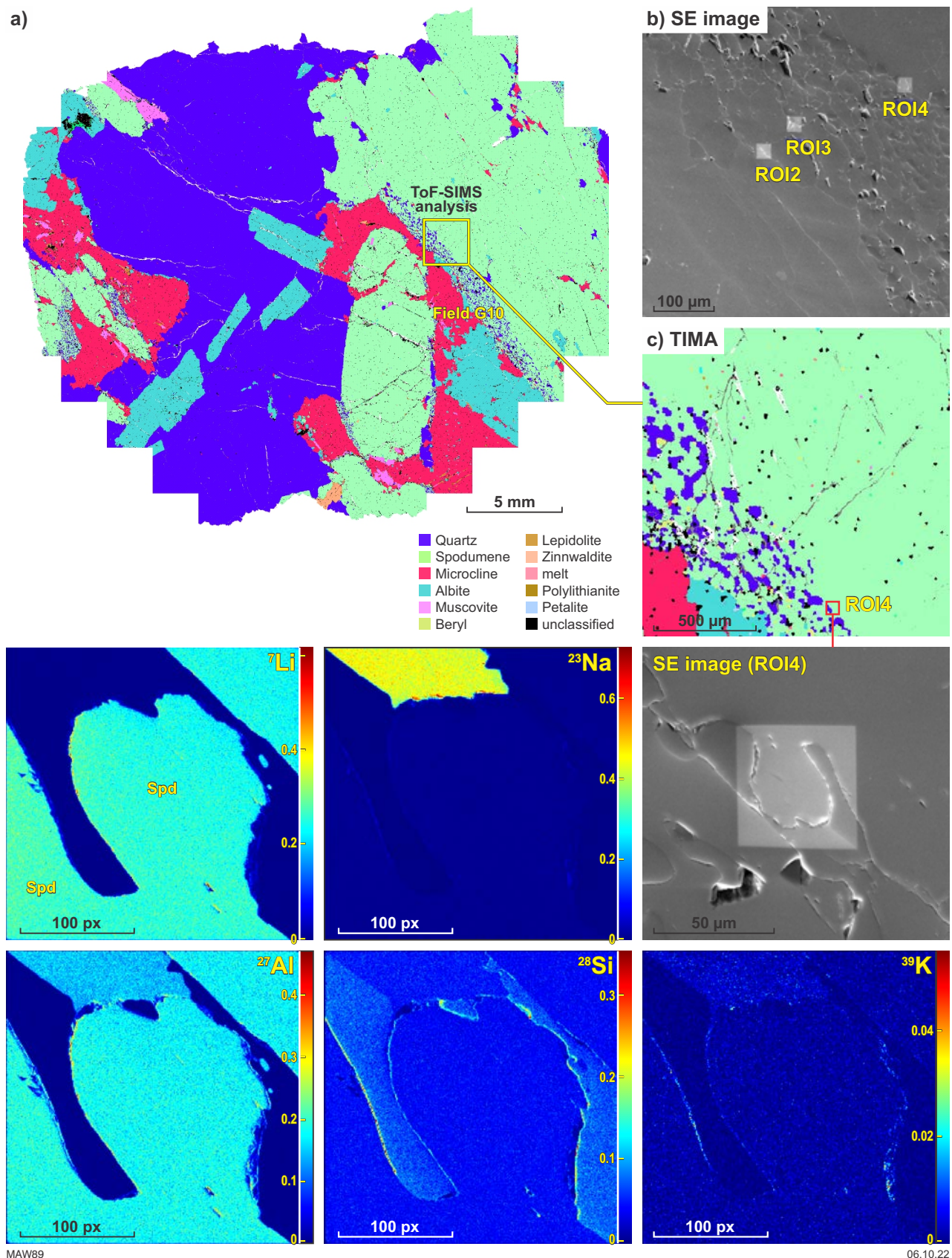


Figure 76. TIMA mineral map of graphic-textured spodumene-quartz alteration between spodumene and K/Na-feldspar for the complex spodumene-type pegmatite example from Pilgangoora (a). Secondary-electron (SE) imaging (b) and the TIMA mineral map at (c) show detail of the area selected for element distribution mapping using ToF-SIMS analysis. Selected ToF-SIMS element distribution maps for Li, Na, Al, Si and K (blue = low element content; red = high element content) are shown for the selected region of interest (ROI4) as shown in the SE image (b) and TIMA map (c). ToF-SIMS Li and Al distribution maps demonstrate the abrupt change in composition associated with the replacement of spodumene, where only 'quartz' (Si) remains

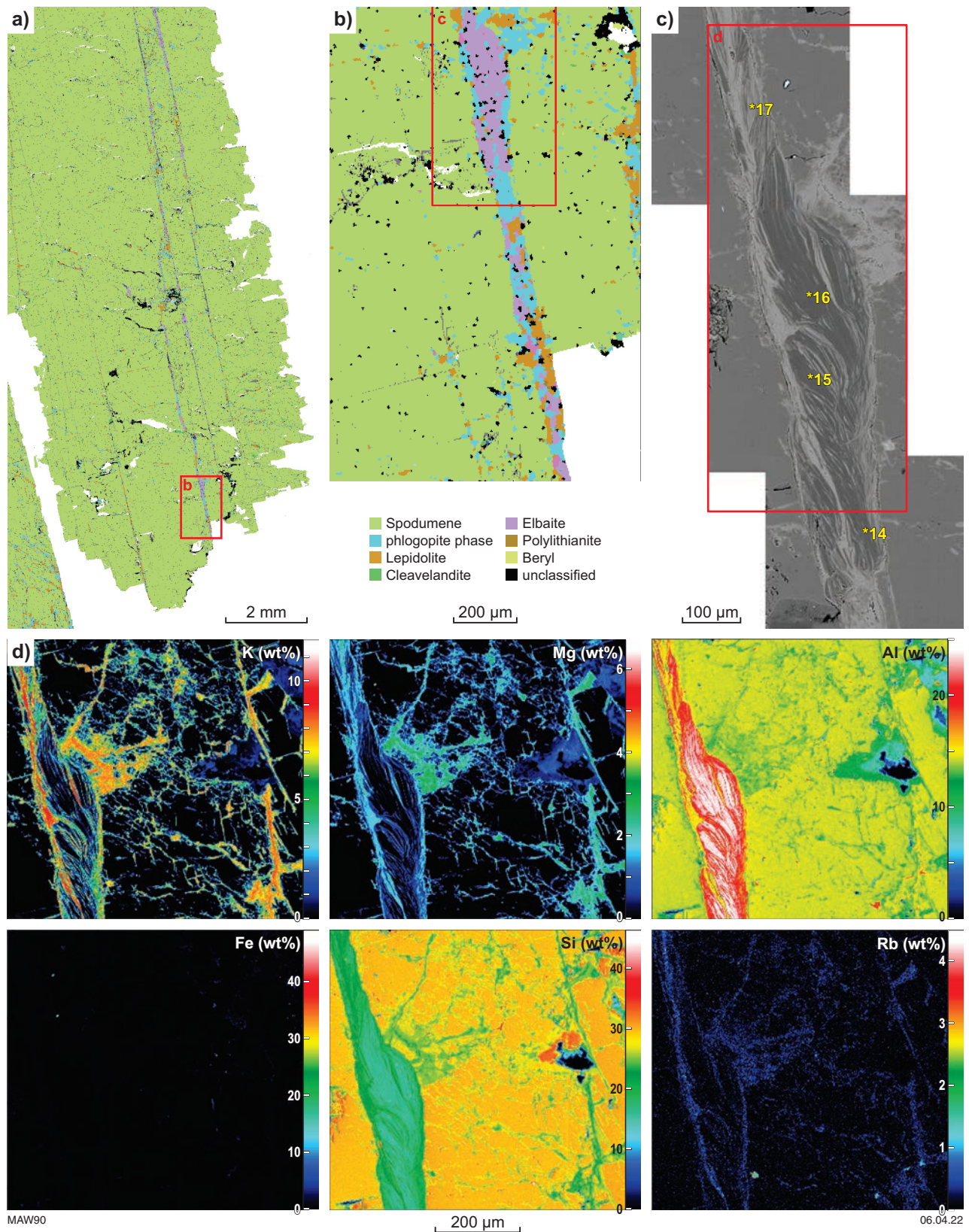


Figure 77. TIMA mineral maps of Mt Cattlin spodumene (a and b) showing extensive development of fracture and cleavage-controlled vein alteration. Contrast variation in the BSE images (c) of the area boxed in red in the TIMA map (b) reveal the textural complexity and intimate nature of the mineral associations. Quantitative, element distribution maps for K, Mg, Al, Fe, Si and Rb (d) highlight the compositional complexity, which indicates the presence of two phases: a high K–Mg–Rb/low-Al phase (high BSE contrast) and a low K–Mg–Rb/high-Al phase (low BSE contrast). Scale bar in the BSE images is 40 µm. Numbered spots (e.g. *17) show locations selected for EMPA measurement

(U–Pb) dating

The U–Pb dating results are summarized in Table 7. During the course of zircon analysis, some cassiterite grains were inadvertently analysed. The cassiterite was not a matrix-match with the primary zircon reference material so downhole fractionation between U and Pb could not be accurately modelled during data reduction. However, given the minimum fractionation between Pb isotopes, and the age of the samples, a weighted mean $^{207}\text{Pb}/^{206}\text{Pb}$ date for cassiterite may still be informative, although should be treated with caution. Future matrix-matched dating of cassiterite is warranted, with even larger laser-ablation spots to accommodate the very low U and Pb contents. In samples dominated by cassiterite, in which little or no zircon was recovered, shaded area in (Table 7), a weighted mean cassiterite ^{207}Pb – ^{206}Pb age is provided in Table 7. Despite a zircon age measured for the Kathleen Valley sample, the high U contents (6000–9000 ppm, Appendix 3) and high mean squared weighted deviation (MSWD) of 6.2 (Table 7), does not support a reliable age determination. Hence, the bracketed ^{207}Pb – ^{206}Pb date for this sample (Table 7).

We filter data for discordance using $((^{207}\text{Pb} - ^{206}\text{Pb} \text{ age} - ^{206}\text{Pb}/^{238}\text{U} \text{ age}) / ^{207}\text{Pb} - ^{206}\text{Pb} \text{ age}) * 100$. Data with >10% discordance are considered to have lost radiogenic-Pb and are not considered further. We use weighted mean ^{207}Pb – ^{206}Pb age as this isotopic system has more chronometric power for Archean aged material and we apply an old primary reference material (OGC-1; 3465.4 ± 0.6 Ma; Stern et al., 2009). Weighted mean ^{207}Pb – ^{206}Pb ages for samples are given in Table 7 with full data tables and weighted mean plots provided in Appendix 3 as a supplementary data spreadsheet, with cathodoluminescence (CL) transmitted and reflected light images also presented as a supplementary presentation, attached with Appendix 3. Note that imaging data is not presented for samples PDRC319 or BH1480 due to the lack of viable analyses nor are the associated concordia plots for samples listed in the shaded part of Table 7. This is because of the high (MSWD) (e.g. KD0076) or the U–Pb ages for cassiterite dominated samples were not properly matrix-matched.

Zircon U–Pb ages for the Greenbushes, Pilgangoora, Dalgaranga, Bald Hill and Londonderry pegmatites overlap within uncertainty (Table 7). Comparable ages were also established for other LCT pegmatites not included in the current study, such as the Mt Deans pegmatite (Dittrich et al., 2019). However, the chemistry and form of most zircon analysed in this work suggests they are inherited grains, not crystallized in the pegmatite. The relatively low-U content (<500 ppm and usually <100 ppm) in the analysed zircon from these samples, and their relatively small size (predominantly ≤ 100 μm but in cases up to 200 μm) suggest that they are not pegmatitic zircon. If these ages reflect the age of the pegmatite host, it follows that they provide a maximum constraint on pegmatite crystallization (i.e. the pegmatite must be younger than the host). It should be noted that these ages broadly coincide with a major period of global pegmatite emplacement at 2650–2600 Ma (Bradley et al., 2017; Dittrich et al., 2019). Peak periods of pegmatite emplacement are considered to correlate with increased crustal magmatism, associated with cycles of supercontinent break-up and formation (e.g. Bradley et al., 2017). In the Yilgarn, the 2650–2600 Ma interval correlates with the formation of low-Ca granitoid melts also accompanied with the intrusion of mantle derived, adakitic granitoids (Dittrich et al., 2019).

While the cassiterite ages should be viewed with caution as indicated above, we note that the Pb–Pb ages for C1-100_Pink and PD005 are significantly younger than those obtained on the inherited zircon from the pegmatites. Future matrix-matched analysis using larger spots would confirm this and provide a further indication of whether cassiterite yields a pegmatitic crystallization age.

The Greenbushes inherited zircon date of 2631 ± 4 Ma is significantly older than the age of three pegmatites dated at 2527 ± 2 Ma as previously reported by Partington and colleagues (1995). The Logue Brook Granite, dated at 2612 ± 5 Ma (Compston et al., 1986), was proposed as the source of the pegmatite but a genetic link with the granitoid is considered unlikely due to the age disparity (Partington et al., 1995). The revised zircon age obtained in the current study

Table 7. Summary of the U–Pb dating results for zircon and cassiterite from the Greenbushes, Pilgangoora, Dalgaranga, Bald Hill and Londonderry pegmatites

Sample ID	Location	GSWA ID	$^{207}\text{Pb}/^{206}\text{Pb}$	MSWD	Number of analyses	Mineral
			date (Ma)			
C3DD0024	Greenbushes	219863	2631 ± 4	0.29	25	zircon
Altura	Pilgangoora	219864	2629 ± 13	0.64	3	zircon
DD1	Dalgaranga		2630 ± 9	0.13	6	zircon
BH2250	Bald Hill		2643 ± 10	0.064	4	zircon
LHDD07	Londonderry		2643 ± 9	0.67	6	zircon
C1-100_Pink	Greenbushes	219861	2458 ± 16	0.27	15	cassiterite
PD005	Pilgangoora	219865	2386 ± 24	0.62	14	cassiterite
PD008	Pilgangoora	219862	2837 ± 16	0.58	22	cassiterite
KDD0076	Kathleen Valley		(2339 ± 5)	-6.2	8	zircon
PDRC319	Dome North		No viable analyses	No viable analyses	5	zircon
BH1480	Bald Hill	219860	No viable analyses	No viable analyses		cassiterite

still suggests that they are not temporally linked, although a review of Logue Brook samples may be warranted.

A weighted mean U–Pb age of 2643 ± 10 Ma was determined from four concordant zircon grains from the Bald Hill site (refer to Appendix 3). The younger age of these grains is consistent with the older age determined for the Mount Belchers formation (MBF) at 2666 ± 5 Ma, which hosts the pegmatite (refer to the section Bald Hill).

$^{40}\text{Ar}/^{39}\text{Ar}$ analysis: spodumene and muscovite

$^{40}\text{Ar}/^{39}\text{Ar}$ geochronology was attempted on spodumene separated from the Bald Hill, Pilgangoora and Mt Cattlin LCT pegmatites (Fig. 78). The analytical results for the Mt Cattlin MC1700 sample generated a robust inverse isochron corrected plateau date of ~ 1.1 Ga, however the Pilgangoora and Bald Hill results are highly uncertain due to excess radiogenic argon (Fig. 78 inset). The corrected plateau dates $\sim 0.6 - 1.3$ Ga and $\sim 0.8 - 1.3$ Ga respectively, are open to interpretation. Collectively, they likely represent post-emplacement fluid alteration events.

An alternative argon geochronology approach involved the analysis of muscovite separates from the Bald Hill and Mount Cattlin samples (Fig. 79). An aliquot of Mount Cattlin muscovite, along with a replicate, did not return statistically significant plateau dates although total fusion error ages of 2.4 Ga and 2.6 Ga (Fig. 79a). Two separate aliquots of Bald Hill muscovite, however, did return statistically significant muscovite plateau ages of 2602.5 ± 2.75 Ma and 2605.2 ± 1.99 Ma (Fig. 79b). These ages are interpreted as a regional cooling age through the closure temperature of the argon system in muscovite. Comparing the Bald Hill muscovite $^{40}\text{Ar}/^{39}\text{Ar}$ ages to the zircon U–Pb age ($2643 \text{ Ma} \pm 10 \text{ Ma}$) indicates that post-emplacement cooling to closure temperature of the Ar-isotope system took ~ 40 million years.

Given the disparate results between spodumene and muscovite ages, and the observation of pervasive microscopic scale spodumene alteration as described in section, spodumene morphology and alteration: indicators of pegmatite crystallization evolution, we infer that the radiogenic argon measured during spodumene analysis was predominantly contributed from the sericite alteration zones. Accordingly, the spodumene argon dates likely reflect a late-stage hydrous alteration event.

It is highly recommended that follow-up dating of known mafic dykes at Mt Cattlin (and at Bald Hill) and further dating of spodumene alteration at both pegmatites (and at other Western Australian pegmatite deposits) be undertaken to provide a relative age constraint on the timing of dyke emplacement and to test whether mafic dyke intrusion led to the alteration observed at these pegmatites.

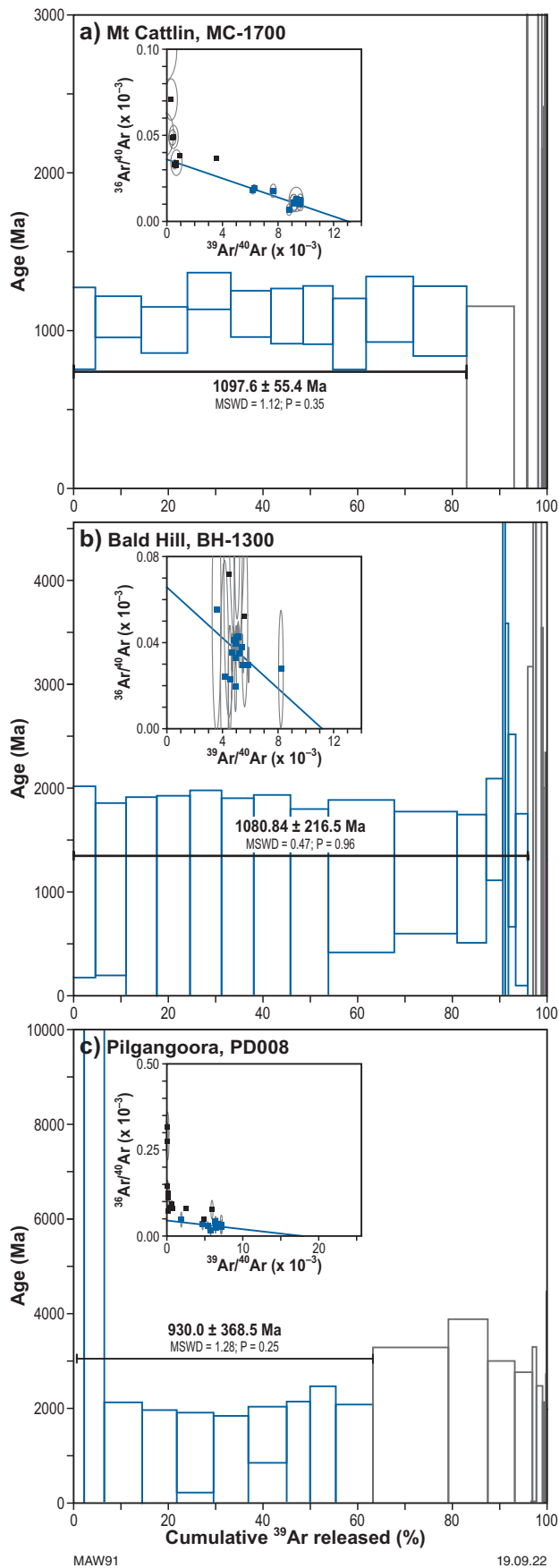


Figure 78. $^{40}\text{Ar}/^{39}\text{Ar}$ apparent age spectra for spodumene from Mt Cattlin, Bald Hill and Pilgangoora that resulted in resolvable age information. $^{40}\text{Ar}/^{39}\text{Ar}$ apparent age spectra plotted against the cumulative percentage of ^{39}Ar released. MSWD and probability of fit (P) are indicated. Errors on plateau ages are quoted at 2σ and do not include systematic errors (i.e. uncertainties on the age of the monitor and on the decay constant). Blue filled boxes within the inverse isochron inset for each sample are the steps used to determine the $^{40}\text{Ar}/^{39}\text{Ar}$ intercept for age corrections. Blue unfilled boxes within the age spectra plots indicate the steps used for the plateau age calculation

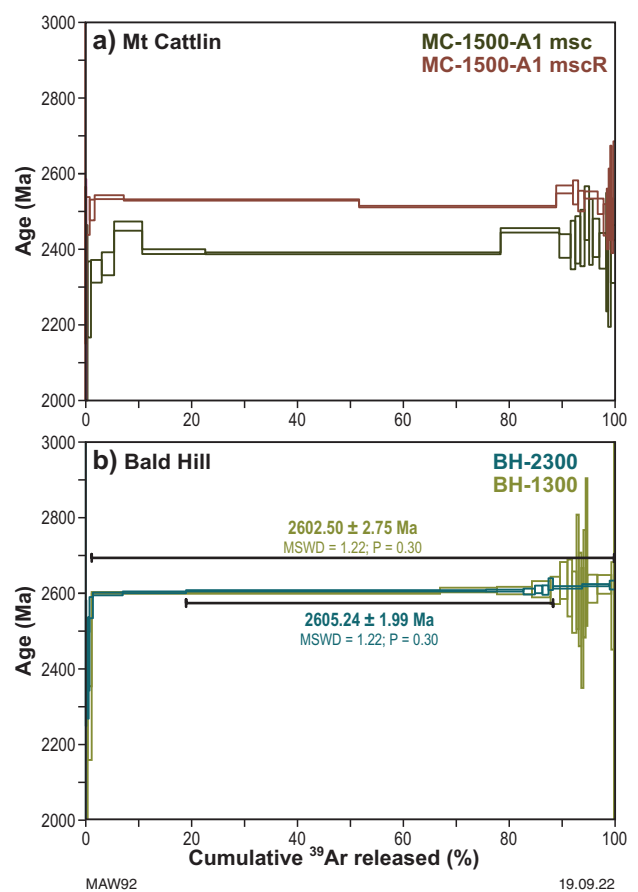


Figure 79. $^{40}\text{Ar}/^{39}\text{Ar}$ age spectra for muscovite from Mt Cattlin and Bald Hill as single grain analyses plotted against the cumulative percentage of ^{39}Ar released. Where plateau ages were able to be determined, MSWD and probability of fit (P) are indicated. Errors on plateau ages are quoted at 2σ and do not include systematic errors (i.e. uncertainties on the age of the monitor and on the decay constant)

Quantitative assessment of pegmatite minerals by LIBS analysis method

The application of LIBS was tested as an independent assessment of the practical limitations and requirements in exploration and mining operations focused on LCT pegmatites. This section provides a brief explanatory background of the technique and of the advantages and disadvantages as applied to the quantitative analysis of Li(spodumene)-bearing pegmatites. In summary, the main findings of this work were:

- Quantification of pegmatite Li and associated element (Al, Si, Fe, K, Mg) contents was assessed by application of partial least squares (PLS) analysis of LIBS analysis of representative powders of known (XRF) composition.
- Calibration PLS cross-validation (CV) models were developed from a standard data set of 37 pegmatite samples with four samples chosen as unknown validation samples.

Predicted PLS CV models of the pegmatite Li, Si and Al content in the validation data set were close to the known Li, Si and Al contents with relative percentage errors of mainly <12%.

- However, Li content of the four validation samples could not be consistently predicted.
- Similarly, modelled contents of the Fe, K and Mg content were not reliably predicted.

The LIBS technique is known to suffer from a few inherent, sample-related effects. The robustness and precision of PLS-LIBS quantification would be improved by developing CV-calibration models from a larger, more extensive sample set and by paying close attention to more consistent sample preparation to minimize sample surface (granularity, textural) and chemical matrix effects.

It is recommended that the existing calibration sample set be expanded to include a minimum of 200–250 representative examples from all significant WA LCT pegmatites to ensure the range of sample compositional variability is accounted by the prediction models.

LIBS methodology

LIBS is a relatively recent technique finding increasing application as a geoanalytical tool. Some recent applications include gold analysis and quantification (e.g. Harhira et al., 2017), gemstone (e.g. McMillan et al., 2014) and garnet (e.g. Alvey et al., 2010) provenance discrimination, and a range of applications for mineral analysis (e.g. McMillan et al., 2007; Harmon et al., 2013). A LIBS system has been adapted for use on board NASA's Curiosity Rover, as the 'ChemCam' system for distal compositional analysis of Martian soil and rock exposures (e.g. <https://mars.nasa.gov/msl/spacecraft/instruments/chemcam/>).

The LIBS technique employs a nano-second, pulsed laser to ablate a 20–100 µm diameter spot of the sample surface being investigated, thereby vaporizing approximately 1 ng of material to form a localized, high temperature

(5000–20 000 K) plasma plume (e.g. McMillan et al., 2014). As the plasma cools, electron decay from excited energy levels to their ground state condition emits characteristic element emission lines typically over the 200–1000 nm wavelength range (e.g. McMillan et al., 2014). The emitted light is collected and transmitted through optical fibres and the polychromatic radiation is dispersed in one or more diffraction gratings and recorded using a charged-couple device or CCD (e.g. McMillan et al., 2014).

LIBS instruments are available in a wide range of configurations with several hand-held, field portable systems (e.g. Bruker, Hitachi and SciApp) available to enable geochemical analysis to be performed at mine or pit faces or be included as part of a core logging campaign. Available LIBS instrumentation can measure and collect both quantitative, multi-element analysis of samples as well as surface, elemental distribution maps, typically of 2 mm x 2 mm areas to characterize the distribution and mineral-element correlation of geological material. A major advantage of the technique is that LIBS enables the simultaneous detection and quantitative analysis of all elements in the periodic table, particularly the emission lines of light elements ($Z < 10$) such as B, Be and Li (e.g. Sweetapple and Tassios, 2015).

Early studies demonstrated the potential of LIBS for phase identification (e.g. McMillan et al., 2007) and for quantitative analysis of Li in Li-bearing phases, such as spodumene, petalite and eucryptite, associated with LCT pegmatites (e.g. Fabre et al., 2002). More recent LIBS applications as a means of Li quantification have met with mixed success, with relative errors of up to 20% reported for Li contents measured using LIBS compared to results from EPMA and LA-ICP-MS techniques (e.g. Rossi et al., 2014; Sweetapple and Tassios, 2015).

As summarized by Sweetapple and Tassios (2015), the precision of LIBS measurements can be affected by instrumental factors relating to spectrometer calibration and plasma effects (e.g. self-absorption) that may induce peak broadening. Despite the significant advantages of the LIBS technique, such as enabling the rapid (real-time) analysis of a high sample volume throughput and requiring little to no sample preparation, the LIBS technique suffers from a few inherent, sample-related effects, such as the condition of the sample surface (granularity, surface texture and density) and chemical (element concentration) matrix effects (Sweetapple and Tassios, 2015). As noted throughout our investigation, spodumene rarely occurs in a pristine, unaltered condition and almost universally displays some level of fine-scale alteration, often not visible to the naked eye (e.g. refer to the section Spodumene morphology and alteration: indicators of pegmatite crystallization evolution).

Sample selection for mineral standards

To test the application of field portable LIBS for quantitative compositional analysis, well characterized mineral samples were selected for use as calibration and validation samples. Pressed-powder discs of pulped standards were then made to generate calibration curves using samples with known composition.

Laser-induced breakdown spectroscopy: application for field quantification of pegmatite composition

LIBS quantification of LCT pegmatite composition

To overcome issues related to sample heterogeneity and surface textural or granularity effects, a pilot study using material pulverized for XRF analysis was undertaken to assess the application of LIBS analysis for quantitative geochemical analysis of a suite of LCT pegmatite samples (Table 3.5, Appendix 3). For the sample series being tested, a LIBS spectrum of a pressed powder 'biscuit' of spodumene from Mt Cattlin (#MC300) is presented in Figure 80. It is interesting to note the detection of emission lines for K and Na (Fig. 80) and other elements present in trace amounts, given the widespread development of fine-scale alteration as previously described for this sample (e.g. refer to section, Spodumene morphology and alteration: indicators of pegmatite crystallization evolution). Use of an aliquot of the XRF sample pulp has the advantage of ensuring a coherent and well characterized data set is used as a means of validating the LIBS compositional analysis against the XRF geochemical results through application of multi-variate, PLS analysis. Refer to Appendix 3 for details of the PLS method and development of LIBS spectral calibration models.

Cross-validation models as plots of the CV-predicted component (i.e. element content) against the known weight percent element concentration for Li, Si, Al and Fe are shown in Figure 81. Cross-validation models for other elements, including Mn, K and Mg, were developed but were less successful (data not shown). Predicted (r^2) values of the Si, Al and Li contents are strongly correlated to the known concentration of these elements, although standard error of prediction (SEP) values for Al (1.25%) and Si (1.46%) may be considered high (Fig. 81). Sample points from which the CV calibration models were produced are coloured by the F-Parameter, with red data points sitting outside (i.e. the green shaded region in each case) the F-Parameter cut-off value of 0.9 (Fig. 81). The F-Parameter value gives a measure of the size of the residual, defined as:

$$\text{F-Parameter} = (\text{known concentration} - \text{predicted concentration})^2$$

for the element in question for each sample. This provides a means of identifying possible outlier samples, and the calibration models could benefit by further refinement to assess if these samples could indeed be excluded from the calibration model.

The CV-predicted element concentrations, derived by applying the PLS calibration models for each element, were compared against the known (i.e. XRF assay) concentration for Li, Si, Al, Fe, K and Mg (Table 8). The CV-predicted contents of Li, Si and Al were close to the known Li, Si and Al contents of the validation samples, with percentage relative errors mostly $< \approx 12\%$. Estimates of the silica content for the unknown samples were the most reliably predicted compared to their known SiO_2 contents (Table 8). However, estimates of the CV-predicted Li content for two

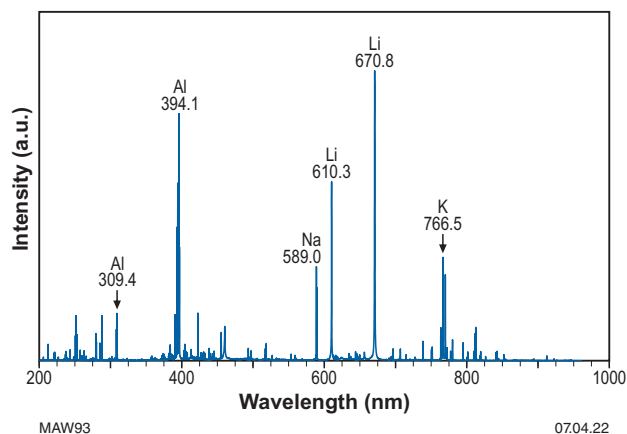


Figure 80. LIBS spectrum for Mt Cattlin spodumene (MC300) over the 200–1000 nm wavelength range. Relative spectral intensity is given in arbitrary units (au). The wavelength position of emission lines for some of the elements detected (Al, Li, K, Na) are labelled

of the validation samples were significantly underestimated compared to the known Li contents in these cases (Table 8). Relative errors of the CV-predicted Fe, K and Mg contents were significant and did not show a consistent trend in either their over or under estimation compared to the known Fe, K or Mg contents for the validation samples (Table 8).

Reasons for the discrepancy between the CV-predicted and known element concentrations are unknown but likely are related to sample physical and chemical effects (e.g. Sweetapple and Tassios, 2015). During LIBS measurement, it was noted there were differences in the competency of the compressed 'biscuit' surface, causing the laser to couple inconsistently during ablation (i.e. greater shot-to-shot variability). In some instances, during LIBS measurement laser shots explosively ejected material from the sample surface. Hence, there would be insufficient energy transfer to generate the plasma plume. In situations where this occurred, sample LIBS measurements were not included in the CV modelling.

In addition, the inclusion of near mono-mineralic samples with more typically mixed-phase samples (i.e. drillcore – Table 3.5, Appendix 3) would induce matrix-matching effects with some samples predominantly comprising a single phase compared to the typical multiphase mineralogy of a rare-element pegmatite, where mineral proportions can vary. Self-absorption effects can also be important. For example, emission lines of Li and Na can be affected by self-absorption, which can induce peak broadening and a reduction in peak intensity (e.g. Rossi et al., 2014; Sweetapple and Tassios, 2015). Finally, CV prediction and PLS model robustness would be improved by including a much larger and more extensive sample suite in the study by incorporating LCT pegmatite examples from other rare-element deposits but still pay close attention to a more consistent matrix matching between samples.

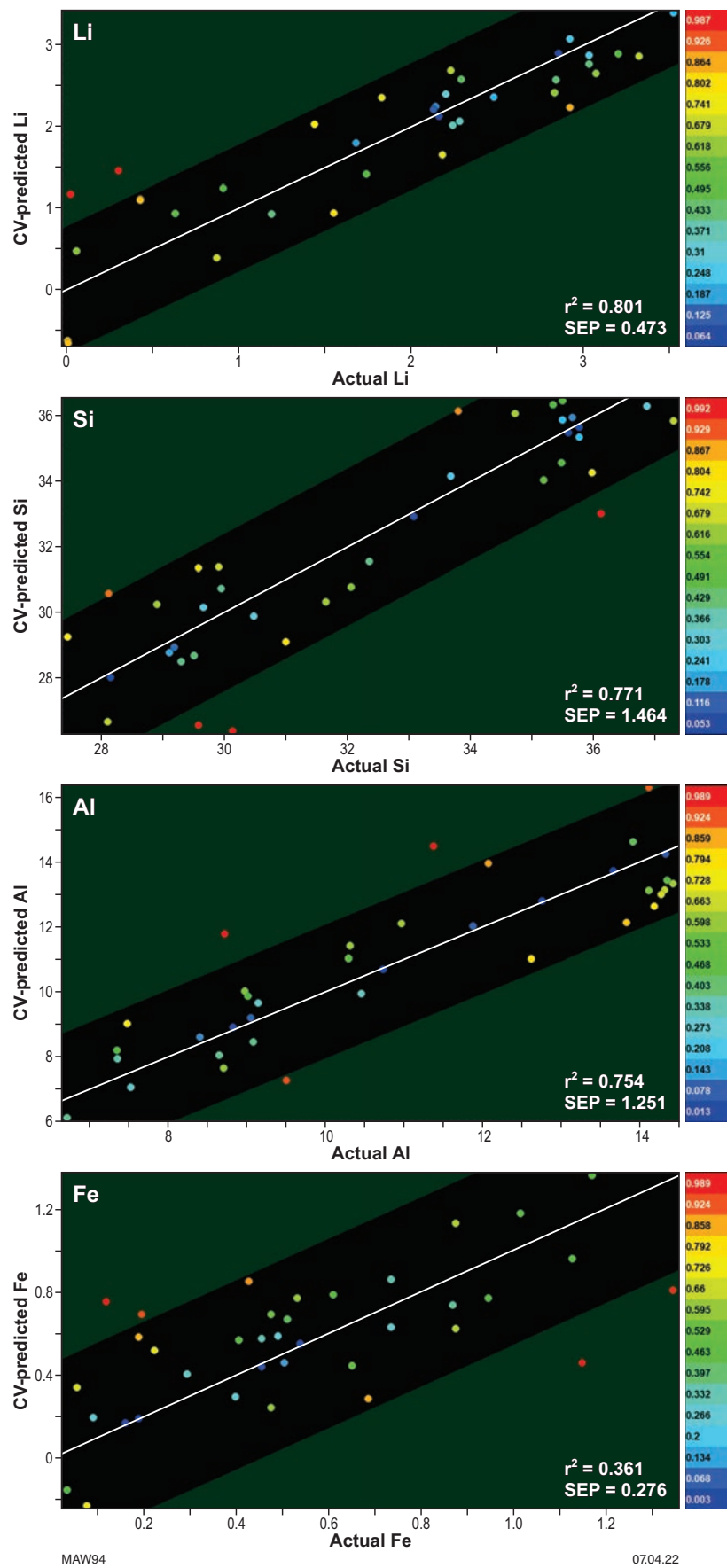


Figure 81. PLS models of the CV-predicted vs measured concentration for Li, Si, Al and Fe. Sample points are coloured by the F-Parameter value set at a cut-off value of 0.9. Hot colours (i.e. red) denote samples with a high F-Parameter value above the cut-off (i.e. green-shaded zone), which may be useful in identifying outlier samples. SEP values have the same units as concentration (i.e. wt%). The co-efficient of determination, r^2 values, carry the same meaning as the Pearson's correlation (r^2) co-efficient

Table 8. Comparison of PLS-predicted and known-element concentrations for Li, Si, Al, Fe, K and Mg in the validation samples

Sample	%Li	PLS-Pred_Li	%Diff.	%Si	PLS-Pred_Si	%Diff.	%Al	PLS-Pred_Al	%Diff.
MC0300	2.92	3.01	3.05	29.2	28.3	-3.00	13.9	15.3	9.73
PD004_67.75m	1.09	-0.12	-110.83	34.8	34.1	-2.03	8.5	9.4	10.72
Bald_Hill_(conc.)	2.9	2.62	-9.69	30.6	29.8	-2.62	12.9	13.2	2.90
GB_241174_New	1.19	0.82	-31.18	29.3	30.4	3.85	11.9	10.4	-12.46

Sample	%Fe	PLS-Pred_Fe	%Diff.	%K	PLS-Pred_K	%Diff.	%Mg	PLS-Pred_Mg	%Diff.
MC0300	1.13	0.98	-13.41	0.49	0.59	22.02	0.20	0.26	29.65
PD004_67.75m	0.70	0.42	-39.34	0.34	0.12	-64.14	0.36	0.04	-88.76
Bald_Hill_(conc.)	0.58	0.69	18.76	0.29	0.41	41.52	0.16	0.14	-8.92
GB_241174_New	1.01	0.67	-34.12	1.55	1.63	5.49	0.21	0.13	-36.97

Assessment of physical and chemical processing behaviour of LCT pegmatites

The metallurgical response of different pegmatite ores was evaluated in terms of:

- Mineral liberation characteristics for beneficiation properties
- Thermal behaviour and lithium extractability associated with conventional calcination and sulphate roasting refining for recovering Li.

Assessment of physical separation behaviour

An understanding of the liberation characteristics or particle composition distribution of an ore is important in comminution circuit design and for optimizing beneficiation processes, such as flotation, density, and magnetic and electrostatic separation in operating plants.

Key findings

Key findings observed in this work are as follows:

- Twenty-one samples that represent different deposits and lithologies from Mt Cattlin, Bald Hill, Greenbushes and Pilgangoora regions were examined. The main source of lithium is spodumene in these deposits, with regions containing Li micas (lepidolite and zinnwaldite) and petalite.
- Generally, the coarse nature of spodumene within quartz, feldspar and muscovite mineral matrix allows for >90% recovery of spodumene, with expected Li grades above 3 wt%.
- Factors identified that limit recovery and grade are regions with:

- Graphic-textured, spodumene–quartz alteration intergrowth between spodumene and K/Na-feldspar, as observed in most samples but extensively in samples elevated from Pilgangoora
- Partially altered spodumene containing micas in fine interstitial veins in voids and fractures and as inclusions within spodumene grains. This is prevalent at both Mt Cattlin and Bald Hill where high grade, white spodumene in quartz, feldspar and muscovite zones transitions to low grade, highly altered green to dark-green spodumene
- Separation of middlings containing high mica and/or quartz/feldspar contents and finer grinding would improve the recovery of spodumene in these orebodies
- In Greenbushes samples, spodumene can be well liberated from the main gangue mineral quartz, with high recovery and Li grades of 3.5 wt%. Fine grinding would be required to liberate spodumene associated with graphitic texture intergrowths with quartz and, in some areas, with feldspars.
- Tantalum minerals in all deposits examined are mainly associated with the gangue minerals or are freely liberated under the particle sizes examined in this study. Hence, Ta minerals can be upgraded and concentrated separately from spodumene, as is practised by industry.
- At Greenbushes, antimony and arsenic are present as stibiomicrolite and parabrandidite, respectively, as finely disseminated grains within spodumene. There are also associations of pollucite with spodumene.
- A high percentage of cassiterite in most samples are locked and associated with spodumene and, therefore, will report along with spodumene grains in the concentrate.
- Analysis of the liberation characteristics of spodumene concentrates collected from the beneficiation circuits at five mines reveal high contamination content of gangue mineral, up to 20 wt%. Of this only around 5 wt% is associated and locked with spodumene. Techniques such as ore sorting can be used to reduce mineral impurities to the beneficiation circuit.

Sample selection and methodology

The samples examined in this study were from Pilgangoora, Bald Hill, Mt Cattlin and Greenbushes regions. Budget constraints limited the evaluation to these four areas. Samples which represent different deposits and lithologies were selected and are outlined in Table 9.

In addition, five concentrates produced from the beneficiation circuits of five mine sites were examined. These are discussed in section, Liberation characteristics-concentrates. Figure 82 outlines the procedure used for sample preparation and analysing mineral liberation properties.

The selected samples were crushed to pass 3.5 cm using a jaw crusher. Sub-samples were then subjected to electrodynamic fragmentation and screened to pass –4 mm. The particle size was chosen to allow comparisons between samples and not to optimize comminution. The electrodynamic fragmentation technique allows for detailed studies of the original morphology and shape, crystal structure, physical and textural features, and the chemical composition of mineral phases without the damaging effects associated with sample preparation by crushing. Sub-sampling was carried out using a rotating splitter technique to ensure representative samples were obtained for detailed mineralogical and metallurgical test work.

Table 9. Sample descriptions

Region	Sample type	Sample description
Pilgangoora Samples from mafic and ultramafic zones	Drillcore	<ul style="list-style-type: none"> • Pegmatite hosted mainly in mafic rock (PD005) • Pegmatite hosted mainly in ultramafic rock (PD008)
	Sample specimens from mine site	<ul style="list-style-type: none"> • Mine site containing spodumene, moderate quartz and mica content (PIL1) • Mine site containing spodumene, high feldspar and mica content (PIL2) • Mine site containing spodumene, high feldspar and quartz content (PIL3)
Bald Hill Samples from high-grade (BH1-series) and low-grade (BH2-series) zones	Sample specimens from mine site	<ul style="list-style-type: none"> • Mine site high-grade zone, rich in white spodumene and low mica (BH1300) • Mine site high-grade zone, containing green spodumene with high feldspar and mica content (BH1480) • Mine site low-grade zone, containing green spodumene with high beryl and mica content (BH2700) • Mine site low-grade zone, containing green spodumene with high feldspar, quartz and mica content (BH2250) • Mine site containing feldspar and chlorite content (BH2800)
	Sample specimens from mine site	<ul style="list-style-type: none"> • ROM pad, rich in white spodumene (MC200) • ROM pad, containing green spodumene with low mica content (MC100) • Mine site containing green spodumene partially altered spodumene (MC500) • Mine site containing green spodumene with high feldspar, quartz and mica content (MC1500) • Mine site 2SE Stage 1 pit, of highly altered spodumene, containing feldspar and chlorite content (MC600) • Mine site 2SE Stage 1 pit, spodumene containing lepidolite (MC1700)
Greenbushes Samples with different lithologies that cover the C3 (Lithium pit) and C1 (Central lode) that represent high-grade Li- and Na-enriched zones	Sample specimens from mine site	<ul style="list-style-type: none"> • Central lode mine containing high-grade spodumene zone (Na enriched zone) with quartz, feldspar and pollucite content (C1200) • Central lode mine containing high-grade pink spodumene zone with high quartz content (C1100P) • Central lode mine containing high-grade white spodumene zone with high quartz and feldspar content (C1100WH) • Lithium pit mine containing high-grade pink spodumene zone with quartz, mica and feldspar content (C3300H) • Lithium pit mine containing high-grade spodumene with high quartz content (C3300HWH)

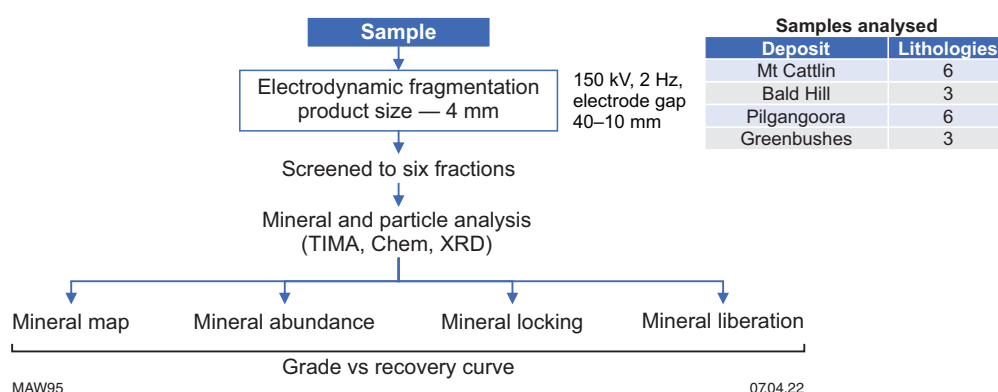


Figure 82. Outline of sample preparation and test work for characterization of ore materials

Electro-fragmented samples were sieved to yield six size distributions (between +2000 μm and -75 μm) and prepared for mineralogical analyses. Polished sections of the sized fractions were produced and studied to determine the relationship of Li-bearing silicates liberated from gangue minerals. Figure 83 shows the particle size distribution following electrodynamic fragmentation where a large percentage of the material resides in the coarse fraction with minimal fines produced. Between 60 and 80% of particles were greater than 1 mm in size. All samples have a similar particle distribution, except two from Greenbushes, which are associated with high and low quartz content. Electrodynamic fragmentation and screening to pass -4 mm reduced the formation of fine particles.

Optical imaging and automated digital imaging assessment of the different size fractions was carried out on polished mounts to determine the modal mineralogy, mineral textures and liberation characteristics of lithium ore samples using TIMA. The deportment of the major elements was also assessed. Using the mineralogical liberation analysis routines within TIMA software, the mineral particles within the polished mounts were categorized in terms of:

- *Mineral locking properties*, which are used to describe how much free surface of a given mineral is exposed, and the type and number of minerals that are intergrown with it
- *Mineral liberation characteristics* based on the distribution of Li-bearing minerals across particle composition classes (locked, middling and liberated) for both bulk composition (volume mineral liberation) and surface composition of particles (surface mineral liberation) analysis
- *Theoretical grade-recovery curves* developed to provide an estimate of the maximum expected recovery that can be achieved by physical separation of a mineral at a given grade. Test work is always required to validate the results.

A comparison between samples and their influence on beneficiation properties was then evaluated.

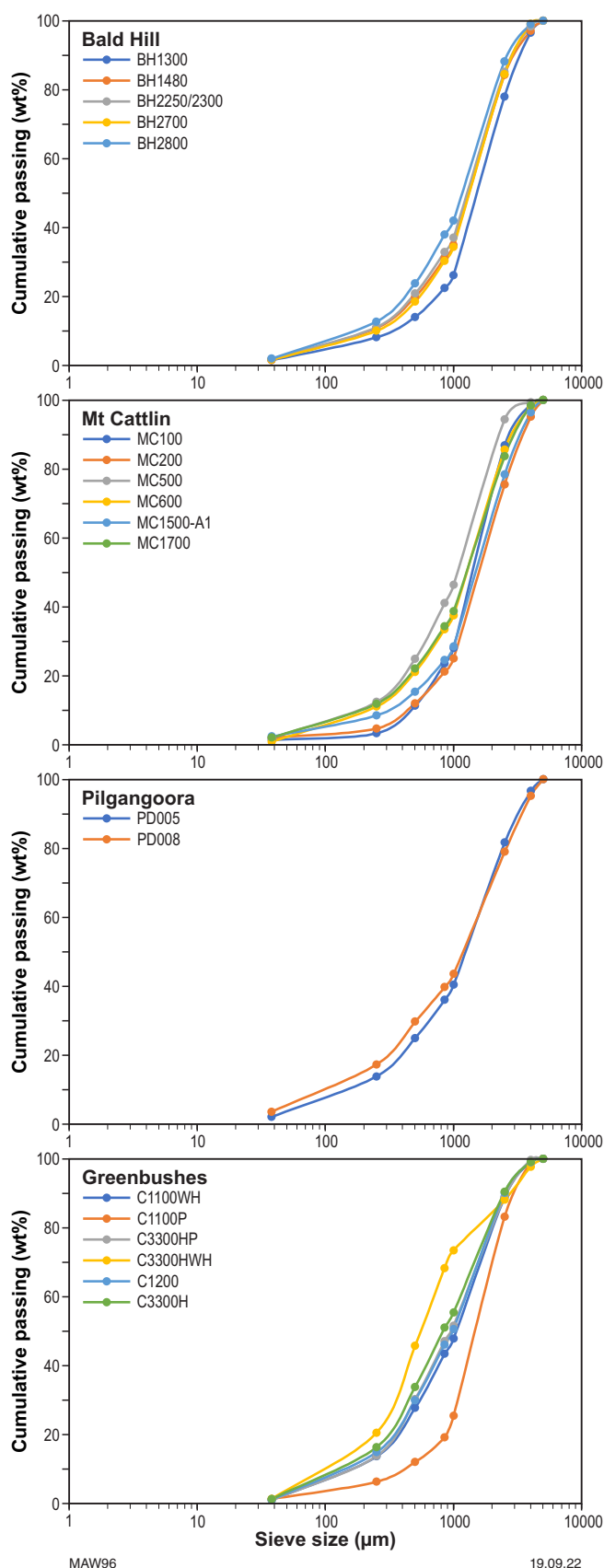


Figure 83. Particle size distribution of samples from all four deposits

Assessment of mineral content

The mineralogical composition acquired from TIMA liberation analysis for samples selected from the four mine sites are shown in Table 10. The mineral mass of a phase is calculated based on percentage area in polished sectioned mounts using an assumed density for each mineral.

In all samples analysed, the main Li-bearing mineral is spodumene, with minor amounts of eucryptite, petalite and lepidolite. The main gangue minerals are feldspars, quartz and micas. The main feldspar tends to be the Na-rich form, albite, with K-rich feldspar more abundant in some Bald Hill and Pilgangoora samples. Chlorite and phlogopite micas rich in Fe, Mg and Mn are associated with both Mt Cattlin and Bald Hill samples. Apatite, tourmaline and beryl appear in most samples. Pollucite is present as a minor phase in the Greenbushes samples, except in C1200, where it is more abundant. Calcite is present in most samples in trace amounts but occurs in slightly higher concentration in some of the Bald Hill and Pilgangoora samples. Tin in the form of cassiterite and Ta in form of tantalite are present in trace amounts. Lepidolite and muscovite, although present in all samples, are more abundant in the Greenbushes and Pilgangoora samples.

The accuracy and consistency of the derived data calculated by TIMA was compared with the whole rock bulk chemistry and the results are shown in Figure 84 and Table 11. An R^2 value is presented for each sample. This value describes the deviation of the results from a perfectly linear relationship ($R^2 = 1$). The minerals in the mineral classification file used to classify which phases in the polished mounts have fixed, average chemical compositions. Both MC500 and MC600 contain highly altered spodumene with varied compositions that may account for some variation in values. Overall, the data are in excellent agreement and provide confidence in the results.

The abundance of spodumene and gangue minerals in the different size fractions in the Pilgangoora, Bald Hill, Mt Cattlin and Greenbushes samples are shown in Appendix 7. The majority of the spodumene in most samples examined occur in the coarse fractions, with the fine fractions containing higher gangue mineral content. The coarse nature of spodumene within the ore reflect its association with the coarse particle size. Depending upon the nature of the minerals associated with spodumene, high-residual contents of micas, feldspars and quartz occur in the coarse fractions.

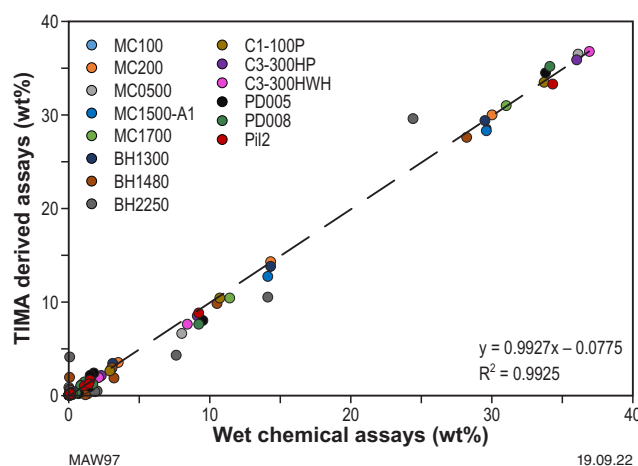


Figure 84. Correlation between the chemistry for selected samples from Mt Cattlin (MC), Bald Hill (BH) and Greenbushes (C1, C3) and Pilgangoora (PD, Pil), derived from TIMA and wet chemical analyses showing good agreement

Table 10. Modal mineral abundance from TIMA
(a) Mt Cattlin and Bald Hill samples

<i>Minerals (wt%)</i>	<i>Mt Cattlin</i>						<i>Bald Hill</i>				
	<i>MC100</i>	<i>MC200</i>	<i>MC600</i>	<i>MC500</i>	<i>MC1500</i>	<i>MC1700</i>	<i>BH1300</i>	<i>BH2800</i>	<i>BH1480</i>	<i>BH2250</i>	<i>BH2700</i>
Spodumene	94.0	97.6	36.7	23.6	80.2	44.6	91.5	5.0	31.5	0.1	16.0
Eucryptite	0.02	0.02	0.01	0.02	0.1	0.1	0.1				0.1
Petalite	0.02	0.02	0.04	0.02	0.1	0.1	0.1	0.1	0.1		0.1
Albite	0.4	0.1	23.8	12.8	5.1	4.8	0.9	26.7	35.0	47.1	13.8
Anorthite	0.3	0.5	0.8	0.1	2.3	1.7	0.1	0.1	0.9	0.2	0.1
Microcline	0.03	0.03	0.4	0.2	0.1	0.3	0.5	2.1	1.2	20.7	1.1
Quartz	1.6	0.1	30.7	50.0	5.1	22.1	0.6	48.5	9.8	5.8	3.3
Beryl	0.08	0.09	0.72	0.08	0.18	0.1	0.3	0.1	0.1		50.8
Biotite										0.2	
Lepidolite	0.1	0.04	1.3	1.0	2.7	18.9	0.1	0.1	0.3		0.1
Muscovite	0.1	0.04	0.9	8.2	0.2	2.8	1.1	8.3	5.4	3.7	2.1
Chlorite/phlogopite	0.3	0.01	0.8	0.2	0.04	0.1	1.6	6.2	1.4	19.1	4.7
Apatite –Mn	0.03	0.1	0.1	0.1	0.1	0.1		0.1	10.0	0.2	0.1
Calcite								0.1	0.2	0.2	0.1
Cassiterite/tantalite/zircon			0.01			0.03			0.1		
Garnet			0.03	0.01	0.03						
Tourmaline	0.9	0.1	0.1	0.9	0.3	0.6	1.2	0.4	0.4	0.5	4.2
Hematite/Magnetite	0.01		0.03		0.01						
Pollucite											
The rest	0.04	0.1	0.1	0.03	0.8	0.3	0.1	0.1	0.4	0.3	0.1
Total	97.8	98.7	96.5	97.0	97.4	96.5	98.2	97.9	96.8	98.1	96.7

Table 10. Modal mineral abundance from TIMA
(b) Greenbushes and Pilgangoora samples

<i>Minerals (wt%)</i>	<i>Greenbushes</i>							<i>Pilgangoora</i>				
	<i>C1-100P</i>	<i>C1-100WH</i>	<i>C1-200</i>	<i>C3-100</i>	<i>C3-300H</i>	<i>C3-300HP</i>	<i>C3-300HWH</i>	<i>PD005</i>	<i>PD008</i>	<i>Pil1</i>	<i>Pil2</i>	<i>Pil3</i>
Spodumene	69.7	56.0	65.8	1.0	53.1	56.6	52.1	11.1	12.3	37.4	41.2	29.5
Eucryptite	0.04	0.1	0.04		0.1	0.04	0.03					
Petalite	0.02	0.02	0.03	0.04	0.02	0.02	0.01	0.1	0.1	0.04	0.1	0.04
Albite	2.7	8.2	9.9	59.5	3.4	3.3	1.9	24.8	23.4	9.9	11.4	10.6
Anorthite	0.04	0.04	0.1	0.1	0.1	0.1	0.02		0.5	0.5	0.1	0.1
Microcline	1.3	1.0	0.7	28.3	2.9	0.8	0.1	11.0	3.6	6.3	4.7	19.8
Quartz	23.8	30.2	13.6	3.2	36.1	37.3	43.9	44.5	50.9	27.3	31.2	33.5
Beryl	0.08	0.06	0.08	0.06	0.05	0.09	0.05	0.3	0.2	0.8	0.3	0.1
Biotite									0.1			
Lepidolite	0.3	0.7	0.7	0.1	0.6	0.1	0.02	0.9	1.1	8.4	0.5	0.7
Muscovite	0.8	1.3	1.2	2.6	1.5	0.3	0.2	6.5	6.5	2.7	4.8	3.3
Chlorite/phlogopite												
Apatite –Mn	0.01	0.1	0.1	0.5	0.6	0.1		0.2	0.4	0.1	0.2	0.1
Calcite										2.5		0.03
Cassiterite/tantalite/zircons		0.1	0.1	0.04	0.01					0.05	0.04	0.06
Garnets									0.5			
Tourmalines	0.0	0.7	0.1	2.2	0.2	0.03	0.03			0.02	0.1	0.1
Hematite/Magnetite								0.2				
Pollucite	0.1	0.1	5.8			0.03	0.01					
The rest	0.01	0.03	0.04	0.2	0.1	0.03	0.04	0.3	0.5	2.4	1.2	1.7
Total	98.8	98.5	98.2	97.9	98.5	98.8	98.4	99.9	100.1	98.3	95.6	99.5

Table 11. Calculated TIMA chemistry vs measured chemical analysis
(a) Mt Cattlin and Bald Hill samples

Element	Mt Cattlin										Bald Hill							
	MC100		MC200		MC0500		MC0600		MC1500		MC1700		BH1300		BH1480		BH2250	
(wt%)	Meas	Calc	Meas	Calc	Meas	Calc	Meas	Calc	Meas	Calc	Meas	Calc	Meas	Calc	Meas	Calc	Meas	Calc
%Li	3.2	3.3	3.5	3.5	1.1	0.8	0.1	1.2	3.0	2.8	2.2	2.0	3.1	3.4	1.7	1.5	0.1	0.1
%F	0.02	0.01	0.00	0.01	0.05	0.12	0.32	0.08	0.05	0.16	1.03	1.12	0.02	0.01	0.10	0.17	0.21	0.07
Na %	0.16	0.33	0.24	0.13	1.02	1.25	0.36	2.30	0.88	1.10	0.78	0.66	0.05	0.16	3.06	2.93	0.05	4.09
Mg %	0.16	0.03	0.00	0.02	0.17	0.02	2.15	0.03	0.01	0.01	0.07	0.01	0.13	0.05	1.17	0.04	2.00	0.45
Al %	14.3	13.6	14.3	13.9	8.0	6.6	15.2	8.4	14.1	12.7	11.4	10.4	14.3	13.8	10.5	9.8	14.1	10.5
Si %	29.7	28.6	30.0	29.2	36.1	36.5	23.8	33.3	29.6	28.3	31.0	31.0	29.5	29.4	28.2	27.6	24.4	29.6
P %	0.01	0.01	0.03	0.02	0.02	0.01	0.01	0.01	0.05	0.01	0.09	0.03	0.01	0.00	0.04	1.92	0.03	0.03
K %	0.63	0.10	0.13	0.04	0.00	0.83	7.70	0.37	0.20	0.32	2.08	1.90	0.71	0.28	0.04	0.68	7.61	4.28
Ca %	0.05	0.06	0.11	0.09	1.34	0.16	0.06	0.26	0.24	0.34	0.29	0.22	0.02	0.13	1.49	1.74	0.09	0.54
Ti %					0.34		0.01	0.00	0.01				0.01		0.61		0.01	0.00
Mn %	0.10	0.09	0.06	0.06	0.01	0.05	0.08	0.08	0.13	0.14	0.19	0.15	0.05	0.09	3.19	1.83	0.05	0.01
Fe %	0.19	0.28	0.08	0.20	0.07	0.13	1.07	0.21	0.73	0.37	0.12	0.11	0.41	0.21	1.15	0.72	1.83	0.37
R ²	0.999		0.999		0.998		0.820		0.997		0.999		0.999		0.999		0.840	
Rb (ppm)	216	30	42	10	447	420	4830	300	361	640	7460	5470	217	200	408	400	2160	2700
Cs (ppm)	57	10	179	10	197	20	353	90	497	70	1300	430	164	0	240	0	340	100
Ta (ppm)	1	0	1	0	15	0	10	20	20	0	513	100	4	0	62	0	7	0
Be (ppm)	6	70	2	50	297	1030	649	2160	24	470	10	420	159	200	7	2700	1030	3600

Table 11. Calculated TIMA chemistry vs measured chemical analysis
(b) Greenbushes and Pilgangoora samples

Element	Greenbushes										Pilgangoora					
	C1-100P		C3-300HP		C3-300HWH		PD005_46.4m		PD008_66.45m		Pil1		Pil2		Pil3	
(wt%)	Meas	Calc	Meas	Calc	Meas	Calc	Meas	Calc	Meas	Calc	Meas	Calc	Meas	Calc	Meas	Calc
%Li	2.9	2.6	2.3	2.1	2.1	1.9	1.5	0.9	1.7	1.2	1.5	1.5	1.5	1.6	1	1.1
%F	0.03	0.05	0.01	0.02	0.00	0.01	0.04	0.06	0.03	0.08	0.11	0.48	0.05	0.09	0.03	0.07
Na %	0.38	0.32	0.37	0.36	0.24	0.23	1.77	2.37	1.10	1.41	0.8	0.9	1.1	1	1.1	0.9
Mg %	0.01	0.08	0.01	0.06	0.00	0.05	0.03	0.03	0.24	0.06	0.2	0.1	0.03	0	0.04	0.01
Al %	10.7	10.4	9.1	8.5	8.4	7.6	9.5	8.0	9.2	7.6	9.5	9.1	9.2	8.8	7.9	8.1
Si %	33.7	33.5	36.0	35.9	36.9	36.8	33.8	34.5	34.1	35.2	29.7	32	34.3	33.3	30	34.8
P %	0.02	0.00	0.03	0.01	0.00	0.00	0.02	0.01	0.03	0.03	0.015	0.0189	0.045	0.0359	0.035	0.0176
K %	0.31	0.32	0.16	0.20	0.02	0.08	1.51	2.12	0.84	1.04	1.8	1.8	1.4	1.2	2.7	3.2
Ca %	0.03	0.08	0.04	0.08	0.01	0.06	0.69	0.16	0.51	0.24	1.4	1.2	0.12	0.2	0.09	0.1
Ti %	0.00	0.00	0.00	0.00	0.00	0.00	0.00	0.00	0.00	0.00						
Mn %	0.03	0.07	0.03	0.06	0.01	0.05	0.06	0.05	0.14	0.29	0.202	0.318	0.0994	0.1388	0.0656	0.051
Fe %	0.09	0.10	0.06	0.07	0.03	0.06	0.15	0.18	0.23	0.22	0.12		0.11		0.08	0.02
R ²	0.999		0.999		0.999		0.996		0.997		0.94		0.96		0.99	
Rb (ppm)	607	601	334	338	51	126	910	2282	774	1369	2700	2789	2360	2300	2740	2412
Cs (ppm)	309	250	211	136	66	52	48	152	43	90	233	300	109	36	218	18
Ta (ppm)	16	1	18	9	4	2	13	1	76	36	108	132	279	116	197	83
Be (ppm)	2	241	5	296	1	170	12	183	413	130	585	368	61	114	62	50

Department of lithium and major elements

The department of the main elements that impact the lithium extraction and recovery process efficiency (Li, Fe, Mg, Mn, Na, K, Cs, Ca, P, Rb, Ta, F) were calculated by evaluating the laser-ablation data and relating the measured concentrations in discrete minerals to the derived TIMA modal abundance of the minerals in the sample. It is important to track and limit the amount of Fe and alkaline metals reporting to the concentrate during beneficiation, as they can cause clinker formation and slagging issues in the downstream calcination process (Harman, 2019).

Figure 85 shows the department of lithium in the Pilgangoora, Bald Hill, Mt Cattlin and Greenbushes samples. The department of other major elements in the samples are shown in Appendix 8.

Lithium is predominantly associated with spodumene in most samples analysed. In Pilgangoora, minor amounts are also associated with lithian muscovite and lepidolite. At Bald Hill, in regions of the deposit containing more altered mineralogy, some Li is associated with the phosphate mineral sicklerite, $\text{Li}(\text{MnFe})\text{PO}_4$, and in a sample rich in beryl. Minor amounts of Li also exist in lepidolite grains and chlorite minerals. At Mt Cattlin, Li is also contained in lepidolite in some regions of the orebody.

In Pilgangoora samples, the Fe content is mainly associated with muscovite (2.4 wt%) and in spodumene (0.58 wt%). Sodium is predominantly in the mineral albite. Potassium and Rb are associated with microcline and micas, whereas Ca is associated with calcite (PIL3) and some feldspars. The high content of Rb (1 wt%) in some of the feldspars would make the K-feldspar a potential source of Rb. Manganese is associated mainly with spessartine and with moderate amounts in Li minerals (0.15 wt%). Phosphorus is associated with minor mineral apatite. Caesium and F are mainly associated with Li micas, although there are traces in feldspar minerals and beryl. Magnesium is present mainly in one sample (PD008) associated with biotite and chlorite minerals.

At Bald Hill, most of the Fe content is associated with the micaceous chlorite (~1.68 wt%) phases and the mineral sicklerite in sample BH1480. Only trace amounts of Fe appear in the spodumene (~0.04 wt%). Manganese and P is rich in sicklerite grains, as observed in sample BH1480. Potassium, along with Rb, is associated with microcline, Fe–Mg rich micas and muscovite. Caesium appears mainly limited to beryl. Sodium is largely associated with albite present in all samples. Calcium is associated with albite and apatite grains. Fluorine is present mainly in apatite grains and muscovite.

In Mt Cattlin samples, a strong association of Fe (016 wt%), Mn (0.1 wt%) and Mg (trace) occurs with spodumene in these samples due to the high content of micas containing Mg, Fe. Manganese, K, Cs, Rb and F are associated with lepidolite found mainly in sample MC1700. Sodium is associated with albite. Calcium is associated mainly with feldspars and apatite although small quantities of Ca are also associated with calcite. Phosphorus is associated with apatite in all samples. Tantalum in the form of tantalite exists in trace amounts in most samples but is more abundant in the lepidolite-enriched sample.

In Greenbushes, only trace amounts of Fe (0.17 wt%), Mg (0.02 wt%), Ca (trace) and Mn (0.07 wt%) are associated with spodumene. Muscovite and tourmaline are minor minerals

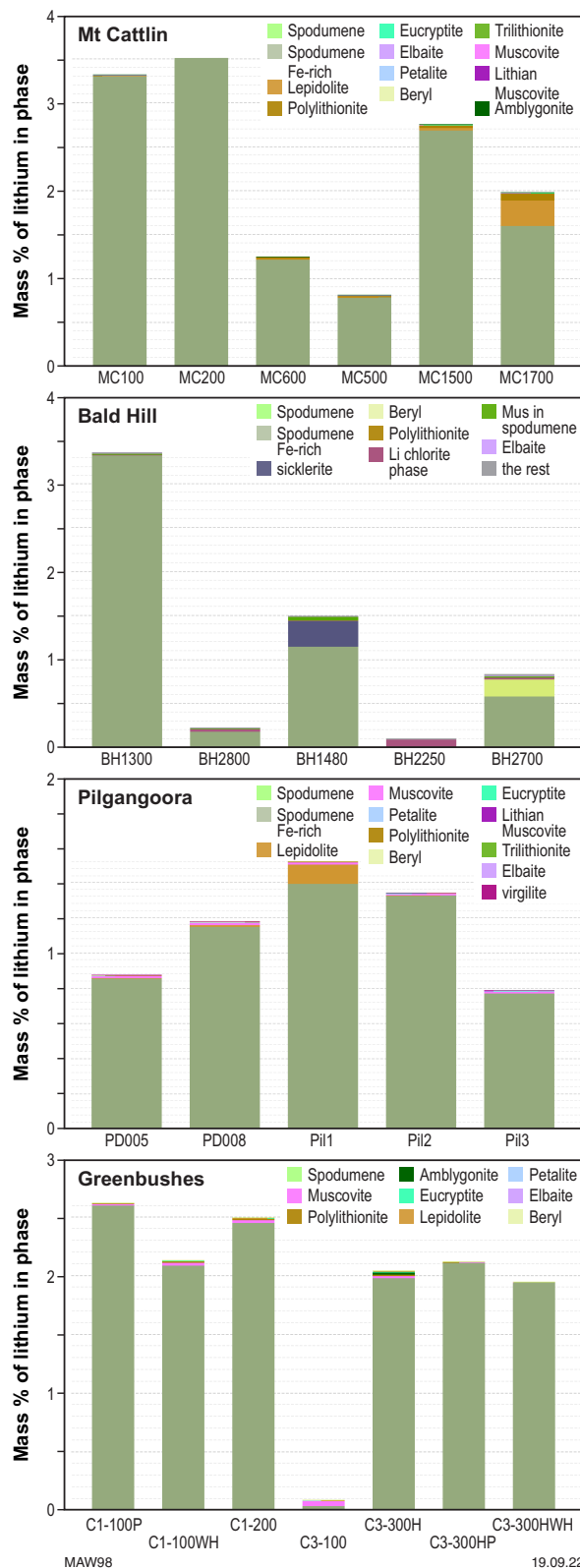


Figure 85. The lithium department in Pilgangoora, Bald Hill, Mt Cattlin and Greenbushes samples

containing Fe, Mg and Mn. Sample C1200 contains Cs associated with the mineral pollucite, which is discussed in more detail in later section. Sodium and K are associated with feldspar minerals which are more abundant in sample C3100. Rubidium is associated with micas (4 wt%) and microcline (0.16 wt%) especially in sample C3100. Fluorine is predominantly associated with mica. Tantalum in the form

of tantalite and stibiomicrolite (Sb-bearing oxide mineral) is associated mainly with samples taken from the Central lode region of the mine.

Iron is also present in Ta–Nb oxides and garnet (mainly as spessartine) as well as the micas, Fe–chlorite (as locally developed at Pilgangoora). Manganese is present in Ta–Nb oxides, garnet (as spessartine) and apatite (nearly all F–apatite is Mn-bearing, 2–6%; as well as the Mn-phosphate, beusite at Mt Cattlin).

Overall, all spodumene samples contain Fe and Mn, which will report along with spodumene in concentrates as discussed later. The high Fe and Mg, K contents of the micas, largely associated with Bald Hill and Mt Cattlin samples, will need to be limited. Apatite appears present in many of the samples. Although apatite appears as a trace mineral, it will need to be limited in concentrates to prevent accumulation of phosphate in downstream processing. Where present, calcite is a minor phase in samples and is unlikely to cause problems in refining of concentrates to extract lithium.

Liberation characteristics of spodumene

Figures 86 to 95 show representative mineral composition maps of all samples in the polished mounts for the +500 µm fractions, together with liberation distribution data for spodumene.

Pilgangoora samples

All samples are abundant in spodumene with many particles low in other mineral inclusions, even within the coarse size fractions (Figs 86–89). All samples exhibit grains with fine intergrowths of quartz, feldspar and spodumene. The intergrowths range in size from 5 to 50 µm. In PIL1 some of the spodumene particles have undergone alteration with spodumene being replaced by micaceous minerals, such as muscovite, lepidolite and trillithionite, as well as occurring with calcite. These alterations occur along margins and fractures, and form aggregates or veinlets of mixed assemblages. The measured particle-composition distribution or liberation characteristics reveal around between 10 and 20% of the spodumene particles contain gangue minerals of quartz, feldspar and some muscovite. While spodumene appears readily liberated from coarse quartz and feldspar mineralization, between 10 and 20% of the spodumene particles contain quartz–spodumene, graphitic textured regions. To separate quartz from spodumene in these graphitic textures would require grinding and separation at a finer grain size (<250 µm). The micaceous rich sample (PIL1) would also require finer grinding down to <75 µm to liberate the micas and calcite from spodumene. Overall, it would be expected that some feldspar and quartz will be carried and reported to the concentrate for treatment downstream. In some samples muscovite (not Li-bearing) also reports with spodumene in the concentrate. While not tested in this work, similar liberation characteristics may be expected in high-grade ores from Mt Marion and Kathleen Valley, which also exhibit fine intergrowths of quartz, feldspar and spodumene features in regions (e.g. refer to Appendix 4).

Bald Hill samples

Mineral composition maps of samples that represent zones from unaltered spodumene through to parts of the post-crystallization, alteration regions are shown in Figures 90 and 91. In the Bald Hill samples, many of the spodumene grains are liberated from the main gangue minerals and range from 90% for mainly high grade, unaltered spodumene (BH1300) to 17% in low grade, altered spodumene samples (BH2700). However, in all samples a proportion of spodumene grains contain networks of fine micaceous inclusions associated with spodumene, from zones within the orebody that have undergone post-crystallization alteration. The samples contain between 10% and 30% micas locked within spodumene particles and are present in all size fractions evaluated. In the areas where post-crystallization alteration is prominent, ultrafine grinding will be essential to liberate unaltered spodumene if these ores are to be treated for lithium extraction. In sample BH2700, beryl is well liberated and can be separated from spodumene by gravity or dense media separation (DMS) techniques. Overall, while spodumene is readily liberated from quartz, feldspar and muscovite minerals, fine disseminated micas associated within spodumene will report to the concentrate. As indicated in the deportment section, most of the fine mica contains high Fe, Mg and K contents. The extent will depend upon on ore selection at the mine.

Mt Cattlin samples

Mineral composition maps, together with the accompanying spodumene liberation analysis, are shown in Figures 92 to 95. Similar to Bald Hill, Mt Cattlin exhibits zones of high-grade, unaltered spodumene (MC200, MC100, MC1500) through to low-grade, highly altered spodumene in post-crystallized, altered regions of the deposit (MC500, MC600). As discussed earlier, these micaceous zones have formed by post-crystallization alteration and replacement of spodumene by finely crystalline mica. While spodumene particles can be well liberated from coarse quartz and feldspar grains in the low-grade altered zones, even at the coarse sizes, many spodumene particles contain veins of Mg- and Fe-enriched mica. The samples from high-alteration zones (MC500 and MC600 samples) contain between 10% and 30% micas locked within spodumene particles. The extent of mica locked within spodumene in samples from altered zones is similar in all the size fraction ranges examined. Fine grinding (<38 µm) would be expected to liberate more of the spodumene. However, full liberation would be limited due to the intergranular nature of the micaceous zones within the unaltered parts of spodumene. Even the high-grade, white spodumene contains small proportions of mica (up to 2% in samples MC100 and MC200). Muscovite is readily liberated from spodumene (MC500). Lepidolite observed in some regions of the orebody can be readily liberated in coarse fractions (MC1700). Hence, while not the predominant form of lithium in the orebody, it may be concentrated for treatment in a separate process to spodumene. Overall, coarse unaltered and altered spodumene grains can be liberated from quartz and feldspar associations. However, micas associated with spodumene as fine interstitial veins in voids and fractures, coarse inclusions within spodumene grains and as complex alteration zones within spodumene grains, will restrict the full recovery of spodumene.

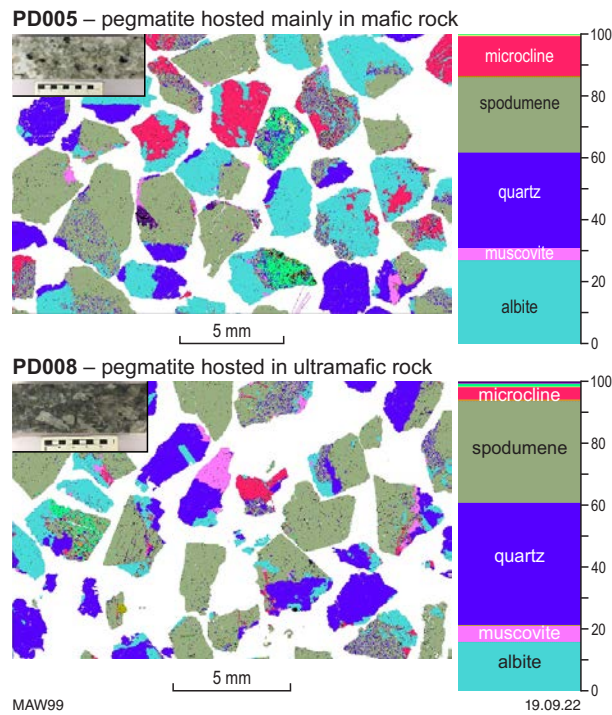
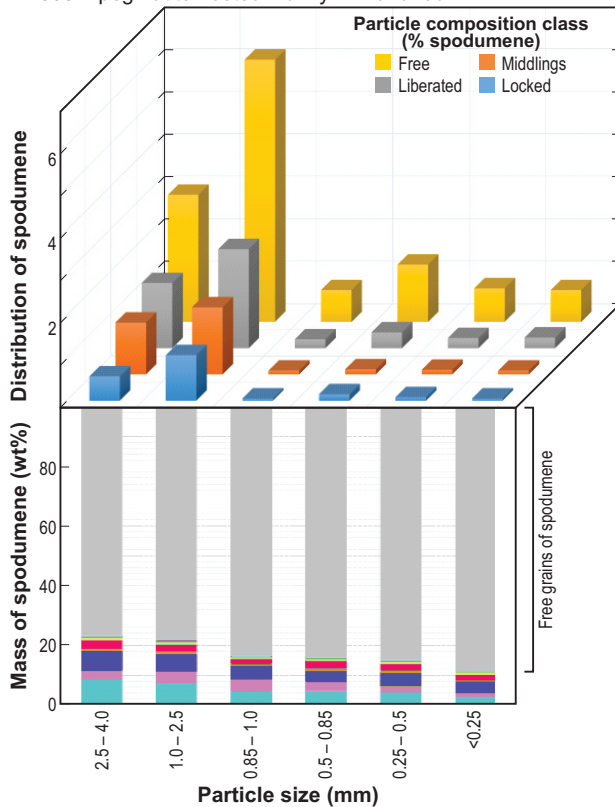


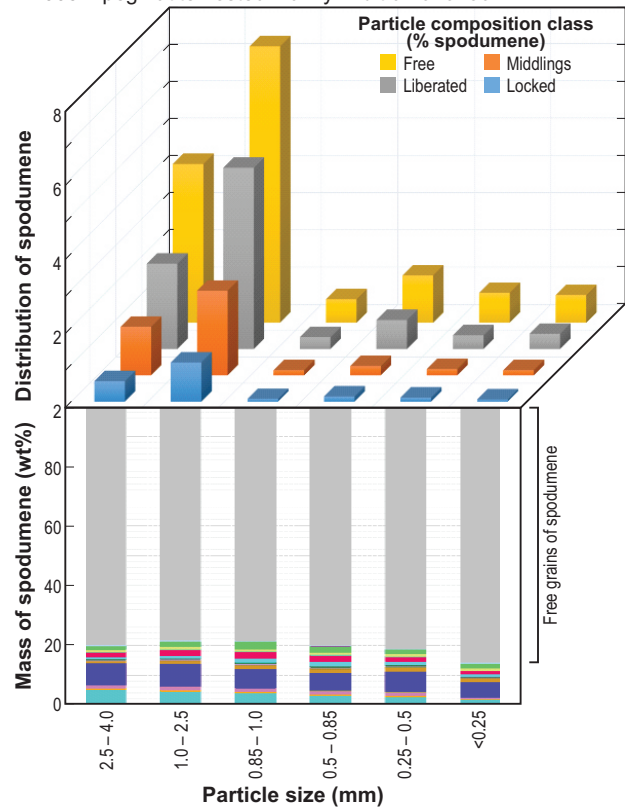
Figure 86. TIMA mineral composition map and mineral abundance in Pilgangoora Altura samples. Spodumene is present as free particles and contains graphic intergrowths of quartz and feldspar

PD005 – pegmatite hosted mainly in mafic rock



MAW100

PD008 – pegmatite hosted mainly in ultramafic rock



19.01.23

Figure 87. Locking characteristics of spodumene, together with liberation distribution of spodumene for Pilgangoora Altura samples. Around 80% of spodumene grains are liberated. Liberation classes were classified based on the surface area of spodumene as: free ($\geq 90\%$), liberated ($< 90\%$, $\geq 70\%$), middling ($< 70\%$, $\geq 30\%$) or locked ($< 30\%$)

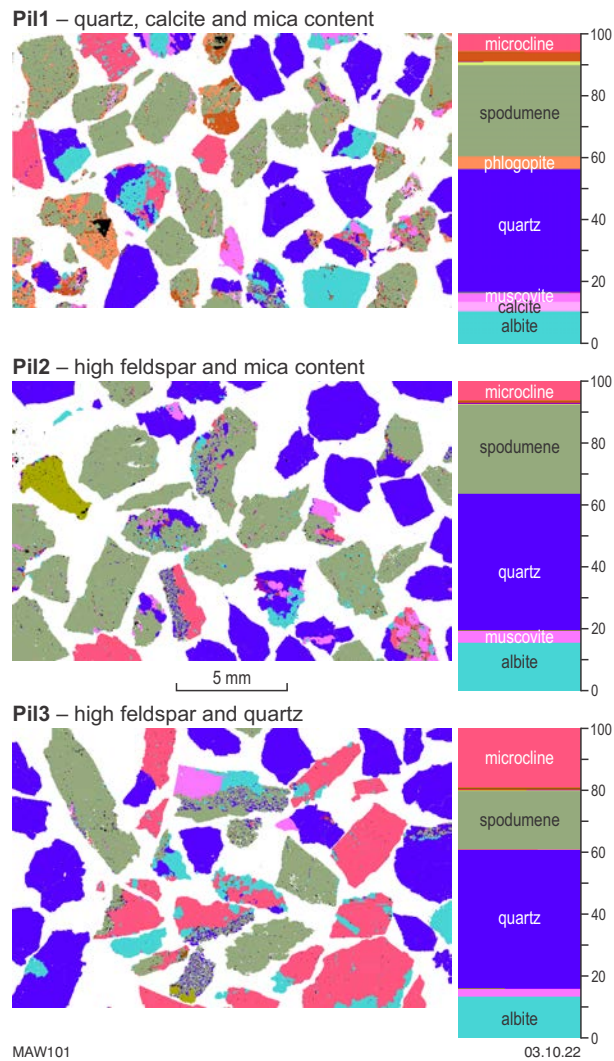
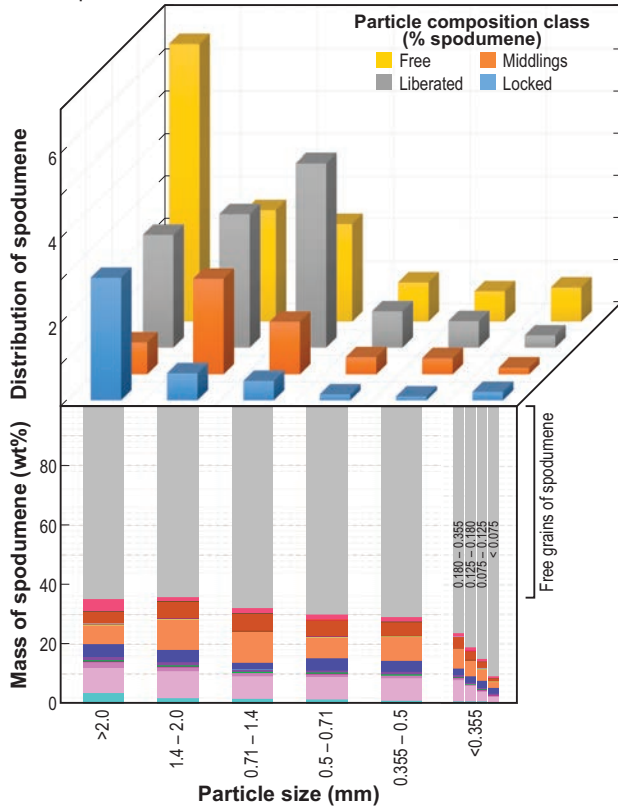
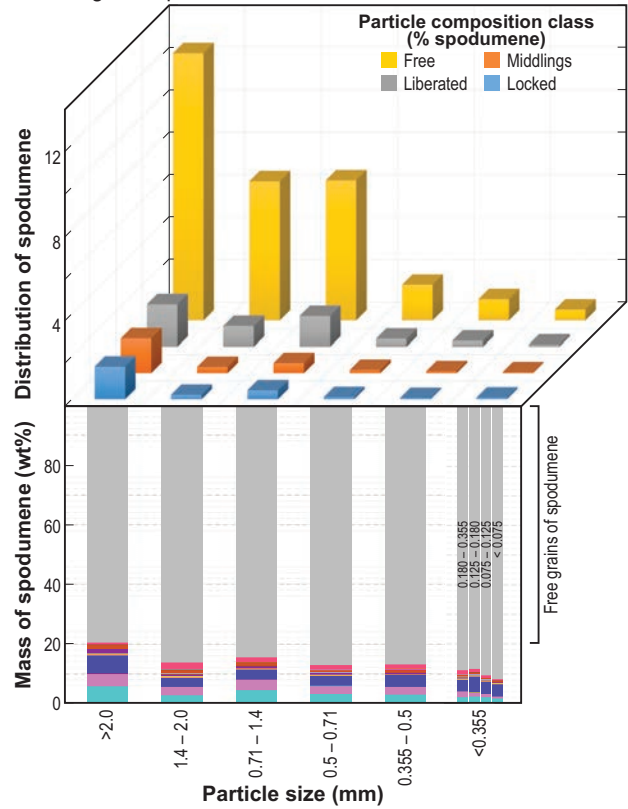


Figure 88. TIMA mineral composition map and mineral abundance for Pilgangoora Pilbara Minerals samples. Many spodumene grains are liberated, but some spodumene is associated with graphic intergrowths of quartz, feldspar, mica and calcite

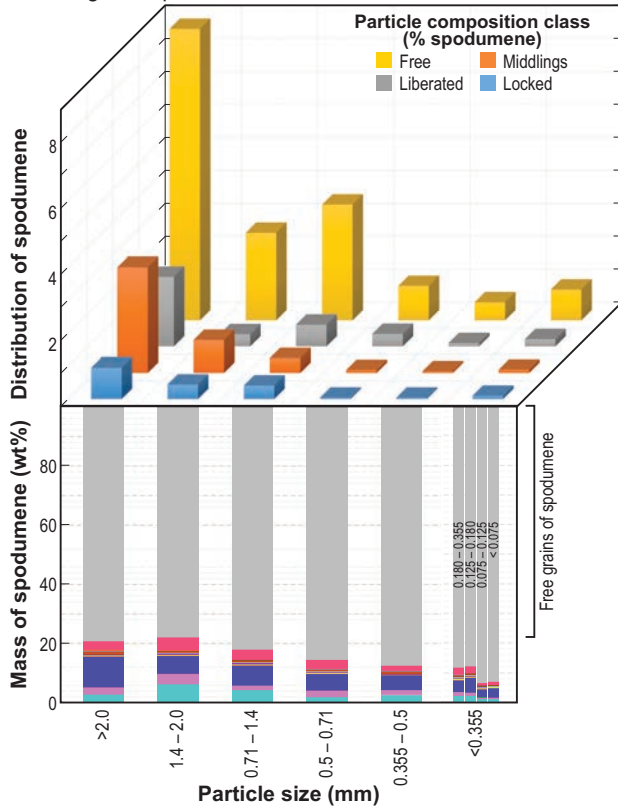
Pil1 – quartz and mica content



Pil2 – high feldspar and mica content



Pil3 – high feldspar and mica content



MAW102

20.01.23

Figure 89. Locking characteristics of spodumene, together with liberation distribution of spodumene for Pilgangoora Pilbara Minerals samples. Liberation classes were classified based on the surface area of spodumene as: free ($\geq 90\%$), liberated ($< 90\%$, $\geq 70\%$), middling ($< 70\%$, $\geq 30\%$) or locked ($< 3\%$)

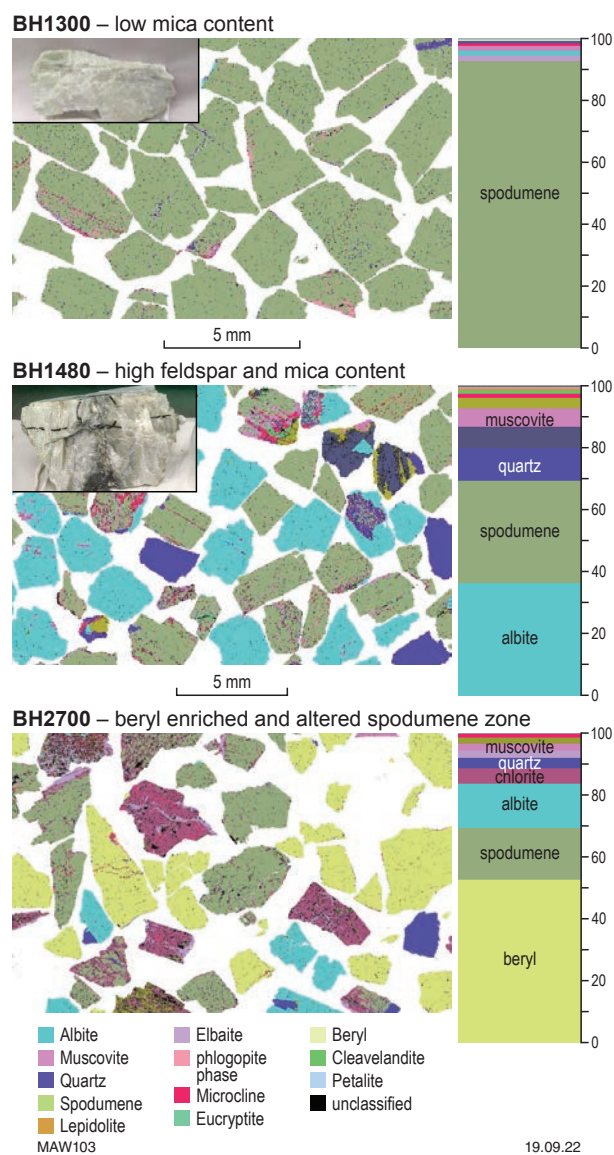
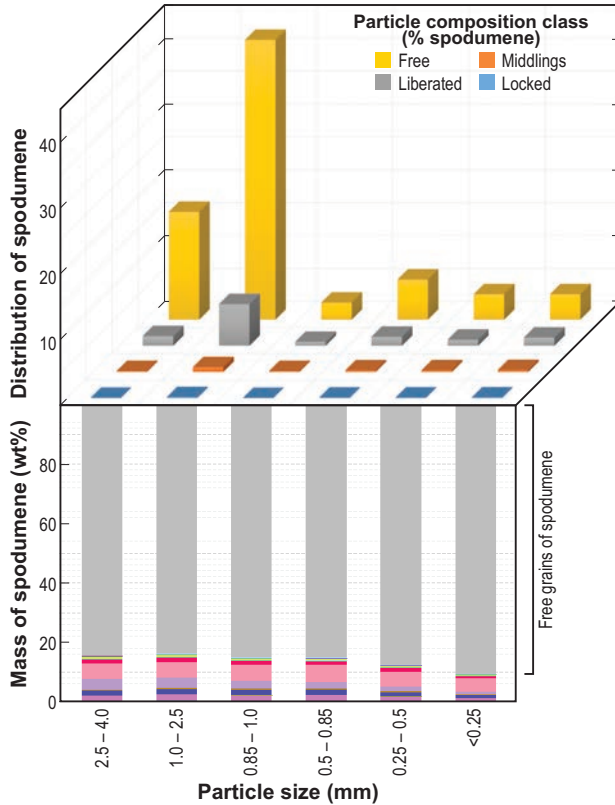
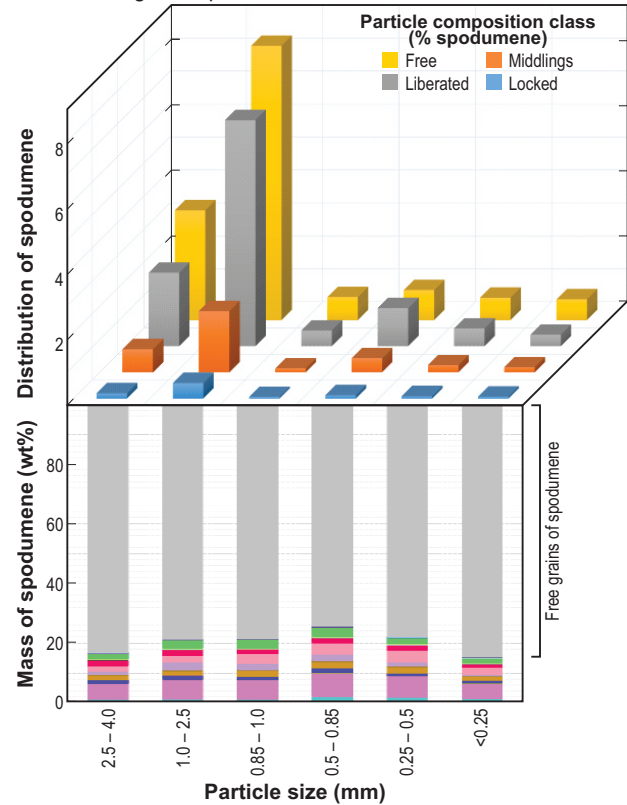


Figure 90. TIMA mineral composition map and mineral abundance for Bald Hill samples. Spodumene is mostly free but has some association with K, Fe, Mg-rich micas

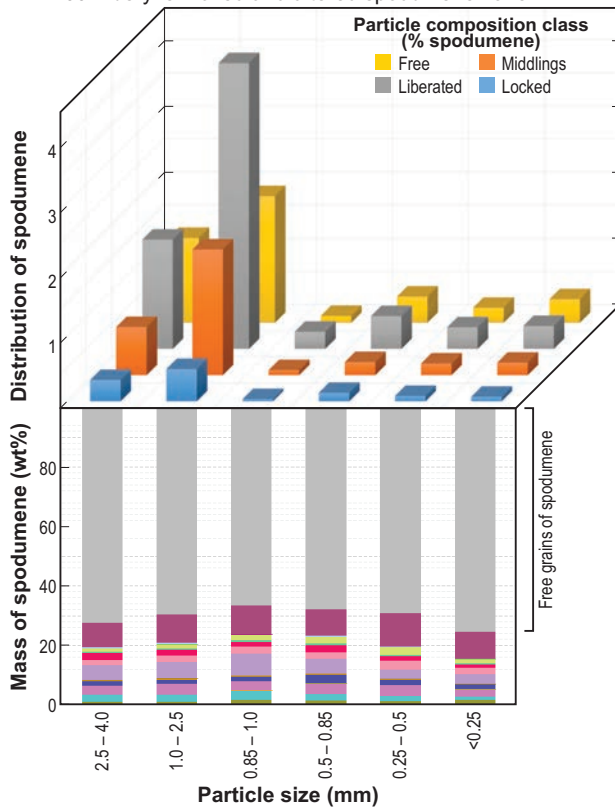
BH1300 – low mica content



BH1480 – high feldspar and mica content



BH2700 – beryl enriched and altered spodumene zone



MAW104

19.01.23

Figure 91. Locking characteristics of spodumene, together with liberation distribution of spodumene for Bald Hill samples. Liberation classes were classified based on the surface area of spodumene as: free ($\geq 90\%$), liberated ($< 90\%$, $\geq 70\%$), middling ($< 70\%$, $\geq 30\%$) or locked ($< 30\%$)

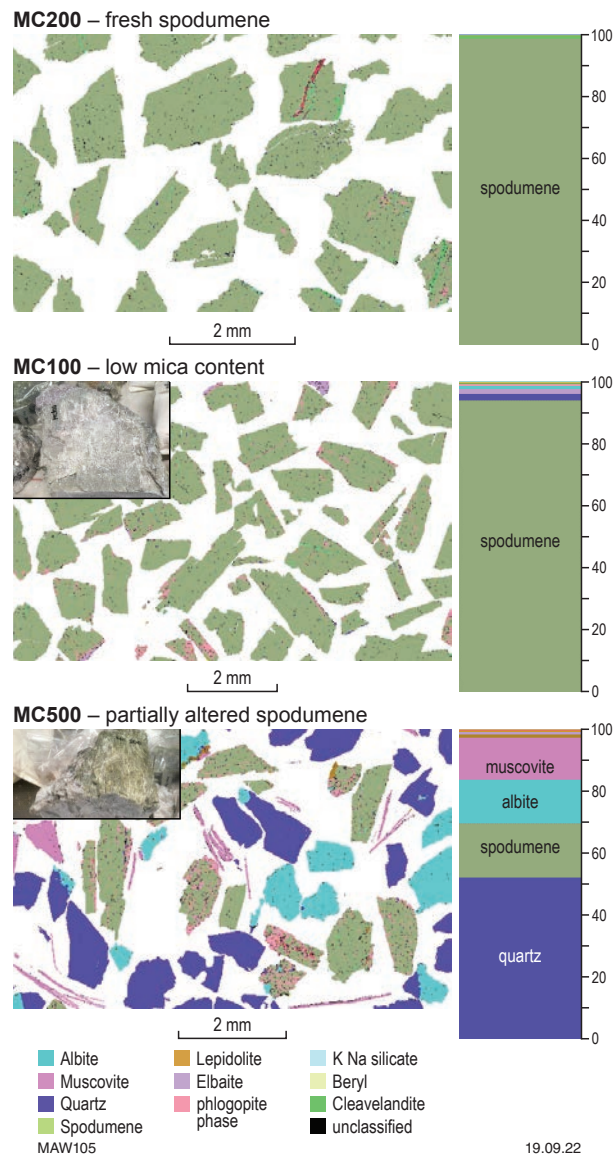
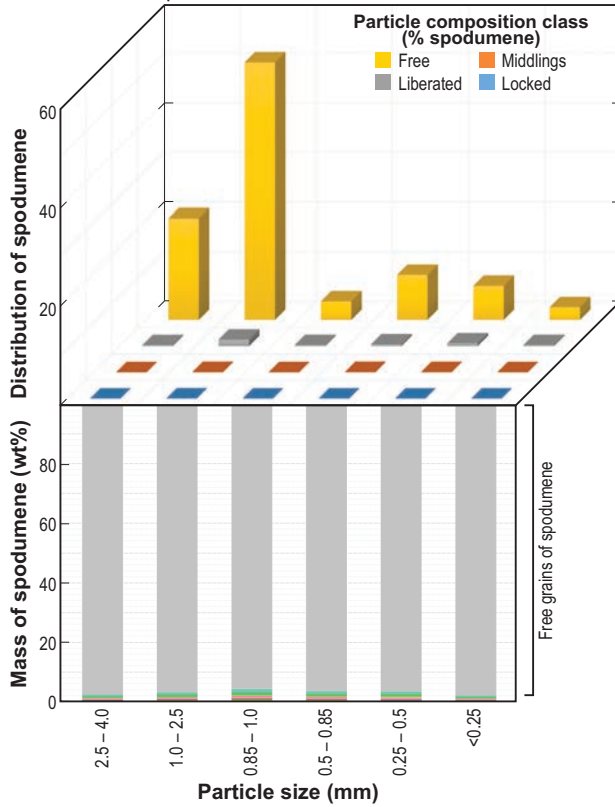
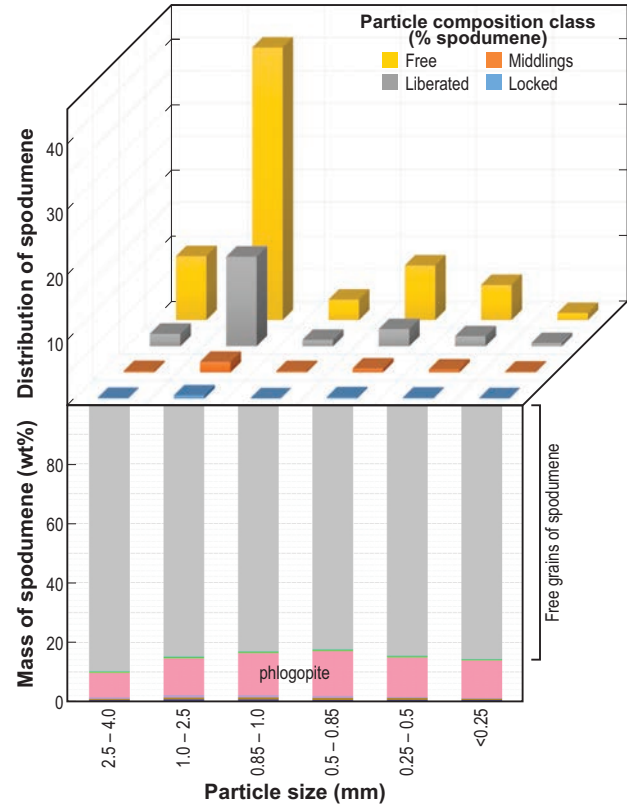


Figure 92. TIMA mineral composition map, and mineral abundance for Mt Cattlin samples. Spodumene is mostly free with some association with Fe, Mg rich micas. Muscovite mainly liberated from spodumene in the final sample

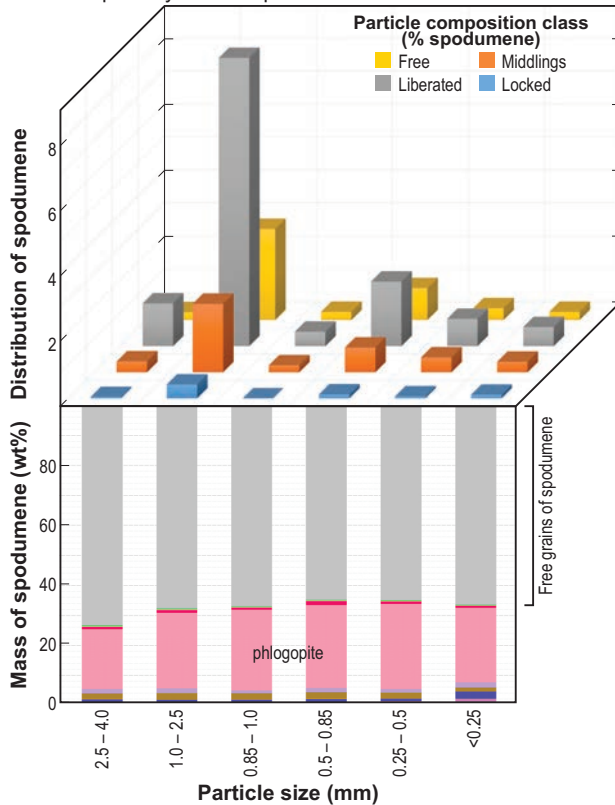
MC200 – fresh spodumene



MC100 – low mica content



MC500 – partially altered spodumene



MAW106

19.01.23

Figure 93. Locking characteristics of spodumene, together with liberation distribution of spodumene for Mt Cattlin samples. Liberation classes were classified based on the surface area of spodumene as: free ($\geq 90\%$), liberated ($< 90\%$, $\geq 70\%$), middling ($< 70\%$, $\geq 30\%$) or locked ($< 30\%$)

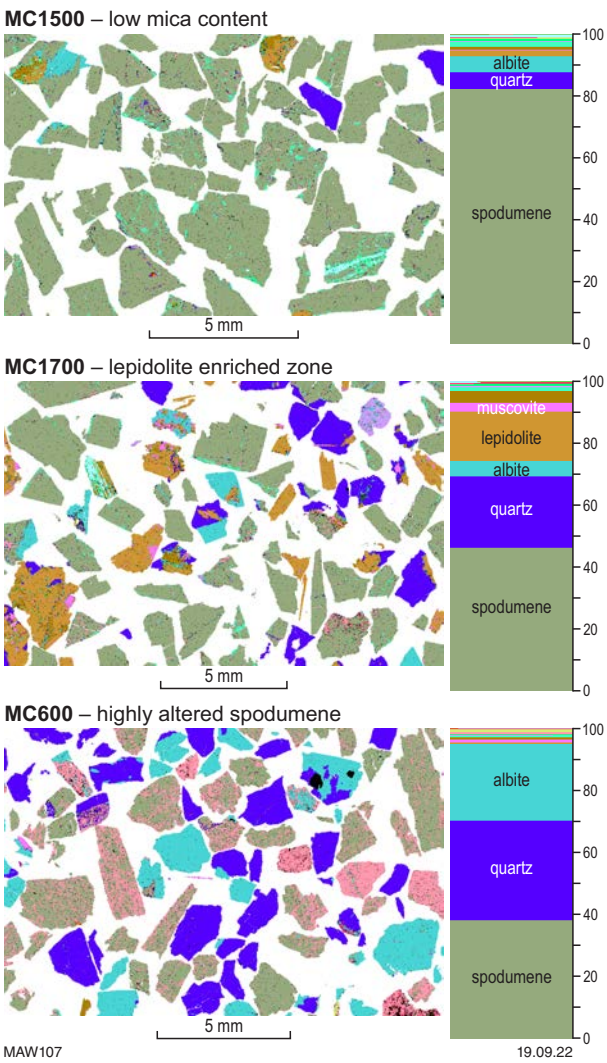
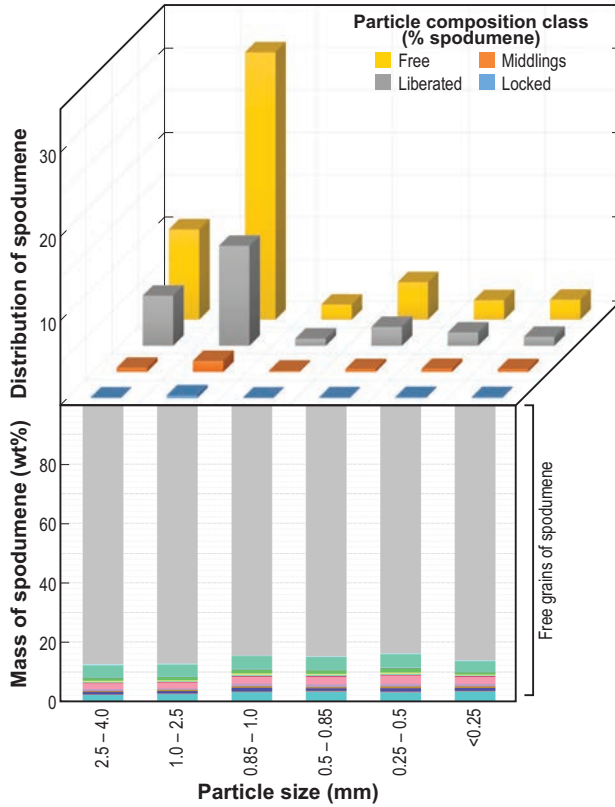
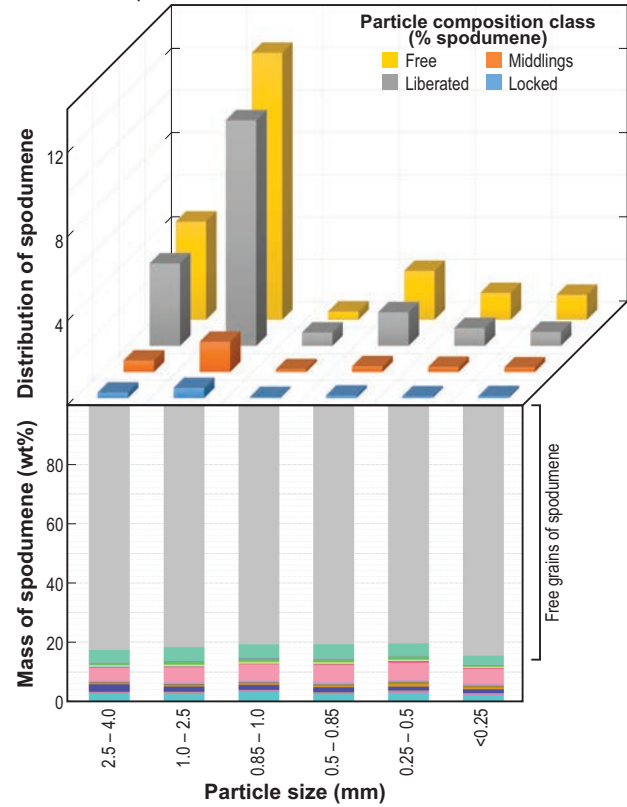


Figure 94. TIMA mineral composition map and mineral abundance for Mt Cattlin samples

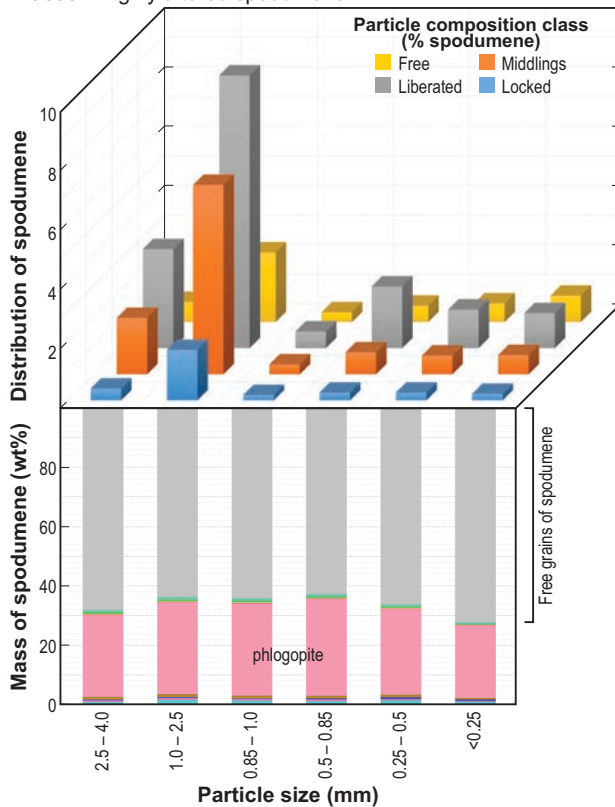
MC1500 – low mica content



MC1700 – lepidolite enriched zone



MC600 – highly altered spodumene



MAW108

19.01.23

Figure 95. Locking characteristics of spodumene, together with liberation distribution of spodumene for Mt Cattlin samples. Liberation classes were classified based on the surface area of spodumene as: free ($\geq 90\%$), liberated ($< 90\%$, $\geq 70\%$), middling ($< 70\%$, $\geq 30\%$) or locked ($< 30\%$)

Greenbushes samples

Mineral composition maps, together with the accompanying spodumene-liberation analysis, are shown in Figures 96 to 99. The ore is dominated by coarse spodumene-quartz textural intergrowths, and regions with fine spodumene-quartz intergrowths as observed in the C3 pit samples described earlier. In all samples examined, the spodumene is mainly liberated, with only minor contents of quartz and trace amounts of feldspar. Sample C1200 has around 5% of the spodumene locked and associated with pollucite (liberation of pollucite is discussed later). Around 10% of the spodumene is locked within quartz and feldspars in the 2.5 to 4 mm size fractions, whereas at particle size <250 μm , less than 2% of the spodumene has quartz or feldspar (mainly albite). Hence, the majority of spodumene can be recovered, with very low gangue mineral reporting to the concentrate.

The physical liberation characteristic behaviour of different lithologies for concentrating spodumene

To allow comparison between the different deposits, the information collated from size-by-size data was converted into theoretical grade-recovery curves. The theoretical grade-recovery curves expected for each of the four deposits with different lithologies passing a 4 mm size screen are shown in Figure 100.

The theoretical grade-recovery curve for an ore is defined as the maximum expected recovery that can be achieved by physical separation of a mineral at a given grade (McIvor and Finch, 1991). This is determined by the surface area liberation of the mineral of interest and is directly related to the grind size. Theoretical grade-recovery curves generated from 2D-liberation measurements tend to overestimate the true liberation characteristics and test work is always required to validate the results. The modal mineralogical distribution of spodumene within each size fraction is represented on the curve as the grade value at 100% recovery. The proportion of fully liberated spodumene particles, based on the exposed surface area, is represented on the curve as the recovery value achieved at 100% spodumene grade. The further the whole curve shifts to the right in the graphs, the better the expected grade and recovery of spodumene.

In all Pilgangoora samples examined, >90% recovery of spodumene can be achieved with expected Li grades above 3 wt% (equivalent to 6.5 wt% Li_2O). These are the types of grades reported by Pilbara minerals and Altura Resources (now part of Pilbara minerals). Full recovery is limited in samples PD005, PD008 and PIL3 due to spodumene grains containing fine graphic intergrowths of quartz and feldspar. Sample PIL1 is further limited by the presence of finely disseminated micas within the spodumene particles. Sample PIL2 has less fine graphic intergrowths of quartz and feldspar than PIL3 and micas present are made up of mainly coarse, liberated muscovite particles.

Samples from both Mt Cattlin and Bald Hill show variations in spodumene recoveries (60 to >95%) with

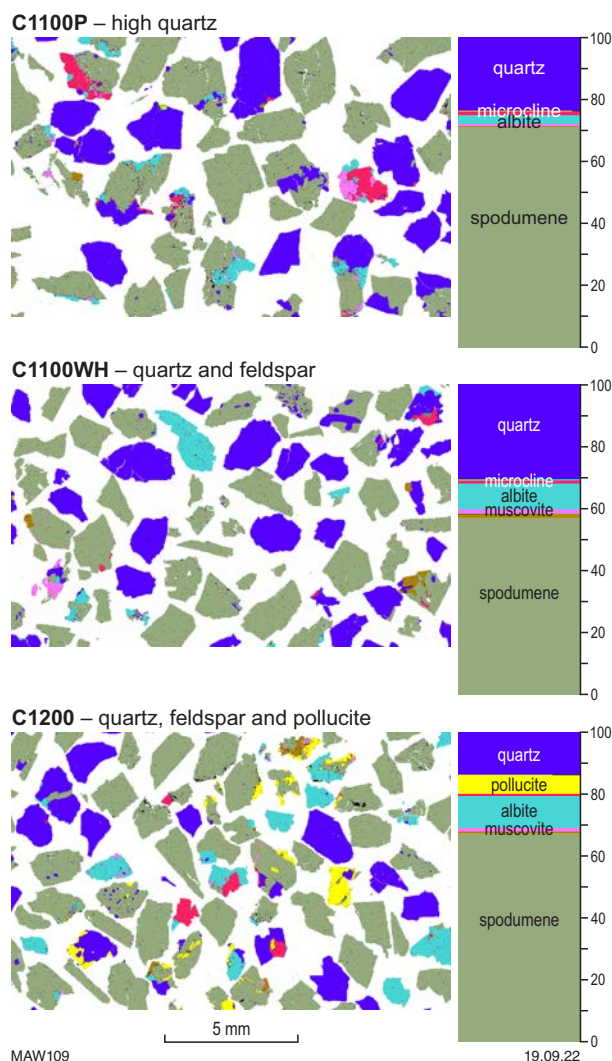
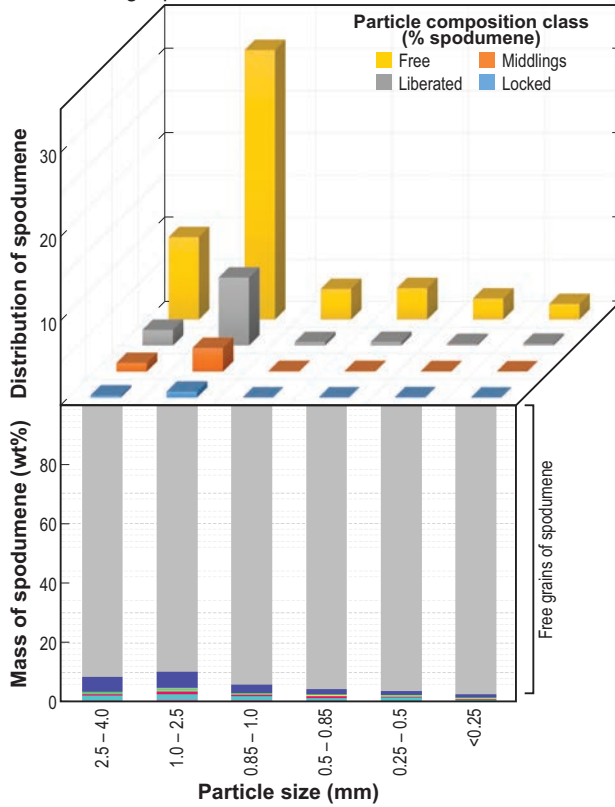


Figure 96. TIMA mineral composition map, mineral abundance and locking characteristics of spodumene, together with liberation distribution of spodumene for Greenbushes samples from the Central lode pit

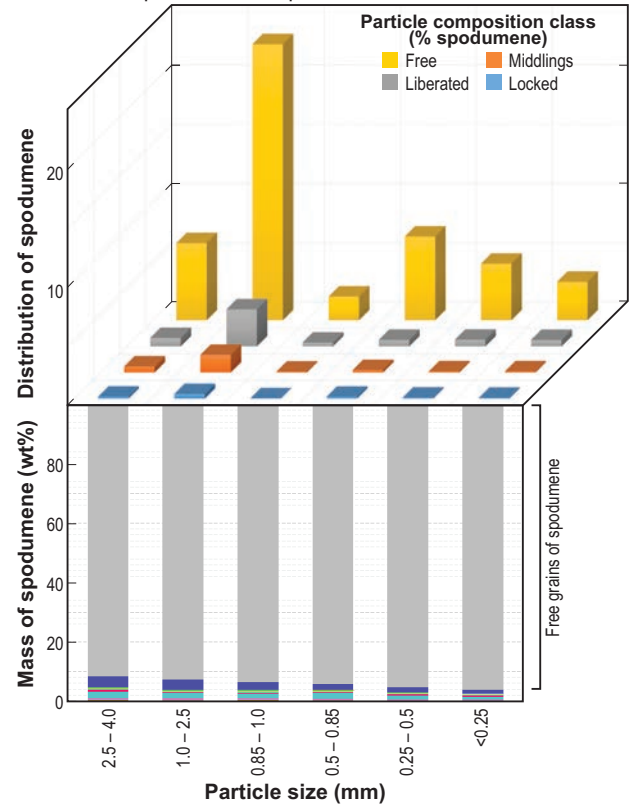
grades ranging from 3 wt% to 3.5 wt% Li (6.5 – 7.5 wt% Li_2O). These values are higher than has been reported by Galaxy Resources (Mt Cattlin) and at Bald Hill. This is probably due to gangue material reporting to the concentrate at both sites and possibly reflecting non-optimal DMS circuit operations. The theoretical curves illustrate liberation and recovery of spodumene increases going from highly altered spodumene 60% in BH2700, MC1700) to fresh spodumene (>95% in BH100, MC100 and MC200) particles. The fine, disseminated micas within many spodumene particles observed in both these deposits, reduces the expected recovery of spodumene. Separation of middlings containing high mica and feldspar contents through fine grinding would improve the recovery of spodumene in this orebody.

Greenbushes samples are well liberated with high recovery and Li grades of 3.5 wt% (7.5 wt% Li_2O) over all samples. This is largely associated with spodumene being readily liberated from the main gangue mineral, quartz.

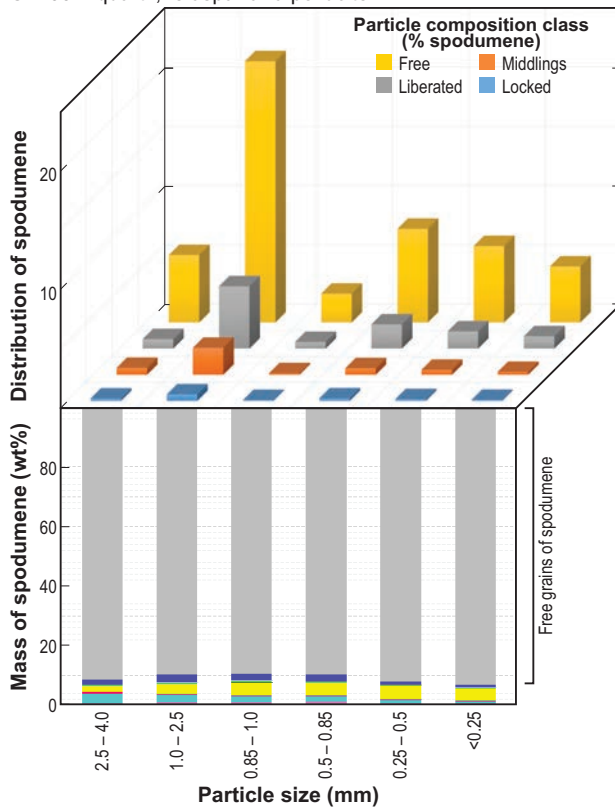
C1100P – high quartz



C1100WH – quartz and feldspar



C1200 – quartz, feldspar and pollucite



MAW110

19.01.23

Figure 97. TIMA mineral composition map, mineral abundance and locking characteristics of spodumene, together with liberation distribution of spodumene for Greenbushes samples. Liberation classes were classified based on the surface area of spodumene as: free ($\geq 90\%$), liberated ($< 90\%$, $\geq 70\%$), middling ($< 70\%$, $\geq 30\%$) or locked ($< 30\%$)

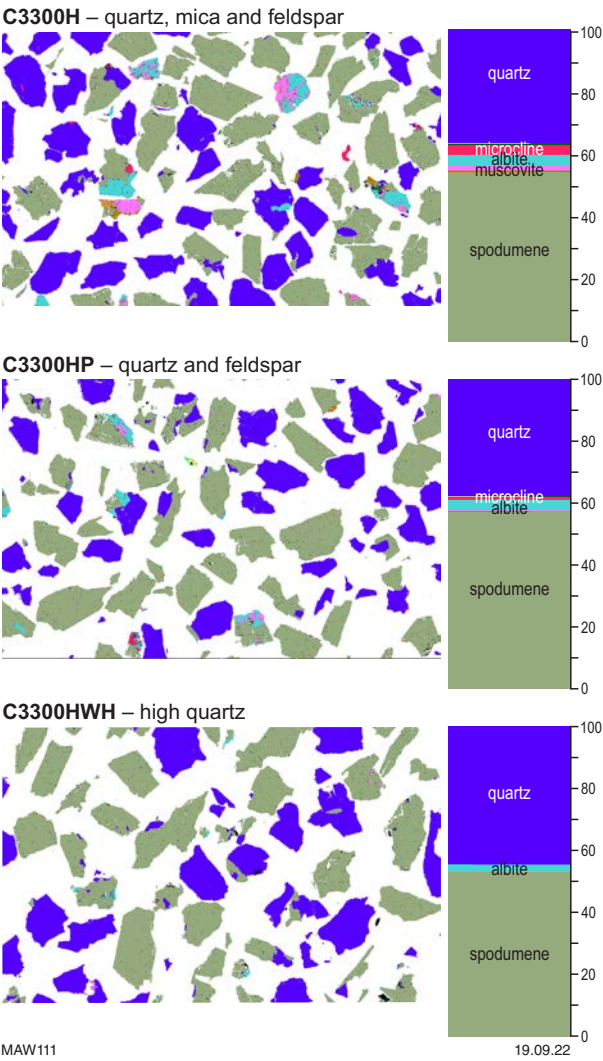
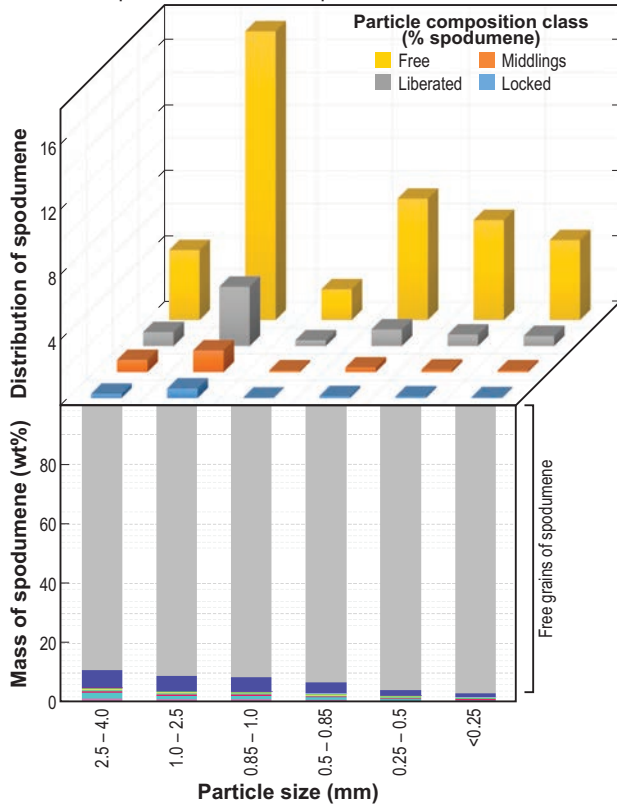
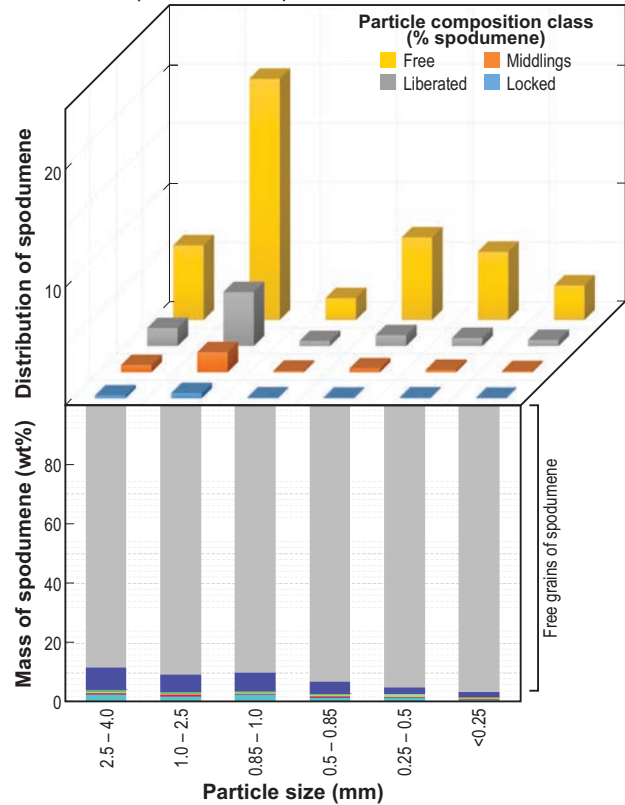


Figure 98. TIMA mineral composition map, mineral abundance and locking characteristics of spodumene, together with liberation distribution of spodumene for Greenbushes samples

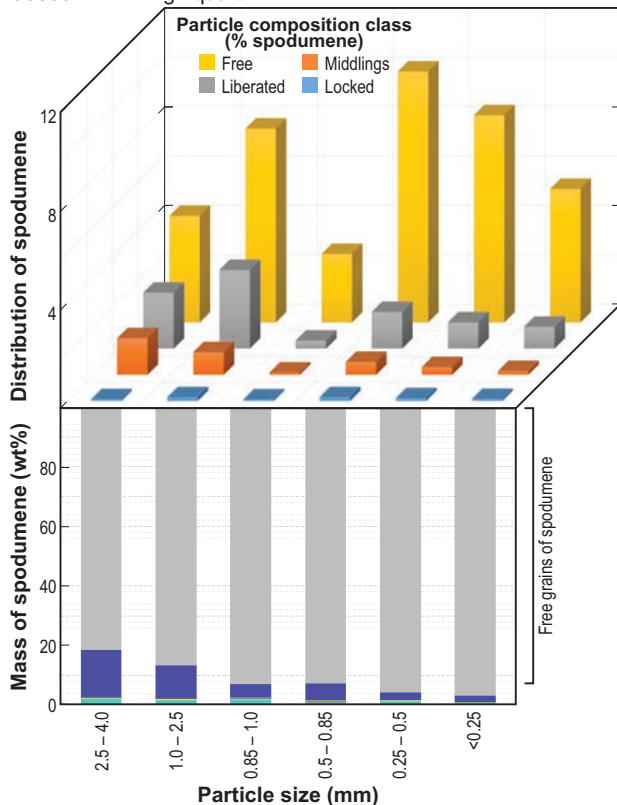
C3300H – quartz, mica and feldspar



C3300HP – quartz and feldspar



C3300HWH – high quartz



MAW112

19.01.23

Figure 99. TIMA mineral composition map, mineral abundance and locking characteristics of spodumene, together with liberation distribution of spodumene for Greenbushes samples. Liberation classes were classified based on the surface area of spodumene as: free ($\geq 90\%$), liberated ($< 90\%$, $\geq 70\%$), middling ($< 70\%$, $\geq 30\%$) or locked ($< 30\%$)

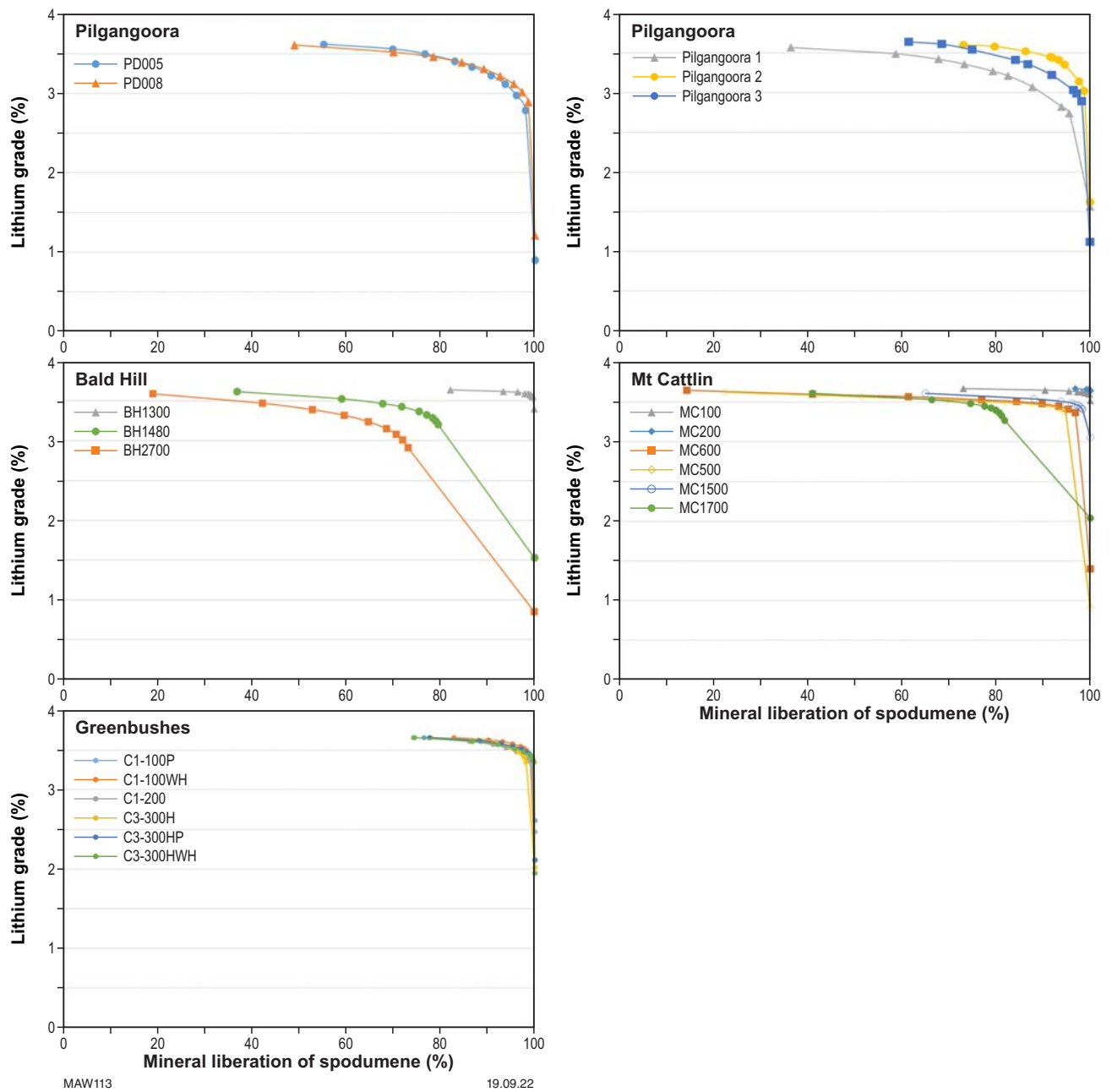


Figure 100. Theoretical grade-recovery curves for recovering spodumene for all Pilgangoora, Bald Hill, Mt Cattlin and Greenbushes samples with different lithologies

Liberation characteristics of heavy minerals and pollucite

While the focus is largely on lithium, the pegmatite ores contain recoverable Ta, Sn and, in some cases, Cs minerals, which have been mined and sold as an extra mineral product.

In Pilgangoora samples, while the bulk concentration observed in chemical assays is not high, most of the Ta, Nb and Sn minerals identified in samples were well liberated in some samples (Fig. 101) and can be separated and concentrated by heavy mineral separation techniques. The mineral particles range in size from ~5 µm to 500 µm. Cassiterite makes up between 0.01 and 0.03 wt% of samples, with 33% free grains and the rest associated with spodumene grains. Tantalite makes up only 0.05 wt% of the PIL1 sample, whereas it is only 0.02 wt% and 0.03 wt% in the PIL2 and PIL3 samples, respectively.

In the Mt Cattlin (Fig. 102) and Bald Hill (Fig. 103) samples both tantalite and cassiterite grains vary from very fine (<5 µm) to coarse sizes (~300 µm). Tantalum minerals are associated with low-grade samples from the highly altered zones of the deposit (MC600 and MC1700) and mostly locked in gangue minerals. Cassiterite is mostly locked up and associated with spodumene in Mt Cattlin samples.

At Greenbushes tantalite, stibiomicrocline, cassiterite, pollucite and tourmaline exist in a range of particle sizes from <5 µm to ~0.5 mm, as illustrated in Figure 104. Around two-thirds of the tantalite and stibiomicrocline grains are liberated in sample C1100WH, which contains the highest abundance of these minerals. In the C3100 sample, cassiterite is liberated from a matrix high in feldspar and quartz content. The rest is associated with, and locked in, spodumene and albite. Approximately two-thirds of the pollucite observed in the C1200 sample is liberated. A significant proportion of the remaining third is associated with spodumene and the rest is associated with feldspar and quartz. Tourmaline (present as schorl and elbaite) is well liberated and occurs in abundance in two of the samples (C1-100WH and C3-100). Greenbushes also contains the arsenic mineral parabrandidite, which was observed in three of the samples (C1-100P and C3-300HP, C1200P). The deportment and size of parabrandidite particles are shown in Figure 105. Parabrandidite concentration is small and exists mainly as inclusions with albite and spodumene. Some of the parabrandidite would report to the concentrate as a contaminant, and accordingly would have to be managed during the refinery stage.

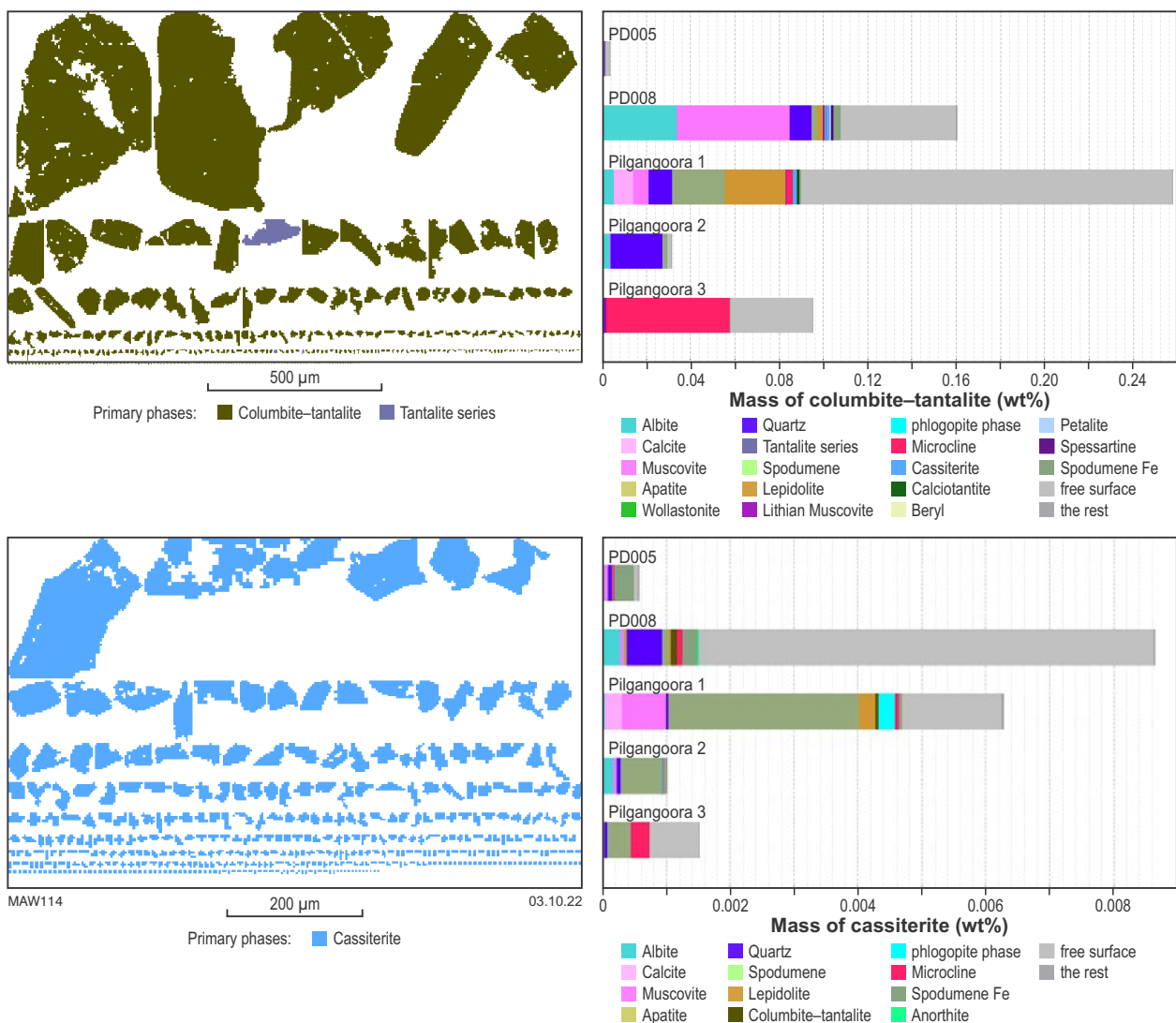


Figure 101. Line-up of grains of tantalite (olive green) and cassiterite (blue) for Pilgangoora samples

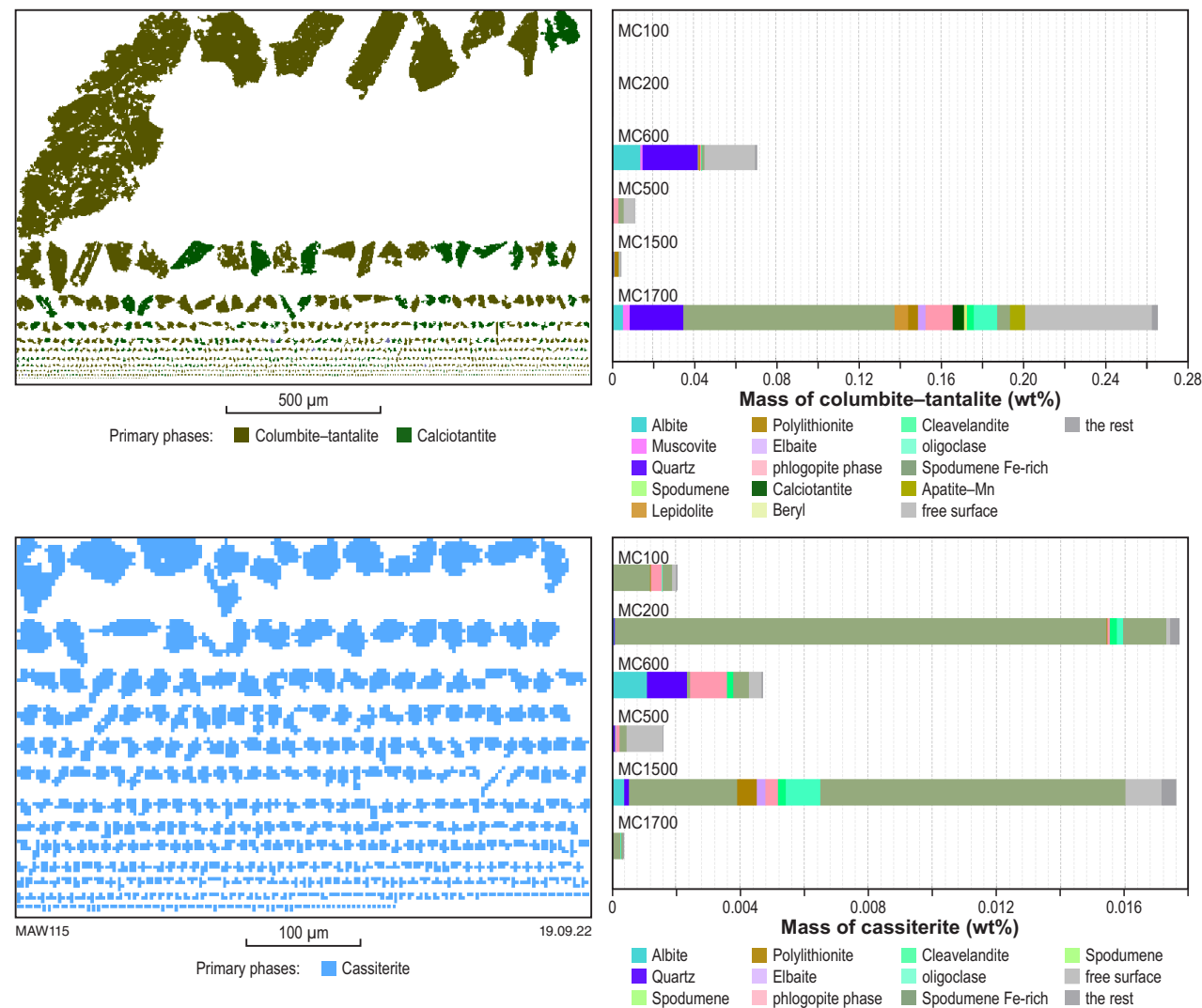


Figure 102. Line-up of grains of tantalite (olive green) and cassiterite (blue) observed in Mt Cattlin samples and the associated mineral-locking characteristics

Overall, Ta minerals in all deposits examined are mainly associated with the gangue minerals or are freely liberated under the particle sizes examined in this study. From a mineral processing point of view, this makes it easier to segregate Ta minerals from spodumene and allow for treatment to upgrade separately via gravity separation techniques, as is performed by mining companies with high-grade Ta resources. Some minor associations occur within spodumene in some of the Mt Cattlin and Greenbushes samples. A high percentage of cassiterite in most samples are locked and associated with spodumene and, therefore, will report along with spodumene grains in the concentrate. Treatment to recover cassiterite would have to occur during the refinery stage. As observed in Table 10 (refer to section, Sample selection and methodology), most of the Ta minerals contain Nb, with the presence of Fe and Mn associated to the columbite-tantalite series. Antimony-bearing, Ta oxide (stibiomicrolite) was only observed in pegmatite samples from Greenbushes. Tourmaline present in samples were mainly liberated or associated with feldspars.

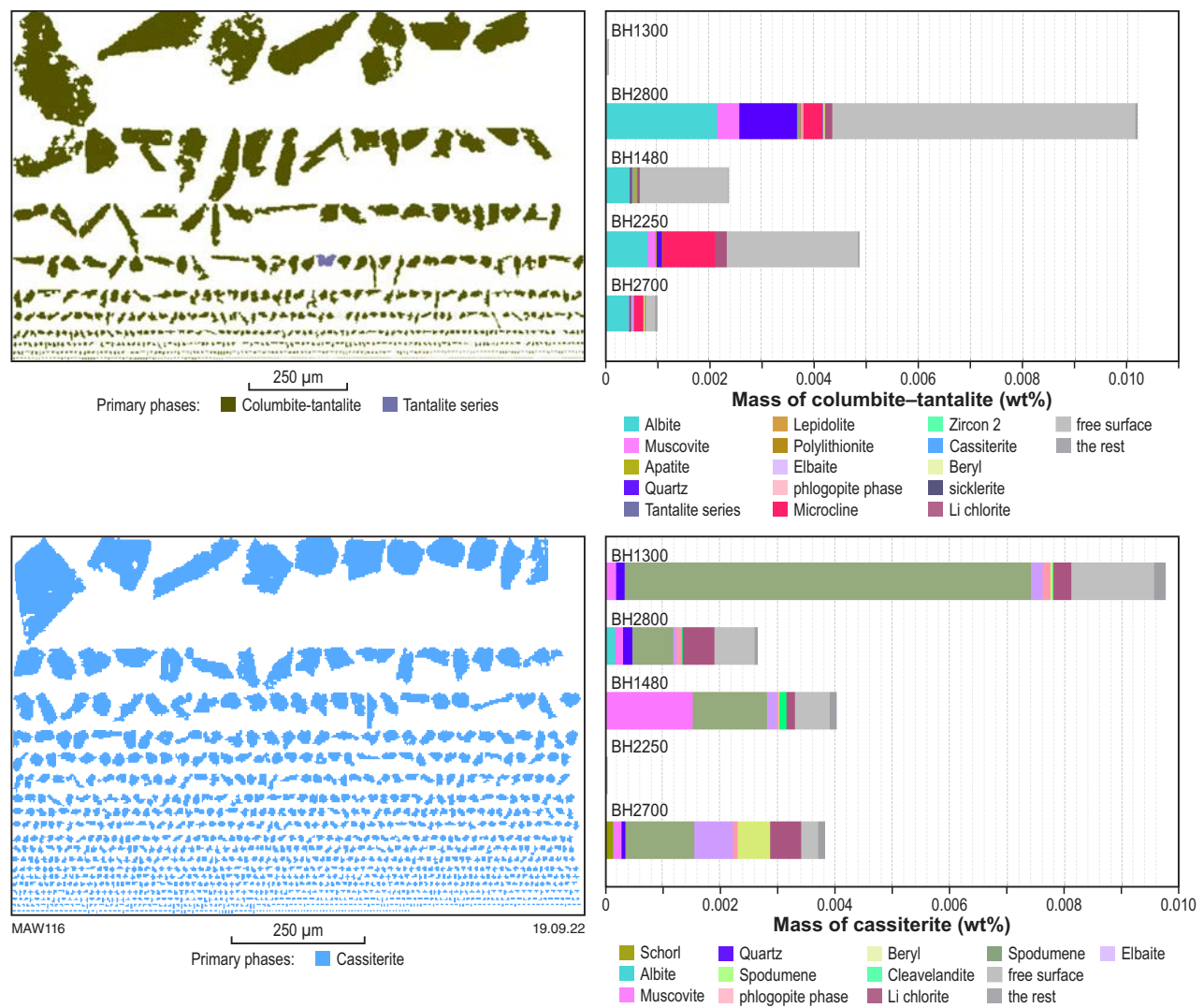


Figure 103. Line-up of grains of tantalite (olive green) and cassiterite (blue) observed in Bald Hill samples and the associated mineral-locking characteristics

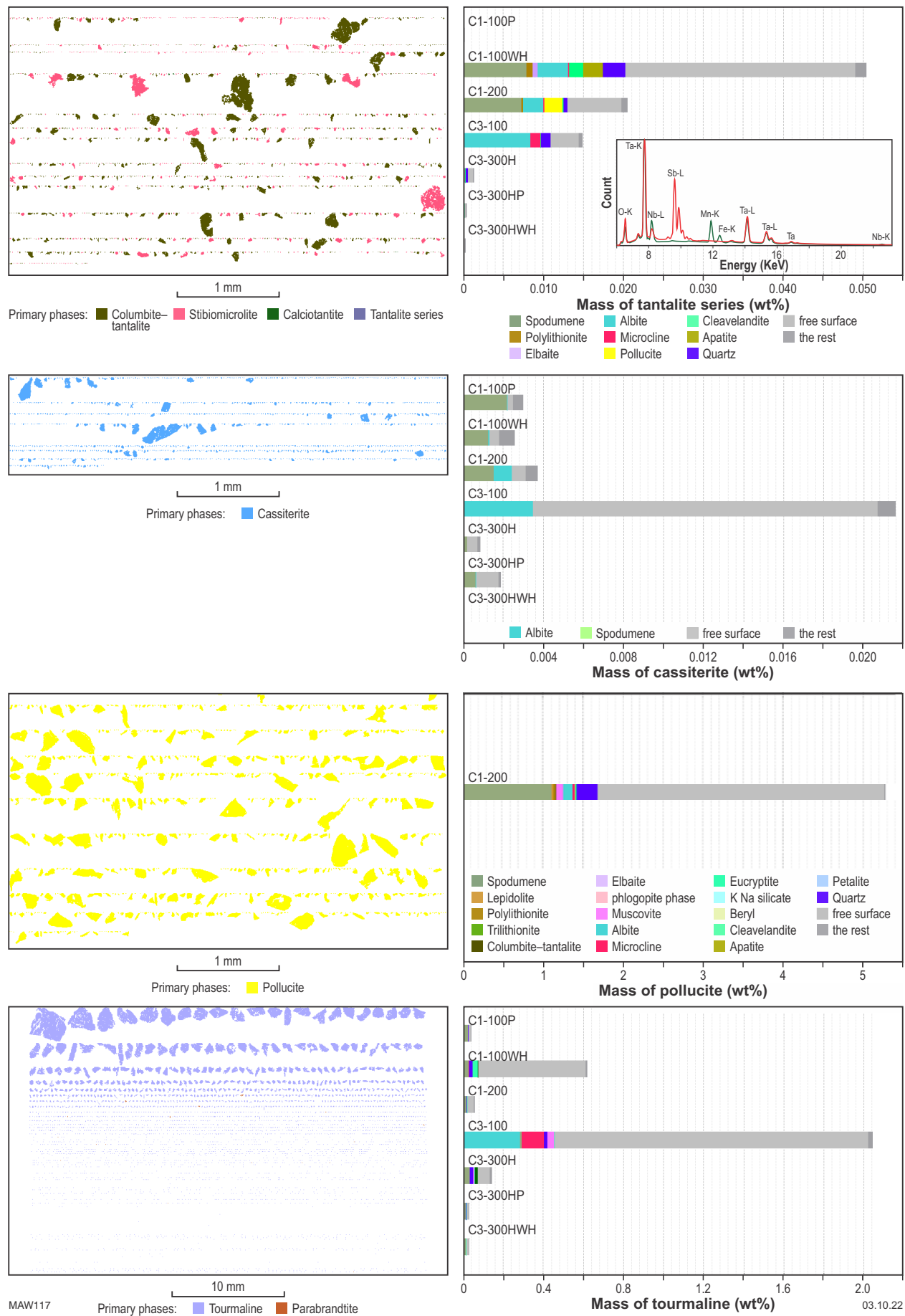


Figure 104. Line-up of grains of tantalum minerals (olive green), cassiterite (blue), pollucite (yellow) and tourmalines (purple) observed in Greenbushes samples and the associated mineral-locking characteristics

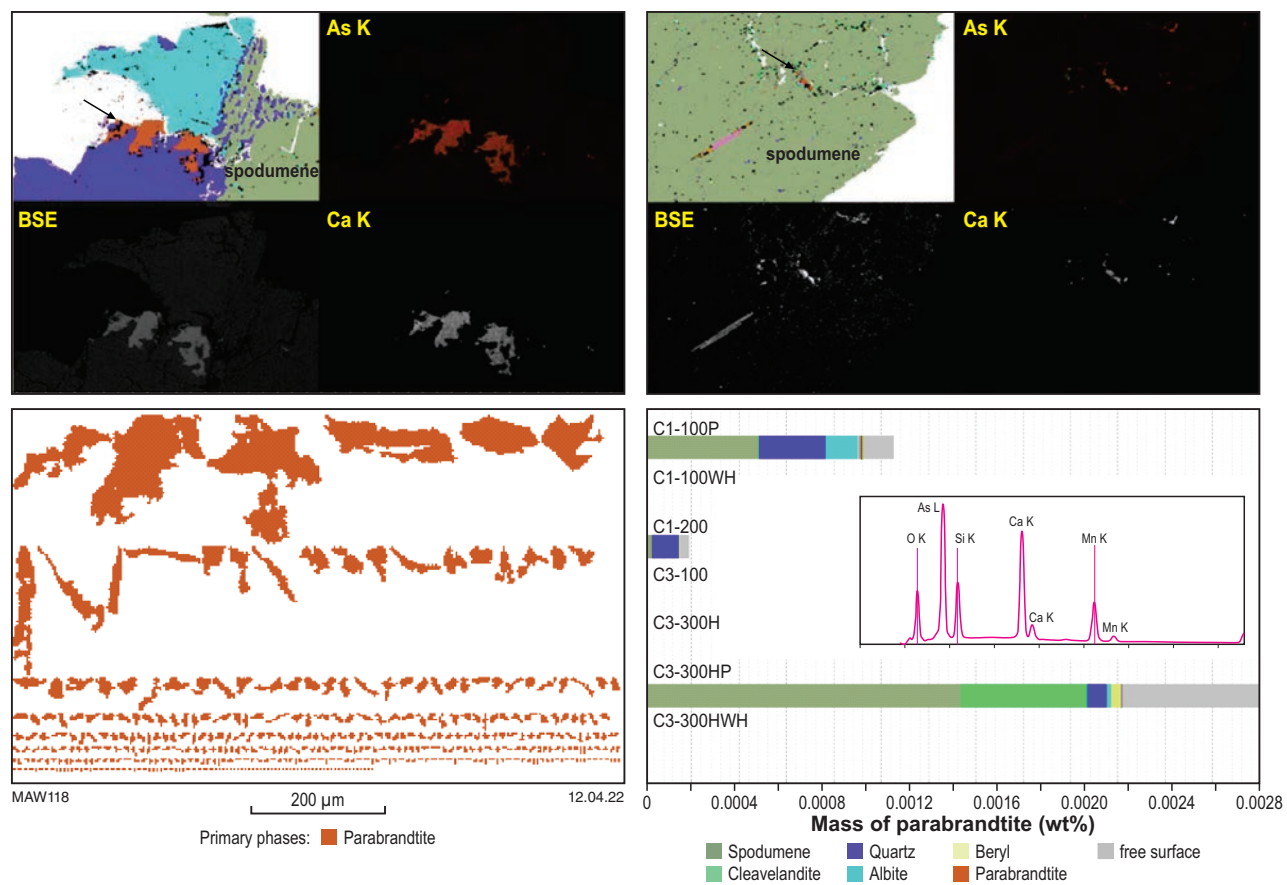


Figure 105. Cross-sections of parabrandidite ($\text{Ca}_2\text{Mn}(\text{AsO}_4) \cdot 2\text{H}_2\text{O}$) grains present as inclusions as illustrated in mineral composition maps, backscatter images and As and Ca distribution maps, together with line-up of grains of parabrandidite and associated mineral-locking characteristics (EDS analysis) for Greenbushes samples (C1100P, C330HP)

Liberation characteristics – concentrates

Spodumene concentrates collected from the beneficiation circuits at five mines were also examined to assess the efficiency of the existing process and compared with the collected samples.

Figure 106 shows images of the concentrates from two mine sites. Closer inspection reveals a higher content of gangue materials associated within these concentrates. This includes country rock (black basalt materials) and platy mica fragments. The majority of the gangue materials appear liberated from the spodumene grains, which indicates that further processing could be achieved to reduce the gangue content.

Figure 107 shows the range of different particle sizes of products from the different mine sites. These concentrates are shipped to refineries in China to recover Li. Both Bald Hill and Mt Cattlin use circuits consisting of spiral classification, reflux classifier and heavy medium separation, targeting coarse concentrate products >12 mm in size. Greenbushes concentrate is fine resulting from milling, collection of ~250 µm size through cyclone classification and flotation steps. The Pilgangoora mines use a combination of staged heavy media separation, grinding, flotation and low/high intensity magnetic separation to generate chemical grade spodumene. Around 35 to 45% of the particles from Pilgangoora concentrates are above 250 µm in size. Fines generated in these plants are either stockpiled or potentially treated as separate products. Gravity separation techniques are also used to collect and concentrate tantalite in several of these mines.

Table 12 shows the main elemental composition of the different concentrates and illustrates the variation between different deposits. Generally, mines are looking to produce high-grade concentrates in the order of +6% Li₂O, with an Fe₂O₃ content at <1.0% and a mica content <0.5%. The Li grades shown in Table 12 are similar or slightly less than those observed in the theoretical liberation analysis carried out in section, Liberation characteristics of spodumene. The difference is associated with the efficiency of the mineral separation techniques used to concentrate the spodumene from the gangue materials. Figure 108 shows the mineral abundance derived from TIMA modal analysis of polished mounts, together with mineral associations with spodumene (expressed as a percentage of the spodumene that is fully liberated). Greenbushes has the lowest elemental impurity levels compared with the other concentrates, with most spodumene grains fully liberated and only a small residual quartz and mica content exists in the concentrate sample. Iron and K are higher in Mt Cattlin reflecting the abundance of micas and the Fe content of spodumene.

Overall, the Li grades vary between 2.9 and 3.2 wt%, with a range of Fe contents (0.16, 0.87 and 1.87 wt% Fe₂O₃). Particle size P80 ranges from 4 mm to 18 mm. Up to 20% gangue material reports along with spodumene to the concentrate. Of these, between 5 and 10% gangue are locked or occur with spodumene in the concentrate. The physical association of spodumene with gangue material is similar to that observed in section, Liberation characteristics of spodumene. The presence of quartz, feldspar and micas in the spodumene concentrates will report to the lithium refinery (calcination and acid baking). Optical ore sorting, prior to the heavy mineral separation circuits, is currently being used by both Pilbara minerals and Galaxy Resources Ltd to improve Li grades and reduce gangue content in the concentrators.



MAW119

19.09.22

Figure 106. Examples of concentrates showing spodumene with variation in colour and the presence of gangue minerals, which have been collected along with spodumene in the beneficiation circuits

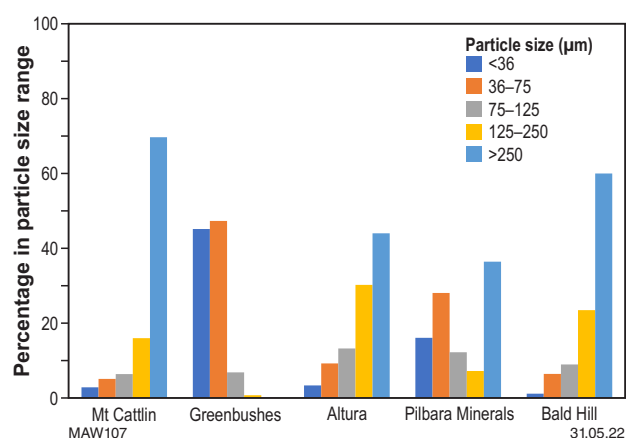


Figure 107. Particle size distribution of concentrate samples from the different mine sites evaluated

Table 12. Chemical assays of main elements in concentrates

	%Li	%Li ₂ O	%SiO ₂	%Al ₂ O ₃	%Fe ₂ O ₃	%CaO	%MgO	%MnO	%K ₂ O	%Na ₂ O	%P ₂ O ₅
Mt Cattlin (Gconc)	3.13	6.74	62.83	24.64	1.87	0.85	0.66	0.19	1.01	0.51	0.02
Greenbushes (Tconc)	3.16	6.80	66.55	25.34	0.16	0.08	0.02	0.05	0.34	0.27	0.16
Altura (Aconc)	2.84	6.11	65.20	24.11	0.87	0.76	0.39	0.24	0.64	0.80	0.08
Pilbara minerals	2.94	6.33	64.03	24.49	0.87	0.52	0.28	0.31	0.81	0.67	0.14
Bald Hill (BHconc)	2.90	6.24	65.44	24.31	0.83	0.21	0.26	0.14	0.70	0.80	0.17

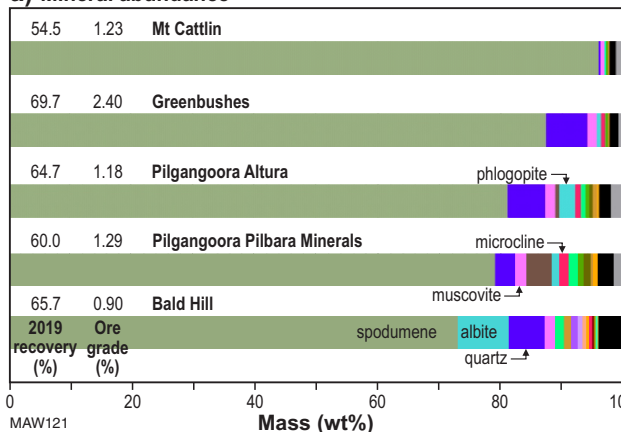
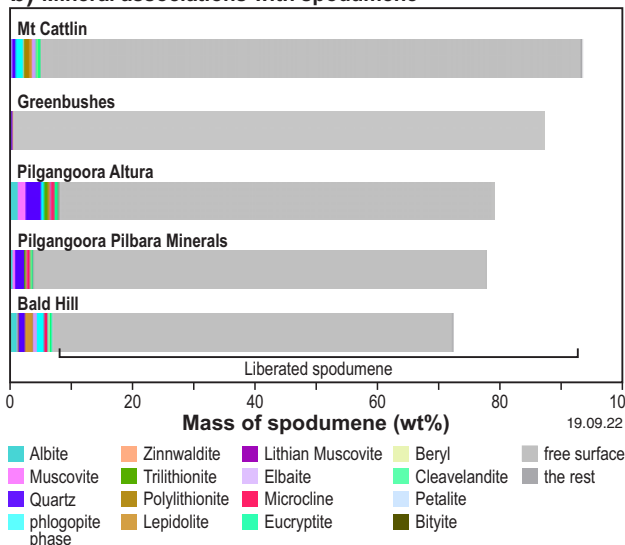
a) Mineral abundance**b) Mineral associations with spodumene**

Figure 108. Mineral abundance (a) and mineral associations (b) with spodumene for concentrate samples taken from site. Data on the average ore grade and amount of spodumene recovered during beneficiation is also shown

Calcination behaviour of mineral constituents

To recover lithium from spodumene concentrate requires a calcination step to render lithium in the spodumene structure amenable to extraction. Although studies in the literature have alluded to lithium recovery affected by conditions and processing, very little is published on the behaviour and effect of impurities and mineral constituents associated with spodumene during the calcination step. It also appears that little work has been done in the lithium industry to develop an understanding of the fusibility of different mineral and elemental components associated with spodumene concentrates during calcination (Harman, 2019).

Key findings

Factors identified in this work that affect the calcination of spodumene concentrates from the deposits examined are as follows:

- All spodumenes have Li content ranging from 3.5 to 3.8 wt% and show some minor variation in Mn, Fe, K, Na and Ca content. Of most significance is Fe and Mn, which can be present in the 0.01 to 1.5 wt% range.
- Spodumene concentrates can have high mineral impurities. For example, mica exists in several forms ranging from fine interstitial veins in voids and fractures to coarse inclusions within spodumene, and as complex alteration zones within spodumene. The micas have high and varying Fe, Mn, Mg and K concentrations relative to spodumene and are identified as muscovite, lepidolite and chlorite/cookeite phases. Feldspars and quartz are also present as minor inclusions within some spodumene grains. Apart from some Pilgangoora samples, calcite occurs as a minor inclusion phase.
- The temperature range that favours the α-β conversion of spodumene required to make lithium amenable to extraction ranges from 1050 °C to 1100 °C. At 950 °C the α-form is stable. At 1050 °C, α-spodumene has mainly converted to β-spodumene via an intermediate γ-phase that is less 'massive' in appearance with marked porosity. At 1100 °C, spodumene exists in the β-form with coarse porosity and is highly fragmented. The porosity and texture of spodumene particles calcined at 1050 °C and 1100 °C appeared favourable for acid baking, followed by water leaching to extract lithium.
- The thermal transformation of spodumene is affected by the exothermic reaction of the oxidation of Fe and Mn present within both micas and spodumene grains.

- The exothermic oxidation of Mn and Fe promotes both the thermal transformation to β -spodumene at a lower temperature and physical disintegration into fine particles during calcination. Hence, some control of the rate of heating and oxidation during the calcination process of high-Fe spodumene may be required to reduce the development of fines.
- The content of gangue minerals in the ore concentrate needs to be minimized as many of the gangue minerals have melting points or decomposition temperatures below the spodumene transformation temperature (e.g. micas and carbonates). Melting contributes to the formation of clinker which tends to line the internal surface of the calcine roaster. Large deposits of clinker may lead to production delays and increased maintenance costs.
- Micaceous minerals (particularly those high in Fe, Mg, K and Na) melt early during calcination and this melt phase may coat and infiltrate spodumene grains, which can prevent full conversion of spodumene to the β -form. However, the highly exothermic nature of the oxidation of Fe and Mn in Fe/Mn-bearing micas during calcination can also promote spodumene transformation. As observed in this study, micas are prevalent in spodumene grains from Mt Cattlin and Bald Hill deposits.
- Feldspars form partial melting eutectics that coat spodumene grains and increase the refractory nature of spodumene. Maintaining the kiln temperature at $\sim 1100^\circ\text{C}$, if possible, would reduce the impact of feldspar-melt formation.

Overall, a controlled heating rate and prevention or reduction of mineral impurities in the spodumene concentrate will favour conversion of spodumene.

Methodology for assessment of thermal properties of major mineral components within pegmatites

Major mineral components in each pegmatite sample were collected by carefully breaking off pieces with a hammer and chisel or cutting with a fine diamond saw. The specimens were characterized using optical imaging and automated digital imaging on polished sample mounts to determine the modal mineralogy of lithium ore and gangue minerals. Bulk mineralogy by X-ray powder diffraction studies and chemical assays were obtained on all specimens. The concentrations of Li and the distribution of elements (e.g. B, Rb, Cs, Fe, Mn, F) within selected mineral grains were quantified by LA-ICP-MS and EPMA. EPMA measurement of the Si content of spodumene, feldspar and mica was used to normalize the trace element data generated by LA-ICP-MS analysis. A sub-microscopic evaluation on selected lithium mineral grains was undertaken to study the variability of lithium and other elements within minerals. This work used a combination of the FIB-SEM with ToF-SIMS, electron backscatter diffraction (EBSD), and XRD to study the compositional variation in minerals. Details of procedures are outlined in Appendix 3.

The thermal properties of a selection of Li-ore and gangue minerals, which represent different mineral constituents within pegmatite ores were evaluated. For XRD and thermal gravimetric studies, representative sub-samples were

prepared by lightly crushing the samples with a mortar and pestle followed by micronizing in ethanol to generate fine powders and to prevent contaminants caused by mechanical grinding. Samples were evaluated using the following techniques:

- **Thermal gravimetric analysis (TGA)** – Thermal gravimetric analysis was performed using a TA Instruments SDT Q600 simultaneous differential thermal analysis (DTA)–TGA. Approximately 20 mg of a sample was weighed into a 90- μL alumina crucible with a matched empty crucible as a reference. The sample was heated from ambient to 1200°C at 20°C per minute in an air atmosphere flowing at 100 mL per minute. The temperature scale of the instrument was calibrated using the melting points of 99.999% indium (156.60°C), 99.99+% tin (231.93°C), 99.99+% zinc (419.53°C), 99.99% silver (961.78°C), and 99.999% gold (1064.18°C). The balance was calibrated over the temperature range using alumina mass standards provided by the instrument manufacturer. The heat flow between the pans was calibrated using a sapphire disk provided by the instrument manufacturer. The cell constant was fine-tuned using the heat of fusion of zinc (113 J/g).
- **In situ XRD thermal analysis** – To characterize changes in mineralogy during calcination, in situ XRD thermal analysis was undertaken using a Thermo Fisher ARL Equinox 5000 XRD with an Anton Paar HTK 1200N oven, parallel beam and Mo K α incident radiation. Tests were carried out on a white spodumene sample, with little impurity content and a green spodumene with partial alteration, at heating rates of $5^\circ\text{C}/\text{min}$ and $20^\circ\text{C}/\text{min}$ to 1200°C before cooling. Data were collected continuously every 10°C . Phase abundance was quantified by Rietveld refinement using Topas™ software.
- **Muffle furnace studies** – For calcination tests, cubic blocks ($\approx 1\text{ cm}^3$) of representative examples of different spodumene types were made by taking large, single spodumene crystals and cutting them into cubes with a diamond saw. Prepared spodumene cubes were photographed, weighed and the dimensions measured before and after heating tests. Spodumene cube samples in duplicates were placed on a ceramic plate at the base of a Thermo Scientific FB1300 Thermolyne electric muffle furnace. Samples were heated by ramping up at $20^\circ\text{C}/\text{min}$ and then held at a fixed temperature for two hours, before cooling to room temperature. The temperature was set and monitored by a calibrated thermocouple, located near the sample. Fresh samples were heated separately at 950°C , 1050°C and 1100°C in an ambient atmosphere. Polished section mounts of mineral blocks before and after heat treatment were produced and studied separately to track the thermal transformations of spodumene and associated gangue minerals.

Selection and characteristics of samples

Images, mineral composition and chemical analyses of different spodumene and associated gangue mineral specimens selected for testing are illustrated in Figure 109, with mineralogical abundance and chemical composition presented in Tables 13 and 14, respectively. The spodumene



Figure 109. Images of different spodumenes and associated gangue minerals. Spodumene can exist in different colours depending upon element impurities (BH–Bald Hill, MC–Mt Cattlin, PIL–Pilgangoora) in Western Australia

samples vary from white to green hues, which is related to colouration from impurities within the mineral structure, as well as from fine inclusions or alteration products. Spodumene with impurities, such as Fe and Mn, which substitute for Al in the spodumene crystal structure, are responsible for colour variation.

There are different types of micas present in pegmatite samples. Primary mica is associated with the main crystallization of pegmatite and typically exists as silvery muscovite flakes (BH-2500) that appear as a 'book-like' texture or disseminated in ring patterns around host spodumene laths. The other micaceous type has formed by post-crystallization alteration and replacement of spodumene by finely crystalline mica (e.g. BH2600-refer to the section Spodumene morphology and alteration: insight into pegmatite crystallization evolution). These secondary micas have a variable mineral composition but occur as a combination of muscovite and chlorite. Feldspars also vary in composition depending on whether they formed during

early or post crystallization events. X-ray diffraction studies revealed all spodumene specimens contain trace amounts of mineral impurities, mainly in the form of micas (Table 13). The feldspar specimens examined in this study (MC400 and BH2300) are a mixture of albite and microcline associated with solid solution variations between Na and K rich varieties and contain some quartz. The secondary micas range in mineral composition but are a combination of muscovite and chlorite.

Table 14 shows the bulk chemical composition of the mineral specimens. Mt Cattlin spodumene samples (MC200, 300, 1500) have higher Fe and Mn contents than Bald Hill spodumene samples (BH0100, 1300, 1425). The Pilgangoora spodumenes (PIL100, PD001, PD006 and PD008) have a range of Fe contents, whereas Bald Hill spodumene samples have moderate concentrates of Fe. Pilgangoora samples have a greater Mn and Ca content than other samples associated with the presence of calcite.

Table 13. Mineralogical analysis by X-ray diffraction studies of mineral specimens

Sample no.	Sample type	Quartz	Spodumene	Muscovite/ Phlogopite	Tainiolite	Cookeite/ chlorite	Celadonite	Microcline	Albite	Orthoclase	Analcime	Calcite
wt%												
Bald Hill												
BH-0100	spodumene	4	95	0.8					0.1		0.4	
BH-1300	spodumene	1	92	7					1			
BH-1425	spodumene	tr	94	6					tr			
BH-2250	spodumene	tr	86	11								
Mt Cattlin												
MC-200	spodumene		94	6		0.4						
MC-300	spodumene		88	7			5					
MC-1500	spodumene	tr	93	3					4			
Pilgangoora region												
PIL-100	spodumene	10	74	9								7
PD001	spodumene	1	84	8		2			3	1		
PD006	spodumene	1	96	3					tr			
PD008	spodumene	2	92	1		2			4			
Mineral accessories												
BH-2200	2 nd micas			87		13						
BH-2300	feldspar	6						69	25			
BH-2500	muscovite/quartz	48		52								
BH-2600	2 nd micas	1		30	57	12						
MC-400	albite/mica	1		10		16		10	63			

Table 14. Bulk chemical composition of mineral specimens

Sample No.	Sample type	SiO ₂	Al ₂ O ₃	CaO	Fe ₂ O ₃	K ₂ O	MgO	Na ₂ O	P ₂ O ₅	SO ₃	TiO ₂	MnO
wt%												
BH-0100	spodumene	64	27	0.1	0.7	0.2	0.02	0.4	0.0	0.0		0.09
BH-1300	spodumene	63	27	0.0	0.6	0.9	0.2	0.6	0.0	0.0	0.01	0.07
BH-1425	spodumene	62	27	0.4	0.7	1.1	0.1	0.4	0	0	0	0.10
MC-200	spodumene	64	27	0.01	2.1	0.001						0.13
MC-300	spodumene	62	26	0.3	1.6	1.2	0.3	0.3	0.0	0.0	0.01	0.16
MC-1500	spodumene	63	27	0.3	1.1	0.2	0.01	1.2	0.1	0	0	0.20
PIL-100	spodumene	64	23	2.0	0.6	1.2	0.4	0.2	0.0	0.0	0.01	0.22
PD001	spodumene	69	21	0.1	1.4	1.4	0.1	0.4	0.0	0.0	0.01	0.10
PD006	spodumene	82	11	0.1	0.8	2.1	0.1	0.7	0.0	0.0	0.01	0.10
PD008	spodumene	73	18	0.3	0.7	1.0	0.3	1.5	0.1	0.0	0.0	0.20
BH-2200	altered micas	52	27	0.1	2.6	9.2	3.3	0.4	0.1	0.0	0.01	0.07
BH-2300	feldspar	98	0.4	0.1	0.6	0.1	0.0	0.1	0.02	0.00	0.01	0.01
BH-2500	muscovite/quartz											
BH-2600	micas	52	26	0.1	3.6	10.3	3.0	0.2	0.1	0.03	0.01	0.06
MC-400	albite/mica	63	27	0.3	1.1	0.2	0.0	1.2	0.1	0.0	0.01	0.17

Sample No.	Sample type	LOI1000 %	Ba ppm	Cs	Nb	Rb	Ta	Be	Li	Zn	F	Cl
BH-0100	spodumene	0.2	35	162	1	68	4	72	33200	12	0.01	0.01
BH-1300	spodumene	0.5	159	164	2	217	4	9	30700	16	0.02	0.00
BH-1425	spodumene	0.9	176	373	0.3	319	1	10	29200	12	0.02	0.00
MC-200	spodumene											
MC-300	spodumene	0.6	359	257	29	815	36	7	29200	32	0.14	0.00
MC-1500	spodumene	0.4	24	497	2	361	20	2	30300	22	0.05	0.01
PIL-100	spodumene	2.1	33	110	12	1470	56	42	24800	80	0.10	0.00
PD001	spodumene	0.8		3080	52	22400	190	21	19800	86	5.46	0.00
PD006	spodumene	0.3	2	117	31	2400	10	17	3030	106	0.11	0.00
PD008	spodumene	0.4	2.5	38.2	51	545	31	221	8710	66	0.16	0.01
BH-2200	altered micas	4.9	1030	340	20	2160	7	125	1280	6	0.21	0.03
BH-2300	feldspar	0.1	3	4	0.3	30	0	13	181	2		0.02
BH-2500	muscovite/quartz											
BH-2600	micas	4.2	1220	235	10	2890	4	56	1330	16	0.51	0.02
MC-400	albite/mica	0.4	24	497	2	361	20	2	30300	22	0.05	0.01

Morphology and composition of spodumene specimens

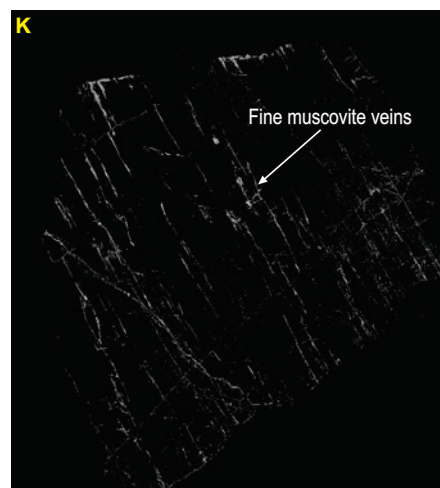
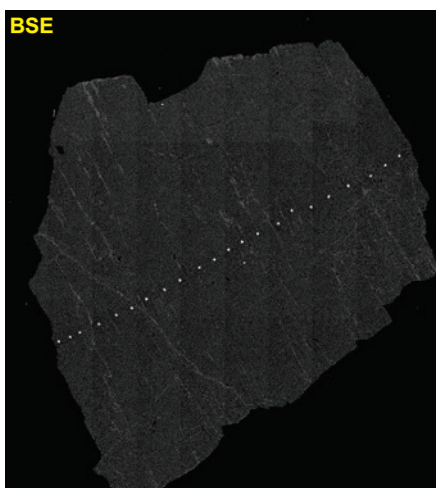
Images of the different spodumene samples showing variations in textures are illustrated in Figures 110 and 111. The composition of lithium and main impurity elements in spodumene and the associated mica inclusions/alterations are shown in Table 15 and Table 16, respectively.

All spodumenes have Li contents between 3.5 and 3.8 wt% (Table 15), but vary in Mn, Fe, K, Na and Ca as the minor constituents. Notable variations occur in the Fe, Mn, Sn and Ta contents between the different spodumenes. While spodumene compositions do not show any significant deviation from the ideal formula, $\text{LiAlSi}_2\text{O}_6$, they can contain minor contents of Fe, Mn, Na, K, Mg and Ca in the structure (London and Burt, 1982; Deer et al, 1992; refer to the section Spodumene composition). Mica exists in several forms as fine interstitial veins in voids and fractures, as coarse inclusions within spodumene grains and as complex alteration zones within spodumene grains. The micas have high and varying contents of Fe,

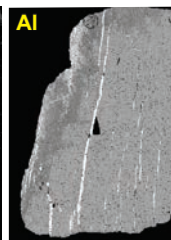
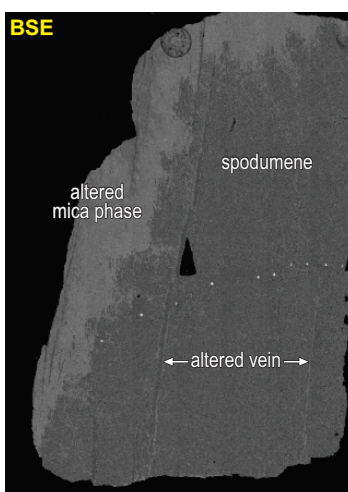
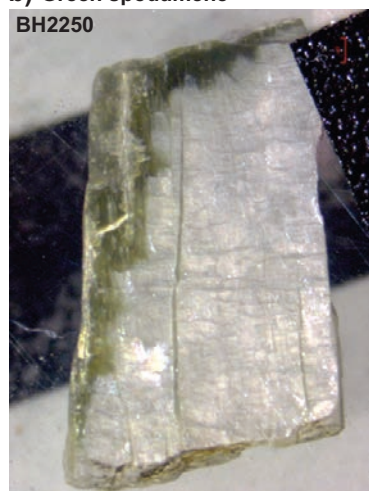
Mn, Mg and K relative to spodumene and are identified as muscovite, lepidolite and chlorite/cookeite phases (e.g. section, Spodumene morphology and alteration: insight into pegmatite crystallization evolution). Feldspars and quartz are also minor inclusions within some spodumene grains, with a sample tested from Pilgangoora containing calcite.

The presence of Rb and Cs in spodumene are likely artefacts from closely associated, fine-grained mica. The Mt Cattlin spodumene samples have higher Fe (average 1500 ppm) and Mn (386–836 ppm) contents than Bald Hill, whereas Pilgangoora spodumenes range in Fe contents (135–1340 ppm) that is similar to Bald Hill, but higher in Mn (average 1160 ppm) and calcium content (average 370 ppm). The Mn content is higher in the Pilgangoora spodumene. Tin and Ta contents vary markedly between the different spodumene, with Sn contents highest in the light-grey spodumene (MC200) (Table 15). The purple colour of the Pilgangoora (PIL100) spodumene may be due to the greater Mn content incorporated within spodumene.

a) White spodumene
BH0100



b) Green spodumene
BH2250



MAW123

12.04.22

Figure 110. Cross-section image and backscatter electron micrograph of: a) white spodumene and potassium Ka energy dispersive elemental map revealing fine muscovite veins in white spodumene crystal; and b) green spodumene with energy dispersive elemental maps revealing an altered micaceous zone along spodumene enriched in K, Fe and Mg

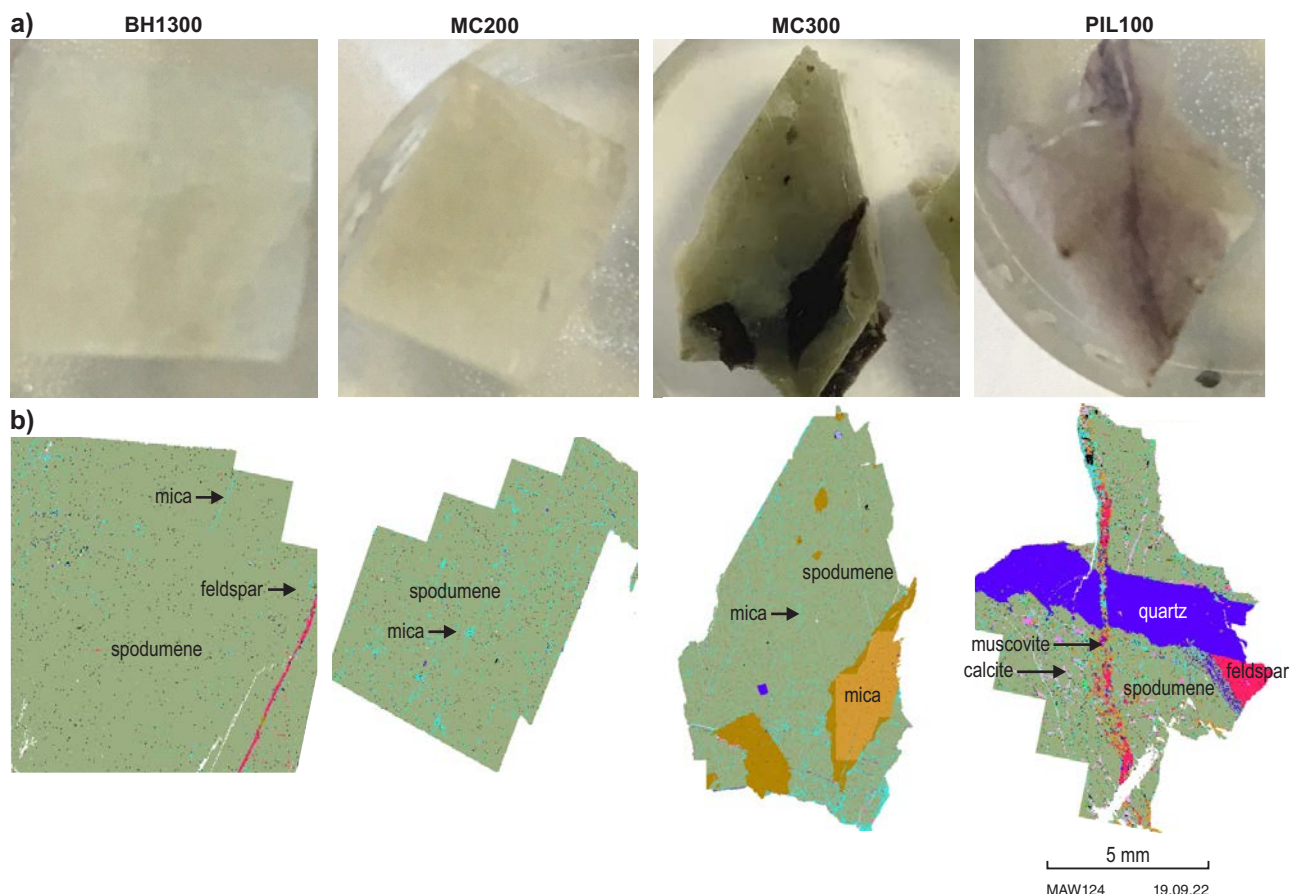


Figure 111. Optical (a) and mineral (b) composition maps showing mineral impurities within spodumene from Mt Cattlin and Pilgangoora (spodumene – olive green, micas – light-blue, feldspar – red, calcite – light-pink, K and Mn-rich mica – brown, quartz – blue)

In hand-specimen and optical images of the material examined, spodumene appears relatively ‘clean’ in appearance showing little or no alteration. However, TIMA mineral mapping highlights a pervasive, finely developed network of micaceous alteration, developed along cracks or cleavage fractures as highlighted in the K–K element distribution maps for the Bald Hill spodumene examples (Fig. 110) and as detected by TIMA mineral mapping of representative examples of spodumene selected for calcination study (Fig. 111; muscovite shown in light-blue). Both the Bald Hill example (BH1300) and Pilgangoora (PIL100) spodumene contain veins mapped as feldspar (red) (Fig. 111). The Pilgangoora spodumene also has a high quartz (blue) content and displays later-stage, calcite veining that crosscuts earlier quartz and spodumene (Fig. 111).

BSE imaging and element distribution mapping show the extent and compositional complexity of the micaceous alteration (Figs 110, 111). Mapping of the K–K α distribution in BH0100 reveals trace quantities of ‘muscovite’ that exist as fine, interstitial veins along cracks and cleavage fractures (Fig. 110). Micaceous alteration (green) of BH2250 is significantly more developed, making up about 25% of the particle (Fig. 110), with the altered micaceous zone enriched in Al, K, Fe and Mg (Fig. 110), and significantly reduced in Li (Table 16). Micaceous alteration of spodumene also results in significant concentration of the minor element content compared to the precursor spodumene (Fig. 110).

The light-grey, Mt Cattlin spodumene (MC200) also contains fine mica disseminated throughout the spodumene, whereas the green spodumene (MC300) contains fine, K and Mg-mica veins, and coarse inclusions of a K–Fe–Mn mica, celadonite–montdorite phase. The micas associated with spodumene grains contain high levels of Fe and Mn relative to spodumene. The high K, Rb and, in some cases, Cs contents are characteristic of Li-bearing micas. The Li content is low (~1000 ppm) except in sample MC300, which has a high Li content similar to zinnwaldite type composition.

Table 15. Average Li and trace elements composition and standard deviation by LA-ICP-MS analysis of spodumene particles

	<i>Li</i>	<i>Mg</i>	<i>Ti</i>	<i>Mn</i>	<i>Fe</i>	<i>Cu</i>	<i>Zn</i>	<i>Na</i>	<i>K</i>	<i>Ca</i>	<i>Nb</i>	<i>Sn</i>	<i>Cs</i>	<i>Rb</i>	<i>Sr</i>	<i>Ta</i>
<i>ppm</i>																
White spodumene (BH0100)																
Mean	37832	0.3	83	309	667	1.3	2.3	839	36.5	45	0.04	254	0.1	0.1	0.0	16
SD	228	0.1	4	88	47	0.3	4.4	91	33.2	21	0.03	581	0.1	0.1	0.0	40
Min	37515	0.2	80	208	582	0.9	0.3	705	1.1	13	0.00	6	0.0	0.0	0.0	0
Max	38334	0.5	93	523	713	1.9	13.9	965	105.5	84	0.1	1804	0.3	0.2	0.0	126
Green altered spodumene (BH2250)																
Mean	34644	195	28.5	414	1822	2.8	11.9				0.04	126	3.2		0.63	0.3
SD	927	147	4.4	56	143	1.2	1.8				0.05	22	4.2		0.63	0.4
Max	36270	477	36.9	521	2101	4.8	14.5				0.15	157	14.4		2.16	1.0
Min	33270	9.2	21.9	303	1566	0.93	8.3				0.0	82	0.3		0.06	0.0
Light-grey spodumene (MC200)																
Mean	35753	<8	63	817	1560	1.1	20.7	813	<30	371	<0.07	640	<0.3	<0.8	<0.1	0.9
SD	358		7	16	35	0.6	1.5	15		664		56				0.5
Min	35135		56	794	1504	0.8	19.3	792		0		591				0.5
Max	36254		78	836	1599	1.3	22.7	832		2252		722				1.8
Green spodumene (MC300)																
Mean	37221	1.6	81	624	3627	0.13	4.7	706	0.9	52	0.004	13	0.004	0.000	0.007	0.006
SD	147	1.2	5	165	296	0.08	3.4	48	0.5	33	0.002	2	0.002	0.000	0.005	0.004
Min	36980	0.4	75	386	2940	0.02	0.9	625	0.5	9	0.003	10	0.003	0.000	0.003	0.003
Max	37436	4.4	88	844	4056	0.25	10.2	780	1.5	95	0.005	17	0.005	0.000	0.013	0.011
Purple spodumene (PIL100)																
Mean	35993	8	39	1163	567	1.7	6.3	693	12	371	1	215	88	1.0	0.02	3.9
SD	420	13	18	235	353	0.8	1.6	68	21	664	1	173	122	0.3	0.00	8.2
Min	35268	0	24	715	135	1.1	3.7	590	0	0	0	18	0	1.0	0.02	0.0
Max	36558	42	73	1437	1342	2.5	8.5	793	64	2252	3	500	319	1.0	0.02	27.5

Table 16. Average Li and trace elemental composition and standard deviation by LA-ICP-MS analysis of micas associated with spodumene particles

	<i>Li</i>	<i>Mg</i>	<i>Ti</i>	<i>Mn</i>	<i>Fe</i>	<i>Cu</i>	<i>Zn</i>	<i>Na</i>	<i>K</i>	<i>Ca</i>	<i>Nb</i>	<i>Sn</i>	<i>Cs</i>	<i>Rb</i>	<i>Sr</i>	<i>Ba</i>	<i>Ta</i>
<i>ppm</i>																	
Vein in altered spodumene (BH2250)																	
	31330	603	36.8	148	8610	16.6	69.2				2.32	1453	60.3	38	4.38	5.1	
Mica phase in altered spodumene (BH2250)																	
Mean	2298	22897	22.4	711	27350	9.3	28.9				0.5	371	653	4624	20.5	89	4.3
SD	575	770	5.3	98	620	1.7	5.1				0.3	61	76	122	1.5	12	3.5
Max	2960	23610	28.1	824	27980	11.1	34.0				0.7	438	739	4731	22.2	102	8.0
Min	1924	22080	17.6	646	26740	7.8	23.8				0.2	318	595	4491	19.3	80	1.2
Mica in green spodumene (MC300)																	
Mean	25080	849	987	16150	24033	1	1337	1753		177	170	722	5957	44194	0	2	406
SD	1793	318	303	1113	883	0	58	297	2272	37	22	171	2206	1965	0	2	58
Min	23188	629	370	14248	22203	0	1194	1272		103	146	341	4801	39223	0	0	266
Max	29791	1570	1319	18039	25196	1	1399	2204		245	224	937	12044	45853	0	7	462
Mica in purple spodumene (PIL100)																	
Mean	8924	36291	55	4489	2279	36	372	2616		3833	8		8924	36291	55	4489	2279
SD	3080	11906	16	1241	656	36	345	6096	15294	7171	2		3080	11906	16	1241	656
Min	1118	6275	9	875	448	5	75	643		277	2		1118	6275	9	875	448
Max	13635	48934	70	5426	2756	135	1380	20991		19359	11		13635	48934	70	5426	2756

Thermal transformation of primary spodumene and altered spodumene

The mineralogical transformations during heating of primary white and altered green spodumene were characterized and tracked by in-situ, XRD studies. Rietveld-refined XRPD data for the white spodumene (BH1300) and green spodumene (BH2250) prior to heating are shown in Figure 112. The white spodumene is mainly α -spodumene with minor quartz and trace muscovite, whereas the green spodumene contains a significant amount of mica. The mica in the green spodumene matches a combination of muscovite and lepidolite structures described in the literature. Using the internal standard method, the amorphous content in both spodumene samples was calculated to be ~15 wt%. Careful sample preparation should have minimized amorphous material formed during pulp milling. However, quantification of the amorphous content is hard to determine as calculation of the amorphous content is sensitive to how well the experimental and the calculated data match.

A contour plot tracking the transformation of α -spodumene to β -spodumene via an intermediate γ -spodumene phase for the green spodumene is shown in Figure 113a. The measured content of crystalline phases derived from refinement of XRD patterns for both white and green spodumene (Bald Hill) as a function of temperature, θ is shown in Figure 113b. Figure 113c illustrates an example of one of the Rietveld-refined XRD data patterns for calcined white spodumene at 1030°C. Under the same heating conditions, the α - β spodumene transformation begins at different temperatures with conversion of α -spodumene to γ -spodumene starting at 40 °C to 50 °C lower for white spodumene (930 °C) compared to green spodumene (970 °C) (Fig. 113b).

β -spodumene is reported to form at temperatures in the range 950 °C to 1100 °C (White and McVay, 1958; Barbosa et al., 2014; Peltosaari et al., 2015; Welsch et al., 2015; Salakjani et al., 2016; Rosales et al., 2019) and γ -spodumene forms in the temperature range of 800 °C to 950 °C (Peltosaari et al., 2015; Salakjani et al., 2016). Four reaction pathways during the transition of spodumene have been reported in the literature (Abdullah et al., 2019; Salakjani et al., 2019). At a slow-heating rate an intermediate γ -spodumene phase is produced from α -spodumene, whereas at a fast-heating rate direct transition of crystalline α -spodumene to β -spodumene is expected. Evidence of an intermediate γ -spodumene phase is apparent in data collected in the current study as exemplified by the presence of 010 and 020 peaks in Figure 113a, and observed in the modelling and measurement of phase abundance in Figure 113b. The presence of γ -spodumene over the range of α -spodumene transformation indicates that direct transition of crystalline α -spodumene to β -spodumene would not be the main pathway to β -spodumene in the current study.

Work reported in the literature also indicates that spodumene can convert to an intermediate, disordered phase before transforming to γ -spodumene (Gasalla and Pereira, 1990; Peltosaari et al., 2015; Salakjani et al., 2017; Moore et al., 2018). In the current study, the amorphous content was estimated based on the addition of corundum as an internal standard to the sample during sample preparation. However, results were inconclusive and further work is required to provide a more accurate measurement of phase abundance.

Plots of the logarithmic concentration of α -spodumene as a function of time and the calculated rates of α -spodumene transformation are shown in Figure 114.

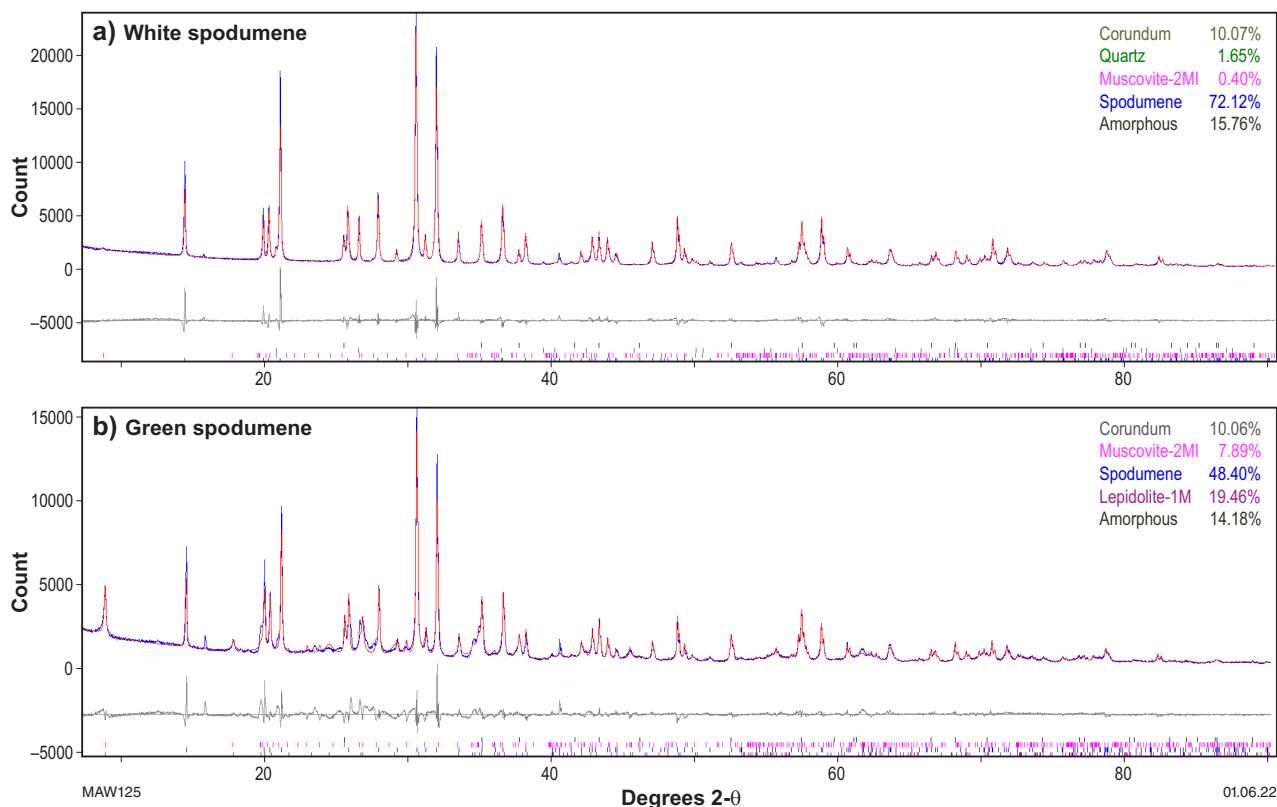


Figure 112. Rietveld refined X-ray powder diffraction patterns of: a) white spodumene showing minor contents of quartz and muscovite; and b) green spodumene with high mica impurities (corundum added as an internal standard)

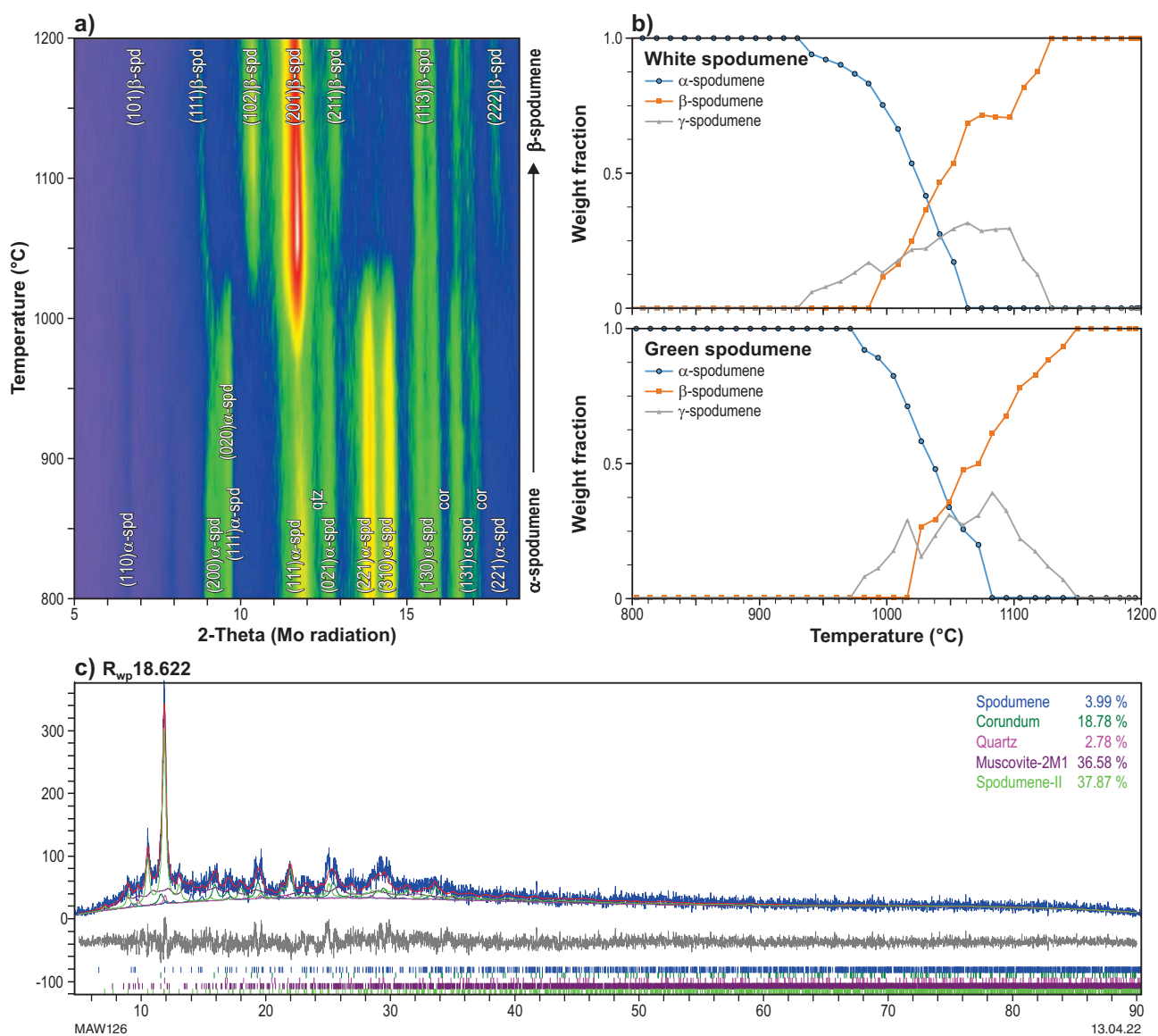
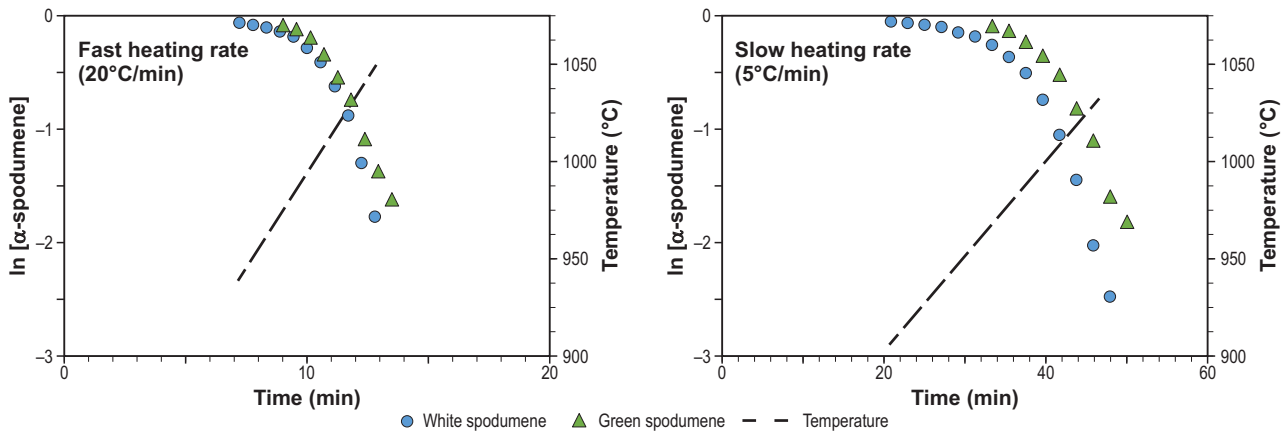


Figure 113. XRD analysis of the α -spodumene to β -spodumene transformation: (a) a contour plot of X-ray power diffraction data (red – peaks with the greatest intensity; blue – background); b) relative weight percent from Rietveld analysis as a function of temperature for white and green spodumene; and c) example of the Rietveld refined X-ray powder diffraction data of calcined white spodumene at 1030 °C, matching α , γ and β spodumene



Heating rate	White spodumene				Green spodumene			
	20°C/min		5°C/min		20°C/min		5°C/min	
Stage	Temp. (°C) ¹	Rate (s ⁻¹)	Temp. (°C) ¹	Rate (s ⁻¹)	Temp. (°C) ¹	Rate (s ⁻¹)	Temp. (°C) ¹	Rate (s ⁻¹)
1	941	4.69 x 10 ⁻²	907	7.40 x 10 ⁻³	983	6.09 x 10 ⁻²	961	3.33 x 10 ⁻²
2	986	2.03 x 10 ⁻¹	949	3.49 x 10 ⁻²	1006	4.41 x 10 ⁻¹	992	1.49 x 10 ⁻¹
3	1020	7.03 x 10 ⁻¹	990	1.94 x 10 ⁻¹				

¹Starting temperature of transformations

MAW127

19.09.22

Figure 114. The logarithmic concentration of α-spodumene as a function of time at fast and slow heating rates and a tabulation of the calculated rates of α-spodumene transformation at different temperature for both Bald Hill white and green spodumene

The logarithmic, kinetic curves show that spodumene transformation as a first order reaction, and as the temperature increases the rate of conversion of α-spodumene increases three-fold for white spodumene and two-fold for green spodumene. The initial rate of α-spodumene transformation in both spodumene samples is slower at the beginning and accelerates towards the end with increasing temperature. While the α-spodumene transformation occurs at a lower temperature for white spodumene, the rate of conversion is faster for green spodumene (Fig. 114). At >900 °C the conversion rate of white spodumene is much faster than green spodumene.

Cross-sectioned mounts of calcined spodumene samples (Fig. 115) show that the product formed from white spodumene is free-flowing, fine-powdered β-spodumene. ToF-SIMS analysis indicated that lithium in calcined spodumene is evenly dispersed in the powder (Fig. 115a). In contrast, the green spodumene sample has fused into a mixture of β-spodumene and melt to form beads. ToF-SIMS analysis shows the melt, which contains K from the micaceous zones, has encapsulated β-spodumene represented by the Li-rich zone (Fig. 115b).

The slower α-β conversion of green spodumene can be interpreted as a result of decomposed mica encapsulating spodumene and reducing the rate of heat transfer rate to spodumene for phase transformation to occur.

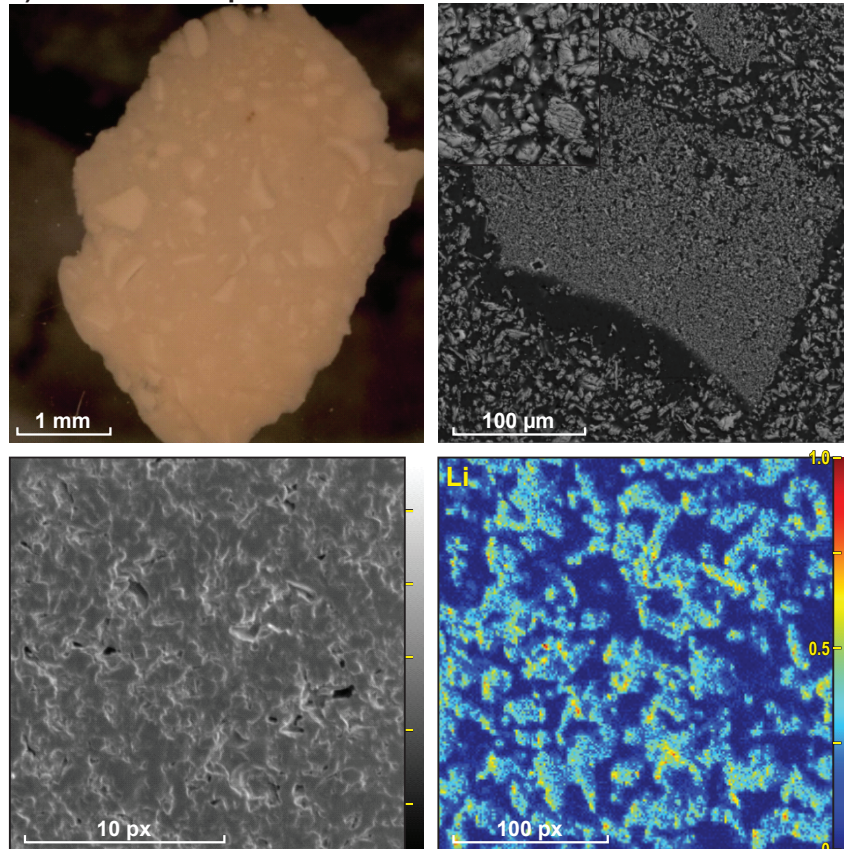
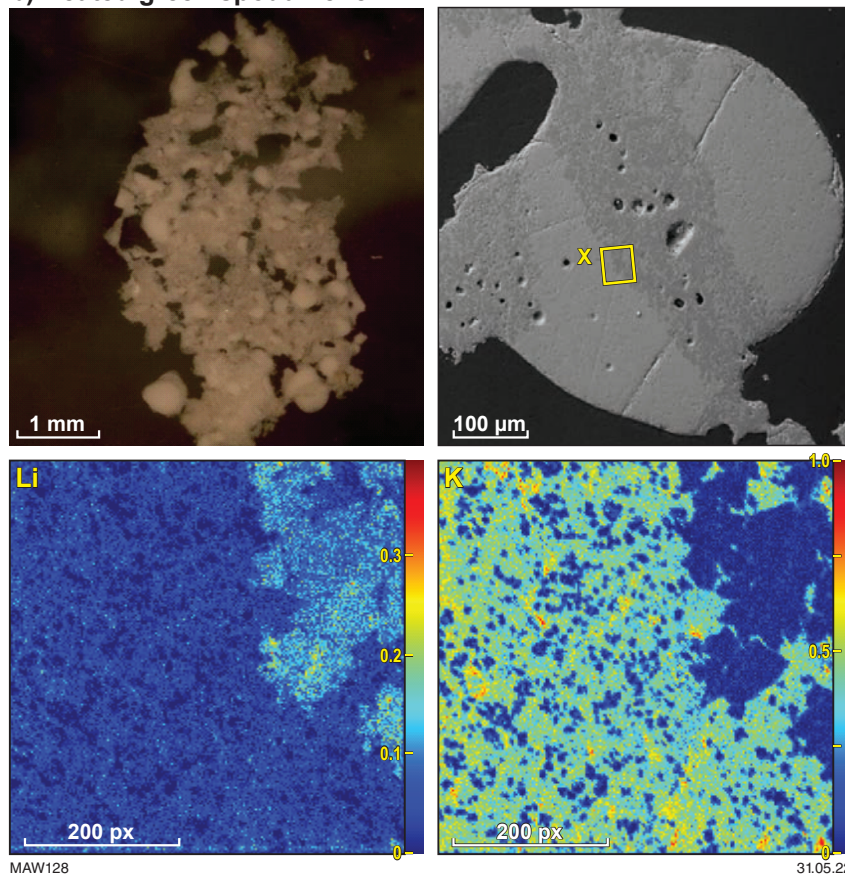
Thermal gravimetric analysis of spodumene and common LCT pegmatite minerals

Comparison of the thermal properties of spodumene with common LCT pegmatite minerals

To understand better the nature of the thermal decomposition of LCT pegmatites, a comparative TGA of spodumene and the gangue phases, mica and feldspar was undertaken from hand-picked minerals collected in this study. An overlay of the different differential thermogravimetric analysis (DTGA) graphs for the different minerals is shown in Figure 116. The temperature range associated with loss of adsorbed water and the dehydroxylation stages for micas is also shown in Figure 116. The TGA of most mineral components found in pegmatites have been reported (e.g. Földvári, 2011) and can aid in the interpretation of results.

As shown in Figure 116, the thermal alteration of spodumene shows a strong endothermic peak (blue line) that is distinguishable from thermal transformations of other common, LCT pegmatite minerals.

Under the operating conditions, the conversion of α-spodumene to β-spodumene is represented as an endothermic peak (Fig. 116; blue line), which starts at around 950 °C and is completed at around 1110 °C. The α-β transformation temperature range is similar to that depicted earlier in Figure 113b. Apart from a slight

a) Heated white spodumene**b) Heated green spodumene**

MAW128

31.05.22

Figure 115. Optical and backscatter electron micrographs, together with ToF-SIMS elemental maps of cross-sections of (a) white and (b) green spodumene powdered samples following heating. β -spodumene formed from heating green α -spodumene is partially encapsulated by melt from micaceous material, whereas the white spodumene remains as a fine powder

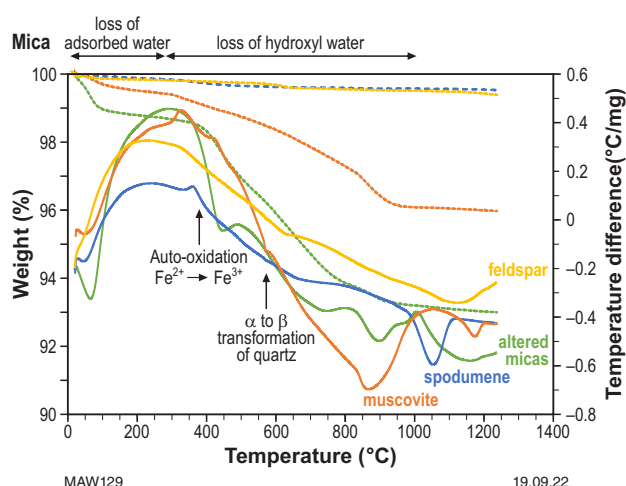


Figure 116. Comparison of the thermo gravimetric analysis of representative mineral examples observed in LCT pegmatites (heating rate 20 °C/min). The percentage weight lost is shown on the left-hand axis and corresponds to the dotted line data. The differential thermal analysis curve for each corresponding phase is shown as a solid line. The temperature range associated with loss of adsorbed water and the dehydroxylation stages for micas is also illustrated

loss in weight (~0.5 wt%) associated with dehydration of minor mineral impurities within the spodumene at lower temperatures, there is no significant loss in weight associated with spodumene transformation. While both α - and γ -spodumene undergo endothermic reactions when transforming to β -spodumene, the direct conversion of α - to γ -spodumene is reported to be an exothermic reaction (Botto et al., 1976; Gasalla and Pereira, 1990; Salakjani et al., 2016, 2017). A slight increase in the temperature difference curve occurs around 950 °C. However, any exothermic peak is masked by the corresponding endothermic transformation to β -spodumene.

The thermal analysis curves for muscovite (orange dotted and full lines) show a loss of ~0.5 wt% associated with the desorption of surface water. Muscovite dehydroxylates in the temperature range 820–920 °C, which is accompanied by a loss in weight of ~3.5 wt%. With increasing temperature, non-equilibrium melting of muscovite with compositionally different layer types produces a melt phase, corundum and leucite (Barlow and Manning, 1999). At temperatures between 1100 °C and 1200 °C, another endothermic peak associated with further muscovite dehydroxylation occurs (Schomburg and Zwahr, 1997; Foldvari, 2011). The muscovite sample also contains quartz and the endothermic transition representing alpha to beta crystal inversion can be observed at 573 °C (Schelz, 1976).

In both spodumene and muscovite samples, a small exothermic peak between 300 °C and ~450 °C was accompanied by a small decrease in weight of spodumene and coincides with the start of continued loss in weight for muscovite. In mica this can be attributed to the auto-oxidation of ferrous to ferric Fe ($\text{Fe}^{2+} \rightarrow \text{Fe}^{3+}$) present in the mineral structure and is normally accompanied by a dehydroxylation endotherm (Foldvari, 2011). Oxidation of Fe^{2+} to Fe^{3+} normally results in an increase in weight. However, changes in weight may be offset by initiation of the loss of structural OH/water.

The thermal analysis curve for feldspar yields a very broad endothermic peak from 1060 °C to 1200 °C and is associated with feldspar melting over a large temperature interval (Fig. 116; yellow line). The melting transformation of feldspar occurs toward completion of spodumene transformation (Fig. 116). Studies reported for albite indicate that increasing heat rate increases the melting point (1143 °C at 5 °C/min to 1167 °C at 20 °C/min) (Johnson and McCauley, 2005). However, with rapid heating the higher the temperature of melting, the more quickly albite melts.

The thermal analysis curve for a sample of secondary mica reveals a series of endothermic peaks and one exothermic peak associated with the decomposition of a mixture of chlorite and muscovite (Fig. 116; green line). As observed, decomposition of secondary mica occurs at a lower temperature than the spodumene transformation. For chlorite, dehydroxylation takes place generally in two steps with an endothermic peak between 470 °C and 650 °C associated with dehydroxylation of the interlayer hydroxide in the chlorite structure and a second endothermic peak between 650 °C and 1000 °C associated with the dehydroxylation of the mica layer (Foldvari, 2011). The number of hydroxyls belonging to the hydroxide sheet is three times more than in the mica layer. The exothermic peak (at ~1020 °C) represents the chlorite recrystallizing into new minerals (e.g. olivine, spinel and enstatite). The temperature interval between the second dehydroxylation and the following exothermic peak varies for different chlorites and has been shown to correlate with the Mg content in the structure (the greater the MgO content, the larger the interval) (Smykatz-Kloss, 1974).

The cause of a small endothermic peak at 450 °C is unclear and is aligned with ~0.35 wt% loss in weight but appears prominent in all micas collected from samples formed during late-stage alteration and crystallization of the pegmatite deposits (Fig. 116).

While factors such as heating rate, mineral composition and particle size influence mineral transformations, it is evident in Figure 116 that micaceous minerals present in pegmatite-mineral assemblages alter at lower temperatures before the transformation of spodumene occurs. The partial melting of feldspars can be avoided if the temperature can be sufficiently controlled below 1100 °C.

In the calcination process, it is important to establish conditions which favour the α - β conversion of spodumene without interference from other minerals associated with spodumene concentrates. Studies reported in the literature have alluded to lithium extraction decreasing with the impurity content in the feed material and suggest that lithium recovery may be limited by impurities coating some β -spodumene particles (Lajoie-Leroux et al., 2018).

Comparison of the thermal properties of different spodumenes

A comparison of the thermal gravimetric curves of spodumene from the Bald Hill, Mt Cattlin and Pilgangoora sites are shown in Figure 117. As described earlier, Mt Cattlin sample has higher Fe content than spodumene collected from the other deposits (Table 15). In all thermal gravimetric curves, the weight loss is largely associated

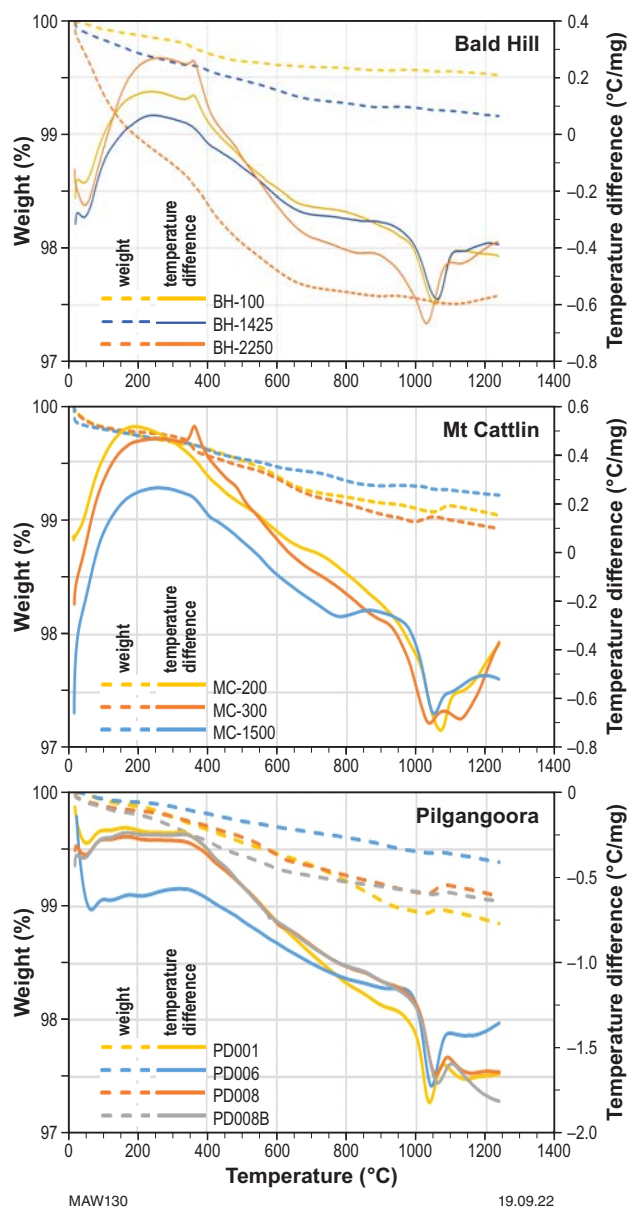


Figure 117. Comparison of the thermal gravimetric curves of spodumene from Bald Hill, Mt Cattlin and Pilgangoora (heating rate 20 °C/min). The percentage weight lost is shown on the left-hand axis and corresponds to the dotted line data. The differential thermal analysis is plotted on the right-hand axis

with the dehydroxylation of mica within spodumene grains. Sample BH-2250 has a significantly greater mica content (11 wt%) than other samples consistent with the greater loss in weight compared with the other samples. A weight loss of between 0.5 and 2.5 wt% occurs depending upon the amount of mica associated with spodumene.

While the endothermic peak associated with the conversion of α -spodumene to β -spodumene is at around 1050 °C, there are significant differences between the thermal transformation of spodumene from Bald Hill and spodumene from Mt Cattlin. The endotherm recorded for the Mt Cattlin spodumene occurs as a doublet with a generally weaker, high temperature shoulder on the main α - β transformation endotherm (Fig. 117). Development of the doublet suggests that the α - β transformation is partly inhibited or is slowed until a certain temperature is attained before going to completion. No such doublet was

observed for the Bald Hill samples evaluated. The doublet can be attributed to the greater Fe content (1.1 – 1.6 wt%) associated with mica in the Mt Cattlin spodumene compared to spodumene at Bald Hill, with an Fe content of 0.7 wt%. The exothermic peak at around 370 °C in both sets of data in Figure 117 is attributed to the oxidation of ferrous ion in the mica as discussed earlier.

The shift in the endothermic peak position correlates with the Fe content in the spodumene structure and the Fe content of mineral impurities associated with spodumene particles (Fig. 118a). High Fe-rich mica has a significant effect on spodumene transitional temperature (Fig. 118b; Table 16). Similarly, Na, K, and Ca correlate with the thermal transformation of Fe-bearing mica contained within spodumene. Manganese that tends to be in the divalent state within micas is also oxidized and shows a similar correlation as Fe but is not as pronounced.

High-impurity contents within spodumene grains have been attributed to lower conversion temperatures (White and McVay, 1958; Salakjani et al., 2019). Spodumene is considered a poor conductor of heat and it has been inferred that elemental impurities may affect the thermal conductivity leading to faster heat transfer within spodumene (White and McVay, 1958; Botto et al., 1976). The results reported in the current study conclusively demonstrate that the exothermic reaction of the oxidation of Fe and Mn within both micas and spodumene grains promotes the thermal transformation

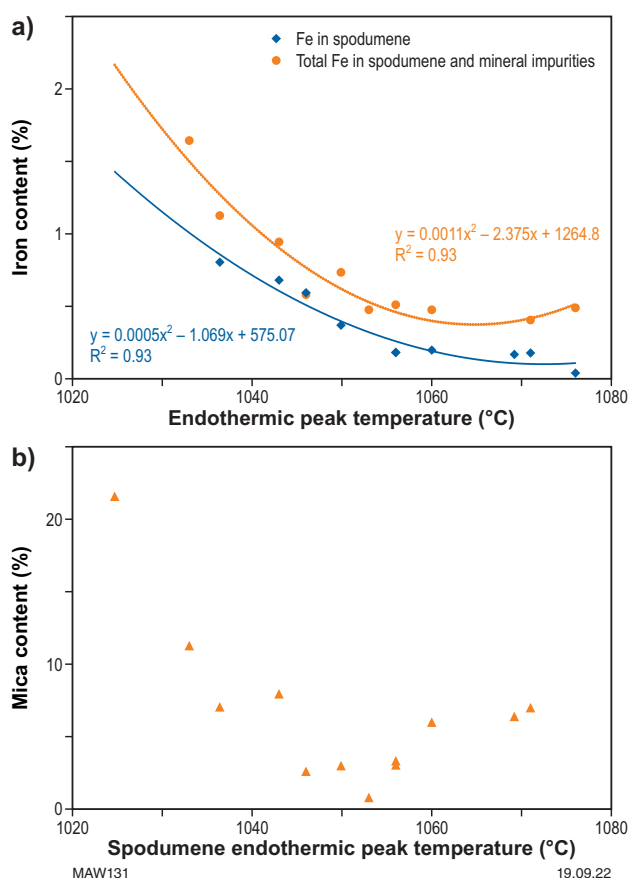


Figure 118. Correlation of the thermal α - β spodumene conversion temperature with: a) Fe content in spodumene and bulk Fe content of combined spodumene and mineral impurities; and b) mica content

of spodumene at a lower temperature. However, if mica is present in high abundance, the melts formed during the decomposition of mica at elevated temperatures can encapsulate spodumene and reduce the rate of conversion of α -spodumene to β -spodumene, as observed earlier in section, Thermal transformation of primary spodumene and altered spodumene.

Morphology and texture changes during calcination of different spodumenes

Spodumene samples of BH1300, MC200, MC300 and PIL100 depicted in Figure 110 were heated and the textures characterized at 950 °C, 1050 °C and 1100 °C to gauge the effect calcination has on different spodumene types.

Phase transformations of different spodumenes at different temperatures

The relative abundance of crystallized phases as a function of temperature for the different spodumenes is shown in Figure 119. Calcination of all spodumenes followed similar phase transitions under the heating conditions used in these experiments with the original α -spodumene transforming to β -spodumene via γ -spodumene. Mica that was observed in original samples could not be detected in the heated samples. While α -spodumene is depleted at 1050 °C, the transformation to β -spodumene is not complete with γ -spodumene present (Fig. 119). The slow transfer of heat through the coarse particles undoubtedly reduced the rate of complete conversion of γ -spodumene to β -spodumene. Extending the heating time would have completed the transformation to β -spodumene. Almost complete conversion to β -spodumene is observed in samples heated at 1100 °C. Quartz content remains similar in samples at different temperature, except for the final Pilgangoora sample that had a slightly higher quartz content than the other samples. Notably, the transformation of α -spodumene to β -spodumene appears to start at a lower temperature in the Fe-rich MC300 spodumene than for other samples, with around 20 wt% of the α -spodumene converted to γ -spodumene at 950 °C. This correlates with the effect of Fe content on spodumene thermal transformation reported in the previous section.

Physical characteristics of calcined spodumene grains

The dimensions of the spodumene blocks before and after heating were measured to track the expansion of spodumene at different temperatures. A plot of the ratio of the final volume over the initial volume as a function of temperature is shown in Figure 120. The spodumene volume remained the same up to around 1000 °C. At temperatures >1050 °C, the volume doubles in size, consistent with total conversion of α -spodumene. All calcined spodumene samples exhibited an expansion of about double the volume of the uncalcined samples. However, there is a variation in volume for the different calcined spodumene that appears related to spodumene composition as illustrated in the next section.

The results are consistent with that reported by Salakjani et al. (2016), who observed that the specific gravity of α -spodumene converted to β -spodumene decreased from

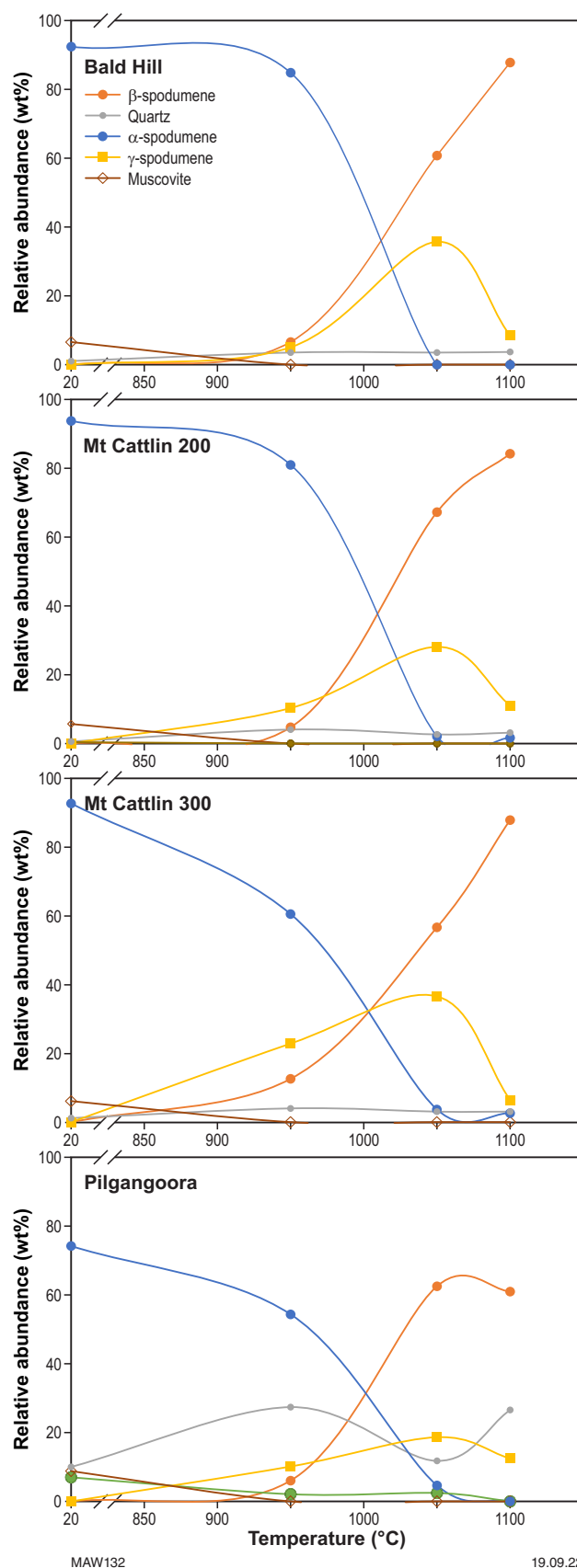


Figure 119. Relative weight percentage of crystalline phases from Rietveld analysis as a function of temperature for different spodumene samples heated in a muffle furnace (samples heated at 20 °C/min and then held at fixed temperature for two hours before cooling at 20 °C/min)

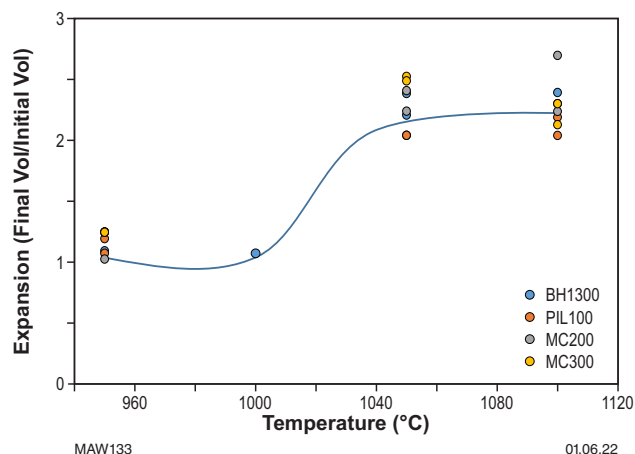


Figure 120. The volume change in spodumene vs temperature. Volume change is expressed as a ratio of final volume after heating over the initial volume of unheated spodumene (samples heated at 20 °C/min and then held at fixed temperature for two hours before cooling at 20 °C/min)

about 3.2 g/cm³ to around 2 g/cm³, and with an apparent increase in surface area from 0.1 to 1 m²/g.

Surface morphology and textures of calcined spodumene samples

Optical images of different spodumene samples before and after heating show marked differences in the appearance between the different samples of spodumene (Fig. 121). At temperatures >1000 °C, the white spodumene samples (Bald Hill and Mt Cattlin) produced a white, chalky product. A light-brown, glassy melt phase was observed to have formed on the white calcined spodumene, whereas the glassy phase that formed on the purple spodumene is light-yellow. At 950 °C, the white spodumene samples have a marbled, mottled appearance. In contrast to the other spodumenes, the calcined green spodumene (MC300) is light-brown with a woody appearance, which was observed under all heating conditions (950 °C, 1050 °C and 1100 °C). The dark-black, 'burnt-out' regions within the calcined green spodumene, MC300, are associated with K, Fe and Mn mica (celadonite) inclusions, which were oxidized during heating. Cross-sections of the calcined particles from Mt Cattlin (MC300) and Bald Hill (BH1300) have an iron stained appearance, whereas the purple Pilgangoora spodumene remained white. The calcined green Mt Cattlin spodumene is significantly darker brown in colour than calcined BH1300 and MC300 samples (Fig. 121).

BSE images (Fig. 122) reveal the calcined spodumene particles have fragmented surfaces. The calcined green spodumene (MC300) shows fine, iron oxide particles, which appear attached and imbedded within the calcined spodumene surface, indicating exsolution and oxidation of Fe from spodumene during heating. Some fine particles of iron oxide were observed in the other calcined spodumene samples but were not as abundant as for the calcined spodumene, MC300.

The smooth, porous melt coats the calcined spodumene grains as illustrated for white (BH1300) and purple (PIL100) spodumenes (Fig. 121). EDS analysis confirmed the

composition of these melts to be K and Mg-rich aluminium silicate, similar to that observed for mica in the original unheated spodumene (Table 16).

Figure 123 shows the effect that Fe content in spodumene has on the calcined particle morphology. Apart from causing Fe oxide staining on calcined grains, the highly exothermic nature of the oxidation of Fe during calcination causes the calcined spodumene to disintegrate into small particles. Hence, during the calcination step to convert spodumene into the β -form, high-Fe spodumene is likely to create issues with the management of finer particles in both the calcination and the acid-bake leach. The fine particles will also create issues (blockages) with the filtering of solids to recover the liquor for lithium recovery. Hence, some control on the rate of heating and oxidation during the calcination process of high-Fe spodumenes (>~0.5 wt%) may be required to reduce the development of fines.

Textures of calcined spodumene at different temperatures

Samples of the Mt Cattlin, high-grade spodumene were heated for two hours in a muffle furnace at a range of temperatures (950 °C, 1050 °C and 1100 °C) separately and mounted in cross-section to study the calcined texture. BSE imaging and TIMA mineral distribution mapping of the internal structure of calcined Mt Cattlin (MC200) illustrates the development of melt formation and changes in spodumene texture with increasing temperature (Fig. 124). At 950 °C, spodumene in the α -form is stable, with only minor melt formation occurring along cleavage-controlled cracks (Fig. 124a). At 1050 °C, α -spodumene has mainly converted to β -spodumene that is less 'massive' in appearance with marked porosity and contains patchy melt developed with a vesicular nature (Fig. 124b). At 1100 °C, spodumene exists in the β -form and is significantly fragmented, together with fluid-flow textures, such as vapour bubble casts encapsulated by melt formation (Fig. 124c).

Band contrast imaging and orientation maps reveal the calcined spodumene particles, in the Mt Cattlin example (MC200), consist of fine crystallites in different orientations (Fig. 125). At 1050 °C, calcined grains are predominately β -spodumene (blue in phase map) with some relict γ -spodumene (yellow in phase map) dispersed irregularly. At temperatures above 1050 °C, the melted mica (yellow) is mobile and forms liquid coatings in fractures and pores of the calcined spodumene as discussed in the next section.

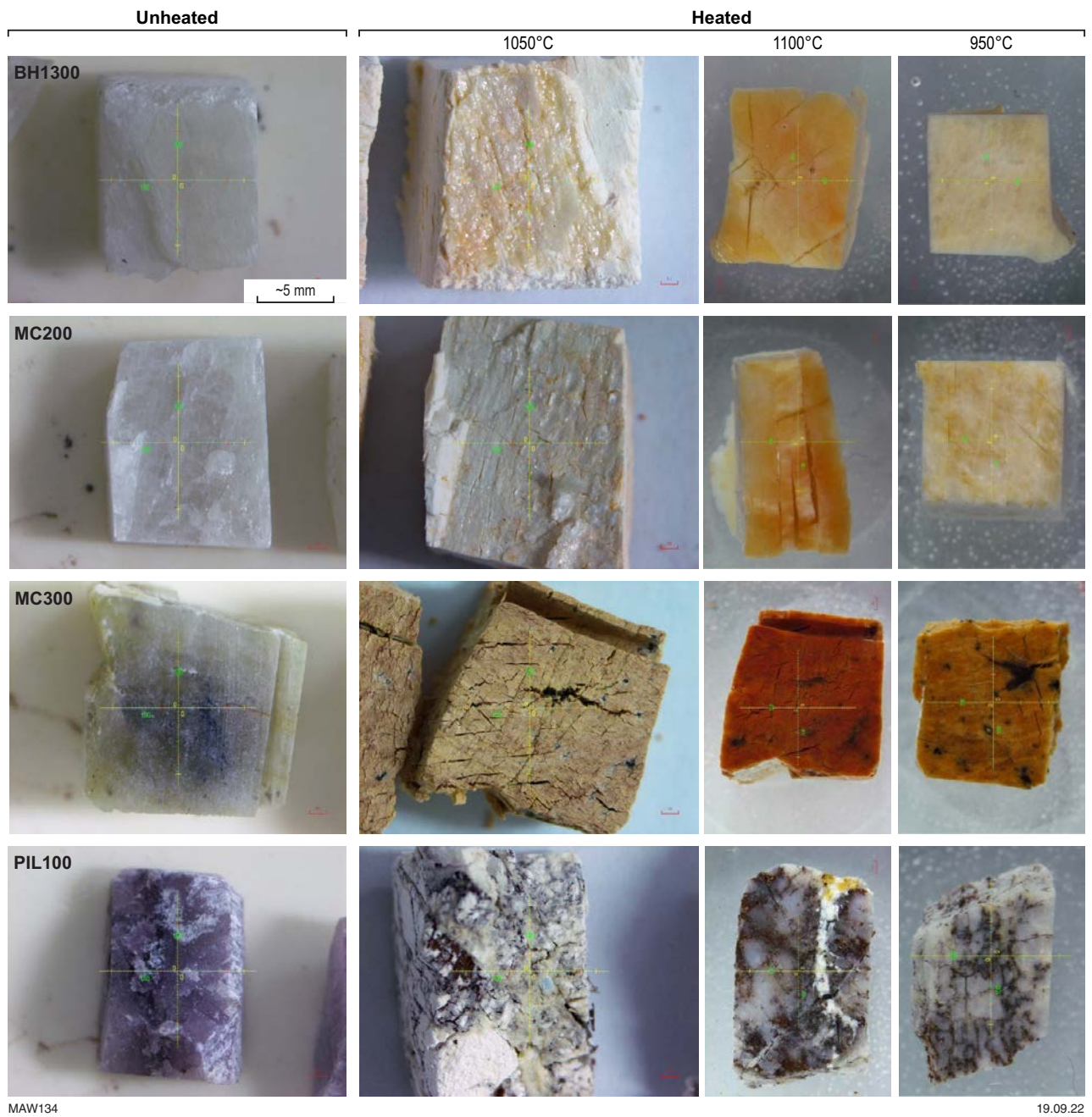


Figure 121. Optical images of sample blocks of spodumene (BH1300, MC200, MC300, PIL100) before and after heating at 950 °C, 1050 °C and 1100 °C. Cross-sections of blocks after heating are also shown

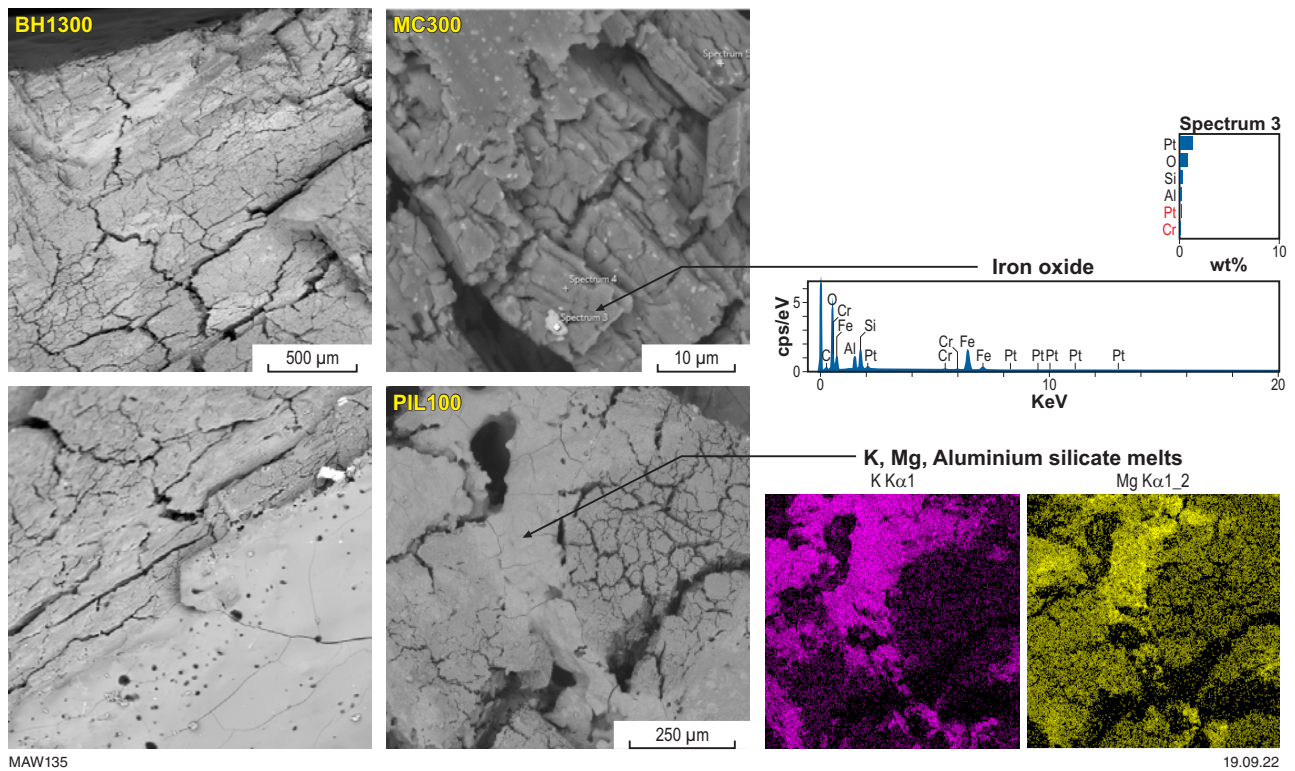


Figure 122. Backscatter electron micrographs showing the fragmented surface of calcined spodumenes following heating and conversion to β -spodumene at 1100 °C. MC300 shows surficial formation of fine iron oxide particles, which is confirmed by EDS analysis. A smooth, porous melted phase coats part of the calcined spodumene in BH1300. EDS elemental distribution maps show the melt phase formed at the surface of PIL100 contains K and Mg

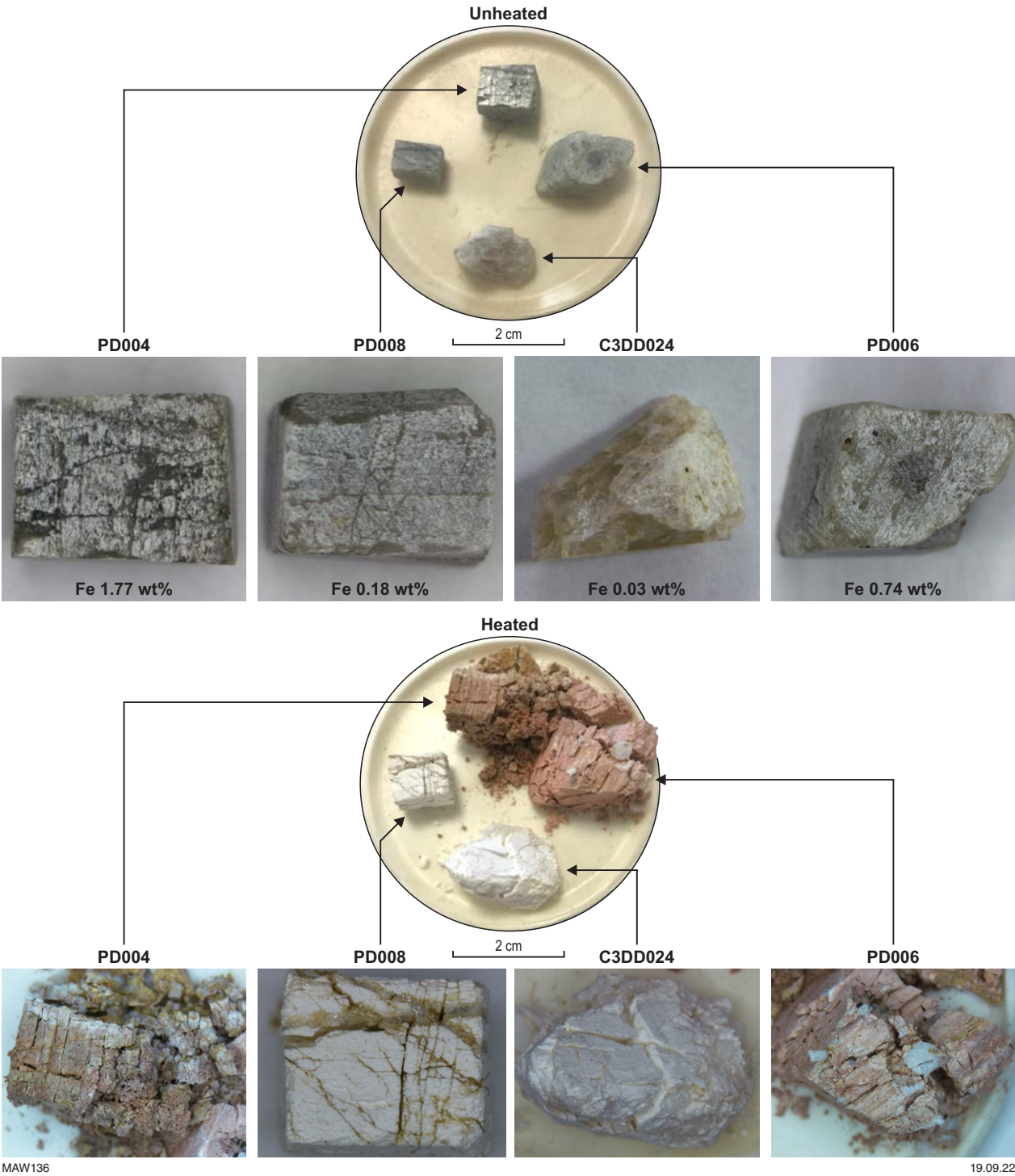


Figure 123. Optical images of sample blocks of spodumene with different Fe contents before and after heating at 1050 °C. Note spodumene with high Fe content fragments into finer particles during heating

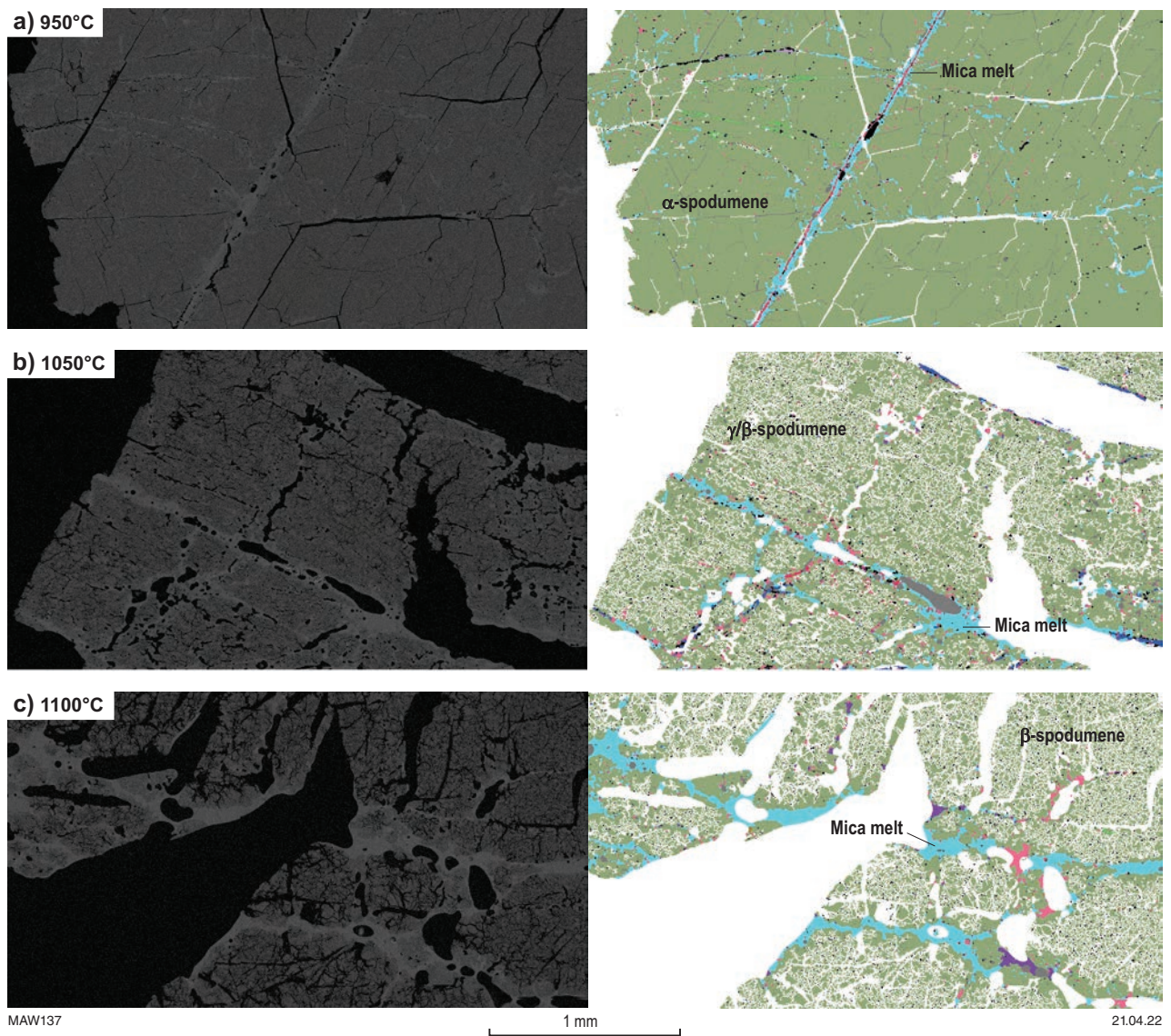


Figure 124. Backscatter electron micrographs and mineral composition maps showing a cross-section of calcined spodumene heated at different temperatures (MC200) (spodumene – green, melted mica – blue)

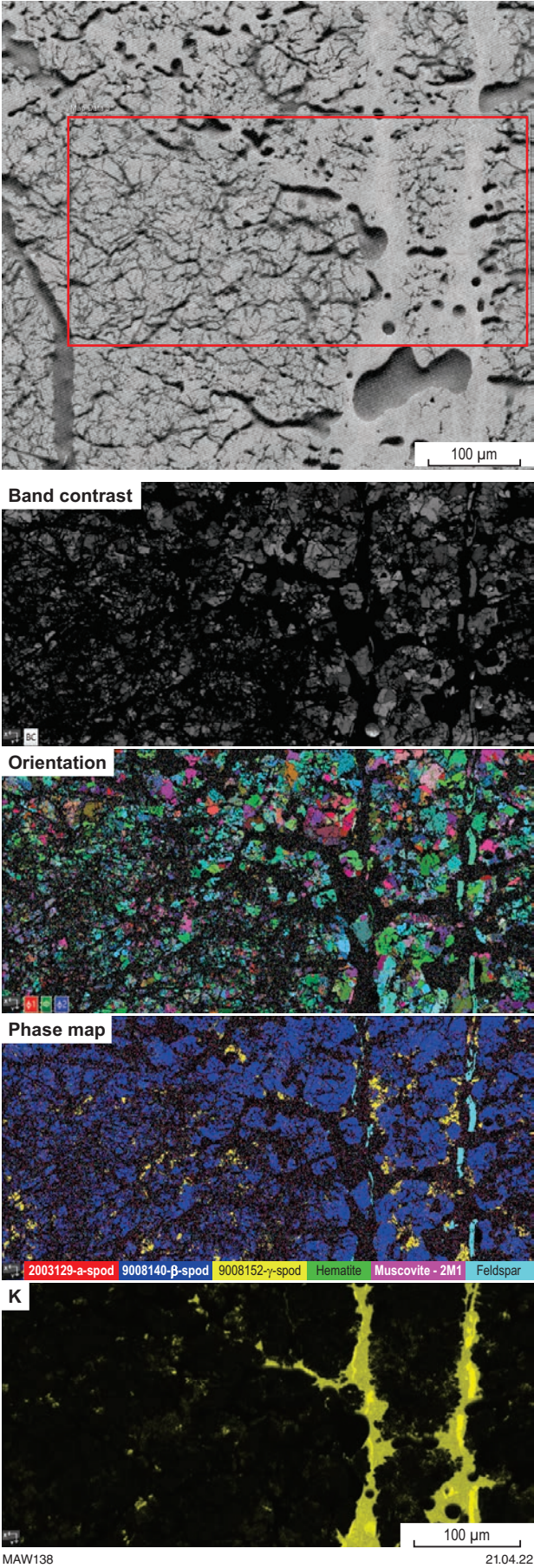


Figure 125. Backscatter electron micrograph images together with band contrast, orientation, phase (blue – β -spodumene) and K-K α EDS maps of a cross-section of spodumene calcined at 1050 °C

Partial melting of mica in calcined spodumene

The composition of mica associated with spodumene in the samples examined is markedly varied. Figure 126 shows the melting product of two micas associated with spodumene samples, MC300 and MC200. In both cases, the melted

micras have coated the calcined spodumene under the conditions used to promote the α - β transformation. The black-sintered ('burnt-out') regions observed in the calcined MC300 spodumene sample is associated with the oxidation of Fe(II) and Mn(II) during mica decomposition, resulting in the formation of fine (1–10 μm) particles of Fe and Mn oxides. EBSD analysis reveals the Fe and Mn particles have

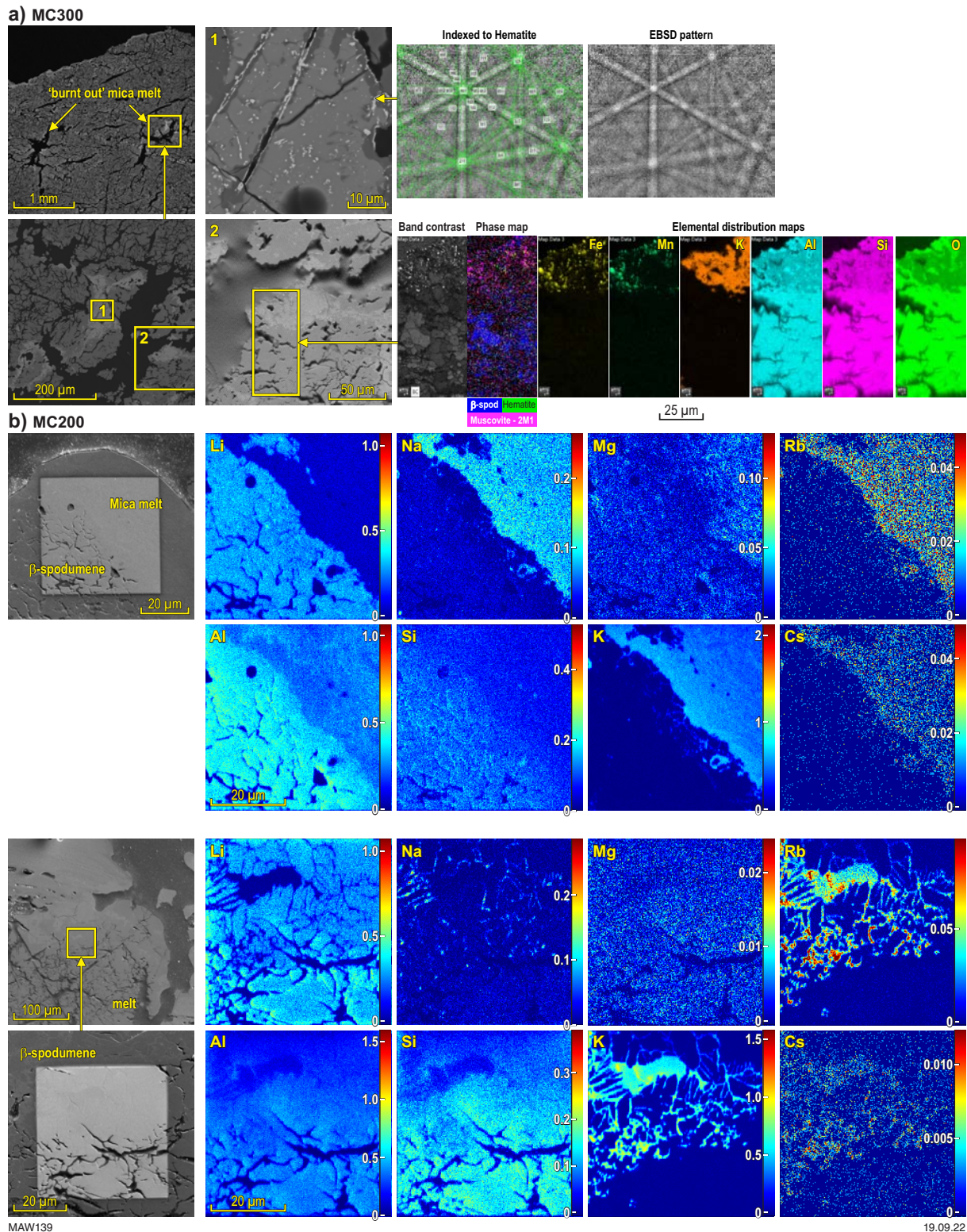


Figure 126. Backscatter electron micrographs showing regions of partial melting of mica coating and encapsulating spodumene: a) Fe and Mn oxide grains in matrix of melt coating spodumene in burnt-out regions of the calcined particle (1050 °C); b) K, Si and Al-rich melt coating on the edge of calcined spodumene

a hematite structure. As illustrated in the band contrast, phase and elemental (EDS) maps, Fe- and Mn-rich, hematite particles are concentrated along the edge or suspended in the K-, Si- and Al-rich melt matrix, coating the β -spodumene surface (Fig. 126a). The black-sintered regions within the calcined spodumene particles result from the highly exothermic reaction of the oxidation of ferrous ion and Mn from mica.

For sample MC200, ToF-SIMS analysis reveals the melt phase coating the porous, calcined spodumene surfaces is enriched in Mg, K, Cs and Rb associated with melted potassium–magnesium–aluminium–silicate mica inclusions (Fig. 126b). The mica contains no detectable Fe and there is no evidence of black-sintered regions within spodumene particle. Similar findings were observed for micas calcined with spodumene in samples BH1300 and PIL100 (Fig. 127).

Primary muscovite and secondary micas generally follow similar decomposition trends. However, during calcination

muscovite appears to retain much of its morphological structure as observed in Figure 128, relative to the more reactivated secondary micas with higher Fe, Mg and Na abundances. The presence of muscovite particles in the kiln is not desirable as they will be prone to become airborne and would likely end up near the hot flame zone at levelled temperature ($\sim 1800^\circ\text{C}$) of the rotary kiln.

It is well known that Fe has a marked effect on the thermal decompositional behaviour of mica minerals (Schomburg and Zwahr, 1997). As observed in the DTGA curves, the exothermic reaction of the oxidation of ferrous ion within mica promotes the dehydroxylation of mica and ultimately melt formation. Mica decomposition has been reported to occur via a topotactic breakdown mechanism with the oxidation of Fe and Mn cations and their displacement from the mica octahedral structural layer (Barlow and Manning, 1999). The production of Fe and Mn oxide within micaceous melt zones, within calcined spodumene, was illustrated in

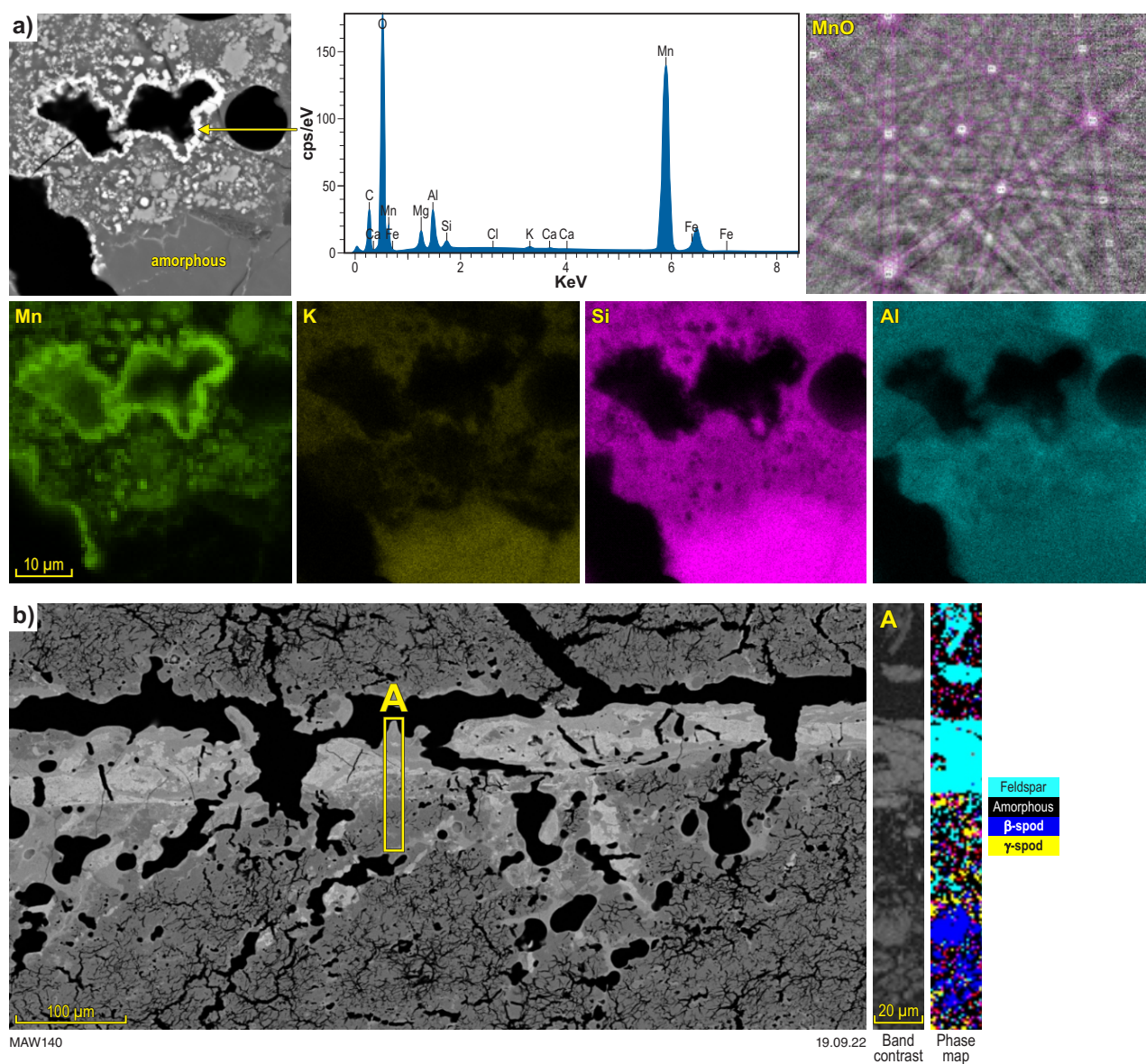


Figure 127. Backscatter electron micrographs showing regions of partial melt of micas coating and encapsulating spodumene: a) Fe and Mn oxide grains in matrix of melt coating spodumene in burnt-out regions of the calcined particle (1050°C); b) K, Si and Al-rich melt coating on the edge of calcined spodumene

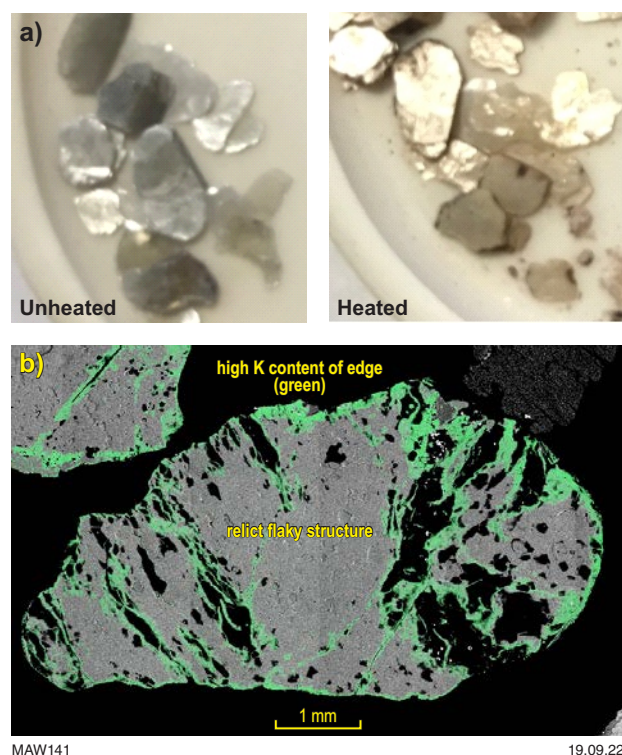


Figure 128. Optical images of: a) muscovite before and after heating; and b) backscatter electron micrograph of a cross-section of calcined muscovite showing partial melting and retainment of mica structure (1100 °C)

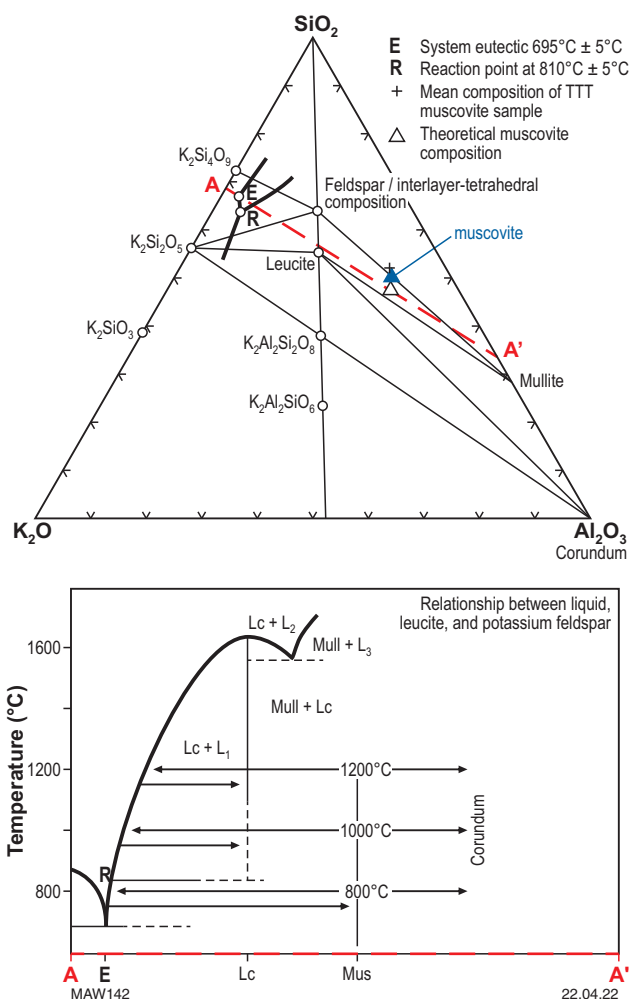
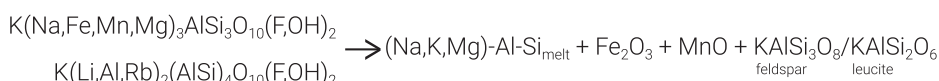


Figure 129. Ternary diagram for the system $K_2O-Al_2O_3-SiO_2$ and temperature and phase dominance graph show the impact of temperature on mineral composition

earlier figures. The formation of the melt phase is attributed to a combination of interlayer cations (K, Mg, Na) and the breakdown of the tetrahedral sheets:



The ternary diagram for the system $K_2O-Al_2O_3-SiO_2$ predicts that the composition of the first melt to form from a feldspar composition would contain 30% K_2O , 67% SiO_2 and 3% Al_2O_3 (point E) (Fig. 129). Melting contributes to the formation of clinker which tends to line the internal surface of the calcine roaster. Hence, the mica content needs to be limited.

Feldspar in calcined spodumene

Feldspar (albite and microcline) exists as coarse primary grains and fine secondary veins in the spodumene samples examined. The effect of calcination on coarse-grained and vein feldspar/mica in cross-sections of sample BH1300 is shown in Figure 130. In all calcined samples heated above 1050 °C, coarse feldspar, present as inclusions in spodumene, appear as fractured particles. In the example shown in Figure 130a, feldspar occurs as albite and orthoclase. Clear contacts across boundaries indicate no interaction of feldspar with calcined spodumene. In mica (K,

Mg, Na-rich) and Ba-rich feldspar veins, the mica has altered to an amorphous melt phase with relict feldspar (Fig. 130b).

Feldspar is observed to undergo partial melting over a large temperature interval (1060 °C to 1200 °C) that overlaps spodumene transformation. Studies reported by Peltosaari et al. (2015) observed particle agglomeration in spodumene concentrates from the partial melting of gangue-based alkali-feldspar at temperatures above 1025 °C. In the temperature range (950–1100 °C) observed in this study, feldspar appears to only have fractured with no obvious melted phase. This is probably due to slow heat transfer through the coarse particles used in these tests and the slow heating rate. It has been reported that increasing the heating rate increases the melting point of feldspars, but also increases the rate of melting (Johnson and McCauley, 2005). Hence, if calcination temperature can be suitably controlled, the effect of feldspar melting can be mitigated. Like micas, melted feldspars would contribute to the formation of clinker in furnaces.

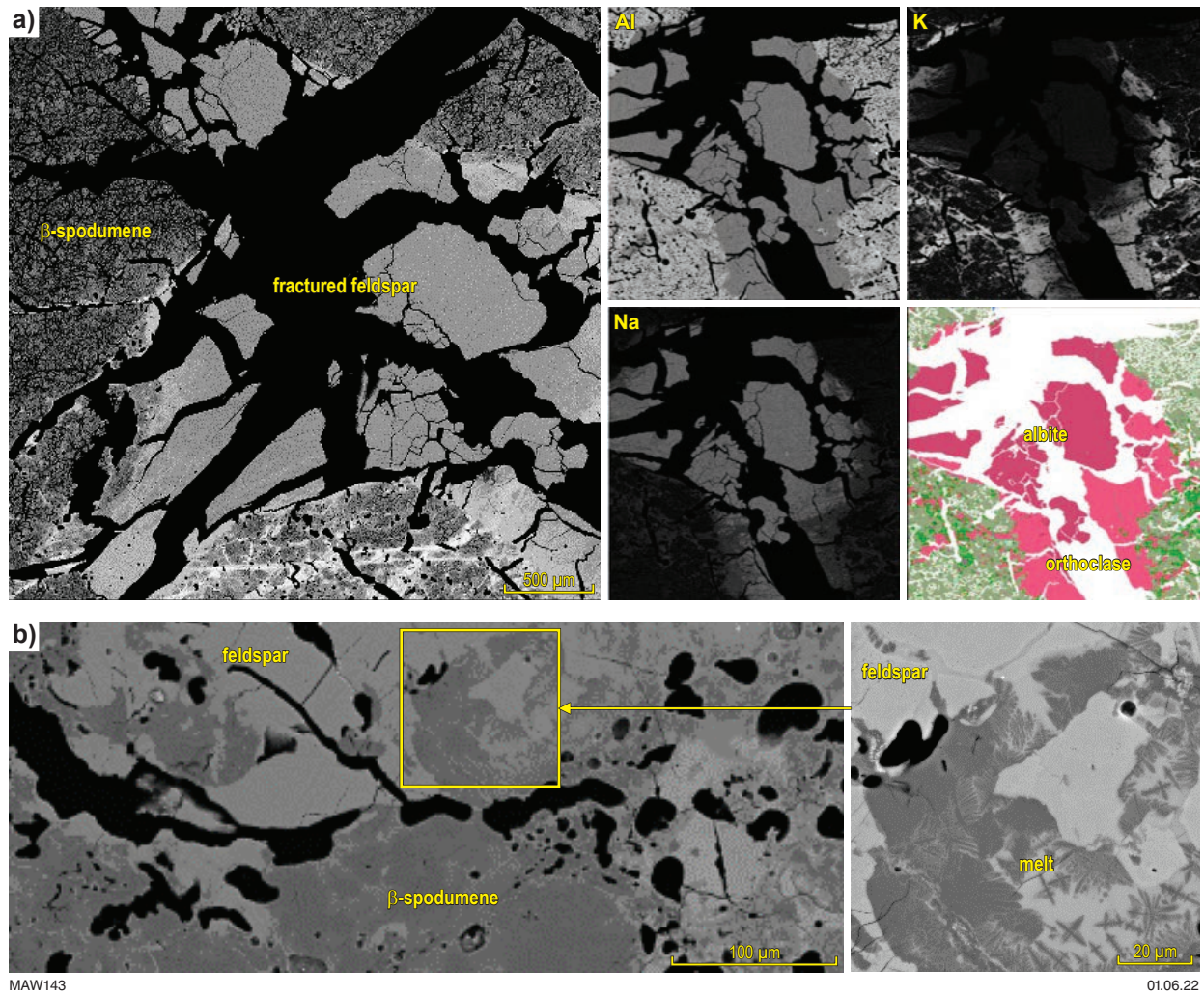


Figure 130. Backscatter electron micrographs of a cross-section of calcined spodumene showing fractured feldspar particle a) and partial melted feldspar and mica mixture b) along a fracture in calcined spodumene particle (1050 °C, BH1300)

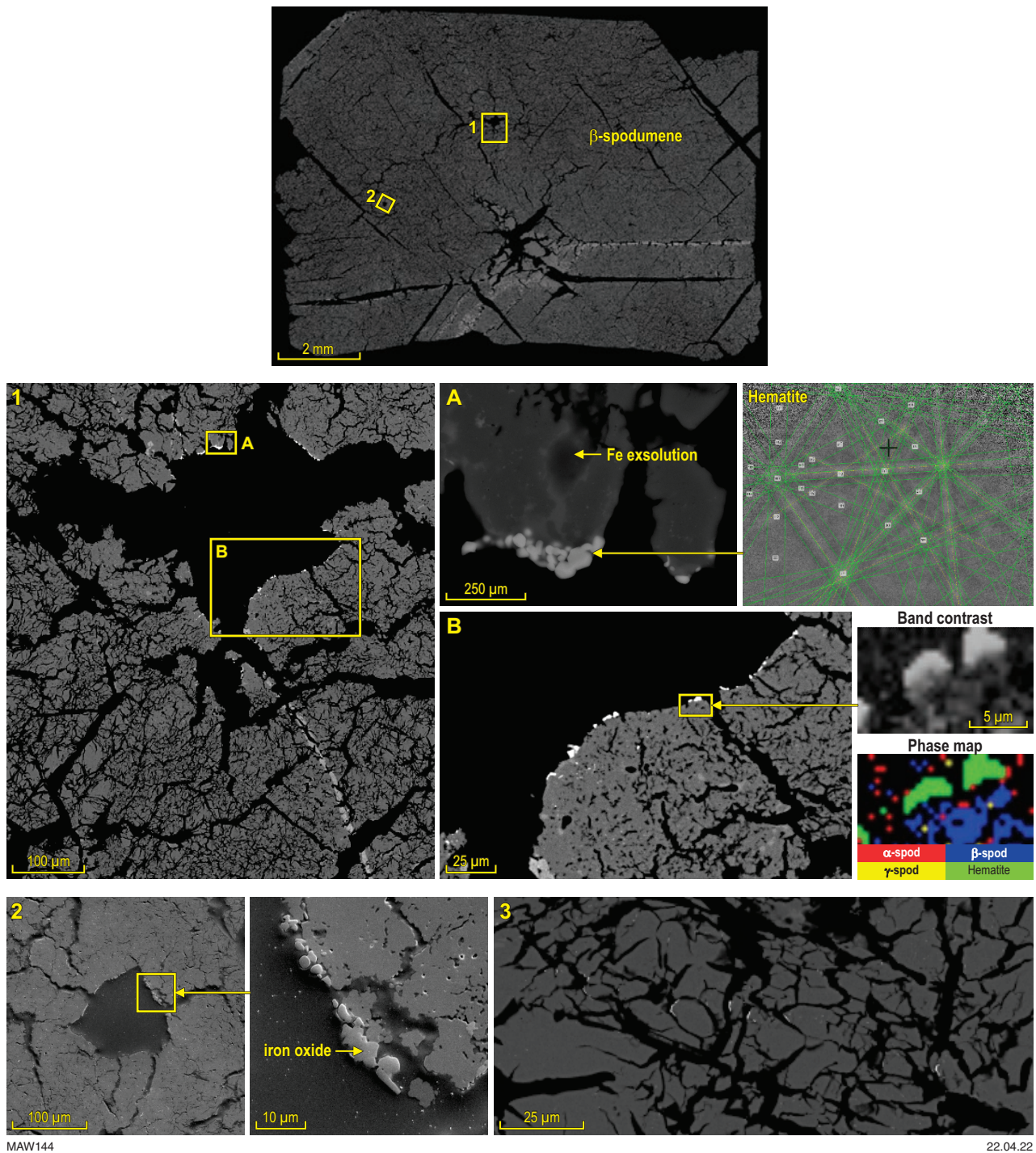


Figure 131. Backscatter electron micrographs showing cross-sections of calcined spodumene and exsolution of iron-oxide grains (1 and 2) on the edge of open vented structures within β-spodumene particles from sample MC300 (1050 °C). The calcination texture shown in (3) is from another calcined particle from MC300 (not shown here)

Exsolution and oxidation of iron from calcined spodumene

As observed in the laser ablation data earlier, the Fe content of α -spodumene examined in this study varied between 500 and 4000 ppm. Surface imaging of calcined Fe-rich spodumene, such as the MC300 sample, revealed finely disseminated ($\leq 5 \mu\text{m}$), roundish grains associated with ‘holes’ in the former, calcined spodumene. EBSD analysis reveals the Fe-oxide particles have a hematite structure attached to the edge of β -spodumene (Fig. 131–1). The BSE image shows evidence of exsolution, migration and cementation of Fe-oxide grains where high, BSE contrast, vein-like structures within β -spodumene can be observed to develop and congregate into grains (Fig. 131–2). It is inferred that during calcination ferrous ions present in monoclinic α -spodumene are exsolved and oxidize to a ferric oxide (hematite) phase during the conversion to tetragonal β -spodumene.

Quartz in calcined spodumene

Quartz undergoes an α - β crystal inversion at 573°C (Schelz, 1976). Interactions of α - β quartz conversions and α -spodumene reactions have been observed in rapid heating tests in fine particles (Abdullah, et al., 2019). In this study, quartz appeared fractured but no real interaction between quartz and spodumene transformation was observed in the coarse particles examined and temperature range of experiments.

Calcination of other gangue minerals

Depending upon the efficiency of the concentrator during the beneficiation step, spodumene concentrates can also contain other unwanted gangue materials, including country rock (e.g. basalts containing amphiboles, calcium-rich feldspar and biotite).

Table 17. Mineral transformation of other minerals at different temperatures

Mineral	Temperature ($^\circ\text{C}$)	Comments
Tourmaline	950	Dehydroxylation ($>980^\circ\text{C}$ with higher Mg content), melting, F and B_2O_3 escape
Amphibole	400–800, >850	Ferrous oxidation (oxidative conditions) Dehydroxylation, meta-phase transformation
Apatites	~ 1600	Melting
Biotite	500–600, 900–1200	Oxidation of ferrous iron, dehydroxylation, phlogopite decomposition
Limestone	~ 900	Decomposes to $\text{CaO} + \text{CO}_2$ influenced by CO_2 partial pressure
Gypsum	60–150, 105–240, >1200	Forms hemihydrate ($\text{CaSO}_4 \cdot 0.5\text{H}_2\text{O}$) Forms anhydrite (CaSO_4) $\text{CaSO}_4 \rightarrow \text{CaO} + \text{SO}_2 + 0.5\text{O}_2$
Clays	530–630	Dehydroxylation
Lepidolite	883	Dehydroxylation, release of HF, decomposition
Zinnwaldite	300, 300–800, 800, 900	Oxidation of ferrous ions, dehydroxylation release of HF, decomposition
Pollucite	>1400	Stable at high temperature

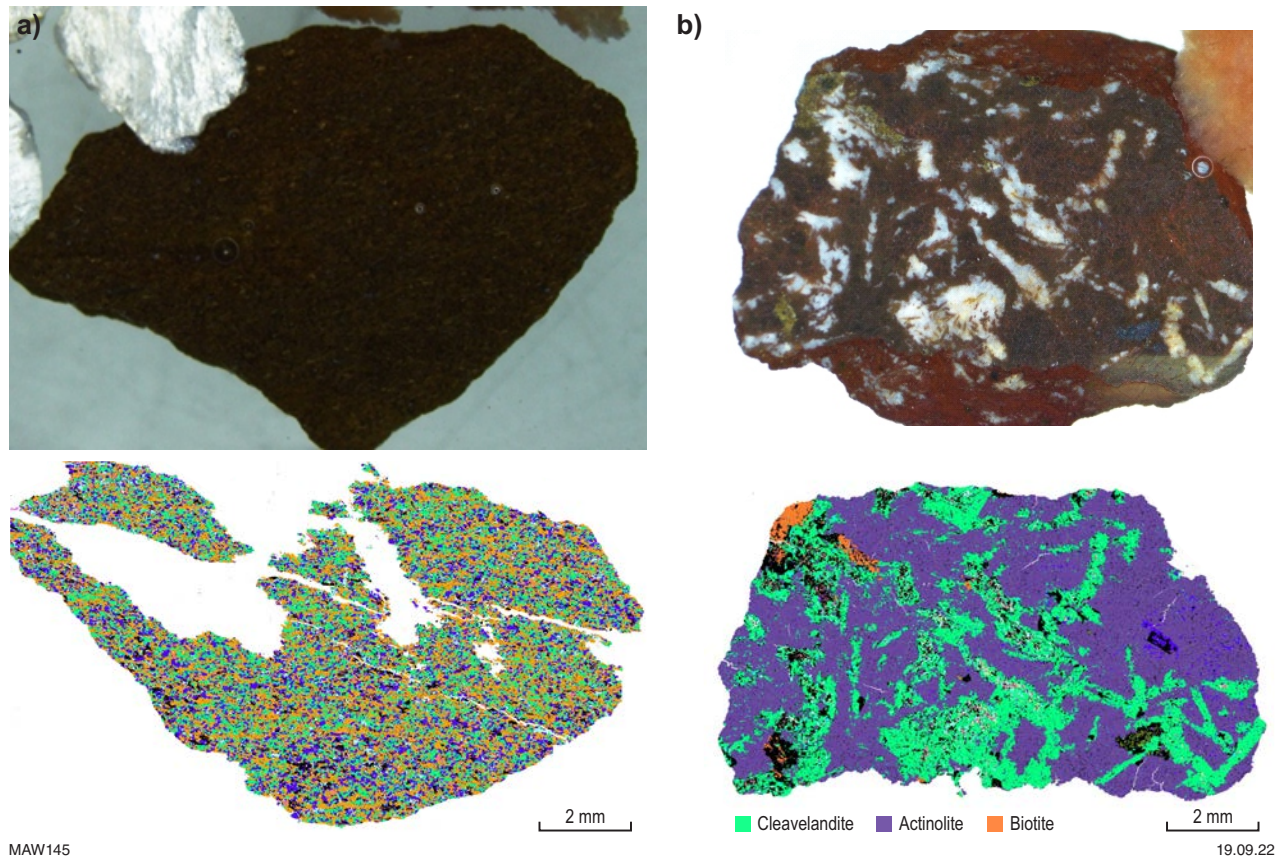
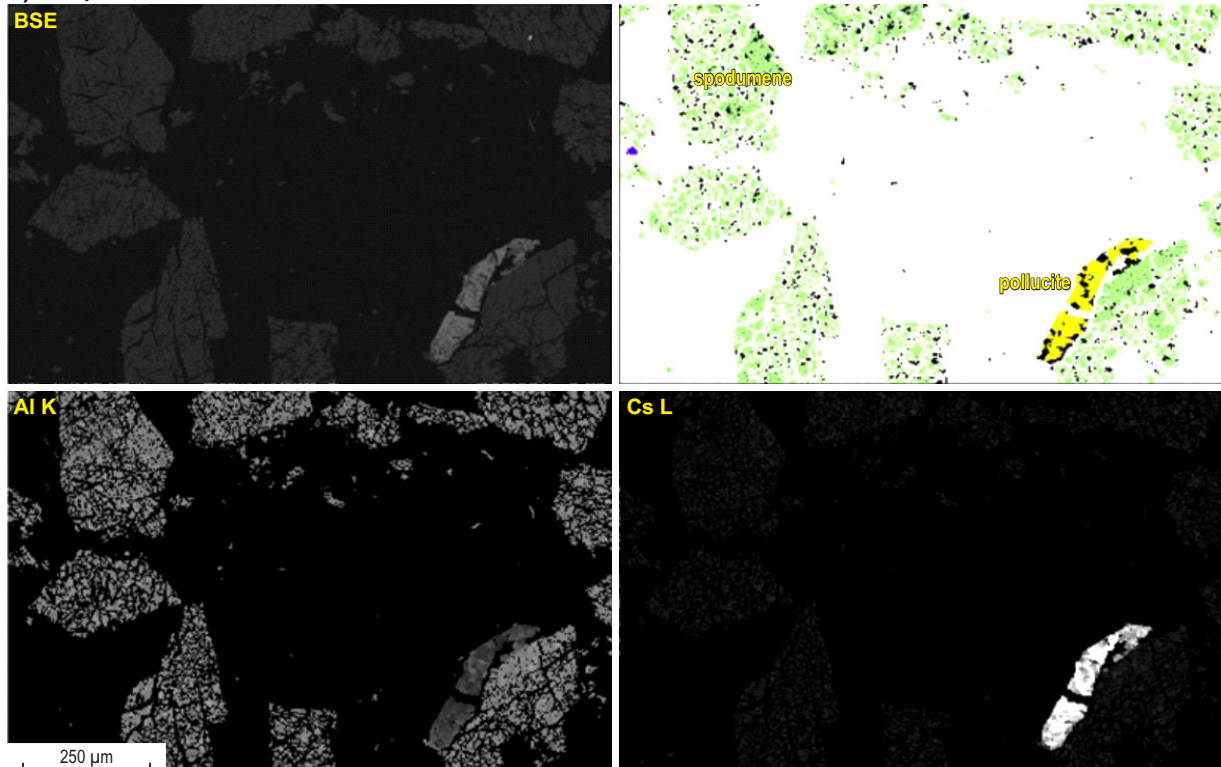
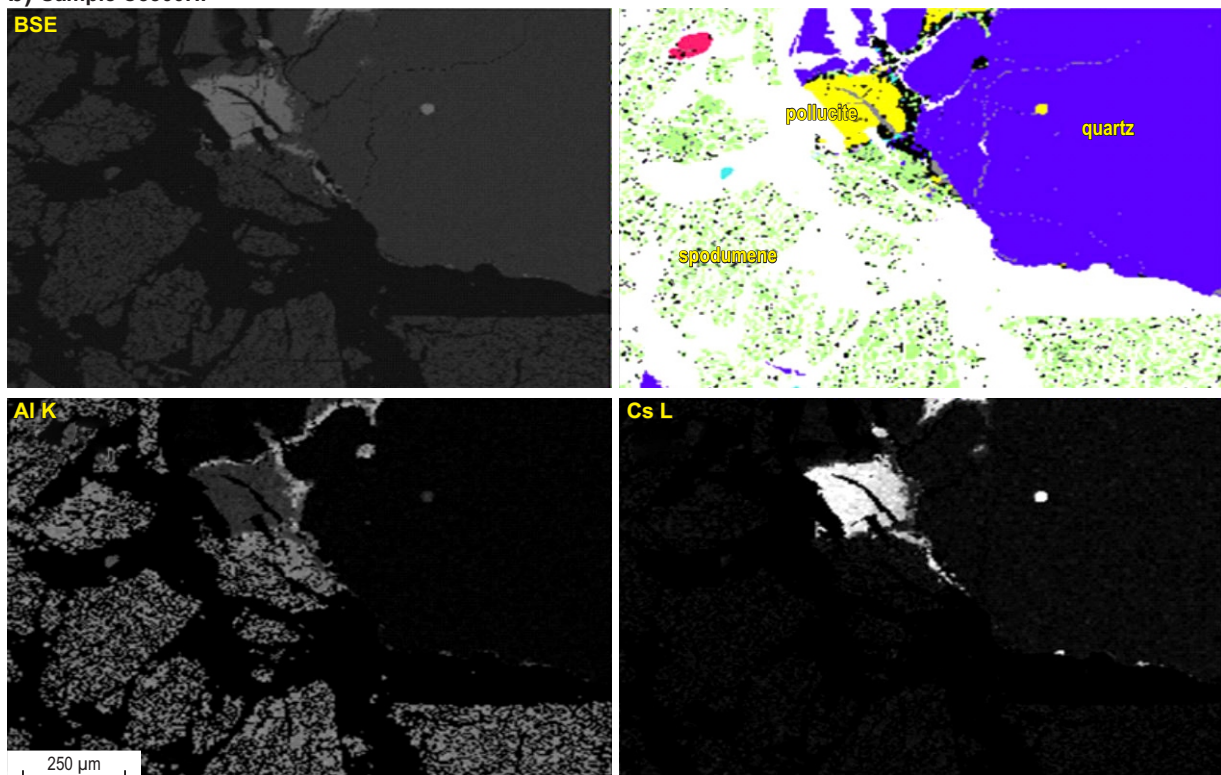


Figure 132. Optical images and mineral composition maps of country rock in: a) Mt Cattlin; and b) Bald Hill samples

a) Sample C1100P**b) Sample C3300HP**

MAW146

19.09.22

Figure 133. Backscatter electron images, mineral composition maps, and Al and Cs element maps showing the association and presence of pollucite (yellow) with β -spodumene in Greenbushes samples (1050 °C): a) C1100P; and b) C3300HP samples

Samples of country rock heated under conditions favourable for the transformation of α -spodumene to β -spodumene are shown in Figure 132. While minerals present in the samples appear to have undergone significant change, the overall rock particles appear to remain intact. Hence, providing the temperature range in the furnace is controlled to around the spodumene α - β transformation temperature, the impact of country rock materials may be minimal.

Pollucite is reported to be stable up to 1400 °C (Vance et al., 1981). Figure 133 illustrates pollucite observed in Greenbushes samples remains unaltered and stable under the calcine conditions. Hence, it will report as pollucite to the acid-bake leach step.

Table 17 shows the mineral transformation of other minerals observed in pegmatite ores at different temperatures. With the exception of apatite and pollucite, all other phases have decomposition temperatures below that of the optimum α - β spodumene calcined temperature.

Lithium extractability of different lithologies by conventional calcination and sulphate-roasting method

A two-stage calcination – sulphate-roast testing procedure was used to simulate and assess the Li-extraction process for ores with different lithologies.

Key findings

Factors identified that affect the extraction of lithium from the samples evaluated are as follows:

- Mica melt encapsulation of the spodumene grains prevents lithium extraction.
- Slow rate of diffusion of acid into large particles to facilitate lithium extraction.
- Potentially insufficient acid for dissolution of lithium and other acid soluble phases.
- Incomplete conversion of γ -spodumene to β -spodumene during calcination may have contributed to poor lithium extraction during the acid-baked and water-leaching stage.

Sample selection

Eight samples from those illustrated in Table 9 were selected to study and compare the calcination and leaching properties of different pegmatite ores. The mineral abundance of samples chosen for this study are shown in Figure 134. The samples show a range of common mineral impurities in addition to the main Li-bearing mineral spodumene.

The samples were treated as received, without any upgrade to allow the determination of the effect of gangue minerals have on the calcination and sulphate baking process, as well as the liberation and extraction of lithium from spodumene.

Calcination and sulphate roasting for lithium recovery methodology

Figure 135 outlines the test procedure used for evaluating lithium recovery.

Selected samples from different deposits with different lithologies were examined in the following way:

- **Calcination** – Approximately 250 g of sample (particle size 1–4 mm) on a flat ceramic plate was placed directly in a muffle furnace set at 1100 °C. The timer was started once the furnace had equilibrated to 1100 °C. After two hours, the calcined sample was removed and left to cool under ambient conditions.
- **Sulphate roasting** – Calcined samples were acid baked according to the optimum conditions observed in a study involving feed from Greenbushes and reported by Salakjani et al. (2019). The acid dosage was set to 180% of the stoichiometric acid dosage (0.9 mol H_2SO_4 /mol Li) based on the Li grade of the sample with the highest grade, which equated to 46.5 g acid per 100 g ore. Samples were baked at 250 °C for one hour. Acid bakes were carried out in two batches of six. Approximately 18 g of Li concentrate was added to each crucible, followed by ~8.4 g of concentrated sulphuric acid. The concentrate and acid mixture were mixed for around 30 seconds with a glass rod. The samples were not ground. The crucibles were inserted into the furnace over the span of around five minutes and the timer started once the last sample had been inserted. After one hour, the crucibles were removed and allowed to cool for 20 minutes.

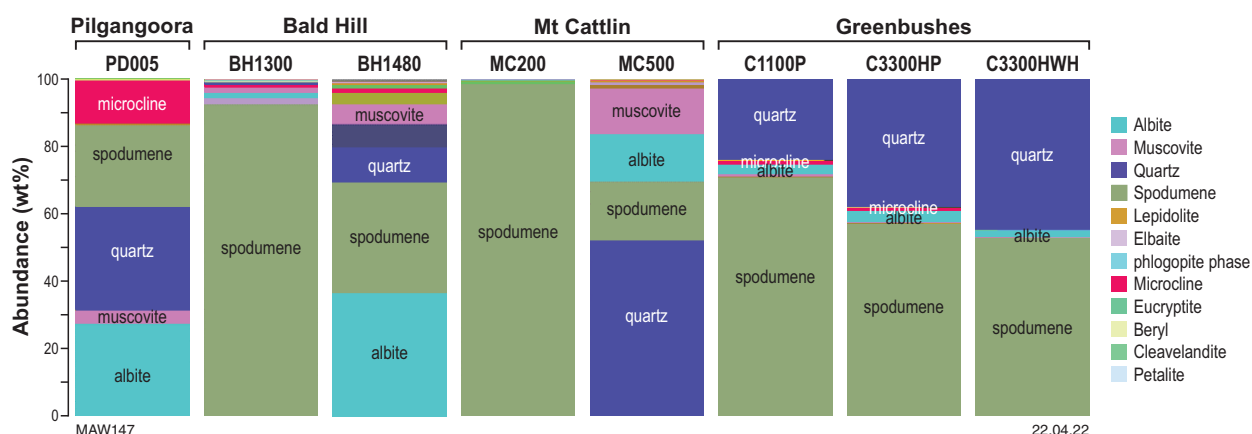


Figure 134. Mineral abundance of samples chosen for calcination and sulphate-roast evaluation showing variations in mineral composition

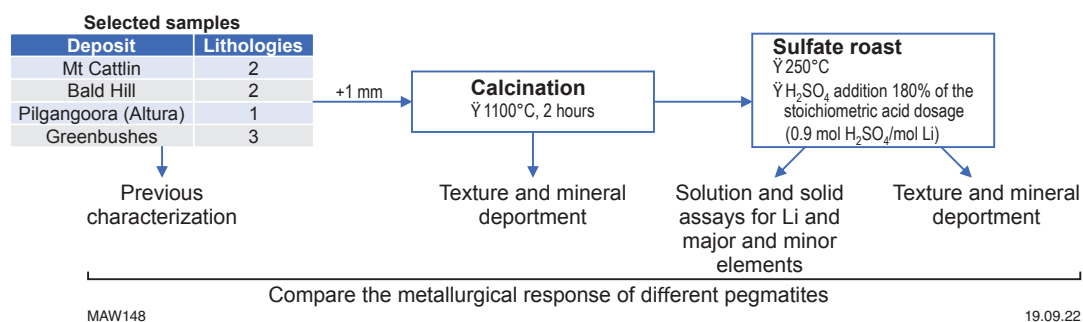


Figure 135. Outline of sample calcination–sulphate-roast testing and test work for characterization of ore materials

- Lithium extraction** — Water leaching was carried out at 50 °C for two hours, with leaching commencing 30 minutes after the crucibles had been removed from the calcination furnace. A mass of 20–25 g of baked concentrate (all that could be removed from the crucible) was added to 100 mL of deionized water in a 250-mL conical flask and placed in a water bath/shaker set to 50 °C for two hours. As with the acid-bake treatments, leaching was carried out in two batches of six, with leaching commencing 30 minutes after the removal of the baked samples from the furnace.

Both sulphate roasting and leaching were carried out using Murdoch University facilities under the supervision of Prof Alek Nikoloski. Polished mounts of samples before and following treatment were produced and examined for textural, compositional and mineralogical changes. Compositional and structural changes in minerals were evaluated using a combination of TIMA, XRPD and FIB-SEM with ToF–SIMS instruments.

Comparison of the calcination properties of different deposits

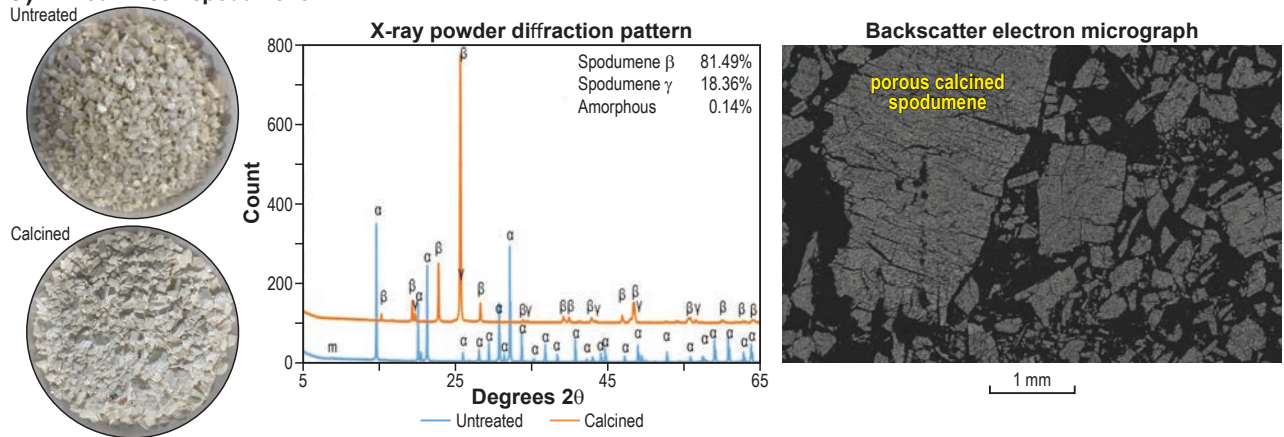
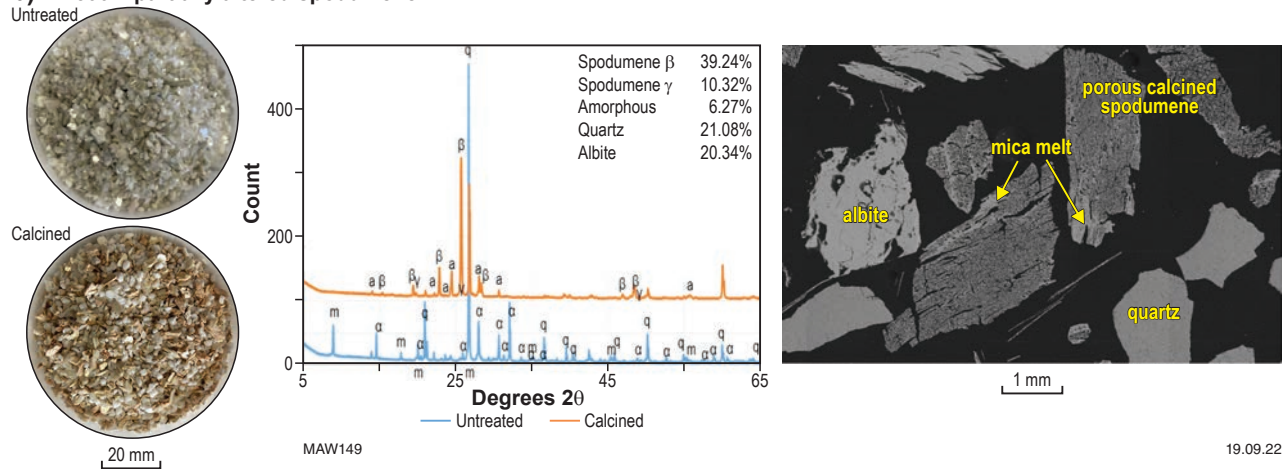
Figures 136 to 139 show images of untreated and calcined sample grains, together with XRPD patterns and BSE micrographs of calcined particle cross-sections for the different orebody samples.

Figure 136 shows the effect of calcination of an unaltered spodumene (MC200) and partially altered spodumene (MC500) from Mt Cattlin following heating to 1100 °C. The white, unaltered spodumene (MC200) yielded a chalky, friable, white product, whereas the greenish, partially altered spodumene (MC500) produced a brown product. Quartz present in the sample remains white. Muscovite present in the altered spodumene sample is also a brownish colour. XRD studies reveal around 80% of α-spodumene was converted to β-spodumene, with the balance converted to γ-spodumene. The BSE micrograph of cross-sections of grains shows that the calcined spodumene particles have uniformly porous textures, with expansion cracks associated with expansion of spodumene from calcination. The mica associated with the partially altered spodumene (MC500) has decomposed to a melt structure similar to that shown in the section Partial melting of mica in calcined spodumene and altered spodumene. Albite present in sample MC500 has partially melted.

The calcination of Bald Hill unaltered spodumene (BH1300) and partially altered spodumene (BH1480) resulted in the samples exhibiting similar products and textures as the Mt Cattlin samples (Fig. 137). However, the BH1480 sample that contains feldspar and micas, as well as the Li-, Mn-phosphate mineral (sicklerite), show dark-brown and black calcined grains, in addition to the chalky, friable, white product. The dark-brown and black calcined grains are associated with the highly exothermic oxidation of Fe within gangue minerals during calcination, to produce a burnt texture (Fig. 137). The BSE micrographs of cross-sections of calcined grains reveals the presence of iron oxide (bright areas covering grain surface) and melts from the decomposition of mica. XRPD show most of the spodumene on both samples was converted to β-spodumene. Mica present in both samples has decomposed.

The Pilgangoora sample (PD005), presented in Figure 138, reveals that the calcination of the white, lime-hued, unaltered spodumene produced a brownish chalky, friable product. XRPD results indicate that 86% of the α-spodumene was converted to β-spodumene, with the balance present as γ-spodumene (14%). Feldspar minerals and quartz appear fractured. Calcination of particles containing fine intergrowths of quartz and spodumene show no obvious interaction between the two minerals. This is consistent with earlier findings.

Figure 139 shows that the calcination of the Greenbushes samples (C1100P, C3300HWH and C3300HP), consisting mainly of white spodumene and quartz, produced white powdered products, which appeared less friable (when pinched between fingers) than those observed in the calcined products of other samples. The XRPD results revealed that, in contrast to other samples, only about 58% of the spodumene converted to β-spodumene, with the rest as γ-spodumene. This is despite the Greenbushes samples being heated under the same temperature for the same period of time as the other samples. Incomplete conversion of γ-spodumene to β-spodumene during calcination has been contributed to poor lithium extraction during the acid bake and water leaching stage (Dessemond et al., 2020).

a) MC200 – fresh spodumene**b) MC500 – partially altered spodumene**

19.09.22

Figure 136. Untreated and calcined images of grains and X-ray powder diffraction patterns, together with backscatter electron micrographs showing cross-sections of calcined particles. The quantity of γ - and β -spodumene and other phases are shown in the diffraction patterns (Mt Cattlin)

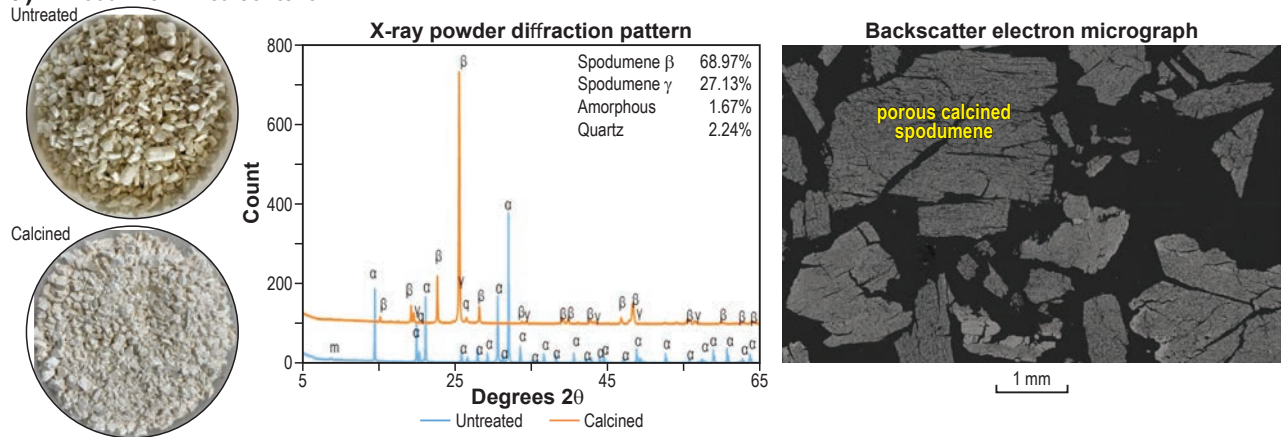
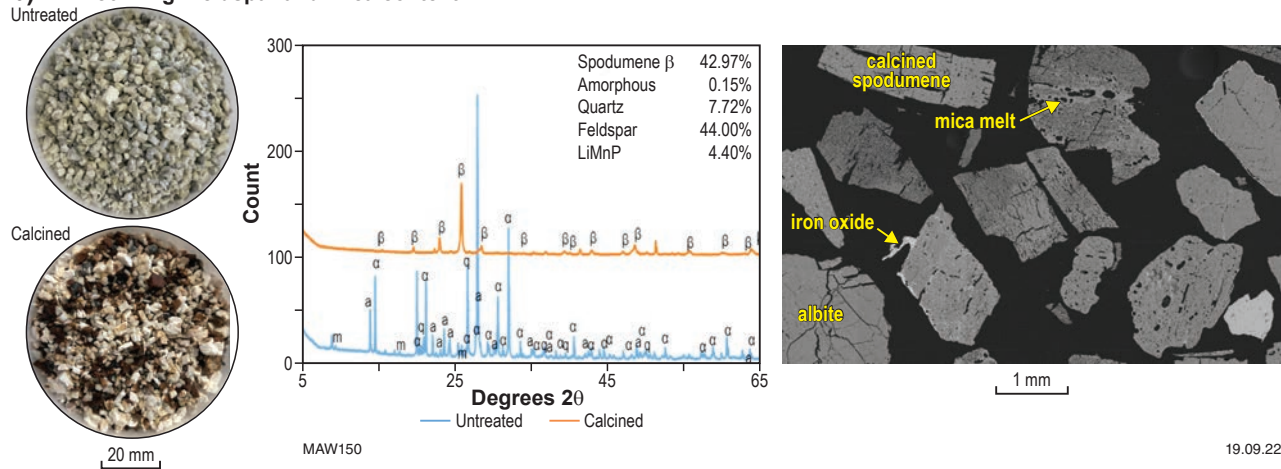
a) BH1300 – low mica content**b) BH1480 – high feldspar and mica content**

Figure 137. Untreated and calcined images of grains and X-ray powder diffraction patterns, together with backscatter electron micrographs showing cross-sections of calcined particles. The quantity of γ - and β -spodumene and other phases are shown in the diffraction patterns (Bald Hill)

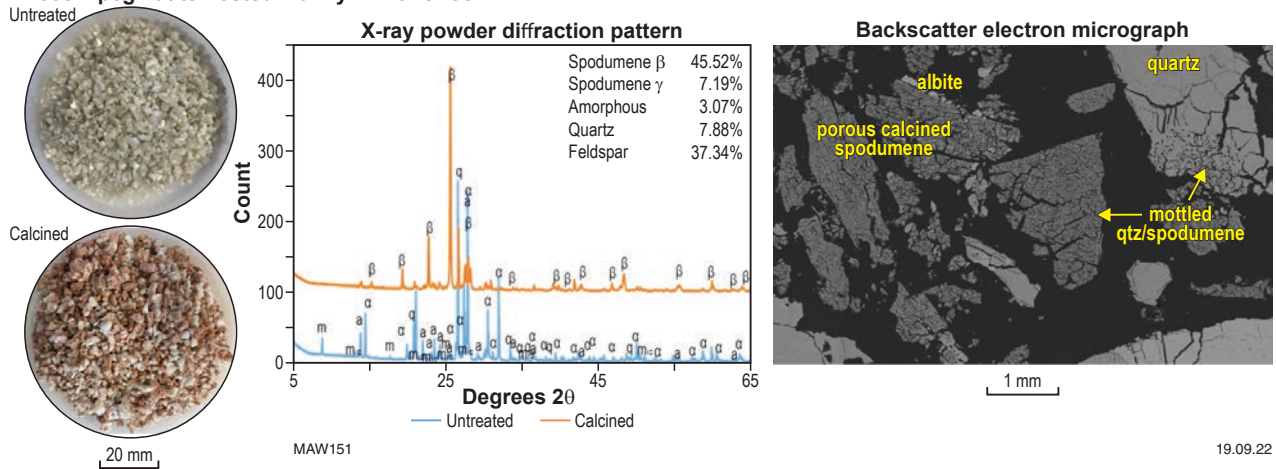
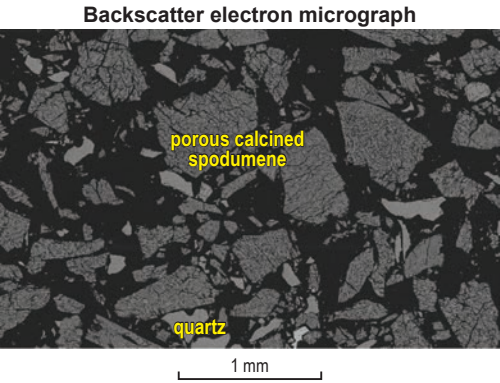
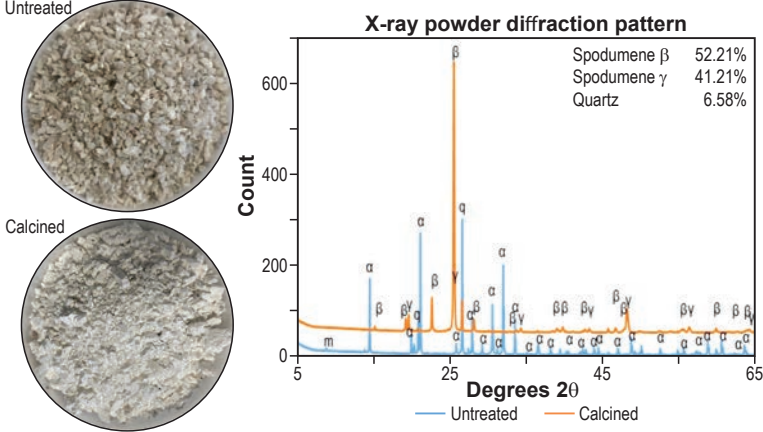
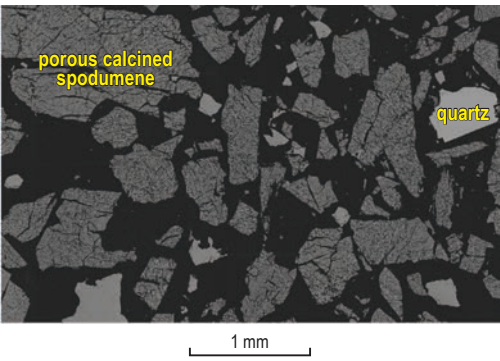
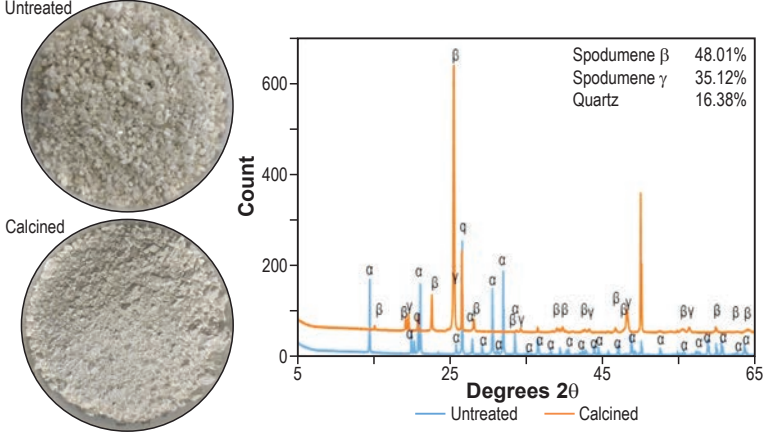
PD005 – pegmatite hosted mainly in mafic rock

Figure 138. Untreated and calcined images of grains and X-ray powder diffraction patterns, together with backscatter electron micrographs showing cross-sections of calcined particles. The quantity of γ - and β -spodumene and other phases are shown in the diffraction patterns (Pilgangoora)

a) C1100P – high quartz



b) C3300HWH – high quartz



c) C3300HP – quartz and feldspar

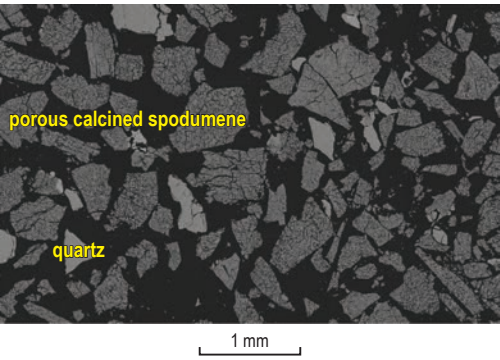
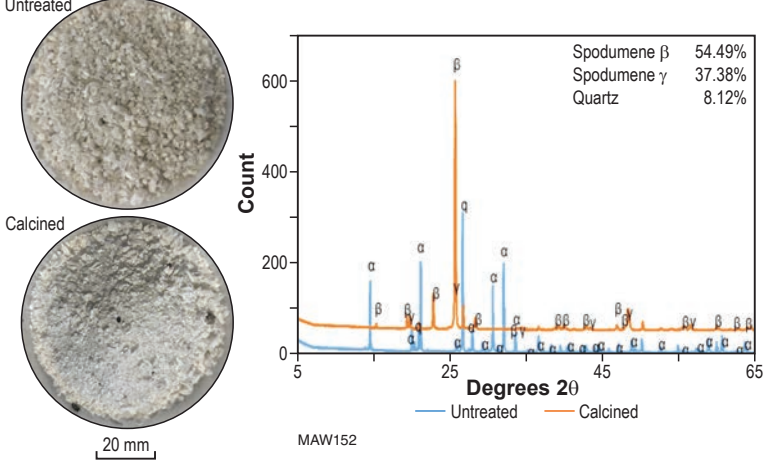


Figure 139. Untreated and calcined images of grains and X-ray powder diffraction patterns, together with backscatter electron micrographs showing cross-sections of calcined particles. The quantity of γ - and β -spodumene and other phases are shown in the diffraction patterns (Greenbushes)

Effect of calcination time on spodumene product

To assess the differences between the spodumene conversion rates between Greenbushes and the other samples, tests were carried out over a time series to establish the length of time required to convert most of the α -spodumene to β -spodumene. A run was conducted on a Mt Cattlin sample along with a Greenbushes sample as a control sample for comparison.

Figure 140 shows a graph of the change in mineralogy with heating time for the main phases present in Greenbushes and Mt Cattlin samples heated to 1100 °C over a period of three hours. A plot of the β -spodumene conversion rate expressed as $\beta/(\beta+\gamma)\%$ with time is also presented. Rapid conversion of α -spodumene to γ -spodumene occurred in both samples within the first half an hour. However, the conversion from γ -spodumene to β -spodumene appeared to be delayed in the Greenbushes sample, similar to that observed in section, Comparison of the calcination properties of different deposits. It is not until after three hours that the majority of the spodumene (~90%) converts to the β -form. Whereas in the Mt Cattlin sample, the majority of the spodumene is converted to β -spodumene after around two hours.

The reason for the difference in the Greenbushes is uncertain but may be related to the insulating properties of the high quartz content (44 J/molK) over spodumene (160 J/molK). In addition, the slower conversion rate of Greenbushes samples is probably related to the lower Fe content within spodumene that would provide an additional insulating effect compared with the other spodumene samples.

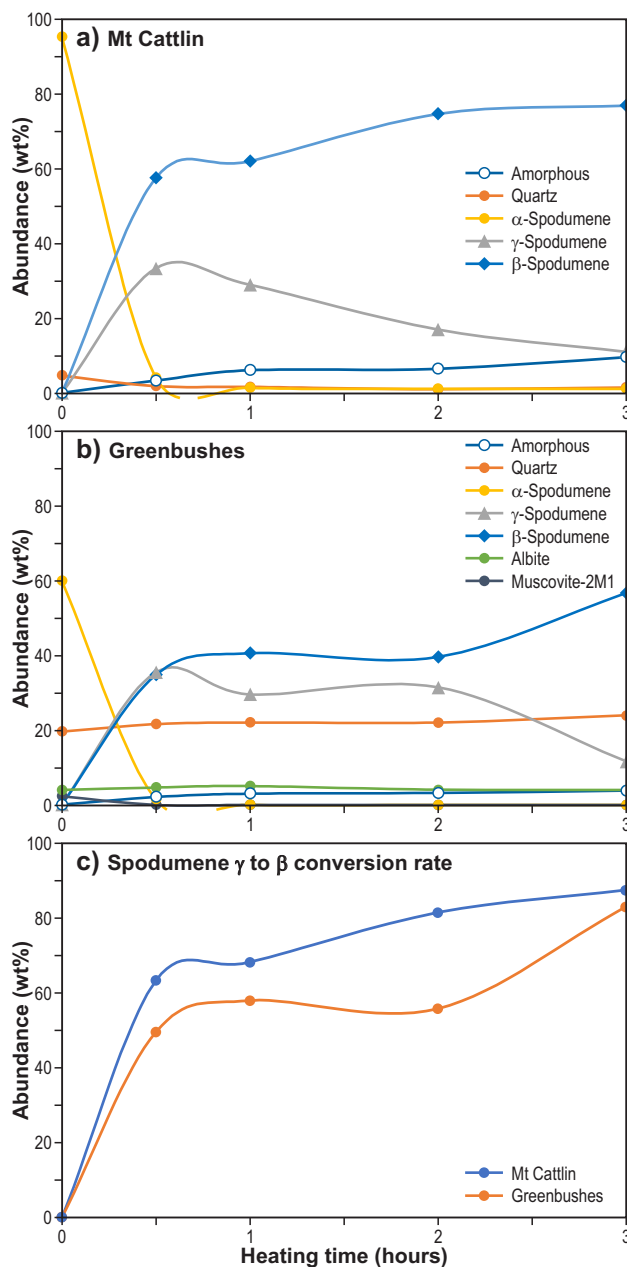
Calcination of concentrates

Four concentrate samples obtained from different mine sites were subjected to the same calcination process as the individual samples above. The composition and mineral association of these concentrates were illustrated in the concentrate liberation analysis section in section, Liberation characteristics-concentrates. As indicated earlier, spodumene in the Greenbushes concentrate is largely liberated, whereas the other concentrates have about 5% of spodumene interlocked with gangue minerals (mica, quartz and feldspar).

Figure 141 shows BSE micrographs, mineral maps, K-K and Al-K elemental maps of calcined concentrate samples, together with XRD patterns showing spodumene converted to β -spodumene. The calcined spodumene in the concentrates show similar texture and features as those observed in the sample specimens. In particular, the Mt Cattlin and Bald Hill concentrate samples have melt structures associated with decomposition and partial melting of contained mica and feldspar, respectively. The Greenbushes concentrate is finer grained than the other concentrates and appears well liberated with a porous calcined product.

Sulphate roast and lithium extraction

The eight calcined samples and four calcined spodumene concentrates described above were acid baked at 250 °C.



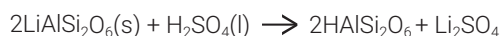
Abundance (wt%)	Mt Cattlin MC200					Greenbushes C1100P				
Heating time (hrs)	0	0.5	1.0	2.0	3.0	0	0.5	1.0	2.0	3.0
Amorphous		3	6	6	10		2	3	3	4
Quartz	5	2	2	1	1	20	22	22	22	24
α -Spodumene	95	4				60	2			
γ -Spodumene		33	29	17	11		35	30	31	12
β -Spodumene		58	62	75	77		35	41	40	57
Albite						4	5	5	4	4
Muscovite-2M1						2				
$\beta/(\gamma + \beta)$ % conversion	-	63	68	81	87	-	50	58	56	83

MAW153

19.09.22

Figure 140. Graphs showing mineral transformations with time for samples heated at 1100 °C for three hours in a muffle furnace for: a) Mt Cattlin; b) Greenbushes; and c) the ratio $\beta/(\beta+\gamma)$ spodumene. The mineral phase abundance at different times is shown in the table

In the acid-bake process, concentrated sulphuric acid is mixed with dry lithium concentrate and heated, forming lithium sulphate as proposed in the following reaction (Salajani et al., 2019).



Lithium sulphate readily dissolves in water, with a solubility of 34.2 g/100 g of water at 25 °C (CRC, 2005).

The lithium was extracted in a water-leach stage and the residues washed and dried for chemical and mineralogical analyses following the methodology outlined in section, Calcination and sulphate roasting for lithium recovery methodology.

Effect of lithology and ore deposit on lithium extraction

Figure 142 shows the extraction of Li and Al for each of the samples and concentrates. The extraction of Li appears related to the extraction of some of the Al. The impact of Al dissolution on Li extraction is discussed later. The moderate content of lithium in the washings illustrate the importance of ensuring samples are washed sufficiently to prevent loss of lithium.

For Pilgangoora, Bald Hill and Mt Cattlin samples, lithium extraction can be considered a function of the mineral impurities associated within these samples. High mineral impurity contents yield a poorer extraction. The concentrates (Aconc, BHconc and Gcon) and BH1300 and MC200 have high lithium extractions and <5% mineral impurity content to interfere with the spodumene conversion and leaching processes. Samples PD005, BH1480 and MC500 contain a moderate to high gangue content, which clearly affected lithium extraction. Studies reported in the literature have indicated that lithium extraction decreases with the impurity content in the feed (Lajoie-Leroux et al 2018; Yelatontsev and Mukhachev, 2021). In contrast, Greenbushes samples appear to have a low lithium extraction, with low mineral impurity content. Figure 143 shows that lithium extraction is not completely dependent on having full conversion of α -spodumene via γ -spodumene to β -spodumene, with the $\beta/(\beta+\gamma)$ ratio varying between 60 and 100%. As discussed in section Effect of calcination time on spodumene product, the slow rate of conversion to β -spodumene has possibly affected the efficiency of lithium extraction, and would likely be ameliorated through finer grinding, similar to the Greenbushes concentrate (Tconc).

Relationship of lithium extraction to impurity contents

The chemical composition of both uncalcined solids and the calcined acid-bake and water-leach residues is shown in Figure 144. The chemical composition of the filtrate and washing solutions are shown in Figure 145. The raw data are presented in Appendix 8.

In the uncalcined samples (Fig. 144a), the Li content ranges from 1.7 wt% for a sample with high impurities to 3 – 3.5 wt% with relatively low levels of impurity. The majority of the samples are made up of Al and Si, with high Si contents associated high quartz content. Iron and Mn are prominent in seven of the samples, largely associated with spodumene and micas as discussed earlier. One exception is BH1480, which contains sicklerite. Sample BH1480 also contains a high impurity content (~10 wt%) due to the high mica content. The Greenbushes samples and MC200 have only trace amounts of elemental impurities. Samples MC500 and BH1300, although with a high Li grade of >3%,

have ~3 wt% of impurities associated with intergranular micas in the spodumene grains as illustrated in earlier studies.

Figure 144b shows that in the leached solid residue following calcination, acid baking and water leaching, the Li content is low (0.0 – 0.2 wt%) in nine of the samples. High Li content remains in the BH1480, C3300HP and C1100P samples (1 – 1.7 wt%) and moderate amounts of residual Li (0.2 – 0.4 wt%) in samples PD005 and C3300HWH. However, there appears to be no relationship between the quantity of mineral impurities and residual lithium content. This is probably due to differences in the thermal and leaching behaviour of the impurities in the different samples. The Greenbushes samples have a high quartz content, which should be relatively inert in the acid-bake treatment, whereas the other samples contain decomposed mica and phosphate minerals. Sample BH1480 has a high content of impurities in the solids compared with PD005, despite having similar quantities of mineral impurities. Mass loss from acid baking and water leaching was high (3 – 5 wt%) in the Mt Cattlin samples (MC200 and MC500) and the high-grade spodumene from Bald Hill (BH1300), as well as for all mine concentrates. In the Pilgangoora sample (PD005) and Greenbushes samples (C300HP, C3300HWH and C1100P), the mass loss was low (0.5 and 2 wt%, respectively). Mass loss is associated with the dissolution of reactive, calcined minerals (e.g. calcium oxide and phosphate dissolution in sulphuric acid). Notably, Fe is detected in all residue samples and is concentrated following the acid-bake and water-leaching process. Mass loss of all concentrates was high compared with the majority of the other samples at around 4 wt%. This reflects the dehydroxylation of some of the mineral impurities associated with these samples during calcination.

Figure 145a shows the elemental content of the filtrate solution expressed as a weight percentage of the sample following the water leach of the acid-bake materials. Lithium in solution follows roughly the reverse trend of the leached solid residues (i.e. high Li in solution, low Li in solids). The samples with a greater impurity content mirror the mass loss illustrated in Figure 144. Dissolution of Na and Al is prevalent in all samples. As indicated earlier, dissolution of some Al is related to Li dissolution from spodumene. Iron dissolution is associated with samples containing high Fe content in spodumene and micas, with the Greenbushes samples having the least amount of Fe. Calcium and P dissolution is prevalent in BH1480, MC200 and in concentrate samples associated with acid dissolution of apatite, while sicklerite ($\text{Li}(\text{MnFe})\text{PO}_4$) in sample BH1480 also contributing to elevated Mn and Fe concentrations. The Greenbushes samples had the lowest level of impurities in solution (~0.3 wt% of sample or total impurity content 500 mg/L in solution) compared with other ores (~1 to 2 wt% of sample or 1500 to 3000 mg/L), reflecting the relative purity of the sample comprising only spodumene and quartz. The concentrates appear to have a high Al, Na and Fe contents in solution. These concentrates are finer in particles size than the other samples, which make some of the gangue material more reactive to acid dissolution.

The chemical composition of the washing solution expressed as a weight percentage of the sample where the filter residue was washed in water is shown in Figure 145b. Similar trends in the solution composition to the

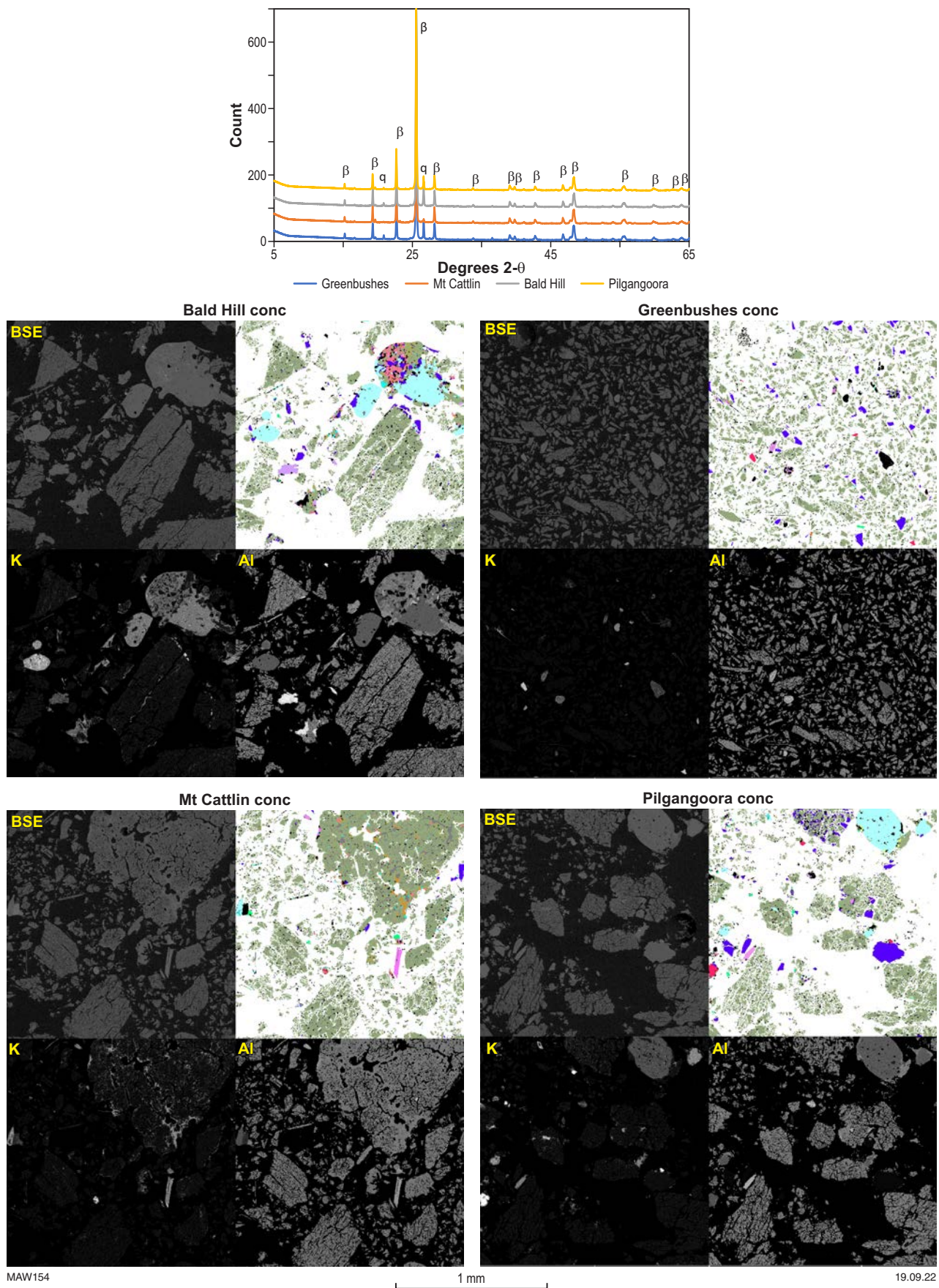


Figure 141. Backscatter micrographs, mineral maps, and K and Al elemental maps of calcined concentrate samples. (In mineral composition maps, olive green is spodumene, light-blue is albite, pink is muscovite and deep blue is quartz with reddish brown melts and red microcline)

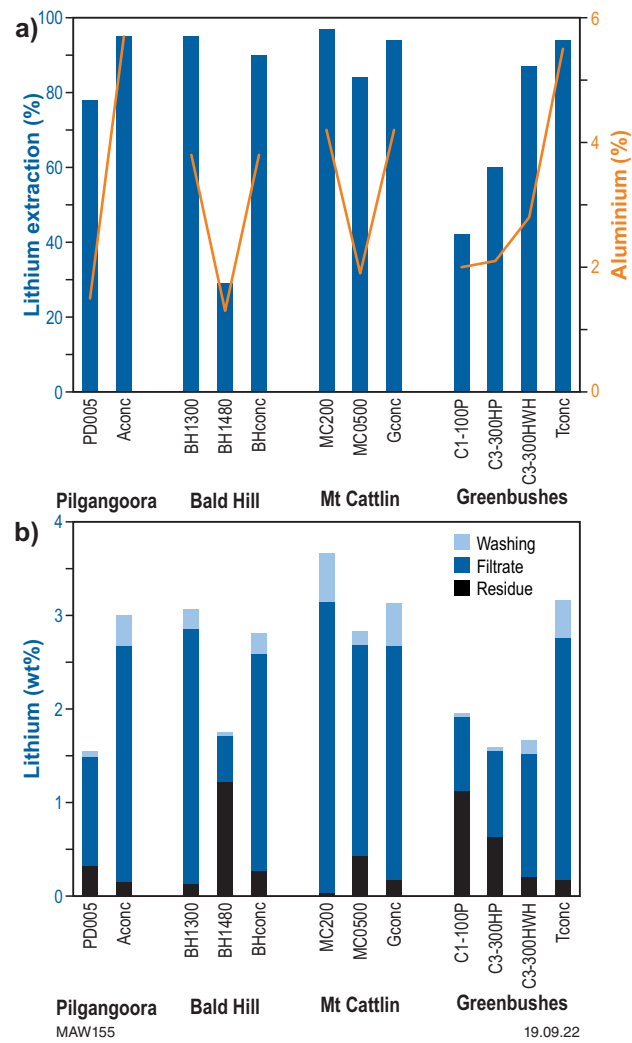


Figure 142. Comparison of the leaching efficiency of samples and concentrates for different lithologies, expressed as: a) percentage of Li (left-hand axis) and aluminium (right-hand axis) extracted; and b) as departments of lithium in filtrate, wash solution and residue as a function of total Li grade

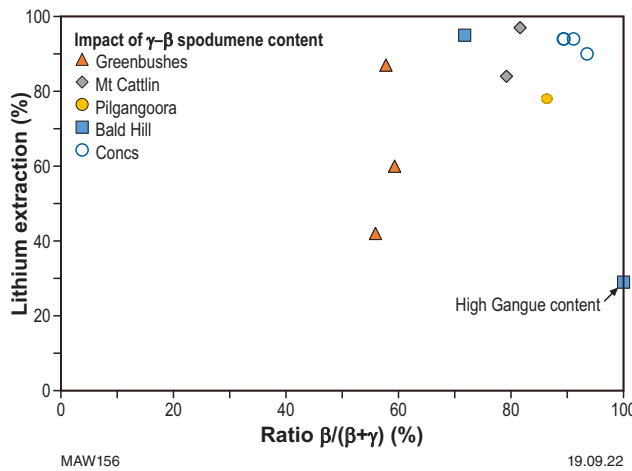


Figure 143. Comparison of Li extraction as a function of spodumene conversion ratio expressed as $\beta/(\beta+\gamma)$

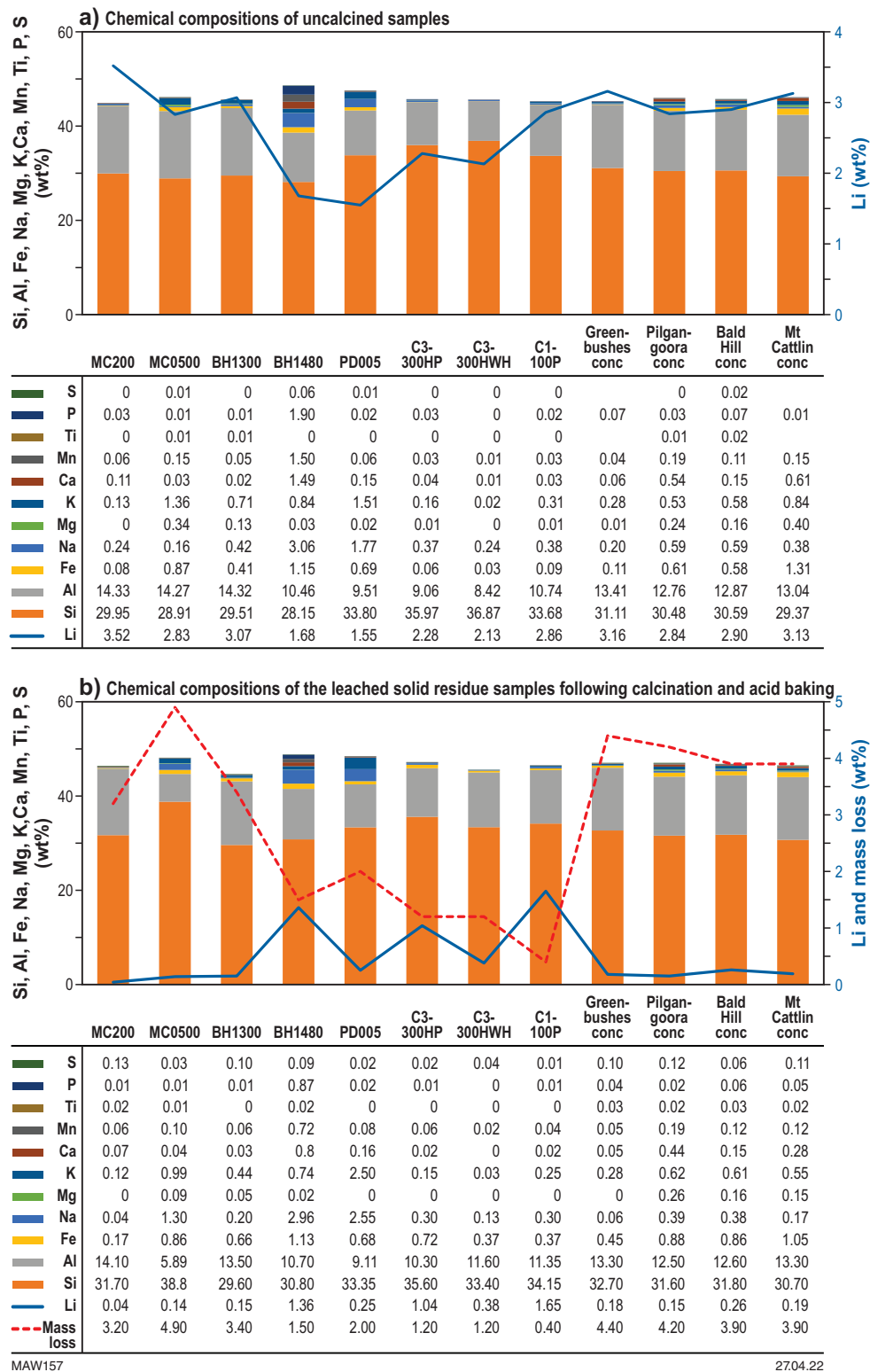


Figure 144. Chemical composition of: a) uncalcined solids; and b) calcined acid-bake and water-leach residues. The majority of elements are illustrated as a histogram of values on the left-hand axis and table below. Lithium content is plotted as a blue line, with units on the right-hand axis

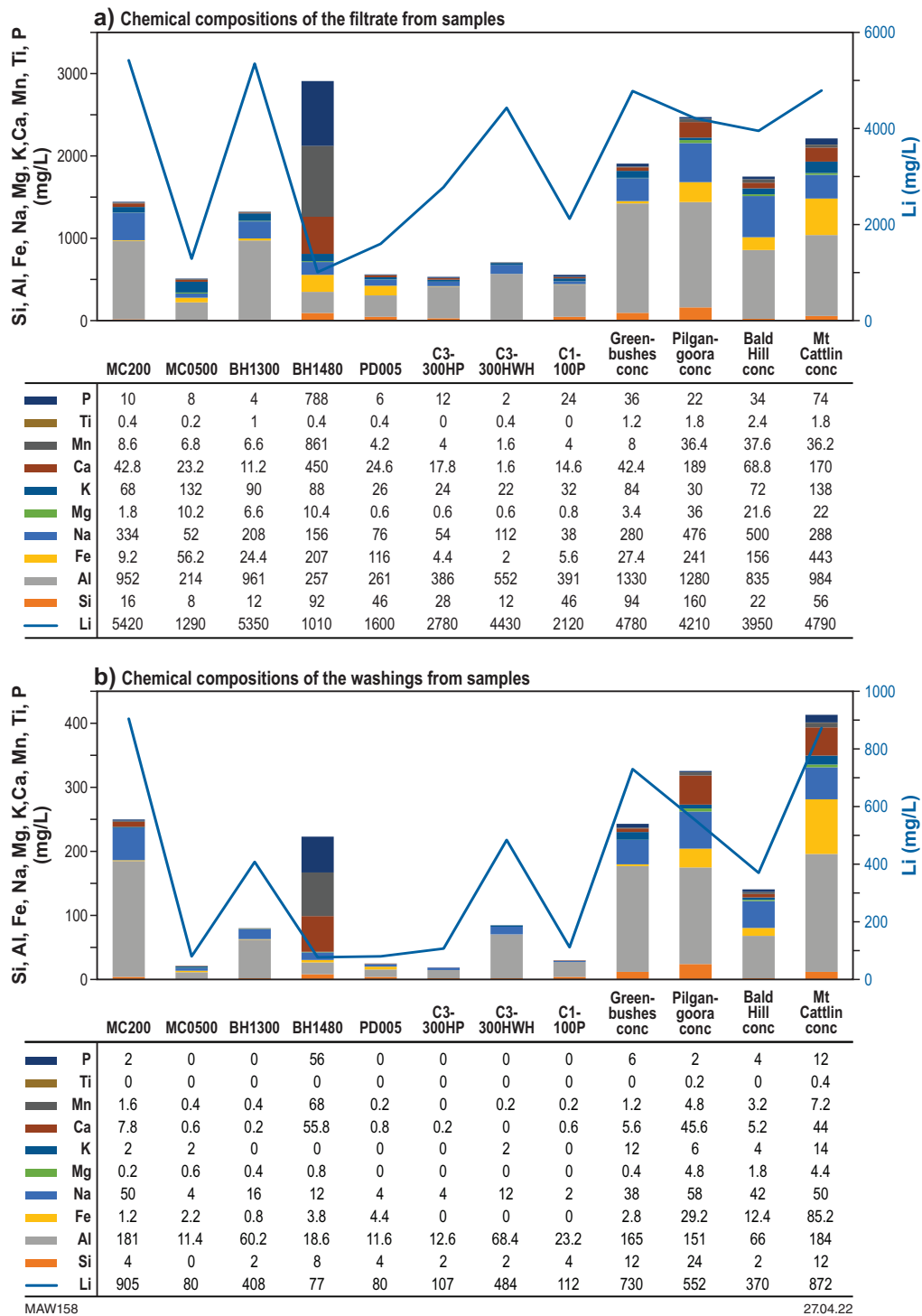


Figure 145. Chemical composition of: a) filtrate from filtered solid leached residue following leaching; and b) washings from washing the solid leached residue expressed as a weight % in sample. The majority of elements are illustrated as a histogram of values on the left-hand axis and table below. Lithium content is plotted as a blue line with units on the right-hand axis

filtrate solutions are observed in the wash solutions but are more dilute. Around 0.5 wt% of the Li in some samples is collected in the washings, which illustrates the importance of washing the filter residues to ensure all interstitial lithium is recovered.

Morphology and deportment of lithium in acid-baked water-leached residues

The deportment of lithium in acid-baked residues and associated grain morphology, as well as their chemical composition, was examined in cross-sections of particles to determine the properties favourable for lithium extraction in the different samples.

Figures 146 and 147 show BSE images of cross-sectioned grains of calcined spodumene after acid baking and water leaching of the Bald Hill sample (BH1480), together with ToF-SIMS elemental maps of major cations.

In Figure 146, the ToF-SIMS scans reveal that an amorphous glass phase (regions of high K, Na, and Rb) has formed a partial encapsulation coating around calcined spodumene. The glassy texture is interpreted as the product of partial melting of contained mica. The glass phase acts to reduce the efficiency of Li extraction during the acid-baking and water-leaching stage. The results demonstrate that sulphuric acid used in the baking stage does not dissolve the mica melt which coats the calcined spodumene grains. The second set of data shows the presence of Fe- and Mn-oxide grains (Fe- and Mn-enriched areas in ToF-SIMS analysis), which formed by the oxidation of Fe and Mn within the melted mica, during initial calcination. Areas enriched in lithium are also encapsulated by melt media containing Na and K from the decomposition of micas.

Figure 147 a and b show BSE images of the cross-sections of two spodumene grains, with accompanying ToF-SIMS Li and Al maps. The cross-section of particles of acid-baked, calcined spodumene have flat, fractured textures, which are common and observed for all calcined spodumene grains that have undergone acid-bake treatment. During the acid baking and subsequent water leaching, the amount of lithium extracted from acid-baked particles varied. In Figure 147a, the majority of lithium was leached from the particle, whereas Figure 147b shows the partial dissolution of lithium within the particle. Notably, in areas where the Li is depleted, the Al concentration (green vs yellow colouration representing different concentrations in the ToF-SIMS Al map) was also depleted, indicating some dissolution and loss of Al, as depicted in the correlation between Li and Al dissolution in the leaching data (see Fig. 143).

Figure 148 shows the cross-sections of particles from the Greenbushes sample illustrating similar textures and lithium deportment following acid baking and water leaching as described above on part of a coarse particle (~250 µm) and a fine particle (~40 µm).

Close examination of the particles at higher resolution (Fig. 148b) reveals a 'white-ant wood' textured framework and rippled structures in areas barren in lithium, compared to Li-rich areas where the particles have a smoother texture. While lithium extraction is considered an ion exchange process, where hydrogen ions replace Li in the residual calcined spodumene structural matrix (Salakjani, et al.,

2016; Han et al, 2018), a proportion of Al is also removed during the sulphuric acid baking and water leaching, which causes shrinkage of the residual mineral particles. The displacement of Al occurring to liberate and extract Li suggests that the direct ion exchange mechanism of Li⁺ for H⁺ following acid baking, as illustrated in the equation above, is non-unique.

The agglomeration and shrinkage of particle grains observed in these tests may impede full extraction within the particles. To facilitate efficient extraction of lithium, the calcined particles for acid-bake leaching need to be ground fine enough to allow diffusion and leaching of lithium from within the particles.

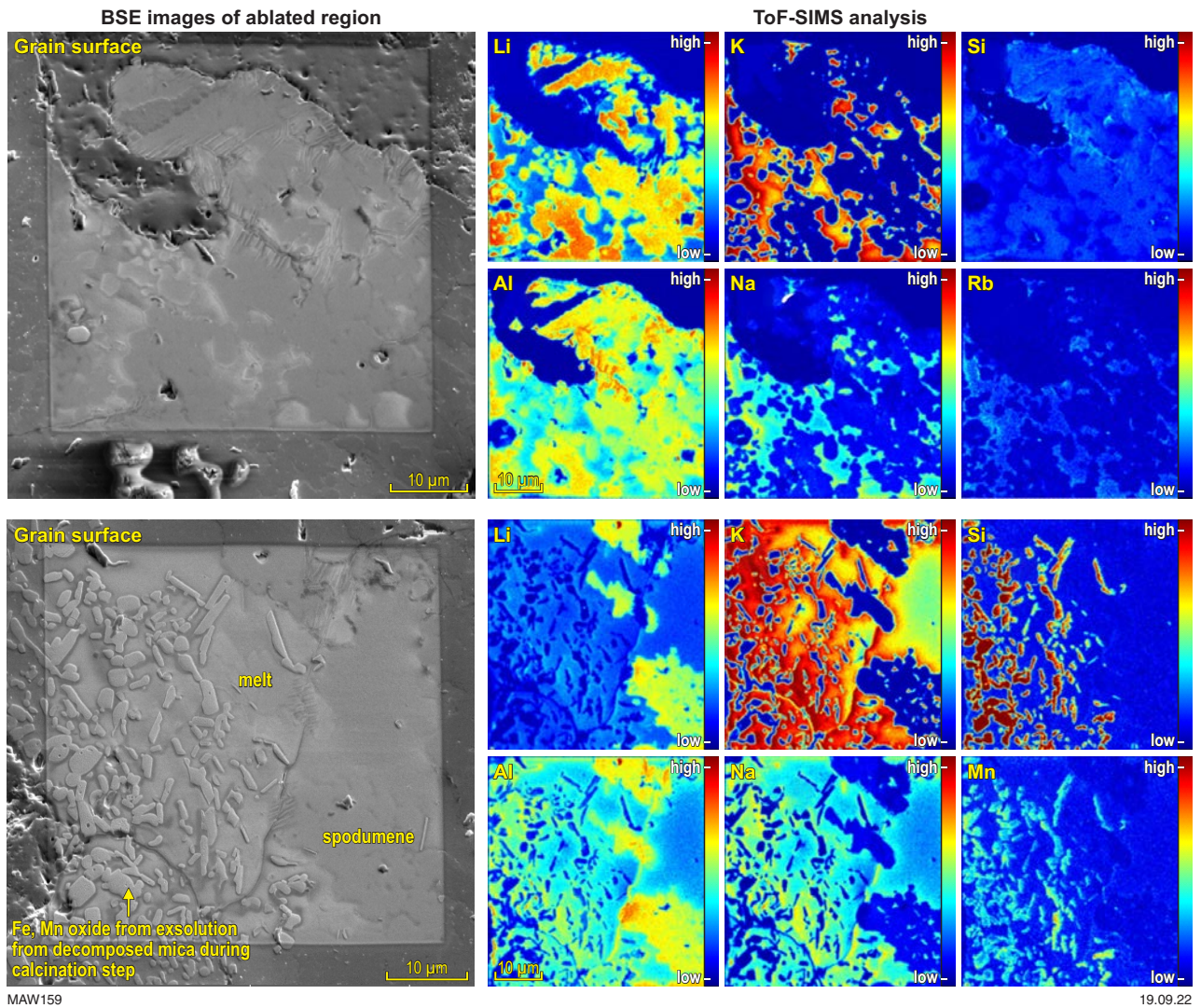


Figure 146. Backscatter images and ToF-SIMS analyses of leaching residue grains following calcination and sulphate roasting (BH1480). The coloured scale bar for each element map shows the relative abundance in each case, with cool colours (blue) indicating a low content and hot colours (red) indicating a high content

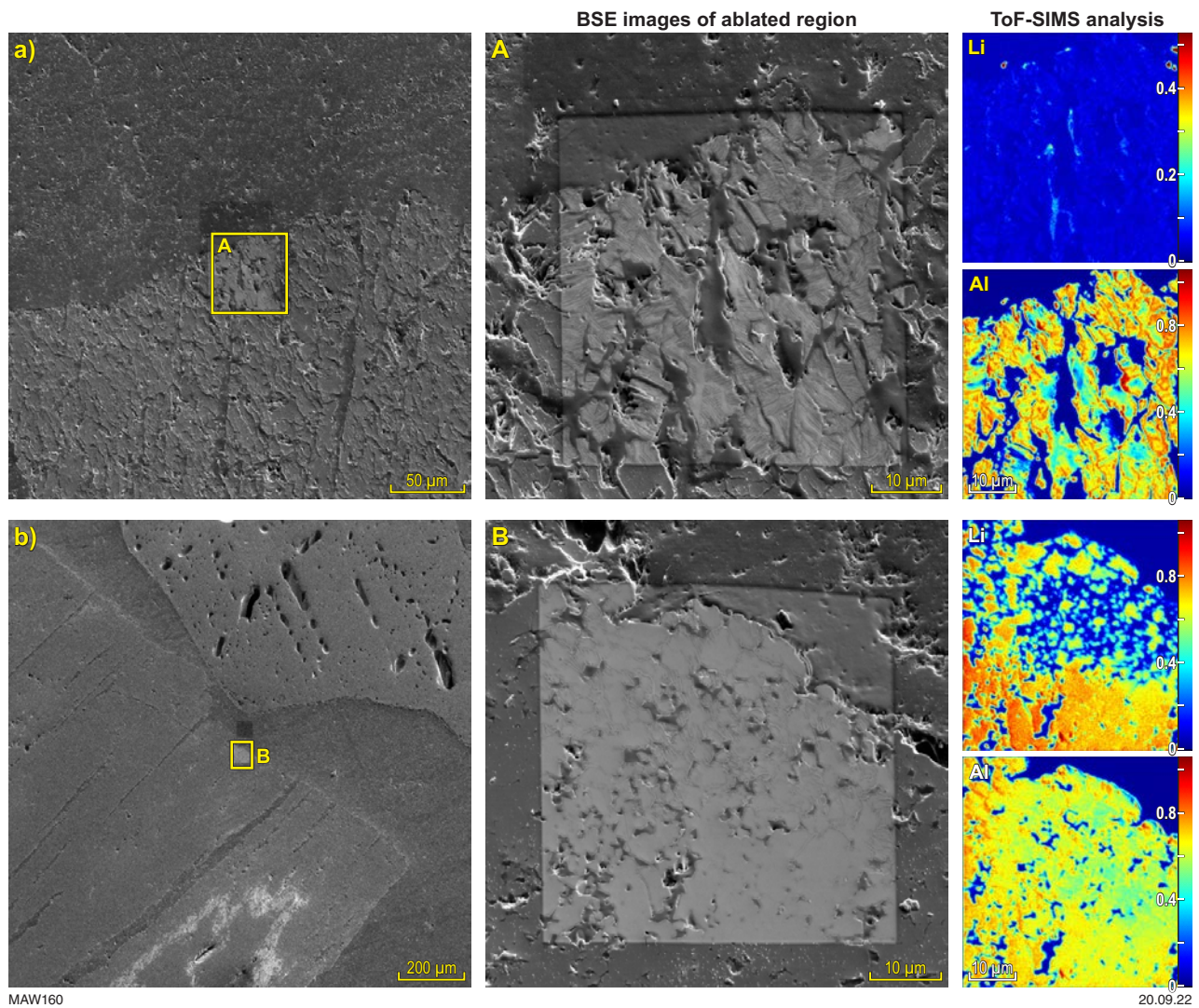


Figure 147. Backscatter images and ToF-SIMS analyses of leaching residue grains following calcination and sulphate roasting (BH1480)

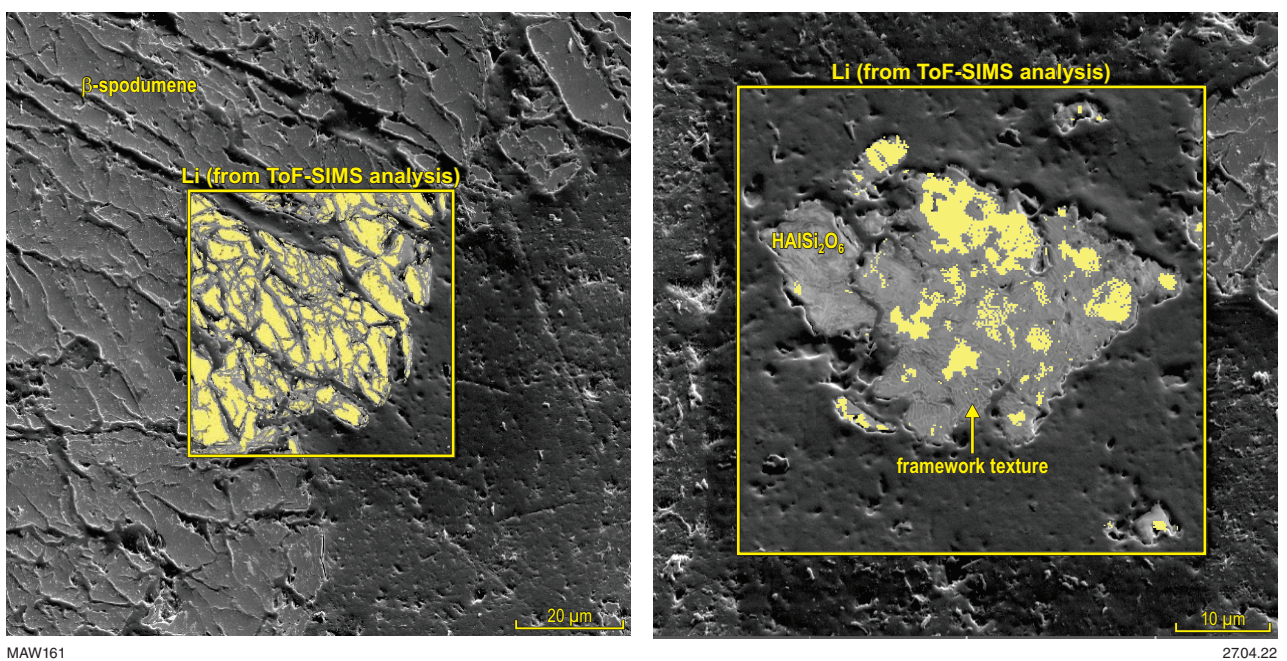


Figure 148. Backscatter images and overlaid with Li distribution (in yellow) scanned by ToF-SIMS (C1100P). Close-up image shows a 'white-ant' wood textured framework and rippled structures in areas barren of Li

Geometallurgical framework

Processing trends in WA LCT pegmatites examined in this study

A comparison between pegmatite ore types and the processing options that are either currently used or are reported as suitable for processing WA pegmatite type ores examined in this study is shown in Table 18. Mines at Pilgangoora, Greenbushes, Mt Cattlin, Mt Marion and Bald Hill have been established with beneficiation process plants producing spodumene concentrates. Information about their process plants is provided in Table 18, where possible.

Beneficiation

Although many of the processing details are not fully published, in general terms the beneficiation process flowsheets can be categorized as one of three types:

1. A heavy media separation circuit
2. Combined heavy media separation and flotation circuit
3. Whole of ore flotation circuit.

The treatment of Kathleen Valley ore is currently at the final investment decision (FID) stage for the development of the mine and process plant by Liontown Resources. Other deposits listed, such as Londonderry, Pioneer Dome, Sinclair and Dalgara, are mainly in the exploration stage, with some metallurgical test work in progress by the respective companies.

Based on the ore types and process plant configurations, the different mines can be categorized into groups that have similar ore properties and processing routes as shown by different colour shades in Table 18 as follows:

- **LCT albite–spodumene pegmatite, LCT complex spodumene pegmatite:** High quartz and feldspar, with moderately sized spodumene pegmatites – staged crushing incorporating high-pressure grinding rollers (HPGR), production of coarse concentrate by DMS and a fine concentrate by flotation with no DMS circuit (Pilgangoora, Mt Marion and Kathleen Valley).
- **LCT albite–spodumene pegmatite:** Quartz, feldspar, with high mica content and coarse to very coarse spodumene pegmatite – staged crushing and liberation of spodumene and concentration with staged DMS cyclone configuration (Bald Hill, Mt Cattlin).
- **LCT complex spodumene pegmatite:** Quartz with moderate to fine spodumene pegmatite – staged crushing and grinding followed by DMS and flotation to generate concentrates (Greenbushes).
- **LCT albite pegmatite:** Zinnwaldite, albite, quartz pegmatite – primary crushing semi-autogenous grinding (SAG) or rod mill followed by magnetic separation to generate concentrate (Dalgara).
- **LCT complex petalite pegmatite:** Petalite zoned with feldspar and quartz pegmatite – excavation, crushing and grinding to produce direct shipping ore (DSO) (Londonderry and Pioneer Dome).

In the Pilgangoora samples examined in this study, coarse tabular spodumene is the main Li-source and hosted within a quartz and feldspar matrix. As observed in the liberation studies (refer to the section Liberation characteristics of spodumene), high spodumene recoveries are possible. However, processing of spodumene associated with fine, graphitic textured intergrowth with quartz and feldspars, and some spodumene–mica alteration zones will lead to reduced recoveries. The two flow sheets available for the Pilgangoora region are from Pilbara Minerals and Altura Resources' plants (now owned by Pilbara Minerals). Both Pilbara Minerals and the Altura concentrator plants are designed for processing ore feed from opposite sides of the same pegmatite ore deposit. However, only the Pilbara Minerals Deposit is considered enriched with Ta. Both plants are of similar design and consist of crushing, feed preparation, DMS, gravity separation, grinding, flotation, magnetic separation and dewatering. The Pilbara Mineral's plant has spirals after the milling circuit to recover tantalite. During operation of the Altura plant, the ore from the ROM pad was crushed to 28 mm through a closed crushing circuit utilizing a primary jaw crusher, secondary cone crusher and dry vibrating screen. The –28 mm material was stockpiled to delink the crushing circuit from the remainder of the plant. The ore was then crushed with HPGR to reduce the particle size to –6 mm and wet screened to a 6 x 1 mm DMS feed and –1 mm fines fraction. Mica was removed from the DMS feed via a classifier prior to a two-stage DMS plant producing a high density, on-grade spodumene product, medium-density middlings and low-density reject streams. The –1 mm fines from the HPGR were subjected to further classification to remove mica prior to further processing. Middlings from the DMS and pre-concentrated fines report to a closed-circuit, ball mill to reduce the particle size to a P80 of 106 µm. The milled ore was de-slimed by removing the –20 µm fines before reporting to the flotation circuit. A rougher cleaner and recleaner circuit upgraded the fines to an on-grade +6% Li₂O concentrate. The flotation concentrate was subject to high intensity, magnetic separation to reduce Fe levels in the concentrate. The fine concentrate was de-watered and stockpiled for blending with the coarse concentrate before shipping. A similar type of plant configuration to the Altura plant has been developed by Covalent Lithium in treating ores from Mt Holland, which contain mineralogical domains consisting of spodumene, petalite, mixed spodumene–petalite, alteration (cookeite), and barren albite zones.

The Greenbushes ore is a high-grade ore consisting of a mixture of spodumene and quartz (section Greenbushes). Greenbushes has three processing plants: one producing technical grade, see section, Greenbushes samples, Li concentrates and two producing chemical-grade Li concentrate. Ore containing Li₂O is fed into the processing plants, which upgrades the lithium using gravity, heavy media, flotation and magnetic processes to produce a range of lithium concentrates for bulk and bagged shipments. The process employs a crushing and grinding circuit, followed by screening to separate coarse and fine particles. The fine fraction is de-slimed, conditioned and treated through a flotation circuit to produce a concentrate. The concentrate is treated through gravity separation and magnetic separation steps to remove heavy minerals and tourmaline to produce a spodumene concentrate. Concentrate produced from this plant feeds the Talison lithium refinery plant at Kwinana in Western Australia. As illustrated in liberation studies

Table 18. Ore and process characteristics of pegmatites examined in this study

Region	Location	Lithologies1	Mineral characteristics				Liberation characteristics			Process implications	
			Lithium associations		Form	Elemental impurities	Mineral associations	Tantalum & tin minerals	Other minerals	Benefication approach	
			Li host	Minor - micas						Comminution	Benefication
Pilbara	Pilgangoora region	<u>LCT albite-spodumene pegmatite</u> <ul style="list-style-type: none">quartz-spodumene-albite-microcline;quartz-microcline-albite (acc. muscovite)quartz-muscovite-microcline (+accessory cassiterite and plagioclase)	Main - spodumene Minor - micas	Spodumene range from 20 mm to 50 mm in tabular form	High iron content in spodumene (0.6-1.2 wt%) High Mn content associated with micas within some spodumene	<ul style="list-style-type: none">Coarse liberated spodumene separated from coarse quartz and feldspars (major form)Fine graphitic texture intergrowth with quartz and feldsparsIn parts mica in aggregate and veins within some spodumene grains.	Columbite-tantalite Cassiterite	Rb enrich feldspar zones calcite	Existing plant ROM feed to Primary - jaw crusher, Secondary - cone crusher, screened and stockpiled, followed by a Tertiary HPGR HPGR → screen • Screen U/F → Secondary screen • Screen O/F → Oversize recycled to crushing • Secondary screen U/F → classification • Secondary screen O/F → Ball mill • Ball mill discharge → Classification	Existing plant (<u>Pilbara minerals plant ~330kt/a, Altura plant 206kt/a</u>) Classification U/F → Spirals Classification O/F (coarse) → Two -stage DMS circuit First stage DMS circuit O/F → Ball mill Second stage DMS circuit O/F → Final HMS concentrate Second stage DMS circuit U/F → Spirals Spirals heavy fraction → Filtration as Ta ₂ O ₅ product Spirals light fraction → Classifier Classifier O/F → Tails Classifier U/F → Flotation Flotation rougher cleaner and recleaner circuit followed by high intensity magnetic separation to reduce iron levels → Chemical grade spodumene concentrate product (6% wt% Li ₂ O)	Main concentrate shipped overseas <ul style="list-style-type: none">Potential treatment of fines by Calix calcination process or LIENA to produce a mid stream lithium salt product
Southern Region	Greenbushes	<u>LCT complex spodumene pegmatite</u> <ul style="list-style-type: none">K-feldspar zone (microcline-quartz)Na-feldspar zone (albite-quartz) containing the main Ta mineralisationLi-zone (spodumene-quartz), as the main source of Li mineralisation	Main - spodumene Minor - micas	<ul style="list-style-type: none">In high-grade, Na- and Li-zone samples spodumene occurs as megacrystic (+10 cm sized)Tabular spodumene as white, pale-grey and pink crystals, fine-grained spodumene with quartz	Low impurity content in spodumene (Fe 0-0.2 wt%)	<ul style="list-style-type: none">Coarse liberated spodumene separated from coarse quartz and feldspars (major form)Fine graphitic texture intergrowth mainly with quartz and some areas with feldspars-	Tantalite and stibiomicrolite (Antimony-bearing oxide mineral) and associated mainly with Central lode region of the deposit	Pollucite	<u>Existing plants (1 technical grade (0.15Mt/a; 2 chemical grade concs (1.2Mt/a)</u> <ul style="list-style-type: none">Primary & secondary jaw crushing,Tertiary cone crushing crushed to ~16 mm, or High pressure grinding rolls (HPGR) Ball milled → screenScreen U/F (~250 µm) → CycloneScreen O/F Oversize (+250 µm) screened at 800 µmOversize to ball mill Undersize is subjected to a magnetic separation to produce a glass grade spodumene & non-magnetic fraction	Existing plant <ul style="list-style-type: none">Cyclone O/F → slimes (~20 µm) to tailingCyclone U/F to flotation circuit Flotation circuit, involves roughing, cleaning and recleaning stages, using fatty acid collector and soda ash to produce a flotation conc of spodumene & tourmaline Gravity separation employed on flotation concentrate to recover heavy minerals (cassiterite and tantalite)Magnetic separation to remove tourmaline High grade spodumene conc (7.5–7.7% Li₂O and <0.1% Fe₂O₃)	Existing plant Li refinery plant commissioned Calcination followed by acid baking and water leaching Production of LiOH
	Mt Cattlin	<u>LCT albite-spodumene pegmatite</u> <ul style="list-style-type: none">Western Pegmatite Sheet coarse-grained (megacrystic) spodumene zone that comprises ~80% of mineralisation overlying a medium-coarse grained spodumene zoneEastern Pegmatite Sheet - mega-crystic, spodumene-albite pegmatite, some lepidolite mineralisationZones of partially to fully altered spodumene	Main - spodumene Minor - micas Lepidolite rich zones SE of pit 1c	Large (metre lengths) to coarse (cm lengths) spodumene laths. Unaltered and partially altered spodumene is mainly hosted by a highly fractured, pale-blue albite-quartz matrix (with minor Li-mica/ muscovite and accessory tourmaline), compared to the massive, milky white (secondary?) albite matrix where spodumene alteration has gone to completion	High iron content in spodumene (0.6-1.2 wt%) Mega-crystic spodumene exhibits marked differences in colour and various alteration textures (Mg, Fe, Na, K contaminates from mica)	<ul style="list-style-type: none">Coarse- liberated spodumene separated from coarse quartz, muscovite and feldspars (major form)Micas exist in a number of forms with spodumene as:<ul style="list-style-type: none">Fine interstitial veins in voids and fracturesCoarse inclusions within spodumene grainsComplex alteration zones within spodumene grains	Columbite-tantalite & microlite - located within the matrix mineralogy mainly albite and not as inclusions in spodumene or K-feldspar		<u>Existing plant (~1Mt/a)</u> <ul style="list-style-type: none">Ore sorter installed to improve gradeThree stage crushing circuit target -6mm crushed ore size and stockpiled Screened	Existing plant Crushed ore screened • Screen U/F (0.5mm) → Spirals and shaking tables used to separate the high-grade tantalite-bearing ore. • Screen O/F (+ 0.5 mm) → DMS circuit • Two -stage DMS cyclone circuit. Overflow rejected to tails U/F from secondary DMS cyclones is the main chemical grade spodumene concentrate product. (1.11 wt% →5.95% Li ₂ O,) 185-200kt	No Li refinery plant planned - concentrate shipped overseas
Goldfields	Bald Hill	<u>LCT albite-spodumene pegmatite</u> Spodumene-muscovite-quartz-albite association	Main - spodumene Minor - micas Minor - sicklerite	High-grade megacrystic spodumene is highly fractured with tabular habit Range from white to dark green with Fe, Mg and K micaceous alteration prismatic, lath-like Spodumene megacrysts (+10-15 cm in length)	Moderate Fe content in spodumene (0.2-0.4 wt%) (Mg, Fe, Na, K contaminates from mica)	Coarse unaltered and altered spodumene can be liberated from quartz and feldspar associations. Micas exist in a number of forms within spodumene as: <ul style="list-style-type: none">Fine interstitial veins in voids and fractures <ul style="list-style-type: none">Coarse inclusions within spodumene grainsComplex alteration zones within spodumene grains	Columbite-tantalite - associated with feldspars and quartz		<u>Existing plant (not operational)</u> <ul style="list-style-type: none">ROM crushed to ~12 mm particle size with jaw and cone crusher	Existing plant <ul style="list-style-type: none">Screen U/F (~1mm) → Spirals and shaking tables used to separate the high-grade tantalite-bearing ore Screen O/F (~12 + 1 mm) → coarse screen which separates feed into a ~12 + 5 mm (coarse fraction) and ~5 + 1 mm (fines fraction) Coarse fraction → Two -stage DMS cyclone circuit. Overflow rejected to tails Fines fraction → Reflux classifier to remove mica & slimes and collected in the O/FReflux classifier U/F → Two -stage DMS cyclone circuit. Overflow rejected to tails U/F from both the coarse and fines secondary DMS cyclones are the main spodumene concentrate product	No Li refinery plant planned - concentrate shipped overseas
	Mt Marion	<u>LCT complex spodumene pegmatite</u> Spodumene-quartz-muscovite-albite-microcline association	spodumene	10 to 30 cm long, and ~1.5 cm in diameter, pale pink, pale green or grey-white tabular spodumene crystals	Fe 0.34- 74% Mn ~0.01%	Two main forms of spodumene associations: <ul style="list-style-type: none">Fine to medium grained pegmatites composed primarily of quartz, feldspar, spodumene and muscovite, without any significant zoning of mineral assemblagesFine graphitic texture intergrowth with quartz and feldspars	Trace tantalite-columbite as blocky laths, Nb>ta (Fe, Mn-bearing)		<u>Existing plant 2.4Mt/a</u> Three -stage crushing circuit with a primary Jaw crusher, secondary cone crusher, a tertiary crushing and HPGR	Existing plant Circuit consists of a primary and secondary DMS with cyclones circuit. A coarse (+1mm) concentrate at 6 wt % Li ₂ O and a fine concentrate at 4 wt% Li ₂ O is produced	No Li refinery plant planned - concentrate shipped overseas. PFS level study (Proposed Li refinery plant for treatment of concentrate from Wodgina mine in Pilbara)
	Londonderry	<u>LCT complex petalite pegmatite</u> <ul style="list-style-type: none">Albite-quartz-muscoviteQuartz-petalite/petalite ore zone	petalite	Massive >10cm	Barren of mineral impurities	Petalite-quartz Petalite-quartz-albite-muscovite associations	Columbite-tantalite - euhedral crystals up to 200 mm associated with quartz-muscovite-albite	Zircons, about 30–50 mm in muscovite Xenotime-Y: euhedral grains to 200 mm, partly fragmented zones associated with zircon and columbite/tantalite	<ul style="list-style-type: none">Primary & secondary jaw crushingTertiary cone crushing	For petalite zones ore excavated and then crushed and ground for transport as a concentrate	No Li refinery plant planned
	Pioneer Dome and Dome North	<u>LCT complex petalite pegmatite</u> Petalite-rich zone	petalite spodumene	Massive >30cm	Barren of mineral impurities	Massive petalite zones Poikiloblastic intergrowths of quartz-spodumene-petalite Fine and medium grained spodumene with quartz, albite and muscovite	Laths of Ta-Nb-oxides (Nb>Ta), Mn/Fe-bearing (<50 mm but up to 250 mm long)		<ul style="list-style-type: none">Primary & secondary jaw crushingTertiary cone crushing	For petalite zones ore excavated and then crushed and ground for transport as a concentrate	No Li refinery plant planned Potential Li refinery plant - Calcination followed by acid baking and water leaching Production of LiOH
	Sinclair Cs deposit	<u>LCT complex lepidolite pegmatite</u> Albite-lepidolite-quartz pegmatite, albite highly fractured, in-filled with spodumene, entrapped grains of quartz/elbaite Pollucite zone	pollucite petalite lepidolite spodumene	Lepidolite, petalite as large crystals up to 20 m in length	Mn, Rb, Cs & F	<ul style="list-style-type: none">Lepidolite - Quartz, elbaite, topaz intergrained with other micas and contacts with feldspar and quartzPollucite barren of impuritie exist as massive zones		Pollucite Zones of pollucite-amblygonite-albite interspersed within the pollucite zone	Primary crusher and then ground in a rod mill to liberate lepidolite (K80~ 0.16mm)	Lepidolite concentration Crushed product deslimed by hydro-cyclone to remove very fine particles (cut size <0.060 mm) Flotation to produce a high Li grade concentrate (4.7 % Li ₂ O) Pollucite concentration – two approaches: <ul style="list-style-type: none">For pure pollucite zones ore excavated and then crushed and ground for transport as a concentrateFor mixtures, pollucite concentrated by three stage reverse flotation technique to flot and remove quartz, mica, and other gangue. Ground feed is conditioned with sulfuric acid to a pH of 1.4-2.7. Addition of hydrofluoric acid to depress pollucite, aluminum sulfate added for froth control; a cationic reagent e.g. Armac CD* (a cocoamine acetate); Tails collected to produce collucite concentrate	No Li refinery plant planned - concentrate shipped overseas
Gascoyne	Kathleen Valley	<u>LCT complex spodumene pegmatite</u> Quartz-albite-lepidolite-spodumene Albite Quartz-spodumene Albite/microcline Quartz-spodumene Quartz-spodumene (lilac)-lepidolite Fine-grained, quartz-albite-lepidolite with high Ta-bearing zone	Spodumene lepidolite	spodumene mainly 5 to 10 cm laths Very coarse spodumene present (megacrystic laths)	Low Mn <0.15-0.17 wt%) Fe up to 0.6%	<ul style="list-style-type: none">Mainly spodumene elongated laths in association with quartz and feldsparsSpodumene laths pseudo-morphic replaced by quartz-elbaite-cleavelandite-calcite-beryllepidolite zones - finely disseminated grains within albite/quartz independent of spodumene	Blocky laths of Ta-Nb-oxides, to 600 mm and some microlite		DFS level study 2.5Mt/a Two -stage crushing followed by SAG milling to P80 grind size of 180 µm	DFS level study (~500kt/a of spodumene concentrate) Magnetic separation to remove iron materials Gravity separation of tantalum concentrate (~12% upgraded off site to 30% Ta ₂ O ₅) Whole of ore three- stage flotation to produce Spodumene concentrate (6% Li ₂ O, 76%)	DFS level study Proposed Li refinery plant - Calcination followed by acid baking and water leaching Production of LiOH
Murchison	Dalgaranga	<u>LCT albite pegmatite</u> zinnwaldite zone, albite-zinnwaldite zone, grey quartz	zinnwaldite	Fine to 10's of cms	Fe, Mn, Rb, Cs & F	Zinnwaldite mainly associated with quartz and albite and muscovite	Ta mineralisation occurs mainly as tapiolite and tantalite, with lesser microlite		Primary crusher and then ground in a rod mill or semi autogenous (SAG) mill to liberate zinnwaldite	Crushed product deslimed by hydro-cyclcone to remove very fine particles Wet High Intensity Magnetic Separation (WHIMS) to separate out the lithium bearing micas (zinnwaldite) and produce a magnetic mica concentrate providing there are no other major paramagnetic minerals where applicable non magnetic fraction spiral or gravity circuit - heavy minerals	Sulphate roasting with CaSO ₄ and Ca(OH) ₂ , followed by water leaching Zinnwaldite decomposed into Ca ²⁺ Fe ³⁺ (SiO ₄) ₃ , Ca(Al ³⁺ Si ³⁺ O ₄), Ca ²⁺ Si ³⁺ O ₄ F ²⁻ , traces of CaF ₂ , and leachable LiKSO ₄ . Fluorine fixed by the formation of F-containing compounds

(refer to section, Liberation characteristics of spodumene), fine grinding would be required to liberate spodumene associated with graphitic textural intergrowths with quartz and feldspar.

The Mt Cattlin and Bald Hill ores are characteristic of high-grade, white spodumene in quartz, feldspar and muscovite zones, transitioning to low-grade, highly altered green to dark-green spodumene present in a quartz and feldspar matrix. The mineralization of spodumene is fairly coarse (metre to coarse centimetre in length) compared with the other deposits, which make it conducive to produce only a coarse concentrate using DMS circuits. As illustrated in this study, Fe-, Mn- and Mg-enriched micas exist in several forms as fine interstitial veins in voids and fractures, as coarse inclusions within spodumene grains and as complex alteration zones within spodumene grains, see section Bald Hill.

Both concentrate plants have similar process configurations and consist of staged crushing with jaw and cone crushers, although the crushed size reporting to the concentrator circuit varies between the two plants (+14 and +18 mm). Ore sorting has recently been installed at Mt Cattlin to improve the quality of the feed going to the concentrator. The crushed ore is screened, and the underflow treated with spirals and shaking tables to recover the Ta product. In the Mt Cattlin circuit, the screen overflow is treated through a DMS cyclone circuit to produce spodumene concentrate. In the Bald Hill plant, the screen overflow is further screened and treated through a two-stage DMS circuit to produce a coarse spodumene concentrate. The fines are first treated through a classifier to remove slimes and mica before treatment through a two-stage DMS circuit to produce a fine spodumene concentrate.

The Londonderry and Pioneer Dome ores contain zones of massive petalite as illustrated in sections Dome North and Londonderry. Neither of these deposits are currently mined for lithium. Selected mining of the region may allow a simple excavation, crushing and grinding circuit targeted at these zones to yield a concentrate. However, processing of petalite in regions with coarse quartz, feldspar and mica associations would require a staged crushing circuit. As petalite has a similar density ($\rho = 2.42 \text{ g.cm}^{-3}$) to most of the gangue material found in LCT pegmatites (i.e. quartz, $\rho = 2.65 \text{ g.cm}^{-3}$ and feldspar, $\rho \approx 2.65 \text{ g.cm}^{-3}$), the recovery of petalite cannot be carried out by DMS cyclone or other gravity type circuits and would require a flotation circuit configuration.

The Sinclair Deposit contains regions of petalite, lepidolite and spodumene, but it is mainly the Cs mineral pollucite which is of interest. Pollucite exists as a massive zone, with minimum impurity content (see section Sinclair Caesium Deposit), which allowed Pioneer Resources (now owned by Essential Metals) to recently mine and process pollucite as a DSO and only involved direct crushing and grinding to make a concentrate.

The Kathleen Valley Deposit is characterized by having medium to coarse spodumene as elongated laths that are associated with quartz and feldspars as described in section, Kathleen Valley. The proposed process will consist of a two-stage crushing circuit followed by SAG to produce a P80 180 μm feed to a flotation circuit. The crushing and grinding circuit feeds a gravity circuit to produce a Ta concentrate. The SAG mill will accommodate

the initial base production of 2.5 Mt/a, and the planned expansion to 4 Mtpa in the sixth year of the mine plan. Magnetic separation is used to reduce the Fe level (by 55%). A flotation circuit will be used to concentrate spodumene. The circuit differs from the Pilgangoora plants in that no DMS circuit is used. Both pre-feasibility study (PFS) and DFS indicated better recoveries (80%) and grade (>6% Li_2O) were obtained by a direct flotation route rather than involving a DMS circuit (Liontown presentation 2020, Liontown ASX announcement 11 Nov 2021).

The Mt Marion Deposit is characterized by spodumene associated with quartz, muscovite and albite (see section Mt Marion). The process plant consists of a three-stage crushing and HPGR circuit. The ground product is screened to produce a coarse (+1 mm) and fine (<1 mm) fraction. Both streams are treated through reflux classifiers separately to remove mica and de-slime. The coarse feed is then processed through the primary DMC circuit to produce a 6% Li_2O grade spodumene concentrate. The coarse rejects are processed along with fine fraction through the secondary DMC circuit to produce a 4% Li_2O grade spodumene concentrate.

The Dalgaranga Deposit contains the Li- and Fe-rich mica, zinnwaldite. No lithium has been mined at Dalgaranga. Treatment of zinnwaldite ores usually involve jaw crushing ROM followed by either rod milling or SAG milling to liberate the zinnwaldite. Beneficiation can be by wet high-intensity magnetic separation (WHIMS) to separate out the Li-bearing micas (zinnwaldite) and produce a magnetic mica concentrate. The ability to use WHIMS is unique to zinnwaldite ore because zinnwaldite contains Fe in its lattice and is paramagnetic. The magnetic susceptibility of zinnwaldite is about $270 \times 10^{-9} \text{ m}^3\text{kg}^{-1}$ (Leißner et al., 2016). Magnetic separation has been shown to be effective in separating zinnwaldite using a relatively broad magnetic induction range ($3500\text{--}7200 \times 10^{-4}$ Tesla) from Sn-W tailings in the Czech Republic (Botula et al., 2005). European Metals Ltd are proposing to recover zinnwaldite by magnetic separation in their plant development at Cinovec in the Czech Republic (European Metals ASX announcement, 2017).

Lithium refineries in Western Australia

As of the fourth quarter 2021, only Talison has built and commissioned a lithium refinery processing plant with a production nameplate of 48 000 tpa battery grade lithium hydroxide from Greenbushes spodumene concentrate at Kwinana. Covalent Lithium has commenced construction works at its Kwinana refinery site following approval from the WA Department of Water and Environmental Regulation. The refinery plan is to process ore from the Mt Holland mine to produce 50 000 tpa of lithium hydroxide, LiOH, over a 40-year project life, with production of battery-grade LiOH forecast for 2024. United States company Albemarle Corporation and its local partner, Mineral Resources, are also looking to build a 50 000 tpa refinery at Kemerton.

While full details of the refinery operations are not published, the refinery process normally consists of spodumene concentrate being heated in a rotary kiln to 1100 °C to convert α -spodumene to β -spodumene. The calcined product is then cooled and ground (74 to 150 μm) in a mill to break up the particles. The ball mill discharge is fed to an acid mixer where sulphuric acid is blended with the calcined

feed. The blended acidic calcined mixture is fed to a second rotary kiln to undertake a sulphate roast at ~250 °C. The baked product is cooled and water leached to extract the lithium from the baked product. The pregnant lithium liquor is filtered from the baked residue and processed through a caustization step.

Direct production of lithium hydroxide is preferred over lithium carbonate product in response to changes in requirement for EV battery materials. The impurities are removed by increasing the pH by the addition of series of bases to precipitate the impurities. Lime is used to increase the pH to remove Al and Fe from solution. Sodium carbonate is then added to remove Ca and Mg. The liquor is treated with 1.5 – 1.7-fold excess NaOH to increase solution pH. The solution is cooled to between –5 and 3°C for around 12 hours to form crystals of Glauber salt, $\text{Na}_2\text{SO}_4 \cdot 10\text{H}_2\text{O}$. These crystals are removed by centrifuge and dried for disposal. The remaining solution is heated to evaporate water and crystallize $\text{LiOH} \cdot \text{H}_2\text{O}$ through a crystallizer. Several stages of dissolution and recrystallization are undertaken to further purify the product.

Lithium refining to make LiOH from Mt Holland and Kathleen Valley ores is in the development stage. Pilbara Minerals is investigating options for treating their fines, which include using the Calix flash vertical kiln to calcine the fines and also investigating the use of the Liena™ process, a pressure alkaline approach developed by Lithium Australia and ANSTO. At this stage, most of the other mines are still processing ores to make a DSO concentrate.

The treatment of petalite ores such as at Londonderry and Pioneer Dome follows a similar treatment process to that used for spodumene (Sitando and Crouse, 2012). For the treatment and extraction of Li from lithium mica ores, sulphate roasting is best undertaken with CaSO_4 and $\text{Ca}(\text{OH})_2$, followed by water leaching. Zinnwaldite decomposes into $\text{Ca}_3\text{Fe}_2(\text{SiO}_4)_3$, $\text{Ca}(\text{Al}_2\text{Si}_2\text{O}_8)$, $\text{Ca}_4\text{Si}_2\text{O}_7\text{F}_2$, and traces of CaF_2 . In this process, F is fixed by the formation of F-containing compounds to prevent HF formation. Other processes such as the SiLeach and L-Max Technology have been tested on pilot scale to recover Li from micas (e.g. lepidolite). The halogen-based SiLeach process uses the addition of ground fluoride minerals followed by sulphuric acid to process slurry to generate F^- in solution and preferentially react with silicates without any accumulation of HF in the slurry (Griffin, 2017). A 6 kg/h pilot plant campaign reported lithium extractions of 95%. Lepidico Ltd have also tested their atmospheric process on a high-grade, Li mica concentrate to yield Li recoveries greater than 80% and following purification steps claim to produce >99.88% Li_2CO_3 (lepidico.com, 2017).

Comparison with other orebodies

Granite pegmatite deposits around the world, where lithium mineralization is mostly hosted by the mineral spodumene, tend to have similar process plant designs as illustrated in this report for the Australian industry. Processing of Li-bearing pegmatites involves three-stage crushing (primary jaw, secondary cone and tertiary HPGR), DMS to produce a spodumene concentrate and gravity concentration to produce separate Sn and Ta concentrates. As illustrated in Figure 3 many of the world deposits are small in comparison with those present in Australia.

Process implications

Key mineralogical factors that are important in selecting a processing option for Li ores are:

- Lithium mineral host and impurities (Fe, Mn) within the mineral structure
- Size of mineral host
- Mineral assemblage, texture and associations with the Li-host mineral.

While orebody and stakeholders can influence the design, increasingly environmental and social governance factors are also becoming important in considering options for processing orebodies. There are several publications which have broadly reviewed the beneficiation and extraction processing of Li-bearing minerals (Grammatikopoulos et al., 2009; Meshram et al., 2014; Tran and Luong, 2015; Tadesse et al., 2019; Karrech et al., 2020; Li et al., 2019; Welham, 2019; Gibson et al., 2021). Details of plant design for individual plants are limited in reported PFS and DFS. A summary of the major issues and impediments of processing of lithium WA ores are listed in Table 19. Specific details of equipment used to treat ores are outlined in the following sections.

Crushing and grinding

The crushing circuits of albite–quartz–feldspar pegmatite ores containing spodumene in Western Australia is generally undertaken using open-circuit primary and closed-circuit secondary crushing.

Tertiary and quaternary crushers are used for ores that need to undergo physical separation, whereas primary crushing followed by SAG milling is used in circuits where the feed goes directly to flotation (Welham, 2019).

Where crushing and dry screening are used, a coarse particle size is favoured. Spodumene pegmatite ores are generally hard (unconfined compressive strength index ~150 MPa) and abrasive (abrasive index ~0.5). The crushing work index of around 15 kWh/t (10–18 kWh/t) typifies moderately hard crushing duties, with ball mill work indexes ranging from 11 kWh/t for coarse product to 20.4 kWh/t for fine P_{80} , ~150 μm products. SAG mill comminution test work data reported for the Kathleen Valley Deposit showed high competency ($A \times b$) values of 55.8 to 65.8, which leads to Liontown favouring SAG milling over staged comminution processes used by other process plants. Apart from higher power consumption, finer crushing requires high-circulating loads, which causes high-liner wear and consequent increased downtime for maintenance. In addition, finer size screening can result in screen pegging and blinding, especially in ores containing a high mica content. Coarse feed can also improve screening efficiencies in downstream DMS circuits. The coarse nature of spodumene in Western Australian ores has allowed companies to favour coarse product sizes (4 to 18 mm).

Overgrinding of ores containing micaceous material can result in preferential sliming of mica, which presents a problem when fed to the beneficiation circuit. To reduce overgrinding, a classifier and screening prior to milling is recommended.

Table 19. A summary of the impact of different ore components on processing for extraction of Li
 a) Comminution and liberation;

Aspects	Issues	Impediments	Potential solutions
Coarse-grain, high siliceous content	High abrasion and wear on comminution circuit	Frequent maintenance and replacement of liners	Stage crushing and use of HPGRs
Particle size	Generation of fine particles	Loss of Li grade and revenue	Ensure particle size reduction is in line with spodumene liberation characteristics and not overground
		High contamination with gangue materials	Ensure particle size reduction is in line with spodumene liberation characteristics and not overground
		Limited treatment options for low grade	Fines treated via flotation to concentrate
Graphitic texture intergrowths of spodumene quartz and/ or feldspars	Incomplete liberation of spodumene	Loss of Li grade and revenue	Finer grinding downstream to liberate and treat via flotation or DMS to concentrate
	Little difference in SG between the gangue minerals and spodumene for dense media or gravity separation	High SG material report to concentrate and dilute grade	
Fe, Mn and Mg-enriched micas as fine interstitial veins in voids and fractures, and as coarse inclusions within spodumene	Incomplete liberation of spodumene	Loss of Li grade and revenue	Minimize processing such materials via ore sorting and/or selective mining
	Little difference in SG between the gangue minerals and spodumene for dense media or gravity separation	High-SG material report to concentrate	
Iron oxides	Reports along with spodumene in DMS circuits	Iron contamination in spodumene concentrate	Magnetic separation to remove Fe-bearing minerals
Micas and clay contents	Overgrinding	Sliming	Remove prior to milling via a classifier and screening
		Reporting to beneficiation circuit	
		Increased costs to remove	
High-petalite content in ore	Reports along with gangue minerals in gravity and DMS techniques	Loss of Li grade and revenue	Treatment via flotation to concentrate
Tourmaline	Reports along with spodumene in the DMS step	Dilution in spodumene concentrate	Spirals and shaker tables after the milling circuit to recover tantalite
	Breakage of coarse grains to generate fines		
Country rock contamination (amphibole, ferro magnesium minerals)	Poor separation during DMS process	Reports and dilutes concentrate to calcination circuit	Ore sorting to remove prior to processing ore

b) Lithium refinery - calcination and acid baking process followed by water leaching

Aspects	Issues	Impediments	Potential solutions
Rotary kiln	In homogeneous axial and radial temperature distributions and varying residence time within the kiln	Incompletion conversion of α-spodumene Overheating and sintering Poor Li extraction	Ensure a steady controlled feed rate
High fines content	Unconverted spodumene is recycled back to the calciner feed	Reduces the capacity of the plant as dust load increases in the kiln	Agglomeration of fines prior to mixing with coarse feed Treat fines by an alternative process
Calcite and other carbonates	High CO ₂ levels in kiln, reduce oxidation of minerals Formation of acid soluble CaO	High content of Ca reporting to liquor – gypsum formation and scaling	Minimize in upstream processing
Micas (particularly high in Fe Mg, K and Na)	Decomposition forming melts (450 to 950°C)	Encapsulation of the spodumene grains preventing Li extraction	Minimize in upstream processing
Feldspars (mainly orthoclase and albite)	Form eutectic melts	Encapsulation of the spodumene grains preventing Li extraction	Minimize in upstream processing Operate kiln at <melting point of feldspars
Calcination of α-spodumene to β-spodumene	Incomplete conversion of spodumene	Poor Li extraction downstream	Extend calcination time Reduce particle size feed to kiln Ensure gangue mineral content minimized
High Fe and Mn impurities within spodumene	Highly exothermic reaction through exsolution of Fe and Mn from spodumene and oxidation Incomplete oxidation of Fe and Mn in spodumene	Rapid α- to β-spodumene conversion and sintering and disintegration of spodumene particles producing more fines Increase Fe and Mn content in water leach	Temperature and air monitored and controlled
Li micas	Liberation of HF during decomposition Formation of melts	Safety and environmental issues Lithium locked melts not recovered during acid bake and water leaching Elevated levels of Rb, Cs Mn and Fe in water leach	Sufficient agitation of particles in contact with air Treated separately to spodumene concentrate via reverse flotation of spodumene Mica treated via a sulphate roast with CaSO ₄ and Ca(OH) ₂ to fix F
Tourmaline	Dehydroxylation with F or B emissions during calcination stage	Safety and environmental issues	Minimize in upstream processing
Apatite (Mn and F)	F form stable during calcination temperature up to ~1600°C Reacts with sulphuric acid during acid bake	Increased Ca and P, Mn and F content in water leach Increased costs in reagents usage to remove during purification stage	Minimize in upstream processing
Acid to calcined ratio in acid-baking stage	Insufficient acid to consume all reactive materials	Poor Li extraction	Ensure excess acid present to cover both Li extraction and acid consuming minerals
Acid and calcine mixing	Limited contact of acid with calcined materials	Poor Li extraction	Optimize particle grind size enough for contact
Addition of lime to raise pH to remove Al, Fe from acid-baked filtered liquor	Precipitation of gypsum through reaction of Ca and SO ₄ ions in solution	Scaling and increased tails residue	Use NaOH as precipitating agent (but increases Na to be discarded)
Impurity levels in final liquor	Low levels of Al, Fe, Mg, Ca	Impurity reports to LiOH product	Ion exchange to remove impurity ions from liquor

For ores that predominantly consist of Li-mica, a primary crushing process followed by rod or SAG milling to liberate the mica is favoured as this reduces the sliming of mica. This type of process could be used to process zinnwaldite at Dalgaranga and possibly the Li-mica at Lepidolite Hill (a predominantly lepidolite ore) near Mt Marion.

HPGR have been successfully used to reduce feed to appropriate size (3–6 mm) for downstream processing via techniques such as DMS and cyclone process. HPGR can reduce the complexity of the crushing circuit allowing for reduced maintenance costs associated with wear life of liners, and less downtime compared with conventional crushing processes. However, HPGR can produce a high content of fines, which can be reduced by choosing a coarse crush size and suitable process downstream for treating fines (Daniel et al., 2019). The use of HPGR has been implemented in the process flowsheet for ores from Pilgangoora and Mt Marion.

Electrodynamic fragmentation (EDF), electrical pulse disaggregation, high-voltage pulse disaggregation, or 'Selfrag' processing techniques can be used as an alternative to conventional comminution techniques to enhance mineral liberation in various metallurgical applications. As applied to a zinnwaldite ore, EDF and traditional comminution size reduction yielded similar locking and liberation characteristics (Sandmann and Gutzmer, 2013). The integrated use of EDF and optical sorting as a combined method to enrich Li minerals has been examined and achieved selective liberation of spodumene and several of the gangue mineral components from a lithium pegmatite rock from Finland (Brandt and Haus, 2010). The EDF technique can reduce power consumption, allow breakage of particles at coarse size and produce fewer fines compared with standard crushing techniques. However, throughput on a large scale suitable for commercial scale production is limited.

Beneficiation

Following the crushing stage, ores with a high Ta mineral content in the form of columbite–tantalite undergo a classification step to remove the high-density, heavy fraction that is treated to concentrate the Ta minerals through spirals and sometimes shaker tables. As illustrated in this report, Ta minerals in all deposits examined are mainly associated with the gangue minerals and can be freely liberated and treated separately from the spodumene concentrate.

During the crushing process of quartz–feldspar spodumene pegmatites, both a coarse and fine fraction are generated. Typically, DMS using cyclones for gravity separation is conducted on the 0.5 to 15 mm size fraction, with the undersize at <250 µm feeding a flotation circuit. In some cases, a middlings DMS product containing unliberated spodumene associated with silicate gangue is combined with the undersize to feed the flotation circuit.

DMS can be an effective means to separate spodumene from lighter silicate minerals in a pre-concentration stage in hard rock operations. This has the benefit of less feed to the grinding and flotation circuits, achieving subsequent capital, energy and operating cost savings. The fines can either be discarded, stockpiled for future exploitation or treated through a flotation process.

Spodumene has a specific gravity between 3.1 and 3.2 g.cm⁻³, while quartz and feldspar have specific gravities between 2.5 and 2.6 g.cm⁻³, whereas mica has a specific gravity between 2.8 and 3.0 g.cm⁻³. Hence, the separation of these minerals from spodumene by dense media is possible.

Factors that contribute to the efficiency of DMS in pegmatite minerals beneficiation are as follows:

- Degree of spodumene liberation at coarse particle sizes. Poor spodumene liberation yields significant lithium losses to the float product and negates economic justification for its use.
- Due to the close relative densities, spodumene liberation must be high at larger particle sizes to minimize lithium losses.
- Fe-bearing silicates, such as amphibole, tend to have higher densities (2.9 – 3.2 g.cm⁻³) and are, therefore, not separated from spodumene through DMS. Hence, this highlights the importance of removing country rock from the process.
- The mineralogical transformation of spodumene to micaceous and clay minerals reduces the specific gravity (SG) of spodumene compared with its pure form and, as a result, there is effectively little difference in SG between the gangue minerals and spodumene.
- The spodumene behaves like micaceous and clay minerals in heavy media separation and, thus, its separation is affected.

The limitations of DMS were shown in spodumene concentrates obtained from both Mt Cattlin and Bald Hill in this study, as shown in section Liberation characteristics – concentrates, where the presence of both country rock and mica was observed in high abundance. In recent times, ore sorting technology has been applied at Mt Cattlin to improve the feed to the DMS circuit. Using this technology, white and green spodumene can be distinguished optically from dark country rock and platy mica. The treatment of pegmatite zones with fine, graphic intergrowths of quartz and feldspar with spodumene (e.g. observed in some Pilgangoora samples tested) will also dilute the grade through DMS circuit and would need to be monitored during grade control.

Froth flotation is a technique which has been widely used in recent years for the beneficiation of spodumene (Gibson et al., 2017; Tadesse et al., 2019). Pre-treatment of Li-ores prior to flotation is an important step of the separation process to 'clean' or modify the surface of minerals before flotation. Reagents NaOH, Na₂S and NaF are used in the pre-treatment of Li-pegmatite ores (Moon and Fuerstenau, 2003; Yu et al., 2015a,b). The more weathered the material, the more cleaning is required for selective flotation. At the Kings Mountain operations in the US, cleaning of spodumene was conducted by the addition of NaOH to the grinding mill before it was fed to the flotation circuit (Redeker, 1981). Typically, the dosage of NaOH used for pre-treatment ranges from 0.5 to 2 kg/t and conditioning is conducted for 20–30 mins (Bulatovic, 2015).

Anionic collectors such as oleic acid, sodium oleate, sulphonated and phosphorated fatty acids are widely utilized for the flotation of spodumene from pegmatite ores (Bulatovic, 2015). Spodumene recoveries of >90% and a

concentrate grade of 6.52% Li₂O can be achieved with oleic acid. New collector mixtures have been tested (e.g. Xu et al., 2016), and the collector adsorption, pH, and isoelectric point that favours spodumene have been investigated in detail (Moon and Fuerstenau, 2003). Actual reagents used by several mine sites to float fine spodumene are confidential in nature. Several different collectors developed by Badische Anilin und Soda Fabrik are also available. Certain dissolved cations can affect spodumene flotation performance (Moon and Fuerstenau, 2003). Notably, both Ca²⁺ and Fe³⁺ in the flotation pulp promotes spodumene activation. However, calcium hydroxide and ferric species are likely to precipitate on the surface of other silicate gangue minerals and spodumene surfaces, which can be the cause of concentrate grade dilution (Gibson et al., 2017). Therefore, process water chemistry is likely to have a significant effect on overall flotation performance of spodumene, an area that warrants further study.

Few studies exist on the flotation of lepidolite or petalite (Tadesse et al., 2019) and further studies on the mechanism of collector adsorption and the effects of activators and depressants are required for a better understanding. However, flotation has been used to separate mica from spodumene concentrate to improve spodumene grade in more complex ores in Canada (Gibson et al., 2017). In this example, a reverse silicate, gangue mineral flotation process is used to float mica and suppress spodumene. Mica flotation is conducted in acidic pulp conditions (pH 2–2.5) using H₂SO₄ as a pH modifier and an amine-based, cationic collector (Bulatovic, 2015). Petroleum sulphonate has also been used to float mica under acidic pulp conditions (Redeker, 1981). Mica pre-flotation offers the added benefit in removing Fe silicates and reducing the overall Fe content of the final spodumene concentrate. For ores with high zinnwaldite contents, beneficiation can be carried out on liberated grains by magnetic separation techniques, as mentioned earlier.

Magnetic separation is also frequently used to reject Fe-bearing minerals so that the spodumene concentrate is suitable for use in ceramics and glass applications. The effectiveness of magnetic separation is related to particle dispersion in the feed (Jirestig and Forssberg, 1994).

Pretreatment calcination processing

The purpose of the calcination step is to convert refractory α -spodumene into β -spodumene, which is more amenable for extracting lithium from the calcined structure. Factors that affect the design and selection of the calcination process are the melting characteristics of the material at high temperature, the feed particle size distribution, abrasiveness and the ability to handle dust (Harman, 2019).

Calcination is conventionally carried out in a rotary kiln (Garrett, 2004). Rotary kilns have temperature gradients along the reactor length with the highest temperature in the flame zone of the burner (Gasafi and Pardemann, 2020). Hence, while the set temperature in the kiln is around 1100 °C, the temperature can exceed 1800 °C near the flame formed by the burner. The inhomogeneous axial and radial temperature distributions and varying residence time within the kiln, means that gangue materials that are associated with spodumene and with different thermal properties (i.e. different melting points) will have a significant effect on the performance of the calcination process.

As illustrated in this study, the texture and appearance of calcined spodumene is related to the elemental and mineral impurities associated with the spodumene. Spodumene with high Fe and Mn content converts to β -spodumene at a slightly lower temperature. The exsolution of Fe and Mn from the spodumene structure during calcination results in fine Fe and Mn oxide particles providing there is sufficient oxygen in the furnace. It is important that Fe and Mn associated with spodumene and other minerals, such as mica, are fully oxidized during the calcination step; otherwise, high dissolution of these elements may be expected in the downstream leaching process. However, some control in the rate of heating and oxidation during the calcination process of high-Fe spodumenes (1–1.5 wt%) needs to be taken, as the highly exothermic nature of the oxidation of Fe during calcination causes the calcined spodumene to disintegrate into smaller particles. This can create issues with the management of finer particles in the acid-bake leach, and the filtering of solids to recover the liquor for recovering lithium from solution.

As illustrated in this study, the decomposition of micaceous materials forming melts may result in the following problems:

- Coating spodumene grains to render calcined spodumene refractory to lithium extraction during the sulphate-roasting and water-leaching step. The finer the particle size distribution the more serious the issue.
- Accumulation, agglomeration of particles and coating of melts in cooler zones along the furnace walls. This will lead to frequent maintenance shutdowns to remove layers of a glass-like phase (clinker) that accumulates during operation.

As observed in the calcination studies, both primary and secondary forms of mica associated with spodumene undergo thermal decomposition at temperatures (<950 °C) below the spodumene transformation temperature. In particular, secondary micas (normally containing Mg, Fe, Na and K) have a recrystallization state that coincides with the spodumene transformation temperature range.

Other gangue material, such as feldspar, can cause particle agglomeration in spodumene concentrates from the partial melting of alkali-feldspar at temperatures above 1025 °C.

The coarse nature of feldspar, quartz and muscovite observed in spodumene concentrates examined in this study suggests they can potentially be liberated and removed by further treatment and upgrade of the concentrates. In concentrate samples examined in this report, liberated gangue particles of country rock materials and muscovite are evident and can easily be removed following a further cleaning separation stage or by ore sorting techniques. However, the fine integrated nature of micas associated within the alteration zone and those associated with fine fractures within spodumene are unlikely to be liberated without costly fine grinding and cleaning processes prior to treatment through the calcination process. Sintering needs to be avoided because leachability is reduced due to limiting access of the reagent to the β and γ -spodumene.

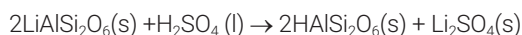
Different pre-treatment options to reduce the refractive nature of spodumene to lithium extraction have been discussed in the literature (Salakjani et al., 2019). These have included microwave-assisted heating, flash calcination, mechanical activation and fluidized-bed calcination. A

general advantage of fluidized-bed over rotary kiln calcination is the establishment of a homogenous temperature profile in the reactor and more accurately controlled residence time (Gasafi and Pardemann, 2020). However, spodumene concentrates are very abrasive and need a narrow particle size range to operate in a fluidized-bed. Harman (2019) considered a tunnel furnace where material is batch loaded as a fixed bed into a large, long kiln and heated in the presence of a gas, which remove issues with abrasion, dust as well as allow regulation of temperature.

Fines in the calciner feed stream tend to be elutriated out of the kiln with the off-gases, which tends to be unreacted α -spodumene (Harman, 2019). Unconverted spodumene is recycled back to the calciner feed, which reduces the overall capacity of the plant as the dust load increases in the kiln. Fine spodumene concentrates are also more susceptible to melting in kilns, causing blockages, and rendering the lithium unrecoverable. Furthermore, lower grade ores can contain other elements, which lower the melting point of spodumene leading to melting, fusing and blockages within the rotary kiln. Sodium, K and Fe are known to lower the melting point of spodumene. Calix have developed the BATMn reactor which has been tested on Pilbara Minerals and Greenbushes ore. The results are not published, but the process involves a fines-feed, flash-heated in an externally heated, vertical reactor (Calix.global.com). This reactor may provide a more suitable approach to calcining fine spodumene concentrate and low-grade ores containing high-gangue mineral content and reduce clinker effects.

Acid bake and water leaching

While there are many studies on alternative processes to extract lithium from spodumene, there have been very few attempts to improve the traditional process or to understand the causes behind its limitations. Approximate favoured conditions of 40% stoichiometric excess of H_2SO_4 , a 250 °C roasting temperature and 30-minute roasting duration have been determined by an orthogonal design of experiments (Tian et al., 2011). The test work conditions used in the current study were those designed by Murdoch University and are proven effective in maximizing lithium extraction from spodumene. The acid dosage was set to 180% of the stoichiometric acid dosage (0.9 mol H_2SO_4 /mol Li) for the reaction:



As shown in this study, incomplete lithium extraction can be limited by:

- Mica melt encapsulation of spodumene grains preventing extraction of Li
- Partial melting of feldspar minerals
- Slow rate of diffusion of acid into calcined spodumene particles
- Potentially insufficient acid for dissolution of Li and other acid soluble phases
- Incomplete conversion of γ -spodumene to β -spodumene during calcination may contribute to poor Li extraction during the acid-baked and water-leaching stage.

Studies by Lajoie-Leroux et al. (2018) also indicated that lithium extraction decreases with the impurity content in the feed material and suggest that lithium recovery may be limited by the impurity coating of some β -spodumene particles.

While lithium extraction is considered an ion-exchange process, where hydrogen ions replace Li in the residual calcined spodumene structural matrix, a proportion of Al is also removed during the sulphuric acid-baking and water-leaching process that causes shrinkage of the mineral particles. The agglomeration and shrinkage of particle grains may impede full extraction from particles. Hence, the feed for acid baking needs to be ground fine enough to allow diffusion and leaching of lithium from within particles, but not too fine to cause sliming and blockages during solid-liquid filtration step.

Lithium recovery

Recovery of lithium from liquors was not examined in this study. However, some inferences can be made from the water-leach studies. The current industry method of lithium recovery involves a purification step followed by crystallization steps to crystallize Li as a lithium-hydroxide product and a waste product of sodium sulphate separately (as described in section, Lithium refineries in Western Australia).

Chemical composition of liquors from the acid-baked and water-leach test in the current study showed elevated levels of Na, Al, Fe and Ca in solution. The Greenbushes samples had the lowest level of impurities in solution (500 mg/L) compared with other ores (1500 to 3000 mg/L), reflecting the low impurity content within spodumene, with unreactive quartz being the main mineral contaminant. The dissolution of minerals, such as apatite, with high-phosphate contents contributed to high-Ca and high-Mn yields in some solutions.

To recover Li as a lithium hydroxide product, impurities in the Li pregnant solution are precipitated out by increasing the pH. As the pH is increased, the solubility of the main contaminants (Fe, Al, Mn, Mg, Ca) decreases until they precipitate (Monhemius, 1977). The process is carried out in stages with Fe and Al being removed first by addition of lime. Hydrogen peroxide can be used to oxidize any ferrous ion to the less soluble ferric ion (Welham, 2019). Manganese, Ca and Mg are then precipitated at higher pH using sodium carbonate. Hence, reagent consumption at this stage will be governed by the concentration of these impurities in the acid-baked filtered solutions.

Elements which are reported to be detrimental to battery production are halides (Cl, F and Br as potential powerful oxidizers), Na and K (impact cathode crystal formation) and base metals (Fe, Co, Ni and Cr as redox active metals) (Harman, 2019; Welham, 2019).

Other mineral recoveries

Other minerals and associated elements of significant interest are as follows:

- Columbite – tantalite – Nb Ta
- Cassiterite – Sn
- Feldspars – high in Rb
- Pollucite – Cs.

Processing to produce Ta concentrates is carried out in several existing plants as described above. The nature of the association of Ta minerals with gangue minerals over spodumene, as illustrated in this study, allows for separation and upgrading by gravity separation techniques to produce a concentrate separate to the spodumene concentrate.

The association and fine dissemination of cassiterite within spodumene in many of these pegmatite deposits means some of the cassiterite will report to the spodumene concentrate. Hence, full recovery of cassiterite would need to consider all process streams. As coarse spodumene concentrates are favoured as products for export markets, the potential revenue from Sn may be lost.

Pollucite, from previous mining at Sinclair and in samples evaluated from Greenbushes, have been and are amenable to concentrating as a product for Cs. The high concentration of Rb (0.9 – 3.6 wt%) in feldspar in some of the Pilgangoora ores make it a favourable resource for Rb. Feldspars can be floated by reverse flotation method from the spodumene float quartz tails by conditioning the slurry with hydrofluoric acid and adjusting the pH to 2–2.5, adding tallow amine acetate collector, kerosene and a frother (Heyes et al., 2012). Further upgrade of Rb feldspar from albite is by the addition of NaCl during flotation.

Summary and conclusions

Lithium is a key component in the production of rechargeable batteries for use in a wide range of products including portable electronic devices (mobile phones), e-bikes/scooters and energy storage systems. However, electric and hybrid vehicles exert the strongest demand, accounting for ~70% of Li end-use applications in 2020, which is forecast to increase to ~90% by 2031. In 2020, Australia produced nearly 49% of global Li output, largely from mines in Western Australia. While WA deposits have been generally classified as LCT pegmatites, there is limited published information on their geology, mineralogy and processing characteristics. The aim of this work was to develop a geometallurgical framework for WA lithium pegmatite deposits that would potentially lead to improved efficiencies in exploration, mineral beneficiation and processing techniques. The project was divided into three integrated modules of geology, mineralogy and metallurgy. The project deliverables for each module and the outcomes in each case are summarized below.

The Geology module focused on assessing the geology of LCT pegmatites in WA in terms of the formation, texture and deposition.

Deliverables	Outcomes
1. Field studies to target the main LCT pegmatites and regions in Western Australia	<p>Drillcore and representative examples of LCT pegmatites were obtained for 10 deposits in the Archean Yilgarn and Pilbara Cratons of Western Australia for detailed petrological, mineralogical, geochemical and geochronological analysis. The LCT pegmatites examined in this study were:</p> <p>Southern Yilgarn: Greenbushes, Mt Cattlin</p> <p>Eastern Yilgarn: Bald Hill, Mt Marion, Sinclair Caesium Deposit, Dome North, Londonderry, Dalgaranga, Kathleen Valley</p> <p>Pilbara: Pilgangoora.</p> <p>The LCT pegmatites examined in the current investigation included most of the significant (e.g. Greenbushes, Kathleen Valley and Pilgangoora) LCT pegmatites in Western Australia.</p>
2. Petrochronological and geochemical synthesis of LCT pegmatite mineral systems in Western Australia	<p>Geochronological characterization of the Greenbushes, Pilgangoora, Dalgaranga, Bald Hill and Londonderry LCT pegmatites was undertaken by:</p> <ul style="list-style-type: none">• U–Pb dating of zircon• ⁴⁰Ar/³⁹Ar-dating of spodumene• ⁴⁰Ar/³⁹Ar-dating of muscovite <p>Zircon U–Pb ages of 2643–2629 Ma were obtained for project samples, a range consistent with other WA LCT pegmatites and which coincides with a major period of global pegmatite emplacement from 2650–2600 Ma. The size (mainly <100 µm) and low U content (mainly <100 ppm) of zircon suggests they are inherited and did not crystallize during pegmatite formation. Therefore, measured U–Pb ages provide a maximum constraint to the relative timing of pegmatite crystallization. A revised, older age for the emplacement of the Greenbushes pegmatite at 2631 ± 4 Ma is a significant new finding. It remains to be confirmed if the zircon grains examined may be xenocrysts.</p> <p>⁴⁰Ar/³⁹Ar dating established a plateau age of ~2605 Ma for muscovite from Bald Hill which compares with a zircon U–Pb age of 2643 ± 10 Ma indicating that cooling took place deep in the crust over a period of ~40 Ma. A similar interpretation was made for the Londonderry LCT pegmatite.</p> <p>⁴⁰Ar/³⁹Ar dating of spodumene at Mt Cattlin established a robust plateau age of ~1100 Ma, interpreted to represent the alteration of spodumene by a hydrothermal resetting event, possibly related to fluid flow associated with mafic-dyke emplacement.</p> <p>Mineral–textural relationships were assessed in relation to the <i>P–T</i> phase relationship of the Li–Al–Si system and allowed crystallization pathways for the Londonderry, Dome North and Greenbushes pegmatites to be determined. This informs the resulting style of Li mineralization on a case-by-case basis and enables a prediction of the style of Li mineralization and, therefore, the appropriate processing option for other locally associated pegmatite bodies.</p> <p>Mineral–textural relationships can also inform the inferred emplacement history and genetic association of pegmatites at the deposit scale. For example, the pseudo-morphic alteration of spodumene and the occurrence of lepidolite at the Mt Mann pegmatite swarm, coupled with the different structural aspect relative to the Kathleen’s Corner pegmatite at Kathleen Valley, argues against an ultimately larger, merged pegmatite body at depth, as previously interpreted.</p>
3. Geochemistry signature of minerals to identify pegmatite associations, which can assist in targeting LCT pegmatites	<p>The mineral composition of spodumene and associated phases, such as mica and Ta–Nb oxides were evaluated to establish elemental signatures as useful tools for targeting potential pegmatite mineralization.</p> <p>Spodumene typically has Li–Al–Si contents close to the expected contents for stoichiometric LiAlSi₂O₆. However, alteration of spodumene results in the systematic removal of Li from the spodumene structure. For example, altered spodumene from Mt Cattlin contains 5.15 wt% Li₂O compared to 8.03% Li₂O for pure spodumene. In spodumene:</p> <ul style="list-style-type: none">• Fe and Mn are the main impurities with a combined value of 1.2 wt%.• Sodium, at 500–1200 ppm, was the only other trace element present at consistently elevated amounts.• Trace element patterns were highly variable, with overall depletion in REEs.• No regional differences in the major, trace or REE composition of spodumene, useful as a potential provenance indicator, were identified. <p>Changes in mica (muscovite/lepidolite) composition followed well-correlated and highly predictable trends in relation to their Li and F contents, Li:Al and Li:Si, and K:Rb ratios:</p> <ul style="list-style-type: none">• The F content is a useful proxy for estimating the Li content of mica.• Changes in the K and Rb content of mica can be used to determine the relative degree of pegmatite fractional crystallization and are potentially useful in assessing Li prospectively.• Low K:Rb ratios established all WA LCT pegmatites as being highly fractionated compared to other global pegmatites.• The Greenbushes Deposit was the most highly fractionated of the WA pegmatites examined and is equivalent to the Tanco and Red Cross Lake LCT pegmatites in Canada <p>Thus, from the changes in mica composition described, it is recommended that in greenfields/brownfields exploration, assessment of pegmatite mineralization potential be based on mica composition as in the field:</p> <ul style="list-style-type: none">• Mica (muscovite/lepidolite) is more easily identified compared to the typically white, Li-bearing and barren (feldspar and quartz) phases that also occur.• Mica is typically present as coarsely crystalline ‘books’ of well-defined crystals.• This makes mica highly amenable to compositional analysis using hand-held or field portable instruments (e.g. XRF, LIBS). <p>The Cs and Ta content of muscovite can be used as an exploration tool for identifying potential Ta mineralization:</p> <ul style="list-style-type: none">• Pegmatites that host muscovite with a Ta content >65 ppm and a Cs content >500 ppm are likely to host Ta–Nb mineralization.• The high Cs and Ta contents of muscovite at Greenbushes, Mt Cattlin, Dome North and Londonderry are consistent with the common occurrence of Ta mineralization (Ta>>Nb) at these deposits.• However, the low Cs (<500 ppm) and Ta (<65 ppm) contents for all but one muscovite examined at Dome North does not support the potential of Ta mineralization at this pegmatite. <p>Changes in the Ta–Nb mineralogy, as reflected in their composition (Ta:Nb and Mn:Fe ratios), provide an additional exploration tool useful for assessing pegmatite fractionation and the potential enrichment style of mineralization (i.e. Ta vs Nb content).</p> <ul style="list-style-type: none">• TIMA-EDS measured Ta:Nb and Mn:Fe ratios showed that the majority of tantalite–columbite analysed was manganiferous (Mn>Fe with Ta≈Nb)• Columbite–tantalite from Kathleen Valley was the most manganiferous, with an average Mn content of ~10.2%.• At Dome North, limited EDS analysis revealed that Ta:Nb and Mn:Fe ratios supported a ferrocolumbite dominated mineralogy, with Nb>>Ta and Fe>Mn.• This is consistent with the current, relatively low, resource estimate of 33 ppm Ta₂O₅ for the Cade Deposit.
4. Classification scheme produced that is useful in exploration targeting for economic LCT pegmatites and grade control in mining operations	<p>From the main Li-host identified by TIMA mineral mapping, all pegmatites investigated in this study were classed as part of the LCT family following the scheme of Černý et al. (2012).</p> <p>The majority of pegmatites belong to one of three main complex sub-types:</p> <ul style="list-style-type: none">• Spodumene – Greenbushes, Kathleen Valley, Dome North, Mt Marion• Petalite – Londonderry• Lepidolite – Sinclair Caesium Deposit <p>Exceptions are Mt Cattlin, Bald Hill and Pilgangoora, classed as albite-spodumene types, and the Dalgaranga pegmatite, which is classed as an albite-type.</p> <p>Pegmatite classification is important to informing the most appropriate processing route that accommodates differences in the main Li-host and associated mineralogy.</p> <p>For example, the presence of massive petalite, as identified at Londonderry and Dome North, requires a different processing approach due to the lighter density of petalite (2.4 gm.cm⁻³) compared to spodumene (3.0 gm.cm⁻³). Hence, as the recovery of petalite cannot be achieved by use of gravity/density separation techniques, alternative recovery (i.e. flotation) techniques are required.</p> <p>Mineral–textural characteristics are also a significant factor in the implementation of the most appropriate processing scheme. The development of the characteristic SQL texture that results by the alteration of petalite (e.g. Dome North pegmatite) or by the (inferred) alteration of the high-temperature Li-phase vergilite (e.g. Greenbushes) requires the application of alternative processing options, as described in section, Geometallurgical framework, to optimize the recovery of Li.</p> <p>Similarly, the occurrence of mica (muscovite/lepidolite) as described at the Sinclair and Kathleen Valley LCT pegmatites would require a different processing route (refer to the section Geometallurgical framework).</p>

The Mineralogy module focused on understanding the deportment of Li and other elements of interest in pegmatite deposits and improving the accuracy and precision of analytical techniques used to measure mineral components in pegmatites.

<i>Deliverables</i>	<i>Outcomes</i>
5. Refine the analytical techniques (TIMA, EPMA, LA-ICP-MS) to improve precision and accuracy to quantify pegmatite samples	<p>Due to the very coarse crystalline nature of LCT pegmatites, large, polished mounts (to 75 x 50 mm) were prepared for TIMA measurement so that a more representative sample could be scanned to better characterize mineral–textural features than otherwise could be achieved with a standard, 25-mm round mount.</p> <p>Reliable EPMA quantification of mineral composition requires a detailed understanding of sample chemical matrix (e.g. peak interference and overlap) effects that can influence the quality of the analysis.</p> <ul style="list-style-type: none">Initial wavelength scans identified interference of Si on the Rb (L-α) peak. This required substituting the commonly used RbZnSi-glass standard for a CaAlGeRb-glass standard to avoid over-estimating Rb abundance. This was particularly important for mica EPMA analysis, where the Rb content is used (along with the K content) as a measure of pegmatite fractionation.Similarly, allowance for the interference of Mn on Fe analyses was also required. This too was important for quantifying, for example, the Fe impurity content of spodumene. The Fe content is one of the key measures used by the WA Li industry to assess the purity of a spodumene concentrate. <p>For LA-ICP-MS analysis, the condition of the sample surface as presented to the laser is important in ensuring consistent and reliable analyses. Care was taken not to over-polish the sample surface presented for analysis due to problems with efficient coupling of the laser for well-polished, highly transparent samples (e.g. petalite and spodumene). This can result in incomplete ablation and affect the reliability of the analysis, resulting in under-estimating element content.</p> <p>TIMA characterization identified spodumene from the Greenbushes pegmatite as a candidate for development as Li-isotope standard and isotope analysis protocol.</p> <p>Sample characterization using LA-ICP-MS analysis confirmed the isotopic homogeneity of spodumene with δ⁷Li measurements within ≈1 permil. Independent isotopic compositional analysis, conducted by the Queen's Facility for Isotopic Research, Queens University, Ontario, confirmed the suitability of the Greenbushes spodumene as a Li-isotopic standard.</p> <p>The Greenbushes spodumene is now used as a Li-isotope measurement standard, as part of an FBI-CRC funded project, which aims to develop trace element/Li-isotope signatures as provenance indicators of LCT pegmatites.</p>
6. Assessment of the deportment of Li and other elements of interest and associated minerals in pegmatite deposits. Produce a quantitative understanding of the mineralogical deportment of both economically important (Li, Nb, Ta) and environmentally deleterious (F, Mn) elements within mineral associated with pegmatite ores	<p>The mineral composition and element deportment of the principal Li-host (spodumene) and associated gangue phases was quantified by application of combined EPMA, LA-ICP-MS, TIMA mapping/EDS analysis and ToF-SIMS analysis.</p> <p>Spodumene, as the principal Li-host, was essentially compositionally ‘clean’, with Li–Al–Si contents close to that expected for pure LiAlSi₂O₆. The main element impurities hosted by spodumene are:</p> <ul style="list-style-type: none">Fe and Mn to a combined maximum of 1.2 wt%.Na (between 500 and 1200 ppm) <p>A significant outcome was the characterization of two main pegmatite-alteration styles that preferentially impact spodumene defined as:</p> <p>1. Complete/near-complete, pseudo-morphic replacement of spodumene by a massive, dark-green to black, fine-grained, Li-mica/cookeite assemblage.</p> <ul style="list-style-type: none">Cookeite is an Fe/Mg-bearing, Li-chlorite, containing up to 2.86 wt% Li₂OAlteration imparts a dull to waxy-mottled textureOnly spodumene at Bald Hill and Mt Cattlin affectedAssociated by a thermal overprinting event (dyke intrusion?) as previously describedAlteration introduces significant K (and other element impurities, such as Fe, Mg, Rb and Mn) and results in near-complete loss of Li. <p>2. Symplectic (graphic-textured), in-situ alteration where spodumene is in contact with Na/K-feldspar:</p> <ul style="list-style-type: none">Co-eval to early-post crystallization replacement alteration of spodumeneForms a microscopic, graphic-textured, SQI typeNot associated with petalite alterationResults in complete loss of LiLeaves residual, low-Al-bearing (1–2 wt%) ‘quartz’Affects nearly all examples of LCT pegmatites examined (the Sinclair Caesium Deposit is the exception). <p>Related to the first alteration style, spodumene almost universally displays some level of secondary, sericitic-like alteration as microscopic veining:</p> <ul style="list-style-type: none">Developed along internal fractures and cleavage planesAlteration is predominantly K-rich but also introduces F, Mn, Fe, Mg and Rb. <p>Numerous (primary and secondary) mineral inclusions within spodumene crystals were also detected. Primary phases and their associated element impurities include:</p> <ul style="list-style-type: none">Feldspar (mainly albite; lesser K-feldspar)—Na, KQuartz—SiMica (muscovite/lepidolite)—K, Rb, CsTourmaline—B, Mn, Fe, NaTa–Nb oxides—Fe, Mn, Ta, NbApatite—F, Mn, CaCassiterite—Sn, TaGarnet—Fe, Mn, CaFluorite—Ca, FBeryl—BePollucite (only at Greenbushes)—Cs, Na. <p>Additional, secondary mineral inclusions and their associated element impurities include:</p> <ul style="list-style-type: none">Fe-chlorite—Fe, Mn (locally developed at Pilgangoora)Calcite—Ca‘Feldspathic’—F, Rb. <p>Alteration and primary mineral impurities hosted by spodumene are ultimately carried through to the final ore (spodumene) concentrate, especially for coarse (14–18 mm) size fractions preferred by some hard-rock, Li producers (deliverable 8).</p>
7. An independent assessment on the practical application of LIBS technology in exploration and mining operations	<p>Quantification of pegmatite Li and associated element (Al, Si, Fe, K, Mg) contents was assessed by application of PLS analysis of LIBS analysis of representative powders of known (XRF) composition.</p> <p>Calibration PLS, cross-validation models were developed from a standard data set of 37 pegmatite samples with 4 samples chosen as unknown, validation samples.</p> <p>Predicted PLS, cross-validation models of the pegmatite Li, Si and Al content in the validation data set were close to the known Li, Si and Al contents with relative percentage errors of mainly <12%.</p> <ul style="list-style-type: none">However, Li content of the four validation samples could not be consistently predicted.Similarly, modelled contents of the Fe, K and Mg content were not reliably predicted. <p>The LIBS technique is known to suffer from a few inherent, sample-related effects. The robustness and precision of PLS-LIBS quantification would be improved by developing cross-validation-calibration models from a larger, more extensive sample set and by paying close attention to more consistent sample preparation to minimize sample surface (granularity, textural) and chemical matrix effects.</p> <p>It is recommended that the existing calibration sample set be expanded to include a minimum of 200–250 representative examples from all significant WA LCT pegmatites to ensure the range of sample compositional variability is accounted by the prediction models.</p>

In the metallurgy module, the physical liberation characteristics of Li-bearing mineral particles and chemical processing behaviour of LCT pegmatites were correlated to the mineralogy data generated in the geology and mineralogy studies.

Deliverables	Outcomes
8. Assess the mineral liberation characteristics of mineral components within pegmatite ores	<p>Twenty-one samples that represent different deposits and lithologies from Mt Cattlin, Bald Hill, Greenbushes and Pilgangoora regions were examined. The main source of Li is spodumene in these deposits, with regions containing Li micas (lepidolite and zinnwaldite), as well as petalite.</p> <p>Generally, the coarse nature of spodumene within quartz, feldspar and muscovite mineral matrix allows for >90% recovery of the spodumene, with expected Li grades above 3 wt%.</p> <p>Factors that limit recovery and grade are regions with:</p> <ul style="list-style-type: none">• Graphic-textured spodumene-quartz alteration intergrowth between spodumene and K/Na-feldspar, as observed in most samples but extensively in samples from Pilgangoora.• Partially altered spodumene containing micas in fine interstitial veins and fractures and as inclusions within spodumene grains. This is prevalent at both Mt Cattlin and Bald Hill where high-grade, white spodumene in quartz, feldspar and muscovite zones transitions to low-grade, highly altered green to dark-green spodumene.• Separation of middlings containing high mica and/or quartz/feldspar contents and finer grinding them would improve the recovery of spodumene in these orebodies.• In Greenbushes samples, spodumene can be well liberated from the main gangue mineral quartz, with high recovery and Li grades of 3.5 wt%. Fine grinding would be required to liberate spodumene associated with graphitic texture intergrowths with quartz and in some areas with feldspars. <p>Tantalum minerals in all deposits examined are mainly associated with the gangue minerals or are freely liberated under the particle sizes examined in this study. Hence, Ta minerals can be upgraded and concentrated separately from spodumene, as is practised in industry.</p> <p>At Greenbushes, antimony and arsenic are present as stibiomicrolite and parabrandidite, respectively, as finely disseminated as grains within spodumene. There are also associations of pollucite with spodumene.</p> <p>A high percentage of cassiterite in most samples are locked and associated with spodumene and therefore will report along with spodumene grains in the concentrate.</p> <p>Analysis of the liberation characteristics of spodumene concentrates collected from the beneficiation circuits at five mines reveal high contamination content of gangue mineral of up to 20 wt%. Of this only around 5 wt% is associated and locked with spodumene. Techniques such as ore sorting can be used to reduce mineral impurities to the beneficiation circuit.</p>
9. Diagnostic method to allow prediction of the metallurgical response of different pegmatite ores to existing processes used to extract Li. Examine the thermal and chemical response and link them to the mineralogical properties	<p>A two-stage calcination–sulphate-roast testing procedure at fixed particle size, temperature, retention time and acid-to-Li content dosage rate was used to simulate and assess the Li-extraction process.</p> <p>Temperature conditions that favour α–β conversion of spodumene required to make the Li amendable to extraction are 1050 °C to 1100 °C.</p> <p>The content of gangue minerals in concentrate needs to be minimized as many of the gangue minerals have melting points or decomposition temperatures below the spodumene transformation temperature (e.g. micas, carbonates). Melt products contribute to clinker formation that lines the internal surface of the calcine roaster leading to production delays and increased maintenance costs.</p> <p>The key factors affecting the extraction of Li from spodumene ores include:</p> <ul style="list-style-type: none">• Incomplete conversion of γ-spodumene to β-spodumene during calcination may contribute to poor Li extraction during the acid-baking and water-leaching stage. Some gangue minerals (e.g. quartz) may prevent complete heat transfer to spodumene during calcination and act as an insulator that impedes the spodumene α–β transformation process. Hence finer grinding, longer heating periods and more effort at removing gangue will be required.• The exothermic reaction of the oxidation of Fe and Mn within both mica and spodumene grains can promote the thermal transformation of spodumene. Some control on the rate of heating and oxidation during the calcination process of high-Fe spodumenes may be required to reduce the development of fines. All ferrous iron in concentrate feed to calcination stage should be converted to ferric iron to reduce Fe solubility and interference in downstream processing.• Micaceous minerals (particularly ones high in Fe, Mg, K and Na) form melts that armour coat spodumene grains during the calcination step, which can prevent full conversion of spodumene to the β-form, as well as render calcined spodumene refractory to extraction through the sulphate-roasting and water-leaching step. Regions of highly altered spodumene with chlorite-mica content in Mt Cattlin and Bald Hill deposits will have to be treated by alternative processes (e.g. alkaline pressure leaching).• Feldspars also form partial melting products that coat spodumene grains and increase the refractory nature of spodumene. Maintaining the kiln temperature at ~1100 °C, if possible, would reduce the impact of feldspar.• The slow rate of diffusion of acid into large particles causes slow and incomplete Li extraction. Finer grinding will favour improved Li extractions up to ~95%.• While Li extraction is considered an ion-exchange process, where H ions replace Li in the residual calcined spodumene structural matrix, this work has shown that Al is also extracted during the sulphuric acid-baking and water-leach processing phase, which causes shrinkage and agglomeration of particles that may reduce full Li extraction. Accordingly, an optimum grind size must be established prior to acid baking to allow diffusion and leaching of Li from within calcined spodumene particles.
10. Practical geometallurgical model useful as a benchmarking tool to identify factors which favour or limit full recoveries in different ore deposits and improve the economic returns of mining operations	<p>Process options for treating different orebodies were categorized based on the classification of 10 pegmatite deposits examined in this study.</p> <ul style="list-style-type: none">• LCT albite-spodumene pegmatite, LCT complex spodumene pegmatite (High quartz and feldspar, with moderate size spodumene) – Staged crushing incorporating HPGR, production of coarse concentrate by DMS and a fine concentrate by flotation (Pilgangoora, Mt Marion Greenbushes and Kathleen Valley).• LCT albite-spodumene pegmatite (Quartz, feldspar, with high mica content and coarse to very coarse spodumene) – Staged crushing and liberation of spodumene and concentration with staged DMS cyclone configuration (Bald Hill, Mt Cattlin)• LCT albite pegmatite, LCT complex lepidolite pegmatite (zinnwaldite, Lepidolite, albite, quartz) – Primary crushing, SAG or rod mill followed by magnetic separation to generate concentrate for zinnwaldite (Dalgara) or flotation for lepidolite (Sinclair, Lepidolite Hill).• LCT complex petalite pegmatite (Petalite zoned with feldspar and quartz) – Excavation, crushing and grinding to produce DSO (Londonderry and Pioneer Dome). <p>The major issues and impediments of treating pegmatite orebodies and solutions were listed, covering the effects of mineralogy and specific details of equipment used to treat ores. Key factors important in selecting a processing option for treating ores include:</p> <ul style="list-style-type: none">• Li mineral host and impurities (Fe, Mn) within the mineral structure.• Grain size of mineral host• Mineral assemblage, texture and associations with the Li host mineral.

Further work

Orebody knowledge

Targeting of LCT pegmatites — The current study provides a comprehensive evaluation of several significant WA LCT pegmatites. However, for a more complete overview of the hard-rock, Li resources of WA, it is recommended further work be conducted to include other known LCT pegmatites including the Wodgina (Albermarle/Mineral Resources), Pilgangoora (Pilbara Minerals) and Mt Holland (Wesfarmers/SQM) deposits, and the Mt Deans (Aruma Resources Ltd.) and Buldania Lithium Projects (Liontown Resources). Such work would determine, for example, if the same mineral fractionation trends identified in the current study are inherent across all of Western Australia's hard-rock Li deposits. Indeed, future work would benefit by including other LCT deposits Australia-wide, such as Core Lithium's Finnis Lithium project, located approximately 20 km south of Darwin.

For the purposes of completeness and to extend and further support (or otherwise) the findings of the current study, it is recommended that representative examples of the main ore types at these deposits also be characterized following the same approach as the M532 study.

This will provide a more comprehensive pegmatite classification for Li-ores in Western Australia, and test the assertion that each pegmatite type has an optimal processing route (e.g. grind-size, dense medium separation [DMS] vs flotation).

Inclusion of additional drillcore — mineralogical and compositional characterization of the Mt Cattlin and Bald Hill LCT pegmatites relied on the evaluation of only pit-exposed material. To understand better the mineral, compositional and geo-petrological evolution and fractionation of the host pegmatite at these deposits, drillcore intersecting the main pegmatite bodies should also be examined using the same protocols as applied in this study.

Geochronology — $^{40}\text{Ar}/^{39}\text{Ar}$ dating of muscovite from Bald Hill established this as a suitable technique for dating muscovite, and enabled assessment of the cooling/closure period of the Ar-isotope system, when compared to zircon U–Pb ages. Follow-up dating of muscovite and lepidolite of other LCT pegmatites (e.g. Kathleen Valley, Sinclair Caesium Deposit, Dome North) will be undertaken as part of the AuScope National Argon Map initiative. For example, at Kathleen Valley, the different pegmatite architecture and differences in mica composition between the Mt Mann and Kathleen Valley pegmatite swarms suggest two separate emplacement events that may also be temporally distinct. Ar–Ar dating of mica from both pegmatite swarms will help to establish the relative timing of their formation. Future $^{40}\text{Ar}/^{39}\text{Ar}$ -dating of mica from other LCT deposits, not included in the forthcoming round (e.g. Wodgina and Pilgangoora), should also be included in a later sample suite that will help in establishing a statewide, temporal framework of pegmatite formation. In conjunction with this, it is recommended that U–Pb dating of cassiterite also be undertaken. While cassiterite ages obtained in the current study should be treated with caution, the measured Pb–Pb ages were significantly younger than those obtained for inherited zircon. Future matrix-matched analyses using

larger, ablation spots would confirm this, and provide a further indication of whether cassiterite yields a pegmatitic crystallization age.

Fluid inclusion studies — Analysis of crystal-fluid inclusions within Li-bearing alumino–silicates (e.g. spodumene), as applied to the Tanco (e.g. London, 2017) and Greenbushes (e.g. Partington et al., 1995; Partington, 2017) LCT pegmatites, inform the cooling history and crystallization evolution of the pegmatite melt. Hence, it is recommended that fluid inclusion studies of other WA LCT pegmatites be undertaken. This will aid in refining the cooling and crystallization evolution of the pegmatite melt to understand better pegmatite genesis and will more precisely establish the *P–T* conditions required as useful indicators in terranes that may host other LCT pegmatites.

Mineralogical analysis

LIBS quantification of pegmatite mineral composition — Application of the LIBS technique showed promise as a means of quantitative analysis of pegmatite composition. However, the LIBS technique is known to suffer from a few inherent, sample-related effects, such as the condition of the sample surface and chemical matrix effects. The robustness of PLS modelling and quantitative prediction of pegmatite composition would be improved by inclusion of a much larger and more extensive LCT pegmatite sample suite and in paying close attention to more consistent matrix matching between sample unknowns and those used as calibration standards.

Quantitative analysis of Ta–Nb-oxide mineralogy — Current assessment of Ta–Nb mineralogy and inferred fractionation (Ta:Nb, Mn:Fe) trends of the host LCT pegmatite was based on (at best) semi-quantitative, TIMA-EDS analysis. Quantitative analysis, by use of EPMA measurement, of Ta–Nb oxides and associated heavy mineral phases will establish a more reliable assessment of the heavy-mineral fraction composition, and of the fractionation trends that may be inferred. In addition, such an approach will:

- Establish if a unique mineralogical or mineral chemistry fingerprint can be assigned to distinguish the various LCT pegmatite types.
- Determine if mineralogy and mineral chemistry of Ta–Nb oxides and associated (resistate) heavy minerals can be applied as a prospect ranking and/or vectoring tool in greenfields/brownfields exploration.

Metallurgy considerations

While there are considerable studies on alternative processes to extract lithium from spodumene, there have been very few attempts to improve the traditional process or to understand the causes behind its limitations. The results from the current study will provide a guidance to the factors that influence recovery and allow improvement in efficiencies in mineral beneficiation and processing of pegmatite ores. Factors that need to be considered are as follows:

Comminution and beneficiation — Recovery yields of Li-bearing minerals from comminution and beneficiation circuits often do not meet design specifications. Western

Australia spodumene producers sometimes sacrifice recovery for grade, achieving Li recoveries of 50–75% to meet Chinese converter specifications, which leads to poor resource utilization and loss of valuable spodumene to waste. In particular, losses to fines generated during comminution are not recovered (20–40%). Comminution is also power intensive and the highest energy cost of the whole comminution and beneficiation plant, which contributes the most to carbon emissions. Assessment of different comminution methodologies to reduce energy cost emissions and fines is necessary. The use of HPGR have improved efficiency, but other processes such as electrodynamic fragmentation (e.g. SelfFrag) could be investigated, particularly if industrial fragmentation systems begin production for commercial operation. The work in this study and existing process plants has shown that high recoveries at coarse size fraction are possible.

Further work also needs to examine the improvement in the efficiency of removing gangue material prior to the beneficiation stage. Several companies are already examining ore sorting technologies that can eliminate the processing of waste material through the DMS circuits.

Actual reagent mixtures used by several mine sites to float fine spodumene are confidential in nature. Flotation of silicates such as spodumene is difficult, with the presence of clays and slimes affecting recovery. Oleic acid has traditionally been used as the collector but needs to be conditioned with soda ash or sodium hydroxide to form water soluble oleates. In addition, process water chemistry is likely to have a significant effect on overall flotation performance of spodumene and is an area that warrants further study.

The processing of Ta minerals to make concentrates should be considered in all LCT pegmatite processing. Tantalum is used in electrolytic capacitors and corrosion-resistant chemical equipment. Many of the Ta minerals contain Nb, which is a highly valuable element used for strengthening alloys but can also be used to improve the electrochemical behaviour and stabilize high-nickel cathodes in the Li-battery industry (Xin et al., 2021). Options for improving the processing and extraction of cassiterite should also be considered.

Calcination and acid baking — Existing technology for refining lithium is not designed for fit for purpose in treating the variability in Li-bearing pegmatite ores. With push for downstream development of lithium refineries, companies will be able to tailor their processing of Li to maximize Li recovery from their orebodies. This includes treating both high- and low-grade materials through separate process routes.

Further work is required to establish an effective calcination procedure for maximizing lithium recovery and reducing the impact of mineral impurities. In particular, furnaces which provide a uniform temperature gradient, such as flash calcination furnaces (e.g. Calix), or static block furnaces need to be examined to regulate and control the mineral conversion process during calcination. Potentially, the use of electric furnaces can promote the use of renewable energy sources rather than conventional furnaces, which use carbon fuels, such as gas heaters. Water balances and production of sodium sulphate wastes also must be managed effectively, which entails additional liability and risks.

Further studies are required on the full flowsheet to ensure Australia remains competitive in the global market. Problems

associated with conventional conversion processes can potentially be overcome by replacing the thermal roast/bake step with an alkaline conversion conducted at low temperature (~250 °C) and pressure. Such processes have been developed by Outotec (Carbonate leach, <https://www.mogroup.com/portfolio/lithium-processing/>) and Lithium Australia (Liena™ process).

The processing of Li-rich, micaceous deposits has yet to be developed on a commercial scale in Australia. These were previously considered as uneconomic. However, process options are available (e.g. halide based SiLeach process, L-Max Technology, Sulphate calcination processing) that may allow treatment of more complex Li-feedstock.

Several novel alternative processes have been developed for the concentration and recovery of lithium from solution that may warrant further investigation. These include an electrodialysis approach, such as the ELi® process co-developed by Neometals and Minerals Resources, and the Nemaska Lithium's electromembrane process (Nemaska Lithium Inc., 2019; Butcher, 2020). Other processes involving manganese Oxide Ion Sieves (Chitrakar et al., 2001), ion-exchange technology (Francis, 2020; Lilac Solutions Inc., 2021) and solvent extraction (Tenova Advanced Technologies, 2021) have been developed mainly for chloride or brine solutions. The PosLX process involves the preparation of a Li-phosphate solution. Apart from the Nemaska Lithium's electromembrane process, most of the other technologies require the recovery of Li from brine solutions.

Linkage with other projects

The mineralogical understanding and geochemical nature of many of the pegmatite ores presented in this report forms the basis for at least two follow-on applied research activities:

- 1 A geomaterials research consultancy will be made available in the John de Laeter Centre to undertake work with industry linking ore body knowledge to geomaterials behaviour that will improve the beneficiation and chemical processing efficiency of lithium minerals
- 2 A 'Trusted Supply Chain' project underway in the Future Battery Industries CRC will test whether geochemical fingerprinting techniques can discriminate batteries produced from Australian ores by:
 - building a chemical database for battery minerals and processed materials sourced from Australian and international producers
 - using provenance data to build a digital platform that will allow consumers to track ethically sourced battery materials through the EV supply chain.

References

- Abdullah, AA, Oskierski, HC, Altarawneh, M, Senanayake, G, Lumpkin, G and Dlugogorski, BZ 2019, Phase transformation mechanism of spodumene during its calcination: *Minerals Engineering*, v. 140, p. 105883.
- Ahtola, T, Kuusela, J, Käpyaho, A and Kontoniemi, O 2015, Overview of lithium pegmatite exploration in the Kaustinen area in 2003–2012: Geological Survey of Finland, Report of Investigation 220, 28p.
- Alvey, DC, Morton, K, Harmon, RS, Gottfried, JL, Remus, JJ, Collis, LM and Wise, MA 2010, Laser-induced breakdown spectroscopy-based geochemical fingerprinting for the rapid analysis and discrimination of minerals: *Applied Optics*, v. 49, p. C168–C180.
- Aylmore, MG, Merigot, K, Rickard, W, Evans, N, McDonald, B, Catovic, E and Spitalny, P 2017, Assessment of Li ore to determine its amenability to processing for the extraction of lithium in Proceedings of European Metallurgical Conference 2017, 20p.
- Aylmore, MG, Merigot, K, Quadira, Z, Rickard, W, Evans, N, McDonald, B, Catovic, E and Spitalny, P 2018a, Applications of advanced analytical and mass spectrometry techniques to the characterisation of micaceous lithium-bearing ores: *Minerals Engineering*, v. 116, p. 182–195.
- Aylmore, MG, Merigot, K, Rickard, W, Evans, N, McDonald, B, Catovic, E and Spitalny, P 2018b, Assessment of a spodumene ore by advanced analytical and mass spectrometry techniques to determine its amenability to processing for the extraction of lithium: *Minerals Engineering*, v. 119, p. 137–148.
- Baker, DEL, Seccombe, PK, and Collins, WJ 2002, Structural history and timing of gold mineralization in the Northern East Strelley Belt, Pilbara Craton, Western Australia: *Economic Geology*, v. 97, p. 775–786.
- Barbosa, LI, Valente, G, Orosco, RP and González, JA 2014, Lithium extraction from β -spodumene through chlorination with chlorine gas: *Minerals Engineering*, v. 56, p. 29–34.
- Barlow, SG and Manning, DAC 1999, Influence of time and temperature on reactions and transformations of muscovite mica: *British Ceramic Transactions*, v. 98, no. 3, p. 122–126.
- Batt, GE, Crook, D, Brand, N and Kerr, S 2020, Agile management and long-term strategy in exploration: The 'lucky' discovery of the Sinclair Pollucite Deposit, Eastern Goldfields, Western Australia: *Australian Journal of Earth Sciences*, v. 68, no. 5, p. 684–696.
- Blewett, RS, Czarnota, K and Henson, PA 2010, Structural-event framework for the eastern Yilgarn Craton, Western Australia, and its implications for orogenic gold: *Precambrian Research*, v. 183, no. 2, p. 203–229.
- Bobos, I, Vieillard, P, Charoy, B and Noronha, F 2007, Alteration of spodumene to cookeite and its pressure and temperature stability conditions in Li-bearing apatite-pegmatites from Northern Portugal: *Clays and Clay Minerals*, v. 55, no. 3, p. 295–310.
- Botto, IL, Arazi, SC and Krenkel, TG 1976, Estudio cinético de la transformación polimórfica espodumeno I en espodumeno II. *Boletín de la Sociedad Española de Cerámica y Vidrio* v. 15, p. 5–10.
- Botula, J, Rucky, P and Repka, V 2005, Extraction of zinnwaldite from mining and processing wastes: Technical University of Ostrava – *Geologická LI*, v. 2, p. 9–16.
- Boyle, RW and Jonasson, IR 1984, The geochemistry of antimony and its use as an indicator element in geochemical exploration: *Journal of Geochemical Exploration*, v. 20, p. 223–302.
- Bradley, D and McCauley, A 2013, A preliminary deposit model for lithium–caesium–tantalum (LCT) pegmatites, Open-File Report 2013–1008, US Department of the Interior: US Geological Survey, 7p.
- Bradley, D, McCauley, AD and Stillings, LM 2017, Mineral-deposit model for lithium–caesium–tantalum pegmatites: US Geological Survey scientific investigations report 2010-5070-0, 48p.
- Brandt, F and Haus, R 2010, New concepts for lithium minerals processing: *Minerals Engineering*, v. 23, p. 659–661.
- Bulatovic, SM 2015, Beneficiation of lithium ores. *Handbook of flotation reagents: Chemistry, Theory and Practice*, p. 41–56.
- Bunting, JA and Williams, SJ 1979, Sir Samuel, Western Australia: Geological Survey of Western Australia: 1:250 000 Geological Series Explanatory Notes, 45p.
- Butcher, D 2020, Review of membrane technology as a process tool: ALTA 2020 Uranium-REE, Perth, Western Australia, ALTA Metallurgical Services Publications, p. 19–24.
- Cameron, M, Sueno, S, Prewitt, CT and Papike, JJ 1973, High-temperature crystal chemistry of acmite, diopside, hedenbergite, jadeite, spodumene, and ureyite: *American Mineralogist*, v. 58, p. 594–618.
- Cano, ZP, Banham, D, Ye, S, Hintennach, A, Lu, J, Fowler, M and Chen, Z 2018, Batteries and fuel cells for emerging electric vehicle markets: *Nature Energy*, v. 3 no. 4, p. 279–289.
- Cassidy, KF, Chamion, DC, Krapez, B, Barley, ME, Brown, SJA, Blewett, RS, Groenewald, PB and Tyler, IM 2006, A revised geological framework for the Yilgarn Craton Western Australia; Record 2006/8: Geological Survey of Western Australia, 8p.
- Černý, P 1991, Rare-element granitic pegmatites: Part 1: Anatomy and internal evolution of pegmatite deposits: *Geoscience Canada*, v. 18, p. 49–67.
- Černý, P, Ercit, TS and Vanstone, PT 1996, Petrology and mineralization of the Tanco rare-element pegmatite, southeastern Manitoba: Field Trip Guidebook A4 in Geological Association of Canada/Mineralogical Association of Canada Annual Meeting, Winnipeg, Manitoba, 27–29 May 1996, 63p.
- Černý, P, London, D and Novák, M 2012a, Granitic pegmatites as reflections of their sources: *Elements*, v. 8, no. 4, p. 289–294.
- Černý, P, Teertstra, DK, Chapman, R, Selway, JB, Hawthorne, FC, Ferreira, K, Chackowsky, LE, Wang, X-J and Meintzer, RE 2012b, Extreme fractionation and deformation of the leucogranite-pegmatite suite at Red Cross Lake, Manitoba, Canada (IV. Mineralogy): *Canadian Mineralogy*, v. 50, p. 1839–1875.
- Champion, DC and Huston, DL 2016, Radiogenic isotopes, ore deposits and metallogenic terranes: Novel approaches based on regional isotopic maps and the mineral systems concept: *Ore Geology Reviews*, v. 76, p. 229–256.
- Chitraker, R, Kanoh, H, Miyai, Y and Ooi, K 2001, Recovery of lithium from seawater using manganese oxide adsorbent ($\text{H}_{1.6}\text{Mn}_{1.6}\text{O}_4$) derived from $\text{Li}_{1.6}\text{Mn}_{1.6}\text{O}_4$: *Indian Engineering and Chemistry Research*, v. 40, p. 2054–2058.
- Choubey, PK, Kim, M, Srivastava, RR, Lee, J-C and Lee, J-Y 2016, Advance review on the exploitation of the prominent energy-storage element: Lithium: Part I: From mineral and brine resources: *Minerals Engineering*, v. 89, p. 119–137.
- Compston, W, Williams, IS and McCulloch, MT 1986, Contrasting zircon U–Pb and model Sm–Nd ages for the Archean Logue Brook Granite: *Australian Journal of Earth Sciences*, v. 33, p. 193–200.
- Crook, DJ, Kerr, ST, Booth, JA, Brand, NW and Panting, R 2019, The discovery and geology of Sinclair, Australia's first caesium deposit: Australian Exploration Geoscience Conference, AEGC2019, Data to Discovery, Perth, Western Australia, 2–5 September 2019, 5p.
- Czarnota, K, Champion, DC, Goscombe, B, Blewett, RS, Cassidy, KF, Henson, PA and Groenewald, PB 2010, Geodynamics of the eastern Yilgarn Craton: *Precambrian Research*, v. 183, p. 175–202.
- Daniel, M, Klein, B and Wang, C 2019, High-pressure grinding roll technology, in *SME Mineral Processing and Extractive Metallurgy Handbook*, Chapter 3.7 edited by K Kawatra and CA Young: Society for Mining, Metallurgy and Exploration, Colorado, p. 443–464.
- Deer, WA, Howie, RA and Zussman, J 1992, An introduction to the rock forming minerals (2nd edition): Longman, John Wiley and Sons, New York, 696p.
- Dessemond C, Gervais Soucy G, Jean-Philippe Harvey J-P and Ouzilleau P 2020, Phase transitions in the α - γ - β spodumene thermodynamic system and impact of γ -spodumene on the efficiency of lithium extraction by acid leaching: *Minerals*, v. 2020, no. 10, p. 519, doi:10.3390/min10060519.

- Dittrich, T, Seifert, T, Schulz, B, Hagemann, S, Gerdes, A and Pfänder, J 2019, Archean rare-metal pegmatites in Zimbabwe and Western Australia, *Geology and Metallogeny of Pollucite Mineralizations*, in Springer Briefs in World Mineral Deposits edited by A Camprubi: Springer, Switzerland, p. 125.
- Drummond, MJ and Wyche, S 2022, Eastern goldfields superterrane greenstones (A-og-YEG), Explanatory Notes extract: Geological Survey of Western Australia, WA Geology Online, viewed 27 January 2022, <www.dmirs.wa.gov.au/ens>.
- Duuring, P 2020, Rare-element pegmatites: A mineral systems analysis: Geological Survey of Western Australia, Record 2020/7, 6p.
- Ellestad, RB and Leute, KM 1950, Method of extracting lithium values from spodumene ores: US Patent No. 2516109.
- Essential Metals 2020, Presentation to the Annual General Meeting of ESS Shareholders, 15 December 2020, viewed 15 June 2021, <https://wcsecure.weblink.com.au/pdf/ESS/02381182.pdf>.
- Essential Metals 2021, Investor presentation–Paydirt Battery Minerals Conference, Perth, 2 June 2021, 22p, <02380700.pdf (weblink.com.au)>.
- European Metals 2017, ASX announcements, <www.europeanmet.com/announcements/>.
- Fabre, C, Boiron, M-C, Dubessy, J, Chabiron, A, Charoy, B and Crespo, TM 2002, Advances in lithium analysis in solids by means of laser-induced breakdown spectroscopy: An exploration study: *Geochimica et Cosmochimica Acta*, v. 66, no. 8, p. 1401–1407.
- Fetherston, JM 2004, Tantalum in Western Australia: Geological Survey of Western Australia, Mineral Resources Bulletin 22, 162p.
- Filip, J, Novák, M, Beran, A and Zboril, R 2006, Crystal chemistry and OH defect concentrations in spodumene from different granitic pegmatites: *Physics and Chemistry of Minerals*, v. 32, p. 733–746.
- Földvári, M 2011, Handbook of thermogravimetric system of minerals and its use in geological practice: Geological Institute of Hungary, Budapest, 180p.
- Foster, JM, Lambert, DD, Frick, LR and Mass, R 1996, Re–Os isotopic evidence for genesis of Archean nickel ores from uncontaminated komatiites: *Nature*, v. 382, p. 703–706.
- Francis, CFJ, Kyratzis, IL and Best, AS 2020, Lithium-ion battery separators for ionic-liquid electrolytes: A review: *Advanced Materials*, v. 32, 1904205.
- Garrett, DE 2004, Handbook of lithium and natural calcium chloride: Their deposits, processing, uses and properties (1st edition): Elsevier, 488p.
- Gasafi, E and Pardemann, R 2020, Processing of spodumene concentrates in fluidized-bed systems: *Minerals Engineering*, v. 148, p. 106205.
- Gasalla, HJ and Periera, E 1990, Activation-deactivation mechanisms in spodumene samples: *Solid State Ionics*, v. 42, p. 1–6.
- Geological Survey of Western Australia 2020, Lithium Investment Opportunities, September 2020 flyer, <www.dmirs.wa.gov.au/ens>.
- Geological Survey of Western Australia 2022, Lithium Investment Opportunities, January 2022 flyer, <www.dmirs.wa.gov.au/ens>.
- Gibson, C, Aghamirian, M and Grammatikopoulos, T 2017, The beneficiation of lithium minerals from hard rock deposits: *Mining Engineering*, v. 69, no. 8, p. 8.
- Gibson, CE, Aghamirian, M, Grammatikopoulos, T, Smith, DL and Bottomer, L 2021, The recovery and concentration of spodumene using dense media separation: *Minerals*, v. 11, p. 649.
- Graham, J 1975, Some notes on α -spodumene, $\text{LiAlSi}_2\text{O}_6$: *American Mineralogist*, v. 60, p. 919–923.
- Grammatikopoulos, TA, Pearse, G, Gelcich, S and Gunning, C 2009, Quantitative characterization of spodumene ore by automated mineralogy from the Moblan rare metals pegmatite deposit: Proceedings of the 48th Annual Conference of Metallurgists of CIM (MetSoc), Quebec, Canada, p 65–76.
- Griffin, A 2017, Hydrometallurgical processes for the recovery of lithium from silicates, abstract: Alta 2017 Nickel-Cobalt-Copper: Uranium-REE and Gold-PM Conference and Exhibition, Perth, Australia, 20–27 May 2017.
- Griffin, TJ 1989, Widgiemooltha, Western Australia: Geological Survey of Western Australia, 1:250 000 Geological Series Explanatory Notes.
- Grigson, M 2011, Mineralogical and textural description of selected photographs of Mount Cattlin pegmatitic ore, and a discussion of their likely paragenesis: *Galaxy Resources report*, April 2011, 26p.
- Grosjean, C, Miranda, PH, Perrin, M and Poggi, P 2012, Assessment of world lithium resources and consequences of their geographic distribution on the expected development of the electric vehicle industry: *Renewable and Sustainable Energy Reviews*, v. 16, p. 1735–1744.
- Guo, H, Kuang, G, Wan, H, Yang, Y, Yu, H and Wang, H 2019, Enhanced acid treatment to extract lithium from lepidolite with a fluorine-based chemical method: *Hydrometallurgy*, v. 183, p. 9–19.
- Hall, CE 2022a, Explanatory Notes for Burra Monzogranite (A-br-gm): Geological Survey of Western Australia, WA Geology Online, viewed 27 February 2022, <www.dmirs.wa.gov.au/ens>.
- Hall, CE 2022b, Explanatory Notes for Dardie Monzogranite (A-da-gm): Geological Survey of Western Australia, WA Geology Online, viewed 27 February 2022, <www.dmirs.wa.gov.au/ens>.
- Hall, CE 2022c, Explanatory Notes for Mount Herbert Gabbro (A-LVmh-og): Geological Survey of Western Australia, WA Geology Online, viewed 29 January 2022, <www.dmirs.wa.gov.au/ens>.
- Hall, CE 2022d, Explanatory Notes for Woolgangie Monzogranite (A-wo-gm): Geological Survey of Western Australia, WA Geology Online, viewed 27 January 2022, <www.dmirs.wa.gov.au/ens>.
- Hall, CE and De Paoli, MC 2020, Explanatory Notes for Hampton Hill Formation (A-KGhh-ux): Geological Survey of Western Australia, WA Geology Online, viewed 27 January 2022, <www.dmirs.wa.gov.au/ens>.
- Hall, CE and Wyche, S 2020a, Explanatory Notes for Kambalda Komatiite (A-KGkm-uk): Geological Survey of Western Australia, WA Geology Online, viewed 27 February 2022, <www.dmirs.wa.gov.au/ens>.
- Hall, CE and Wyche, S 2020b, Explanatory Notes for Lunnon Basalt (A-KGlu-bb): Geological Survey of Western Australia, WA Geology Online, viewed 23 May 2022, <www.dmirs.wa.gov.au/ens>.
- Hall, CE and Wyche, S 2020c, Explanatory Notes for Paringa Basalt (A-KGpa-bb): Geological Survey of Western Australia, WA Geology Online, viewed 10 May 2022, <www.dmirs.wa.gov.au/ens>.
- Hall, CE, Wyche, NL and Sapkota, J 2022, Explanatory Notes for Black Flag Group (A-BF-xf-s): Geological Survey of Western Australia, WA Geology Online, viewed 29 January 2022, <www.dmirs.wa.gov.au/ens>.
- Hall, CE, Wyche, S, Wyche, NL and Sapkota, J 2022, Explanatory Notes for Kalgoorlie Group (A-KG-bb): Geological Survey of Western Australia, WA Geology Online, viewed 27 January 2022, <www.dmirs.wa.gov.au/ens>.
- Hall, SJ 1988, Mt. Farmer PL59/214: Annual report for Pancontinental Mining Limited, Report P88–06, 13p.
- Han, G, Gu, D, Lin, G, Cui, Q and Wang, H 2018, Recovery of lithium from a synthetic solution using spodumene leach residue: *Hydrometallurgy*, v. 177, p. 109–115.
- Harhira, A, Bouchard, P, Rifai, K, Haddad, J-El, Sabsabi, M, Blouin, A and Laflamme, M 2017, Advanced laser-induced breakdown spectroscopy (LIBS) sensor for gold mining in Canadian Institute of Mining, Metallurgy and Petroleum Proceedings: The Conference of Metallurgists, Hosting World Gold and Nickel Cobalt, 2017, 11p.
- Harman, G, 2019, The nature of lithium mineral physical properties in selecting calcination and roasting equipment in Lithium Processing Proceedings: 24th Annual Processing Conference, Alta Metallurgical Services, Melbourne, Australia, 16p.

- Harmon, RS, Russo, RE and Hark, RR 2013, Applications of laser-induced breakdown spectroscopy for geochemical and environmental analysis: A comprehensive review: *Spectrochimica Acta, Part B*, v. 87, p. 11–26.
- Heyes, GW, Allan, GC, Bruckard, WJ and Sparrow, GJ 2012, Review of flotation of feldspar: *Mineral Processing and Extractive Metallurgy*, v. 121, no. 2, p. 72–78.
- Hrstka, T, Gottlieb, P, Skála, R, Breiter, K and Motl, D 2018, Automated mineralogy and petrology: Applications of TESCAN Integrated Mineral Analyzer (TIMA): *Journal of Geosciences*, v. 63, p. 47–63.
- Ivanic, TJ 2019, Explanatory Notes for Yalgowra Suite (A-SDY-og): Geological Survey of Western Australia, WA Geology Online, viewed 07 February 2022, <www.dmirs.wa.gov.au/ens>.
- Jacobson MI, Calderwood, MA and Grguric, BA 2007, Guidebook to the pegmatites of Western Australia: Hesperian Press, Perth, Australia, 356p.
- Jirestig, JA and Forssberg, KSE 1994, Dispersion of flotation concentrates before magnetic separation: *Minerals Engineering*, v. 7, p. 1505–1516.
- Johnson, LA and McCauley, RA 2005, The thermal behavior of albite as observed by DTA: *Thermochimica Acta*, v. 437, p. 134–139.
- Karrech, A, Azadi, MR, Elchalakani, AM, Shahin, MA and Seibi, AC 2020, A review on methods for liberating lithium from pegmatites: *Minerals Engineering*, v. 145, p. 106085.
- Kendall-Langley, LA, Kemp, AIS, Grigson, JL and Hammerli, J 2020, U–Pb and reconnaissance Lu–Hf isotope analysis of cassiterite and columbite group minerals from Archean Li–Cs–Ta type pegmatites of Western Australia: *Lithos*, v. 352–353, p. 105231.
- Kesler, SE, Gruber, PW, Medina, PA, Keoleian, GA, Everson, MP and Wallington, TJ 2012, Global lithium resources: Relative importance of pegmatite, brine and other deposits: *Ore Geology Reviews*, v. 48, p. 55–69.
- Kinny, PD 2000, U–Pb dating of rare-metal (Sn–Ta–Li) mineralized pegmatites in Western Australia by SIMS analysis of tin and tantalum-bearing ore minerals in *Beyond 2000: New Frontiers in Isotope Geoscience (incorporating ACOG 4) Abstracts and Proceedings*, p. 113–116.
- Lajoie-Leroux, F, Dessemond, C, Soucy, G, Laroche, N. and Magnan, J-F 2018, Impact of the impurities on lithium extraction from β -spodumene in the sulfuric acid process: *Minerals Engineering*, v. 129, p. 1–8.
- Laznicka, P 2006, *Giant metallic deposits*: Springer, Berlin, 847p.
- Leißner, T, Bachmann, K, Gutzmer, J and Peuker, UA 2016, MLA-based partition curves for magnetic separation: *Minerals Engineering*, v. 94, p. 94–103.
- Li, H, Eksteen, J and Kuang, G 2019, Recovery of lithium from mineral resources: State-of-the-art and perspectives: A review: *Hydrometallurgy*, v. 189, p. 105–129.
- Li, P, Li, J, Chen, Z, Liu, X, Huang, Z and Zhou, F 2021, Compositional evolution of the muscovite of Renli pegmatite-type rare-metal deposit, northeast Hunan, China: Implications for its petrogenesis and mineralization potential: *Ore Geology Reviews*, v. 138, p. 104380.
- Libby, CB and Wyche, S 2019, Explanatory Notes for Maloney's Dam Metagranite (A-md-mg): Geological Survey of Western Australia, WA Geology Online, viewed 27 January 2022, <www.dmirs.wa.gov.au/ens>.
- Lide, DR (editor) 2005, *Handbook of Chemistry and Physics (86th edition)*: CRC Press, 2616p.
- Liera, AR, Fuertes-Fuente, M, Cepedal, A and Martin-Izard, A 2019, Barren and Li–Sn–Ta mineralized pegmatites from NW Spain (Central Galicia): A comparative study of their mineralogy, geochemistry, and wallrock metasomatism: *Minerals*, v. 9, p. 739.
- Lilac Solutions Inc. 2021, *New extraction methods: Technology*, viewed 4 November 2021, <http://lilacsolutions.com/technology/>.
- Lima, A and Dias, F 2019, Spodumene and quartz intergrowth: Textural and genesis point of view: *Geophysical Research Abstracts*, v. 21, EGU2019-13404.
- Linnen, RL, Van Lichtenvelde, M and Cerny, P 2012, Granitic pegmatites as sources of strategic metals: *Elements*, v. 8, no. 4, p. 275–280.
- Liontown Resources 2021, Kathleen Valley, viewed 11 June 2021, <www.ltresources.com.au/kathleen-valley-lithium-project>
- Liontown 2022, June 2022 Quarterly Report, 21p, viewed 10 October 2022, <https://www.ltresources.com.au/investors/corporate-reports>
- London, D 2008, Pegmatites: The Canadian Mineralogist Special Publication, v. 10, p. 347.
- London, D 2017, Reading pegmatites: Part 3: What lithium minerals say: *Rocks and Minerals*, v. 92, no. 2, p. 144–157.
- London, D and Burt, DM 1982, Lithium aluminosilicate occurrences in pegmatites and the lithium aluminosilicate phase diagram: *American Mineralogist*, v. 67, p. 483–493.
- London, D and Morgan, GB 2012, The pegmatite puzzle: *Elements*, v. 8, p. 263–268.
- Lu, Y, Wingate, MTD, Kirkland, CL and Hall, CE 2016, 182288: metagranodiorite, Horse Rocks; *Geochronology Record 1350*: Geological Survey of Western Australia, 4p.
- Mclvor, RE and Finch, JA 1991, A guide to interfacing of plant grinding and flotation operations: *Minerals Engineering*, v. 4 (1), p. 9–23.
- McMillan, NJ, Rees, S, Kochelek, K and McManus, C 2014, Geological applications of laser-induced breakdown spectroscopy: *Geostandards and Geoanalytical Research*, v. 38, no. 3, p. 329–343.
- McMillan, NJ, Harmon, RS, De Lucia, FC and Miziolek, AM 2007, Laser-induced breakdown spectroscopy analysis of minerals: Carbonates and silicates: *Spectrochimica Acta, Part B*, v. 62, p. 1528–1536.
- Martens, H and Naes, T 1989, *Multivariate calibration*: Wiley, Chichester, 440p.
- Meshram, P, Pandey, BD and Mankhand, TR 2014, Extraction of lithium from primary and secondary sources by pre-treatment, leaching and separation: A comprehensive review: *Hydrometallurgy*, v. 150, p. 192–208.
- Mohr, SH., Mudd GM and Giurco, D 2012, Lithium resources and production: Critical assessment and global projections: *Minerals*, v. 2, p. 65–84.
- Monhemius, A 1977, Precipitation diagrams for metal hydroxides, sulphides, arsenates and phosphates: *Transactions of the Institution of Mining and Metallurgy*, 86p, C202.
- Moon, KS and Fuerstenau, DW 2003, Surface crystal chemistry in selective flotation of spodumene ($\text{LiAl}[\text{SiO}_3]_2$) from other aluminosilicates: *International Journal of Mineral Processing*, v. 72, p. 11–24.
- Moore, DM and Reynolds, RC 1997, *X-ray diffraction and identification and analysis of clay minerals (2nd edition)*: Oxford University Press, New York, 378p.
- Moore, LR, Mann, JP, Montoya, A and Haynes, BS 2018, In situ synchrotron XRD analysis of the kinetics of spodumene phase transitions: *Physical Chemistry Chemical Physics*, v. 55, no. 13, p. 6426–6434.
- Morozova, LN, Sokolova, EN, Smirnov, SZ, Balagansky, VV and Bazai, AV 2020, Spodumene from rare-metal pegmatites of the Kolmozero lithium world-class deposit on the Fennoscandian shield: Trace elements and crystal-rich fluid inclusion: *Mineralogical Magazine*, v. 85, p. 149–160.
- Myers, JS 1993, Precambrian history of the West Australian Craton and adjacent orogens: *Annual Review of Earth and Planetary Science*, v. 21, p. 453–485.
- Nelson, DR 1997, Evolution of the Archean granite-greenstone terranes of the Eastern goldfields, Western Australia: SHRIMP U–Pb zircon constraints: *Precambrian Research*, v. 83, p. 57–81.
- Nemaska Lithium Inc. 2019, NI 43-101 Technical Report: Report on the Estimate to Complete for the Whabouchi Lithium Mine and Shawinigan Electrochemical Plant, viewed 3 November 2021, <www.nemaskalithium.com/assets/documents/NMX_NI4301_20190809.pdf>.

- Painter, GM and Groenewald, PB 2001, Geology of the Mount Belches 1:100 000 sheet: Geological Survey of Western Australia, 1:100 000 Geological Series Explanatory Notes, 38p.
- Partington, GA 2017, Greenbushes tin, tantalum and lithium deposit, *in* Australian Ore Deposits *edited by* GN Phillips: The Australian Institute of Mining and Metallurgy, Melbourne, p. 6.
- Partington GA, McNaughton, NJ and Williams IS 1995, A review of the geology mineralization, geochronology the Greenbushes pegmatite Western Australia: Economic Geology, v. 90, p. 616–635.
- Peltosaari, O, Tanskanen, P, Heikkinen, E-P and Fabritius, T 2015, α - γ - β -phase transformation of spodumene with hybrid microwave and conventional furnaces: Minerals Engineering, v. 82, p. 54–60.
- Pollard, PJ 2017, Australian rare element granitic pegmatites, *in* Australian Ore Deposits *edited by* GN Phillips: The Australian Institute of Mining and Metallurgy, Monograph 32, Melbourne, p. 67–74.
- Porter, TM 2017, Other significant deposits, *in* Australian Ore Deposits *edited by* GN Phillips: The Australian Institute of Mining and Metallurgy, Monograph 32, Melbourne, p. 857–864.
- PorterGeo Database 2019, Yilgarn Craton: geology, structure and mineralization, viewed 13 June 2019, <<http://portergeo.com.au/database/mineinfo.asp?mineid=mn1626>>.
- Quentin de Gromard, R, Ivanic, TJ and Zibra, I 2021, Pre-Mesozoic interpreted bedrock geology of the southwest Yilgarn, 2021, digital data layer: Geological Survey of Western Australia, 23p.
- Redeker, IH 1981, Flotation of feldspar, spodumene, quartz and mica from pegmatites in North Carolina, USA, *in* 13th Canadian Mineral Processors Annual Meeting, Ottawa, Ontario.
- Roddick, JC, Compston, W and Durney, DW 1976, The radiometric age of the Mount Keith Granodiorite, a maximum age estimate for an Archean greenstone sequence in the Yilgarn Block, Western Australia: Precambrian Research, v. 3, p. 55–78.
- Romano, SS 2022, Explanatory Notes for Greensleeves Formation (A-POg-mhs): Geological Survey of Western Australia, WA Geology Online, viewed 7 February 2022, <www.dmirs.wa.gov.au/ens>.
- Rosales, GD, Resentera, ACJ, Gonzalez, JA, Wuilloud, RG and Rodriguez, MH 2019, Efficient extraction of lithium from β -spodumene by direct roasting with NaF and leaching: Chemical Engineering Research and Design, v. 150, p. 320–326.
- Roskill 2021, Lithium-ion batteries: Outlook to 2028 (3rd edition): London: Roskill Information Services.
- Rossi, M, Dell'Aglio, M, De Giacomo, A, Gaudiuso, R, Senesi, GS, De Pascale, O, Capitelli, F, Nestola, F and Ghiara, MR 2014, Multi-methodological investigation of kunzite, hiddenite, alexandrite, elbaite and topaz, based on laser-induced breakdown spectroscopy and conventional techniques for supporting mineralogical characterization: Physics and Chemistry of Minerals, v. 41, p. 127–140.
- Salakjani, NK, Singh, P and Nikoloski, AN 2016, Mineralogical transformations of spodumene concentrate from Greenbushes, Western Australia: Part 1: conventional heating: Minerals Engineering, v. 98, p. 71–79.
- Salakjani, NK, Singh, P and Nikoloski, AN 2017, Mineralogical transformations of spodumene concentrate from Greenbushes, Western Australia: Part 2: microwave heating: Minerals Engineering, v. 100, p. 191–199.
- Salakjani, NK, Singh, P and Nikoloski, AN 2019, Acid roasting of spodumene: Microwave vs. conventional heating: Minerals Engineering, v. 138, p. 161–167.
- Sandmann, D and Gutzmer, J 2013, Use of mineral liberation analysis (MLA) in the characterization of lithium-bearing micas: Journal of Minerals and Materials Characterization and Engineering, v. 1, p. 285–292.
- Sapkota, J 2022a, Explanatory Notes for Jimberlana Norite Member (P_-wz-ow): Geological Survey of Western Australia, WA Geology Online, viewed 27 February 2022, <www.dmirs.wa.gov.au/ens>.
- Sapkota, J 2022b, Explanatory Notes for Theatre Rocks Monzogranite (A_-tr-gm): Geological Survey of Western Australia, WA Geology Online, viewed 27 February 2022, <www.dmirs.wa.gov.au/ens>.
- Sapkota, J 2022c, Explanatory Notes for Pioneer Monzogranite (A_-pi-gm): Geological Survey of Western Australia, WA Geology Online, viewed 27 February 2022, <www.dmirs.wa.gov.au/ens>.
- Sapkota, J 2022d, Explanatory Notes for Mount Kirk Formation (A-KGmk-bk): Geological Survey of Western Australia, WA Geology Online, viewed 27 February 2022, <www.dmp.wa.gov.au/ens>.
- Sapkota, J and Wyche, S 2022, Explanatory Notes for Yilgarn Craton Granites (A-mgss-Y): Geological Survey of Western Australia, WA Geology Online, viewed 27 January 2022, <www.dmirs.wa.gov.au/ens>.
- Schelz, JP 1976, The detection of quartz in clay minerals by differential thermal analysis: Thermochimica Acta, v. 15, p. 17–28.
- Schomburg, J, and Zwahr, H 1997, Thermal differential diagnosis of mica mineral group: Journal of Thermal Analysis, v. 48, no. 1, p. 135–139.
- Selway, JB, Breaks, FW and Tindle, AG 2005, A review of rare-element (Li–Cs–Ta) pegmatite exploration techniques for the Superior Province, Canada, and large worldwide tantalum deposits: Exploration and Mining Geology, v. 14, no. 1–4, p. 1–30.
- Shannon, RD 1976, Revised effective ionic radii and systematic studies of interatomic distances in Halides and Chalcogenides: Acta Crystallographica, v. A32, p. 751–767.
- Shaw, RA, Goodenough, KM, Roberts, NMW, Horstwood, MSA, Chenery, SR and Gunn, AG 2016, Petrogenesis of rare-metal pegmatites in high-grade metamorphic terranes: A case study from the Lewisian Gneiss Complex of north-west Scotland: Precambrian Research, v. 281, p. 338–362.
- Sitando, O and Crouse, PL 2012, Processing of a Zimbabwean petalite to obtain lithium carbonate: International Journal of Mineral Processing, v. 102–103, p. 45–50.
- Smith, B and Ross, J 2017, Mount Marion lithium pegmatite deposit, *in* Australian Ore Deposits *edited by* GN Phillips: The Australian Institute of Mining and Metallurgy, Monograph 32, Melbourne, p. 161–162.
- Smykatz-Kloss, W 1974, Contribution to the classification of chlorites, *in* Differential Thermal Analysis: Minerals and Rocks, vol. 11., Springer, Berlin, Heidelberg, p. 122–128.
- Stern, RA, Bodorkos, S, Kamo, SL, Hickman, AH and Corfu, F 2009, Measurement of SIMS instrumental mass fractionation of Pb isotopes during zircon dating: Geostandards and Geoanalytical Research, v. 33, p. 145–168.
- Stilling, A, Černý, P and Vanstone, PJ 2006, The Tanco pegmatite at Bernic Lake, Manitoba, XVI: Zonal and bulk compositions and their petrogenetic significance: The Canadian Mineralogist, v. 44, p. 599–623.
- Sweetapple, M 2017, Pilgangoora lithium–tantalum pegmatite deposit, *in* Australian Ore Deposits *edited by* GN Phillips: The Australian Institute of Mining and Metallurgy, Melbourne, Monograph 32, p. 339–342.
- Sweetapple, MT and Collins, PLF 2002, Genetic framework for the classification and distribution of Archean rare metal pegmatites in the North Pilbara Craton, Western Australia: Economic Geology, v. 97, p. 873–895.
- Sweetapple, MT and Tassio, S 2015, Laser-induced breakdown spectroscopy (LIBS) as a tool for in situ mapping and textural interpretation of lithium in pegmatitic minerals: American Mineralogist, v. 100, p. 2141–2151.
- Tadesse, MF, Albijanic, B and Dyer, L 2019, The beneficiation of lithium minerals from hard rock ores: A review: Minerals Engineering, v. 131, p. 170–184.
- Talbot, P and Watts, J 2020, Li-ion battery cathode manufacture in Australia, a scene setting project, Future Battery Industries CRC report, 144p.
- Tarascon, J-M 2010, Is lithium the new gold? Nature Chemistry, v. 2, no. 6, p. 510.

- Tawana Resources NL and Alliance Mineral Assets Ltd 2018, Bald Hill ore reserve report 2018: Lithium ore reserve increase of 105% at Bald Hill: Report to Australian Securities Exchange, 6 June 2018, 33p.
- Tenova Advanced Technologies 2021, Lithium-processing, viewed 4 November 2021, <<https://www.tenova.com/product/lithium-processing/#:~:text=TAT's%20lithium%20recovery%20process%20consists,a%20LiOH%20solution%2C%20using%20electrolysis>>.
- Tian, Q, Chen, B, Chen, Y, Ma, I and Shi, X 2011, Roasting and leaching behaviour of spodumene in sulfuric acid process: Chinese Journal of Rare Metals, v. 35, p. 118–123.
- Tran, T and Luong, VT 2015, Chapter 3: Lithium production processes, in *Lithium process chemistry: Resources, extraction, batteries, and recycling* edited by A Chagnes and J Swiatowska: Elsevier Science, p. 81–124.
- Urgine, S 2016, Mineralogical and textural changes with pit development, Mt Cattlin: Galaxy Resources Report, September 2016, p. 18.
- US Geological Society 2022, Minerals commodity summaries 2022, US Department of the Interior, US Geological Society, Reston, Virginia, 202p.
- Van Kranendonk, MJ, Ivanic, TJ, Wingate, MTD, Kirkland CL and Wyche, S 2013, Long-lived, autochthonous development of the Archaean Murchison Domain, and implications for Yilgarn Craton tectonics: Precambrian Research, v. 229, p. 49–92.
- Vance, ER, Scheetz, BE, Barnes MW and Bodnar BJ 1981, Studies of pollucite: MRS Online Proceedings Library, v. 6, p. 31–35, doi:10.1557/PROC-6-31.
- Wedepohl, KH 1995, The composition of the continental crust: *Geochimica et Cosmochimica Acta*, v. 59, no. 7, p. 1217–1232.
- Welham, NJ 2019, Lithium, in *SME mineral processing and extractive metallurgy handbook*, Volume 21 edited by RC Dunne, K Kawatra and CA Young: Society for Mining, Metallurgy and Exploration, p. 839–1853.
- Wells, MA and Chia, J 2011, Ni laterite mineralogy and chemistry – A new approach to quantification: The First AusIMM International Geometallurgy Conference, Brisbane, Queensland, 5–7 September, p. 187–194.
- Welsch, A-M, Murawski, D, Prekajski, M, Vulic, P and Kremenovic, A 2015, Ionic conductivity in single-crystal $\text{LiAlSi}_2\text{O}_6$: Influence of structure of lithium mobility: *Physics and Chemistry of Minerals*, v. 42, p. 413–420.
- White, GD and McVay, TN 1958, Some aspects of the recovery of lithium from spodumene: Oak Ridge National Laboratory: Metallurgy and Ceramics, Union Carbide Corporation, US Atomic Energy Commission, Report ORNL-2450, 17p.
- Wietelmann, U and Klett, J 2018, 200 years of lithium and 100 years of organolithium chemistry: *Zeitschrift für Anorganische und Allgemeine Chemie*, v. 644, no. 4, p. 194–204.
- Wilde, SA, Middleton, MF and Evans, BJ 1996, Terrance accretion in the southwestern Yilgarn Craton: Evidence from a deep seismic crustal profile: *Precambrian Research*, v. 78, no. 1–3, p. 179–196.
- Wingate, MTD and Romano, SS 2022a, Explanatory Notes for Binneringie Dolerite Member (P_-wx-o): Geological Survey of Western Australia, WA Geology Online, viewed 27 February 2022, <www.dmp.wa.gov.au/ens>.
- Wingate, MTD and Romano, SS 2022b, Explanatory Notes for Widgiemooltha Dolerite (P-ww-o): Geological Survey of Western Australia, WA Geology Online, viewed 27 January 2022, <www.dmirs.wa.gov.au/ens>.
- Witt, WK 1999, The Archaean Ravensthorpe Terrane, Western Australia: Synvolcanic Cu–Au mineralization in a deformed island arc complex: *Precambrian Research*, v. 96, p. 143–181.
- Witt, WK, Cassidy, KF, Lu, Y-J and Hagemann, SG 2020, The tectonic setting and evolution of the 2.7 Ga Kalgoorlie–Kurnalpi Rift, a world-class Archaean gold province: *Mineralium Deposita*, v. 55, p. 601–631.
- Wood, SA and William-Jones, AE 1993, Theoretical studies of the alteration of spodumene, petalite, eucryptite and pollucite in granitic pegmatites: Exchange reactions with alkali feldspars: *Contributions to Mineralogy and Petrology*, v. 114, p. 255–263.
- Wyche, S 2021, Explanatory Notes for Kathleen Valley Gabbro (A-_kv-o): Geological Survey of Western Australia, WA Geology Online, viewed 09 May 2022, <www.dmirs.wa.gov.au/ens>.
- Wyche, S, Ivanic, TJ, Chen, S, Wyche, NL, Sapkota, J and Zibra, I 2022, Explanatory Notes for Yilgarn Craton Granites (A-g-Y): Geological Survey of Western Australia, WA Geology Online, viewed 27 February 2022, <www.dmirs.wa.gov.au/ens>.
- Wyche, S and Sapkota, J 2022a, Explanatory Notes for Fifty Mile Tank Gneiss (A-_fi-mgn): Geological Survey of Western Australia, WA Geology Online, viewed 27 February 2022, <www.dmirs.wa.gov.au/ens>.
- Wyche, NL and Sapkota, J 2022b, Explanatory Notes for Black Flag Group (A-BF-xf-s): Geological Survey of Western Australia, WA Geology Online, viewed 27 February 2022, <www.dmp.wa.gov.au/ens>.
- Wyche, NL and Wyche, S 2017, Yilgarn Craton geology, in *Australian Ore Deposits* edited by GN Phillips: The Australian Institute of Mining and Metallurgy, Melbourne, Monograph 32, p. 89–94.
- Xin, F, Zhou, H, Zong, Y, Zuba, M, Chen, Y, Chernova, NA, Bai, J, Pei, B, Goel, A, Rana, J, Wang, F, An, K, Piper, LFJ, Zhou, G and Whittingham, MS 2021, What is the role of Nb in nickel-rich layered oxide cathodes for lithium-ion batteries?: *ACS Energy Letters*, v. 2021, no. 6, p. 1377–1382.
- Xu, L, Hu, Y, Tian, J, Wua, H, Yang, Y, Zeng, Z and Wang, J 2016, Selective flotation separation of spodumene from feldspar using new mixed anionic/cationic collectors: *Mineral Engineering*: v. 89, p. 84–92.
- Yelatontsev, D and Mukhachev, A 2021, Processing of lithium ores: Industrial technologies and case studies: A review: *Hydrometallurgy*, v. 201, p. 105578.
- Yu, F, Wang, Y and Zhang, L 2015a, Effect of spodumene leaching with sodium hydroxide on its flotation: *Physicochemical Problems of Mineral Processing*, v. 51, p. 745–754.
- Yu, F, Wang, Y, Zhang, L and Zhu, G 2015b, Role of oleic acid-molecular complexes in the flotation of spodumene: *Minerals Engineering*, v. 71, p. 7–12.
- Zibra, I 2022, Explanatory Notes for Cullculi Suite (A-ANC-mgga): Geological Survey of Western Australia, WA Geology Online, viewed 07 February 2022, <www.dmirs.wa.gov.au/ens>.

Appendices

Appendices 1–6 are available with the PDF online as an accompanying digital resource

Appendix 7

Department of lithium and major elements in liberation analysis samples

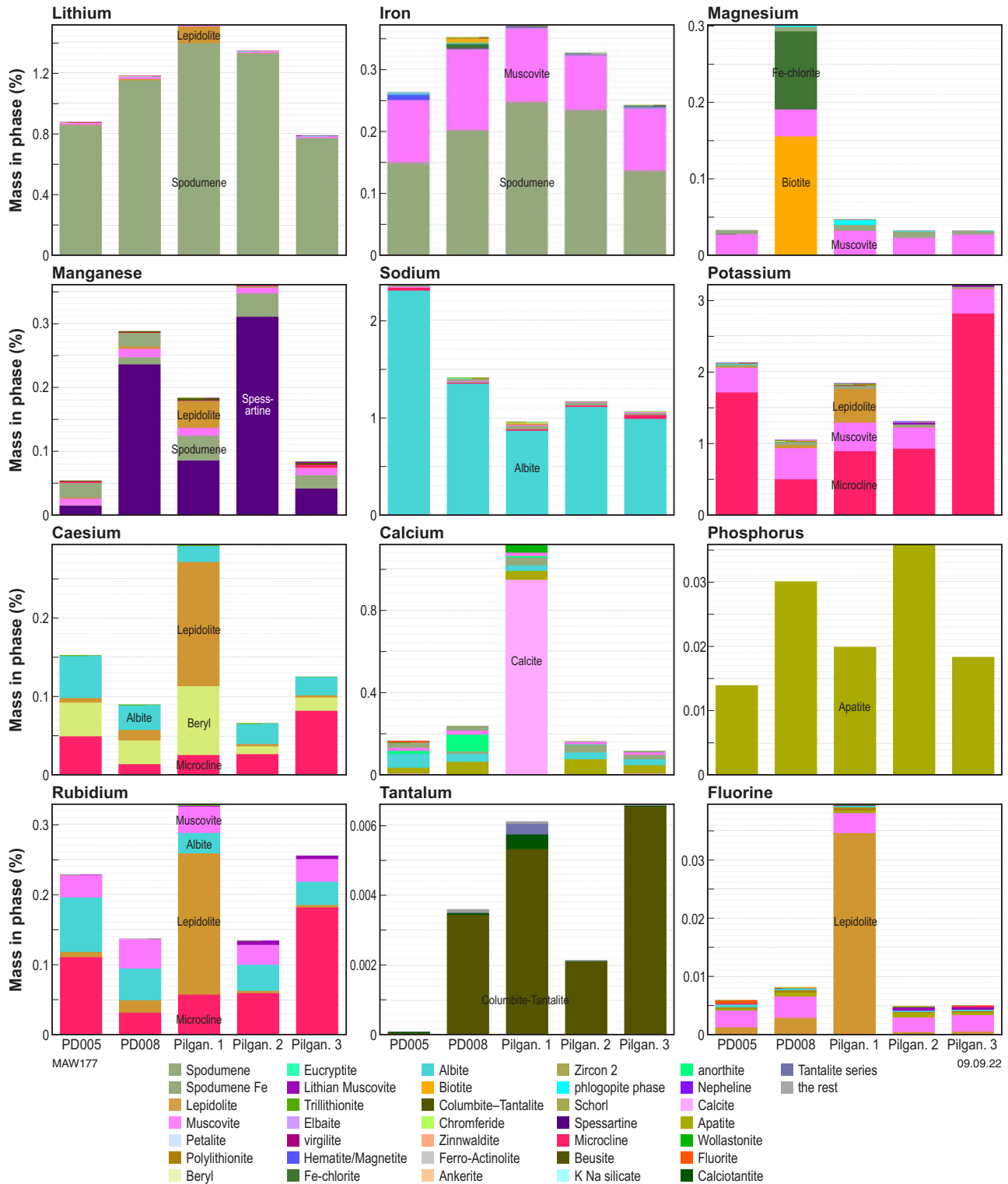


Figure 7.1. Department of Li, Fe, Mg, Mn, Na, K, Cs, Ca, P, Rb, Ta and F in Pilgangoora samples

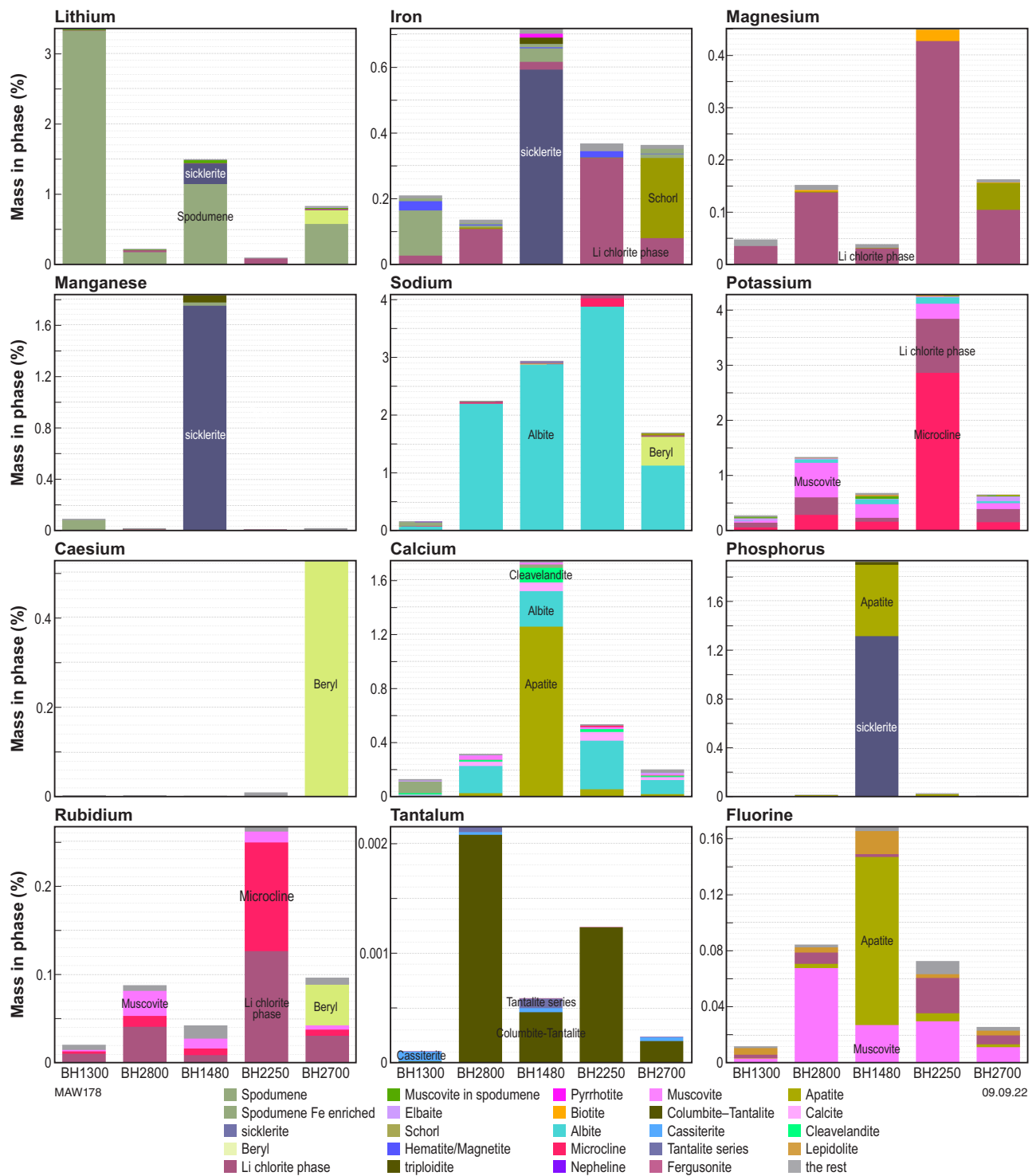


Figure 7.2. Department of Li, Fe, Mg, Mn, Na, K, Cs, Ca, P, Rb, Ta and F in Bald Hill samples

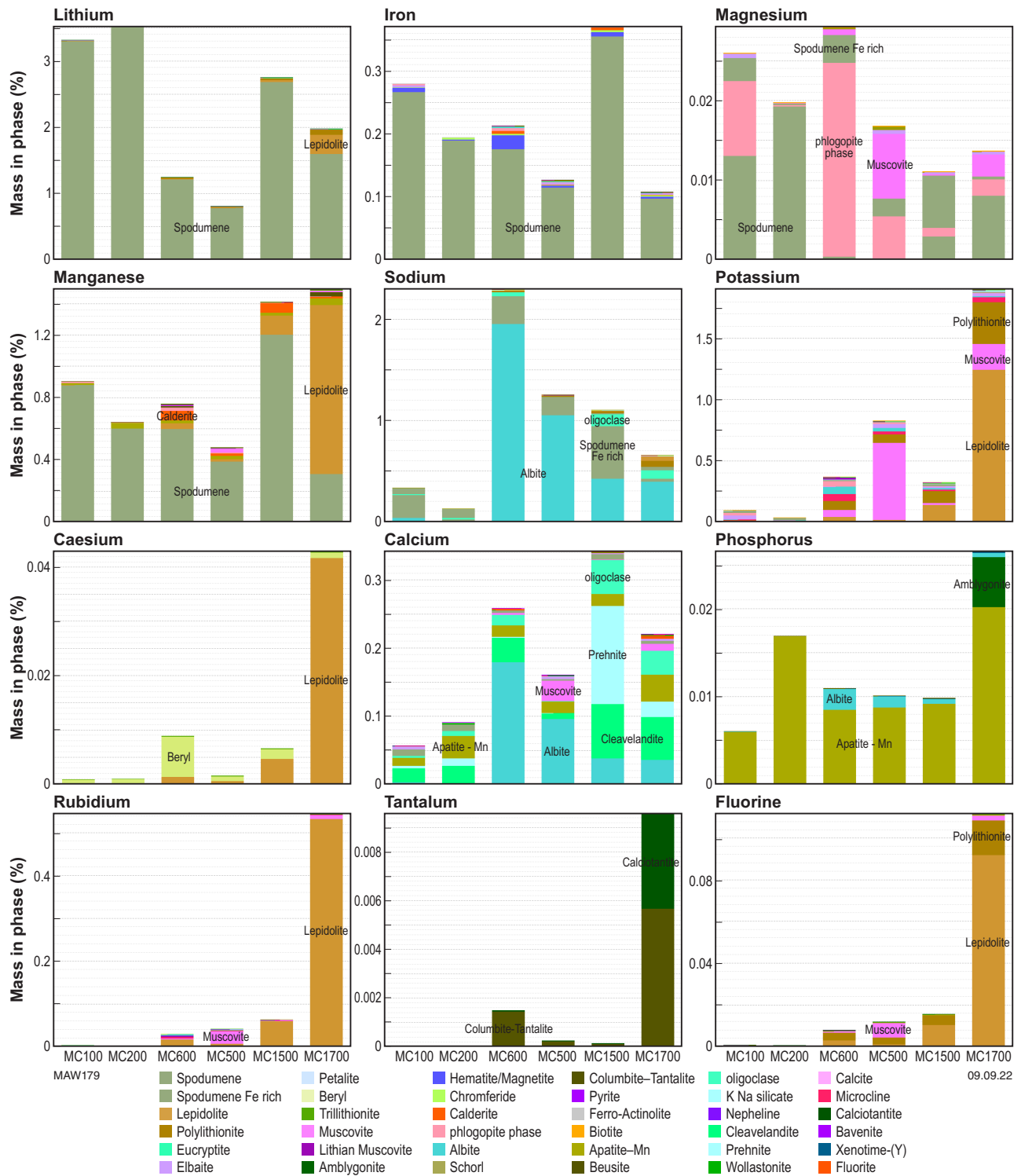


Figure 7.3. Department of Li, Fe, Mg, Mn, Na, K, Cs, Ca, P, Rb, Ta and F in Mt Cattlin samples

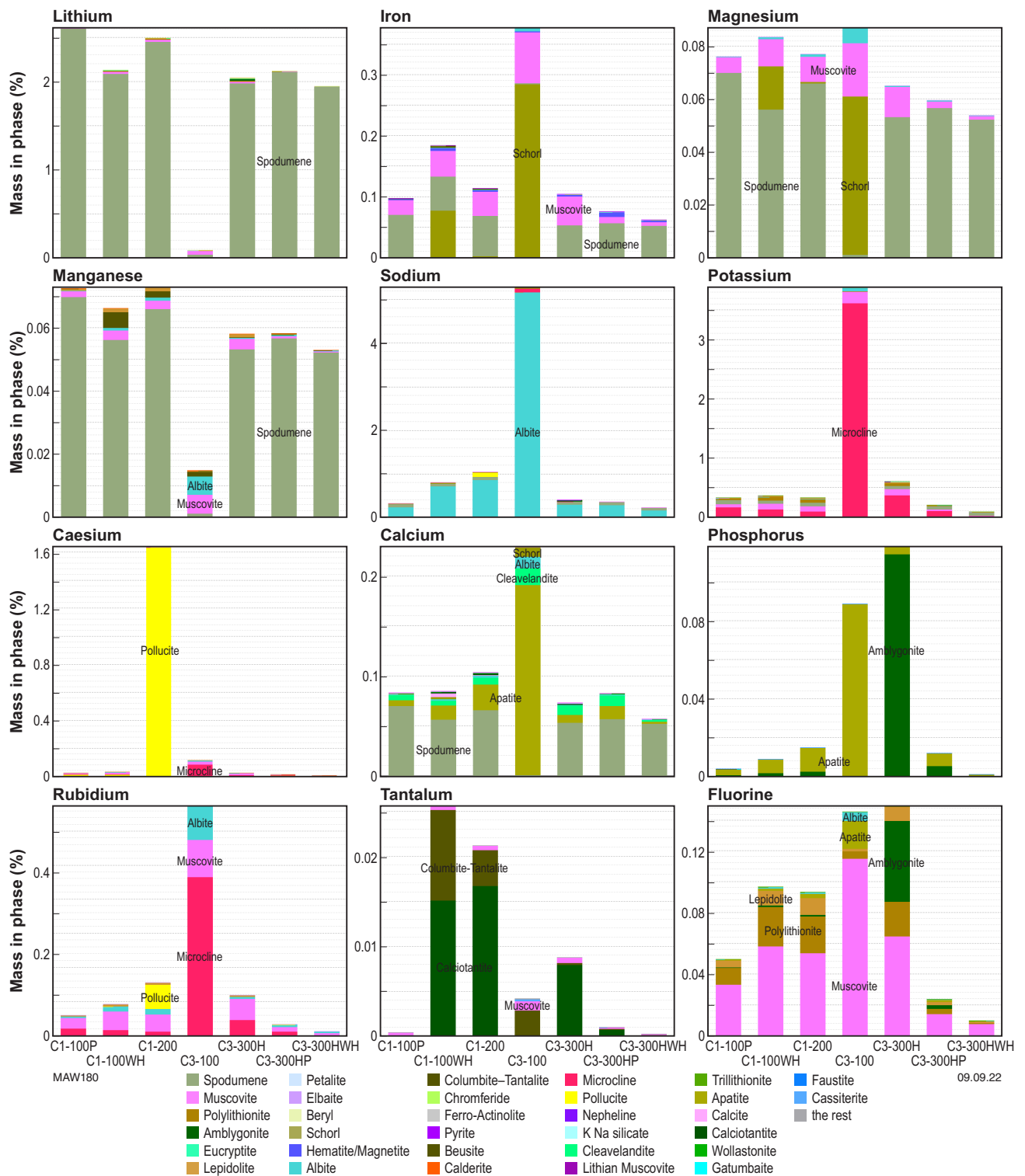


Figure 7.4. Department of Li, Fe, Mg, Mn, Na, K, Cs, Ca, P, Rb, Ta and F in Greenbushes samples

Appendix 8

Acid-bake and water-leaching tests

Table 8.1 Acid-bake conditions

<i>Sample</i>	<i>Li con, g</i>	<i>Conc. acid, g</i>	<i>Residue, g</i>	<i>Mass loss</i>	<i>Acid/Li mole ratio</i>	<i>Acid/ore mass ratio</i>
MC200	18.12	8.98	17.54	3.20	96%	50%
MC0500	18.12	9.31	17.23	4.90	128%	51%
BH1300	18.42	8.91	17.79	3.40	112%	48%
BH1480	18.59	9.09	18.31	1.50	198%	49%
PD005	18.22	8.71	17.86	2.00	218%	48%
C3300HP	18.46	8.84	18.24	1.20	213%	48%
C3300HWH	18.54	8.88	18.32	1.20	203%	48%
C1100P	18.28	8.8	18.21	0.40	174%	48%
Tconc.	18.08	8.97	17.28	4.40	111%	50%
Aconc.	18.04	8.92	17.28	4.20	117%	49%
BHconc.	18.12	8.8	17.41	3.90	122%	49%
Gconc.	18.15	8.99	17.44	3.90	112%	50%

Table 8.2 Head grade assays (wt%)

<i>Sample</i>	<i>Li</i>	<i>Si</i>	<i>Al</i>	<i>Fe</i>	<i>Na</i>	<i>Mg</i>	<i>K</i>	<i>Ca</i>	<i>Mn</i>	<i>Ti</i>	<i>P</i>	<i>S</i>
MC200	3.52	29.95	14.33	0.08	0.24	0	0.13	0.11	0.06	0	0.03	0
MC0500	2.83	28.91	14.27	0.87	0.16	0.34	1.36	0.03	0.15	0.01	0.01	0.01
BH1300	3.07	29.51	14.32	0.41	0.42	0.13	0.71	0.02	0.05	0.01	0.01	0
BH1480	1.68	28.15	10.46	1.15	3.06	0.03	0.84	1.49	1.5	0	1.9	0.06
PD005	1.55	33.8	9.51	0.69	1.77	0.02	1.51	0.15	0.06	0	0.02	0.01
C3-300HP	2.28	35.97	9.06	0.06	0.37	0.01	0.16	0.04	0.03	0	0.03	0
C3-300HWH	2.13	36.87	8.42	0.03	0.24	0	0.02	0.01	0.01	0	0	0
C1-100P	2.86	33.68	10.74	0.09	0.38	0.01	0.31	0.03	0.03	0	0.02	0
Greenbushes conc.	3.16	31.11	13.41	0.11	0.2	0.01	0.28	0.06	0.04		0.07	
Pilgangoora conc.	2.84	30.48	12.76	0.61	0.59	0.24	0.53	0.54	0.19	0.01	0.03	0
Bald Hill conc.	2.9	30.59	12.87	0.58	0.59	0.16	0.58	0.15	0.11	0.02	0.07	0.02
Mt Cattlin conc.	3.13	29.37	13.04	1.31	0.38	0.4	0.84	0.61	0.15		0.01	

Table 8.3 Residues assays (wt%)

Sample	Li	Si	Al	Fe	Na	Mg	K	Ca	Mn	Ti	P	S
MC200	0.04	31.7	14.1	0.17	0.04	0	0.12	0.07	0.06	0.02	0.01	0.13
MC0500	0.14	38.8	5.89	0.86	1.3	0.09	0.99	0.04	0.1	0.01	0.01	0.03
BH1300	0.15	29.6	13.5	0.66	0.2	0.05	0.44	0.03	0.06	0	0.01	0.1
BH1480	1.36	30.8	10.7	1.13	2.96	0.02	0.74	0.8	0.72	0.02	0.87	0.09
PD005	0.25	33.35	9.11	0.68	2.55	0	2.5	0.16	0.08	0	0.02	0.02
C3300HP	1.04	35.6	10.3	0.72	0.3	0	0.15	0.02	0.06	0	0.01	0.02
C3300HWH	0.38	33.4	11.6	0.37	0.13	0	0.03	0	0.02	0	0	0.04
C1100P	1.65	34.15	11.35	0.37	0.3	0	0.25	0.02	0.04	0	0.01	0.01
Greenbushes conc.	0.18	32.7	13.3	0.45	0.06	0	0.28	0.05	0.05	0.03	0.04	0.1
Pilgangoora conc.	0.15	31.6	12.5	0.88	0.39	0.26	0.62	0.44	0.19	0.02	0.02	0.12
Bald Hill conc.	0.26	31.8	12.6	0.86	0.38	0.16	0.61	0.15	0.12	0.03	0.06	0.06
Mt Cattlin conc.	0.19	30.7	13.3	1.05	0.17	0.15	0.55	0.28	0.12	0.02	0.05	0.11

Table 8.4 Filtrate assays (mg/L)

Sample	Li	Si	Al	Fe	Na	Mg	K	Ca	Mn	Ti	P	S
MC200	5420	16	952	9.2	334	1.8	68	42.8	8.6	0.4	10	23700
MC0500	1290	8	214	56.2	52	10.2	132	23.2	6.8	0.2	8	6440
BH1300	5350	12	961	24.4	208	6.6	90	11.2	6.6	1	4	18700
BH1480	1010	92	257	207	156	10.4	88	450	861	0.4	788	5080
PD005	1600	46	261	116	76	0.6	26	24.6	4.2	0.4	6	7640
C3300HP	2780	28	386	4.4	54	0.6	24	17.8	4	0	12	15600
C3300HWH	4430	12	552	2	112	0.6	22	1.6	1.6	0.4	2	18100
C1100P	2120	46	391	5.6	38	0.8	32	14.6	4	0	24	15500
Greenbushes conc.	4780	94	1330	27.4	280	3.4	84	42.4	8	1.2	36	18500
Pilgangoora conc.	4210	160	1280	241	476	36	30	189	36.4	1.8	22	20500
Bald Hill conc.	3950	22	835	156	500	21.6	72	68.8	37.6	2.4	34	19300
Mt Cattlin conc.	4790	56	984	443	288	22	138	170	36.2	1.8	74	20400

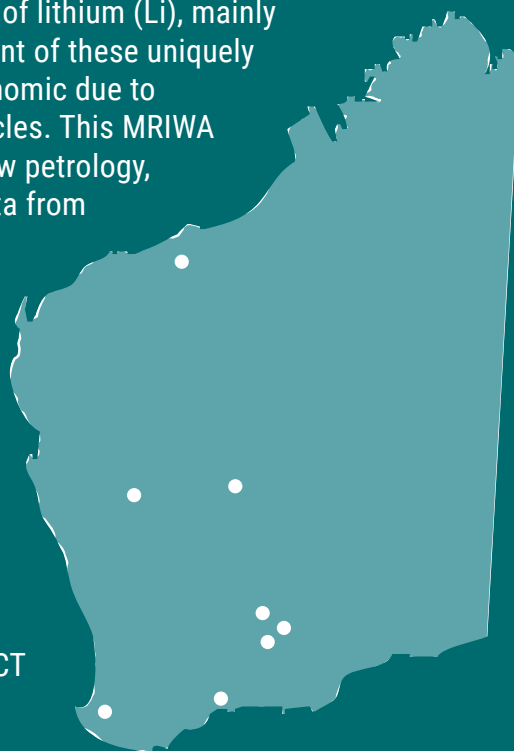
Table 8.5 Washings assays (mg/L)

Sample	Li	Si	Al	Fe	Na	Mg	K	Ca	Mn	Ti	P	S
MC200	905	4	181	1.2	50	0.2	2	7.8	1.6	0	2	3430
MC0500	80	0	11.4	2.2	4	0.6	2	0.6	0.4	0	0	365
BH1300	408	2	60.2	0.8	16	0.4	0	0.2	0.4	0	0	1310
BH1480	77	8	18.6	3.8	12	0.8	0	55.8	68	0	56	370
PD005	80	4	11.6	4.4	4	0	0	0.8	0.2	0	0	360
C3300HP	107	2	12.6	0	4	0	0	0.2	0	0	0	565
C3300HWH	484	2	68.4	0	12	0	2	0	0.2	0	0	1830
C1100P	112	4	23.2	0	2	0	0	0.6	0.2	0	0	763
Greenbushes conc.	730	12	165	2.8	38	0.4	12	5.6	1.2	0	6	2390
Pilgangoora conc.	552	24	151	29.2	58	4.8	6	45.6	4.8	0.2	2	2410
Bald Hill conc.	370	2	66	12.4	42	1.8	4	5.2	3.2	0	4	1580
Mt Cattlin conc.	872	12	184	85.2	50	4.4	14	44	7.2	0.4	12	3420

MRIWA REPORT M532 –
THE GEOLOGY, MINERALOGY AND GEOMETALLURGY OF
EV MATERIALS DEPOSITS IN WESTERN AUSTRALIA

M Wells, M Aylmore and B McInnes

Western Australia is the world's largest producer of lithium (Li), mainly as spodumene concentrate. However, development of these uniquely complex deposits has only recently become economic due to rising demand for Li in batteries for electric vehicles. This MRIWA and industry-supported project has generated new petrology, mineralogy, geochemistry and geochronology data from some key Li–Cs–Ta (LCT) pegmatite deposits in Western Australia. Characterization and analysis techniques applied include XRD, SEM-EDS, EPMA, LIBS, LA-ICP-MS, SHRIMP U–Pb dating, $^{40}\text{Ar}/^{39}\text{Ar}$ dating, FIB-SEM and ToF-SIMS. The mineralogy results are used to produce a comparative geometallurgical classification framework for Western Australian LCT pegmatites. Project samples were assessed using physical liberation, calcination and thermogravimetric methods. The project has built new capability and capacity in the area of LCT pegmatite characterization. It also demonstrates that ore body knowledge and geometallurgical data are critical factors in the production of quality feedstock, and optimizing the economics of lithium mining operations in Western Australia.



Further details of geoscience products are available from:

First Floor Counter
Department of Mines, Industry Regulation and Safety
100 Plain Street
EAST PERTH WESTERN AUSTRALIA 6004
Phone: +61 8 9222 3459 Email: publications@dmirs.wa.gov.au
www.dmirs.wa.gov.au/GSWApublications